Faculty of Aerospace Engineering

Flight Dynamics Analytically-Derived Mathematical Model of Tiltrotor Aircraft

The development of an approachable tilt-rotor flight mechanics model, with clearly defined limitations, suitable for performance and piloted flight simulation.

Piotr Sokołowski

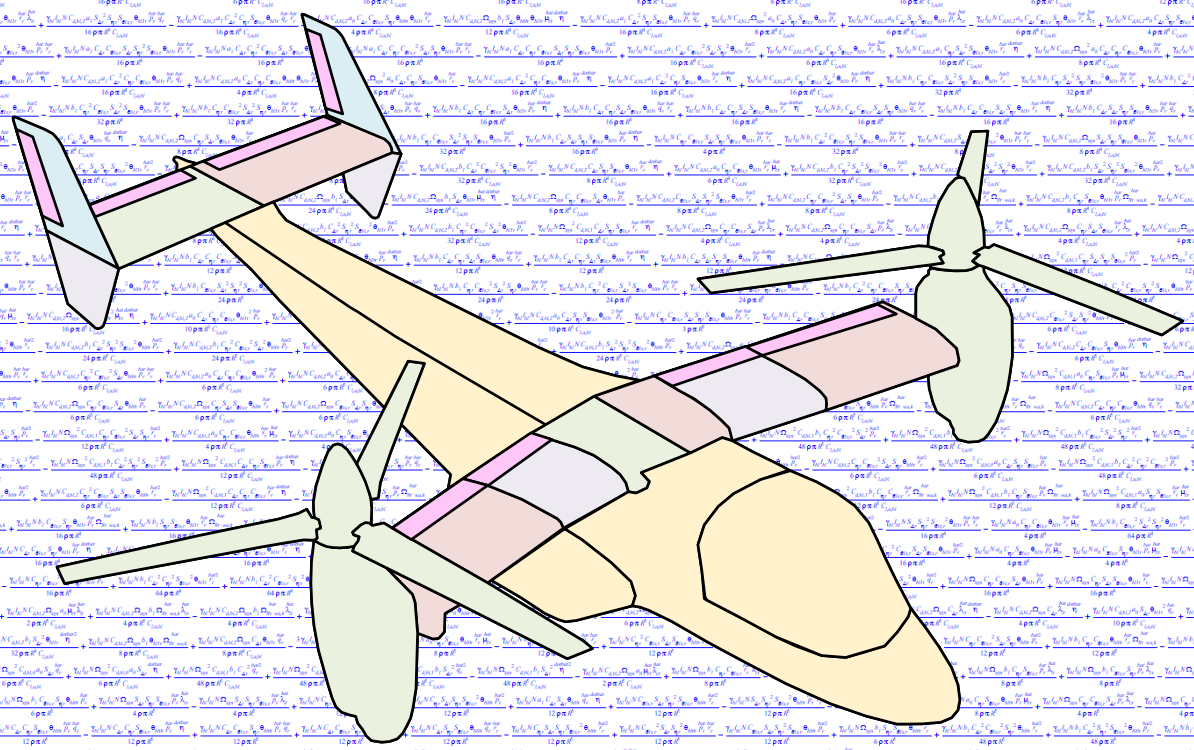

TU Delft Delft University of Technology

Challenge the future

Flight Dynamics Analytically-Derived Mathematical Model of Tiltrotor Aircraft

The development of an approachable tilt-rotor flight mechanics model, with clearly defined limitations, suitable for performance and piloted flight simulation.

by

Piotr Sokołowski

in partial fulfillment of the requirements for the degree of

Master of Science
in Aerospace Engineering

at the Delft University of Technology,
to be defended publicly on Monday December 12, 2022 at 14:00.

Supervisor:	Dr. ir. M.D. Pavel
Thesis committee:	Dr. ir. M.D. Pavel
	Dr. ir. E. van Kampen
	Dr. ir. W.A.A.M. Bierbooms
Student number:	4344499

An electronic version of this thesis is available at `http://repository.tudelft.nl/`.

TU Delft Delft University of Technology

Preface

The following report documents the work performed as part of the Master's Thesis research project concerned with the development of an analytically derived tilt-rotor flight mechanics model in the Control and Operations track of the Aerospace Engineering Faculty at the Delft University of Technology (TU Delft). My motivation to pursue a research project related with rotorcraft has stemmed from the Helicopter Performance, Stability and Control elective course provided at the Aerospace Faculty led by Dr.ir. Marilena Pavel who later became my thesis supervisor providing me with this great research opportunity that has ever since been slowly growing into a passion which I hope to pursue someday in my professional career.

This Master's Thesis report is mainly aimed at an academic audience with an engineering background in the aerospace field. The resources, tools, and results accompanying this research project have been developed and obtained with the hopes of them being used in future related research projects at the TU Delft Aerospace Engineering Faculty.

I would like to thank my thesis supervisor, Dr.ir. Marilena Pavel, for her academic guidance and moral support provided to me over the course of this research project, and for her time spent during our in-person and online meetings. I would also like to thank the Aerospace Faculty of TU Delft for the provided facilities and resources.

Next I would like to thank my friends at the Faculty for all the time that we have spent and worked together during the bachelor and master, making this challenging academic journey enjoyable and a memory I will treasure for years to come. I would also like to thank my friends from outside the Faculty who were always eager to hear how my Master's Thesis is going.

Finally I would especially like to thank my parents and brother for supporting me in my entire academic endeavor. Thank you for believing in me and allowing me to pursue what I love doing most.

Piotr Sokołowski
Delft, December 2022

Summary

State-of-the-art tilt-rotor flight mechanics models appear to be inadequate to predict flight behavior across the entire flight envelope due to a lack of experimental data, which has already resulted in fatalities, suggesting the need for more generic models. To circumvent this problem, some models resort to extensive coefficient tables or empirical relations requiring more experimental data and thus rendering the models inflexible. Other models based on analytical or numerical approaches tackle this problem by employing more complex equations or using more computational power, however this too may result in inflexibility. The research project at hand attempts to find the middle ground between flexibility (genericity) and accuracy through the development of a generic analytically derived tilt-rotor flight mechanics model. The development process is focused on highlighting the effects of the tiltable nacelle on the rotor expressions and flight mechanics.

The developed tilt-rotor model consists of fuselage, lifting surface, and rotor models, the latter being the focus of this study. The rotor model consists of an analytical differential flapping equation derived with the use of the Blade Element Method (BEM) which is solved with the use of the disk tilt approximation yielding a first order presumed quasi-static solution. The rotor forces and moments are also derived with the BEM and are defined in the non-rotating control (swashplate) plane with the use of the disk tilt angles.

The analytical derivation of the rotor model is performed in the symbolic manipulation program Maple, taking advantage of similarities between different expressions, named Common Integrals, in order to reduce the derivation workload and improve model flexibility. The insignificant terms of the rotor expressions are removed with the use of the Automatic Ordering Scheme developed for the purposes of this study in order to improve model clarity. The complete tilt-rotor model is implemented in the programming language Matlab and in the simulation environment Simulink.

The effect of the tiltable nacelle on the rotor is determined by inspecting the analytical rotor expressions and the simulation results consisting of trimmed flight curves, conversion corridors, and climbing flight Haffner diagrams. The model is also validated against the XV-15 tilt-rotor implementation of the NASA Generic Tilt-Rotor Simulation model.

It is concluded that the tiltable nacelle affects the rotor expressions through the velocity experienced by the rotor hub and blade element. Both the nacelle tilt rate and acceleration are considered significant contributors to many, but not all, rotor expressions. Orthogonal body rotational rates that phase each other out as a function of nacelle tilt appear frequently in the expressions. Simple summation of the nacelle tilt rate with the body pitch rate is common, however not permissible in all instances. It is also found that the nacelle tilt rate always increases the flapping angle. Apart from the implicit effect through the rotor hub velocity, the nacelle tilt rate does not have a significant (explicit) effect on the constant coning angle a_0, and rotor thrust and torque. Several terms that only exist in conversion flight also appear making them unique to tiltable proprotors such as the tilt-yaw Coriolis effect in the flapping equation.

It is also concluded that the conversion from helicopter (H-mode) to airplane (A-mode) configuration necessitates more nose-up pitch attitude, a greater nose-down stick deflection, and initially less collective which later increases near A-mode. Furthermore, as the tilt-rotor converts to A-mode the rotor exhibits smaller disk tilt angles and generates a lower induced velocity, lower thrust, lower in magnitude side force, an initially higher hind force which decreases near A-mode, lower torque, greater rolling moment, and a lower pitching moment. Near hover the collective, induced velocity, side force, pitching moment, and longitudinal and lateral disk tilt angles are not affected by the nacelle tilt angle. The Haffner diagram of the tilt-rotor drastically changes when converting to A-mode showing much lower induced velocities than those indicated by the Haffner diagram of an isolated rotor. Finally, the nacelle tilt rate has an effect on both handling and performance requiring more power and initially more nose-down stick deflection while converting from helicopter to airplane when compared to flight where the nacelle tilt rate is zero. Near A-mode more nose-up stick deflection is required.

The developed tilt-rotor model shows good flight mechanics characteristics that are representative of a generic tilt-rotor aircraft based on the high similarity in trim curve trends when compared to the GTRS model. However, the model does not predict the flight characteristics of the specific XV-15 aircraft well enough for it to be considered valid for performance and piloted flight simulation. It is hypothesized that this specific validity may be considerably improved by selecting more accurate model parameters without changing or re-deriving the governing equations.

The effect of the gravitational acceleration on the flapping equation is verified to be negligible while the assumption that the transient response resolves within two blade revolutions is shown to be true. The assumption that the blade element (BE) lift is much greater than its drag is considered verified, however the BE small inflow angle and simplified BE total velocity assumptions are shown to be grossly violated.

It is recommended that the critical assumptions employed in the derivation be revisited in the future, especially the ones that have been shown to be grossly violated. The encountered anomalies in the generated results should also be further investigated. Finally, the identified deficiencies of the model should be addressed. Most importantly the rotor model should be expanded to include disk tilt and inflow dynamics, a non-uniform inflow distribution, and it should be ensured that the rotor wake has an effect on the tail. Furthermore the tilt-rotor model should employ more sophisticated lifting surface and control surface models, while in addition to the drag, the fuselage should be modeled to produce the remaining force and moment components.

Contents

List of Figures

List of Tables

List of Acronyms and Abbreviations

AC	Aerodynamic Center
AFM	Aerodynamic Flapping Moment
AOS	Automatic (Extended) Ordering Scheme
adv.	advance
aero.	aerodynamic
arpln	airplane
BEM	Blade Element Method
BL	BLade
CI	Common Integral
CoG	Center of Gravity
CoM	Center of Mass
CP	Control Plane
ccw	counter-clockwise
col.	collective
const.	constant
cw	clockwise
DoF	Degrees of Freedom
DP	Disk Plane
EoM	Equation of Motion
EOS	Extended Ordering Scheme
ext.	external / excitation
GTRS	Generic Tilt-Rotor Simulation
HP	Horse Power
HSO	Highest Significant Order
heli.	helicopter
h-stab	horizontal stabilizer
IGE	In Ground Effect
infl.	inflow
LHS	Left-Hand Side
MAC	Mean Aerodynamic Chord
NoT	Number of Terms
OGE	Out of Ground Effect
OOP	Object-Oriented Programming
PoT	Product of Terms
perio.	periodic
pow	power
RAC	Root Aerodynamic Center
RHS	Right-Hand Side
RPM	Revolutions Per Minute
SCAS	Stability and Control Augmentation System
SoT	Sum of Terms
SP	Shaft Plane
SPO	Smallest Present Order
TPP	Tip Path Plane
VTOL	Vertical Take-Off and Landing
v-stab	vertical stabilizer
w.a.	wind axis

List of Symbols

$\boldsymbol{A}$	disk tilt system dependent $m \times n$ matrix
$\overline{AC}$	aerodynamic center of mean aerodynamic chord
$A_{11} \dots A_{mn}$	disk tilt system A-matrix elements
A_{eq}	equivalent flat plate area
$\boldsymbol{a}$	linear acceleration vector
$\widehat{\boldsymbol{a}}$	disk tilt system unknown $n \times 1$ vector
a	linear acceleration scalar
a_0	rotor coning angle
$\overline{a}_0$	blade precone angle
a_1	longitudinal rotor disk tilt angle; $a_1 > 0$ if TPP tilts backwards
a_{in}	axial induction ratio
$\boldsymbol{B}$	disk tilt system independent $m \times 1$ vector
BL	buttock line / lateral disposition
$B_1 \dots B_m$	disk tilt system B-vector elements
b_1	lateral rotor disk tilt angle; $b_1 > 0$ if TPP tilts rightward
$b_{1/2,ls}$	lifting surface half span
$\overline{C}$	mean aerodynamic chord length
C_D	drag coefficient
$C_{d_0,bl}, C_{d_1,bl}, C_{d_2,bl}$	blade drag coefficient parameters
C_L	lift coefficient
C_{l_α}	lift coefficient curve slope
C_M	pitching moment coefficient
C_X	cosine function of X
c	chord length
D	drag force
d_{sgn}	mounting side parameter; d_{sgn}=1 when right-mounted
d_{xrf}	reference frame origin longitudinal disposition w.r.t. body CoG
d_{yrf}	reference frame origin lateral disposition w.r.t. body CoG
d_{zrf}	reference frame origin vertical disposition w.r.t. body CoG
$\{\boldsymbol{E}\}$	reference frame column unit vector
E_{EOS}	maximum allowable fractional error introduced by ordering scheme
$e_0 \dots e_3$	quaternion elements
e_{EOS}	maximum allowable value error introduced by ordering scheme
$\boldsymbol{F}$	force vector
F	force scalar
H	rotor hind force; positive rearward
$HP_{RO,max}$	maximum optimum engine power
I_{bl}	blade flapping moment of inertia
I_{xx}	tilt-rotor rolling moment of inertia
I_{xz}	tilt-rotor roll-yaw product of inertia
I_{yy}	tilt-rotor pitching moment of inertia
I_{zz}	tilt-rotor yawing moment of inertia
i_{ls}	lifting surface incidence angle; $i_{ls} > 0$ leading edge up
K_β	flapping spring stiffness
$K_{\epsilon T}$	inflow solver convergence-rate constant
k_{max}	inflow solver maximum number of iterations
L	lift force
l_n	nacelle length
$\boldsymbol{M}$	moment vector
M	moment scalar
$M_{1,bl}$	blade first mass moment
M_O	arithmetic mean of evaluated orders
m	tilt-rotor mass
m_{bl}	blade mass
$\mathbb{N}$	natural numbers set
N	number of blades per rotor
O	rotor rolling moment; positive TPP right side up
O_X	X^{th} order
O^X	X^{th} order power
$O(\epsilon^n)$	n^{th} order term in basis ϵ
P	rotor pitching moment; positive TPP fore down
p	body roll rate; $p > 0$ right-wing-down

Q	rotor torque; positive ccw
Q_{AV}	available engine torque at rotor shaft
Q_{REQ}	required average torque at the rotor shaft
$\boldsymbol{q}_4$	4-value quaternion
q	body pitch rate; $q > 0$ nose-down
R	rotor radius
RF	automatic ordering scheme rounding factor
RPM_{SEL}	rotor RPM selector
R_{SHP}	commanded engine power
r	body yaw rate; $r > 0$ nose-right
r_{BE}	blade element radial position
S	rotor side force; positive leftward
S	lifting surface area
SL	station line / longitudinal disposition
SHP_{acc}	engine accessory power loss
S_X	sine function of X
$\boldsymbol{s}$	position vector
$\boldsymbol{T}$	transformation matrix
T_{ext}	threshold extension parameter
T_i	i^{th} term
T_{tail}	tailored significance threshold
T	rotor thrust; positive upward
$T_{\epsilon T}$	inflow solver thrust error threshold
U_P	blade element perpendicular velocity component
U_R	blade element radial velocity component
U_T	blade element tangential velocity component
u	body longitudinal velocity; $u > 0$ forwards
$\boldsymbol{V}$	linear velocity vector
V	linear velocity scalar
V_{pc}	perpendicular CP velocity component
V_{tc}	tangential CP velocity component
V_{tc1}	longitudinal tangential CP velocity component
V_{tc2}	lateral tangential CP velocity component
v	body lateral velocity; $v > 0$ rightwards
v_{in}	rotor induced velocity
WL	water line / vertical disposition
w	body vertical velocity; $w > 0$ downward
X_{COL}	total collective quasi-stick deflection; $X_{COL,pilot} > 0$ for higher collective pitch
$X_{COL,gov}$	collective governor stick-equivalent deflection
$X_{COL,pilot}$	pilot collective stick deflection; $X_{COL,pilot} > 0$ for higher collective pitch
$X_{COL,pilot,\eta}$	pilot nacelle phased collective stick deflection
$X_{COL,thr}$	collective-throttle stick deflection
X_{FLA}	pilot flap lever deflection; $X_{FLA} > 0$ for flap deflection
X_{LAT}	pilot lateral stick deflection; $X_{LAT} > 0$ for stick leftwards
X_{LON}	pilot longitudinal stick deflection; $X_{LON} > 0$ for stick forwards
X_{PED}	pilot pedals deflection; $X_{PED} > 0$ for left pedal forwards
X_{rf}	reference frame X-axis
X_{TIL}	pilot nacelle tilt lever deflection; $X_{TIL} < 0$ to tilt towards airplane mode
x_{cg}	body north position
$\overline{Y}$	mean aerodynamic chord spanwise position
Y_{rf}	reference frame Y-axis
y_{cg}	body east position
Z_{rf}	reference frame Z-axis
z_{cg}	body altitude
α	angle of attack
α_{0L}	zero-lift angle of attack
α_i	induced angle of attack
α_{loc}	local angle of attack
β	blade flapping angle; $\beta > 0$ if blade above CP
β_b	body angle of sideslip; $\beta_b > 0$ when velocity vector is to the right of the nose
β_{loc}	local angle of sideslip
$\beta_{SP,absmax}$	maximum allowable flapping angle w.r.t. shaft plane
Γ_{ls}	lifting surface dihedral angle; $\Gamma_{ls} > 0$ for wing tips up
γ_b	body flight path angle; $\gamma_b > 0$ for climb
γ_{bl}	blade lock number
Δ	wind shift angle
Δ_O	difference between the highest significant order and smallest present order
ΔC_D	change in lifting surface C_D due to control surface deflection

ΔC_L	change in lifting surface C_L due to control surface deflection
ΔC_M	change in lifting surface C_M due to control surface deflection
$\Delta\alpha_{0L}$	change in lifting surface α_{OL} due to control surface deflection
δ_{B1}	θ_{1s} offset rigging constant
δ_{cs}	control surface deflection
ϵ	ordering scheme basis
η	nacelle tilt angle; $\eta < 0$ when tilting forward
$\dot{\eta}$	nacelle tilt rate; $\dot{\eta} < 0$ when tilting forward
η_{XMSN}	drivetrain transmission efficiency
θ_0	swashplate collective angle
$\theta_{0,COL,\eta}$	collective stick θ_0 nacelle phased contribution
$\theta_{0,gov}$	governor swashplate collective deflection
$\theta_{0,gov,max}$	governor maximum swashplate collective deflection
$\theta_{0,gov,min}$	governor minimum swashplate collective deflection
$\theta_{0,LAT,\eta}$	lateral stick θ_0 nacelle phased contribution
$\theta_{0,LL,0.75R,\eta}$	θ_0 nacelle phased lower limit at 3/4 blade length
$\theta_{0,LL,\eta}$	θ_0 nacelle phased lower limit
$\theta_{0,LL,mod,\eta}$	nacelle phased global blade pitch modified
θ_{1s}	swashplate longitudinal cyclic angle; positive for stick forwards
$\theta_{1s,LON,\eta}$	longitudinal stick θ_{1s} nacelle phased contribution
$\theta_{1s,offset,\eta}$	θ_{1s} nacelle phased offset
$\theta_{1s,PED,u\eta}$	pedals θ_{1s} velocity and nacelle phased contribution
θ_b	body pitch angle; $\theta_b > 0$ nose up
θ_{BE}	blade element pitch angle
$\theta_{bl,1}$	blade linear twist rate; $\theta_{bl,1} < 0$ for washout
$\theta_{bl,g}$	blade constant twist
θ_{XPT}	rotor turbine gear ratio
Λ	sweep angle; $\Lambda > 0$ for aft sweep
λ	lifting surface taper ratio
λ_i	non-dimensional rotor induced velocity
λ_{pc}	CP inflow ratio / non-dimensional CP perpendicular velocity
λ_{tot}	CP total inflow ratio
μ_{tc}	CP advance ratio / non-dimensional CP tangential velocity
ρ	air density
ϕ_b	body roll angle; $\phi_b > 0$ right-wing-down
ϕ_{BE}	blade element inflow angle
ψ	blade azimuthal position
ψ_b	body heading angle; $\psi_b > 0$ nose-right
Ω	rotor axial rotational velocity
Ω_{sgn}	rotation direction parameter; Ω_{sgn}=1 when ccw
Ω_{tot}	total rotor rotational rate
$\boldsymbol{\omega}$	angular velocity vector
ω	angular velocity scalar

List of Subscripts and Superscripts

Subscripts

$\|rf$	defined in reference frame
0	drag induced
AC	aerodynamic center
$\overline{AC}$	mean aerodynamic chord aerodynamic center
a	aerodynamic
ail	flaperon
$arpln$	in airplane configuration
aw	aileron wing segment
BE	blade element
BEM	derived with the blade element method
BL	blade reference frame
b	tilt-rotor body
bl	blade
C	non-rotating flat Earth-fixed
$COL, pilot$	pilot collective stick
CP	control plane
cg	tilt-rotor center of gravity
cls	complete lifting surface
cs	control surface
DP	disk plane
E	vehicle-carried normal-to-Earth
eff	effective rate
ele	elevator
ext	external / excitation
FLA	flaps
fla	flap
flw	flap wing segment
frw	free wing segment
fus	fuselage
$heli.$	in helicopter configuration
hs	horizontal stabilizer
i	lift induced
i	inertial
L	left
LAT	lateral stick
LON	longitudinal stick
loc	local
ls	lifting surface
M	derived according to the simplified momentum/Glauert theory
NR	non-rotating
n	nacelle
nom	nominal
np	nacelle pivot
O	origin
PED	pedals
PIL	pilot
$prod$	product
R	right
R	rotating reference frame
RAC	root chord aerodynamic center
r	root
r	rotor
rf	reference frame
rud	rudder
rw	rotor wash
SP	shaft plane
s	segment
s	spring
TIL	nacelle tilt
TPP	tip-path plane
t	tip
tot	total rate
u	velocity phased
vs	vertical stabilizer
vsb	bottom vertical stabilizer segment
vst	top vertical stabilizer segment
w	wash rate
w	wing
x	acting along/around the X-axis
y	acting along/around the Y-axis
z	acting along/around the Z-axis
η	nacelle tilt phased

Superscripts

$\bar{x}$	non-dimensional rotational rate	$\widehat{x}$	defined in the wind axis system
$\dot{x}$	time derivative		

1 Introduction

A tilt-rotor aircraft combines the vertical take-off and landing (VTOL) capability of a helicopter and the high speed cruise and range capability of an airplane. Its airframe resembles that of an airplane with the addition of a proprotor and nacelle assembly attached to each tip of the main wing through a pivoting mechanism. This pivot axis allows the rotor assembly to be dynamically orientated anywhere from an upright helicopter rotor position to a front facing airplane propeller position, all the while the tilt-rotor is airborne. As a result modeling the flight mechanics of a tilt-rotor requires the combination of knowledge about both airplanes and helicopters providing quite the challenge, albeit an interesting one which shall hopefully be demonstrated in this master's thesis.

This research project consists of investigating past and state-of-the-art tilt-rotor flight mechanics models with respect to performance and piloted flight simulation, focusing on the recommended elements required for accurate prediction and the approaches of implementing these elements. The goal of this thesis work is to develop an analytically derived tilt-rotor flight mechanics model based on the recommended elements and suitable combination of existing approaches to achieve an accurate, flexible, and clear model based on and validated against the XV-15 VTOL aircraft.

This introductory chapter starts with section 1.1 which briefly describes the history of tilt-rotors leading up to the creation of the XV-15 tilt-rotor. Next the background and motivation behind this research project is given in section 1.2 while the definition of the problem to be challenged by this thesis work is described in section 1.3. The formal research objective and accompanying research question and sub-questions are then defined in section 1.4. Finally the structure of this complete document is explained at the end of this chapter in section 1.5.

1.1. Tilt-Rotor History

According to [7], the first tilt-rotor to become airborne was the Transcendental Model 1-G (fig. 1.1), which lifted off the ground for the first time in 1954. Although many designs and numerous attempts were made prior to this event, none of the aircraft that did eventually fully fly agreed with the definition of a tilt-rotor. However, in 1951 a thorough investigation into this type of aircraft had already begun, initiated with the joint U.S. Army and U.S. Airforce Convertiplane Program. A design competition for a vehicle that could achieve a precisely controllable and sustained hover, high speed and range, and allow for rescue operations was announced yielding three candidates: the McDonnell XV-1 compound helicopter; the Sikorsky XV-2 stoppable rotor aircraft; and the Bell XV-3 tilt-rotor. Eventually, the XV-3 proved to be superior with regard to the convertiplane requirements. Although many problems were encountered during testing, the design was considered a success mainly because it demonstrated the feasibility and unique capability of the tilt-rotor concept. Unfortunately the development ended in 1968 with a catastrophic full-scale wind tunnel test during which the proprotors broke away from the wings due to unexpected fatigue cracks.

As told by [7], tilt-rotor research continued nonetheless with focus on solving the shortcomings of the XV-3. Once again, the Bell Helicopter Company was awarded a government contract to perform full-scale wind tunnel tests on in-house designed proprotors, with emphasis on understanding the issue of aeroelastic

Figure 1.1: Transcendental Model 1-G tilt-rotor in flight. [1]

instability in tilt-rotors. Later, scale tests were performed on the Bell Model 300, an independently designed tilt-rotor, leading to improvements in the stability augmentation control system. In parallel, Boeing Vertol was contracted to carry out experiments to expand the performance limitations of proprotors as a result of contradicting design requirements for helicopter and airplane modes.

Positive results brought by the investigations of Bell and Boeing justified further research, which lead to both companies being individually awarded government contracts to conduct preliminary tilt-rotor design studies in 1971 and 1972. The competitive efforts brought forth two candidates, namely the newly designed Boeing Vertol Model 222 and the Bell Model 301, successor of the previously mentioned Model 300. A Source Evaluation Board was gathered to assess the two aircraft and ultimately scored the Bell Model 301 higher, resulting in the Bell Helicopter Company being awarded a governmental contract to design and manufacture the next iteration of the tilt-rotor aircraft, now known as the XV-15.

The purpose of this next iteration was to finally develop a tilt-rotor that satisfied the "minimum size required to perform proof-of-concept flight investigations" [8, p1]. The XV-15 design was directly based on the Bell Model 301 [9], and was thoroughly tested in simulation [10] as well as in practice [7], with experiments starting at an isolated subsystem level [11, 12], expanded to scale [7] and full-scale [9] wind tunnel tests and full-scale ground tie-down tests [7], and ending at full-scale flights [2, 13]. It performed experimental and demonstration flights for over a decade generating a large database of flight test data [7]. It is for this reason that the XV-15 is chosen as the basis for the tilt-rotor model developed in this research project.

1.2. Background and Motivation

The mission profile of a tilt-rotor may contain all the possible flight phases of an airplane and helicopter combined, including autorotation, and vertical and rolling take-off and landing. The tilt-rotor can perform all flight phases at (almost) any possible nacelle conversion angle, as deemed most suitable by the pilot, providing a range of operational speeds broader than for an airplane or helicopter. The tilt-rotor aircraft concept has been already employed in the military, for example the Bell-Boeing V-22 Osprey, and is in the development phase for civil use, e.g. the Augusta-Westland AW-609 [14]. A large impact of the civil application concerns airports as it has the potential to reduce the number of short distance flights requiring the use of the main runways, allowing for an increased airport capacity and fewer delayed flights [15].

Tilt-rotor flight mechanics modeling incorporates elements from both the airplane as well as helicopter engineering fields, resulting in a broad and complex task that makes tilt-rotor modeling challenging. For this reasons many authors either decide to make numerous bold assumptions yielding oversimplified and inaccurate models, or choose to thoroughly approach the task and create a tilt-rotor model that is too complex to be traceable, and relies too much on existing experimental data to be modified or applied to other tilt-rotor aircraft. Therefore the main challenge of interest is to be able to develop a flight mechanics model for such a complex vehicle while at the same time retaining accuracy, flexibility, and clarity of the model.

The flight mechanics model may serve as a tool to determine the flight envelope, structural and aeroelastic stability, and the origin of undesirable flight behavior of a tilt-rotor which may lead to a faster, cheaper, and

safer aircraft development process. Unfortunately even current state-of-the-art models seem to be unreliable as was the case with the SIMRX flight simulator used to investigate the fatal crash of the AW-609 tilt-rotor [16]. The simulation was not able to predict flight behavior that led to the fatal crash in 2015, and the inability of the model was determined to be caused by a lack of experimental data [17]. This highlights the necessity and provides the motivation for the development of tilt-rotor flight mechanics models that are based on fundamental physical equations and not on experimental data.

1.3. Problem Definition

Many of the tilt-rotor flight mechanics models available in literature possess most of the elements that are considered necessary. Unfortunately the more accurate models often resort to coefficient table lookup or empirical relations which require experimental data rendering the model inflexible. On the other hand, models that are based on analytical or numerical approaches are more flexible however they come at a cost. In the case of numerical models higher accuracy is achieved with higher computational intensity challenging real-time simulation, while in the case of analytical models some compromise must be made between accuracy and simplicity. Paradoxically each side of the compromise-spectrum introduces its own inflexibilities in the form of hindered clarity and expansion as a result of accurate but convoluted governing equations, or limited validity as a result of oversimplification.

This research project will try to find the middle ground, taking into account the recommendations and existing approaches, with the hopes of developing an accurate yet approachable and flexible tilt-rotor flight mechanics model capable of future expansion. Emphasis shall be put on the assumptions and simplifications that are employed in order to obtain a flight mechanics model that remains within the scope of this research, and the resulting limitations shall be highlighted. The scope of the research is limited to performance and piloted flight simulation.

It has been decided that the rotor model of the tilt-rotor flight mechanics model developed for this thesis shall be derived analytically. The rotor is considered the most significant subsystem in this thesis therefore the complete tilt-rotor flight mechanics model is colloquially referred to as being analytically derived, however not all subsystems shall be derived in a similar manner. Nonetheless, an analytically derived rotor provides more insight into the workings of the model and potentially has greater academic and scientific value since the expressions of complete subsystem may be analyzed as opposed to a numerical model which is based on localized governing equations that only collectively (after numerical integration) provide meaningful data. Additionally the analytical model is expected to be less computationally expensive (and thus more accessible) than its numerical counterpart since most of the expression integration shall be performed analytically during the model development stage as opposed to numerical models which perform the integration during simulation run-time.

1.4. Research Objective and Questions

As mentioned previously, many tilt-rotor flight mechanics models find themselves at either end of the complexity spectrum, with some being oversimplified in order to be flexible, while others are complex and tailored for a specific aircraft yielding accurate results at the cost of flexibility. This leaves an opportunity for innovation which may be formulated into the main research objective of this thesis:

> **To achieve a clear, expandable, and flexible tilt-rotor flight mechanics model with clearly defined limitations and capable of accurate performance and piloted flight simulation, obtained by means of a rigorous model development process based on an analytical derivation approach to increase the understanding of the problem and consequences of simplifications.**

The main research objective is achieved in several intermediate steps defined by the sub-goals described below.

First of all a good overview and understanding of the recommended tilt-rotor flight mechanics model elements shall be established. This shall be followed by a study of the existing modeling approaches employed in works focused on tilt-rotor performance flight mechanics modeling, taking note of the strengths and deficiencies of the approaches which is advantageous in the development of the scope of the synthesized model.

In parallel, a simpler preliminary three degrees of freedom (DoF) tilt-rotor flight mechanics model (referred to as the 3DoF model) shall be developed giving light to model development issues which would have otherwise been encountered for the first time when developing the final tilt-rotor model (referred to as the 6DoF model). Validation data in the form of existing modeling results and flight test data shall also obtained in the meantime.

The information gathered from literature and the experience obtained during the development of the preliminary model shall then be combined throughout the design and synthesis stage of this thesis work yielding the 6DoF tilt-rotor flight mechanics model. The parameters of the 6DoF model shall then be set to correspond to those of the XV-15 tilt-rotor in order to generate data which shall be used to validate the 6DoF model against flight data available in literature. Once complete, the extent of reaching the research objective shall be assessed concluding the research project.

In order to present the development of a clear, expandable, and flexible tilt-rotor flight mechanics model, the following research question is asked:

> **What effect does the tiltable proprotor have on the tilt-rotor flight mechanics when compared to a conventional helicopter within the realistic flight envelope?**

The main research question is split into several sub-questions which help in the answering of the main question. The sub-questions are divided into literature- and thesis work-related as follows:

Research Sub-Questions to be Answered in Literature

- What constitutes a tilt-rotor?
- How is a tilt-rotor controlled?
- What methods exist to model flight mechanics of a tilt-rotor?
  - What methods are suitable for real-time simulation?
  - What methods satisfy the accuracy requirements for a tilt-rotor performance simulation?
- What is the required extent of the tilt-rotor flight mechanics model required for performance and piloted flight simulation?
  - What are the minimally required number of degrees of freedom?
  - What dynamic motion of the blades of the proprotor must be included?
- How are the helicopter flight mechanics modeled in a performance and piloted flight simulation?
- What are the differences between the helicopter and tilt-rotor flight mechanics models in performance and piloted flight simulation?

Research Sub-Questions to be Answered by Inspection of the Thesis Work

- What effect does the tiltable proprotor have on the analytical rotor expressions?[1]
  - How are the velocity components experienced by the rotor hub affected?
  - How are the velocity components experienced by the blade element affected?
  - How is the flapping equation expression affected?
    - ◇ How is the inertial flapping moment affected?
    - ◇ How is the aerodynamic flapping moment affected?
  - How are the disk tilt angles affected?
  - How are the rotor force and moment expressions affected?
- What effects does the tiltable proprotor have on the simulation results?
  - In what ways does the flight envelope change for an aircraft with a the tiltable proprotor?
  - How are the climbing-flight Haffner diagrams affected?
  - How are the trim curves affected?
    - ◇ How is the induced velocity required for trim affected?
    - ◇ How are the disk tilt angles required for trim affected?
    - ◇ How are the pilot inputs required for trim affected?
    - ◇ How is the body angle of attack required for trim affected?
    - ◇ How are the rotor thrust and torque required for trim affected?
    - ◇ How are the rotor hind H-force and side S-force required for trim affected?

[1] Note that in this thesis only the significant effects are considered. Some expressions are additionally supplied to a reduction scheme which determines the possible maximal magnitude of each term and only retains the terms that are large enough to be considered significant. In those cases only the reduced expressions are inspected for the (significant) effect of the tiltable proprotor.

1.5. Document Structure

This entire thesis report is divided into four main parts with Part I presenting the findings of this research project in the form of a scientific article.

Part II consists of the literature review of tilt-rotor flight mechanics modeling shown in chapter 2 which aims at answering the first set of research sub-questions to be answered in literature, and the preliminary results presented in chapter 3 which describes the 3DoF tilt-rotor model and summarizes the preliminary simulation results.

Part III covers the main focus of this research project, namely the complete development process of the final 6DoF tilt-rotor flight mechanics model, starting with chapter 4 which presents a general overview of the model and may later serve as a guide summarizing all basic elements of the model which the reader may return to for reference when reading the remaining chapters of Part III. It is recommended that this chapter is read first before continuing to chapter 5 which presents the applied theories and summarizes the derivation of the governing equations of the 6DoF model and its components. These expressions are also analyzed throughout the chapter addressing the second set of research sub-questions concerned with the effect of the tiltable proprotor on the analytical rotor expressions. Obtaining the governing equations has proven to be a challenge due to the complex nature of the analytical derivation, therefore chapter 6 describes the approach that has been taken in executing this derivation in practice with the use of Maple[18], a symbolic manipulation program. The application of the derived governing equations to a simulation environment is then treated in chapter 7 which presents the implementation of the equations in the Matlab programming language[19] and its Simulink simulation environment making it possible to generate simulation data. The employed trimming routine is also described in this chapter. Chapter 8 then describes all the simulation results, generated with the Matlab and Simulink 6DoF model, which are used to verify several assumptions, validate the model against the XV-15 tilt-rotor, and to address the second set of research sub-questions concerned with the effect of the tiltable proprotor on the simulation results. The findings of the thesis work are summarized in chapter 9 while a list recommendations for the future regarding the 6DoF model is shown in chapter 10 concluding the main body of this thesis.

Finally Part IV contains a number of appendices with appendix A summarizing all the parameters used in the 6DoF model XV-15 tilt-rotor implementation. Next, appendix B lists all the identified model assumptions and simplifications used throughout the equation derivation stage, while appendix C presents several disk-tilt-approximation-specific expressions. Appendix D and appendix E include supplementary material related to the practical derivation of the analytical expressions, while appendix F presents similar supplementary material related with the implementation of the 6DoF model in Matlab and Simulink. Finally appendix G presents simulation results that are reference to in the results section, yet are not considered impactful enough to be included in the main thesis body.

Part I

Scientific Article

Development, Validation, and Analysis of an Analytically Derived Tilt-Rotor Flight Mechanics Model

P.M. Sokolowski*
Aerospace Engineering, Delft University of Technology, 2629HS Delft, The Netherlands

State-of-the-art tilt-rotor flight mechanics models appear to be inadequate in predicting the flight dynamics behavior across the entire flight envelope due to a lack of experimental data suggesting the need for more generic models. This paper presents a middle ground between model flexibility (genericity) and accuracy. For this purpose a generic 7-degrees-of-freedom tilt-rotor flight mechanics model is derived analytically. A novel ordering scheme is employed ensuring a bounded expression simplification error which is not found in existing tilt-rotor models. The research highlights the effects of the tiltable nacelle on the rotor analytical expressions and static flight mechanics. The model is validated against the XV-15 implementation of the NASA GTRS model showing promising overlap. It is concluded that the tiltable nacelle mainly affects the rotor expressions through the velocity experienced by the rotor hub and blade element, and that the nacelle tilt rate and acceleration are considered significant contributors to many rotor expressions. It is also shown that the nacelle tilt rate has an observable effect on handling and performance. Terms unique to tiltable proprotors are shown to exist, most notably the Coriolis effect of the nacelle tilt on the flapping dynamics. Several assumptions common in tilt-rotor modeling are also shown to be grossly violated. The future recommendation is to incorporate more sophisticated wing, control surface, and fuselage models, while the rotor model should include disk tilt and inflow dynamics, and a non-uniform inflow distribution.

Keywords: **tilt-rotor, XV-15, GTRS, BEM, analytical, flapping equation, proprotor, flight mechanics, ordering scheme, Haffner.**

Nomenclature

AC	Aerodynamic Center
BEM	Blade Element Method
BL	BLade
BE	Blade Element
CoG	Center of Gravity
CP	Control Plane
ccw	counter-clockwise
cw	clockwise
DoF	Degrees of Freedom
DP	Disk Plane
GTRS	Generic Tilt-Rotor Simulation
LHS	Left-Hand Side
MAC	Mean Aerodynamic Chord
RHS	Right-Hand Side
RPM	Revolutions Per Minute
SP	Shaft Plane
TPP	Tip Path Plane
w.a.	wind axis
a_0	rotor coning angle
$\overline{a}_0$	blade precone angle
a_1	longitudinal rotor disk tilt angle; $a_1 > 0$ if TPP tilts backwards
b_1	lateral rotor disk tilt angle; $b_1 > 0$ if TPP tilts rightward
$C_{d_0,bl}, C_{d_1,bl}, C_{d_2,bl}$	blade drag coefficient parameters
C_{l_α}	lift coefficient curve slope
C_X	cosine function of X
c	chord length
D	drag force
d_{sgn}	mounting side parameter; d_{sgn}=1 when right-mounted
$\{\boldsymbol{E}\}$	reference frame column unit vector
H	rotor hind force; positive rearward
I_{bl}	blade flapping moment of inertia
K_β	flapping spring stiffness
L	lift force
l_n	nacelle length
$M_{1,bl}$	blade first mass moment
N	number of blades per rotor
O	rotor rolling moment; positive TPP right side

*M.Sc. Student at Delft University of Technology, Faculty of Aerospace Engineering, Control and Simulation Department, Delft, The Netherlands.

	up		pedal forwards
$O(\epsilon^n)$	n^{th} order term in basis ϵ	X_{TIL}	pilot nacelle tilt lever deflection; $X_{TIL} < 0$ to tilt towards airplane mode
P	rotor pitching moment; positive TPP fore down		
p	body roll rate; $p > 0$ right-wing-down	x_{cg}	body north position
Q	rotor torque; positive ccw	y_{cg}	body east position
q	body pitch rate; $q > 0$ nose-down	z_{cg}	body altitude
R	rotor radius	α	angle of attack
r	body yaw rate; $r > 0$ nose-right	β	blade flapping angle; $\beta > 0$ if blade above CP
r_{BE}	blade element radial position	γ_{bl}	blade lock number
S	rotor side force; positive leftward	Δ	wind shift angle
S_X	sine function of X	δ_{cs}	control surface deflection
$\boldsymbol{s}$	position vector	ϵ	ordering scheme basis
$\boldsymbol{T}$	transformation matrix	η	nacelle tilt angle; $\eta < 0$ when tilting forward
T	rotor thrust; positive upward	θ_0	swashplate collective angle
U_P	blade element perpendicular velocity component	θ_{1s}	swashplate longitudinal cyclic angle; positive for stick forwards
U_R	blade element radial velocity component	θ_b	body pitch angle; $\theta_b > 0$ nose up
U_T	blade element tangential velocity component	θ_{BE}	blade element pitch angle
u	body longitudinal velocity; $u > 0$ forwards	$\theta_{bl,1}$	blade linear twist rate; $\theta_{bl,1} < 0$ for washout
v	body lateral velocity; $v > 0$ rightwards	$\theta_{bl,g}$	blade constant twist
v_{in}	rotor induced velocity	λ_i	non-dimensional rotor induced velocity
w	body vertical velocity; $w > 0$ downward	λ_{pc}	CP inflow ratio / non-dimensional CP perpendicular velocity
X_{COL}	total collective quasi-stick deflection; $X_{COL,pilot} > 0$ for higher collective pitch	μ_{tc}	CP advance ratio / non-dimensional CP tangential velocity
$X_{COL,pilot}$	pilot collective stick deflection; $X_{COL,pilot} > 0$ for higher collective pitch	ρ	air density
X_{FLA}	pilot flap lever deflection; $X_{FLA} > 0$ for flap deflection	ϕ_b	body roll angle; $\phi_b > 0$ right-wing-down
X_{LAT}	pilot lateral stick deflection; $X_{LAT} > 0$ for stick leftwards	ϕ_{BE}	blade element inflow angle
X_{LON}	pilot longitudinal stick deflection; $X_{LON} > 0$ for stick forwards	ψ	blade azimuthal position
X_{PED}	pilot pedals deflection; $X_{PED} > 0$ for left	ψ_b	body heading angle; $\psi_b > 0$ nose-right
		Ω	rotor axial rotational velocity
		Ω_{sgn}	rotation direction parameter; Ω_{sgn}=1 when ccw

I. Introduction

A tilt-rotor aircraft combines the vertical take-off and landing capability of a helicopter and the high speed cruise and range capability of an airplane. Due to its broad mission profile the tilt-rotor aircraft concept has already been employed in military operations, such as the Bell XV-15 and its successor the Bell-Boeing V-22 Osprey, and is in the development phase for civil use, e.g. the Augusta-Westland AW-609 [1]. A large impact of the civil application concerns airports, as it has the potential to reduce runway use, allowing for an increased airport capacity and fewer delayed flights [2].

Tilt-rotor flight mechanics modeling incorporates elements from both the airplane, as well as helicopter engineering fields, resulting in a broad and complex task that makes tilt-rotor modeling challenging. For this reasons many available tilt-rotor models either employ numerous assumptions yielding oversimplified and inaccurate models, or achieve high accuracy through increased complexity and dependence on vast amounts of experimental data (see next section for elaborated discussion). Flight mechanics models may serve as tools to determine the flight envelope, structural and aeroelastic stability, and the origin of undesirable flight behavior of a tilt-rotor which may lead to a faster, cheaper, and safer aircraft development process. Unfortunately even modern models seem to be unreliable as was the case with the SIMRX flight simulator used to investigate the fatal crash of the AW-609 tilt-rotor in 2015 [3]. It was concluded that the simulation was not able to predict flight behavior that led to the tragic incident due to a lack of experimental data [4]. This highlights the necessity for the development of tilt-rotor flight mechanics models that are based on fundamental physical equations instead of data-driven approaches.

This research presents a middle ground between model accuracy and flexibility, taking into account recommendations and existing approaches available in literature, with the hopes of developing an accurate yet approachable and generic tilt-rotor flight mechanics model capable of future expansion. Emphasis is put on the effect of the tiltable nacelle on the rotor analytical expressions and static flight mechanics. The scope of the research is limited to performance and piloted flight simulation purposes only. Assumptions and simplifications that are employed in order to obtain a flight mechanics model that remains within this scope are clearly indicated, and the resulting limitations are highlighted.

A. Tilt-Rotor Models Available in Literature

Previous attempts at capturing the flight mechanics of a tilt-rotor may be grouped into: 1) those that solve the rotor equations analytically; 2) and those that solve them numerically. Starting with the former, the most often referenced model in different research works is the Generic Tilt-Rotor Simulation (GTRS) which is based on the Bell Model 301 tilt-rotor model [5], first formalized as the GTRS in [6], and later revised in [7–9]. This model has been extensively validated against the Bell XV-15 tilt-rotor aircraft [10–12], mostly using scale wind tunnel tests [13]. Due to the good accessibility and documented validity, the GTRS model is therefore often used as the basis for the validation of novel tilt-rotor models, which is also the case of the research work at hand. In general, this model may be considered a gray box model as it combines analytically derived equations and empirical relations.

Other analytical models that are validated against the GTRS can be found in the works of [14] and [15] which both develop generic tilt-rotor models for the purpose of trim, stability, and control analyses. More recent models are found in [16] which focuses on real-time simulation application, and in the work of [17] which investigates the effect of aerodynamic interactions on tilt-rotor flight mechanics. Other analytical models can be found in the works of [18] and [19], however the former is additionally validated against the successor of the XV-15 tilt-rotor, namely the V-22 [12], while the latter is solely validated against the V-22. Furthermore, the model of [18] investigates the control and stability of a linear state space model, capable of longitudinal flight only, in either helicopter or airplane configuration, not allowing for the investigation of conversion flight. The model of [19] is non-linear and is developed for the purpose of performance, simulated flight, and stability and control analyses. The author of [20] also derives an analytical non-linear model, however for educational purposes only, providing a good introductory resource for tilt-rotor modeling.

Notable numerical tilt-rotor models validated against the XV-15 include the work of [21] which was developed for the purpose of exploring aeromechanical phenomena with emphasis on aeroelastic stability, or the black-box model of [22] which has been created for commercial purposes.

B. Tilt-Rotor Model Requirements

According to [23], the tilt-rotor model should not be linearised, allow for six degrees of body motion freedom, and be valid across the entire flight envelope, which includes forwards, backwards, sideways, and vertical flight. Furthermore the model should exhibit the basic dynamic modes characteristic to helicopters and airplanes. Finally, the power requirements should be estimated realistically.

Based on the recommendations of [20, 24], the equations describing the aerodynamics of the rotor should contain axial and in-plane airflow velocity components, which also includes the airflow resulting from body rotations. It is sufficient to only consider axial inflow, however it should have a non-uniform distribution across the rotor disk. If a uniform inflow distribution is used, the tip-loss factor [25] must be incorporated as a correction factor [9, 20]. If resources allow, the inflow model may be extended to include in-plane and rotational velocity components. Furthermore, it is recommended to model the inflow as a dynamic system (see [9, 20, 24, 26, 27]). It is sufficient to describe the flapping and lagging motion of the blade with one harmonic, and to only consider the steady state response. It is recommended, however, that a quasi-static description of the blade flapping and lagging motion is used, incorporating first order dynamics to the steady state response [20, 23]. The rotor forces and moments acting on the body may be averaged around one revolution, therefore neglecting load periodicity. It is suggested that an additional rotor rotational degree of freedom is introduced allowing to simulate autorotation [23]. Finally, modeling the effect of the flow reversal region has a high impact on handling qualities and hence should be included for piloted flight simulation.

Apart from the necessary fuselage, wing, and tail aerodynamics, [9] recommends to model the aerodynamics of the tilting nacelles and the effect of ground proximity on rotor power, thrust, and downwash. Furthermore, [9, 17] suggest that the effect of the wing-nacelle interaction be considered, as well as the aerodynamic downwash effect of the rotor

and wing on the horizontal stabilizer, and the effectiveness of the ailerons as a function of nacelle angle. Finally, [24] recommends incorporating the tandem rotor effect in sideways flight, and the effect of the Mach number on the lift and drag coefficients.

II. Generic Tilt-Rotor Model Development

The tilt-rotor model developed for the purposes of this research work has six degrees of body motion freedom (hence it is referred to as the 6-degrees-of-freedom model, or 6DoF model in short) and thus is capable of three-dimensional flight simulation. It consists of tiltable simplified articulated rotors, trapezoidal planform lifting surfaces that mostly exhibit flat plate aerodynamics, and a fuselage model that only produces drag. A schematic representation of all these components is shown in fig. 12 in the appendix. The tiltable rotor model was derived analytically based on the blade element method (BEM) with the use of Maple [28], a symbolic manipulation program. The 6DoF model is implemented in simulation with the use of Matlab and Simulink [29], additionally incorporating rotor RPM dynamics (a 7th DOF of the model) allowing for the simulation of autorotation. The parameters of the 6DoF model are set to those corresponding to the real-life XV-15 tilt-rotor aircraft in order to generate simulation results and validate the model. The most critical simplifications applied during the development of the model include the small-angle-approximation of the blade element inflow angle, the lack of any aerodynamic ground effects and mutual rotor wake effects, a rotor-induced velocity that is uniform across the rotor disk, the omission of the flapping and inflow dynamics, and a fuselage that is assumed to produce only drag and no lift.

The rotors of the 6DoF model tilt together with the nacelles with the angle η and tilt rate $\dot{\eta}$. In helicopter configuration the nacelles are orientated vertically and the nacelle angle η is equal to 0, while in airplane configuration the nacelles are tilted forward and the nacelle angle is equal to $-90°$ (note the negative sign). The reference frames, states, and control angles (and their positive conventions) are summarized in fig. 1. Note that all reference frames are defined according to the right-hand-rule.

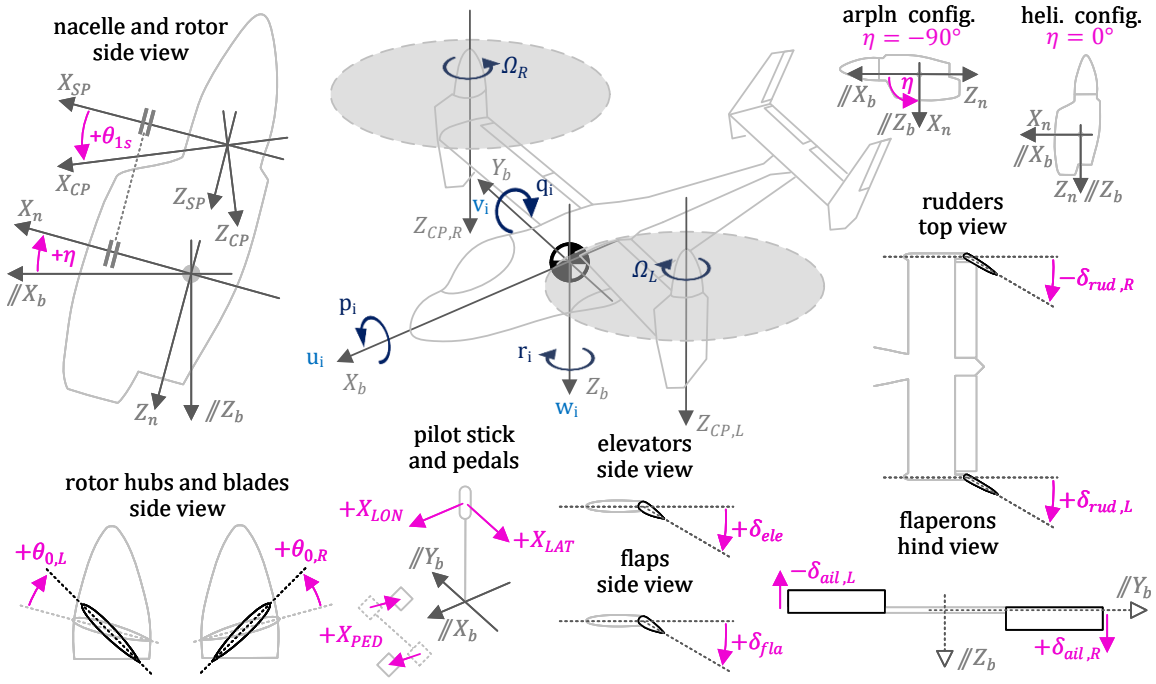

Fig. 1 Summary of positive sign conventions of the tilt-rotor states, control inputs, and control outputs.

The tilt-rotor equations of motions are defined in the body reference frame $\boldsymbol{E}_b$, with the state derivatives being a non-linear function of the states $\boldsymbol{x}$, aircraft inputs $\boldsymbol{u}_{aircraft}$, external forces $\boldsymbol{F}_b$ and moments $\boldsymbol{M}_b$ acting on the body, and time as formalized in eq. (1). The tilt-rotor body is assumed rigid.

$$\dot{\boldsymbol{x}} = f\left(\boldsymbol{x}, \boldsymbol{u}_{aircraft}, \boldsymbol{F}_b, \boldsymbol{M}_b, t\right) \tag{1}$$

The state vector is given by eq. (2) and consists of the: body longitudinal u_i, lateral v_i, and vertical w_i inertial linear velocities; body CoG north x_{cg}, south y_{cg}, and (negative) altitude z_{cg} position in a non-rotating flat-Earth reference frame; body roll p_i, pitch q_i, and yaw r_i inertial rotational velocities; roll ϕ_b, pitch θ_b, and heading ψ_b attitude angles defined in the same Earth reference frame; nacelle tilt angle η; and interconnected rotors' rotational rate Ω. Note that the body attitude angles are ultimately defined with quaternions in simulation.

$$\boldsymbol{x} = \left[u_i, v_i, w_i, x_{cg}, y_{cg}, z_{cg}, p_i, q_i, r_i, \phi_b, \theta_b, \psi_b, \eta, \Omega\right] \tag{2}$$

The aircraft control inputs are a function of the pilot inputs $\boldsymbol{u}_{pilot}$ and nacelle tilt (through control mixing and phasing), as shown in eq. (3), and consist of the: left and right rotor (indicated with the L and R subscripts) longitudinal cyclic θ_{1s} and collective θ_0 swashplate angles; commanded engine power R_{SHP}; aileron δ_{ail}, elevator δ_{ele}, rudder δ_{rud}, and flap δ_{fla} deflections; and the nacelle tilt rate $\dot{\eta}$.

$$\boldsymbol{u}_{aircraft} = f(\boldsymbol{u}_{pilot}, \eta) = \left[\theta_{1s,L}, \theta_{1s,R}, \theta_{0,L}, \theta_{0,R}, R_{SHP}, \delta_{ail}, \delta_{ele}, \delta_{rud}, \delta_{fla}, \dot{\eta}\right] \tag{3}$$

The pilot inputs are given in eq. (4) which consist of the: longitudinal X_{LON}, lateral X_{LAT}, and pilot-collective $X_{COL,pilot}$ stick deflections; pedal deflection X_{PED}; flap X_{FLA} and nacelle tilt-rate X_{TIL} lever deflections; and the rotor rotational rate selector RPM_{SEL}. The 6DoF model approximates the control mixing and phasing scheme of the XV-15 tilt-rotor with analytical expressions as described in detail in [30].

$$\boldsymbol{u}_{pilot} = \left[X_{LON}, X_{LAT}, X_{COL,pilot}, X_{PED}, X_{FLA}, X_{TIL}, RPM_{SEL}\right] \tag{4}$$

The external forces and moments acting on the body CoG, on the other hand, are the summation of multiple contributions which, in the case of this model, are limited to the rotors (subscript r), wings (w), horizontal stabilizers (hs), vertical stabilizers (vs), and fuselage (fus) components only (see eq. (5)). For notation compactness the forces $\boldsymbol{F}$ and moments $\boldsymbol{M}$ are presented in vector form. It can be seen that the total moment (eq. (5b)) consists of pure moments and additional moments as a result of the generated forces acting at a distance from the CoG represented by the position vectors $\boldsymbol{s}$. Note that the force and moment vectors are defined in the body (b) reference frame ($\boldsymbol{E}$) as indicated by the column unit vector $\{\boldsymbol{E}_b\}$. This convention shall be used for other reference frames as well.

$$\begin{pmatrix} F_{bx} & F_{by} & F_{bz} \end{pmatrix} \{\boldsymbol{E}_b\} = \boldsymbol{F}_b = \boldsymbol{F}_r + \boldsymbol{F}_w + \boldsymbol{F}_{hs} + \boldsymbol{F}_{vs} + \boldsymbol{F}_{fus} \tag{5a}$$

$$\begin{aligned} \begin{pmatrix} M_{bx} & M_{by} & M_{bz} \end{pmatrix} \{\boldsymbol{E}_b\} = \boldsymbol{M}_b = \boldsymbol{M}_r + \boldsymbol{M}_w + \boldsymbol{M}_{hs} + \boldsymbol{M}_{vs} + \boldsymbol{M}_{fus} \\ + \boldsymbol{s}_r \times \boldsymbol{F}_r + \boldsymbol{s}_w \times \boldsymbol{F}_w + \boldsymbol{s}_{hs} \times \boldsymbol{F}_{hs} + \boldsymbol{s}_{vs} \times \boldsymbol{F}_{vs} + \boldsymbol{s}_{fus} \times \boldsymbol{F}_{fus} \end{aligned} \tag{5b}$$

The 6DoF model also distinguishes between between inertial (i subscript), aerodynamic wash (w), and total aerodynamic rates (no subscript). The inertial terms correspond to the movement of a point within the inertial Earth reference frame, the wash rates correspond to the movement of air (originating from wind gusts or the rotor wash, for example), while the total aerodynamic rates are the combined inertial and wash rates as defined in eq. (6). All of these velocities are defined in the body reference frame. Note that the wash velocity is indicated with the subscript $w|b$, with the left-hand-side (LHS) of the subscript indicating the wash (w) velocity, while the right-hand-side (RHS) indicating the body (b) reference frame in which this velocity is defined. This convention shall be used for other linear and rotational velocities, forces and moments, position vectors, and reference frames as well.

$$\boldsymbol{V}_{b|b} = \boldsymbol{V}_{b,i|b} - \boldsymbol{V}_{w|b} \tag{6a}$$

$$\boldsymbol{\omega}_{b|b} = \boldsymbol{\omega}_{b,i|b} - \boldsymbol{\omega}_{w|b} \tag{6b}$$

In order to generalize the derivation of longitudinally symmetric components, two so-called sign change parameters are also introduced, namely d_{sgn} and Ω_{sgn}, which serve the purpose of changing the sign of a term or expression depending on either the mounting position of a component (the former parameter) or the direction of rotation of the rotor (the latter parameter), as defined in eq. (7).

$$\Omega_{sgn} = \begin{cases} 1 & \text{if counter-clockwise, viewed from above} \\ -1 & \text{if clockwise, viewed from above} \end{cases} \qquad d_{sgn} = \begin{cases} 1 & \text{if right-mounted, viewed from aft} \\ -1 & \text{if left-mounted, viewed from aft} \end{cases} \tag{7}$$

A. Analytical Tiltable Proprotor Derivation

The rotor force and moment vectors are decomposed into three orthogonal components acting along or around the negative wind axis (w.a. in short, indicated with the caret symbol, treated later) control plane (CP) axes according to the right hand rule as graphically summarized in fig. 2 for the left (L) and right (R) rotor. The mathematical definitions of these forces and moments are provided in eq. (8) where the subscript $r|X\widehat{CP}$ indicates the force (or moment) of the rotor (r) acting along the x-axis (X) of the w.a. control plane ($\widehat{CP}$). This convention shall be used throughout this paper. Analogously, the $\boldsymbol{T}_{\widehat{CP}|b}$ term indicates the transformation from the w.a. CP frame to the body frame. The rotor force and moment components are also referred to as the hind H-force, side S-force, thrust T-force, rolling O-moment, pitching P-moment, and torque Q-moment. All of these forces and moments are derived with the blade element method (subscript BEM), therefore the blade element velocity components must also be defined.

$$\boldsymbol{F}_r = \begin{pmatrix} F_{r|X\widehat{CP}} \\ F_{r|Y\widehat{CP}} \\ F_{r|X\widehat{CP}} \end{pmatrix}^T \boldsymbol{T}_{\widehat{CP}|b}\{\boldsymbol{E}_b\} = -\begin{pmatrix} \widehat{H}_{\text{BEM},L} + \widehat{H}_{\text{BEM},R} \\ \widehat{S}_{\text{BEM},L} + \widehat{S}_{\text{BEM},R} \\ \widehat{T}_{\text{BEM},L} + \widehat{T}_{\text{BEM},R} \end{pmatrix}^T \boldsymbol{T}_{\widehat{CP}|b}\{\boldsymbol{E}_b\} = -\begin{pmatrix} H_L + H_R \\ S_L + S_R \\ T_L + T_R \end{pmatrix}^T \boldsymbol{T}_{\widehat{CP}|b}\{\boldsymbol{E}_b\} \tag{8a}$$

$$\boldsymbol{M}_r = \begin{pmatrix} M_{r|X\widehat{CP}} \\ M_{r|Y\widehat{CP}} \\ M_{r|X\widehat{CP}} \end{pmatrix}^T \boldsymbol{T}_{\widehat{CP}|b}\{\boldsymbol{E}_b\} = -\begin{pmatrix} \widehat{O}_{s,L} + \widehat{O}_{s,R} \\ \widehat{P}_{s,L} + \widehat{P}_{s,R} \\ \widehat{Q}_{\text{BEM},L} + \widehat{Q}_{\text{BEM},R} \end{pmatrix}^T \boldsymbol{T}_{\widehat{CP}|b}\{\boldsymbol{E}_b\} = -\begin{pmatrix} O_L + O_R \\ P_L + P_R \\ Q_L + Q_R \end{pmatrix}^T \boldsymbol{T}_{\widehat{CP}|b}\{\boldsymbol{E}_b\} \tag{8b}$$

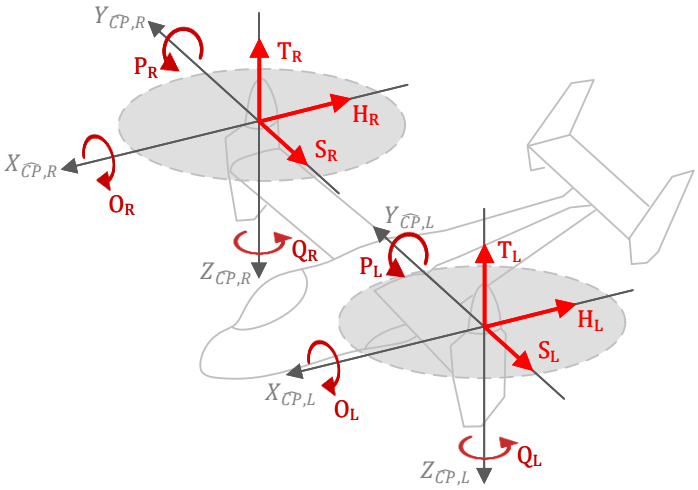

Fig. 2 Positive sign conventions of the rotor forces and moments defined in the wind axis control planes of the left (cw.) and right (ccw.) rotor.

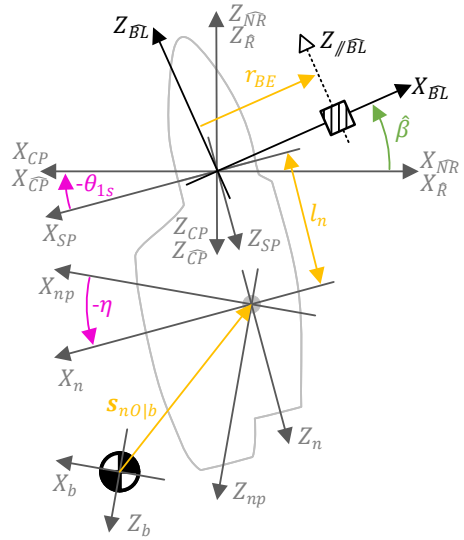

Fig. 3 Schematic side-view of the cascaded reference frame transformations from the tilt-rotor body to the blade element. Wind shift angle Δ is set to zero and blade is positioned at $\psi = \widehat{\psi} = 0$. Blade element represented by striped box. Body CoG and nacelle outline shown in background.

1. Blade Element Velocity Components

The blade element (BE) is defined to be an infinitesimally narrow section of the blade at a radial position r_{BE} away from the rotor hub, and is treated aerodynamically as a two-dimensional airfoil. The velocity experienced by the blade

element ($\boldsymbol{V}_{BE|\widehat{BL}}$) is decomposed into the radial U_R, tangential U_T, and perpendicular U_P orthogonal components (see fig. 13 in the appendix) acting along the blade reference frame ($\boldsymbol{E}_{\widehat{BL}}$) axes as defined in eq. (9).

$$\boldsymbol{V}_{BE|\widehat{BL}} = \begin{pmatrix} U_R & \Omega_{sgn} U_T & U_P \end{pmatrix} \{\boldsymbol{E}_{\widehat{BL}}\} \tag{9}$$

The blade element velocity vector $\boldsymbol{V}_{BE|\widehat{BL}}$ is derived by successively calculating the velocity vectors of the origins of 'child' reference frames, that may be rotating and have an offset with respect to their 'parent' reference frames, with the use of eq. (10). Here $\boldsymbol{\omega}$ and $\boldsymbol{s}$ are angular velocity and position vectors respectively.

$$\boldsymbol{V}_{child|child} = \left(\boldsymbol{V}_{parent|parent} + \boldsymbol{\omega}_{parent|parent} \times \boldsymbol{s}_{child|parent}\right) \boldsymbol{T}_{parent|child} \tag{10}$$

This cascading derivation starts with the body reference frame origin velocity vector which is known to be the body velocities u, v, and w, and continues with the determination of the velocity of the nacelle origin (nO), rotor hub, and finally ends at the velocity of the blade element as summarized in eq. (11). Note that the obtained velocity vectors must be successively transformed from the body, to the nacelle pivot (np), nacelle (n), shaft plane (SP), control plane (CP), w.a. control plane ($\widehat{CP}$), w.a. non-rotating frame ($\widehat{NR}$), w.a. rotating frame ($\widehat{R}$), and finally to the w.a. blade ($\widehat{BL}$) reference frames. All involved rotational transformations and offsets are indicated under the transformation arrows and depicted in fig. 3. These include the nacelle pivot point offset $\boldsymbol{s}_{nO|b} = \begin{pmatrix} -d_{xn} & d_{sgn} d_{yn} & -d_{zn} \end{pmatrix} \{\boldsymbol{E}_b\}$ and the nacelle length (or rotor hub offset) l_n only.

$$\boldsymbol{V}_{bO}\{\boldsymbol{E}_b\} \underset{\boldsymbol{s}_{nO|b}}{\rightarrow} \boldsymbol{V}_{nO}\{\boldsymbol{E}_b\} \underset{\eta}{\rightarrow} \boldsymbol{V}_{nO}\{\boldsymbol{E}_n\} \underset{l_n}{\rightarrow} \boldsymbol{V}_{hub}\{\boldsymbol{E}_n\} \underset{\dot{\theta}_{1s}}{\rightarrow} \boldsymbol{V}_{hub}\{\boldsymbol{E}_{CP}\} \underset{\Delta,\pi,\widehat{\psi},\widehat{\beta}}{\rightarrow} \boldsymbol{V}_{hub}\{\boldsymbol{E}_{\widehat{BL}}\} \underset{\boldsymbol{r}_{BE}}{\rightarrow} \boldsymbol{V}_{BE}\{\boldsymbol{E}_{\widehat{BL}}\} \tag{11}$$

An intermediate step in this cascading derivation is the determination of the hub velocity in the control plane reference frame $\boldsymbol{V}_{hub|CP}$, with its components designated tangential (t) and perpendicular (p) variables names as shown in eq. (12). It should be noted that transforming the rotor hub velocity from the nacelle to the control plane frame should introduce the rotational rate of the control plane $\dot{\theta}_{1s}$ as well. For simplicity's sake this rotational rate is neglected. Also note that at this point the nacelle tilt angle η and rate $\dot{\eta}$ are introduced into the proprotor expressions.

$$\boldsymbol{V}_{hub|CP} = \begin{pmatrix} V_{tc1} & V_{tc2} & V_{pc} \end{pmatrix} \{\boldsymbol{E}_{CP}\} \tag{12}$$

The rotor forces and moments are derived in the wind axis control plane reference frame $\widehat{CP}$ (see fig. 14 in the appendix) which is the nominal control plane reference frame CP that is rotated around its Z_{CP}-axis with the angle Δ defined by eq. (13). The resulting relation between the nominal blade azimuth angle ψ and its w.a. counterpart $\widehat{\psi}$ is defined by eq. (14). The wind shift angle is defined to act in the same direction irrespective of the rotational direction of the rotor. The w.a. CP tangential ($\widehat{V_{tc}}$) and perpendicular ($\widehat{V_{pc}}$) velocity components are then obtained with eq. (15) and eq. (15b) respectively. It is not clear whether the w.a. shift transformation should introduce a new rotational velocity component, namely $\dot{\Delta}$, therefore it is not included in this derivation.

$$\Delta = \arctan\left(\frac{V_{tc2}}{V_{tc1}}\right) \tag{13}$$

$$\psi = \widehat{\psi} - \Omega_{sgn}\Delta \tag{14}$$

$$\widehat{V_{tc}} = \sqrt{V_{tc1}^2 + V_{tc2}^2} \tag{15a}$$

$$\widehat{V_{pc}} = V_{pc} \tag{15b}$$

The transformation of the rotor hub velocity to the w.a. CP is formalized in eq. (16). The rotor induced velocity v_{in} is also introduced into the velocity vector at this point, simplified to be perpendicular to the CP instead of the disk plane (DP). Moreover, the induced velocity is defined to uniform across the rotor disk and quasi-static. Note that several rotor expressions shall make use of the non-dimensionalized versions of these velocities which are defined in eq. (79) in the appendix. Also note that for sake of compactness the shorthand notation for the trigonometric functions is used where the sine and cosine of the wind shift angle Δ are abbreviated with S_Δ and C_Δ respectively. This compact notation shall be used for other trigonometric arguments in this paper as well.

$$\boldsymbol{V}_{hub|\widehat{CP}} = \begin{pmatrix} V_{tc1} \\ V_{tc2} \\ V_{pc} - v_{in} \end{pmatrix}^T \boldsymbol{T}_{CP|\widehat{CP}}\{\boldsymbol{E}_{\widehat{CP}}\} = \begin{pmatrix} V_{tc1}C_\Delta + V_{tc2}S_\Delta \\ -V_{tc1}S_\Delta + V_{tc2}C_\Delta \\ V_{pc} - v_{in} \end{pmatrix}^T \{\boldsymbol{E}_{\widehat{CP}}\} = \begin{pmatrix} \widehat{V_{tc}} \\ 0 \\ \widehat{V_{pc}} - v_{in} \end{pmatrix}^T \{\boldsymbol{E}_{\widehat{CP}}\} \tag{16}$$

Continuing the derivation of the blade element velocity components involves the transformation from the non-rotating to the rotating reference frame, introducing the blade rotational velocity Ω which acts around the $Z_{\widehat{NR}}$-axis and is influenced by the rotor rotational direction through the Ω_{sgn} parameter. The resulting velocity components must then be transformed from the rotating frame into the blade frame which only follows the blade flapping motion around the negative $Y_{\widehat{R}}$-axis, but does not include the lead/lag motion. This introduces both the flapping angle $\widehat{\beta}$ and its time derivative $\dot{\widehat{\beta}}$.

2. Inertial Flapping Moment

In order to transform the rotor forces and moments from the rotating blade frame to the non-rotating w.a. CP frame, the quasi-static disk tilt approximation is employed. The transient response of the blade is assumed to resolve relatively quickly. This approximation requires the prior derivation of the flapping equation defined in the w.a. rotating frame $\boldsymbol{E}_{\widehat{R}}$ which is coplanar with the w.a. CP and follows the azimuthal position of the blade. The flapping motion is presumed to be describable by a second order differential equation as given by eq. (17), neglecting all non-linearities with respect to $\widehat{\beta}$, with I_{bl} being the blade flapping inertia, c the damping gain, k the spring gain, and M_{ext} the excitation moment.

$$I_{bl}\ddot{\widehat{\beta}} + c\dot{\widehat{\beta}} + k\widehat{\beta} = M_{ext} \tag{17}$$

The flapping motion of the blade is assumed to be dictated by inertial and aerodynamic forces only, summing the inertial (subscript i) and aerodynamic (a) moments around the flapping hinge (formally the negative $Y_{\widehat{R}}$-axis) as given by eq. (18a) (and depicted in fig. 15 in the appendix). This rotor model includes a flapping spring hence an additional hub spring moment (subscript s) is included in the summation. The gravitational acceleration is assumed insignificant. Note that eq. (18a) is re-arranged into the form given by eq. (18b) since the derivation of the inertial moment shall include the LHS blade inertial term $I_{bl}\ddot{\widehat{\beta}}$ as described next. The aerodynamic and spring moments shall be treated later.

$$I_{bl}\ddot{\widehat{\beta}} = \sum \overset{+}{\curvearrowleft}_{(-Y\widehat{R})} M = M_{BL|-Y\widehat{R},a} - M_{BL|Y\widehat{R},s} - M'_{BL|Y\widehat{R},i} \tag{18a}$$

$$-M_{BL|Y\widehat{R},i} = M_{BL|-Y\widehat{R},a} - M_{BL|Y\widehat{R},s} \quad \text{with} \quad M_{BL|Y\widehat{R},i} = -I_{bl}\ddot{\widehat{\beta}} - M'_{BL|Y\widehat{R},i} \tag{18b}$$

The inertial flapping moment $M_{BL|Y\widehat{R},i}$ is derived with Newtonian mechanics and obtained by integrating the (orthogonal) forces experienced by the blade element $dF_{BL|\widehat{R}}$ as a result of its acceleration $\boldsymbol{a}_{BE|\widehat{R}}$ along the blade length as defined in eq. (19) (and depicted in fig. 16 in the appendix). , with $\overline{m}$ being the blade mass per length.

$$M_{BL|Y\widehat{R},i} = \int_0^R r_{BE}\left(S_{\widehat{\beta}}dF_{BL|X\widehat{R},i} - C_{\widehat{\beta}}dF_{BL|Z\widehat{R},i}\right)dr_{BE} = \int_0^R r_{BE}\overline{m}\left(S_{\widehat{\beta}}a_{BE|X\widehat{R},i} - C_{\widehat{\beta}}a_{BE|Z\widehat{R},i}\right)dr_{BE} \tag{19}$$

The blade element acceleration vector $\boldsymbol{a}_{BE|\widehat{R}}$ is derived by successively calculating the acceleration of appropriate (possibly moving) points (pnt) within 'parent' reference frames (that may be rotating) with the use of eq. (20). Here $\boldsymbol{a}_{par|par,i}$ is the linear acceleration of the parent frame origin.

$$\boldsymbol{a}_{\text{pnt|par,i}} = \ddot{\boldsymbol{s}}_{\text{pnt|par}} + 2\boldsymbol{\omega}_{\text{par|par},i} \times \dot{\boldsymbol{s}}_{\text{pnt|par}} + \dot{\boldsymbol{\omega}}_{\text{par|par},i} \times \boldsymbol{s}_{\text{pnt|par}} + \boldsymbol{\omega}_{\text{par|par},i} \times \left(\boldsymbol{\omega}_{\text{par|par},i} \times \boldsymbol{s}_{\text{pnt|par}}\right) + \boldsymbol{a}_{\text{par|par,i}} \tag{20}$$

Analogously to the blade element velocity components, this cascading derivation starts with the body reference frame origin acceleration and continues with the nacelle origin (nO), rotor hub, and finally ends at the acceleration of the blade element as summarized in eq. (21). The obtained acceleration vectors must also be successively transformed

from the body to the w.a. rotating ($\widehat{R}$) reference frame, with all involved rotational transformations and offsets already depicted in fig. 3.

$$\boldsymbol{a}_{bO,i}\{\boldsymbol{E}_b\} \underset{\boldsymbol{s}_{nO|b}}{\rightarrow} \boldsymbol{a}_{nO,i}\{\boldsymbol{E}_b\} \underset{\eta}{\rightarrow} \boldsymbol{a}_{nO,i}\{\boldsymbol{E}_n\} \underset{l_n}{\rightarrow} \boldsymbol{a}_{hub,i}\{\boldsymbol{E}_n\} \underset{\theta_{1s},\Delta,\pi,\widehat{\psi}}{\rightarrow} \boldsymbol{a}_{hub,i}\{\boldsymbol{E}_{\widehat{R}}\} \underset{\boldsymbol{r}_{BE}}{\rightarrow} \boldsymbol{a}_{BE,i}\{\boldsymbol{E}_{\widehat{R}}\} \tag{21}$$

During the derivation process both the nacelle tilt acceleration $\ddot{\eta}$ and flapping acceleration $\ddot{\widehat{\beta}}$ are introduced into the rotor expressions. It should be noted that the derivation involves the derivative of the blade azimuthal position $\dot{\widehat{\psi}}$ which is set equal to $\Omega_{sgn}\Omega_{tot}$, where the latter term is the total azimuthal rotational rate of the rotating frame (incorporating the body rates).

Solving the integral of eq. (19) and applying the small angle approximation to $\widehat{\beta}$ yields an extensive expression which may be generalized by eq. (22), where $M_{1,bl}$ is the blade first mass moment. The complete expression shall not be shown in this paper, however its simplified version is presented and analyzed in section III. Returning to the generalized form, it is important to highlight that the linearized inertial flapping moment depends on the nacelle tilt angle, rate, and acceleration, does not depend on the flapping rate $\dot{\widehat{\beta}}$, and both the $B_{\widehat{\beta}}$ and B_{ext} terms are equal to zero in the case that the rotor hub acceleration is equal to zero.

$$\begin{aligned} M_{BL|Y\widehat{R},i} &= f(\eta, \dot{\eta}, \ddot{\eta}, p_i, q_i, r_i, \dot{p}_i, \dot{q}_i, \dot{r}_i) \\ &= -I_{bl}\ddot{\widehat{\beta}} - \left(A_{\widehat{\beta}} I_{bl} + B_{\widehat{\beta}} M_{1,bl}\right)\widehat{\beta} + A_{ext} I_{bl} + B_{ext} M_{1,bl} \end{aligned} \tag{22}$$

3. Aerodynamic Flapping Moment

The aerodynamic moment $M_{BL|Y\widehat{BL},a}$ is derived in the wind axis blade frame $\boldsymbol{E}_{\widehat{BL}}$ with the use of the blade element method (BEM) by integrating the moment as a result of the aerodynamic vertical blade force $F_{BL|Z\widehat{BL},a}$, parallel to the $Z_{\widehat{BL}}$-axis, experienced by the blade element along the blade length as given by eq. (23) (and depicted for clarity in fig. 17 in the appendix). The vertical force itself consists of a BE lift dL_{BL} and drag dD_{BL} component as shown in the same equation (and depicted in fig. 18 in the appendix).

$$M_{BL|-Y\widehat{R},a} = \int_0^R r_{BE} dF_{BL|Z\widehat{BL},a} = \int_0^R r_{BE}\left(dL_{BL} cos(\phi_{BE}) - dD_{BL} sin(\phi_{BE})\right) \tag{23}$$

By assuming that the inflow angle ϕ_{BE} is small and that the BE lift is much greater than the drag, however, the vertical force may be simplified to only consist of the BE lift component yielding an aerodynamic flapping moment that reduces to the form shown in eq. (24). Note that the presented rotor model does not include a hinge offset, tip loss factor, nor any compensation for the flow reversal region.

If $\phi_{BE} \ll 1$ and $dL_{BL} \gg dD_{BL}$, then:

$$M_{BL|-Y\widehat{R},a} = \int_0^R r_{BE} dL_{BL} \tag{24}$$

The BE lift is linear with respect to its angle of attack α_{BE} as defined in eq. (25), where $C_{l_\alpha,bl}$ is the blade lift coefficient slope and c_{bl} is the (constant) blade chord length. The angle of attack depends on the BE inflow angle ϕ_{BE} and the BE pitch angle θ_{BE}, with the latter modeled to vary linearly along the blade length as shown in eq. (27). The total BE velocity $V_{BE|Y-Z\widehat{BL}}$ and inflow angles are simplified, however, yielding a simplified BE lift as shown in eq. (28).

$$dL_{BL} = \frac{1}{2}\rho V^2_{BE|Y-Z\widehat{BL}} C_{l_\alpha,bl} \alpha_{BE} c_{bl} dr_{BE} \tag{25}$$

$$\alpha_{BE} = \theta_{BE} - \phi_{BE} \tag{26}$$

$$\theta_{BE} = \theta_0 + \theta_{bl,1} r_{BE} \tag{27}$$

If $U_T \gg U_P$, then:

$$\phi_{BE} = \frac{U_P}{U_T} \tag{28a}$$

$$V^2_{BE|Y-Z\widehat{BL}} = U_T^2 \tag{28b}$$

$$dL_{BL} = \frac{1}{2}\rho U_T^2 C_{l_\alpha,bl}\left(\theta_0 + \theta_{bl,1} r_{BE} - \frac{U_P}{U_T}\right) c_{bl} dr_{BE} \tag{28c}$$

Solving the integral of eq. (24) and applying the small angle approximation to $\widehat{\beta}$ yields an extensive expression which may be generalized by eq. (29). Here γ_{bl} is the blade lock number defined by eq. (80) in the appendix. The complete expression shall also not be shown in this paper, however its simplified version is presented and analyzed in section III. Returning to the generalized form, it is important to highlight that the linearized aerodynamic flapping moment depends on the nacelle tilt angle and rate and introduces the flapping rate $\dot{\widehat{\beta}}$ into the flapping equation.

$$\begin{aligned}\frac{M_{BL|-Y\widehat{R},a}}{\gamma_{bl} I_{bl}} &= f(\eta, \dot{\eta}, \theta_0, \theta_{bl,1}, \theta_{1s}, p, q, r) \\ &= D_{d\widehat{\beta}}\dot{\widehat{\beta}} + D_{\widehat{\beta}}\widehat{\beta} + D_{ext}\end{aligned} \tag{29}$$

4. Spring Moment

The final portion of the flapping equation consist of the flapping spring moment which is modeled by a linear torsional spring with an angular offset from the un-flapped ($\widehat{\beta} = 0$) position, also referred to as the precone angle $\overline{a}_0$, as given by eq. (30), with K_β being the torsional flapping spring constant. The complete flapping equation shall not be shown in this paper, however its simplified version is shown and analyzed in section III.

$$M_{BL|Y\widehat{R},s} = K_\beta(\widehat{\beta} - \overline{a}_0) \tag{30}$$

5. Disk Tilt Approximation

The disk tilt presumed steady state solution for the flapping motion defined in the w.a. CP reference frame is given by eq. (31a), with the blade motion constrained to the first harmonics only. Here $\widehat{a}_0$ is the coning angle, while $\widehat{a}_1$ and $\widehat{b}_1$ are the longitudnial and lateral disk tilt angles. The conventions for their positive effect on the rotor 'cone' formed by the (rotating) blades is depicted in fig. 4. Here $\overline{TPP}$ is the tip-path-plane. Note that the positive conventions of the disk tilt angles are identical for both the left and right rotor.

$$\widehat{\beta} = \widehat{a}_0 - \widehat{a}_1 cos(\widehat{\psi}) - \Omega_{sgn}\widehat{b}_1 sin(\widehat{\psi}) \tag{31a}$$

The first and second derivatives of the presumed solution are provided in eqs. (31b) and (31c), noting the lack of disk tilt angle dynamics.

$$\begin{aligned}\dot{\widehat{\beta}} &= \Omega_{sgn}\Omega_{tot,i}\widehat{a}_1 sin(\widehat{\psi}) - \Omega_{sgn}^2\Omega_{tot,i}\widehat{b}_1 cos(\widehat{\psi}) \\ &= \Omega_{sgn}\Omega_{tot,i}\widehat{a}_1 sin(\widehat{\psi}) - \Omega_{tot,i}\widehat{b}_1 cos(\widehat{\psi})\end{aligned} \tag{31b}$$

$$\begin{aligned}\ddot{\widehat{\beta}} &= \Omega_{sgn}^2\Omega_{tot,i}^2\widehat{a}_1 cos(\widehat{\psi}) + \Omega_{sgn}\Omega_{tot,i}^2\widehat{b}_1 sin(\widehat{\psi}) \\ &= \Omega_{tot,i}^2\widehat{a}_1 cos(\widehat{\psi}) + \Omega_{sgn}\Omega_{tot,i}^2\widehat{b}_1 sin(\widehat{\psi})\end{aligned} \tag{31c}$$

Substituting the disk tilt approximation into the complete (but linear with respect to $\widehat{\beta}$) flapping equation, collecting aperiodic and first harmonic sine and cosine terms (removing any higher harmonics in the process), and applying the expression reduction scheme (which neglects all terms considered insignificant, treated in more detail later) to the three expression collections yields a linear system of equations for the unknown disk tilt angles, as shown in eq. (32).

$$\begin{bmatrix} A_{11} & A_{12} & 0 \\ A_{21} & A_{22} & 0 \\ A_{31} & A_{32} & A_{33} \end{bmatrix} \begin{pmatrix} \widehat{a}_0 \\ \widehat{a}_1 \\ \widehat{b}_1 \end{pmatrix} = \begin{pmatrix} B_1 \\ B_2 \\ B_3 \end{pmatrix} \tag{32}$$

As a result the expression for the lateral disk tilt may be isolated from the system reducing it to a 2×2 system as shown in eq. (33), with the lateral disk tilt being fully dependent on the coning and longitudinal disk tilt as shown in eq. (34). Note that the non-dimensional rotor induced velocity λ_i is explicitly separated out of the expressions since it is also unknown, highlighting the fact that the system is not yet solvable. In order to be able to solve for all disk tilt angles and the induced velocity (albeit in a numerical manner as shall be described later), two rotor thrust equations are introduced as shall be described next. The analytical solution of the matrix inversion shall shall not be shown due to its extensiveness.

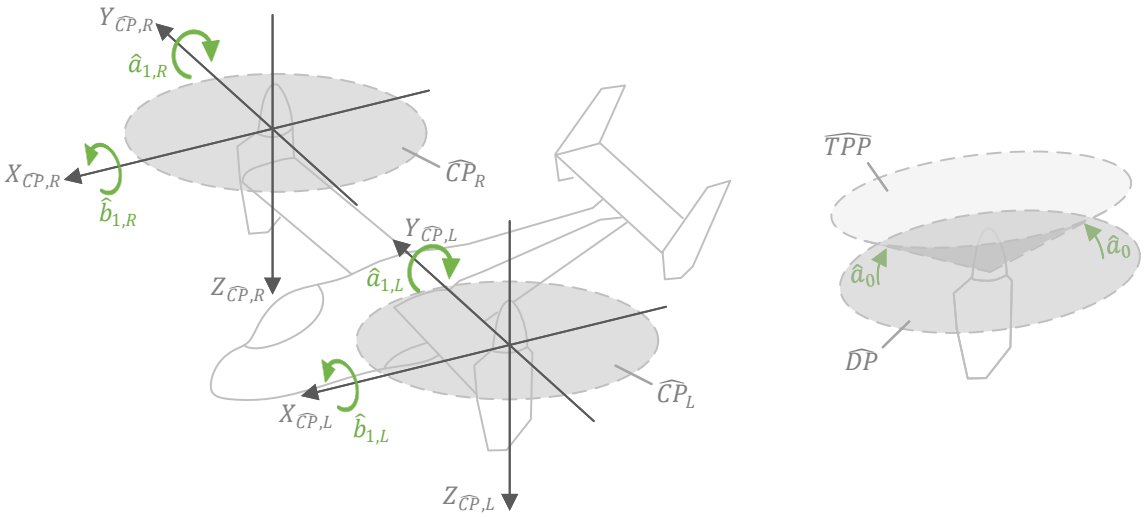

Fig. 4 Positive sign conventions of longitudinal and lateral disk tilt angles (left), and the coning angle (right), for the left (cw.) and right (ccw.) rotor. The wind axis control plane ($\widehat{CP}$), disk plane ($\widehat{DP}$), and tip path plane ($\widehat{TPP}$) are also indicated.

$$\begin{bmatrix} A_{11} & A_{12} \\ A_{21} & A_{22} \end{bmatrix} \begin{pmatrix} \widehat{a}_0 \\ \widehat{a}_1 \end{pmatrix} = \begin{pmatrix} B'_1 \\ B'_2 \end{pmatrix} + \begin{pmatrix} -A_{14} \\ -A_{24} \end{pmatrix} \lambda_i$$

$$\begin{pmatrix} \widehat{a}_0 \\ \widehat{a}_1 \end{pmatrix} = \begin{bmatrix} A_{11} & A_{12} \\ A_{21} & A_{22} \end{bmatrix}^{-1} \begin{pmatrix} B'_1 \\ B'_2 \end{pmatrix} + \begin{bmatrix} A_{11} & A_{12} \\ A_{21} & A_{22} \end{bmatrix}^{-1} \begin{pmatrix} -A_{14} \\ -A_{24} \end{pmatrix} \lambda_i \tag{33}$$

$$\widehat{b}_1 = \frac{1}{A_{33}} \left(B_3 - A_{31}\widehat{a}_0 - A_{32}\widehat{a}_1 \right) \tag{34}$$

Before continuing to the thrust equations, however, it is appropriate to mention at this point that the a lateral disk tilt correction factor is included in the model in the form of eq. (35) in order to compensate for the inaccuracies introduced by using a uniform rotor induced velocity distribution.

$$\widehat{b}_1 \leftarrow \widehat{b}_1 + \Omega_{sgn} \frac{K_{b1}\lambda_i}{1 + \widehat{\mu}_{tc}^2/2} \tag{35a}$$

$$K_{b1} = \frac{1.33\widehat{\mu}_{tc}/\left|\widehat{\lambda}_{tot}\right|}{1.2 + \widehat{\mu}_{tc}/\left|\widehat{\lambda}_{tot}\right|} \tag{35b}$$

It is worth mentioning that solving the system of equations given in eq. (32) yields disk tilt angles that are defined in the wind axis control plane. The definition of these in the non-wind axis CP is given by eq. (81) in the appendix.

6. Blade Element Thrust

The first thrust equation is derived with the BEM and is defined to be perpendicular to the w.a. control plane, while the second thrust equation is based on the momentum theory and is perpendicular to the w.a. disk plane. In order to be able to correctly equate the two forces, the other two orthogonal BEM force components defined in the w.a. control plane, i.e. the H- and S-forces, will also have to be determined first. The BEM thrust is derived first, followed by the H- and S-forces, while the definition of the momentum theory thrust, as well as the method of solving for the disk tilt angles and induced velocity will be treated last.

The BEM thrust $\widehat{T}_{\text{BEM}}$ is obtained by integrating the BE aerodynamic force that is perpendicular to the w.a. CP along the blade length and taking the averaged-over-one-rotor-revolution thrust of all the N blades as shown in eq. (36a).

The perpendicular BE force can be written in terms of the aerodynamic vertical blade force $F_{BL|Z\widehat{BL},a}$, as shown in eq. (36b). Once again, assuming that the inflow angle is small, that the BE lift is much greater than the drag, and that the flapping angle is also small, the BEM thrust may be simplified to only depend on the BE lift as shown in eq. (36c).

$$\widehat{T}_{\text{BEM}} = \frac{N}{2\pi}\int_0^{2\pi}\int_0^R dF_{BL|Z\widehat{R},a}\,d\widehat{\psi} \tag{36a}$$

$$dF_{BL|Z\widehat{R},a} = cos(\widehat{\beta})dF_{BL|Z\widehat{BL},a} = cos(\widehat{\beta})(dL_{BL}cos(\phi_{BE}) - dD_{BL}sin(\phi_{BE})) \tag{36b}$$

If $\phi_{BE} \ll 1$, $dL_{BL} \gg dD_{BL}$, *and* $\widehat{\beta} \ll 1$ *then:*

$$\widehat{T}_{\text{BEM}} = \frac{N}{2\pi}\int_0^{2\pi}\int_0^R dL_{BL}\,d\widehat{\psi} \tag{36c}$$

After applying the small angle approximation to $\widehat{\beta}$ and substituting its remaining instances by the disk tilt angles, solving the integrals, and finally applying the expression reduction scheme yields an extensive expression for the BEM thrust defined in the non-rotating w.a. CP which may be generalized by eq. (37). The complete expression shall not be shown in this paper, however its simplified version is presented and analyzed in section III. Returning to the generalized form, it is important to highlight that the nacelle tilt rate, as well as the coning and lateral disk tilt angles are not considered significant enough to remain in the expression, while the body yaw rate is considered significant. Furthermore the BEM thrust is linear with respect to the longitudinal disk tilt angle and (non-dimensional) induced velocity.

$$\begin{aligned}\widehat{T}_{\text{BEM}} &= f(\eta, \widehat{a}_1, \lambda_i, \theta_{bl,0}, \theta_{bl,1}, \theta_{1s}, p, q, r)\\ &= A_{42}\widehat{a}_1 + A_{44}\lambda_i - B_4\end{aligned} \tag{37}$$

7. Hind H-Force

The H-force $\widehat{H}_{\text{BEM}}$ is obtained by integrating the BE aerodynamic hind force $F_{BL|-X\widehat{CP},a}$ parallel with the $X_{\widehat{CP}}$-axis along the blade length and taking the averaged-over-one-rotor-revolution hind force of all the N blades as given by eq. (38). The BE hind force is a combination of the aerodynamic tangential $F_{BL|-Y\widehat{R},a}$ and radial $F_{BL|-X\widehat{R},a}$ blade forces, as shown in the same equation and depicted on the LHS of fig. 19 provided in the appendix for clarity.

$$\widehat{H}_{\text{BEM}} = \frac{N}{2\pi}\int_0^{2\pi}\int_0^R dF_{BL|-X\widehat{CP},a}\,d\widehat{\psi} = \frac{N}{2\pi}\int_0^{2\pi}\int_0^R \left(\Omega_{sgn}dF_{BL|-Y\widehat{R},a}sin(\widehat{\psi}) - dF_{BL|-X\widehat{R},a}cos(\widehat{\psi})\right)d\widehat{\psi} \tag{38}$$

The blade tangential and radial forces are a combination of the BE lift and drag, as given by eqs. (39) and (40) respectively, which can be graphically derived based on figs. 17 and 18.

$$dF_{BL|-Y\widehat{R},a} = dF_{BL|-Y\widehat{BL},a} = \Omega_{sgn}\left(dL_{BL}sin(\phi_{BE}) + dD_{BL}cos(\phi_{BE})\right) \tag{39}$$

$$dF_{BL|-X\widehat{R},a} = sin(\widehat{\beta})dF_{BL|Z\widehat{BL},a} = sin(\widehat{\beta})(dL_{BL}cos(\phi_{BE}) - dD_{BL}sin(\phi_{BE})) \tag{40}$$

The BE drag is defined by eq. (41a) with the blade drag coefficient $C_{d,bl}$ being described by a second degree polynomial as given in eq. (41b) with $C_{d_0,bl}$, $C_{d_1,bl}$, and $C_{d_2,bl}$ being constants.

$$dD_{BL} = \frac{1}{2}\rho V^2_{BE|Y-Z\widehat{BL}}C_{d,bl}c_{bl}dr_{BE} \tag{41a}$$

$$C_{d,bl} = C_{d_0,bl} + C_{d_1,bl}\alpha_{BE} + C_{d_2,bl}\alpha^2_{BE} \tag{41b}$$

Similarly to the lift, the BE drag is also be simplified by assuming that the tangential BE velocity component is much greater than its perpendicular counterpart yielding the simplified and expanded expression shown in eq. (42).

If $U_T \gg U_P$, *then:*

$$dD_{BL} = \frac{1}{2}\rho c_{bl} U_T^2 \left(C_{d_0,bl} + C_{d_1,bl}\left(\theta_0 + \theta_{bl,1} r_{BE} - \frac{U_P}{U_T}\right) + C_{d_2,bl}\left(\theta_0 + \theta_{bl,1} r_{BE} - \frac{U_P}{U_T}\right)^2 \right) dr_{BE} \tag{42}$$

Applying the same simplifications as in the case of the rotor thrust, it can be seen that the radial blade force only depends on the BE lift, while the tangential force remains to depend on both the lift and drag as given by eqs. (43) and (44) respectively. The resulting rotor H-force simplifies to the expression shown in eq. (45).

If $\phi_{BE} \ll 1$, $dL_{BL} \gg dD_{BL}$, *and* $\widehat{\beta} \ll 1$ *then:*

$$dF_{BL|-Y\widehat{R},a} = \Omega_{sgn}\left(dL_{BL}\phi_{BE} + dD_{BL}\right) \tag{43}$$

$$dF_{BL|-X\widehat{R},a} = \widehat{\beta} dL_{BL} \tag{44}$$

$$\widehat{H}_{\text{BEM}} = \frac{N}{2\pi}\int_0^{2\pi}\int_0^{R}\left[sin(\widehat{\psi})\left(dL_{BL}\phi_{BE} + dD_{BL}\right) - \widehat{\beta}cos(\widehat{\psi})dL_{BL}\right]d\widehat{\psi} \tag{45}$$

After applying the small angle approximation to $\widehat{\beta}$ and substituting its remaining instances by the disk tilt angles, solving the integrals, and finally applying the expression reduction scheme yields an extensive expression for the H-force defined in the non-rotating w.a. CP which may be generalized by eq. (46). The complete expression shall not be shown in this paper, however its simplified version is presented and analyzed in section III. Returning to the generalized form, it is important to highlight that the lateral disk tilt angle is not considered significant enough to remain in the expression, while the nacelle tilt rate, body yaw rate, and all drag coefficient constants are considered significant. Furthermore the H-force is also linear with respect to the coning angle while several products of terms render the expression non-linear with respect to the longitudinal disk tilt angle and induced velocity.

$$\begin{aligned}\widehat{H}_{\text{BEM}} &= f(\eta, \dot{\eta}, \widehat{a}_0, \widehat{a}_1, \lambda_i, \theta_{bl,0}, \theta_{bl,1}, C_{d_0,bl}, C_{d_1,bl}, C_{d_2,bl}, \theta_{1s}, p, q, r) \\ &= A_{61}\widehat{a}_0 + A_{62}\widehat{a}_1 + A_{64}\lambda_i + f(\widehat{a}_1 \cdot \lambda_i) - B_6\end{aligned} \tag{46}$$

8. Side S-Force

The rotor S-force is derived in an analogous manner to the H-force based on the RHS of fig. 19 where the integral of the BE side force $F_{BL|-Y\widehat{CP},a}$ (parallel with the $Y_{\widehat{CP}}$-axis) along the blade length, and the averaged-over-one-rotor-revolution side force of all the N blades are taken as given by eq. (47).

$$\widehat{S}_{\text{BEM}} = \frac{N}{2\pi}\int_0^{2\pi}\int_0^{R} dF_{BL|-Y\widehat{CP},a} d\widehat{\psi} = \frac{N}{2\pi}\int_0^{2\pi}\int_0^{R}\left(dF_{BL|-Y\widehat{R},a}cos(\widehat{\psi}) + \Omega_{sgn}dF_{BL|-X\widehat{R},a}sin(\widehat{\psi})\right)d\widehat{\psi} \tag{47}$$

Once again applying the same simplifications as in the case of the hind force, the rotor S-force simplifies to the expression shown in eq. (45).

If $\phi_{BE} \ll 1$, $dL_{BL} \gg dD_{BL}$, *and* $\widehat{\beta} \ll 1$ *then:*

$$\widehat{S}_{\text{BEM}} = \frac{\Omega_{sgn}N}{2\pi}\int_0^{2\pi}\int_0^{R}\left[cos(\widehat{\psi})\left(dL_{BL}\phi_{BE} + dD_{BL}\right) + \widehat{\beta}sin(\widehat{\psi})dL_{BL}\right]d\widehat{\psi} \tag{48}$$

Performing the S-force derivation in the same way as the H-force, including the application of the expression reduction scheme, yields an extensive expression for the S-force defined in the non-rotating w.a. CP which may be generalized by eq. (49). The complete expression shall not be shown in this paper, however its simplified version is presented and analyzed in section III. Returning to the generalized form, it is important to highlight that this is the only rotor expression where all disk tilt angles are considered significant enough to remain in the expression. Furthermore the nacelle tilt rate, body yaw rate, and all drag coefficient constants are also considered significant. Finally the S-force is only linear with respect to the longitudinal disk tilt angle while several products of terms render the expression non-linear with respect to the coning and lateral disk tilt angles, as well as the induced velocity.

$$\begin{aligned}\widehat{S}_{\text{BEM}} &= f(\eta, \dot{\eta}, \widehat{a}_0, \widehat{a}_1, \widehat{b}_1, \lambda_i, \theta_{bl,0}, \theta_{bl,1}, C_{d_1,bl}, C_{d_2,bl}, \theta_{1s}, p, q, r) \\ &= A_{71}\widehat{a}_0 + A_{72}\widehat{a}_1 + A_{73}\widehat{b}_1 + A_{74}\lambda_i + f(\widehat{a}_0 \cdot \lambda_i) + f(\widehat{b}_1 \cdot \lambda_i) - B_7\end{aligned} \tag{49}$$

9. Solving for Coning Angles, Inflow, and Thrust

The resultant BEM force that is perpendicular to the w.a. disk plane may be finally determined making it possible to equate it with the momentum theory thrust $\widehat{T}_M$. The former is formally obtained with eq. (50a) which, after applying the small angle approximation to the disk tilt angles and performing the transformation, is shown to depend on the orthogonal BEM forces and the longitudinal and lateral disk tilt angles as can be seen in eq. (50b).

If $a_0 \ll 1$, $a_1 \ll 1$, *and* $b_1 \ll 1$ *then:*

$$\boldsymbol{F}_{r|\widehat{DP}} = \begin{pmatrix} -\widehat{H}_{\text{BEM}} \\ -\widehat{S}_{\text{BEM}} \\ -\widehat{T}_{\text{BEM}} \end{pmatrix}^T \boldsymbol{T}_{\widehat{CP}|\widehat{DP}} = \begin{pmatrix} -\widehat{H}_{\text{BEM}|\widehat{DP}} \\ -\widehat{S}_{\text{BEM}|\widehat{DP}} \\ -\widehat{T}_{\text{BEM}|\widehat{DP}} \end{pmatrix}^T \tag{50a}$$

$$\widehat{T}_{\text{BEM}|\widehat{DP}} = \widehat{T}_{\text{BEM}} + \widehat{H}_{\text{BEM}}\widehat{a}_1 - \widehat{S}_{\text{BEM}}\widehat{b}_1 \tag{50b}$$

The momentum theory thrust $\widehat{T}_M$, on the other hand, is inherently defined with respect to the w.a. disk plane and is given by given in eq. (51a). Here $\boldsymbol{V}_{R|\widehat{DP}}$ is the resultant of the combined body and induced velocity, defined in the w.a. disk plane, as given by eq. (51b). Note that the induced velocity is temporarily removed from the rotor hub velocity $\boldsymbol{V}_{hub|\widehat{CP}}$ in order to perform the transformation from the w.a. CP to the w.a. DP, ultimately resulting in the induced velocity being perpendicular to the disk plane in accordance with the momentum theory. The small angle approximation is once again applied to the disk tilt angles when performing this transformation yielding the simplified resultant velocity vector shown on the RHS of eq. (51b). It should be noted that according to [31] the momentum theory is only valid when the rotor is either in propeller state or in windmill brake state with an axial induction ratio a_{in} (simplified to = $v_{in}/\widehat{V}_{pc}$) no greater than 0.5.

$$\widehat{T}_M = 2\Omega R\lambda_i \left(\rho\pi R^2 \|\boldsymbol{V}_{R|\widehat{DP}}\|_2\right) \tag{51a}$$

If $\widehat{a}_0 \ll 1$, $\widehat{a}_1 \ll 1$, *and* $\widehat{b}_1 \ll 1$ *then:*

$$\boldsymbol{V}_{R|\widehat{DP}} = \left(\boldsymbol{V}_{hub|\widehat{CP}} - \begin{pmatrix} 0 \\ 0 \\ -v_{in} \end{pmatrix}^T\right) \boldsymbol{T}_{\widehat{CP}|\widehat{DP}} + \begin{pmatrix} 0 \\ 0 \\ -v_{in} \end{pmatrix}^T \{\boldsymbol{E}_{\widehat{DP}}\} = \Omega R \begin{pmatrix} \widehat{\mu}_{tc} - \widehat{a}_1\widehat{\lambda}_{pc} \\ \widehat{b}_1\widehat{\lambda}_{pc} \\ \widehat{a}_1\widehat{\mu}_{tc} + \widehat{\lambda}_{tot} \end{pmatrix}^T \{\boldsymbol{E}_{\widehat{DP}}\} \tag{51b}$$

Due to the non-linearity of the problem, an iterative feedback algorithm is used to solve for the five unknowns, i.e. the three disk tilt angles, induced velocity, and the rotor thrust, as informally described by eq. (52) where k is the number of iterations. Note that an attempt at linearizing this system of equations is made and discussed in [30, app. C], showing promising results. The presented rotor model, however, employs the non-linear iterative feedback method in order to avoid additional errors introduced by the linearization process.

$$\text{while } k \leq 1\text{e}3 \quad \text{find } \lambda_i \quad \text{such that } \left(\widehat{T}_{\text{BEM}|\widehat{DP}} - \widehat{T}_M\right) \leq 1\text{e}{-6} \tag{52}$$

10. Torque Q-Moment

The rotor derivation is concluded with the determination of the moments that it generates, starting with the torque $\widehat{Q}_{\text{BEM}}$ which is also obtained with the used of the BEM by integrating the moment generated by the BE aerodynamic tangential force $dF_{BL|-Y\widehat{R},a}$ along the blade length and taking the averaged-over-one-rotor-revolution torque of all the N blades as given by eq. (53).

$$\widehat{Q}_{\text{BEM}} = -\frac{N}{2\pi}\int_0^{2\pi}\int_0^R dF_{BL|-Y\widehat{R},a}\, r_{BE} cos(\widehat{\beta}) d\widehat{\psi} \tag{53}$$

Applying similar simplifications as has been done in the case of the BEM forces, the rotor torque simplifies to the expression shown in eq. (54). Note that here the BE lift is multiplied by the sine of the inflow angle. Recalling that the latter is considered small, the resulting product of the two may be of a similar order as the differential drag hence disregarding the BE drag may no longer be valid in this case.

If $\phi_{BE} \ll 1$ *and* $\widehat{\beta} \ll 1$ *then:*

$$\widehat{Q}_{\text{BEM}} = \frac{-\Omega_{sgn} N}{2\pi} \int_0^{2\pi} \int_0^R r_{BE} \left(dL_{BL} \phi_{BE} + dD_{BL} \right) d\widehat{\psi} \tag{54}$$

After applying the small angle approximation to $\widehat{\beta}$ and substituting its remaining instances by the disk tilt angles, solving the integrals, and finally applying the expression reduction scheme yields an extensive expression for the Q-moment defined in the non-rotating w.a. CP which may be generalized by eq. (55). The complete expression shall not be shown in this paper, however its simplified version is presented and analyzed in section III. Returning to the generalized form, it is important to highlight that the nacelle tilt rate, as well as the coning and lateral disk tilt angles are not considered significant enough to remain in the expression, while the body yaw rate and all drag coefficient constants are considered significant. Furthermore the rotor torque is non-linear with respect to the longitudinal disk tilt and, even more so, the induced velocity.

$$\begin{aligned} \widehat{Q}_{\text{BEM}} &= f(\eta, \widehat{a}_1, \lambda_i, \theta_0, \theta_{bl,1}, C_{d_0,bl}, C_{d_1,bl}, C_{d_2,bl}, \theta_{1s}, p, q, r) \\ &= A_{82}\widehat{a}_1 + A_{84}\lambda_i + f(\widehat{a}_1 \cdot \lambda_i) + f(\lambda_i^2) - B_8 \end{aligned} \tag{55}$$

11. Rotor Hub Spring Reaction Moments

The rolling and pitching moments acting on the rotor hub are given by eqs. (56) and (57) respectively, which are assumed to fully originate from the flapping spring reaction moment. The inertial and aerodynamic moments acting around the feathering and (missing) lead/lag hinges are assumed to be negligibly small. It can be seen that these spring reaction moments are only implicitly affected by the nacelle tilt through the lateral $\widehat{b}_1$ and longitudinal $\widehat{a}_1$ disk tilt angles respectively.

$$\widehat{O}_s = M_{hub|-X\widehat{CP},s} = -\frac{NK_\beta \widehat{b}_1}{2} \tag{56}$$

$$\widehat{P}_s = M_{hub|-Y\widehat{CP},s} = -\frac{NK_\beta \widehat{a}_1}{2} \tag{57}$$

B. Rotor Expression Reduction Scheme

The formal description of the reduction scheme used throughout the rotor derivation starts with the definition of the to-be-reduced expressions which are expected to be in polynomial form, also referred to as sum of terms (SoT), as given by eq. (58) where PoT_i and sgn_i is the i^{th} product of terms (PoT) and its sign in the expression, while NoT is the number of terms. Each PoT may be a single variable, or a product of terms (as the name suggests) as defined by eq. (59), where pow_i is the power to which the i^{th} term (T) is raised to.

$$\text{SoT} = \sum_{i=1}^{\text{NoT}} \text{sgn}_i \text{PoT}_i \tag{58}$$

$$\text{PoT} = \prod_{i=1}^{\text{NoT}} \text{T}_i^{\text{pow}_i} \tag{59}$$

Next, the order of each term must be found, indicated with the big-O notation as defined by eq. (60), where y represents the term, ϵ is the order basis, and n is the order (power) of the term. The order basis may be chosen freely (as shall be discussed later), while the order power n (also denoted by O^X) may be obtained with eq. (61) where X is the value of the term at hand. Note that the reduction scheme makes a distinction between the order of the maximum and minimum values of a PoT (the latter may be negative and larger than the maximum in the absolute sense) based on the (anticipated) minimum and maximum values of the constituting terms, enabling a less conservative determination of the order of a PoT (and SoT), as is described in detail in [30].

$$y = O(\epsilon^n) \quad \text{with} \quad 0 < \epsilon < 1 \quad \text{and} \quad n \in \mathbb{Z} \quad \text{such that} \quad |y| \leq \epsilon^n \tag{60}$$

$$n = O^X = \log_\epsilon(X) \tag{61}$$

The ultimate goal of the reduction scheme is to reduce an expression such that the introduced error as a result of the reduction is no greater than a single term that is just considered significant enough to be included in the expression, i.e. a term with the highest significant order (HSO), as formalized by eq. (62). The HSO depends on the order of the (absolute) largest term within the expression, referred to as the smallest present order (SPO), and the chosen Δ_0 parameter which specifies the allowable difference between the SPO and HSO, as given by eq. (63).

$$f = f_{\text{reduced}} + O(\epsilon^{HSO}) \qquad (62) \qquad HSO = \Delta_O + SPO \qquad (63)$$

The resulting expression reduction fractional error E_{EOS}, defined by eq. (64), is then guaranteed to be smaller than or equal to the order basis raised to the power of Δ_0, as shown in [30]. At this point it can be seen that ϵ and Δ_0 may be selected freely to achieve the desired maximum allowable reduction error which has been chosen to be 6.25% in the case of this research work, corresponding to $\epsilon = 0.5$ and $\Delta_0 = 4$.

$$E_{\text{EOS}} = \frac{f - f_{\text{reduced}}}{f_{\text{reduced}}} \leq \epsilon^{\Delta_O} \qquad (64)$$

In order to fulfill the guarantee presented above the tailored significance threshold T_{tail} must be calculated with eq. (65). Any terms that have an order smaller than or equal to T_{tail} are considered significant enough to remain in the reduced expression, while all other terms are removed.

$$T_{tail} = O^{M,\text{SoT}} + T_{ext} \qquad O^X \leq T_{\text{tail}} \implies \text{term } X \text{ is considered significant} \qquad (65)$$

In eq. (65) $O^{M,\text{SoT}}$ is the arithmetic mean of the orders of the terms within the SoT calculated with eq. (66), while T_{ext} is the (generic) threshold extension parameter which is proven to be equal to eq. (67) in [30]. Note that T_{ext} is completely expression independent (and only depends on the selected Δ_0 and ϵ parameters), thus the significance threshold T_{tail} is tailored to the specific expression by $O^{M,\text{SoT}}$ only. Also note that due to this extension the ordering scheme is referred to as the extended ordering scheme (EOS).

$$O^{M,\text{SoT}} = \log_\epsilon \left(\frac{\sum_{i=1}^{\text{NoT}} \epsilon^{\text{pow}_i}}{\text{NoT}} \right) \qquad (66) \qquad T_{ext} = (\Delta_O + 1) - \log_\epsilon \left(\frac{1 + \epsilon^{\Delta_O}}{1 + \epsilon^{-1}} \right) \qquad (67)$$

The presented ordering scheme has been automated with the use of the Python programming language [32], which is referred to as the automatic ordering scheme (AOS), with the inclusion of a rounding factor (RF) which is multiplied by the threshold extension parameter as shown in eq. (68). This parameter extends the threshold even further ensuring that, even in a limit case, all terms that should be kept, will be kept despite any numerical rounding errors introduced by the Python implementation. In this research work this parameter has been set to a value of 1.01 allowing for a 1% numerical rounding error.

$$T_{tail} = O^{M,\text{SoT}} + RF \cdot T_{ext} \qquad (68)$$

It is also worthwhile to highlight that in the case of a numerical model finding the significance of a term would require one to simulate possibly a broad range of limiting conditions in hopes of finding cases where that term is most significant, yet still without the guarantee for it.

C. Lifting Surfaces and Fuselage

The main wing and tail stabilizers are approximated with trapezoidal planforms and flat plate aerodynamics. Most control surfaces have a linear aerodynamic effectiveness with the exception of flaps which are modeled as (movable) flat plates. These components are described in more detail in [30].

The rotor wash effect on the lifting surfaces (ls) is incorporated in the tilt-rotor model by adding the axial rotor wash (rw) component V_{rw} to the velocity vector experienced by the lifting surface mean aerodynamic chord (MAC) aerodynamic center (AC) $\overline{AC}$ as shown in eq. (69). The rotor is assumed not to induce any other wash velocity components.

$$\boldsymbol{V}_{\overline{AC}|ls} \leftarrow \boldsymbol{V}_{\overline{AC}|ls} + \begin{pmatrix} 0 & 0 & V_{rw} \end{pmatrix} \boldsymbol{T}_{CP|ls}\{\boldsymbol{E}_{ls}\} \qquad (69)$$

The rotor wash itself is based on the "contracted stream-tube" [17, p6] model as shown in eq. (70). Here the rotor wash velocity is determined at a perpendicular distance z_{rw} away from the rotor disk, and the lifting surface is only affected by the rotor wash if its MAC AC is located within the cylindrical volume below the rotor disk. This condition is checked with the use of x_{rw} and y_{rw} which are the longitudinal and lateral distances (measured along the $X-$ and Y-axes of the control plane) between the rotor hub and the lifting surface MAC AC. The complete vector between the rotor hub and lifting surface MAC AC is calculated with eq. (71).

$$V_{rw} = \begin{cases} v_{in}\left(1 + \dfrac{z_{rw}/R}{\sqrt{1+(z_{rw}/R)^2}}\right) & \text{if} \quad \sqrt{x_{rw}^2 + y_{rw}^2} \le R \quad \text{and} \quad z_{rw} \ge 0 \\ 0 & \text{otherwise} \end{cases} \tag{70}$$

$$\begin{pmatrix} x_{rw} & y_{rw} & z_{rw} \end{pmatrix} \{\boldsymbol{E}_{CP}\} = \boldsymbol{s}_{\overline{AC}-hub|CP} = \left(\boldsymbol{s}_{hub|b} - \boldsymbol{s}_{\overline{AC}|b}\right) \boldsymbol{T}_{b|CP} \{\boldsymbol{E}_{CP}\} \tag{71}$$

The fuselage is the final airframe component which is simplified to only generate drag based on its equivalent flat plate area.

D. Rotor RPM Dynamics and Collective Governor

The rotor RPM dynamics are implemented based on the GTRS model described in [7, p. A-270], with the torque generated by each rotor taken to be the Q-moment calculated with eq. (54). One of the required inputs for this subsystem includes the torque generated by the engines which is also based on the GTRS model, however only the minimally required portions of the full drivetrain have been implemented for simplicity reasons as described in more detail in [30]. Curve fitting has been employed to obtain a continuous function for the direct relationship between the collective-throttle stick displacement $X_{\text{COL,thr}}$ and the commanded engine horsepower R_{SHP} mentioned in, with the result being a fourth order polynomial as given by eq. (84) in the appendix.

The collective governor is also included in the 6DoF model and is based on the GTRS, however only the minimally-required elements of the primary system described in [7, A-254, fig.A17-1] are implemented, neglecting all failure monitors. This collective governor implementation introduces the operating rotor speed RPM_{SEL}. The top level block diagram of this simplified collective governor model is shown in fig. 20 in the appendix.

E. Trimming Routine

The 6DoF model is trimmed with the use of the Matlab optimization routine *fmincon* which aims to minimize the objective function Z consisting of the absolute largest linear or rotational acceleration of the body as given by eq. (72). As a result the employed trim routine may only provide a trim solution to un-accelerated flight conditions including straight and level flight, climbing flight, sideslip flight, or sideward flight. Each trim solution is also inspected for feasibility by checking whether any of the predefined limits are exceeded, including the pilot stick and pedal travel limits, flapping magnitude, required engine power, collective governor swashplate limits, and the rotor hub swashplate limits.

$$Z = \max\left(\text{abs}\left(\{\dot{u}, \dot{v}, \dot{w}, \dot{p}, \dot{q}, \dot{r}, \}\right)\right) \tag{72}$$

F. Model and Simulation Setup

All the equations that define the flight characteristic model of the 6DoF tilt-rotor have been implemented in Matlab following an object oriented programming (OOP) organization structure with each component group, i.e. the rotors, lifting surfaces, and fuselage, being defined by their own class. All component instances are then collected together by a single instance of the tilt-rotor class which determines the correct order of calculation of all the forces and moments acting on the body, and calculates the body state derivatives. The OOP structure is chosen mainly due to it being widely known and providing more approachable code that is easier to maintain and expand in the future.

The Matlab model is incorporated into a simulation environment with the use of Simulink which takes care of the time integration of all the model states and allows for the connection of the model with a graphical flight simulator such as FlightGear [33]. Figure 5 presents the top level block diagram corresponding to the implementation of the tilt-rotor simulation in Simulink with the 6DoF tilt-rotor Matlab model only being one of the multiple elements that comprise the entire simulation. It should also be noted that the RPM dynamics, drivetrain, and collective governor have been directly implemented in Simulink instead of in the Matlab model.

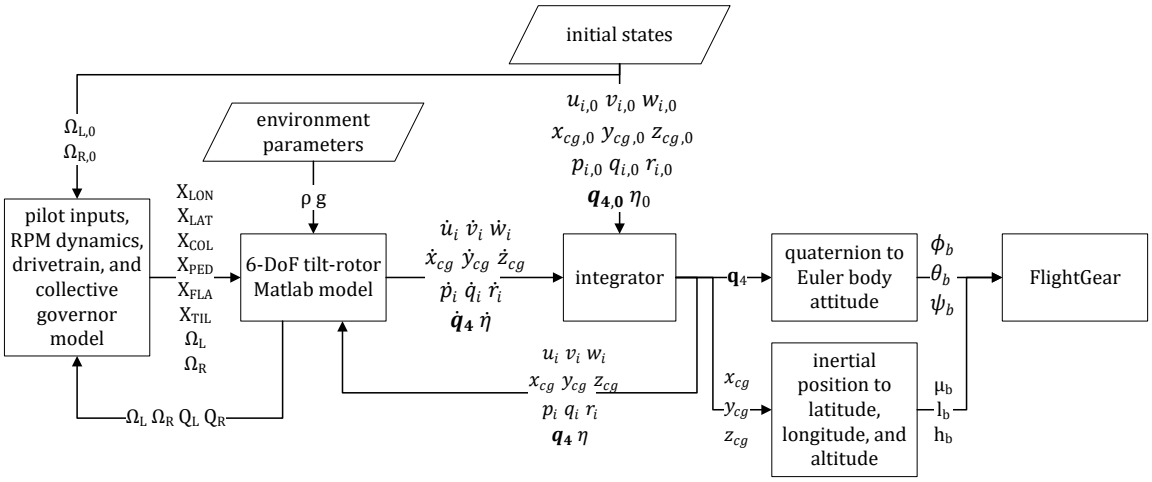

Fig. 5 Top level block diagram of the Simulink simulation implementation.

III. Model Validation and Analysis

The results of the 6DoF tilt-rotor model verification, validation, and analysis process performed in [30] are summarized in this section starting with the validation of the 6DoF model against the GTRS model implementation of the XV-15 tilt-rotor [7–9]. The aircraft and simulation parameters used in the 6DoF model implementation of the XV-15 model are provided in [30]. Next several critical assumptions are briefly verified, and the section is concluded with an analysis of the effect of the tiltable nacelle on the tilt-rotor flight mechanics.

A. Model Validity

The developed 6DoF tilt-rotor model shows good flight mechanics characteristics that are representative of a generic tilt-rotor aircraft based on the high similarity in trim curve trends and dynamic responses when compared to the GTRS model. The 6DoF model does not predict the flight characteristics of the specific XV-15 aircraft well enough for it to be considered valid for this aircraft. It is hypothesized that this specific validity may be considerably improved by selecting more accurate model parameters without changing or re-deriving the governing equations.

1. Conversion Corridor

The 6DoF model is also validated based on its conversion corridor, shown in fig. 6, which is generated based on the unaccelerated, longitudinal, and level flight limits. In general the 6DoF conversion corridor is considered mostly valid, predicting the higher velocity limits close to helicopter mode, and lower velocity limits close to airplane mode, quite well when compared to the real XV-15 conversion corridor. However, the 6DoF model significantly underpredicts the lower velocity limits for nacelle angles ranging between $-10°$ and $-45°$, while greatly overpredicting the upper velocity limits for nacelle angles ranging between $-60°$ and airplane mode. The real XV-15 conversion corridor is hypothesized to be additionally limited by model factors that are outside of the scope of this research project, such as diverging aeroelasticity, exceeded structural loads, or operational safety, resulting in the large differences between the 6DoF model and real life conversion corridors at lower velocities in conversion flight and higher velocities near airplane mode.

The trimming routine used to generate the conversion corridor additionally outputs data about the factors that bound the feasible region of flight of the 6DoF model, plotted onto the conversion corridor in fig. 7. It can be seen that the upper velocity limit of the 6DoF model conversion corridor is bounded by insufficient engine power and throttle range, with the next limiting factor being either the flapping magnitude, a maxed-out swashplate collective angle, or a combination of both. Sparse data is available for the limiting factors of the lower velocity range, however close to helicopter configuration the conversion corridor is limited by an exceeded flapping angle.

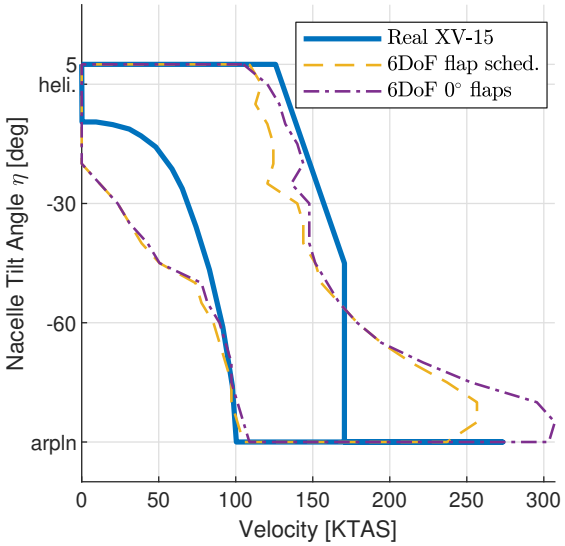

Fig. 6 Comparison between the conversion corridors of the 6DoF tilt-rotor model with and without flap deflection, and the real XV-15 tilt-rotor.

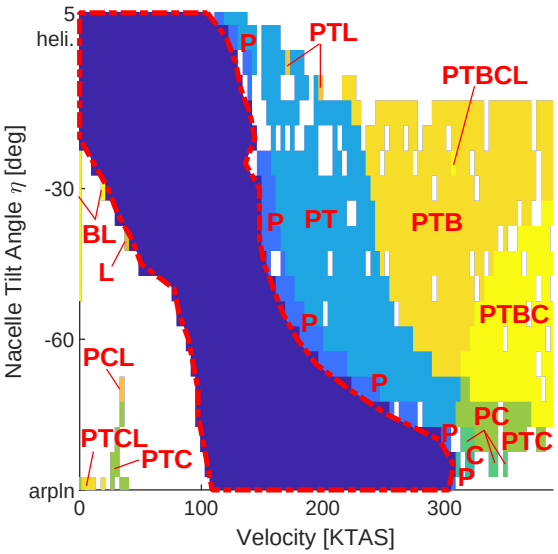

Fig. 7 6DoF tilt-rotor model (without flap deflection) conversion corridor additionally indicating infeasible regions with exceeded limits consisting of the pilot throttle (T) and longitudinal stick (L) deflections, total swashplate collective (C), flapping angle magnitude $|\beta|$ (B), and required engine power (P).

2. Rotor Thrust vs Torque Validity

The rotor model is validated by comparing the relation between the rotor thrust and torque of both the 6DoF and GTRS models as shown in fig. 8. Here it can be seen that both models show a positive parabolic correlation between the thrust and torque, however the 6DoF model overpredicts the torque at low thrust, and underpredicts it at high thrust. This discrepancy is attributed to a mismatch of the blade drag coefficients while the 6DoF model expressions for the rotor thrust and torque are considered valid for a generic tilt-rotor.

B. Lateral Trim and Dynamic Response Validity

The tilt-rotor is also validated by comparing the lateral flight trim curves and dynamic responses of both the 6DoF and GTRS models in helicopter and airplane configurations. The sideward and sideslipping flight trim curves are shown in fig. 21, while the dynamic responses are shown in fig. 22, both provided in the appendix. The validity performance of the 6DoF model is summarized in table 1.

The milder pitch response of the 6DoF model in hover is hypothesized to be caused by a deficiency of the horizontal tail stabilizer which overdamps the pitch response. The initial pitch response, however, hints that the rotor pitch effectiveness is valid. The underestimation of the yaw response is hypothesized to be caused by the invalidity of the vertical tail stabilizers.

C. Assumption Verification

Based on the numerically obtained flapping response (in the time domain) to a vertical rotor hub acceleration, the effect of the gravitational acceleration on the flapping equation has been verified to be negligible resulting in only a 2% difference in steady state solution. Furthermore the transient response settles to within 5% of the final value in under two revolutions, verifying the assumption that the transient flapping response resolves within two blade revolutions.

Based on the simulated variation of the blade element aerodynamic states across the rotor disk, the assumption that the blade element lift is much greater than blade element drag is considered verified for critical flight conditions, and thus is considered acceptable. However, several assumptions have been shown to be violated and thus are due for a revision in future iterations of the 6DoF model. First of all, the the small inflow angle assumption has been shown to be

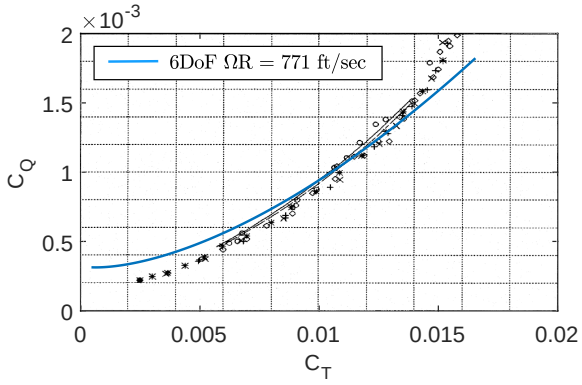

Fig. 8 6DoF tilt-rotor model left clockwise-rotating rotor thrust-torque correlation in a tie-down hover test plotted against the rotor thrust-torque correlation data of the GTRS model (black lines) and real XV-15 tilt-rotor (shapes) [9, p. 14 fig. 3].

Table 1 Summary of lateral trimmed state (trim.) and dynamic (dyn.) response (resp.) validity performance of the 6DoF model in hover and airplane (arpln) modes.

Flight Condition	Validity Performance
trim. hover sideward	lateral stick deflection underpredicted and does not follow piecewise linear trend
trim. arpln sideslip	lateral stick deflection greatly overpredicted but follows linear trend
dyn. hover pitch resp.	similar amplitude but slightly more damped, hypothesized to be caused by a deficiency of the horizontal tail stabilizer; initial pitch response hints that the rotor pitch effectiveness is valid
dyn. hover yaw resp.	small non-linearly growing underprediction
dyn. arpln pitch resp.	only valid when elevator effectiveness halved; short period mode similar amplitude but lower frequency and more damped; phugoid mode observable, heavily damped and distorted by collective governor
dyn. arpln. roll resp.	significantly more damped; highly damped aperiodic mode and (stable) spiral mode observable
dyn. arpln yaw resp.	similar amplitude but lower frequency; clear Dutch-roll mode not observed

grossly violated in airplane mode as expected, while in helicopter mode it is only violated near the rotor hub. Moreover, linearizing the inflow angle (i.e. eq. (28a)) has been shown to introduce large errors across the entire rotor disk in airplane mode, while in helicopter mode significant errors once again only appear near the rotor hub. The absolute percentage differences between the non-linear and linear inflow angles in helicopter and airplane configurations are shown in fig. 9a and fig. 9b respectively. Finally, simplifying the total longitudinal velocity experienced by the blade element to equal to its tangential component (i.e. eq. (28b)) only also introduces considerable errors across entire disk in airplane mode. In helicopter configuration mode the error is much smaller and confined to the rotor hub region. The absolute percentage differences between the nominal and simplified total longitudinal velocity in helicopter and airplane configurations are shown in fig. 9c and fig. 9d respectively.

D. Effect of Tiltable Proprotor on Rotor Expressions

An extensive visual inspection has been carried out in order to determine the effect of the nacelle tilt angle η and tilt rate $\dot{\eta}$ on the analytical rotor expressions mentioned throughout the rotor derivation. The rotor hub velocity components are treated first, followed by the effect on the blade element velocity components, inertial and aerodynamic flapping moment expressions, the disk tilt angles, and rotor forces and moments.

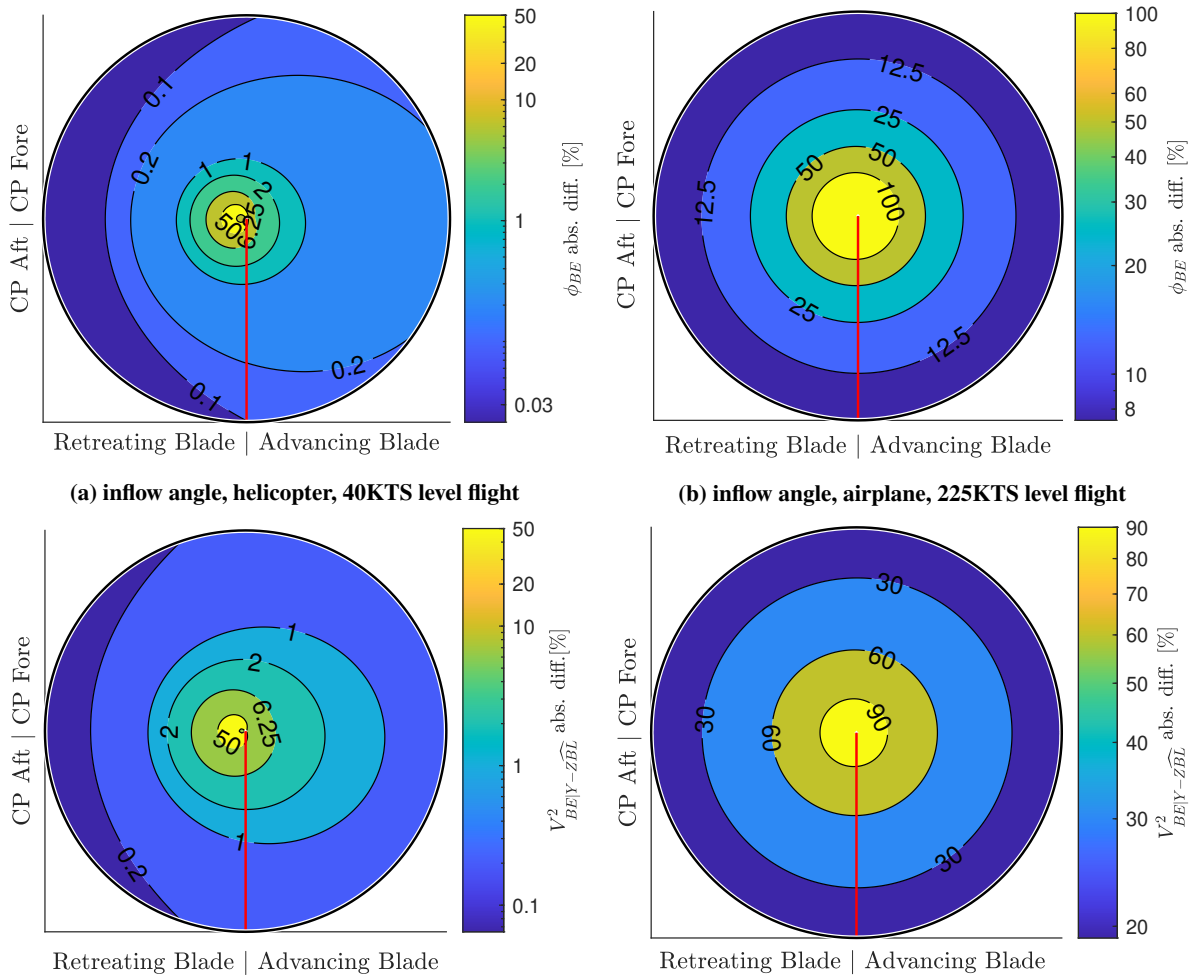

(a) inflow angle, helicopter, 40KTS level flight

(b) inflow angle, airplane, 225KTS level flight

(c) velocity, helicopter, 40KTS level flight

(d) velocity, airplane, 225KTS level flight

Fig. 9 Variation of the percentage difference between the non-linear and linearized blade element inflow angle and total longitudinal velocity across the rotor disk in helicopter and airplane configurations.

1. Rotor Hub Velocity Components in Control Plane

The rotor hub velocity components defined in the control plane are given by eq. (73). Here it can be seen that almost all terms within the rotor hub velocity components' expressions are affected by either a trigonometric function of the nacelle tilt angle η, the nacelle tilt rate $\dot{\eta}$, or the length of the tiltable nacelle l_n. The lateral-tangential velocity component V_{tc2} is not affected by the nacelle tilt rate at all while the longitudinal-tangential V_{tc1} and perpendicular V_{pc} components are. Simply adding the nacelle tilt-rate to the (total aerodynamic) body pitch rate q is not permissible in some cases due to the fact that the velocity experienced by the nacelle pivot point does not depend on the nacelle tilt rate.

$$\boldsymbol{V}_{hub|CP} = \begin{pmatrix} V_{tc1} \\ V_{tc2} \\ V_{pc} \end{pmatrix}^T \{\boldsymbol{E}_{CP}\} = \begin{pmatrix} \begin{array}{l} \left(-d_{sgn}\, d_{yn}\, r - d_{zn}\, q + u\right) C_\eta C_{\theta 1s} \\ -\left(d_{sgn}\, d_{yn}\, p + d_{xn}\, q + w\right) S_\eta C_{\theta 1s} - l_n\, \left(\dot{\eta} + q\right) C_{\theta 1s} \\ +\left(d_{sgn}\, d_{yn}\, p + d_{xn}\, q + w\right) C_\eta S_{\theta 1s} \\ -\left(d_{sgn}\, d_{yn}\, r + d_{zn}\, q - u\right) S_\eta S_{\theta 1s} \end{array} \\ \hdashline \left(-l_n\, S_\eta - d_{xn}\right) r + \left(l_n\, C_\eta + d_{zn}\right) p + v \\ \hdashline \begin{array}{l} \left(d_{sgn}\, d_{yn}\, r + d_{zn}\, q - u\right) C_\eta S_{\theta 1s} \\ +\left(d_{sgn}\, d_{yn}\, p + d_{xn}\, q + w\right) S_\eta S_{\theta 1s} + l_n\, \left(\dot{\eta} + q\right) S_{\theta 1s} \\ +\left(d_{sgn}\, d_{yn}\, p + d_{xn}\, q + w\right) C_\eta C_{\theta 1s} \\ -\left(d_{sgn}\, d_{yn}\, r + d_{zn}\, q - u\right) S_\eta C_{\theta 1s} \end{array} \end{pmatrix}^T \{\boldsymbol{E}_{CP}\} \tag{73}$$

2. Blade Element Velocity Components

All three blade element velocity components, i.e. the radial U_R, tangential U_T, and perpendicular U_P components given in eq. (74), are affected by the nacelle tilt angle, however not all influences are explicit. The radial component is affected only implicitly through the rotor hub velocity, while the tangential and perpendicular components additionally include explicit instances of the nacelle tilt angle giving rise to so-called 'effective' and 'total' rates.

'Effective' rates are defined to be the combination of two orthogonal body rotational rates that phase each other out as a trigonometric function of the nacelle tilt angle, while the 'total' rate corresponds to the combined nacelle tilt rate and body pitch rate. Both of these definitions are applicable to rotational accelerations which are then referred to as 'effective' and 'total' accelerations.

Although 'total' rates appear in both tangential and perpendicular velocity components, in several cases simply adding the nacelle tilt rate $\dot{\eta}$ to the body pitch rate q is not permissible due to the presence of the nacelle pivot velocity terms (which do not depend on the nacelle tilt rate) within the rotor hub velocities.

$$U_R = \left(v_{in} - \widehat{V_{pc}}\right) S_{\widehat{\beta}} - \widehat{V_{tc}} C_{\widehat{\psi}} C_{\widehat{\beta}} \tag{74a}$$

$$\begin{aligned} U_T = \widehat{V_{tc}} S_{\widehat{\psi}} + r_{BE} \Big[& \left(\left[(pS_\eta + rC_\eta) S_{\theta 1s} + (pC_\eta - rS_\eta) C_{\theta 1s} \right] S_\Delta - (q + \dot{\eta}) C_\Delta \right) S_{\widehat{\psi}} S_{\widehat{\beta}} \\ & + \Omega_{sgn} \left((q + \dot{\eta}) S_\Delta + \left[(pS_\eta + rC_\eta) S_{\theta 1s} + (pC_\eta - rS_\eta) C_{\theta 1s} \right] C_\Delta \right) C_{\widehat{\psi}} S_{\widehat{\beta}} \\ & + \left(\Omega + \Omega_{sgn} \left[(pC_\eta - rS_\eta) S_{\theta 1s} - (pS_\eta + rC_\eta) C_{\theta 1s} \right] \right) C_{\widehat{\beta}} \Big] \end{aligned} \tag{74b}$$

$$\begin{aligned} U_P = & \left(v_{in} - \widehat{V_{pc}}\right) C_{\widehat{\beta}} + \widehat{V_{tc}} C_{\widehat{\psi}} S_{\widehat{\beta}} \\ & + r_{BE} \Big[\dot{\widehat{\beta}} - \Omega_{sgn} \left((q + \dot{\eta}) S_\Delta + \left[(pS_\eta + rC_\eta) S_{\theta 1s} + (pC_\eta - rS_\eta) C_{\theta 1s} \right] C_\Delta \right) S_{\widehat{\psi}} \\ & + \left(\left[(pS_\eta + rC_\eta) S_{\theta 1s} + (pC_\eta - rS_\eta) C_{\theta 1s} \right] S_\Delta - (q + \dot{\eta}) C_\Delta \right) C_{\widehat{\psi}} \Big] \end{aligned} \tag{74c}$$

3. Flapping Equation and Disk Tilt Angles

The flapping equation is provided in the appendix (due to its extensiveness) as defined by eq. (82) which combines both the inertial $M_{BL|Y\widehat{R},i}$ and aerodynamic $M_{BL|Y\widehat{R},a}$ flapping moments into one expression. Several terms are grouped together based on their physical interpretation as indicated by the right-hand-side annotations. Note that this expression has already been linearized with respect to $\widehat{\beta}$ and all second and higher flapping harmonics have been removed. Also note that the complete flapping equation has been simplified for the purpose of visual inspection, which includes setting the CP deflection θ_{1s} and w.a. shift angles Δ, as well as the linearly varying blade twist parameter $\theta_{bl,1}$ to zero. The effect of the tiltable proprotor on the inertial terms is treated first, followed by the effect on the aerodynamic terms.

Analogously to the blade element velocity components, instances of 'effective' and 'total' rates and accelerations appear in the inertial terms. To be more precise, the nacelle tilt acceleration $\ddot{\eta}$ may be added to the inertial body pitch acceleration $\dot{q}_i$ when calculating the inertial effect of angular acceleration on the flapping motion, and the nacelle tilt rate may be simply added to the body pitch rate q_i in the centrifugal spring portion of the inertial flapping moment. However, the nacelle tilt rate may not be added to the body pitch rate when calculating the Coriolis effect of the pitching motion on the flapping dynamics, contradicting what is found in [15]. Furthermore the nacelle tilt rate and acceleration may not be simply added to the body pitch rate and acceleration in the rotor hub acceleration components since these contain the pivot acceleration terms that only depend on the body rates and accelerations and not on the nacelle tilt rate and acceleration. The inertial flapping moment also contains terms that are only present in conversion mode and thus are unique to the tiltable proprotors, one of which is the Coriolis effect of the nacelle tilt on the flapping dynamics. Regarding the flapping motion of the blade, the nacelle tilt rate always increases the flapping angle $\widehat{\beta}$, and the nacelle tilt angle swaps the effect of the body roll and yaw rate on the flapping angle where the yaw rate decreases the flapping angle in helicopter mode and increases the flap angle in airplane mode, while the opposite is true for the roll rate.

The aerodynamic flapping moment terms also contain 'effective' and 'total' rates which consist of explicit instances of the nacelle tilt angle and rate. Specifically, the nacelle tilt angle swaps the effect of the body roll and yaw rate on the aerodynamic damping term in the aerodynamic flapping moment, and the nacelle tilt rate may be simply added to the body pitch rate in both the aerodynamic spring and excitation terms of the aerodynamic moment. The nacelle tilt is also implicitly present in the rotor hub linear velocity terms.

Although not shown in this paper, the coning $\widehat{a}_0$, longitudinal $\widehat{a}_1$, and lateral $\widehat{b}_1$ disk tilt angles are also affected by the tiltable proprotor, however only the significant effects (as determined by the extended ordering scheme) are summarized here. The resulting reduced expressions of all three disk tilt angles continue to contain 'effective' rates and rotor hub linear velocities which implicitly contain the nacelle tilt angle and rate. However, the coning angle $\widehat{a}_0$ is not affected by the nacelle tilt rate at all, while there is only one occurrence of the tilt rate in each of the longitudinal and lateral disk tilt angle expressions. In the latter case the nacelle tilt rate may be simply added to the body pitch rate providing the only instance of a 'total' rate among all disk tilt angle expressions.

4. BEM Thrust

Similarly to the disk tilt angles, the BEM rotor thrust $\widehat{T}_{BEM}$ expression has been reduced with the automated ordering scheme leaving only the terms that are considered significant. Therefore only the significant effects of the tiltable proprotor on the BEM thrust are mentioned here. Moreover, the expression has been further simplified for the purpose of visual inspection in an identical manner as the flapping equation. The above also applies to the H- and S-forces, as well as the Q-moment treated later. Note that all 'effective' and 'total' rates henceforth are substituted by single variables identified with 'eff' and 'tot' subscripts for the sake of expression brevity, while several rotational rates are also non-dimensionalized as indicated by an overbar. The formal definitions of all of these are provided by eq. (83) in the appendix. Finally, all force and moment expressions are grouped according to their dependence on the disk tilt angles and their counter-rotating-rotors symmetry as indicated by the right-hand-side annotations.

The BEM thrust, as given by eq. (75), also contains 'effective' rates and is implicitly affected by the nacelle tilt angle and rate through the rotor hub linear velocities. However, the reduction scheme does not consider the (explicit) nacelle tilt rate to be a significant contributor to the BEM thrust therefore this expression does not contain any explicit $\dot{\eta}$ terms. The thrust expression obtained with the use of the momentum theory (not shown here) is also implicitly affected by the tiltable proprotor through the rotor hub linear velocities.

$$
\begin{aligned}
\widehat{T}_{\text{BEM}} = \frac{I_{bl}\gamma_{bl}N\Omega^2}{R}\Bigg[& -\frac{\Omega_{sgn}}{6}\left(\overline{p}_{eff}\theta_0 - \frac{3\overline{r}_{w,eff}\widehat{\mu}_{tc}}{4} + \frac{3\overline{p}_{eff}\widehat{\lambda}_{pc}}{4}\right)\widehat{a}_1 && (\widehat{a}_1\text{-dependent}) \\
& + \frac{\theta_0}{6}\left(\overline{r}_{eff}^2 - \overline{r}^2 C_\eta^2 + \frac{3\widehat{\mu}_{tc}^2}{2} + 1\right) + \frac{\widehat{\lambda}_{tot}}{4} && (\text{free symmetrical}) \\
& - \frac{\Omega_{sgn}}{6}\left(2\theta_0\overline{r}_{eff} + \frac{3\overline{r}_{eff}\widehat{\lambda}_{tot}}{2} - \frac{3\overline{p}_{eff}\widehat{\mu}_{tc}}{4}\right)\Bigg] && (\text{free asymmetrical})
\end{aligned}
\tag{75}
$$

5. Hind H- and Side S-Forces

Almost identical conclusions may be made about the effect of the tiltable proprotor on the (reduced) rotor hind H-force ($\widehat{H}_{BEM}$, given by eq. (76)) and side S-force ($\widehat{S}_{BEM}$, given by eq. (77)). First of all, instances of 'effective' rates are present in both expressions, and the nacelle tilt angle and rate has an implicit effect through the rotor hub velocity components. The nacelle tilt rate may be simply added to the body pitch rate in some cases giving rise to 'total' rates, however in other cases $\dot{\eta}$ is considered insignificant leaving sole q terms. Finally both H- and S-force expressions contain terms that only exist in conversion configuration making them unique to tiltable proprotors.

$$
\begin{aligned}
\widehat{H}_{\text{BEM}} = \frac{\Omega^2 I_{bl}\gamma_{bl}N}{R}\Bigg[& \frac{3\theta_0\widehat{\lambda_{pc}}-2}{24}\overline{q}\widehat{a}_0 && (\widehat{a}_0\text{-dependent}) \\
& + \Bigg(\frac{\overline{r}_{eff}^2-\overline{r}^2C_\eta^2+\overline{r}_{eff}\overline{r}_{i,eff}+2}{12}\theta_0+\frac{3\widehat{\lambda_{tot}}}{8} && (\text{sym. } \widehat{a}_1\text{-dep.}) \\
& - \Omega_{sgn}\left\{\frac{\overline{r}_{eff}+2\overline{r}_{i,eff}}{8}\widehat{\lambda_{tot}}+\frac{3\overline{r}_{eff}+\overline{r}_{i,eff}}{12}\theta_0+\frac{\overline{p}_{eff}\widehat{\mu}_{tc}}{32}\right\}\Bigg)\widehat{a}_1 && (\text{asym. } \widehat{a}_1\text{-dep.}) \\
& + \frac{\overline{p}_{eff}\overline{r}_{eff}-3\widehat{\mu}_{tc}\widehat{\lambda}_{tot}}{12}\theta_0+\frac{\widehat{\mu}_{tc}C_{d_0,bl}}{4C_{l_\alpha,bl}} && (\text{free symmetrical}) \\
& -\Omega_{sgn}\left(\frac{\theta_0}{12}+\frac{\widehat{\lambda}_{tot}}{4}\right)\overline{p}_{eff}\Bigg] && (\text{free asymmetrical})
\end{aligned}
\tag{76}
$$

$$
\begin{aligned}
\widehat{S}_{\text{BEM}} = \frac{\Omega^2 I_{bl}\gamma_{bl}N}{R}\Bigg[& \Bigg(\Omega_{sgn}\frac{3\theta_0+6\widehat{\lambda}_{tot}}{8}\widehat{\mu}_{tc} && (\text{sym. } \widehat{a}_0\text{-dep.}) \\
& + \frac{\overline{p}_{eff}}{12}-\frac{\overline{p}_{eff}\widehat{\lambda}_{tot}+3\overline{r}_{eff}\widehat{\mu}_{tc}}{8}\theta_0\Bigg)\widehat{a}_0 && (\text{asym. } \widehat{a}_0\text{-dep.}) \\
& + \Bigg(-\Omega_{sgn}\frac{7(\overline{q}+\overline{\dot{\eta}})}{32}\widehat{\mu}_{tc} && (\text{sym. } \widehat{a}_1\text{-dep.}) \\
& + \frac{\overline{p}_{eff}\overline{q}\theta_0}{24}\Bigg)\widehat{a}_1 && (\text{asym. } \widehat{a}_1\text{-dep.}) \\
& \Bigg(-\frac{3\widehat{\mu}_{tc}+\overline{r}_{eff}\overline{r}_{i,eff}+2}{12}\theta_0-\frac{3\widehat{\lambda}_{tot}}{8} && (\text{sym. } \widehat{b}_1\text{-dep.}) \\
& + \Omega_{sgn}\left\{\frac{3\overline{r}_{eff}+\overline{r}_{i,eff}}{12}\theta_0+\frac{8\overline{r}_{i,eff}\widehat{\lambda}_{tot}-5\overline{p}_{eff}\widehat{\mu}_{tc}+4\overline{r}_{eff}\widehat{\lambda}_{pc}}{32}\right\}\Bigg)\widehat{b}_1 && (\text{asym. } \widehat{b}_1\text{-dep.}) \\
& - \Omega_{sgn}\frac{(\overline{q}+\overline{\dot{\eta}})(\widehat{3\lambda}_{tot}+\theta_0)}{12} && (\text{free symmetrical}) \\
& + \frac{\overline{\dot{\eta}}\overline{p}S_\eta+\overline{r}_{eff}\overline{q}}{12}\theta_0\Bigg] && (\text{free asymmetrical})
\end{aligned}
\tag{77}
$$

6. Torque Q-Moment

The rotor torque Q-moment ($\widehat{Q}_{BEM}$, given by eq. (78)) also contains 'effective' rates and rotor hub velocity terms presenting both explicit and implicit effects of the tiltable proprotor. However, the explicit instances of the nacelle tilt rate are not considered significant at all therefore the Q-moment expression does not have any explicit $\dot{\eta}$ terms. Finally the rotor torque expression also contains terms that only exist in conversion configuration making them unique to tiltable proprotors.

$$
\begin{aligned}
\widehat{Q}_{\text{BEM}} = \Omega^2 I_{bl}\gamma_{bl} N \Bigg[\frac{1}{8} \Bigg(& \Omega_{sgn}\left(\overline{p}_{eff}\overline{r}_{i,eff} + 2\widehat{\mu}_{tc}\widehat{\lambda}_{tot}\right) && \text{(sym. } \widehat{a}_1\text{-dep.)} \\
& + \frac{2}{3}\left(\overline{r}_{w,eff}\widehat{\mu}_{tc} - \overline{p}_{eff}\widehat{\lambda}_{pc} + \overline{p}C_\eta\lambda_i\right)\theta_0 - \overline{p}_{eff}\Bigg)\widehat{a}_1 && \text{(asym. } \widehat{a}_1\text{-dep.)} \\
& + \Omega_{sgn}\left(\frac{\widehat{\lambda}_{tot}^2}{4} + \frac{\widehat{\lambda}_{tot}\theta_0}{6} + \frac{\overline{p}_{eff}^2}{16} - \frac{C_{d_0,bl}}{8C_{l_\alpha,bl}}\right) && \text{(free symmetrical)} \\
& + \frac{1}{12}\left(\overline{p}_{eff}\widehat{\mu}_{tc} - 2\overline{r}_{eff}\widehat{\lambda}_{tot}\right)\theta_0 \Bigg] && \text{(free asymmetrical)}
\end{aligned} \tag{78}
$$

E. Effect of Nacelle Tilt Rate on Handling and Performance

A set of longitudinal and level flight trim curves has been generated where the instantaneous nacelle tilt rate $\dot{\eta}$ is set to its maximum forward- and backward-tilting values in order to determine the effect of the nacelle tilt rate on the tilt-rotor handling and performance. These two effects are assessed based on the variation of the longitudinal stick X_{LON} and required engine power $HP_{ENG,REQ}$ trim curves as a function of $\dot{\eta}$, as presented in fig. 10. The results show that the nacelle tilt rate affects the performance of the tilt-rotor relatively more than its handling characteristics. When compared to the $\dot{\eta} = 0$ flight trim curves, converting from helicopter to airplane mode requires more power as the total velocity increases throughout the entire conversion process. Furthermore, more nose down longitudinal stick deflection is required in helicopter mode which gradually changes to more nose up longitudinal stick deflection while increasing velocity and nearing airplane mode. The opposite is true when converting back to helicopter mode.

F. Effect of Tiltable Proprotor on Haffner Diagrams

Longitudinal climbing flight trim curves at different flight path angles have also been generated in order to create Haffner diagrams corresponding to the tilt-rotor at different conversion stages (with the exception of airplane mode), shown in fig. 23 in the appendix. The obtained 6DoF model Haffner diagrams are compared to a standard helicopter Haffner diagram generated according to the momentum theory, also referred to as the Glauert Haffner diagram.

In summary the Haffner diagram of a tilt-rotor drastically changes when converting from helicopter to airplane mode resulting in induced velocities that are much lower than the ones calculated with the momentum theory for an isolated rotor. As a result, if the Glauert Haffner diagram were to be used to approximate the induced velocity of a tilt-rotor, the approximated induced velocity would be increasingly overestimated as the tilt-rotor converts from helicopter to airplane mode.

G. Effect of Tiltable Proprotor on Longitudinal and Level Flight Trim Curves

Finally the body attitude, longitudinal stick, induced velocity, disk tilt angles', and rotor forces' and torque trim curves corresponding to longitudinal and level flight have been generated, as presented in fig. 11. The effect of converting from helicopter to airplane mode on the trim curve states is summarized in table 2.

IV. Discussion

This research presents the development of an analytically-derived tilt-rotor model and investigates the effects of the tiltable nacelle on the rotor analytical expressions and tilt-rotor static flight mechanics. The contributions of this work to tilt-rotor modeling are discussed below, followed by the identified shortcomings of the 6DoF model when compared against the tilt-rotor models available in literature. A list of the most critical recommendations for the future are presented last.

A. Research Contributions

The presented work provides a methodology to analytically derive the flapping equation and rotor forces and moments of a generic tiltable proprotor which includes the nacelle tilt angle, rate, and acceleration explicitly in the expressions. Furthermore, sign-change-parameters are introduced which change the signs of terms in the model

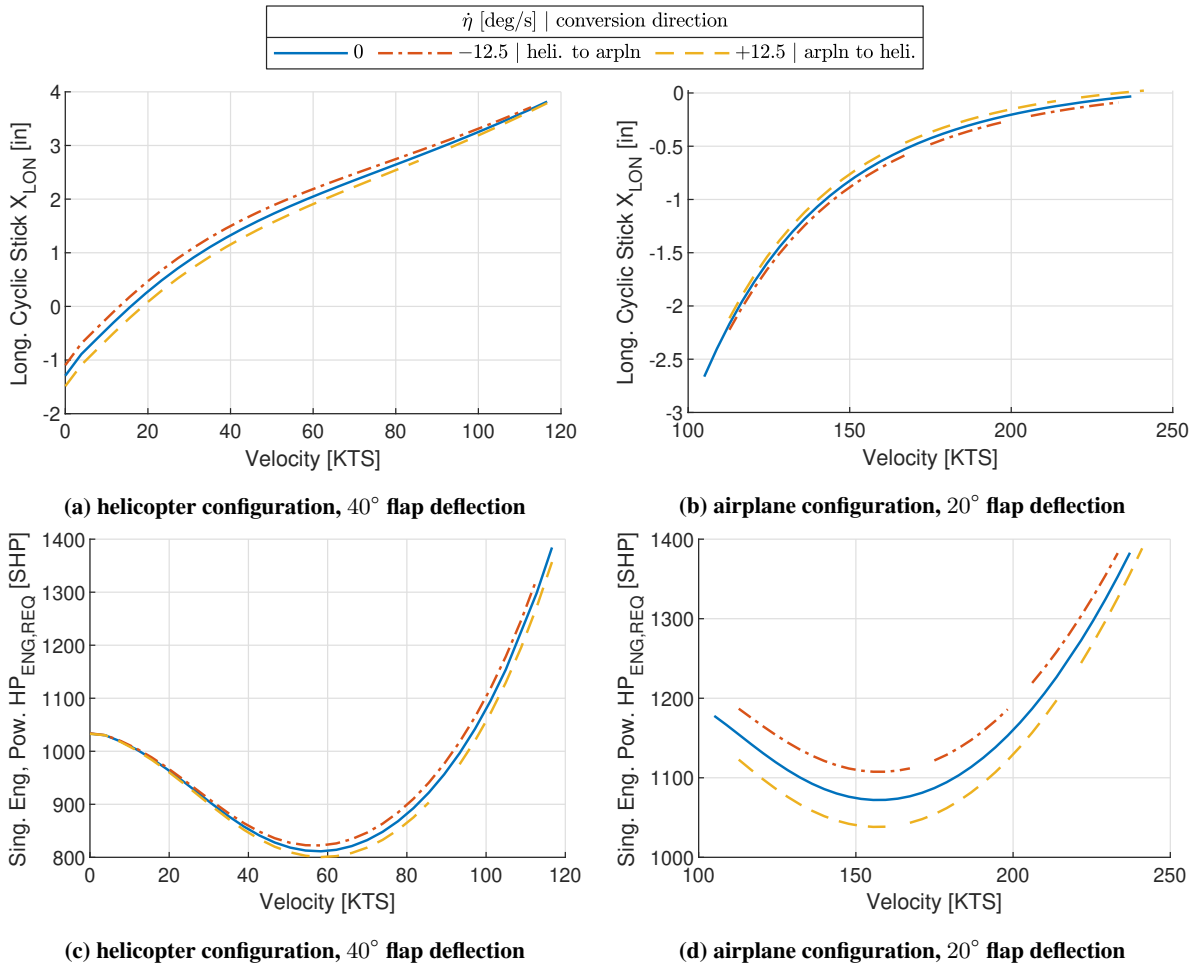

(a) helicopter configuration, 40° flap deflection

(b) airplane configuration, 20° flap deflection

(c) helicopter configuration, 40° flap deflection

(d) airplane configuration, 20° flap deflection

Fig. 10 Effect of nacelle tilt rate on longitudinal stick deflection and engine power required for trimmed level flight in helicopter and airplane configurations. Nacelle tilt rate $\dot{\eta}$ indicated in legend.

expressions depending on the mounting position of a component or the direction of rotation of the rotor. The flapping equation is derived with Newtonian mechanics yielding an expression that explicitly defines the acceleration of the rotor hub. The obtained tilt-rotor model includes a collective governor and allows for the simulation of autorotation. It is shown to have satisfactory first-approximation validity and exhibits the generic static and dynamic characteristics of a tilt-rotor aircraft.

The presented work also introduces the extended ordering scheme, which is essential to achieve an accurate, yet generic tilt-rotor model. The extended ordering scheme removes insignificant terms from the analytical expressions, consciously introducing a guaranteed bounded error in a well-defined manner. This allows the 6DoF model to take into account all body velocities and accelerations in the derivation of the rotor equations, including the body yaw rate and acceleration, as well as the nacelle tilt rate and acceleration, which are oftentimes presumed to be negligible in other works. The significance of these terms is then determined with the ordering scheme based on their expected maximum and minimum values, removing terms with a negligible effect on the flight mechanics of the tilt-rotor. There is no global rule for keeping a certain term since the extended reduction algorithm is expression specific. In contrast, other works employ a fixed and global rule set defining the insignificant terms, as is done in [14]. As a result, the selection of insignificant terms may be considered imprecise, requiring iterations to obtain a sufficient level of accuracy, without the guarantee of boundedness.

Finally, the presented conversion corridor limits, and the Haffner diagrams corresponding to different conversion stages of the tilt-rotor are considered novel results. The same can be said about the plots of the error distribution across

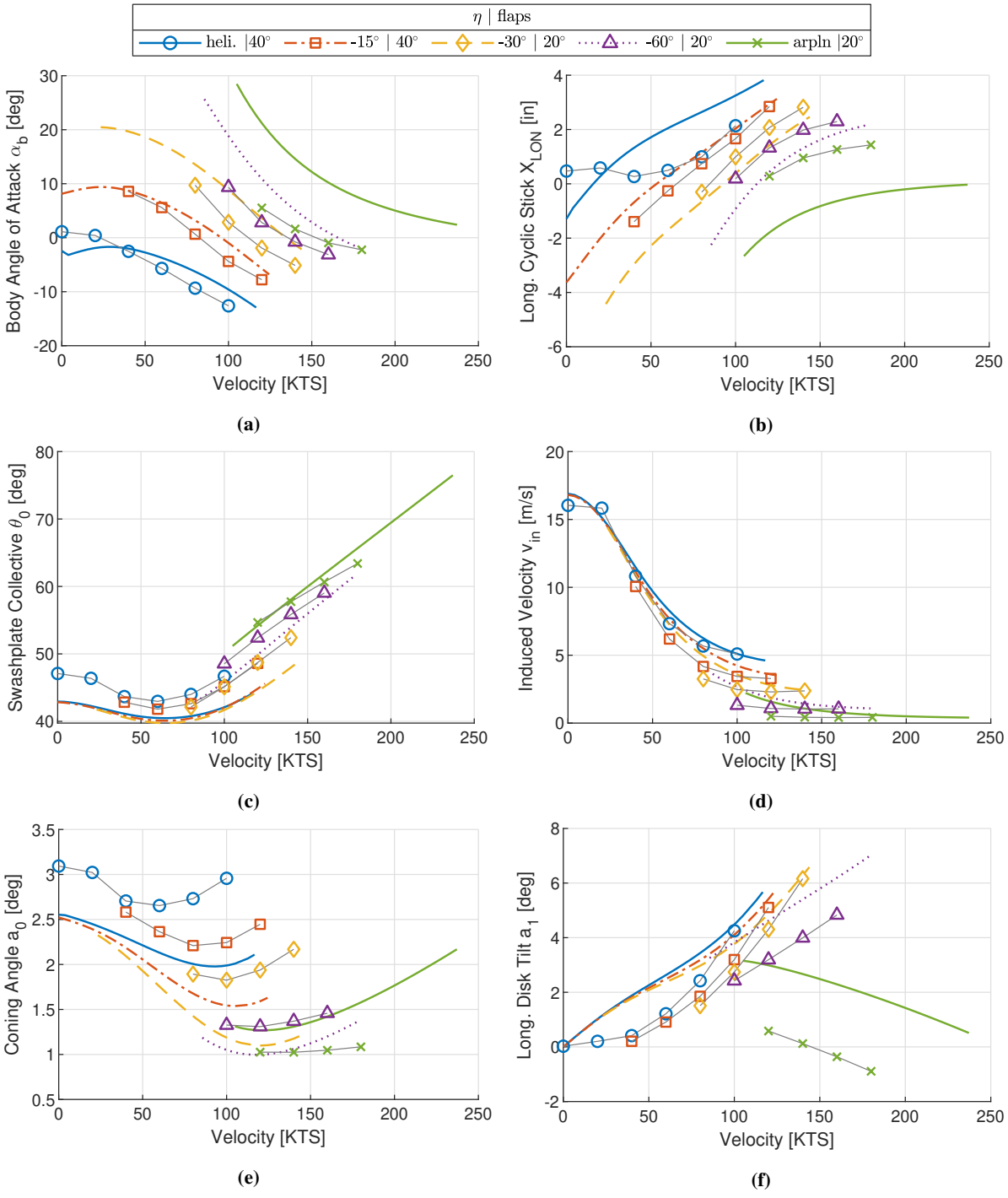

Fig. 11 Comparison between trim curves of the 6DoF tilt-rotor model and the GTRS. Color line patterns correspond to the 6DoF model while shapes connected with gray lines correspond to the GTRS data[9, app. A]. Nacelle tilt η and flap deflection angles indicated in legend.
(figure continued on next page)

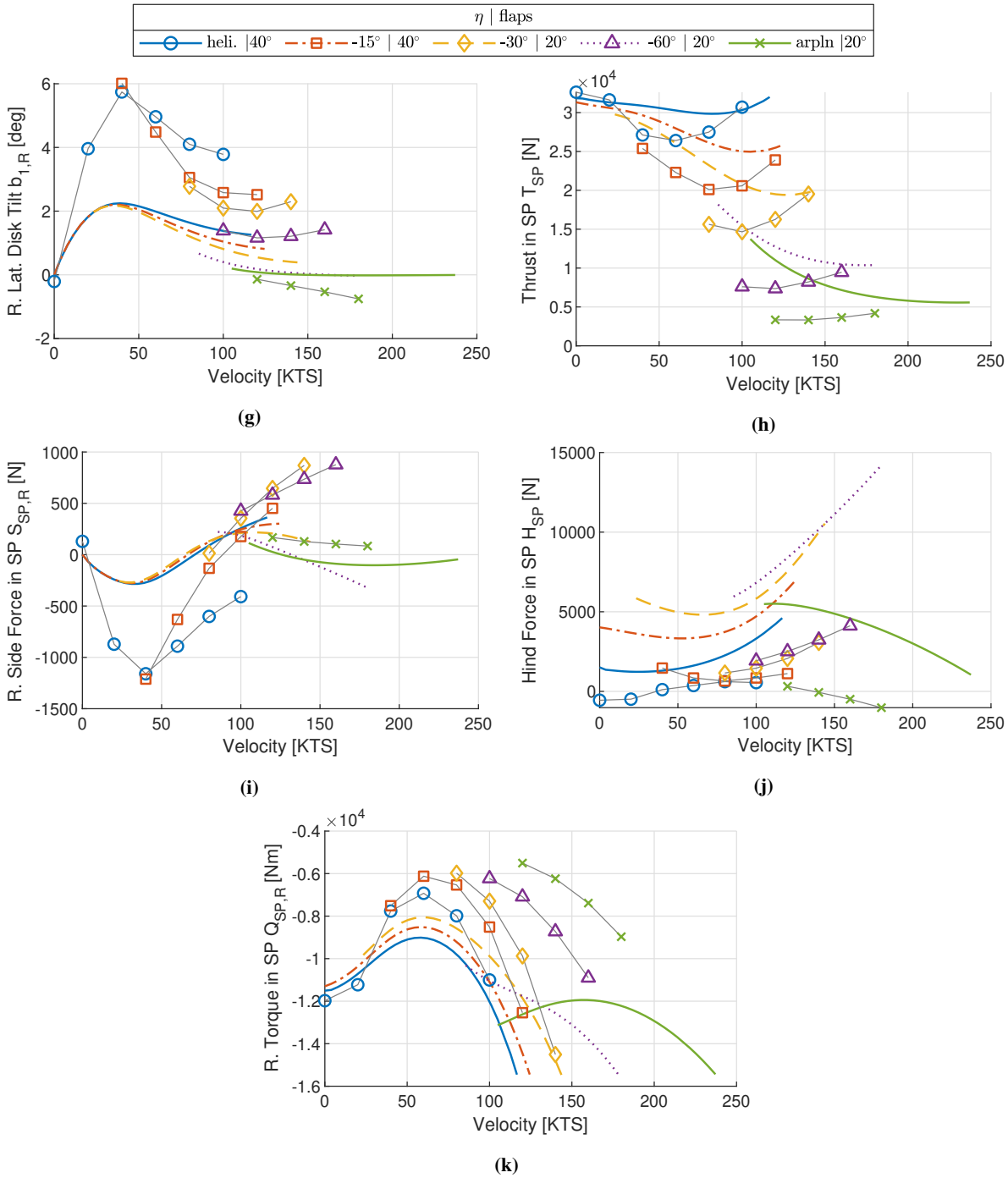

Fig. 11 Comparison between trim curves of the 6DoF tilt-rotor model and the GTRS. Color line patterns correspond to the 6DoF model while shapes connected with gray lines correspond to the GTRS data [9, app. A]. Nacelle tilt η and flap deflection angles indicated in legend.
(figure concluded)

Table 2 Effect of converting from helicopter to airplane mode on trim state.

	Required Action to Remain in Trim When Converting Towards Airplane Mode		
Trim Variable	**In Hover**	**Near Helicopter Mode**	**Near Airplane Mode**
α_b	..... more nose-up attitude		
X_{LON}	..... more nose-down stick		
θ_0	no effect	less collective	more collective
v_{in}	no effect	..... smaller induced velocity	
a_0	..... smaller coning angle		larger coning angle
a_1 and P_{SP}	no effect	..... smaller disk tilt angle / pitching moment	
b_1	no effect	..... smaller lateral disk tilt	
T_{SP}	..... lower thrust		
S_{SP}	no effect	..... smaller side force	
H_{SP}	..... larger hind force		smaller hind force
Q_{SP}	..... smaller torque		larger torque
O_{SP}	..... larger rolling moment		

the rotor disk as a result simplifications commonly employed in tilt-rotor modeling, as well as the trim curves showing the effects of the nacelle tilt on handling and performance.

B. 6DoF Model Shortcomings

Starting with the rotor, the 6DoF tilt-rotor model only defines an articulated rotor type meaning that all other rotor types, such as the gimballed rotor which is used on the XV-15 tilt-rotor, shall have to be approximated with the articulated rotor, possibly introducing significant modeling errors. Other authors such as [17] define the appropriate rotor type when modeling the XV-15 tilt-rotor. Furthermore other authors include a flapping hinge offset [14], lead/lag hinge [21], and pitch-flap coupling [17] in their rotor models, which are all present on the XV-15 proprotor, but are not included in the 6DoF model.

Apart from the rotor hub type, other geometrical discrepancies between the 6DoF model and the XV-15 tilt-rotor include an offset between the blade element CoG and feathering axis producing an additional torque moment due to inertial dynamics [34], blades that can be described with arbitrary planform and airfoil distributions [16, 19] (instead of a constant chord and airfoil as is the case in the 6DoF model), or a non-linear twist distribution [5, 16, 17].

Regarding the rotor aerodynamics, the 6DoF model uses the small angle approximation on the blade inflow angle, while this is avoided in [16] making the corresponding model more applicable to tilt-rotors which experience high inflow angles and have highly twisted blades. Moreover, the 6DoF model rotor induced velocity is static and uniform across the rotor disk, while a more accurate description of reality is the introduction of a non-uniform inflow distribution as is done in [17, 21], and inflow and flapping dynamics as performed in [16]. Other recommended tilt-rotor rotor modeling elements that are not present in the 6DoF model, but are present in other works, include the tip loss factor (e.g. in [17]), the side-by-side rotor aerodynamic interaction, ground proximity effect on the power required for hover, and the the reflected rotor wake effect on the tail as included in the model of [7].

Apart from the rotor model, other airframe components of the 6DoF model possess their own shortcomings. In the 6DoF model the lifting surface forces and moments are calculated based on the velocity of the MAC AC, while a more appropriate approach would be to use strip theory, as is done in [17], enabling a more accurate inclusion of the rotor wake effect on the wing or tail, for example. Regarding the empennage, in [17] the wing downwash has an effect on the horizontal tail stabilizer, and in [19] the rotor wake has an additional delay to simulate the distance the wake has to travel from the rotor to the tail, both of which are not part of the 6DoF model. The 6DoF model also neglects the aerodynamic effect of the nacelles and greatly simplifies the aerodynamics of the fuselage, while in [5, 7, 15, 19] the fuselage and nacelle aerodynamics make use of coefficients taken from experimentally obtained data tables providing a more accurate (yet less generic) model. The 6DoF model greatly simplifies the general aerodynamic calculations of

blades and lifting surfaces by using either constant values or flat plate characteristics, while in [7, 16, 17, 19] the lift, drag, and pitching moment coefficients are found from experimentally obtained look-up tables as well. Finally, highly non-linear aerodynamic behavior such as stall and air compressibility effects are included in the model of [34] per the modeling recommendations which are not fully abided by the 6DoF model.

C. Recommendations

The largest discrepancies between the 6DoF model and GTRS in the static and dynamic simulation results should be further investigated, most notably the milder pitch responses in both helicopter and airplane modes. Moreover, the validity of the phugoid mode with the collective governor turned on and off, and the validity of the Dutch-roll mode, or lack thereof, should also be determined in the future. The assumptions that have been shown to be violated, i.e. the linearization of the BE inflow angle and total velocity, should be appropriately addressed in the future as well, most likely requiring a re-derivation of the governing equations.

Regarding the rotor, a future revision of the model should include disk tilt and inflow dynamics, as well as a non-uniform induced velocity distribution. Alternatively the tip loss factor and flow reversal region should be implemented. Furthermore it is suggested that the lead/lag hinge be modeled as well or, more appropriately, the articulated-type rotor model should be replaced by a gimballed-type rotor altogether to be in accordance with the XV-15 tilt-rotor.

The inclusion of the rotor and wind ground effects, as well as the mutual wake effect of the two rotors in proximity is recommended. It is also suggested for the implemented rotor wash to have a more continuous effect on the lifting surfaces rather than a binary effect acting on the MAC AC only. The control surface aerodynamic effectiveness should not be linear in the future, while the aerodynamic model of the fuselage should be expanded to at least incorporate lift and a pitching moment. Finally, 3-dimensional aerodynamic effects, as well as air compressibility should be included in the complete tilt-rotor model, or at least in the rotor model.

References

[1] R. A. Ormiston, "Revitalising Advanced Rotorcraft Research - and the Compound Helicopter," *Aeronaut. J.*, vol. 120, no. 1223, pp. 83–129, 2016, doi: 10.1017/aer.2015.5.

[2] W. Johnson, G. K. Yamauchi, and M. E. Watts, "Designs and Technology Requirements for Civil Heavy Lift Rotorcraft," presented at the AHS Vert. Lift Aircraft Des. Conf., San Francisco, CA, USA, Jan. 18-20, 2006, Paper 1.

[3] Mark Huber, "AW609 Final Accident Report Issued ," *AINonline*. [Online]. Available: https://www.ainonline.com.[Accessed: Jan.31,2020]

[4] Italy. Italian Civil Aviation Safety Investigation Authority, "Accident Occurred to the AugustaWestland AW609 Aicraft Registration Marks N609AG, in Toronzano Vercellese (VC), on the 30th of October 2015," *ANSV - Agenzia Nazionale per la Sicurezza del Volo*. [Online]. Available: http://www.ansv.it.[Accessed:Jan.31,2020]

[5] P. B. Harendra, M. J. Joglekar, T. M. Gaffey, and R. L. Marr, "V/STOL Tilt Rotor Study - Volume V: A Mathematical Model for Real Time Flight Simulation of the Bell Model 301 Tilt Rotor Research Aircraft," Bell Helicopter Company, A Textron Company, Fort Worth, TX, USA, Contractor Rep. CR114614, Apr. 1973.

[6] G. B. Churchill and D. C. Dugan, "Simulation of the XV-15 Tilt Rotor Research Aircraft," NASA ARC, Moffett Field, CA, USA, Tech. Memo. 84222, Mar. 1982.

[7] S. W. Ferguson, "A Mathematical Model for Real Time Flight Simulation of a Generic Tilt-Rotor Aircraft, Rev. A," Systems Tech., Inc., Mountain View, CA, USA, Contractor Rep. CR-166536, 1988.

[8] H. Gregory D. and F. Samuel W., "Generic Tilt-Rotor Simulation (GTRSIM) User's and Prorammer's Guide, Volume 1: User's Guide, Rev. A," Systems Tech., Inc., Moffett Field, CA, USA, Contractor Rep. CR-166535, 1988.

[9] S. W. Ferguson, "Development and Validation of a Simulation for a Generic Tilt-Rotor Aircraft," Systems Tech., Inc., Mountain View, CA, USA, Contractor Rep. CR-166537, 1989.

[10] M. Maisel et al., "Tilt Rotor Research Aircraft Familiarization Document," NASA ARC, Moffett Field, CA, USA, Tech. Memo. TM X-62, 407, Jan. 1975.

[11] D. C. Dugan, R. G. Erhart, and L. G. Schroers, "The XV-15 Tilt Rotor Research Aircraft," NASA ARC, Moffett Field, CA, USA, Tech. Memo. 81244, 1980.

[12] M. D. Maisel, D. J. Giulianetti, and D. C. Dugan, "The History of The XV-15 Tilt Rotor Research Aircraft: From Concept to Flight," *NASA Special Publication 4517*, 2000.

[13] J. A. Weiberg and M. D. Maisel, "Wind-Tunnel Tests of the XV-15 Tilt Rotor Aircraft," NASA ARC, Moffett Field, CA, USA, Tech. Memo. 81177, Apr. 1980.

[14] K. M. Kleinhesselink, "Stability and Control of Modeling of Tiltrotor Aircraft," Master's thesis, University of Maryland, 2007.

[15] W. Qi and W. Wenhai, "Modelling and Analysis of Tiltrotor Aircraft for Flight Control Design," *Inf. Technol. J.*, vol. 13, no. 5, pp. 885–894, 2014, doi: 10.3923/itj.2014.885.894.

[16] F. Barra, S. Godio, and G. Guglieri, "Implementation of a Comprehensive Mathematical Model for Tilt-Rotor Real-Time Flight Simulation," presented at the 45th ERF, Warsaw, Poland, Sep. 17-20, 2019, Paper 20.

[17] W. Appleton, A. Filippone, and N. Bojdo, "Aeromechanics Modelling of Tiltrotor Aircraft," presented at the 45th ERF, Warsaw, Poland, Sep. 17-20, 2019, Paper 118.

[18] G. D. Klein, "Linear Modeling of Tiltrotor Aircraft (in Helicopter and Airplane Modes) for Stability Analysis and Preliminary Design," Ph.D. dissertation, Nav. Postgraduate School, Monterey, CA, USA, 1996.

[19] M. Miller and J. Narkiewicz, "Tiltrotor Modelling for Simulation in Various Flight Conditions," *J. Theor. Appl. Mech.*, vol. 44, no. 4, pp. 881–906, 2006.

[20] M. E. Dreier, *Introduction to Helicopter and Tiltrotor Simulation*. Reston, VA, USA: AIAA, Inc., 2007.

[21] S. M. Barkai, O. Rand, R. J. Peyran, and R. M. Carlson, "Modeling and Analysis of Tilt-Rotor Aeromechanical Phenomena," *Math. Comput. Model.*, vol. 27, no. 12, pp. 17–43, 1998.

[22] ART, "Flightlab Dynamics Models," *Advanced Rotorcraft Technology*. [Online]. Available: https://www.flightlab.com/flight-dynamics-models.html

[23] R. K. Heffley and M. A. Mnich, "Minimum-Complexity Helicopter Simulation Math Model," Manudyne Systems, Inc., Los Altos, CA, USA, Contractor Rep. CR177476, Apr. 1988.

[24] W. Johnson, "An Assessment of the Capability to Calculate Tilting Prop-Rotor Aircraft Performance, Loads, and Stability," NASA ARC, Moffett Field, CA, USA, Tech. Paper 2291, Mar. 1984.

[25] A. Gessow and G. C. Myers Jr., *Aerodynamics of the Helicopter*. New York, NY, USA: Fredderick Ungar Publishing Co., 1952.

[26] R. T. N. Chen, "A Survey of Nonuniform Inflow Models for Rotorcraft Flight Dynamics and Control Applications," NASA ARC, Moffett Field, CA, USA, Tech. Memo. 102219, Nov. 1989.

[27] D. A. Peters and N. HaQuang, "Dynamic Inflow for Practical Applications," *J. Am. Helicopter Soc.*, vol. 33, no. 4, pp. 64–68, 1988.

[28] *Maple*. (2020.1). Maplesoft.

[29] *Matlab*. (R2020a). MathWorks.

[30] P. Sokolowski, "Flight Dynamics Analytically-Derived Mathematical Model of Tiltrotor Aircraft," Master's thesis, Delft University of Technology, 2022.

[31] F. S. Stoddard, "Discussion of Momentum Theory for Windmills," *Wind Energy Center Reports*, no. 20, pp. Appendix IV, 28–35, 1976.

[32] *Python*. (3.8.6). python.org.

[33] *FlightGear*. (2020.3). https://www.flightgear.org/.

[34] W. Johnson, "Analytical Model for Tilting Proprotor Aircraft Dynamics, Including Blade Torsion and Coupled Bending Modes, and Conversion Mode Operation," NASA, Moffett Field, CA, USA, Tech. Memo. TM X-62, 369, Aug. 1974.

Appendix

Diagrams

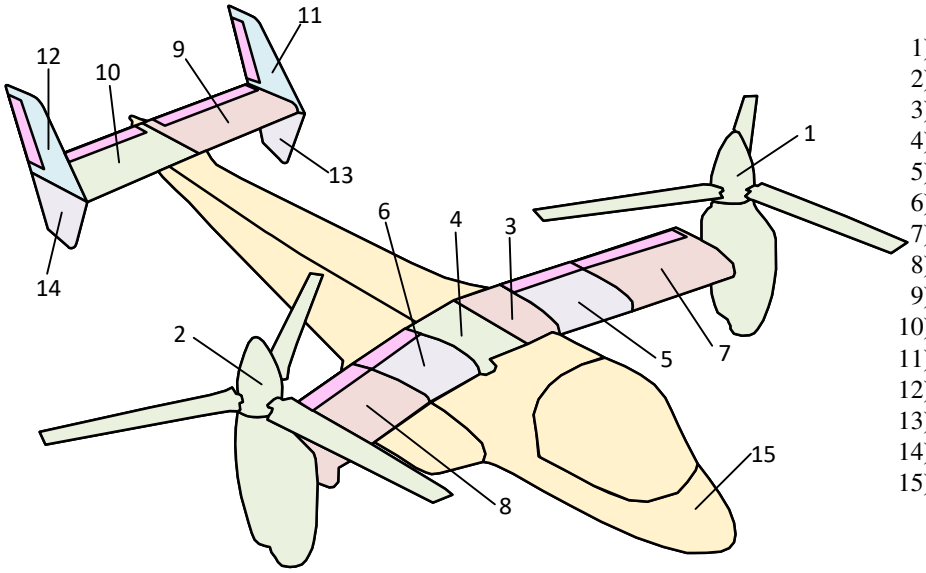

1) Rotor, left
2) Rotor, right
3) Free wing, left
4) Free wing, right
5) Flap wing, left
6) Flap wing, right
7) Aileron wing, left
8) Aileron wing, right
9) H-stab, left
10) H-stab, right
11) V-stab, top left
12) V-stab, top right
13) V-stab, bot. left
14) V-stab, bot., right
15) Fuselage

Fig. 12 Schematic depiction of the XV-15 tilt-rotor showing all of the components and their names that comprise the 6DoF model XV-15 implementation. Colors are used only to differentiate between neighboring components, with the exception of control surfaces which are also shown and are represented collectively by pink rectangles.

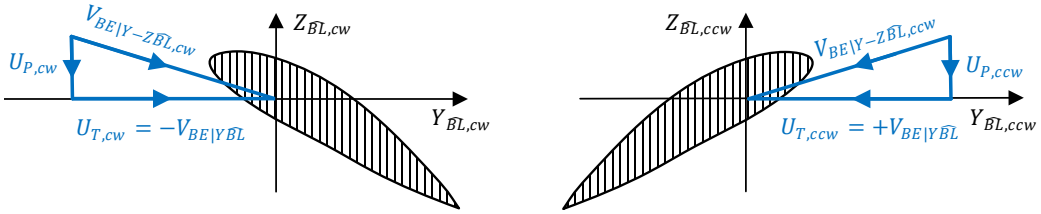

Fig. 13 Positive sign conventions of the clockwise (cw) and counter-clockwise (ccw) rotating blade element tangential and perpendicular velocity components. Arrows indicate air velocity vectors.

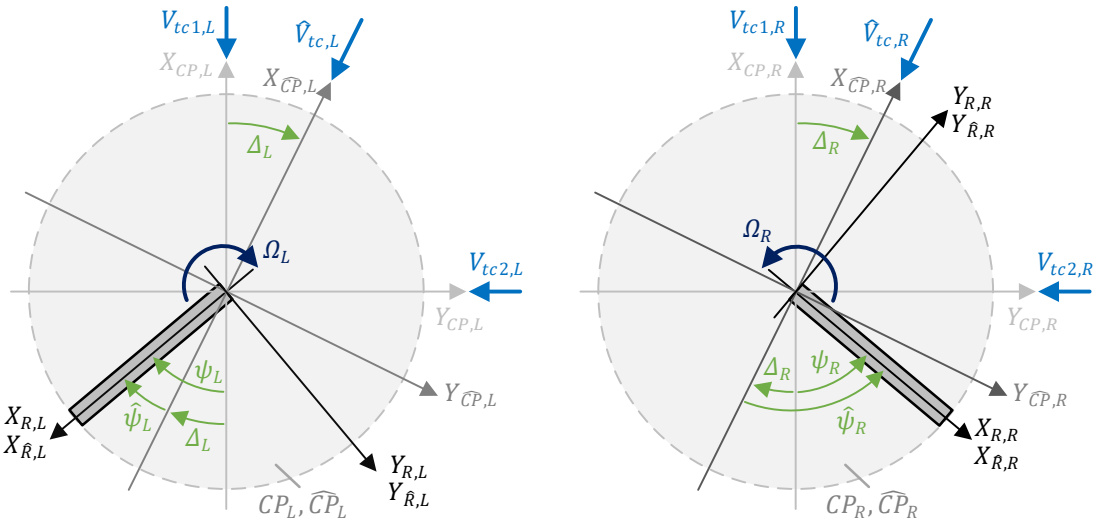

Fig. 14 Schematic depiction of the wind axis control plane of a clockwise (left, L) and counterclockwise (right, R) rotating rotor with respect to the non-wind-axis control plane. Wind axis and non-wind-axis rotating frame axes also shown together with a schematic depiction of a single blade represented by the shaded rectangle. Velocity vectors indicate the direction of air flow.

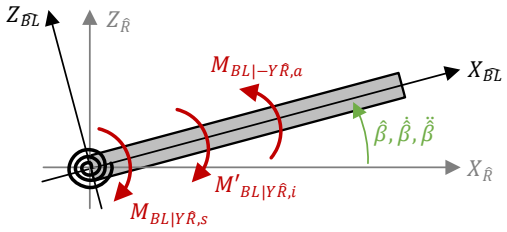

Fig. 15 Direction of action of the inertial, aerodynamic, and spring moments on the flapping motion.

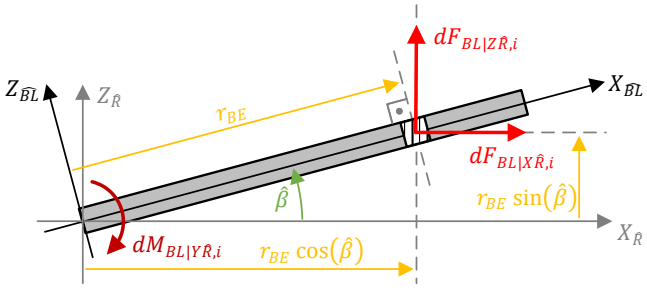

Fig. 16 Contribution of the inertial forces acting on blade element to the inertial flapping moment.

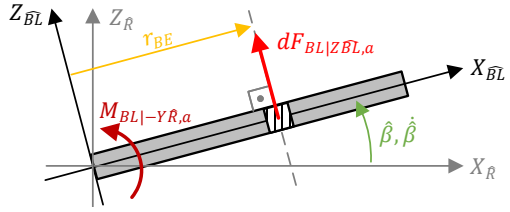

Fig. 17 Schematic front/rear view of the rotor blade showing the contribution of the differential blade vertical force to the blade aerodynamic moment.

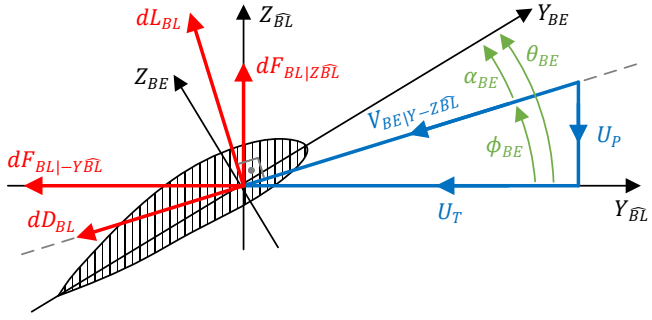

Fig. 18 Schematic representation of the blade element in the wind axis blade element frame of reference. Velocity arrows indicate the direction of the airflow movement.

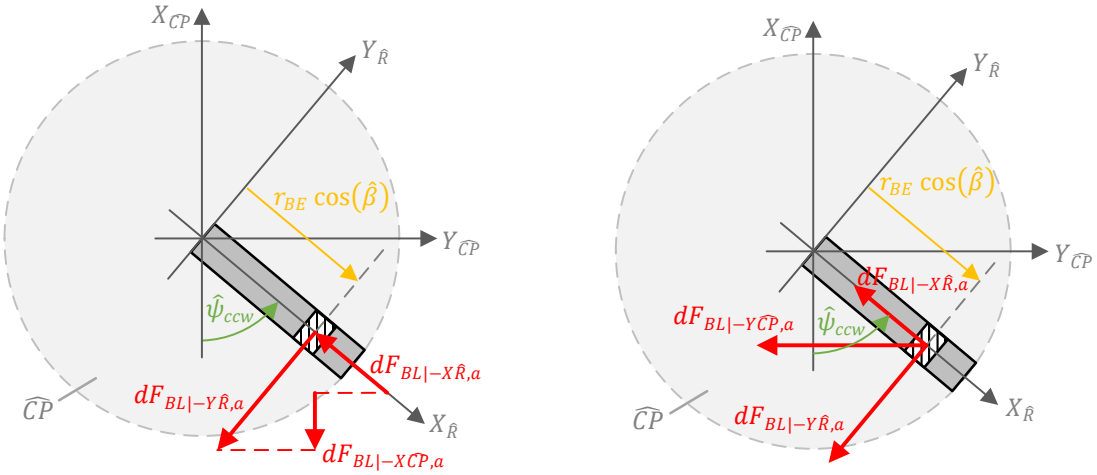

Fig. 19 Schematic top view of a ccw. rotating rotor blade showing the contribution of the blade element radial and tangential forces to the blade element H-force (left) and S-force (right).

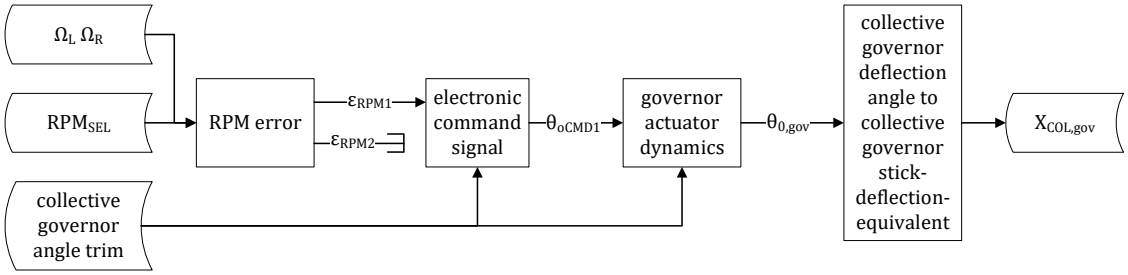

Fig. 20 Block diagram of the simplified collective governor model.

Non-Dimensional Variables

$$\widehat{\mu}_{tc} = \frac{\widehat{V}_{tc}}{\Omega R} \tag{79a}$$

$$\widehat{\lambda}_{pc} = \frac{\widehat{V}_{pc}}{\Omega R} \tag{79b}$$

$$\lambda_i = \frac{v_{in}}{\Omega R} \tag{79c}$$

$$\widehat{\lambda}_{tot} = \widehat{\lambda}_{pc} - \lambda_i \tag{79d}$$

$$\gamma_{bl} = \frac{\rho C_{l_\alpha,bl} c_{bl} R^4}{I_{bl}} \tag{80}$$

Non-Wind Axis Disk Tilt Approximation

$$\beta = a_0 - a_1 cos(\psi) - \Omega_{sgn} b_1 sin(\psi) \tag{81a}$$

$$a_0 = \widehat{a}_0 \tag{81b}$$

$$a_1 = \widehat{a}_1 cos(\Delta) + \widehat{b}_1 sin(\Delta) \quad (81c) \qquad b_1 = \widehat{b}_1 cos(\Delta) - \widehat{a}_1 sin(\Delta) \quad (81d)$$

Complete Flapping Equation

$$\begin{aligned}
&\ddot{\widehat{\beta}} + \gamma_{bl}\left[\frac{\Omega - \Omega_{sgn}\left(pS_\eta + rC_\eta\right)}{8} + \frac{\widehat{\mu}_{tc}}{6}\Omega S_{\widehat{\psi}}\right]\dot{\widehat{\beta}} && \text{(inertia \& aero. damping)} \quad (82a)\\
&+\left[\left(\Omega - \Omega_{sgn}(p_i S_\eta + r_i C_\eta)\right)^2 - \frac{(q_i + \dot{\eta})^2}{2} + A_{\widehat{\beta},\text{prod}}\right. && \text{(centrifugal spring)}\\
&+ \frac{\gamma_{bl}\widehat{\mu}_{tc}}{6}\left(\Omega^2 - \Omega_{sgn}(pS_\eta + rC_\eta)\Omega\right)C_{\widehat{\psi}} && \text{(aero. spring)}\\
&- \Omega_{sgn}\gamma_{bl}(pC_\eta - rS_\eta)\left(\frac{\theta_0}{4}\left(\Omega - \Omega_{sgn}(pS_\eta + rC_\eta)\right) + \frac{\widehat{\lambda}_{tot}}{6}\Omega\right)C_{\widehat{\psi}}\\
&+ \gamma_{bl}(q + \dot{\eta})\left(\frac{\gamma_{bl}\theta_0}{4}\left(\Omega - (pS_\eta + rC_\eta)\right) + \frac{\widehat{\lambda}_{tot}}{6}\Omega\right)S_{\widehat{\psi}}\\
&+ \left.\frac{\theta_0(q + \dot{\eta})\widehat{\mu}_{tc}}{6}\Omega + \frac{K_\beta}{I_{bl}}\right]\widehat{\beta} = && \text{(\& flapping spring)}\\
&\quad = \Omega_{sgn}\left(\dot{p}_i C_\eta + \dot{r}_i S_\eta\right)S_{\widehat{\psi}} - \left(\dot{q}_i + \ddot{\eta}\right)C_{\widehat{\psi}} && \text{(inertia excitation)}\\
&\quad + \Omega_{sgn}2(p_i C_\eta - r_i S_\eta)\left(\Omega - \Omega_{sgn}(p_i S_\eta + r_i C_\eta)\right)C_{\widehat{\psi}} && \text{(roll Coriolis)}\\
&\quad - 2q_i\left(\Omega - \Omega_{sgn}(p_i S_\eta + r_i C_\eta)\right)S_{\widehat{\psi}} && \text{(pitch Coriolis)}\\
&\quad - 2\dot{\eta}\left(\Omega - \frac{\Omega_{sgn}(p_i S_\eta + r_i C_\eta)}{2}\right)S_{\widehat{\psi}} && \text{(tilt Coriolis)}\\
&\quad + \frac{\gamma_{bl}\theta_0}{3}\left(\Omega^2 - \Omega_{sgn}(pS_\eta + rC_\eta)\Omega\right)\widehat{\mu}_{tc}S_{\widehat{\psi}} && \text{(aero. excitation)}\\
&\quad + \frac{\gamma_{bl}\widehat{\lambda}_{tot}}{6}\left(\Omega^2 - \Omega_{sgn}(pS_\eta + rC_\eta)\Omega\right)\\
&\quad + \frac{\gamma_{bl}\widehat{\lambda}_{tot}}{4}\widehat{\mu}_{tc}\Omega^2 S_{\widehat{\psi}}\\
&\quad + \frac{\gamma_{bl}\theta_0}{8}\left(\widehat{\mu}_{tc}^2\Omega^2 + \left(\Omega - \Omega_{sgn}(pS_\eta + rC_\eta)\right)^2\right)\\
&\quad + \Omega_{sgn}\gamma_{bl}\frac{pC_\eta - rS_\eta}{8}\left(\Omega - \Omega_{sgn}(pS_\eta + rC_\eta)\right)S_{\widehat{\psi}}\\
&\quad + \gamma_{bl}\frac{q + \dot{\eta}}{8}\left(\Omega - \Omega_{sgn}(pS_\eta + rC_\eta)\right)C_{\widehat{\psi}}\\
&\quad + \Omega_{sgn}\gamma_{bl}\frac{pC_\eta - rS_\eta}{12}\widehat{\mu}_{tc}\Omega + \frac{K_\beta\overline{a}_0}{I_{bl}} && \text{(\& precone excitation)}
\end{aligned}$$

$$A_{\widehat{\beta},\text{prod}} = \frac{2p_i r_i S_\eta C_\eta - \Omega_{sgn}2\Omega\left(p_i S_\eta + r_i C_\eta\right) - p_i^2 C_\eta^2 - r_i^2 S_\eta^2}{2} \quad (82b)$$

$$\overline{p}_X = \frac{p_X}{\Omega} \quad (83a) \qquad \overline{q}_X = \frac{q_X}{\Omega} \quad (83b) \qquad \overline{r}_X = \frac{r_X}{\Omega} \quad (83c)$$

$$\overline{\eta} = \frac{\dot{\eta}}{\Omega} \quad (83d) \qquad \overline{p}_{eff} = \overline{p}C_\eta - \overline{r}S_\eta \quad (83e) \qquad \overline{r}_{eff} = \overline{p}S_\eta + \overline{r}C_\eta \quad (83f)$$

$$\overline{p}_{i,eff} = \overline{p}_i C_\eta - \overline{r}_i S_\eta \quad (83g) \qquad \overline{r}_{i,eff} = \overline{p}_i S_\eta + \overline{r}_i C_\eta \quad (83h) \qquad \overline{r}_{w,eff} = \overline{p}_w S_\eta + \overline{r}_w C_\eta \quad (83i)$$

$$\dot{p}_{i,eff} = \dot{p}_i C_\eta - \dot{r}_i S_\eta \qquad (83j) \qquad \overline{q}_{tot} = \overline{q} + \overline{\dot{\eta}} \qquad (83k) \qquad \overline{q}_{i,tot} = \overline{q}_i + \overline{\dot{\eta}} \qquad (83l)$$

Table 3 Description of subscripts of combined rotational rates.

Subscript	Description
[none]	Aerodynamic rate - motion of the air wrt. the tilt-rotor, consisting of an inertial rate and a wash rate.
i	Inertial rate - motion of the tilt-rotor wrt. an inertial frame of reference.
w	Wash rate - motion of the air wrt. an inertial frame of reference.
eff	'Effective' rate - combination of two orthogonal rates forming a single rate as a sinusoidal function of the nacelle tilt angle.
tot	'Total' rate - combination of two rates acting around the same axis.
X	Any valid combination of the subscripts i, w, eff, and tot.

Engine Power vs. Throttle Position Approximation

$$\begin{aligned} R_{\text{SHP}} &= f(X_{\text{COL,pilot}}) = \\ &= (0.2513)\left(X_{\text{COL,pilot}}\right)^4 + (4.822)\left(X_{\text{COL,pilot}}\right)^3 - (20.03)\left(X_{\text{COL,pilot}}\right)^2 + (121.7)\left(X_{\text{COL,pilot}}\right) + 89.496 \end{aligned} \qquad (84)$$

Lateral Level Flight Trim Curves

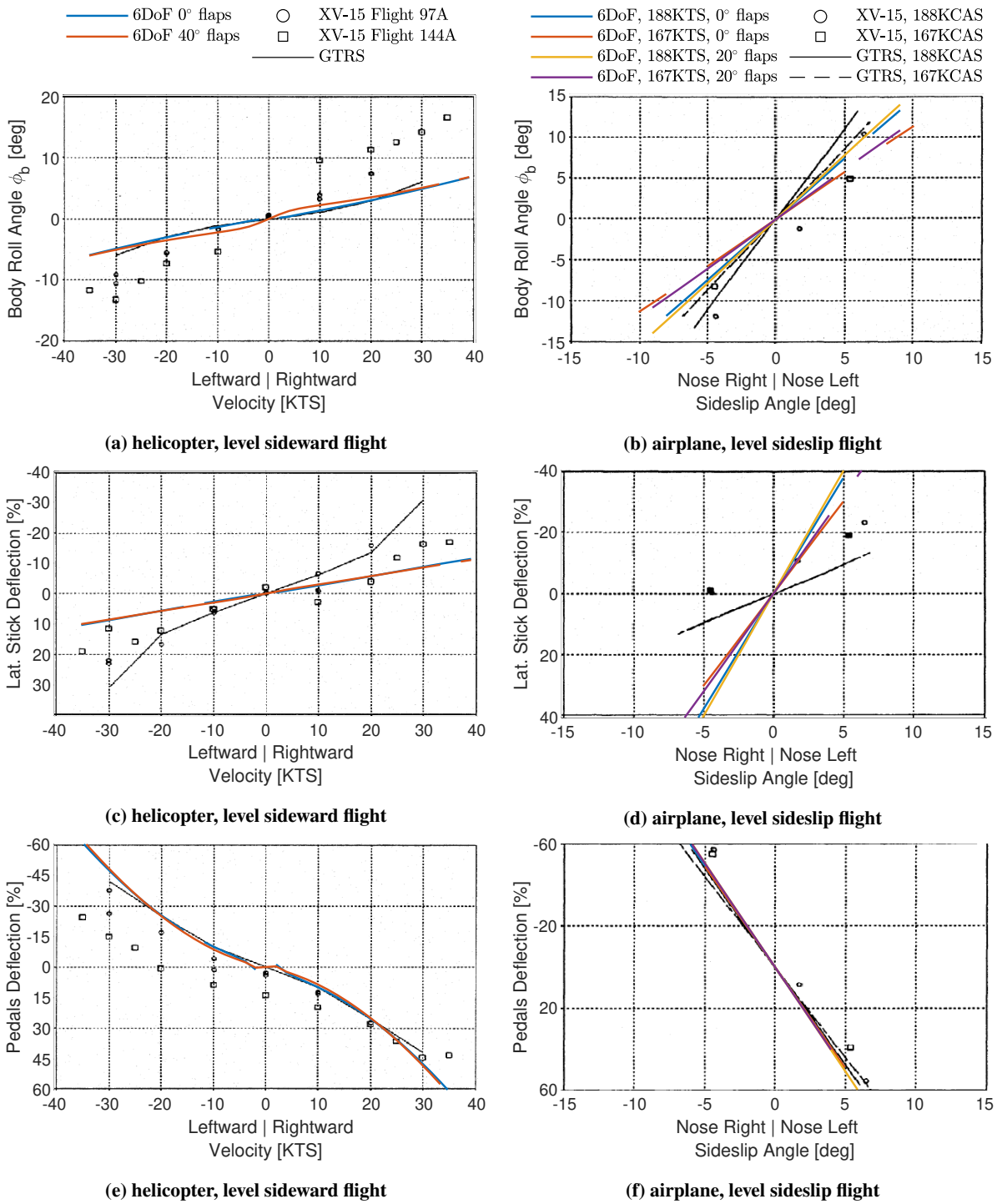

(a) helicopter, level sideward flight

(b) airplane, level sideslip flight

(c) helicopter, level sideward flight

(d) airplane, level sideslip flight

(e) helicopter, level sideward flight

(f) airplane, level sideslip flight

Fig. 21 Comparison between the trim curves of the 6DoF tilt-rotor model, GTRS model, and real XV-15 tilt-rotor in trimmed helicopter level sideward flight [9, p. 26 fig. 9] (left column) and trimmed airplane level sideslip flight [9, p. 45 fig. 19] (right column). 6DoF model flap deflection angles indicated in legends above figure columns.

Dynamic Responses in Time Domain

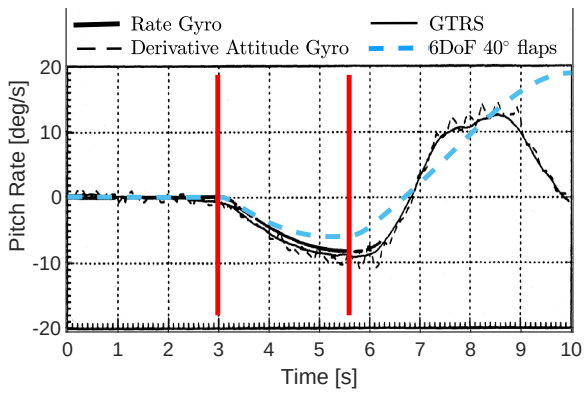

(a) helicopter, long. stick step input

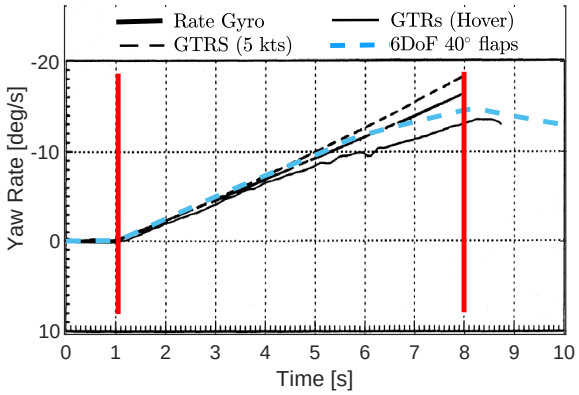

(b) helicopter, pedals step input

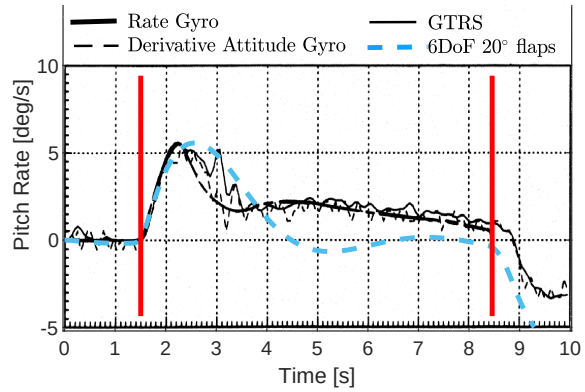

(c) airplane, 175KTS level flight, long. stick step input

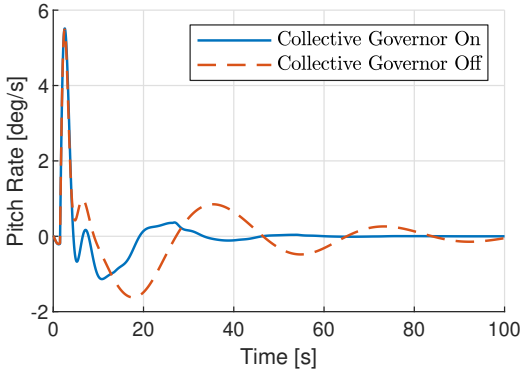

(d) airplane, 175KTS level flight, long. stick step input

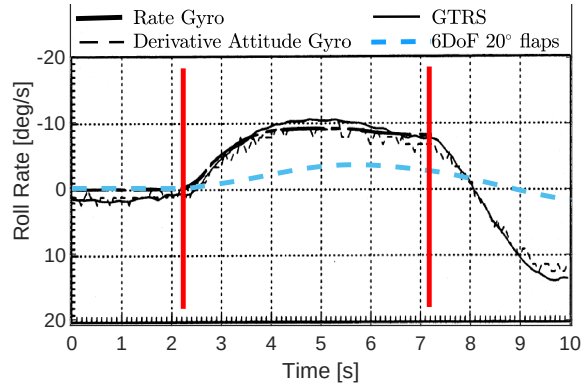

(e) airplane, 178KTS level flight, lat. stick step input

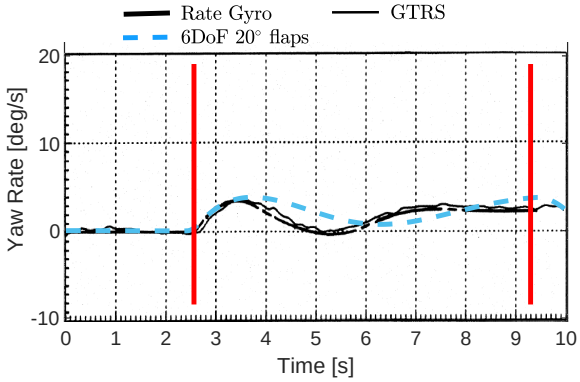

(f) airplane, 176KTS level flight, pedals step input

Fig. 22 Comparison between the step-input responses of the 6DoF tilt-rotor model, GTRS model, and actual XV-15 tilt-rotor in helicopter and airplane configurations. Comparison data taken from [9]. Period of step inputs indicated to be between the vertical red lines.

Haffner Diagrams

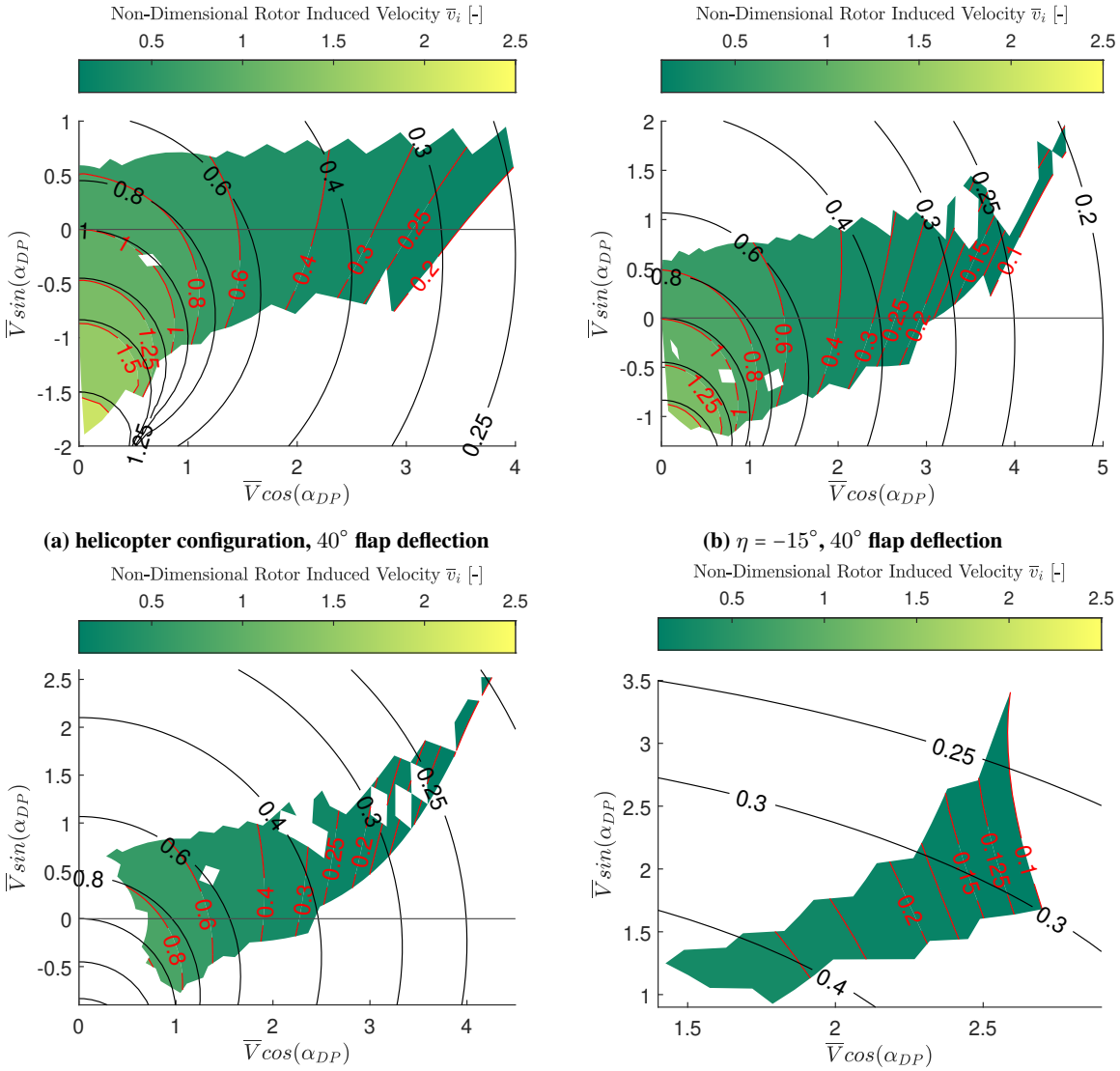

(a) helicopter configuration, 40° flap deflection

(b) $\eta = -15°$, 40° flap deflection

(c) $\eta = -30°$, 20° flap deflection

(d) $\eta = -60°$, 20° flap deflection

Fig. 23 Haffner diagrams corresponding to the 6DoF tilt-rotor for different nacelle tilt angles (green and red), plotted against the Glauert Haffner contours (black).

Part II

Literature Review and Preliminary Results

2

Literature Review of Tilt-Rotor Flight Mechanics Models

The research project at hand starts with a review of literature relevant to tilt-rotor flight mechanics modeling, as presented in this chapter, with focus on performance and piloted flight simulation applications. The literature review provides familiarization with the tilt-rotor aircraft and the associated flight mechanics model development process, simultaneously addressing the first portion of research sub-questions to be answered in literature. Based on this research it is then possible to identify an opportunity for innovation which is targeted by the objective of this thesis.

The chapter begins with section 2.1 which describes the general structure of a tilt-rotor, its mission profile, and briefly assesses its strengths and weaknesses in comparison to helicopters and airplanes, while section 2.2 describes the control strategy of a tilt-rotor based on the XV-15 aircraft. Next section 2.3 explores the possible scope of the models, that is, which elements of a tilt-rotor can be modeled, and section 2.4 summarizes the findings of various authors about what should be included in a tilt-rotor model and the reasoning behind it. For the purpose of this thesis project, elements recommended for performance and piloted flight simulations only are covered. Finally section 2.5 presents the attempts of different authors at modeling the recommended elements, discussing their approaches in the context of the findings of the previous section.

2.1. How Tilt-Rotors Fly

A tilt-rotor consists of a fuselage, empennage, and pair of wings closely resembling an airplane, however it is distinguished from the latter by two proprotors attached via tiltable nacelles at the tips of the wings. At low speeds, the proprotors provides the majority of lift and control, whereas at higher speeds the wings start generating the larger portion of the lift, the tail and control surfaces give control, while the proprotor mainly produces the propulsive force [14].

The main engines may be mounted within the fuselage, such as in the Bell XV-3, and connected to the proprotors via shafts running through the wings, or they may be mounted on the wing tips within the nacelles, such as in the XV-15 [7]. Furthermore, the engines may be interconnected to provide redundancy in case of a one-engine-inoperative condition. Irrespective of the drive connection, the proprotor shaft axis must readily be able to tilt from a vertical helicopter-mode position, to a horizontal airplane-mode position and back in order for the aircraft to be classified as a tilt-rotor. It is possible for the tilting range to be larger than 90 degrees, as for example in the XV-15 which can tilt its nacelles partially backwards providing rearward thrust.

The wings of a tilt-rotor usually have similar control surfaces to those found on an airplane such as ailerons and flaps. The control authority of these surfaces may depend on the nacelle tilt angle, however it is common to find flaps being greatly deflected in helicopter mode in order to reduce the amount of rotor downwash on the wing. Similarly, the tail elevator and rudder maximum deflection also may depend on the nacelle tilt angle.

As in the case of helicopters, tilt-rotors may be designed with different rotor types. For example the classical fully-articulated rotor was used on the Transcendental Model 1-G, the first tilt-rotor, and initially on the XV-3. Later the XV-3 rotor was replaced by a teetering rotor [14]. However, a more popular choice is the gimballed rotor, the multi-bladed variation of the teetering rotor, which is present on both the XV-15 and V-22.[1] Again, similarly to helicopters, tilt-rotors also have collective and longitudinal cyclic inputs via the swashplate. It is not common, however, to find lateral cyclic controls since lateral control can be achieved via differential collective.

The mission profile of a tilt-rotor may contain all the possible flight phases of a helicopter, i.e.: longitudinal and lateral taxiing; vertical and forward take-off and climb; cruise; loitering; hover; and vertical and forward descent and landing, including autorotation. Furthermore the tilt-rotor is capable of performing a rolling short take-off and landing. A rolling take-off is a significant advantage since it allows the tilt-rotor to have a gross take-off weight larger than its maximum vertical take-off weight. Finally the tilt-rotor can perform all of the mentioned mission stages at (almost) any possible nacelle conversion angle, as deemed most suitable by the pilot, providing a range of operational speeds broader than for an airplane.

It is apparent that the tilt-rotor is more capable than a helicopter or airplane in specific areas, but of course there are tasks which are more suited for the helicopter or airplane. It must be noted however, that although tilt-rotors may perform a rolling take-off and landing, usually this is not possible with the nacelles tilted to a horizontal position, i.e. in airplane mode, since the large proprotors would strike the ground. Therefore this type of take-off and landing is typically achieved with the nacelles tilted to some intermediate conversion angle, e.g. a 15 degree forward tilt is required "for minimum ground-roll" [7, p70] in the XV-15.

2.2. Tilt-Rotor Control

The description of the control strategy of a tilt-rotor described in this subsection is based on the XV-15 tilt-rotor. Although differences may exist in other tilt-rotors, it is safe to assume these are minor since the engineers developing the the XV-15 pioneered and extensively tested many control solutions which served as a reliable basis for later tilt-rotor control system designs.

The basic pilot controls consist of a longitudinal-lateral center stick, rudder pedals, power lever, beta governor lever, and a nacelle angle switch. The center stick and rudder pedals are connected to the rotors' swashplate as well as the ailerons, elevator, and rudder. The longitudinal motion of the center stick controls the elevator and swashplate longitudinal cyclic on both rotors in the same direction resulting in a symmetrical pitching motion of the tilt-rotor. Rolling motion is performed with lateral input of the center stick which controls the ailerons and collective. Unlike in helicopters where rolling motion is achieved through swashplate lateral cyclic, in tilt-rotors it is instead achieved through differential collective when in helicopter mode. The difference in thrust of each of the rotors result in a rolling moment. In airplane mode only the ailerons are deflected to achieve rolling motion, however some differential collective may still be applied to counter adverse yaw [8]. Yawing motion is controlled with the rudder pedals which are connected to the rudder and swashplate longitudinal cyclic. Since the tilt-rotor has two counter-rotating rotors, it does not need a tail rotor for yaw stability and control. Instead, yawing motion is achieved through differential longitudinal cyclic while in helicopter mode. In airplane mode only the rudder is deflected to achieve yawing motion.

In helicopter mode, the power lever acts and has the same movement as the collective stick directly controlling the swashplate collective of both rotors in the same direction. The power lever is also directly connected to the throttle providing a feedforward input to the engines [2], improving the rotor RPM disturbance rejection due to the change in load as a result of a collective input. In airplane mode the collective control of the power lever is phased out meaning it only controls the throttle in this mode. Control phasing is explained in more detail in a separate paragraph.

Flight efficiency can be increased by varying the rotor rotational rate (given in revolutions per minute, i.e. RPM) depending on the flight mode, for example in the case of the XV-15 the rate is lowered from 589 RPM in helicopter and conversion modes to 517 RPM in airplane mode [2]. The pilot may select a desired RPM value through a beta governor system, comparable to the one used with a constant-speed propeller [21],

[1] Unfortunately examples of tilt-rotors employing hingeless or bearingless rotors were not found due to a lack of available information on this topic. However, these types rotors have more complex aeroelastic instability characteristics [20], and since aeroelastic instability has been a prevalent problem for tilt-rotors in general, the hingeless and bearingless rotors might not viable for tilt-rotor application.

which controls the swashplate collective in a closed-loop system [8]. The control system was designed such that the power lever does not have direct control of the blade pitch in airplane mode since in this mode the change in rotor torque is very sensitive to a change in collective [22]. Furthermore, this control effectiveness greatly increases as a function of airspeed [22] making it very difficult for the pilot to manually maintain a constant rotor rotational rate.

The pilot can control the nacelle tilt angle with, for example, a three position self-centering switch located on the power lever as in the case of the XV-15. The speed of rotation is typically kept constant, but it is possible for a slower rotation rate to be applied at near-vertical angles for more precise helicopter-mode control. Furthermore, the pilot should be able to start and stop the tilting motion at any nacelle position within the allowable bounds allowing for any conversion configuration to be flown. Finally it is convenient for the pilot to be informed about the current nacelle position with a conversion angle indicator such as the one on the XV-15 shown in fig. 2.1.

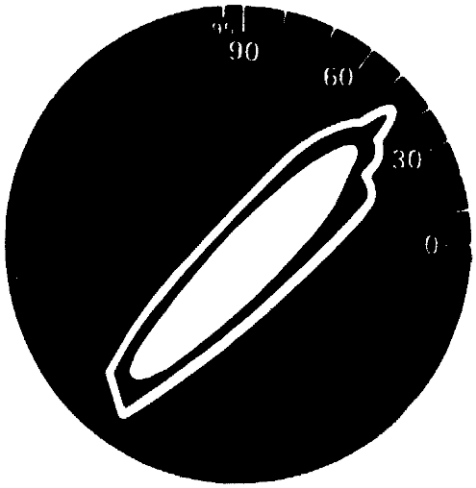

Figure 2.1: Nacelle angle indicator on the Bell XV-15 tilt-rotor. [2]

The effect of the center-stick, collective, and rudder pedal inputs on the proprotor thrust in helicopter-mode is summarized in fig. 2.2. Note that the discussed effects of inputs on the motion of the tilt-rotor do not take into account input cross-coupling effects which are present in reality. These unwanted effects can be partially removed with input mixing.

As mentioned earlier, during conversion controls can be mechanically or digitally phased out as a function of nacelle angle. This means that the amount of maximum deflection of the airplane control surfaces and the maximum amount of swashplate movement in response to pilot inputs changes depending on the nacelle tilt angle. At near-vertical nacelle angles the swashplate retains full movement, but as the tilt-rotor begins to convert into airplane mode, the allowable swashplate movement is gradually decreased until the pilot no longer has direct control over the swashplate (with some exceptions as mentioned earlier). Typically the airplane control surfaces are not phased out since they do not have a large effect on the handling qualities in early stages of conversion from helicopter mode. However swashplate controls must be phased out before the tilt-rotor converts to airplane mode because direct control of the blade pitch angles at higher velocities would make it more difficult for the pilot to fly. The control phasing profile is typically designed such that it minimizes the workload of the pilot during conversion making it an effortless and smooth maneuver [2].

2.3. Possible Modeling Scope

This section explores the elements of a tilt-rotor that can be included in a flight mechanics model. It is organized on a subsystem basis starting with the body motion and continuing with the rotor, airframe, aerodynamic interaction, control system, and concludes by addressing other possible elements that are not considered critical for the purposes of this research work.

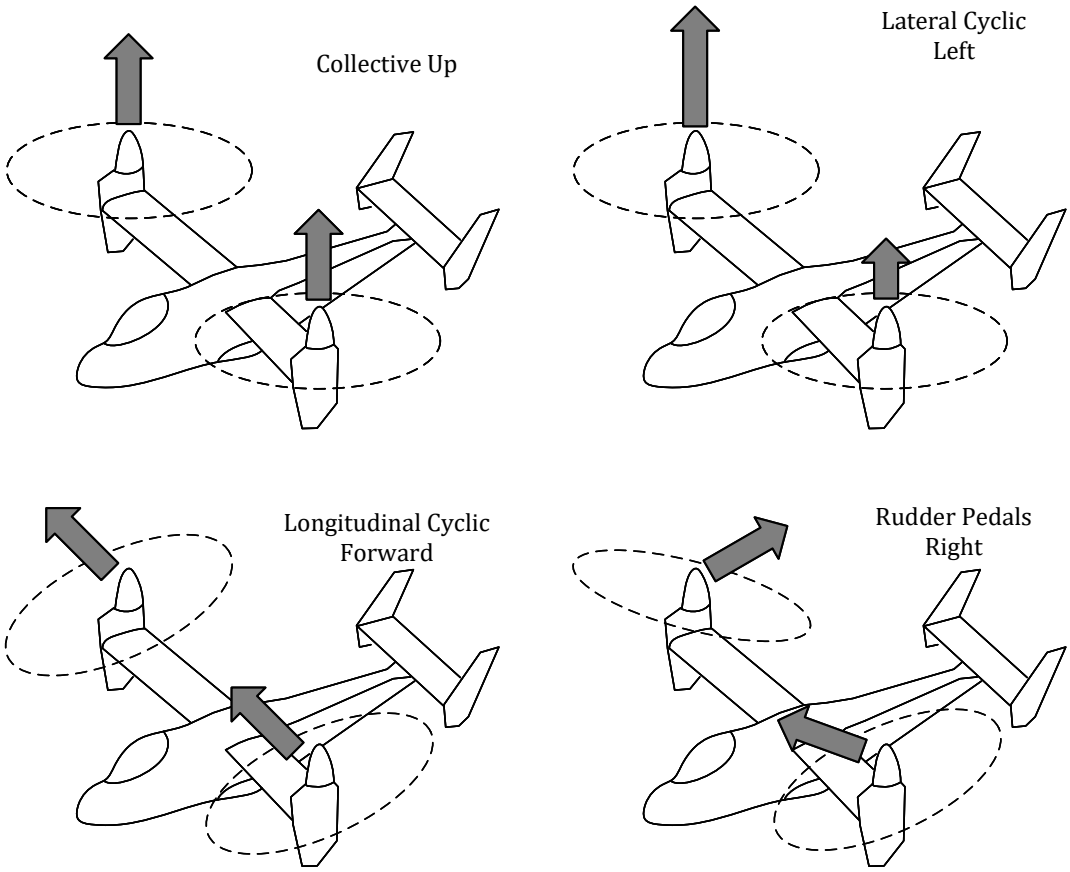

Figure 2.2: Effect of control inputs on proprotor thrust in helicopter mode.

Body Motion

Modeling the body motion of a rigid tilt-rotor differs in no way from modeling other rigid moving bodies, therefore a typical description incorporates six degrees of freedom (DoFs), i.e. three linear and three rotational motions. Since the tilt-rotor has tiltable nacelles with considerable mass and inertia, it is also possible to model the tilting of the nacelle as an additional degree of freedom. Furthermore, fuel consumption and detachable payload can have a large impact on the flight characteristics, therefore mass may also be included as an additional degree of freedom.

In cases where only specific flight behavior needs to be simulated and a simpler model would suffice, the model can be reduced to longitudinal or lateral only motions, decreasing the number of DoFs by three in each case.

Rotor

As in the case of helicopters, the rotor is one of the most complex subsystem of the tilt-rotor, therefore its model can consists of a multitude of elements. Starting with the hub, each hub type has different geometric and dynamic characteristics which can be reflected in their unique models. Therefore it is possible to develop models specifically for articulated rotors with just a flapping hinge or also including a lead/lag hinge. A hinge offset as well as a flapping spring would also require changes to be made to the model. The rotor model would also have to be rederived if the tilt-rotor would employ a teetering, gimballed, hingeless, or bearingless hub type. Additional modifications such as undersling, a precone angle, or a δ_3 hinge (coupling between feathering and flapping motion) would also change the equations in the model. Finally, the effects of cyclic and collective inputs can also be included in the model.

Blade flapping is required in order for any rotor vehicle, including the tilt-rotor, to be able to fly. Therefore this phenomenon can also be modeled either completely dynamically, including the transient motion, or quasi-statically where only the steady state is considered. In the latter case it is common to find that the motion is represented by first or second order harmonics with the fundamental frequency being the rotor rotational

rate. In addition it is possible to treat the parameters describing the quasi-static motion as dynamic, and thus including them as additional DoFs.

In order for the rotor to produce thrust, it must induce a velocity in the air. In reality this induced velocity will most likely have a very complex distribution around the rotor, therefore it is not surprising to find that it is sometimes modeled with computational fluid dynamics analyses. It is also common, however, to find approaches where a greatly simplified induced velocity model is developed where the distribution can be described with relatively simple analytical equations. These models can be made to approximate the full velocity vector of the induced velocity, i.e. the distribution of the three linear and three rotational components, or can be further simplified to only model one component such as the axial flow. In the simplest case the model can assume a uniform distribution as well. As in the case of the blade flapping, the induced velocity distribution can be modeled as static or dynamic. In the latter case additional DoFs would be required.

When modeling the dynamics and aerodynamics of the rotor, a complete approach would incorporate the effects of the rotation of the blades, the linear and rotational velocities and accelerations of the body (including the effect of an offset between the center of gravity of the body and the location of the rotor), and all wash velocity components as a result of, for example, induced velocities or wind gusts. As with the other elements, it is of course possible to neglect some contributions to the loads on the rotor thus simplifying the model.

The blade geometry affects the flight characteristics and performance of a rotor, therefore its effect can also be incorporated into the model. For example the blade twist profile can be implemented into the model as is, or it can be approximated by a simpler description such as linear variation or a constant average with no variation at all. It is also possible to include the effect of a blade that is swept or curved out-of-plane. Root and tip shape as well as blade taper can also be incorporated into the equations.

Finally, the loads of the rotor acting on the body motion through the hub can be modeled with, for example, a resultant thrust force only, or the complete load vector can be used which would include the rearward H-force, sideward S-force, the required torque Q, and the pitching and rolling moments.

Airframe

The airframe can affect the flight mechanics of a tilt-rotor in multiple ways which can be reflected in the model in multiple areas. The largest component of the airframe is the fuselage which, in part, has an effect on the aerodynamics. Therefore it can be modeled as a source of drag only, or can be treated as a lifting body which would additionally introduce lift as well as yaw, pitch, and roll moments. Other external elements such as the landing gear can be modeled separately, but in a similar manner as the fuselage. Another example of external elements of the tilt-rotor airframe are the nacelles which, apart from being modeled as aerodynamic load sources, can also introduce tilting dynamics which can affect the rotor dynamics, and vice versa.

The wings constitute another large portion of the tilt-rotor airframe. These also can be modeled to introduce the six aerodynamic forces and moments affecting the body motion, which can depend on the wing sweep and dihedral angle, and flap and aileron deflections. The horizontal and vertical stabilizers at the tail can be modeled in a similar manner taking into account the elevator and rudder deflections instead. The wing can additionally be modeled to produce a wake.

Aerodynamic Interaction

Up to this point, the mentioned elements of a tilt-rotor that can be modeled were treated as isolated subsystems. In reality, however, aerodynamic interaction has a considerable effect on performance and handling qualities, therefore several significant aerodynamic interactions that can be modeled are listed below:

- the effect of the rotor wake on the wing and empennage
- the effect of wing proximity on the rotor
- the mutual wake effect of the two rotors in proximity
- the effect of the wing downwash on the empennage
- the effect of ground proximity on the wing and rotor
- the effect of wing-nacelle interference on the wing and control surfaces

Control System

Similarly to helicopters and airplanes, the tilt-rotor may have a stability and control augmentation system (SCAS) which of course can be included in the flight mechanics model. What differentiates the tilt-rotor is the conversion flight phase during which helicopter controls are phased into airplane controls, therefore control phasing, as well as control mixing if present, can also be part of a tilt-rotor flight mechanics model.

Non-Critical Elements for Flight Mechanics modeling

The tilt-rotor model can be expanded in many more ways, but not every addition to the complexity of the model may be worth it considering its contribution to the accuracy of the flight mechanics model focused on piloted flight. Large proprotors are infamous for introducing aeroelastic instabilities and vibrational loads, therefore these issues were and continue to be a large area of research in tilt-rotor development. It is not surprising then to find that aeroelasticity and vibrations have also been extensively modeled in literature, especially for the purposes of structural and stability analyses. In these cases the rotor blades, fuselage, wings, and nacelles may be modeled as elastic and exhibit bending dynamics of their own. This would greatly increase the number of DOFs as each elastic element could potentially be modeled with multiple symmetric and asymmetric bending modes. The objective of this thesis work, however, is to obtain a tilt-rotor flight mechanics model capable of accurate performance and piloted flight simulation only, therefore the topics of aeroelasticity and vibrations will not be treated here.[2]

Other elements that have not been mentioned are for example engine and transmission dynamics, the stiff interaction of the landing gear with the ground, and the input dynamics as a result of control-linkage deformation or fly-by-wire delays, and actuator lag.

2.4. Recommended Model Elements

In contrast to the previous section which explored what *may* be modeled, this section summarizes the findings of various authors about what *should* be included in a tilt-rotor flight mechanics model and the reasoning behind it. For the sake of clarity this section is organized on a source basis rather than an model-element basis.

R. Heffley, M. Mnich 1988 [27]

The NASA contractor report written by Heffley and Mnich discusses the minimally required elements that should be included in a helicopter model developed for evaluation of handling qualities, keeping a well-thought-out balance between usefulness and cost as a result of increasing complexity.

According to the authors, the model usefulness increases asymptotically as a function of model complexity, while the costs increases exponentially. The usefulness of the model should be determined based on its intended purpose and the complexity adjusted such that the "point of diminishing returns" [27, p2], the point at which the relative cost and value are equal, is not exceeded. Therefore it is argued that the model should not be made anymore complex than required. It is also pointed out that often the complexity of the flight model is not the limiting factor of the usefulness and fidelity of the simulator, suggesting that a simpler model would suffice.

The authors suggest including the following elements in a helicopter flight mechanics model. First of all, the model should be nonlinear and be valid across the entire flight envelope of the real helicopter, constituting forward, rearward, and sideward flight, as well as hover and transition from hover to forward flight. Hovering flight should be characterized by longitudinal and lateral hover cubics (i.e. longitudinal and lateral hover dynamic modes) coupled with the rotor flapping dynamics, while the forward flight modes should consist of the short period, phugoid, Dutch roll, roll mode, and the rotor-body coupling. In sideward flight the dihedral effect should not be neglected. The dynamics of the blade flapping motion should be modeled as a first-order system at the very least, additionally reproducing the input lag experienced in real flight which is considered important by the authors. This would require three additional degrees of freedom per rotor, corresponding to the coning angle and longitudinal and lateral disk tilt angles. Higher order rotor flapping or structural dynamics should only be considered when dealing with aggressive control systems. The motion of

[2] An introduction to aeroelastic BEM modeling can be found in [23]. The development of tilting gimballed and hingeless proprotor aeroelastic models can be found in [24]. A discussion on the effect of including various DoFs on the aeroelastic behavior of a tilt-rotor wing-rotor system can be found in [25] and [26].

the helicopter should be modeled with the 6DoF rigid body equations of motion. Finally, power requirements and autorotation should be modeled realistically, preferably (but not necessarily) with a varying rotor RPM. A varying rotor would also require the inclusion of an additional degree of freedom in the model, potentially one per proprotor if these would not be interconnected.

This contractor report solely concerns helicopter simulation, nonetheless all these findings are applicable to tilt-rotor modeling due to the high similarity between the two vehicle types, at least in the case of specific flight configurations of the tilt-rotor such as in and near the helicopter-mode. However, since there are significant differences between the helicopter and tilt-rotor, such as the presence of a large main wing and the propeller-like function of the rotor in airplane-mode, there may exist minimally required model elements that are not mentioned in the report since they would be specific only to tilt-rotors. Therefore, as means of precaution, the list of desired model features presented in this report should be treated as incomplete when considering tilt-rotor flight mechanics modeling. To further emphasize this, one subtle example is given. Recalling the highlighted importance of the input lag, in the case of a helicopter, first order flapping dynamics will indeed model both longitudinal as well as lateral cyclic inputs since in the latter case the helicopter achieves roll control through lateral disk tilt, i.e. lateral flapping. In the case of the tilt-rotor, however, roll control is achieved through differential collective, therefore flapping dynamics might not be sufficient to accurately predict the lateral input lag and the model would have to be expanded with, for example, inflow dynamics.

Basing on this document only, however, it can be deduced that a 13DoF tilt-rotor model would suffice for evaluating handling qualities, assuming that the proprotors are interconnected.

M. Dreier 2007 [23]

The book written by Dreier broadly explores the development of a helicopter and tilt-rotor simulation model, includes derivations of numerical and analytical equations, and contains the authors suggestions about what elements he considers to be most important and thus should be included in a model.

Similarly to [27], Dreier suggests that first order flapping dynamics should be included in the rotor model, but he also argues that it is unnecessary to expand to second order dynamics since this introduces more complexity without significantly improving the accuracy of the model. Although this approximation is suitable for performance simulations, the same cannot be said for structural and stability analyses. The higher order dynamics could excite weakly damped high frequency modes of for example the blade, changing the flapping response which, in turn, could considerably alter the stability of the tilt-rotor. As stated before, however, this research work focuses on piloted flight (and performance) simulation and therefore the original suggestion is considered to be more appropriate. Consequently it can be considered almost certain that a performance and handling qualities tilt-rotor model will include 6 additional degrees of freedom (3 per rotor).

When modeling propeller aerodynamics, the author suggest that both axial and in-plane airflow velocity components should be taken into account, stressing that the in-plane flows give rise to moments perpendicular to the shaft axis, one of which (called the p-factor) causes a propeller aircraft to yaw during climb which can sometimes be dangerous. The tilt-rotor usually has counter rotating proprotors which would mean that, in airplane mode, the p-factor would cancel out. Nonetheless, if one proprotor experiences different aerodynamic conditions than the other, the resultant yawing moment could be non-zero and could significantly alter the handling qualities. Therefore modeling the p-factor should also be considered important when modeling tilt-rotor flight mechanics.

The author also mentions that the flow reversal region on a rotor may significantly change handling qualities and performance. It is less likely for the tilt-rotor to develop a large flow reversal region since most high speed flight will be performed in airplane mode. Nonetheless the flow reversal region might temporarily grow large during transition, altering the handling qualities in this flight phase. Therefore it might be of interest to include the flow reversal region in the model.

The author recommends for the inflow model to be described by a non-uniform axial velocity component at the very least. If resources allow, the model should be extended to all 6 velocity components. Furthermore, inflow dynamics should be included and the author highly suggests the Pitt-Peters model which has been shown to perform well in many conditions [28]. This would further increase the number of degrees of freedom by 6 in the case of a tilt-rotor (3 per rotor). If, however, resources are limited and a uniform inflow is implemented, the tip-loss factor must be employed as a correction for the required power.

Regarding general body dynamics, the author states that mass and inertia time derivatives can be neglected in the equations of motion, but it should still be possible to instantaneously change these values during a simulation run. It should be highlighted that a change of the nacelle angle may indeed significantly alter the total inertia of the aircraft, but even in the case of a tilt-rotor the rate of change of the inertia will not have a large impact within the equations of motion.

Basing on the recommendations regarding flight mechanics mentioned in the book, it can be deduced that an 18DoF tilt-rotor model would suffice for a performance and handling qualities simulation.

W. Johnson 1984 [26]

The NASA Technical Paper written by Johnson analyzes the capability of an existing analytical tilt-rotor model, developed by the same author, to predict the performance, loads, and stability characteristics of the XV-15. The author also indicates the model complexity that is required to achieve adequate accuracy in each of these three areas. The summary below focuses on requirements for performance simulations.

The author explicitly states that for performance and load simulations it is sufficient to consider only the periodic solution of the rotor motion, in contrast to stability analyses where the transient solution is also required. In the case of performance prediction, it is sufficient to describe the rotor motion with one harmonic. To put this into perspective, load prediction requires the motion to be described by ten harmonics.

Although coupled flap/lag bending DoFs were included in the performance model, the author states that these did not make a significant difference on the calculations of performance parameters in hover and high-speed cruise. Rigid and elastic torsional blade deformation DoFs showed little effect on performance calculations in hover, but significant changes in required collective (about 1 to 2 degrees) were observed. In airplane mode single-mode elastic torsion resulted in performance parameters that were 'better' by about 1.5% and blade tip rotational deflections of about $-1°$. Higher elastic torsion modes did not make a significant difference and coupling between bending and torsional deformation was not observed. It can be seen that torsional blade deformation has a non-negligible effect on performance calculations, but in the case of the XV-15, it does not improve correlation between the estimate and experimental data and therefore the author does not consider this DoF necessary for performance calculations.

According to the author non-uniform inflow and dynamic stall models should be included in a tilt-rotor simulation as they are expected to improve the prediction accuracy. The author argues, however, that (at the time of writing the technical paper) the available analytical inflow and dynamic stall models (thus including the original Pitt-Peters inflow model but not its later revisions by other authors) do no provide great improvements over uniform inflow and static stall models since these were developed for helicopter rotors and not the highly twisted blades commonly found on a tilt-rotor. Unless more accurate approaches that are specifically developed for real-time tilt-rotor simulation are found, based on this paper it can be concluded that the most accurate analytical option is to employ uniform inflow and static stall models.

When calculating the forces and moments generated by the rotor, the maximum lift and minimum drag coefficients are of particular importance for performance prediction, therefore the variation of these with the Mach number should also be modeled. Furthermore, according to the findings of Johnson in a previous paper [25], variations of these forces and moments during one rotor revolution have a very small effect on the dynamics of a gimballed or hingeless rotor both in helicopter and conversion flight modes. Therefore using the average of these forces and moments over one revolution for tilt-rotor analysis is considered adequate.

S. Ferguson 1989 [5]

The NASA contractor report written by Ferguson summarizes the development, verification, and validation of the Generic Tilt-Rotor Simulation (GTRS) using flight test data of the XV-15, focusing on the measures taken to address the deficiencies of the nominal model.

Contradictory to [27], according to Ferguson it is not necessary to predict hover performance accurately for piloted simulation since it does not make a significant impact on the fidelity. However, it is crucial that the simulated tilt-rotor inherits capabilities within the bounds of the flight envelope of the real aircraft. For this purpose, performance must be modeled correctly and thus it is implicitly also required for piloted simulation.

The author states that the ground effect as well as the tip loss factor play a significant role in hover performance modeling. The ground effect reduces the required power to hover as the distance to the ground decreases. It is not only important to incorporate the necessity to reduce the collective input as a result of

the ground effect into the model, but also to correctly model the required gradual change in collective as a function of height. In accordance with [23], the tip loss factor should also be included as it compensates for the erroneous over prediction as a result of the uniform induced velocity assumption. Although for many helicopters a value of 0.97 is acceptable, in the case of tilt-rotors it can still yield over estimated performance, therefore care must be taken such that a more accurate value is calculated.

It is mentioned that correct aerodynamic modeling of the engine nacelles and the rotor inflow dynamics have a large impact on realistic modeling of sideward flight, however discrepancies still remain even when these elements are modeled more precisely. Therefore it is hypothesized that incorrect rotor downwash effects on the airframe, ground effect in sideward flight, and tandem rotor effect on the trailing rotor may account for the unmodeled sideward flight dynamics. It is also hypothesized that the aerodynamic interaction between the wing and nacelle has a noticeable influence on the control effectiveness of the aileron due to the end plate effect and increased vorticity as a result of the wing-pylon juncture. Furthermore, flap deflection and nacelle angle also have a significant influence on the aileron control effectiveness.

Finally, the author suggests that the ground effect on the wing, wing incidence, and the interaction of the rotor wake on the wing and horizontal tail when in ground effect are model elements that might greatly influence the simulated short take-off and landing performance of the tilt-rotor.

W. Appleton, A. Filippone, N. Bojdo 2019 [29]
The paper written by the authors listed above investigates the effect of various aerodynamic interactions on the attitude and longitudinal stick trim curves of a 3DoF longitudinal XV-15 model. A comparison is made between a baseline model with no aerodynamic interactions and more complex models which successively incorporate different aerodynamic interactions. The following interactions were considered: rotor wake download on the wing; wing downwash on the horizontal stabilizer; and rotor wake effect on the horizontal stabilizer. The results of the study are also verified against trim curves obtained with the Bell Model 301 tilt-rotor mathematical model described in [30].

In summary, the nominal tilt-rotor model, which did not incorporate any aerodynamic interactions, compared moderately to the trim curves of [30], with the best correlation observed when the nacelles were completely vertical in helicopter mode. Significant discrepancy was found in the longitudinal stick trim curves. The rotor wake download on the wing had a negligible effect on the attitude and longitudinal stick trim curves. The wing downwash effect on the tail makes a significant difference on the trim curves and greatly improves the correlation of the longitudinal stick trim curves for most of the conversion angles. The rotor wake effect on the horizontal stabilizer significantly changes the trim curves only at lower flight speeds and conversion angles close to helicopter mode, however by doing so it worsens the correlation. Nonetheless it is shown that it should be included in the tilt-rotor model since, in combination with the wing downwash at the empennage, produces trim curves with better correlation overall.

Based on the results of this paper, it seems that it is worthwhile to model the combined effect of the rotor wake and wing downwash on the horizontal stabilizer, while ignoring the rotor download on the wing due to its negligible effect. Unfortunately the authors did not compare the effect of aerodynamic interactions on the collective stick trim curves. It would be interesting to see the effect of the rotor wake download on the collective trim curve, especially in helicopter mode since in this case the download would act in the opposite direction to the thrust, possibly requiring a significantly higher collective input. This is somewhat discussed by presenting power-required-for-trim curves, stating that the effects are only considerable in the case that the available power is close to the power required for hover. However, collective input limits are not mentioned which might be the actual limiting factors for some tilt-rotors. Thus, the conclusions that could potentially be drawn from a comparison of the collective trim curves might be of importance to tilt-rotor modeling since in the current study, the rotor wake download interaction made a negligible difference, suggesting that it could be neglected.

2.5. Available Tilt-Rotor Models and their Modeling Approaches

Having treated the model elements that should be included in a tilt-rotor flight mechanics model, this section presents various tilt-rotor models and their attempts at incorporating the mentioned recommended elements, discussing their approaches in the context of the findings of the previous section. Note that this section is organized on a model-element basis rather than a model basis. The section starts with the rotor dynamics

and aerodynamics, and continues with the flapping equation, inflow model and solver, the flow reversal region and tip loss factor, varying rotor rotational rates and autorotation, wing and tail aerodynamics, airframe aerodynamics, airfoil characteristics, aerodynamic interaction, the ground effect, and concluding with a description of different trimming routines.

Rotor Dynamics

In order to simulate the flight mechanics of a tilt-rotor it is necessary to calculate the forces and moments developed by the rotors in the body reference frame. Although calculating these loads in the body reference frame directly would not require any additional transformation, it is more convenient to derive the rotor equations of motion in the rotor rotating frame of reference and perform the transformation nonetheless. Therefore this approach is often used in helicopter, propeller, and tilt-rotor analyses.

The forces and moments developed by the rotor can be the result of mass acceleration, aerodynamics, or structural reaction. The latter would, for example, include loads resulting from blade elasticity which, as mentioned before, is not within the scope of this thesis. One exception would be modeling blade elasticity with a rigid blade attached to the hub via springs and dampers. Due to the relative simplicity of this approach it is considered to be within the bounds of this research project. From this point onward, any mention of rotor dynamics refers to loads as a result of mass acceleration and the aforementioned hub springs and dampers. Aerodynamics are treated later.

Depending on the author, rotor dynamics may be derived in different rotating frames, including the shaft/hub plane (as is done in [29] and [31]) which is the plane perpendicular to the shaft, the tip-path plane which is the plane formed by the blade tips, and the control plane which is the plane coincident with the swash-plate. The choice of the rotating frame defines the reference for the blade deflections which comprise blade flapping, lead/lagging, and collective and cyclic inputs.

The total linear acceleration $\boldsymbol{a}$, as observed from an inertial reference frame, experience by a mass element of the rotor blade moving in a non-inertial rotating reference frame can be described by eq. (2.1). As can be observed, the total acceleration is the result of the summation of multiple acceleration terms. Before these terms are treated, it must be mentioned that $\boldsymbol{a}$, $\boldsymbol{s}$, $\boldsymbol{\omega}$, and $\boldsymbol{a}_{hub}$ represent three-dimensional vectors defined within the rotating reference frame. Here $\boldsymbol{s}$ is the position vector of the blade mass element, $\boldsymbol{\omega}$ is the rotational velocity vector of the rotating reference frame, and $\boldsymbol{a}_{hub}$ is the linear acceleration vector of the origin of the rotating reference frame (thus the rotor hub) defined within the rotating reference frame. The time derivatives of the position and rotational velocity vectors are indicated with over-dots.

Returning to the acceleration terms, in eq. (2.1) $\ddot{\boldsymbol{s}}$ is the linear acceleration of the mass elements as observed from the rotating frame, and this would encompass the linear acceleration as a result of blade flapping or lead/lagging rotational accelerations acting at a distance from the appropriate hinges. Next, $2\boldsymbol{\omega} \times \dot{\boldsymbol{s}}$ represents the Coriolis acceleration also caused by the motion of the mass element as a result of flapping and lead/lagging, $\dot{\boldsymbol{\omega}} \times \boldsymbol{s}$ corresponds to the linear acceleration as a result of rotational acceleration acting at a distance from the axis of rotation (due to, for example varying rotor RPM or body rotational acceleration), and finally $\boldsymbol{\omega} \times (\boldsymbol{\omega} \times \boldsymbol{s})$ is the centripetal acceleration mainly resulting from the blade rotation around the shaft.

$$\boldsymbol{a} = \ddot{\boldsymbol{s}} + 2\boldsymbol{\omega} \times \dot{\boldsymbol{s}} + \dot{\boldsymbol{\omega}} \times \boldsymbol{s} + \boldsymbol{\omega} \times (\boldsymbol{\omega} \times \boldsymbol{s}) + \boldsymbol{a}_{hub} \tag{2.1}$$

Depending on the author's choice, the rotor dynamics are either modeled with the complete equation, or some terms are neglected. The most common term to be neglected is the hub acceleration, but it is possible to find models which include, at least partially, the hub acceleration in the rotor dynamics. For example, in [32] the body rotational acceleration and offset between the body center of gravity (CoG) and rotor hub contribute to the hub acceleration, but the linear body acceleration does not. In [33], however, the model is simplified even more by neglecting the contribution of the body rotational acceleration as well. It should be noted at this point that gravitational acceleration can also be included in the $\boldsymbol{a}_{hub}$ vector, but is also often omitted since it is considered to be small when compared to the other acceleration terms. It can be found in some tilt-rotor models nonetheless, such as in [31] or [33].

On a related note, it is common to find tilt-rotor models where several rotational velocity or acceleration terms are partially or completely omitted from the $\boldsymbol{\omega}$ vector. For example oftentimes only the body roll

p and pitch q rates are included in this vector, while the body yaw rate r is neglected, arguing that it is insignificant in comparison to the rotor rotational rate Ω around the shaft. This simplification originates from the helicopter field where the rotor hub has a fixed orientation with respect to the body and therefore the body yaw rate vector is closely aligned with the Ω vector. In the case of tilt-rotors, however, this assumption can be greatly violated since the proprotor can tilt forward by 90° resulting in the two vectors being close to orthogonal. For this reason it is also possible to find models were the body yaw rate remains included in the $\boldsymbol{\omega}$ vector, as is done in [32] for example. In this model, however, the author chose to neglect several rotational rates nonetheless, such as the acceleration of the rotor $\dot{\Omega}$ through the assumption of a constant RPM (which also shows that it is possible to only include a rotational velocity component while neglecting its time derivative, hence the mentioned partial omission), and the nacelle tilt rotational velocity $\dot{\eta}$ and acceleration $\ddot{\eta}$. On the other hand, in [33] the author does include the nacelle rotational rate $\dot{\eta}$ in the $\boldsymbol{\omega}$ vector, but only in the Coriolis acceleration term (which shows that the $\boldsymbol{\omega}$ vector can vary across the different acceleration terms within eq. (2.1), again supporting the mentioned statement of partial omission). In [31] the nacelle rotational rate is completely omitted from all terms, but the model is further simplified by also selectively omitting the blade flapping rate $\dot{\beta}$ and acceleration $\ddot{\beta}$ from the Coriolis acceleration term.

Apart from the linear and rotational velocities and accelerations, the type of rotor hub also has an impact on the generated rotor forces and moments. The rotor hub type will influence the position vector $\boldsymbol{s}$, as well as the mass and inertia of the blades which in turn will affect the acceleration of the blades subject to the aerodynamic forces and moments. A particularly significant difference exists between an articulated and gimballed rotor due to the fact that in the latter case all the blades are connected and pivot together. This difference is magnified in the case that the blades and their connection are assumed to be rigid. Therefore some authors, for example [29], choose to follow reality closely and model the rotor dynamics with the equations corresponding to the appropriate hub type. Others simplify the problem and assume that one hub type may be approximated with the equations corresponding to another hub type, for example in [32] the gimballed hub of the XV-15 is modeled with an articulated hub, but no additional effort is made to compensate for the differences between the two hub types. On the other hand, in [31] although only an articulated hub is modeled, the author identifies that differences may exists and provides some compensation in the form of a tunable flapping spring which can be adjusted to emulate frequency characteristics of different hub types.

As mentioned in section 2.3, rotor hubs can be characterized by other elements as well such as hub restraints (springs and dampers), hinges (flapping, lead/lag, δ_3, and undersling), or various geometries (hinge offsets and precone angles). A notable and unique rotor hub characteristic can be found in [34] where an offset between the cross-sectional blade element CoG and feathering axis is introduced, producing an additional torque acting on the hub (assuming the feathering hinge reacts rigidly to external torques) as a result on inertial mass acceleration.

Rotor Aerodynamics

Continuing from the last subsection, the remaining forces and moments developed by the rotor originate from the aerodynamics of the rotor blades. These loads can be found with the Blade Element Method (BEM) or with the aid of computational fluid dynamics. Unfortunately the latter is computationally expensive and thus not suitable for real-time simulation [35], therefore only the application of the BEM is explored in this literature review.

Similarly to the dynamics, the BEM may be carried out in the different rotating frames and typically it is the same reference frame as the one used for the dynamics. It is common to find the rotor aerodynamics to be derived in a disk reference frame aligned with the oncoming aerodynamic velocity, i.e. the disk-wind axis system, as is done in [29] and [23]. This is achieved through a sideslip angle Δ rotation about the disk normal axis. The sideslip angle is defined in eq. (2.2) where μ_x is the dimensionless longitudinal velocity in the disk plane, and μ_y is the lateral component. Performing the aerodynamic analysis in the wind axis system simplifies the equations by eliminating the lateral velocity component from them. This, however, requires an additional transformation to be performed from the wind axis back to the nominal rotor disk axis in order to obtain the correct aerodynamic loads.

$$\Delta = arctan\left(\frac{\mu_y}{\mu_x}\right) \tag{2.2}$$

The total aerodynamic linear velocity $\boldsymbol{v}_a$ seen by the blade element in the rotating blade element reference frame can be described by eq. (2.3). Similarly to the total acceleration, the total aerodynamic linear velocity $\boldsymbol{v}_a$ is also a summation of multiple velocity terms. Again, $\boldsymbol{v}_a$, $\boldsymbol{s}$, $\boldsymbol{\omega}_i$, $\boldsymbol{\omega}_w$, $\boldsymbol{v}_i$, and $\boldsymbol{v}_w$ represent three-dimensional vectors defined within the rotating frame of reference. In this case $\boldsymbol{v}$ corresponds to linear velocity, and $\boldsymbol{\omega}$ corresponds to rotational velocity, with the subscripts i and w indicating the inertial and wash components respectively. The inertial velocity components originate from the fact that the rotor blade element is moving with respect to an inertial frame of reference, while the wash velocity components comprise all external aerodynamic velocities such as rotor wash (which requires the calculation of the rotor induced velocity, treated in its own section) or wind gusts. Note that in the acceleration equation (eq. (2.1)) only the inertial velocity is used since the wash velocity does not contribute to loads originating from the dynamics.

Returning to the velocity terms, in eq. (2.3) $\dot{\boldsymbol{s}}$ is the linear velocity of the blade element as observed from the rotating frame, and this too would include the linear velocity as a result of blade flapping or lead/lagging rotational rates acting at a distance from the appropriate hinges. Next $(\boldsymbol{\omega}_i + \boldsymbol{\omega}_w) \times \boldsymbol{s}$ represents the linear velocity as a result of the total rotational velocity acting at a distance from the axis of rotation, and this, for example, would include the influence of the body rotational rate, nacelle tilting rate, or the rotational velocity of the rotor wake (if modeled) on the aerodynamics. Finally $(\boldsymbol{v}_i + \boldsymbol{v}_w)$ corresponds to the total linear velocity experienced by the blade element which would include the body translational velocity or linear wake velocity components for example.

$$\boldsymbol{v}_a = \quad \dot{\boldsymbol{s}} \quad + \quad (\boldsymbol{\omega}_i + \boldsymbol{\omega}_w) \times \boldsymbol{s} \quad + \quad (\boldsymbol{v}_i + \boldsymbol{v}_w) \tag{2.3}$$

It is possible to come across tilt-rotor models where the wash velocity component is completely or partially omitted, but more often other models include the rotor or airframe induced wash while neglecting wind gusts. Analogously to the acceleration equation, some authors choose to not include all rotational velocity components in the $\boldsymbol{\omega}$ vector. Apart from neglecting wash rotational velocities, the body yaw rate is also sometimes not included in the $\boldsymbol{\omega}$ vector for the same reasons as mentioned in the preceding subsection on rotor dynamics. Other models, such as the ones found in [32] and [33] do take the body yaw rate into account. The former also does not include the nacelle tilting rotational velocity in the $\boldsymbol{\omega}$ vector.

These rotational velocities result in a linear velocity component because of a distance that exists between the blade element and the axis of rotation. If done correctly, this distance should measure from the appropriate (and possibly unique) rotation axis of each rotational velocity component to the blade element, but some tilt-rotor models are simplified by generalizing or neglecting these distances. For example in [33] body rates orthogonal to the shaft axis introduce a linear velocity component at the rotor hub which is calculated using the distance between the body CoG and the hub. This linear velocity component is then uniformly applied across the rotor disk neglecting the relative distance of each blade element with respect to the hub. This approach simplifies the model but also yields an inaccurate velocity vector since the distance between the body CoG and each blade element should have been used which would result in a non-uniform velocity distribution across the rotor disk. The author does, however, use the correct distance to each blade element in the case of body rates aligned with the shaft axis. An example of a tilt-rotor model where the correct approach is employed for all body rates can be found in [31].

The aerodynamic velocity vector consists of three components described in the blade element reference frame. These components are typically referred to as the radial U_R, tangential U_T, and perpendicular U_P velocities. It is common to find proprotor models where it is assumed that the flow along the blade span can be neglected, treating the blade element as an infinite wing, therefore also completely disregarding the radial velocity component U_R. The other two components are essential, however, in order to find the aerodynamic forces and moments generated by the airfoil. Again the model can be simplified by assuming that the tangential velocity U_T is much larger than the perpendicular velocity U_P (e.g. in [23], [33], or [32]) which makes it possible to, first of all, assume that the total velocity is equal to the tangential velocity, and second of all, assume that the blade inflow angle ϕ_{bl} is small enabling the application of the small angle approximation. Both of these assumptions greatly simplify the lift, drag, and pitching moment equations and might be acceptable for helicopter flight mechanics simulation, but the same cannot be said in the case of a tilt-rotor. Since the proprotors may be tilted forwards into airplane mode, during which the tilt-rotor may fly at high speeds, it is likely for the perpendicular velocity component to become significant with respect to the tangential velocity. In this case regions on the proprotor may experience inflow angles than no longer can be considered small, violating the assumption and yielding inaccurate results.

One of the main reasons why many authors choose to assume that $U_T \gg U_P$ is because this simplification makes it possible to linearise the blade inflow angle which contains the flapping rate $\dot{\beta}$. This in turn makes it possible to linearise the flapping equation with respect to β and its time derivatives yielding a differential equation that is much simpler to solve. Due to the unfitness of the assumption in the case of tilt-rotors, however, the authors of [31] isolate the flapping rate from the other velocity terms within U_T and U_P and only linearised the portion of the inflow angle dependent on the flapping rate. This expanded the validity of the proprotor model to allow for high inflow angles which are likely to occur in the case of a tilt-rotor.

Apart from the velocity vector, the aerodynamic forces and moments also depend on the geometric description of the rotor blade, which differs between models. It has been mentioned that the blades of a tilt-rotor are highly twisted, therefore it is interesting to explore the different approaches of incorporating this twist in the model. Starting with the simplest approach, in [6] the twist is approximated with a constant value equal to the actual twist of the blade at the $3/4$ blade radial position. Although this would result in an inaccurate blade-wise aerodynamic load distribution, the average load per revolution would remain relatively accurate which is sufficient for performance simulations. One important exception is when stall characteristics are included in the model, the reason being that a non-varying twist would greatly alter the angle of attack distribution which dictates which regions of the rotor experience stall. This in turn may have a significant impact even on the mentioned averaged-per-revolution loads, invalidating the appropriateness of the constant-twist assumption for performance simulations. A more appropriate simplification is made in [32] and [33] where the twist is assumed to vary linearly along the blade span. A slightly modified version of this simplification is used in [29] and [30] where the twist is described with a piecewise linear curve that more closely resembles the actual non-linear twist distribution. Finally, in [31] the twist is modeled with a 3^{rd} order polynomial which, in contrast to the previous method, yields a smooth twist distribution.

Similarly to the twist distribution, other geometric characteristics such as blade planform and airfoil distribution [36], or chord distribution [31], may be included in the proprotor aerodynamic model. Once again the tilt-rotor proprotor model developed in [34] includes a notable geometric characteristic, i.e. an offset is introduced between the aerodynamic center of the blade element and the feathering axis which generates an additional periodic torque that acts on the hub.

Flapping Equation

Combining the dynamic and aerodynamic forces and moments yields the equation of motion of the blade in the rotating reference frame. Although this equation of motion may model both flapping and lead/lagging motion, in this subsection it is assumed that only the flapping motion is included in the equation. Hence from this point on it is referred to as the flapping equation.

The blade equation of motion must be transformed back into a body-relative non-rotating reference frame such that the rotor loads acting on the hub can be defined in the body system and incorporated into the body equations of motion. In order to be able to do so, the flapping angle must be know at each calculation cycle, therefore the flapping equation must be solved for the flapping angle. One approach of solving the flapping equation involves performing numerical time integration, as is done in [29] for example. The advantage of this approach is that both the transient and steady-state solution of the flapping equation is obtained. In the case of real-time simulation, time integration might not be suitable due to the high computational cost required to perform calculations at a frequency several times higher than the rotor rotational rate in order to capture the transient response. Recalling the modeling recommendations found in section 2.4, only the periodic solution to the rotor motion is necessary for tilt-rotor performance simulations, therefore the transient solution may be neglected. For this reason the quasi static approach of solving the flapping equation might be more suitable.

The quasi static method assumes that transient rotor motion resolves relatively quickly (e.g. within one or two rotor revolutions) and only provides a presumed solution of the shape of the steady-state flapping response as a function of the azimuth position of the blade, rotor states, and control inputs. The presumed solution consists of an average term and harmonic terms, where the latter may be selected to include different order harmonics. Typically the solution is truncated to the first harmonic (recalling the recommendations, it is unnecessary to include higher harmonic terms) and takes take form of eq. (2.4), therefore the approximated path the flapping blade takes as viewed from the non-rotating body reference frame resembles an inverted cone than may tilt longitudinally and laterally. Here, β is the resolved flapping angle, a_0 is the average term referred to as the coning angle, a_1 is the longitudinal cone tilt, and b_1 is the lateral cone tilt. The quasi

static method is often used in tilt-rotor models, such as [32] and [33], due to its simplicity and suitability for real-time application.

$$\beta = a_0 - a_1 cos(\psi) - b_1 sin(\psi) \tag{2.4}$$

The quasi static method can be expanded to approximate the transient solution of the flapping blade by treating the coning parameters (e.g. a_1) as dynamic states. This approach is employed in [31] where, initially, only the first order flapping dynamics are included, and these are modeled with eq. (2.5). Here $\boldsymbol{C}$ and $\boldsymbol{A}$ are 2x2 matrices, and $\boldsymbol{B}$ is a 2x1 vector, all containing the appropriate terms of the linearised flapping equation. This model was later modified to include second order dynamics, i.e. $\ddot{a}_1$ and $\ddot{b}_1$. According to the recommendations, however, first order flapping dynamics are sufficient for tilt-rotor performance or piloted flight simulations.

$$\boldsymbol{C}\begin{bmatrix}\dot{a}_1\\ \dot{b}_1\end{bmatrix} + \boldsymbol{A}\begin{bmatrix}a_1\\ b_1\end{bmatrix} = \boldsymbol{B} \tag{2.5}$$

Inflow Model

Modeling the rotor with the BEM requires some calculation of the induced velocity in order to determine the resultant velocity on the blade element. The inflow or wash velocity can be described by six velocity elements, three linear and three angular velocities. In literature, however, many authors choose to only consider the axial component of the wash velocity [23], i.e. the one perpendicular to the rotor disk, neglecting the longitudinal, lateral and rotational components. The inflow velocity may be uniform across the rotor disk, or may change according to some linear or non-linear gradient. The simplest rotor analyses assume a uniform inflow distribution (as is done in [32], [33], [34], and [37]) and more accurate ones incorporate the non-uniformity, but still resort to linear gradients. In addition, the inflow model may contain dynamics of its own and thus be dependent on its past state. Again, the simplest rotor models do not incorporate inflow dynamics, while the more accurate ones do.

The induced velocity itself can be calculated according to multiple theories. The momentum theory model (later referred to as the simplified momentum model) is a very popular option and is explored more in depth in the next subsection on solving for inflow. Other options include the vortex models and the lifting line theory model which can be further divided into free wake, semi-prescribed wake, and fully-prescribed wake variations. A more elaborate discussion and comparison of the mentioned models can be found in [35]. The authors of this paper conclude that a simplified version of the momentum theory model, characterized by eq. (2.6), produces results with an accuracy very comparable to the other methods, making it an attractive option considering its simplicity. It should be noted, however, that the analysis was performed for rotors in axial flow only, therefore discrepancies in accuracy might occur in different flow conditions. In the equations below, T is the thrust, Q is the torque applied on the flow, R is the rotor radius, ρ is the air density, V is the oncoming axial airflow velocity, w_a is the axial induced velocity component, w_t is the circumferential or tangential induced velocity component, and the *disk* and *far* subscripts distinguish the values at the rotor disk and far downstream in the rotor wake.

$$T = 2\pi R^2 \rho w_a (V + w_a) \tag{2.6a}$$

$$Q = \frac{2}{3}\pi R^2 \rho w_t (V + w_a) R = \left(\frac{w_t}{3w_a}\right) TR \tag{2.6b}$$

$$w_{a,far} = 2w_{a,disk} \tag{2.6c}$$

$$w_{t,far} = w_{t,disk} \tag{2.6d}$$

As mentioned at the beginning, apart from the different methods of calculating the induced velocities, the inflow model is also defined by the velocity distribution and dynamics. An example of an axial-only and linearly non-uniform inflow model with first order dynamics used for tilt-rotor modeling is the one used in [29]. It is a variation of the Pitt-Peters model modified by Peters and HaQuang in [38] for helicopter analysis. Equation (2.7a) defines the distribution of the inflow ratio λ_i, where ν_0 is the mean inflow, ν_s and ν_c are the

lateral and longitudinal inflow gradients, r is the radial position along the blade, R is the blade radius, and $\bar{\psi}$ is the blade azimuth angle with respect to the longitudinal axis in the wind reference frame. The dynamics of the inflow parameters are described by eq. (2.7b) where $[\boldsymbol{M}]$ is an apparent mass matrix introducing a time delay effect, $[\boldsymbol{L}]_{nl}$ is a gain matrix, and C_T, C_L, and C_M are the rotor thrust, roll, and pitching coefficients in the wind axis system. For brevity purposes the definitions of $\bar{\psi}$ and the mass and gain matrices are not presented here, however these can be found in [38].

$$\lambda_i = \nu_0 + \nu_s \frac{r}{R} sin(\bar{\psi}) + \nu_c \frac{r}{R} cos(\bar{\psi}) \qquad (2.7a)$$

$$[\boldsymbol{M}] \begin{bmatrix} \dot{\nu}_0 \\ \dot{\nu}_s \\ \dot{\nu}_c \end{bmatrix} + [\boldsymbol{L}]_{nl}^{-1} \begin{bmatrix} \nu_0 \\ \nu_s \\ \nu_c \end{bmatrix} = \begin{bmatrix} C_T \\ -C_L \\ -C_M \end{bmatrix} \qquad (2.7b)$$

It is possible to omit the dynamics and only consider a non-uniform distribution, or have a uniform distribution but still model inflow dynamics. According to Chen in [28], the Pitt-Peters model shown above performs well in general, and due to its simplicity, is very well-suited for real time simulation of helicopters and tilt-rotors, e.g. [31]. For this reason other approaches of modeling the inflow are not treated any further in this literature review, however more can be found in [28] which presents an exhaustive overview of the other inflow models.

Solving for Inflow

The inflow velocity cannot be algebraically calculated based on the states of a system because it depends on the thrust, which in turn depends on the inflow velocity itself, resulting in an implicit equation which must be solved in some manner. In [23], the author shows that it is possible to simplify the rotor analysis by neglecting the contribution of the induced velocity in the oncoming airflow. This means that the thrust can be calculated directly without ever needing to calculate the induced velocity. This simplification, however, limits the flight conditions to pure axial flow and high air velocities. Although this might be acceptable for propeller performance analysis in high velocity steady axial flight, the same cannot be said for tilt-rotor modeling. Already in airplane mode the prop-rotors can experience much different flight conditions such as a disk angle of attack which would introduce off-axial flow velocity components, not to mention the vastly different aerodynamic conditions in helicopter mode.

If one chooses to employ the simplification nonetheless, it is possible to improve the approximation accuracy of the model by introducing an empirical correction factor, but this does not provide much insight. A more rigorous approach is to solve the implicit inflow equation which, when neglecting inflow non-uniformity and dynamics, takes the form of a fourth-order polynomial as shown in eq. (2.8) [23]. Here $\overline{w}$, $\overline{\mu}$, and $\overline{\eta}$ are the non-dimensional total induced velocity, horizontal aerodynamic velocity, and vertical aerodynamic velocity respectively, made non-dimensional through a division by the induced velocity in hover. θ_T is the angle between the thrust vector (which is taken to be normal to the disk plane) and the horizon, and thus implicitly incorporates the nacelle tilt angle. The polynomial can be obtained by substituting the expression for the resultant airflow velocity seen by the rotor disk into the Glauert momentum model and made non-dimensional. Several methods to solve the polynomial are described in [23] and summarized below.

$$\overline{w}^4 + 2\Big(\overline{\mu} cos(\theta_T) - \overline{\eta} sin(\theta_T)\Big)\overline{w}^3 + (\overline{\mu}^2 + \overline{\eta}^2)\overline{w}^2 - 1 = 0 \qquad (2.8)$$

The inflow polynomial can be solved with the standard Newton-Raphson method where the non-dimensional induced velocity is approximated in an iterative manner with the use of the polynomial function and its derivative. Fortunately the derivative of the polynomial can also be described analytically therefore no computational power must be expended to numerically obtain it, making it an attractive approach for real time simulation application. The iterative loop can be stopped once eq. (2.8) is sufficiently close to zero upon substitution of the estimated induced velocity.

A different approach to solve for the inflow is the iterative feedback method. Here an initial guess of the inflow velocity is made and the expression for thrust developed according to the BEM is evaluated with this value. This thrust value is then substituted into the Glauert momentum model yielding a different value for the induced velocity. The next guess for the induced velocity is then obtained by taking some weighted average (e.g. 50-50 or 70-30) between this different value and the previous guess. This type of approach is used in, for example, [31] and [6].

The third approach involves the bisection method where the Glauert momentum model expression is first rearranged into standard form with the right-hand side (RHS) set to zero. Next an upper and lower bound for the induced velocity is chosen. The author of [23] suggests that the upper bound be set to 20 times the induced velocity at hover, and the lower bound to be the negative of this value, making it very likely for the solution to be within the bounds. The thrust developed with the BEM is substituted into the rearranged Glauert momentum model and the expression is evaluated at the bounds and at the midpoint between the bounds. Depending on the results, either the midpoint value is taken as the solution, or the iteration continues by replacing one of the bounds with the midpoint value and calculating a new midpoint value. The biggest advantage of this approach is that divisions by zero are eliminated providing a fully defined system. This, however, comes at a price of slower convergence in comparison with the previous methods.

Other approaches involve modeling the inflow as a dynamic system. In this case only a trim solution must be initially found with, for example, one of the above approaches and subsequent values for the inflow velocity are then obtained through time integration of the inflow dynamics, just as is done with the dynamic equations of the aircraft.

Flow Reversal

One of the tilt-rotor model recommendations, specifically desirable for tilt-rotor handling qualities assessment, is the inclusion of the flow reversal region. According to [23], in order to incorporate the effect of the flow reversal region the standard BEM integration of the differential forces and moments along the blade and azimuth is divided into three parts as seen in eq. (2.9). Here $f(r,\psi)$ represents the differential load acting on the blade element, μ is the advance ratio, and ψ is the azimuth angle. The first part on the RHS is the integration along the entire blade radius and the advancing side of the rotor. The second part is the negative integration over the retreating side of the rotor along the blade portion that is within the circular flow reversal region. The third part is the integration over the retreating side of the rotor as well, but along the blade portions that are outside of the flow reversal region.

$$\begin{aligned}\int_0^{2\pi}\int_0^R f(r,\psi)drd\psi &= \\ &= \int_0^{\pi}\int_0^R f(r,\psi)drd\psi - \int_{\pi}^{2\pi}\int_0^{-\mu R sin(\psi)} f(r,\psi)drd\psi + \int_{\pi}^{2\pi}\int_{-\mu R sin(\psi)}^R f(r,\psi)drd\psi\end{aligned} \tag{2.9}$$

Tip Loss Factor

Another mentioned recommended element is the tip loss factor. In [5], Ferguson mentions that the tilt-rotor tip loss factor B may be approximated with eq. (2.10), an equation introduced in [39] and meant for helicopter analysis, where c_t is the blade tip chord and R the rotor radius. Although other methods of estimating the tip loss factor for helicopters are discussed in [39], it seems that Ferguson decided that eq. (2.10) is most suitable for tilt-rotor modeling, or at least achieved the most realistic performance estimation for the XV-15. Therefore it may be the case that this equation was just an elaborate manner of data fitting for the XV-15 model and thus it might be a possible source of error when attempting to model different tilt-rotors.

$$B = 1 - \frac{c_t}{2R} \tag{2.10}$$

One other method of estimating the tip loss factor presented in [40] is given by eq. (2.11), where C_T is the rotor thrust coefficient and N is the number of blades. Although it is explicitly stated by the author of [40] that this equation is best suited for lightly-loaded rotors, it is used nonetheless in [29] to model the tip loss factor for a tilt-rotor, an aircraft with highly-loaded rotors in comparison to helicopters. The reason for this choice is unfortunately not given, however it is reported that the complete tilt-rotor model, using this equation with constant C_T calculated at hover, is accurate enough for piloted flight and performance prediction purposes. This suggests that the method of determining the tip loss factor might not be of highest importance, as long as it has been demonstrated to be accurate enough for tilt-rotor flight mechanics modeling.

$$B = 1 - \frac{C_T}{N} \tag{2.11}$$

Other authors, such as R. Chen in [41], assume the tip loss factor to be 1 despite the fact that they also assume a uniform inflow. It must be noted, however, that R. Chen's goal was to develop a very simple rotor model for piloted simulation, finding it appropriate to resort to such a simplification.

Several authors, such as [29], also take into account the effect of lost lift due to the hub structure or rotor spinner with the use of the root cut-off fraction. The result of this fraction is that instead of summing the forces along the entire span of the rotor blade, it is summed starting from a positive, non-zero value - the root cut-off fraction. By doing so, it is assumed that a fraction of the root portion of the blade produces no lift or drag.

Varying Rotor RPM and Autorotation

The possibility to model autorotation is recommended in [27], and this can be achieved through a varying rotor RPM. A simple dynamic model of the rotor rotational rate is presented in [23] and can be seen in eq. (2.12). Here J is the rotor moment of inertia, $\dot{\Omega}$ is the rotor rotational acceleration, Q_{engine} is the torque supplied by the engine, and Q_{rotor} is the torque absorbed by the rotor which can be derived using BEM.

$$J\dot{\Omega} = Q_{engine} - Q_{rotor} \tag{2.12}$$

In the simplest case it can be assumed that the torque supplied by the engine is equal to the torque absorbed by the rotor, unless the required torque or power exceeds the limits of the engine. In the former case the rotor will have a constant rotational rate, and in the latter the rotational acceleration (or more likely deceleration) will depend on the difference between the maximum available torque and the torque absorbed by the rotor. This simple model also allows to simulate autorotation in which the torque supplied by the engine can be assumed to be zero and thus the rotational acceleration will be proportional to the absorbed torque.

Wing and Tail Aerodynamics

Aside from the rotors, the wing and tail are also significant contributors to the forces and moments acting on the body. In [23] multiple manners of calculating these loads are mentioned, and these methods will be described in terms of the main wing only. Nonetheless the same methods may be employed in the calculation of the forces and moments generated by the horizontal and vertical stabilizers due to their high similarity with the main wing.

The point load approach is the simplest variant. It involves approximating the wing with a planform which is used to calculate the resultant force and moment which is assumed to act at one point, usually at the quarter-chord point of the mean aerodynamic chord (MAC). Although this method does not model a lift distribution, it is still possible to include the effect of the rotor download on the wing, which may be a desired feature of a tilt-rotor flight mechanics simulation, trough empirical relations. An additional problem of the point load method is the incorporation of the body rotational rates on the calculated loads. Since the loads are calculated for the entire wing, an equivalent aerodynamic velocity due to body rotations must be found which would approximate the aerodynamic velocity distribution across the wing span. As an example, in [32] the linear velocity as a result of body roll rate calculated at the 2/3 wing span distance from the root is taken as the velocity representative of the velocity distribution.

A modified version of the point load approach which somewhat combats the troublesome influence of the body rates is the derivative method described in [23]. Here the point load approach is only applied to the aerodynamic loads resulting from linear body motion. The aerodynamic forces and moments resulting from body rates, however, are calculated with the use of load derivatives, such as $\partial L/\partial p$, which are multiplied with the appropriate body rotational rate to yield the desired change in aerodynamic load. The given load example would correspond to a change in the lift as a result of a change in the body roll rate. The load derivatives may be obtained experimentally, numerically, or analytically.

A more commonly used approach, however, involves strip theory which divides the wing into airfoil cross-sections for which the aerodynamic loads are calculated individually and integrated along the wing span, similarly to the BEM approach. The wing strips are discrete, however, and therefore require numerical integration to be performed during the simulation, as is done in [29] for example. Dividing the wing in a continuous manner and thus allowing for analytical integration to be performed during the derivation of the model and not during simulation, as is done in the case of the BEM, has not been observed in any of the mentioned tilt-rotor models. There does not seem to be any serious barrier preventing this approach from

being implemented, but significant modifications would have to be made to the load equations such as a presumed function describing the rotor download on the wing.

Other methods of calculating the aerodynamic loads of a wing include the lifting line theory, lifting surface theory, vortex lattice method, and computational fluid dynamics, however these are not commonly used in real-time tilt-rotor simulations due to their increased computational cost.

All of the above methods require some geometric description of the wing, the extent of which may be limited by either the method or the desired model accuracy. In the case of the most common approach, i.e. strip theory, the limiting factor is typically the latter and thus the author decides whether or not to include certain wing geometric characteristics. For example, in [29], the tilt-rotor wing chord, span, and taper as well as the dihedral, sweep, and incidence angles are included in the model. As a side note, the model is simplified by applying the small angle approximation to the incidence angle. In [36] the wing is additionally described with twist and airfoil distributions.

Airframe Aerodynamics

Although the airframe may comprise a multitude of components, the most common elements to be included in a tilt-rotor model are the fuselage and nacelles as these most likely have the largest impact on the aerodynamics. The nacelles are sometimes omitted as well, e.g. in [32].

The fuselage and nacelles are often modeled with coefficients taken from experimentally obtained data tables, as is done in [33], [6], [36], and . In [5] initially the nacelle drag was modeled empirically as a function of the nacelle tilt angle. In a later revision of the tilt-rotor model this was changed to the experimentally obtained data to improve accuracy.

In order to determine the aerodynamic loads, the velocity experienced by the airframe components must be found. Many models include both the longitudinal as well as lateral velocity components, therefore these aerodynamic loads depend on both the angle of attack and sideslip. Nonetheless, some simplifications can be made in this regard as well, for example in [5] the angle of attack and sideslip of the rotor spinners and pylons do not take into account velocity components resulting from body rotational rates. On the other hand, in [36] the nacelle rotational rate $\dot{\beta}$ is included in the nacelle aerodynamics. From this it can be seen that, depending on the model and its purpose, the airframe aerodynamic effects may only be partially accounted for.

Airfoil Characteristics

Aerodynamic coefficients may be required to calculate the blade, wing, and horizontal and vertical stabilizer aerodynamic loads, but only the experimental data-tables approach of determining these coefficients was mentioned so far. The data-table approach is common in tilt-rotor simulations such as [29], [31], [6], and [36]. Although not as common, other methods of determining the aerodynamic coefficients also exist such as computational fluid dynamics or distributed vorticity. If experimental data is not available, these analytical approaches will most likely provide a more accurate result than rule-of-thumb values such as a 2π lift curve slope. Since these approaches are more computationally demanding than a table look-up procedure, they may not be fit for real-time simulation. It is possible, however, to pre-generate a data-table with the analytical methods as well, circumventing the issue. This approach has not been seen in the studied literature however. Finally, these analytical methods make it possible to directly estimate the airfoil characteristics in specific configurations, such as in the wake of a main wing (thus representing the tail stabilizers), or in ground effect, thus encompassing any tilt-rotor aerodynamic interference within the airfoil characteristics.

Several simplifications related to the airfoil characteristics may be made as well, for example in [32] the lift curve slope and blade drag coefficient is assumed to be constant along the rotor blade span. It should be emphasized that the drag coefficient is assumed to be constant, therefore it does not change with the blade angle of attack. Although this greatly simplifies the rotor blade equations of motion, some may consider it a very optimistic assumption. Therefore other approaches of modeling the rotor blade drag coefficient $C_{d,bl}$ are used instead, for example the one shown in eq. (2.13). This empirical equation is commonly used in helicopter simulations, but also in tilt-rotor models such as the ones found in [5] and [23] for example. Here $C_{d_0,bl}$, $C_{d_1,bl}$, and $C_{d_2,bl}$ are tunable profile drag parameters and α_{bl} is the blade angle of attack. The profile drag parameters must unfortunately be found experimentally, however some authors simply choose these values based on previous works and consider this approach as adequate for a first approximation.

$$C_{d,bl} = C_{d_0,bl} + C_{d_1,bl}\alpha_{bl} + C_{d_2,bl}\alpha_{bl}^2 \tag{2.13}$$

Even in the case that experimental data is not available, the effect of air compressibility on the aerodynamic coefficients can be modeled as well, and may be employed in a tilt-rotor model such as the one in [34]. For example the effect of air compressibility on the lift coefficient can be approximated with the Glauert-Prandtl rule shown in eq. (2.14)[23]. Here C_l is the lift coefficient, a is the lift curve slope, and M is the Mach number. The subscripts c and i indicate the compressible and incompressible lift parameters respectively. This rule can also be applied to the moment and pressure coefficients. Unfortunately the effect of compressibility on the drag coefficient is more complex and cannot be modeled with the equation below. Typically empirical equations are used instead[23].

$$\frac{C_{l,c}}{C_{l,i}} = \frac{a_c}{a_i} = \frac{1}{\sqrt{1-M^2}} \tag{2.14}$$

Finally, if experimental data is not available, many authors choose to omit the effect of stall on the aerodynamic coefficients of the rotor blade or wing. Although this might be acceptable for the aerodynamic analysis of wings (assuming the tilt-rotor remains within a realistic flight envelope), the same cannot be said for the proprotors since it is very likely for regions of the blade to experience stall. For this reason tilt-rotor models such that the ones found in [34] or [29] model airfoil stall characteristics. In the case of the latter model, the post-stall lift is modeled using an extensive empirical relation which can be found in [42].

Aerodynamic Interaction

Some tilt-rotor models, such as the ones found in [32], [33], or [34], neglect all aerodynamic interaction. Recalling the recommendations, however, several aerodynamic interactions are necessary for an accurate tilt-rotor flight mechanics model.

Starting with the rotor and main wing, in [29], the aerodynamic download of the rotor wake on the wing of the tilt-rotor is modeled by a "contracted stream-tube" [29, p6] with the induced velocity incorporated into the strip model of the wing. The induced velocity ratio λ_w at an axially projected distance z is given by eq. (2.15)[3] where λ_0 is the mean inflow ratio at the rotor disk.

$$\lambda_w = \lambda_0\left(1 + \frac{z/R}{\sqrt{1+(z/R)^2}}\right) \tag{2.15}$$

It is important to note that here the rotor wake velocity is assumed to be parallel with the shaft, therefore it is not influenced by the disk angle. This could be a potential source of error if the disk has a considerable angle with respect to the shaft plane, but could be even more problematic if disk dynamics (or flapping dynamics) are modeled. In the latter case only the rotor forces will have an influence on the lag between cyclic input and body roll and pitching motions. However, since the wake effect on the wing and tail also results in body roll and pitching moments, it might be important to consider the effect of disk dynamics when modeling the rotor wake interaction with the wing and tail as well.

The wake velocity is added to the free stream velocity experienced by the wing strip element only if the quarter-chord line of the strip is within the region defined by two wake skew angles originating from the front and rear of the rotor disk at the same spanwise position. The wake skew angle χ is defined in eq. (2.16), where v_z and v_x are the normal and longitudinal rotor hub velocities respectively, both defined in the shaft plane.

$$\chi = arctan\left(\frac{v_z}{|v_x + \lambda_w|}\right) \tag{2.16}$$

[3]Due to uncertainty about the correctness of the equation presented in [29], it is taken from the cited source [43] instead.

Another possible shortcoming of the approach presented above is that the change in download is only gradual when the wing quarter-chord line is within the region bounded by the wake skew angles. Once the quarter-chord line exits this region, the additional wake velocity is immediately set to zero and thus the change in download is discontinuous. This might result in non-realistic flight behavior.

A different approach of determining which portion of the wing is affected by the rotor wake is presented in [44] and [33]. Here the wing is divided into two areas, S_1 and S_2, with the total wing area being $S_w = S_1 + S_2$. The first area S_1 is affected by the rotor wake while the second area S_2 is affected only by the free-stream flow. The area affected by the rotor wake is calculated with eq. (2.17) where i_n is the nacelle tilt-angle (with $i_n = 0$ in airplane mode), u is the longitudinal body velocity, u_{cr} is the critical velocity, a and b are constants, and $S_{max} = 2Rc_w\eta_{ss}$ where c_w is the mean wing chord, and η_{ss} is a constant. Unfortunately the constants u_{cr}, a, b, and η_{ss} are found by fitting experimental data.

$$S_1 = \begin{cases} 0 & \text{if } i_n < 60^\circ \text{ or } u \geq u_{cr} \\ S_{max}\Big(sin(ai_n) + cos(bi_n)\Big)\dfrac{u - u_{cr}}{u_{cr}} & \text{else} \end{cases} \tag{2.17}$$

Since this approach does not specify the spanwise position where the rotor wake starts to affect the wing, only the total wing load can be calculated according to the point load method for each area. The only difference between the two areas is the total velocity and resulting angle of attack due to the additional wake velocity components experienced by S_1.

A similar but more elaborate approach based on defining two wing areas is developed in [6]. Apart from additionally taking into account wake shift and contraction, the method also provides moment arms for each area allowing for the calculation of resultant moments acting on the tilt-rotor body. This method unfortunately uses tabulated coefficients, many parameters, and involves many steps, therefore it will not be shown here.

Moving onto the aerodynamic interaction experienced by the horizontal stabilizer, in [29] the wing downwash angle is simply added to the effective angle of attack seen by the tail in order to incorporate the effect of the wing downwash on the empennage. Unfortunately the downwash angle is not calculated analytically but instead found by interpolating data dependent on the main wing angle of attack and nacelle angle. The rotor wash at the horizontal stabilizer is obtained through an experimentally defined polynomial and presenting it here does not add much value to the study. It is, however, important to mention that the rotor creates an upwash at the tail which counteracts the effect of the wing downwash and thus should be considered for tilt-rotor flight mechanics modeling, preferably via an analytical relation. In [5] only the average rotor induced velocity is incorporated into the flow experienced by the tail, while the rotor wake acting on the wing has a spatial distribution. In [36] the rotor also has an effect on the tail, but the model is further expanded with a wake delay to simulate the distance the wake has to travel from the rotor to the tail. The magnitude of the inflow in this model is adjusted with a correction coefficient.

The rotor download on the fuselage is sometimes neglected, e.g. in [6], due to its smaller magnitude in comparison to the other aerodynamic effects. In the case of the interaction between the two proprotors, in [5] the side-by-side rotor effect is modeled with a tabulated correction factor that is incorporated into the implicit inflow equation.

Ground Effect

According to the recommendations, modeling the ground effect may be desirable in performance and piloted tilt-rotor flight simulations.

In [5], ground proximity has an effect on the power required for hover and is modeled with eq. (2.18)[4]. Here G represents the ratio of the required power for hover in ground effect (IGE) to the required power for hover out of ground effect (OGE), h is the rotor height with respect to the ground, R is the rotor radius, and A_1 and A_2 are tuning constants. Data fitting is required to determine the tuning constants, therefore this approach is not ideal for generic tilt-rotor modeling.

[4] A minus sign was added before the A_2 constant for the purpose of this report to emphasize that the ratio should tend to 1 as the height increases when both tuning constants are positive.

$$G = \frac{P_{hov,IGE}}{P_{hov,OGE}} = 1 - A_1 e^{-A_2(h/2R)} \tag{2.18}$$

A more useful analytical relation between the in and out of ground effect power required for hover is given by eq. (2.19) [23]. This relation is derived by treating the rotor as a wing and modeling it with a horseshoe vortex in ground proximity. Although this approach greatly simplifies the ground effect phenomenon and does not incorporate the effect for forward flight velocity, it can still serve as a first approximation.

$$G = \frac{P_{hov,IGE}}{P_{hov,OGE}} = \frac{8h^2/R^2}{1 + 8h^2/R^2} \tag{2.19}$$

One of the recommended elements involves modeling the rotor wake effect on the tail. Apart from direct effect of the rotor wake on the empennage, through experiments it has been observed that the tilt-rotor experiences an additional nose-down pitching moment while hovering in ground proximity. In [5] it is hypothesized that this is caused by the colliding wakes of the two rotors which are then reflected from the ground and subsequently strike the aft of the airframe. This additional pitching moment is empirically modeled with eq. (2.20) where M_{cc} is the said moment, T_{total} is the combined thrust of the two rotors, and K_1 and K_2 are tuning constants. Apart from the undesired but required data fitting, this equation also does not incorporate the effect of the nacelle tilt-angle which is expected to have a large influence. Therefore, if left unaltered, this equation is not considered very suitable for til-rotor modeling.

$$M_{cc} = K_1(T_{total})e^{-K_2(h/2R)} \tag{2.20}$$

Trimming Routines

An important step in the development of a tilt-rotor flight mechanics simulation is the ability to trim the model, whether it be for model capability and validity assessment or dynamic stability determination purposes. Therefore the final section of this chapter briefly treats various trimming routines that are employed in tilt-rotor model literature.

In the case of airplanes and helicopters, the simplest trim curves are found for a steady, level-flight condition and are a function of velocity only. In the case of a tilt-rotor, however, the trim curves are not only a function of velocity but also a function of nacelle tilt angle. In this case the nacelle tilt angle is not considered as an active pilot input but instead as a pre-determined flight condition. These types of trim curves can be found in [33] for example. Less restricted trimming approaches allow for the definition of additional flight conditions such as the flight path angle [29], or even the turn rate [32].

The difficulty of trimming a tilt-rotor model may originate from the fact that the pilot must control both the prop-rotor swashplates and airplane control surfaces, amounting to a total of 7 control inputs (2 collective, 2 longitudinal cyclic, elevator, aileron, and rudder) in contrast to the 4 control inputs typical to helicopters and airplanes (3 body rate controls and 1 power). In the case of the tilt-rotor, this results in an undetermined system where there are more unknowns (as a result of the 3 additional inputs) than equations. It is possible to solve this problem with, for example, a non-linear least-squares curve fitting method (as is done in [33]), but many authors choose to link the tilt-rotor swashplate controls with the airplane controls through the control stick, pedals, and power lever resulting in only 4 inputs. Any control mixing or phasing can be incorporated as well. This approach is also logical since this type of control-linking is applied to real tilt-rotors as well. Having only 4 inputs yields a fully determined system which can be solved in multiple ways.

If the problem were simple enough, the system of equations could be solved analytically. Unfortunately this is not the case for tilt-rotor models, therefore other methods of finding the trim solution must be employed. For example in the sequential correction approach described in [23] each control variable (which corresponds to the 4 control inputs as well as the pitch and roll angles) is linked to only one of the DoFs (3 forces and 3 moments) and adjusted such that the linked force or moment is equal to zero. The control variables are iteratively adjusted in sequence until all forces and moments are (close to) zero. The biggest shortcoming of this method is that control cross-coupling is not taken into account which means that a single control variable may influence several DoFs, requiring many iterations to find a solution or not being able to find a

solution at all. Due to the inherent cross-coupling, this approach might not be suitable for tilt-rotor model trimming.

Fly-to-trim is another related approach described in [23] where a control scheme is programmed to control the tilt-rotor model with the goal to minimize the forces and moments acting on the aircraft, but in this case all control variables are adjusted in parallel and not in sequence. Besides the fact that this approach may be computationally expensive since the flight mechanics simulation must be run, there is no guarantee that a solution will be found since it is already challenging to develop a robust controller than can stabilize the tilt-rotor across the entire flight envelope.

A more robust and therefore popular method of trimming tilt-rotors is the Jacobi method where the equations of motion are linearised with the Taylor series to obtain the Jacobian matrix comprising the partial derivatives of all DoFs with respect to all control variables, i.e. the amount of change of each DoF as a result of a change in each of the control variables. The Jacobian is typically calculated numerically, but it might be possible to find it analytically if the tilt-rotor model is defined analytically. The Jacobian and body acceleration vector are evaluated at the initially guessed control variable vector and then used to find a new control variable vector that is closer to the trim solution. This new vector is used as the new guess and the procedure continues in an iterative manner until the evaluated acceleration vector is sufficiently close to zero, i.e. the tilt-rotor is sufficiently close to the trim state.

3

Preliminary Results - 3DoF Model

An analytically derived tiltrotor mathematical model with three body motion degrees of freedom (DOFs) referred to as the 3DoF model was developed based on the XV-15 aircraft during the preliminary phase of this research project in hopes of giving insight on the feasibility of different modeling and trimming approaches. In addition the model development process revealed several challenges and gave light to questionable assumptions which would otherwise have not been discovered and investigated. Ultimately the gained knowledge and experience served as a starting point for the development of the final 6DoF tilt-rotor model thoroughly treated in Part III of this thesis.

The development and results of the preliminary 3DoF model documented in [3] are summarized in this chapter, starting with the model scope and the general description of its components which are treated in section 3.1. The model derivation approach is then summarized in section 3.2, while results relevant to this thesis report and a summary of the conclusions of the preliminary research are found in section 3.3.

3.1. Model Scope and Description

The scope of the preliminary 3DoF tilt-rotor model has been purposefully greatly bounded in order to make it easier to develop a first working version of a tilt-rotor mode. As a consequence the body motion has been limited to three degrees of freedom, namely longitudinal and vertical movement, as well as pitching motion, yielding a model that is capable of simulating symmetrical flight only. This in turn made it possible to omit several significant model elements that would otherwise be required in a full-motion simulation, greatly simplifying the development and analysis of the preliminary model. Furthermore the model scope has been limited to require accuracy in performance and piloted flight only, neglecting other simulation domains such as structural dynamics or aeroelasticity. A summarized description and list of scope-limiting assumptions and simplifications applied to the complete 3DoF model and its components is shown below. Other more specific assumptions and simplifications are mentioned in section 3.2 which summarizes the derivation of the 3DoF model.

General Description, Assumptions, and Simplifications

- The tilt-rotor is limited to symmetric motion, i.e. surge and heave translations, and pitch rotations, resulting in a model with three body motion DoFs. It is assumed that this symmetric motion is decoupled from the omitted asymmetric motion.
- The tilt-rotor consists of two rotors, a main wing, a horizontal stabilizer, and a fuselage only.
- All tilt-rotor structural elements are assumed to be rigid.
- The mass of the tilt-rotor is assumed to be constant, however the longitudinal position of the center of mass (CoM) can vary.
- The tilt-rotor airframe geometry and mass distribution is assumed to be symmetrical in the surge-heave plane.
- The pilot longitudinal stick to longitudinal cyclic is phased as a function of the nacelle tilt. The blade pitch lower limit is also adjusted as a function of the nacelle tilt.
- All aerodynamic interactions between components are neglected.

- The fuselage is assumed to generate drag only. The origin of the drag force coincides with the body center of gravity (CoG).
- The simulation environment is defined by a flat, non-rotating Earth.
- Gravity is assumed to be constant therefore the CoM coincides with the CoG.

Rotor Description, Assumptions, and Simplifications

- The rotor is based on an articulated-type rotor with a feathering and flapping hinge, and a flapping spring.
- The flapping dynamics are derived using the Lagrangian Method. Here the nacelle tilt rate is considered a negligible contributor.
- The flapping aerodynamics are derived using the blade element method.
- The rotor angular velocity is assumed to be constant.
- The rotor-induced velocity is assumed to be axial, constant, and uniform across the rotor disk.
- The blade is assumed to have a constant cross-sectional shape and area, and has a constant twist angle.
- The blade is assumed to be rigid.
- The lift coefficient of the blade element is assumed to vary linearly with the blade element angle of attack, and it is assumed that the zero-lift angle of attack is equal to zero.
- The aerodynamic center of the blade profile is assumed to lie at its quarter-chord point.
- The blade feathering axis is assumed to coincide with the blade profile quarter-chord point.
- The left and right rotor models are identical.

Wing and Tail Description, Assumptions, and Simplifications

- All lifting surfaces are modeled as 2-dimensional airfoils.
- The lift coefficient of the lifting surfaces is assumed to vary linearly with the local angle of attack.
- The horizontal stabilizer elevator is the only control surface to be included in the model.

3.2. Model Derivation Approach

The 3DoF tiltrotor model was developed in several phases with each subsequent phase increasing the model complexity, however this section shall combine the development process of each phase presenting the complete derivation as one. This section is structured according to the different parts of the 3DoF model, starting with the body equations of motion. Next the rotor model is summarized and the section is concluded with a brief description of the wing, horizontal tail, and fuselage aerodynamic models.

3.2.1. Body Equations of Motion

The three-degrees-of-freedom body motion is described with eq. (3.1) where u and w are the longitudinal and vertical velocity components acting along the body X and Z axes, q is the body pitch rate. Furthermore m is the tilt-rotor mass, I_{yy} is the body pitch moment of inertia, and F_{bx}, F_{bz}, and M_{by} are the external forces and moment acting on the body.

$$\dot{u} = \frac{F_{bx}}{m} - qw \tag{3.1a}$$

$$\dot{w} = \frac{F_{bz}}{m} + qu \tag{3.1b}$$

$$\dot{q} = \frac{M_{by}}{I_{yy}} \tag{3.1c}$$

The external force and moment vectors acting on the body are defined in eq. (3.2) and consist of the contributions of the rotor (r), fuselage (f), main wing (w), and horizontal stabilizer (ht). Apart from pure moments, the moment vector additionally consists of the contribution of the component force vectors acting at a distance $\boldsymbol{s}$ away from the body CoG. The derivation of these contributions is treated in the following

sections, however only the pitching moment and longitudinal and vertical force components shall be derived since only these forces and moment are needed for the 3DoF body motion described by eq. (3.1).

$$\boldsymbol{F}_b = \begin{pmatrix} F_{bx} \\ F_{by} \\ F_{bz} \end{pmatrix} = \boldsymbol{F}_r + \boldsymbol{F}_f + \boldsymbol{F}_w + \boldsymbol{F}_{ht} \tag{3.2a}$$

$$\boldsymbol{M}_b = \begin{pmatrix} M_{bx} \\ M_{by} \\ M_{bz} \end{pmatrix} = \boldsymbol{M}_r + \boldsymbol{M}_f + \boldsymbol{M}_w + \boldsymbol{M}_{ht} + \boldsymbol{s}_r \times \boldsymbol{F}_r + \boldsymbol{s}_f \times \boldsymbol{F}_f + \boldsymbol{s}_w \times \boldsymbol{F}_w + \boldsymbol{s}_{ht} \times \boldsymbol{F}_{ht} \tag{3.2b}$$

3.2.2. Rotor Model

The rotor model development consists of the derivation of the flapping equation, blade element velocity components, rotor hub forces and moments, and the thrust-inflow solver as described below.

Rotor Flapping Dynamics

The 3DoF model rotor flapping dynamics are derived according to the Lagrangian Method as shown in eq. (3.3a) where the function describing the total energy of the flapping blade L is differentiated with respect to the flapping angle β and time. The total energy of the system is the potential energy V subtracted from the kinetic energy T as seen in eq. (3.3b).

$$\frac{d}{dt}\left(\frac{\partial L}{\partial \dot{\beta}}\right) = \frac{\partial L}{\partial \beta} \tag{3.3a}$$

$$L = T - V \tag{3.3b}$$

In the case of the flapping blade the potential energy is stored in the form of the spring and is defined according to eq. (3.3c) where K_β is the spring constant. The kinetic energy is assumed to originate from rotational velocity only as shown in eq. (3.3d), neglecting any linear components due to an offset from the center of rotation or any purely linear velocity components such as linear body velocity. Here I_{bl} is the blade mass moment of inertia around the blade flapping and lead/lagging hinges, both being equal since the blade is assumed to be a slender rod. Furthermore q_{bl} and r_{bl} are the rotational velocities of the blade around those same axes respectively.

$$V = \frac{K_\beta \beta^2}{2} \tag{3.3c}$$

$$T = \frac{I_{bl}\ q_{bl}^2}{2} + \frac{I_{bl}\ r_{bl}^2}{2} \tag{3.3d}$$

The two rotational velocities are defined in eqs. (3.3e) and (3.3f). Here ψ is the azimuth position of the blade, Ω is the rotor shaft rotational rate, and q is the body pitch rate. The nacelle tilting rate $\dot{\eta}$ is considered negligible in comparison to the other rotational velocities and thus not included here.

$$q_{bl} = q\cos(\psi) - \dot{\beta} \tag{3.3e}$$

$$r_{bl} = \Omega\cos(\beta) - q\sin(\psi)\sin(\beta) \tag{3.3f}$$

Substituting the rotational velocities into eq. (3.3d), combining the kinetic and potential energy in eq. (3.3b), and finally taking the necessary derivatives described in eq. (3.3a) yields the so-called left-hand side (LHS) of the flapping equation which is simplified by neglecting higher order rotational velocity terms (i.e. q^2) and by applying the small angle approximation to the flapping angle β. Rearranging the resulting terms to the left hand side and equating them to a forcing moment M_{bly} yields the simplified flapping equation as shown in eq. (3.4) consisting of the blade inertia, the Coriolis effect, the centrifugal force, and the spring reactive moment terms.

$$I_{bl}\ddot{\beta} + 2qI_{bl}\Omega\sin(\psi) + \beta(I_{bl}\Omega^2 + K_\beta) = M_{bly} \tag{3.4}$$

Rotor Flapping Aerodynamics

The total aerodynamic moment M_{bly} is the result of the lift and drag generated by the blade acting at a distance away from the flapping hinge and is derived in the control plane with the use of the blade element method (BEM). Assuming that the inflow angle experienced by the blade element is small, however, the the drag contribution is neglected resulting in a simplified total aerodynamic moment expression as shown in eq. (3.5). As a result M_{bly} is the integral of the differential lift dL_{bl} the blade element positioned at a radial distance r away from the flapping hinge (which coincides with the rotor hub since there is no flapping hinge offset) evaluated along the entire blade radial length R. No tip-loss factor is taken into account.

$$M_{bly} = \int_0^R r dL_{bl} \tag{3.5}$$

The differential lift is defined by eq. (3.6) where ρ is the air density, V_{bl} is the aerodynamic velocity experience by the blade element, $C_{l_{\alpha,bl}}$ is the lift curve slope of the blade airfoil, α_{bl} is the blade angle of attack, c_{bl} is the blade element chord, and dr is the blade element differential width. The angle of attack depends on the blade element pitch angle θ_{bl} (which is constant in this 3DoF model) and the inflow angle ϕ_{bl} as seen in eq. (3.7).

$$dL_{bl} = \frac{1}{2}\rho V_{bl}^2 C_{l_{\alpha,bl}} \alpha_{bl} c_{bl} dr \tag{3.6}$$

$$\alpha_{bl} = \theta_{bl} - \phi_{bl} \tag{3.7}$$

The inflow angle depends on the velocity experienced by the blade element as shown in eq. (3.8) with V_t and V_p being the tangential and perpendicular blade element velocity components defined with respect to the control (i.e swashplate) plane. The total aerodynamic velocity experienced by the blade element may then be defined by eq. (3.9). Both expressions are simplified by assuming that the blade element tangential velocity component is much greater than the perpendicular component, and as a result the inflow angle is small as shown in the equations. This is done in order to be able to later linearize the flapping equation.

$$\phi_{bl} = arctan\left(\frac{V_p}{V_t}\right) \approx \frac{V_p}{V_t} \tag{3.8}$$

$$V_{bl}^2 = V_t^2 + V_p^2 \approx V_t^2 \tag{3.9}$$

The blade element pitch angle, on the other hand, depends on the swashplate collective angle θ_0 and the thrust-weighted twist $\theta tw,$T-W as shown in eq. (3.10a), while the thrust-weighted twist is obtained with eq. (3.10b) where θ_{tw} is the function that describes the actual blade twist as a function of the radial position r along the blade.

$$\theta_{bl} = \theta_0 + \theta_{tw,\text{T-W}} \tag{3.10a}$$

$$\theta_{tw,\text{T-W}} = \frac{\int_0^R \theta_{tw} r^2 dr}{\int_0^R r^2 dr} \tag{3.10b}$$

Blade Element Velocity Components

The blade element velocity components have been derived graphically yielding the expressions shown in eq. (3.11). Starting with the tangential component, here V_b is the total body velocity, α_b is the body angle of attack, V_{qtc} is the in-plane linear velocity experienced by the blade element, acting parallel to the control plane, as a result of a body pitch rate, and α_{ct} is the control plane angle of attack defined in eq. (3.12). Here θ_{1s} is the longitudinal swashplate cyclic angle and η is the nacelle tilt angle (equal to 0 in helicopter configuration and $-\pi/2$ in airplane configuration). The expanded expression for this in-plane velocity V_{qtc} is not shown here, however it must be mentioned that it depends on the nacelle tilt angle η as well.

$$V_t = \Omega r cos(\beta) + (V_b cos\,(\alpha_{ct}) - V_{qtc})\, sin(\psi) \tag{3.11a}$$

The blade element perpendicular velocity component is defined by eq. (3.11b) where $\dot{\beta}$ is the blade flapping rate, v_i is the rotor induced velocity, and V_{qpc} is the out-of-plane linear velocity experienced by the blade

element, acting perpendicular to the control plane, as a result of a body pitch rate. The out-of-plane velocity also depends on the nacelle tilt angle.

$$V_p = V_b sin\left(\alpha_{ct}\right) cos(\beta) + \left(V_b cos\left(\alpha_{ct}\right) - V_{qtc}\right) cos(\psi) sin(\beta) - V_{qpc} cos(\beta) + \dot{\beta} r + v_i cos(\beta) \quad (3.11b)$$

$$\alpha_{ct} = \left(\theta_{1s} - \eta - \alpha_b\right) \quad (3.12)$$

Complete Flapping Equation

Substituting the (simplified) blade element velocity components, angle of attack, and inflow angle in the the differential lift and solving the integral in eq. (3.5) yields the aerodynamic flapping moment which is substituted back into eq. (3.4) in order to obtain the complete flapping equation. Applying several more simplifications (described in more detail in [3]), non-dimensionalizing several terms, and applying the small angle approximation to β yields the complete flapping equation defined in the rotating control plane frame as shown in eq. (3.13). Here the sine and cosine functions of ψ are abbreviated with S_ψ and C_ψ respectively. The definitions of the non-dimensional variables are given in eq. (3.14) consisting of the blade lock number γ, the control plane advance ratio μ_c and inflow ratio λ_c, the induced velocity inflow ratio λ_i, the pitch rate induced advance ratio μ_{qt} and inflow ratio λ_{qp}. In the latter the r_{cg} variable is the radial distance between the rotor hub and the projection of the body CoG onto the control plane, and whose definition can be found in [3]. The effect of the tiltable proprotor, i.e. the presence of η in the equations, is implicitly found within the μ_c, λ_c, and λ_{qp} variables.

$$\begin{aligned}
&I_{bl}\ddot{\beta} + 2qI_{bl}\Omega sin(\psi) + \beta\left(I_{bl}\Omega^2 + K_\beta\right) = \\
&= -\Omega^2\gamma I_{bl}\left(\frac{\lambda_c}{6} + \frac{S_\psi\lambda_c\mu_c}{4} - \frac{S_\psi\lambda_c\mu_{qt}}{4} + \frac{\lambda_i}{6} + \frac{S_\psi\mu_c\lambda_i}{4} - \frac{S_\psi\lambda_i\mu_{qt}}{4} + \frac{C_\psi\mu_c\beta}{6} + \frac{C_\psi S_\psi\mu_c^2\beta}{4}\right. \\
&\left. - \frac{C_\psi S_\psi\mu_c\mu_{qt}\beta}{2} - \frac{C_\psi\mu_{qt}\beta}{6} + \frac{C_\psi S_\psi\mu_{qt}^2\beta}{4} - \frac{\lambda_{qp}}{6} - \frac{S_\psi\mu_c\lambda_{qp}}{4} + \frac{S_\psi\lambda_{qp}\mu_{qt}}{4}\right) \\
&- \Omega\gamma I_{bl}\left(\frac{\dot{\beta}}{8} + \frac{\dot{\beta}S_\psi\mu_c}{6} - \frac{\dot{\beta}S_\psi\mu_{qt}}{6} - \frac{C_\psi q}{8} - \frac{C_\psi qS_\psi\mu_c}{6} + \frac{C_\psi qS_\psi\mu_{qt}}{6}\right) \\
&+ \frac{\theta_{bl}\Omega^2\gamma I_{bl}}{8}\left(\frac{8\mu_c - 8\mu_{qt}}{3}S_\psi + \mu_c^2 - 2\mu_c\mu_{qt} + \mu_{qt}^2 + 1\right)
\end{aligned} \quad (3.13)$$

$$\gamma = \frac{\rho C_{l_{\alpha,bl}} c_{bl} R^4}{I_{bl}} \quad (3.14a) \qquad \mu_c = \frac{V_b cos(\alpha_{ct})}{\Omega R} \quad (3.14b)$$

$$\lambda_c = \frac{V_b sin(\alpha_{ct})}{\Omega R} \quad (3.14c) \qquad \lambda_i = \frac{v_i}{\Omega R} \quad (3.14d)$$

$$\mu_{qt} = \frac{V_{qtc}}{\Omega R} \quad (3.14e) \qquad \lambda_{qp} = \frac{qr_{cg}}{\Omega R} \quad (3.14f)$$

The flapping equation is then converted from the rotating frame to the non-rotating control plane frame with the use of the presumed quasi-static solution for the flapping angle given in eq. (3.15) where a_0 is the average term referred to as the coning angle, a_1 is the longitudinal cone tilt, and b_1 is the lateral cone tilt. Substituting the disk tilt angles into the flapping equation and separating the sine, cosine, and free terms yields analytical expressions for the disk tilt angles themselves. These analytical expressions are not shown in this thesis document due to their extensiveness, however they are provided in [3].

$$\beta = a_0 - a_1 cos(\psi) - b_1 sin(\psi) \quad (3.15a) \qquad \dot{\beta} = a_1 \Omega sin(\psi) - b_1 \Omega cos(\psi) \quad (3.15b)$$

$$\ddot{\beta} = a_1 \Omega^2 cos(\psi) + b_1 \Omega^2 sin(\psi) \quad (3.15c)$$

Rotor Hub Forces and Moments

The rotor thrust depends on the blade lift and drag. Assuming that the lift is much greater than the drag and that the inflow angle is small, and applying the small angle approximation to the flapping angle, the averaged-per-revolution BEM thrust may be defined to depend on the blade lift only as shown in eq. (3.16). Note that the thrust is defined to be perpendicular to the control plane here, and that N is the number of blades present on one rotor. Substituting the flapping angle by the quasi-static disk tilt solution and solving the integral yields the analytical expression for the BEM thrust as shown in eq. (3.16).

$$\begin{aligned} T_{\text{BEM}} &= \frac{N}{2\pi} \int_0^{2\pi} \int_0^R dL_{bl} d\psi \\ &= \frac{\Omega^2 \gamma I_{bl} N}{4R} \left(\left(\mu_{qt}^2 - 2\mu_c \mu_{qt} + \mu_c^2 + \frac{2}{3} \right) \theta_{bl} - \frac{a_1 \mu_{qt}}{2} + \frac{a_1 \mu_c}{2} + \lambda_{qp} - \lambda_c - \lambda_i \right) \end{aligned} \quad (3.16)$$

The rotor hind H-force also depends on the blade lift and drag, however by applying the same assumptions as mentioned above the averaged-per-revolution blade element method H-force continues to depend on both the lift and drag as shown in eq. (3.17). Here dD_{bl} is the blade differential drag given by eq. (3.18) where $C_{d,bl}$ is the blade drag coefficient approximated with the second-degree polynomial characterized by the $C_{d,0}$, $C_{d,1}$, and $C_{d,2}$ constant parameters as shown in eq. (3.19). Unlike in the case of the BEM thrust, the worked-out H-force expression is not shown in this thesis report due to its extensiveness, however it is provided in [3].

$$H = \frac{N}{2\pi} \int_0^{2\pi} \int_0^R \left(\left(\phi_{bl} sin(\psi) - \beta cos(\psi) \right) dL_{bl} + sin(\psi) dD_{bl} \right) d\psi \quad (3.17)$$

$$dD_{bl} = \frac{1}{2} \rho V_{bl}^2 C_{d,bl} c dr \quad (3.18) \qquad C_{d,bl} = C_{d,0} + C_{d,1} \alpha_{bl} + C_{d,2} \alpha_{bl}^2 \quad (3.19)$$

The only moment that is transmitted to the hub is the pitching flapping-spring reaction moment as defined by eq. (3.20).

$$M_{K_\beta} = \frac{N K_\beta a_1}{2} \quad (3.20)$$

Solving for Induced Velocity and Thrust

In order to be able to solve for the induced velocity and rotor thrust, an additional thrust equation is used in the 3DoF model which corresponds to the simplified momentum model which, in its final form, is given by eq. (3.21a). Here μ_d and λ_d are the disk plane advance and inflow ratios defined by eqs. (3.21b) and (3.21c). Both of these definitions depend on α_{dt} which is the disk plane angle of attack which may be obtained with the use of eq. (3.22).

$$T_M = 2\rho\pi R^4 \lambda_i \Omega^2 \sqrt{(\lambda_d + \lambda_i)^2 + \mu_d^2} \quad (3.21a)$$

$$\mu_d = \frac{V_b cos(\alpha_{dt})}{\Omega R} \quad (3.21b) \qquad \lambda_d = \frac{V_b sin(\alpha_{dt})}{\Omega R} \quad (3.21c)$$

$$\alpha_{dt} = \alpha_{ct} - a_1 \tag{3.22}$$

The inflow solution is obtained with the use of an iterative feedback method where an initial guess for the dimensionless induced velocity is made and substituted into both the non-dimensional BEM ($C_{T,BEM}$) and momentum ($C_{T,M}$) thrust equations. An inaccurate guess results in a difference (D_T) between the two thrust values. The difference is then used to update the next estimate for the inflow velocity. This procedure is repeated until the absolute difference becomes smaller than a predefined value which determines the accuracy of the estimate. A flow diagram of this procedure is included in fig. 3.1.

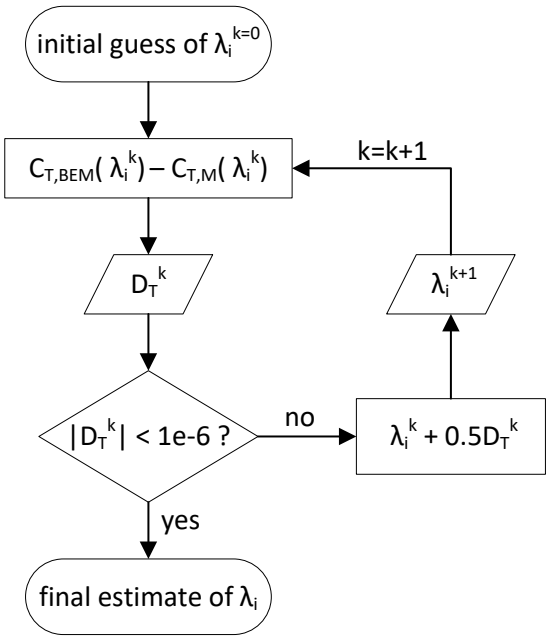

Figure 3.1: Flowchart showing the iterative feedback process of estimating the inflow velocity employed in the 3-DoF model.[3]

3.2.3. Wings, Tail, and Fuselage

The wing is treated as a 2-dimensional airfoil with the lift L_w and drag D_w calculated using eqs. (3.23a) and (3.23b). The lift and drag are assumed to act at the wing aerodynamic center AC_w (assumed to be located at the quarter-chord point of the wing root), and are taken to be perpendicular and parallel to the velocity vector V_w experienced by the wing aerodynamic center (AC) respectively. The total velocity vector V_w takes into account both body linear rates as well as linear rates experienced by the wing as a result of as body pitch rate. In these equations S_w is the wing planform area, $C_{l,w}$ is the wing profile lift coefficient defined by eq. (3.23c), and $C_{d,w}$ is the wing profile drag coefficient defined by eq. (3.23d). The lift coefficient depends on the wing profile lift curve slope $C_{l_{\alpha},w}$, angle of attack α_w, and the zero-lift angle of attack $\alpha_{0L,w}$. The drag coefficient depends on the profile zero-lift drag coefficient $C_{d,0,w}$, wing aspect ratio AR_w, and Oswald efficiency factor e_w. The wing aerodynamic moment is determined with eq. (3.23e) with $C_{m,AC,w}$ being the aerodynamic pitching moment coefficient measured at the wing profile aerodynamic center.

$$L_w = \frac{1}{2}\rho V_w^2 S_w C_{l,w} \tag{3.23a}$$

$$D_w = \frac{1}{2}\rho V_w^2 S_w C_{d,w} \tag{3.23b}$$

$$C_{l,w} = C_{l_{\alpha},w}(\alpha_w - \alpha_{0L,w}) \tag{3.23c}$$

$$C_{d,w} = C_{d,0,w} + \frac{C_{l,w}^2}{\pi(AR_w)e_w} \tag{3.23d}$$

$$M_w = \frac{1}{2}\rho V_w^2 S_w C_{m,AC,w} \tag{3.23e}$$

The horizontal stabilizer aerodynamics are almost identical to the ones of the wing with the exception of the lift coefficient expression which additionally depends on the (constant) aerodynamic effectiveness of the elevator $dC_{l,\delta e}$ and the deflection of the elevator δ_e as shown in eq. (3.24).

$$C_{l,ht} = C_{l_\alpha,ht}(\alpha_{ht} - \alpha_{0L,ht}) + dC_{l,\delta e}\delta_e \tag{3.24}$$

Finally the fuselage aerodynamics consist of a drag term only dependent on the total body velocity V_b and an equivalent flat plate drag area A_{eq} as shown in eq. (3.25).

$$D_f = \frac{1}{2}\rho V_b^2 A_{eq} \tag{3.25}$$

3.3. Preliminary Results Summary

This last section briefly describes the conclusions that have been made based on the preliminary research, and presents only two results which are most relevant to this thesis report. The first being fig. 3.2 which presents the conversion corridor of the 3DoF model compared against the conversion corridor of the real XV-15. Both of these conversion corridors are later compared to the one of the 6DoF model developed for the purposes of this thesis. Figure 3.3, on the other hand, presents the lateral disk tilt trim curves of the 3DoF model which are later mentioned in the analysis of the 6DoF model results in section 8.2. The remainder of the preliminary results are presented and discussed in [3].

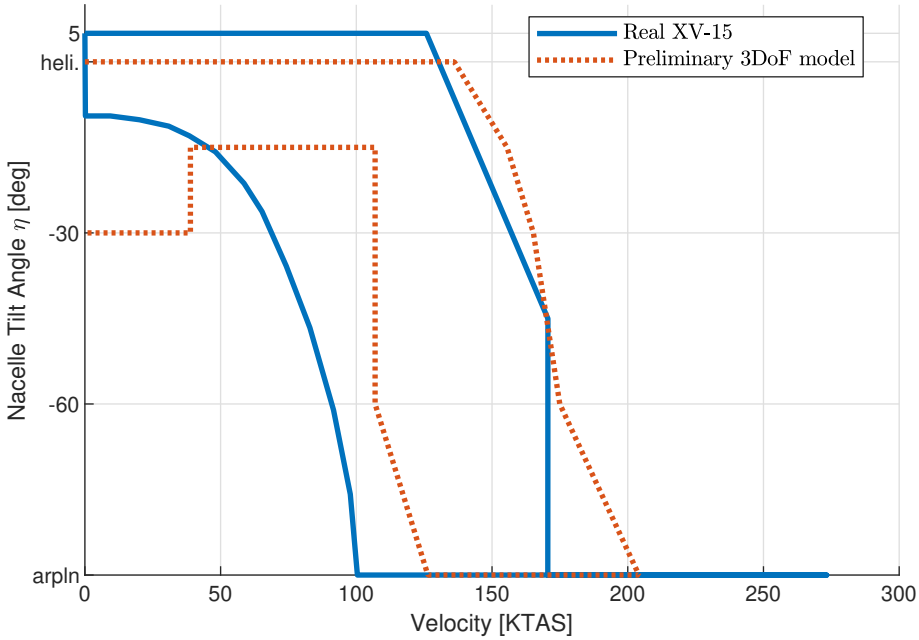

Figure 3.2: Comparison between the conversion corridors of the preliminary 3DoF tilt-rotor model and the real XV-15 tilt-rotor.

The conclusions made based on all of the results of the 3DoF tilt-rotor model presented in [3] are as follows. The effect of the nacelle angle is widely present throughout the model, including the expression for the thrust, coning angle, disk tilt angles, and the hind H-force. Some trim states greatly depend on the nacelle angle, such as the longitudinal and collective cyclic stick inputs, the coning angle, and lateral disk tilt. Other trim states, such as the body pitch, induced velocity, and longitudinal disk tilt depend on the nacelle angle to lesser extent. The wing and horizontal tail expands the conversion corridor allowing for flight at nacelle tilt

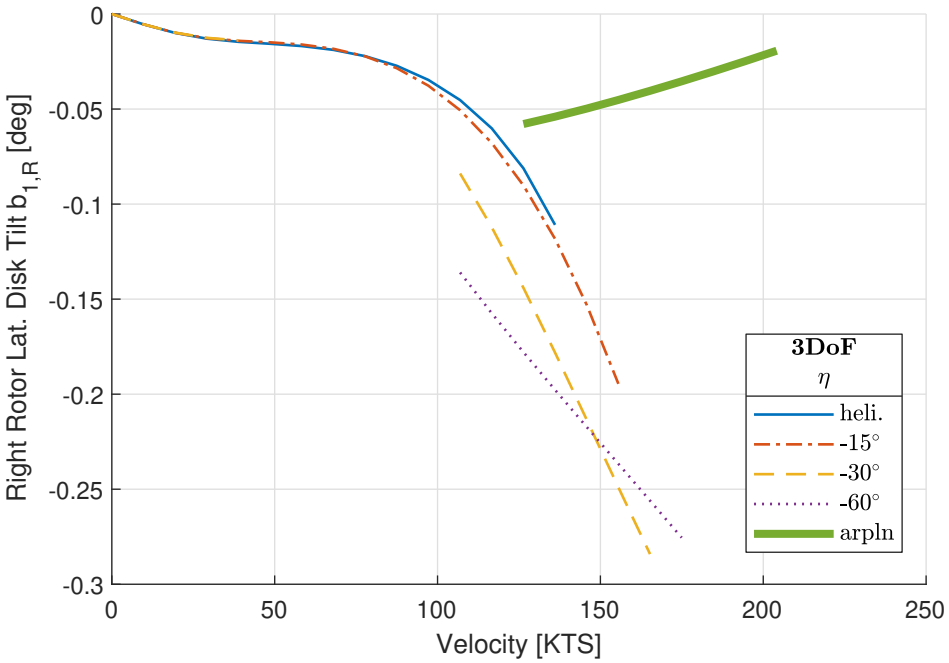

Figure 3.3: Right counter-clockwise rotating rotor control plane lateral disk tilt angle trim curves of the 3DoF tilt-rotor model. Nacelle tilt η indicated in legend. No flap deflection.

angles closer to airplane mode. The inclusion of the H-force significantly contracts the conversion corridor greatly reducing the estimated maximum velocity thereby yielding a more realistic result. Based on the trim curves, the 3DoF model is considered to be somewhat valid, however it is suspected that the lateral disk tilt estimation is erroneous. Based on the conversion corridor the model is not considered valid in its current state mainly due to over-predicted minimum velocity, and under-predicted maximum velocity limits.

Part III

Thesis Work

4

6DoF Model Description

The objectives of this thesis work is to obtain a high-fidelity tilt-rotor flight mechanics model. Therefore, considering the limitations of the presented three degrees of freedom (DoF) model (referred to as the 3DoF model) developed during the preliminary phase of this research project, the next step consists of expanding the preliminary model from two-dimensional longitudinal flight to three-dimensional flight yielding the first iteration of the analytically derived tilt-rotor flight mechanics model, colloquially referred to as the 6DoF model. Before the governing equations of the 6DoF model are derived however, first a general overview of the model is presented in this chapter which later may serve as a guide summarizing all basic elements of the model, such as positive state and input sign conventions or model subsystems, which the reader may return to during the actual derivation of the model presented in the next chapter.

The structure of this chapter is as follows. First the scope, key features, and limitations of the model are declared and briefly explained in section 4.1 while section 4.2 presents the different subsystems of the tilt-rotor modeled as separate components which collectively form the complete tilt-rotor flight mechanics model. Next section 4.3 lists the model states and controls, and graphically presents their positive sign conventions, while section 4.4 defines the phased and mixed relationships between the control inputs and outputs. All the parameters that are required to obtain a functional 6DoF tilt-rotor model instance are listed in section 4.5 while the values of these parameter used to obtain the 6DoF model XV-15 tilt-rotor implementation used to generate results and validate the model in this thesis work are given in appendix A. Next, the most critical assumptions and simplifications made throughout the model derivation phase are summarized in section 4.6 while the complete list is shown in appendix B. Finally, all reference frames relevant to the model derivation are formally defined in section 4.7 concluding this model description chapter.

4.1. Model Scope, Features, and Limitations

Before the specific 6DoF model description is given, first a more general overview is presented consisting of the scope of the model which has been defined to limit the modeling extent and is in accordance with the scope of this research work, a list of features of the final 6DoF model serving as a quick guide for the reader, and finally a summary of the identified limitations of the model which set bounds on the flight conditions in which the used modeling theories are valid.

Scope

Starting with the scope, first and foremost the focus of this thesis work is on the development of a flight mechanics model that aims at achieving accuracy in the domain of piloted and performance flight simulation, therefore other modeling domains such as airframe stresses or structural dynamics shall not be considered. Furthermore dynamic changes in mass or inertia due to for example fuel depletion or a change in nacelle tilt angle shall also not be modeled. The flight dynamics themselves shall be modeled in three dimensions as opposed to two in the case of the preliminary longitudinal 3DoF model. The final output of the model shall consist of the state derivatives while their time integration shall be handled by an outside simulation environment. All environmental factors consisting of air density, gravitational acceleration, and linear and rotational wind gusts only shall be supplied as inputs to the model therefore they must be handled by the outside simulation environment as well.

The 6DoF model shall be based on the XV-15 tilt-rotor therefore any aircraft components that are not present on the XV-15 shall not be implemented, however it must be highlighted that not all components of the XV-15 shall be implemented in the 6DoF model either (such as the landing gear). Among the modeled components, only the rotor model shall be analytically derived yielding functions for the generated forces and moments that shall be symbolically integrated to obtain resultant forces and moments. Moreover, the rotor model aerodynamics shall be derived based on the blade element method, while the inertial dynamics shall be derived according to Newtonian mechanics. The rotor model shall also use the disk tilt approximation limited to the first harmonic static solution. Disk tilt dynamics and inflow dynamics shall be neglected. The remaining modeled tilt-rotor components consist of the main wing (excluding the wing-tip-mounted nacelles), vertical and horizontal tail stabilizers, and the fuselage only. The lifting surfaces shall be approximated by trapezoidal planforms with (adjusted) flat plate aerodynamics and control surfaces, yielding single lift, drag, and pitching moment vectors providing a sufficient first approximation of these components. The fuselage shall be simplified even further by approximating it by its equivalent flat plate area, yielding a resultant drag vector only.

Finally the calculation of aerodynamic forces and moments shall resort to the use of aerodynamic coefficients that will be simply taken from sources in literature instead of being obtained through empirical, analytical, or numerical models. Aerodynamic interactions shall be limited to the rotor wake effect on the lifting surfaces, while all other interactions shall be neglected, including the rotor and wing ground effects.

Key Features

The following list presents key features of the developed and implemented 6DoF tilt-rotor model.

- The 6DoF tilt-rotor model is non-linear and allows for three-dimensional flight simulation.
- The trimmable inputs consist of the longitudinal, lateral, and collective/throttle pilot stick deflections, as well as the pedals.
- The remaining inputs consist of the combined inboard and outboard flap deflections, nacelle tilt rate, and selected rotor revolutions per minute (RPM), as well as two switches to enable and disable the variable RPM and collective governor model options.
- The 6DoF model incorporates pilot input phasing and mixing based on the XV-15 tilt-rotor (model) described in [6].
- The 6DoF tilt-rotor model consists of rotor, lifting surface, and lifting body components only.
- The rotor component is modeled by a simplified articulated rotor type with flapping and feathering (but not lead/lagging) blades, which produces an axial non-rotating wake. A flapping spring and precone angle are included. All hinge offsets are neglected. Due to the convenience and ease of implementation of the wind axis approach, the rotor model is derived in the wind axis control plane reference frame discussed in more detail on page 106.
- The rotor rotational rate is variable and the model allows for the simulation of autorotation.
- The rotor inflow is axial only and uniform across the rotor disk.
- All lifting surfaces are modeled as trapezoidal planforms characterized by incidence, dihedral, and sweep angles. The variation of the lift and drag coefficients as a function of angle of attack correspond to that of a flat plate.
- The rotor wake effect on the lifting surfaces is modeled.
- The lifting body model only takes into account the drag of the body neglecting the produced lift.
- The 6DoF model may consist of any number and combination of components enabling the modeling of different aircraft configurations which may even lie outside of the definition of a tilt-rotor, however the 6DoF model implementation created for the purposes of this thesis resembles the XV-15 tilt-rotor and thus consists of a lifting body fuselage, the main wing and tail stabilizer lifting surfaces, and finally two tiltable rotors.
- The 6DoF model includes a simplified XV-15 drive train model and variable rotor RPM capability with the option to turn it on and off during simulation.
- The 6DoF model includes a simplified XV-15 collective governor implementation with the option to turn it on and off during simulation. In order to turn the collective governor on, the variable rotor RPM option must also be turned on.

Limitations

The 6DoF model is primarily limited to the predefined minimum and maximum variable values supplied to an expression reduction scheme described in section 6.3. Exceeding these limits violates the expected

error introduced by the reduction scheme possibly yielding inaccurate simulation results. The rotor model is additionally limited to the propeller state and the windmill brake state with a maximum allowable axial induction ratio of 0.5 (see eq. (5.93) in section 5.2). Exceeding these bounds violates the momentum theory which is the basis of the rotor model producing inaccurate thrust and induced velocity values. Finally the rotor model thrust and inflow solver (see fig. 5.15) may not find a solution when the aerodynamic conditions experienced by the rotor change sufficiently fast, resulting in a crash of the simulation. Care must be taken not to invoke such rapidly changing conditions during simulation through aggressive pilot inputs.

4.2. Model Components

This next section first provides the geometric description of the 6DoF model components, namely the rotors, main wing, horizontal and vertical tail stabilizers, and the fuselage. All the instances of these generic components that are part of the 6DoF model XV-15 implementation are then identified and briefly described, and their disposition with respect to the tilt-rotor airframe is presented graphically.

4.2.1. Component Geometric Description

The descriptions of the geometric characteristics of the three generic tilt-rotor components part of the 6DoF model are included below and accompanied by diagrams where necessary.

Rotor

The rotor component is based on an articulated-type rotor featuring a feathering (blade pitch control θ_0) and flapping (β) hinge at each blade. The lead/lag hinge as well as any hinge offsets from the rotor shaft have been omitted in the model in a first approximation. The rotor model also includes a flapping spring with a torsional stiffness of K_β and a configurable but constant precone angle $\overline{a}_0$. The chord c_{bl} and airfoil shape of each blade is constant along the entire blade length, however the blade may have a geometric (wash-in) twist that has a constant component ($\theta_{bl,g}$) and a linearly varying component ($\theta_{bl,1}$) as a function of the blade radial position. The pitch of the blade profile (later referred to as the blade element BE) θ_{BE} at a radial distance r_{BE} away from the rotor hub is given by eq. (4.1). A comparison between this linear approximation and the Generic Tilt-Rotor Simulation (GTRS) blade twist is shown in fig. A.1. A diagram of the modeled simplified articulated rotor consisting of the rotor hub, the flapping spring (represented by the coil), and a single blade is shown in fig. 4.1 together with the positive conventions of the mentioned angles. Here the subscript R refers to the right rotor, while the constant R is the rotor radius (which is equivalent to the blade length). The X- and Y-axes of the blade and rotating frames are also shown (indicated with the $\widehat{BL}$ and $\widehat{R}$ subscripts respectively) and are formally defined in section 4.7. Note that $\theta_{bl,g}$ is incorporated into θ_0 therefore it is not shown in the figure.

$$\theta_{BE} = \theta_0 + \theta_{bl,1} r_{BE} \tag{4.1}$$

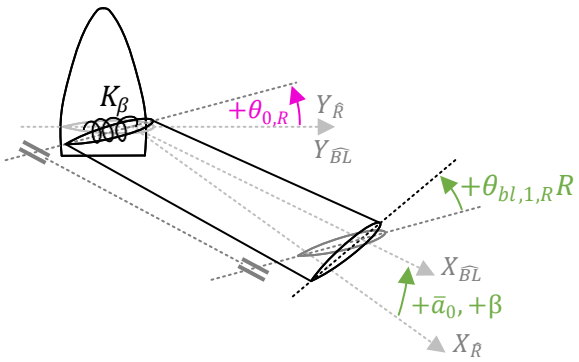

Figure 4.1: Schematic depiction of the rotor hub and blade of a counterclockwise rotating rotor, indicating the positive sign conventions of the blade root collective, twist, precone, and flapping angles.

Lifting Surface

The lifting surface (ls) component has a trapezoidal planform characterized by a root $c_{r,ls}$ and tip $c_{t,ls}$ chord length, distance of the root profile aerodynamic center (AC) from the leading edge $c_{rAC,ls}$, half-span $b_{1/2,ls}$, and a aerodynamic center sweep angle Λ_{ls}. Furthermore the orientation of the lifting surface with respect to the tilt-rotor body is defined by an incidence i_{ls} and dihedral angle Γ_{ls}. The sweep angle is treated as a shear transformation. Finally the lifting surface may contain one or more control surfaces. A diagram of the top, side, and rear view of the lifting surface component is shown in fig. 4.1 together with the dimensions and positive conventions of the mentioned angles. Here the subscript R refers to a lifting surface mounted on the right side of the tilt-rotor when viewed from behind the aircraft while the subscript ls represents a specific lifting surface abbreviation. A list of these abbreviations is provided in table 4.4. The X- and Y-axes of the body, intermediate lifting surface, and final lifting surface reference frames are also shown (indicated with the b, ls', and ls subscripts respectively) and are formally defined in section 4.7.

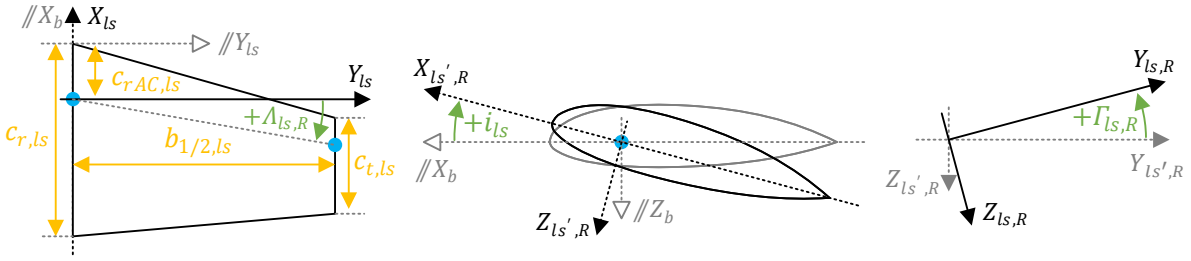

Figure 4.2: Schematic depiction of the top, side, and aft views of a right-mounted trapezoidal lifting surface component showing its defining parameters and positive angle sign conventions. Blue dots indicate the positions of the airfoils' aerodynamic centers.

Lifting Body

The lifting body component is described only by an equivalent flat plate area parameter A_{eq}.

4.2.2. 6DoF Model XV-15 Implementation Components

Since several of the components that are part of the real XV-15 tilt-rotor may be represented by the same generic component, such as the wing and tail stabilizers may both be considered lifting surfaces, the 6DoF model XV-15 implementation also consists of multiple instances of the generic components described in the previous section. This section describes all the instances and names of the components that make up the 6DoF tilt-rotor model. A graphical summary of these components is also presented in fig. 4.3.

Starting with the propulsion, the 6DoF model contains two rotor components, each corresponding to the proprotor mounted on either the left or right tiltable nacelle located on one of the tips of the main wing. The dynamic nor aerodynamic effect of the nacelles themselves is neglected in the 6DoF model however. Note that each component instance that has a longitudinally symmetrical counterpart, such as one of the rotors, is additionally distinguished by a *left* or *right* identifier which refers to its lateral disposition with respect to longitudinal line of symmetry of the tilt-rotor body when looking from behind. This shall also apply to the main wing and tail stabilizer lifting surfaces.

The XV-15 main wing is divided into a left and right half, with each half being further divided along its span into three lifting surface instances based on the location of the control surfaces. As a result the innermost lifting surface instance closest to the fuselage corresponds to the wing segment that has no control surfaces running along its span, therefore it is referred to as the *free wing* segment. The next component instance corresponds to the segment of the wing that is spanned by the inboard flaps, hence it is referred to as the *flap wing* segment. Finally, the last wing segment closest to the nacelle corresponds to the segment of the wing that is spanned by the flaperons, i.e. the combined control surface that acts both as an aileron and a flap, and it is referred to as the *aileron wing* segment. This wing division also closely overlaps with the portions of the wing that are affected by the rotor wake, namely only the *flap wing* and *aileron wing* segments are 'wetted' by the rotor wake. A detailed description of the rotor wake effect on the wings is found in section 5.5.

The XV-15 horizontal stabilizer is also divided into a left and right half with each being its own lifting surface. Each of these halves also has a separate elevator control surface, however both of these elevators are controlled simultaneously as if they were a single control surface.

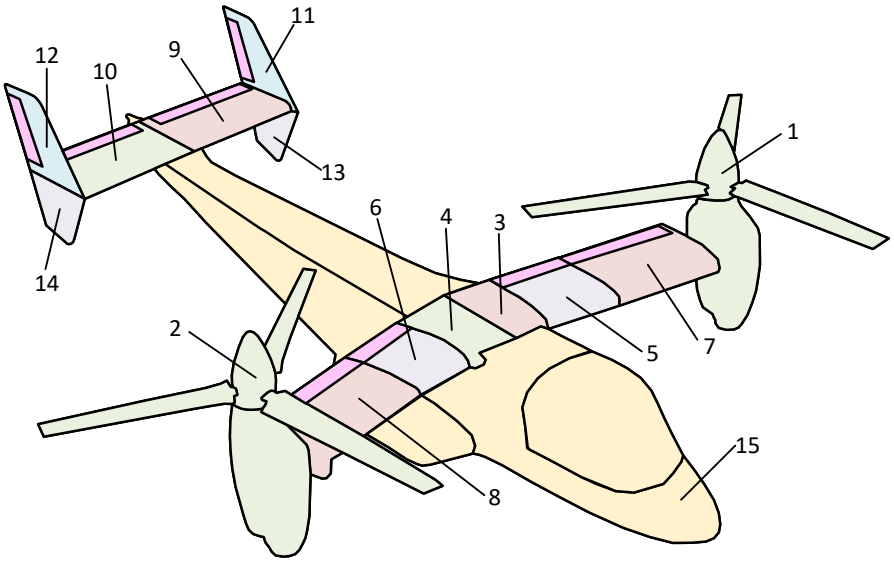

1. Rotor, left
2. Rotor, right
3. Free wing, left
4. Free wing, right
5. Flap wing, left
6. Flap wing, right
7. Aileron wing, left
8. Aileron wing, right
9. H-stab, left
10. H-stab, right
11. V-stab, top left
12. V-stab, top right
13. V-stab, bot. left
14. V-stab, bot., right
15. Fuselage

Figure 4.3: Schematic depiction of the XV-15 tilt-rotor showing all of the components and their names that comprise the 6DoF model XV-15 implementation. Colors are used only to differentiate between neighboring components, with the exception of control surfaces which are also shown and are represented collectively by pink rectangles.

The XV-15 tilt-rotor has an H-tail configuration meaning that it has two vertical stabilizers, one at each tip of the horizontal stabilizer. Furthermore each vertical stabilizer significantly deviates from the trapezoidal planform approximation and instead resembles two conjoined trapezoids. As a result each vertical stabilizer is divided into a top and bottom lifting surface, with only the top surface having a rudder control surface which closely resembles the vertical stabilizer construction of the real XV-15 tilt-rotor.

Finally the XV-15 only has one fuselage which is modeled by the only lifting body component that is part of the 6DoF model.

4.3. Model States and Controls

This section summarizes the states, control inputs, and control outputs of the 6DoF model XV-15 implementation. A diagram depicting all the positive conventions of these model variables is also shown in order to initially familiarize the reader with the model, and later serve as a compact summary for the reader to return to while reading the rest of the report.

Model States

The states of the 6DoF model are defined to be model variables that are obtained by integrating their derivatives, which in turn depend on the past values of the states. Keeping this in mind, the 6DoF model variables that may be classified as states are summarized in table 4.1 showing each state's symbol, description, positive direction of action (i.e. the axis along or around which the state is positive, with angular states being positive according to the right hand rule), and (SI) units. The reference frame axes listed in the *Direction of Action* column are formally defined in section 4.7 while the Ω_{sgn} term in the last row is treated in section 4.5.8. Note that although the drivetrain and collective governor implementations also contain dynamic states, they are not listed here since they correspond to the specific XV-15 model implementation and not a generic tilt-rotor. These subsystems are, however, described in section 7.3. Also note that out of all states, only the nacelle tilt has minimum and maximum limits which are provided in table A.3.

Pilot Control Inputs

All control inputs are directly controlled by the pilot and consist of the variables that affect the control outputs such as the swashplate angle or elevator deflection[1]. The 6DoF model variables that adhere to this

[1]Note that later a distinction between the Matlab 6DoF model and the Simulink 6DoF model shall be made, each having slightly different control inputs. The control inputs summarized in this chapter, however, correspond to the pilot inputs of the more extensive Simulink 6DoF model.

Table 4.1: List of the 6DoF tilt-rotor model states.

Symbol	State Description	Positive Direction of Action	Units
u_i	longitudinal linear body inertial velocity	X_b / forward	m/s
v_i	lateral linear body inertial velocity	Y_b / rightward	m/s
w_i	vertical linear body inertial velocity	Z_b / downward	m/s
x_{cg}	longitudinal body CoG position in inertial space	X_C / north	m
y_{cg}	lateral body CoG position in inertial space	Y_C / east	m
z_{cg}	vertical body CoG position in inertial space	Z_C / negative altitude	m
p_i	rolling angular body inertial velocity	X_b / right wing tip down	rad/s
q_i	pitching angular body inertial velocity	Y_b / nose up	rad/s
r_i	yawing angular body inertial velocity	Z_b / nose right	rad/s
ϕ_b	body roll angle	$X_{b''}$ / right wing tip down	rad
θ_b	body pitch angle	$Y_{b'}$ / nose up	rad
ψ_b	body heading angle	Z_E / nose right	rad
η	nacelle tilt angle	Y_{np} / backward	rad
Ω	rotor axial rotational velocity	$\Omega_{sgn} Z_{\widehat{NR}}$ / -	rad/s

definition are summarized in table 4.2 showing each control input's symbol, description, effect as a result of a positive input (i.e. the *Positive Action* column), and units. Here in refers to inches, RPM to revolutions per minute, and the ranges specified within the brackets mean that the corresponding control inputs may have any real value within the specified range. Apart from the flap lever and nacelle tilt switch, the other control inputs are also bounded and their limits are summarized in table A.14.

Table 4.2: List of the 6DoF tilt-rotor model pilot control inputs.

Symbol	Control Input Description	Positive Action	Units
X_{LON}	longitudinal stick deflection	$-q$, i.e. nose down	in
X_{LAT}	lateral stick deflection	$-p$, i.e. left wing tip down	in
$X_{COL,pilot}$	pilot collective stick deflection	more thrust	in
X_{PED}	pedal position	$-r$, i.e. nose left	in
X_{FLA}	flap lever position	more wing camber	[0 to 1]
X_{TIL}	nacelle tilt switch	from arpln to heli. config.	[-1 to 1]
RPM_{SEL}	rotor RPM selector	-	RPM

Control Outputs

Conversely, the control outputs consist of variables that are affected by the control inputs, however not exclusively. For example the swashplate collective is not only influenced by the pilot collective stick, but also by the collective governor. Since the latter is not directly controlled by the pilot, it has not been listed as a control input, however it is introduced in the control mixing and phasing section (i.e. section 4.4). The effect of the control inputs on the control outputs is also treated in the control mixing and phasing section since in some cases one input may affect multiple outputs, or multiple inputs may affect one output.

The control outputs of the 6DoF model are summarized in table 4.3 showing each control output's symbol, description, positive action, and units with HP being horse power. Although the flapping angle β is not a control output, it is also included at the end of this table showing indicating its positive direction of action. As is presented graphically in fig. 4.4, positive control surface deflections result in an increase in the lift of the parent control surface (defined in its reference frame). Furthermore, positive longitudinal cyclic results in a downward motion of the front of the rotor disk while positive swashplate collective results in an increase in the blade pitch, which in turn (typically) results in more rotor thrust. Finally, more commanded engine power results in more delivered torque at the rotor shaft, which in turn results in an increase in rotor RPM, and a positive tilt rate results in the nacelle being tilted from airplane to helicopter configuration.

Table 4.3: List of the 6DoF tilt-rotor model control outputs.

Symbol	Control Output Description	Positive Action	Units
θ_{1s}	swashplate longitudinal cyclic angle	CP fore downwards	rad
θ_0	swashplate collective angle	increase blade pitch	rad
R_{SHP}	commanded engine power	-	HP
δ_{ail}	flaperon deflection	right flaperon down	rad
δ_{ele}	elevator deflection	elevator down	rad
δ_{rud}	rudder deflection	outward	rad
δ_{fla}	flap deflection	flap and flaperon down	rad
$\dot{\eta}$	nacelle tilt rate	nacelle tilt backwards	rad/s
β	blade flapping angle	above CP	rad

A graphical summary of the sign conventions of the model states, control inputs, and control outputs is shown in fig. 4.4. Here the subscripts L and R refer to components mounted on the left and right sides of the tilt-rotor (when looking from behind) respectively. The axes of the body, nacelle, shaft plane, and control plane are also shown and indicated with the subscripts b, n, SP, and CP respectively. These reference frames are formally defined in section 4.7. It must be highlighted that a nacelle angle of $\eta = 0°$ corresponds to helicopter configuration (heli. config.) while an angle of $\eta = -90°$ corresponds to airplane configuration (arpln config.).

4.4. XV-15 Control Mixing and Phasing

Having defined the control inputs and control outputs of the 6DoF model it is now possible to specify the effects of the inputs on the outputs. The relationships between the inputs and outputs of the 6DoF model are based on the GTRS model tables provided in [6]. Data tables are not continuous, therefore analytical functions have been defined for the 6DoF model instead, providing an approximation for the control input-output relationships.

Before these relationships are defined, it must be first mentioned that the effects of several of the inputs on several of the outputs is influenced by the nacelle tilt or velocity. Furthermore, some of the inputs affect multiple outputs, and some outputs are affected by multiple inputs. These two phenomena are referred to as control phasing and control mixing respectively, and the combined term control phasing and mixing shall refer to the complete relation ship between the inputs and a single output. Finally, terms that are influenced by the nacelle tilt or velocity shall be referred to as being *phased*.

This section is structured according to the control outputs listed in table 4.3, therefore first the swashplate longitudinal cyclic control phasing and mixing is treated, followed by the swashplate collective, commanded engine power, flaperon, elevator, rudder, flaps, and finally nacelle tilt rate control outputs. All constant terms shall not be given in this section and instead are listed in table A.13 in appendix A together with the other 6DoF model implementation parameters. A graphical comparison between the presented analytical functions and the GTRS data tables is also presented in appendix A.

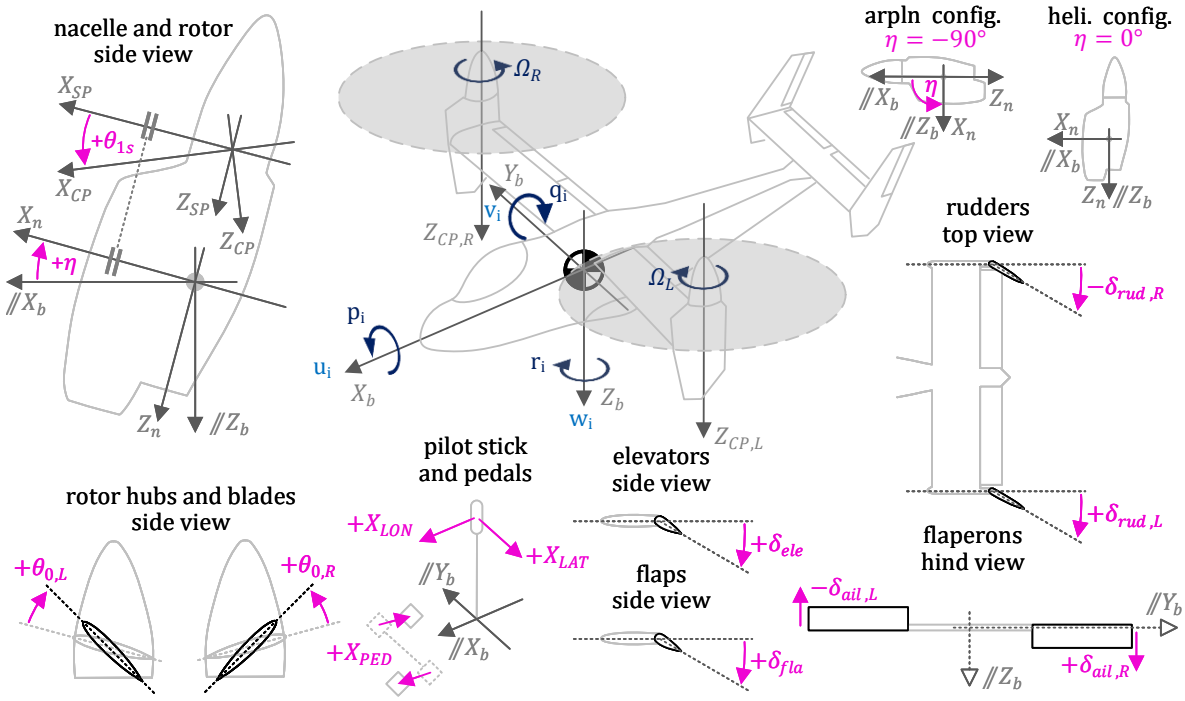

Figure 4.4: Summary of positive sign conventions of the tilt-rotor states, control inputs, and control outputs.

4.4.1. Swashplate Longitudinal Cyclic θ_{1s}

The swashplate longitudinal cyclic output θ_{1s} is a combination of three phased terms, namely an offset term $\theta_{1s,offset,\eta}$, a longitudinal stick term $\theta_{1s,LON,\eta}$, and a differential pedals term $\theta_{1s,PED,u\eta}$ as shown in eq. (4.2) for the left and right rotor indicated by the L and R subscripts. The only difference between the control relationships are the opposite signs in front of the $\theta_{1s,PED,u\eta}$ term. Due to these opposite signs the pedals are categorized as a differential input in this case. Note that θ_{1s} is defined in radians while its constituents are defined in degrees, hence the need for a conversion from degrees to radians. Also note that the phasing variables are indicated in the subscripts, in this case both the nacelle tilt η and longitudinal (aerodynamic) body velocity u appear as phasing variables. The affecting control inputs are also shown in the subscripts.

$$\theta_{1s,L} = \left(\theta_{1s,offset,\eta} + \theta_{1s,LON,\eta} - \theta_{1s,PED,u\eta}\right)\frac{\pi}{180} \tag{4.2a}$$

$$\theta_{1s,R} = \left(\theta_{1s,offset,\eta} + \theta_{1s,LON,\eta} + \theta_{1s,PED,\eta}\right)\frac{\pi}{180} \tag{4.2b}$$

Stick Invariant θ_{1s} Phasing - Offset

The definition of the phased swashplate longitudinal cyclic offset is shown in eq. (4.3) where δ_{B1} is a constant term (given in degrees). This relationship is directly taken from [6, p. A-131] therefore it is not an analytical approximation. $\theta_{1s,offset,\eta}$ may also be referred to as the stick-invariant longitudinal cyclic phasing since it does not depend on any pilot stick inputs. It can be seen that the δ_{B1} constant term is phased-in as the tilt-rotor converts to airplane mode resulting in a nose-down pitching moment, while in helicopter configuration it has no effect on the control plane tilt. The value of δ_{B1} is given in table A.13.

$$\theta_{1s,offset,\eta} = \delta_{B1}\left(1 - cos(\eta)\right) \tag{4.3}$$

Longitudinal Stick θ_{1s} Phasing

The longitudinal stick term $\theta_{1s,LON,\eta}$, on the other hand, is defined in eq. (4.4a) and depends on the longitudinal stick deflection X_{LON}. Here the fraction $\frac{\partial\theta_{1s}}{\partial X_{LON}}$ is referred to as longitudinal-stick-to-longitudinal-cyclic-gearing and its analytical approximation is defined in eq. (4.4b). A graphical comparison between the

analytical approximation and GTRS gearing is shown in fig. A.2. It can be seen that in helicopter configuration the gearing between the stick and swashplate is equal to the constant value $\frac{\partial \theta_{1s}}{\partial X_{LON}}\Big|_{\eta=0}$, while in airplane mode the pilot longitudinal stick control over the swashplate is completely phased out. The value of $\frac{\partial \theta_{1s}}{\partial X_{LON}}\Big|_{\eta=0}$ is given in table A.13.

$$\theta_{1s,LON,\eta} = X_{LON}\frac{\partial \theta_{1s}}{\partial X_{LON}} \tag{4.4a}$$

$$\frac{\partial \theta_{1s}}{\partial X_{LON}} = \frac{\partial \theta_{1s}}{\partial X_{LON}}\Big|_{\eta=0} cos(\eta) \tag{4.4b}$$

Differential Pedals θ_{1s} Mixing and Phasing

The last term $\theta_{1s,PED,u\eta}$ is defined in eq. (4.5a) and depends on the pedals deflection X_{PED} and longitudinal body velocity u. Here the fraction $\frac{\partial \theta_{1s}}{\partial X_{PED}}$ is referred to as pedals-to-longitudinal-cyclic-gearing and its analytical approximation is defined in eq. (4.5b). A comparison between the analytical approximation and GTRS gearing is shown in fig. A.3 for different velocities. Once again it can be seen that in helicopter configuration the gearing between the pedals and swashplate is equal to the $\frac{\partial \theta_{1s}}{\partial X_{LON}}\Big|_{\eta=0}$ term, while in airplane mode the pilot pedal control over the swashplate longitudinal cyclic is completely phased out. This trend is not influenced by the longitudinal velocity u however. In contrast, the $\frac{\partial \theta_{1s}}{\partial X_{LON}}\Big|_{\eta=0}$ term in this case is not constant and instead is influenced by the longitudinal body velocity u. This influence is analytically approximated by a horizontally flipped sigmoid function as defined by eq. (4.5c). A graphical comparison between this analytical approximation and the GTRS velocity phasing is shown in fig. A.4 for different nacelle tilt angles. It can be seen that the pedals-to-longitudinal-cyclic-gearing generally decreases as the velocity increases.

Observing fig. A.4 it can also be seen that the sigmoid relationship does not vary as a function of the nacelle tilt and thus persists throughout the entire tilt-rotor conversion range. However it does depend on four constant parameters, the first two being the upper S_{top} and lower S_{bot} plateau values equal to the pedal-to-longitudinal-cyclic-gearing values at 0 and 100 knots respectively, as shown in eq. (4.5d) and eq. (4.5e). The other two parameters, namely S_{inflex} and S_{slope}, correspond to the velocity at which the sigmoid has its inflection point and the slope of the curve at the inflection point, both of which have been adjusted manually to achieve a satisfactory level of overlap between the analytical approximation and the GTRS gearing. The values of all four sigmoid parameters are given in table A.13.

$$\theta_{1s,PED,u\eta} = X_{PED}\frac{\partial \theta_{1s}}{\partial X_{PED}} \tag{4.5a}$$

$$\frac{\partial \theta_{1s}}{\partial X_{PED}} = \frac{\partial \theta_{1s}}{\partial X_{PED}}\Big|_{\eta=0} cos(\eta) \tag{4.5b}$$

$$\frac{\partial \theta_{1s}}{\partial X_{PED}}\Big|_{\eta=0} = (S_{\text{top}} - S_{\text{bot}})\left(\frac{1}{e^{(u-S_{\text{inflex}})S_{\text{slope}}}+1}\right) + S_{\text{bot}} \tag{4.5c}$$

$$S_{\text{top}} = \frac{\partial \theta_{1s}}{\partial X_{PED}}\Big|_{\eta=0,u=0} \tag{4.5d}$$

$$S_{\text{bot}} = \frac{\partial \theta_{1s}}{\partial X_{PED}}\Big|_{\eta=0,u=100kts} \tag{4.5e}$$

Recalling eq. (4.2), an input on the pedals results in one rotor disk being tilted forwards, and the other backwards, resulting in a moment imbalance making it possible for the tilt-rotor to yaw in helicopter configuration. This yawing moment is reduced as the longitudinal body velocity increases, and is completely phased out in airplane configuration.

4.4.2. Swashplate Collective θ_0

The swashplate collective output θ_0 is a combination of three phased terms, namely a lower limit term $\theta_{0,LL,\eta}$, a collective stick term $\theta_{0,COL,\eta}$, and a differential lateral stick term $\theta_{0,LAT,\eta}$ as shown in eq. (4.6)

for the left and right rotor indicated by the L and R subscripts. The only difference between the control relationships are the opposite signs in front of the $\theta_{0,LAT,\eta}$ term. Due to these opposite signs the lateral stick is categorized as a differential input in this case. Note that θ_0 is defined in radians while its constituents are defined in degrees, hence the need for a conversion from degrees to radians. Also note that the phasing variable η as well as the affecting control inputs are shown in the subscripts.

$$\theta_{0,L} = \left(\theta_{0,LL,\eta} + \theta_{0,COL,\eta} - \theta_{0,LAT,\eta}\right) \frac{\pi}{180} \tag{4.6a}$$

$$\theta_{0,R} = \left(\theta_{0,LL,\eta} + \theta_{0,COL,\eta} + \theta_{0,LAT,\eta}\right) \frac{\pi}{180} \tag{4.6b}$$

Stick Invariant θ_0 Phasing - Pitch Lower Limit

The definition of the phased swashplate collective lower limit is shown in eq. (4.7) which consists of a constant geometric blade root pitch $\theta_{bl,g}$, the phased blade pitch lower limit at a radial distance of $0.75R$ away from the rotor hub $\theta_{0,LL,0.75R,\eta}$, and the value of the geometric blade pitch at that same radial position $\theta_{bl,g,0.75R}$. The GTRS reference data for the phased lower limit given in [6, p. B-92] defines the lower limit only at a radial distance of $0.75R$ away from the rotor hub. Since the 6DoF model requires the lower limit to be defined at the blade root, first the difference between the geometric blade pitch and the lower limit is calculated at $0.75R$ by subtracting the former from the latter, yielding a so-called global pitch modifier $\theta_{0,LL,mod,\eta}$ which indicates the change in blade pitch as a result of the phased lower limit term. Since this global modifier is constant along the blade length it may be simply added to the geometric blade root pitch $\theta_{bl,g}$ yielding the total blade root pitch lower limit $\theta_{0,LL,\eta}$.

$$\theta_{0,LL,\eta} = \theta_{bl,g} + \left(\theta_{0,LL,0.75R,\eta} - \theta_{bl,g,0.75R}\right) = \theta_{bl,g} + \theta_{0,LL,mod,\eta} \tag{4.7}$$

Both $\theta_{bl,g}$ and $\theta_{bl,g,0.75R}$ are constant values provided in table A.2. It must be noted that $\theta_{bl,g,0.75R}$ is interpolated from the data given in [6, p. B-16]. The phased blade pitch lower limit $\theta_{0,LL,0.75R,\eta}$, on the other hand, varies as a function of the nacelle tilt and its analytical approximation is defined in eq. (4.8). Here the terms $\theta_{0,LL,0.75R,heli}$ and $\theta_{0,LL,0.75R,arpln}$ are constant and correspond to the blade pitch lower limits at $0.75R$ in helicopter and airplane configuration respectively. These too are provided in table A.13. A graphical comparison of the global pitch modifier $\theta_{0,LL,mod,\eta}$ between the analytical approximation and the GTRS is shown in fig. A.5. It can be seen that the pitch modifier initially decreases the lower limit in helicopter configuration, however it increases linearly as the nacelle tilts from helicopter to airplane configuration ultimately resulting in an increased lower limit in airplane mode.

$$\theta_{0,LL,0.75R,\eta} = \theta_{0,LL,0.75R,heli}\left(1 + \frac{2\eta}{\pi}\frac{\theta_{0,LL,0.75R,heli} - \theta_{0,LL,0.75R,arpln}}{\theta_{0,LL,0.75R,heli}}\right) \tag{4.8}$$

Collective Stick θ_0 Phasing - Pilot and Governor Inputs

Next, the collective stick term $\theta_{0,COL,\eta}$ is defined in eq. (4.9) where X_{COL} is the total collective quasi-stick deflection and $\frac{\partial\theta_0}{\partial X_{COL}}\Big|_{\eta=0}$ is the (constant) total-collective-quasi-stick-to-swashplate-collective-gearing in helicopter configuration (provided in table A.13).

$$\theta_{0,COL,\eta} = X_{COL}\left.\frac{\partial\theta_0}{\partial X_{COL}}\right|_{\eta=0} \tag{4.9}$$

It is important to highlight that the control deflection X_{COL} is not equal to the pilot collective stick $X_{COL,pilot}$ control input as listed in table 4.2. Instead X_{COL} combines the inputs from both the pilot stick ($X_{COL,pilot,\eta}$) and the collective governor ($X_{COL,gov}$) as shown in eq. (4.10a). The reason for combining the pilot and governor inputs is explained at the beginning of section 7.4. Note that the collective governor subsystem nominally outputs a swashplate collective deflection ($\theta_{0,gov}$, see section 7.3.4) while here the control input of the governor is represented by a stick deflection $X_{COL,gov}$. For this reason the latter is referred to as

being a stick-deflection-equivalent since the nominal collective governor angular output is converted to a stick deflection with the use of eq. (4.10b).

The analytical approximation of the relationship between the pilot collective stick input $X_{COL,pilot}$ and the phased pilot collective stick input $X_{COL,pilot,\eta}$, on the other hand, is given by eq. (4.10c). A graphical comparison between the analytical approximation and the GTRS gearing is shown in fig. A.6. It can be seen that the pilot's control over the swashplate collective reduces linearly as the nacelles tilt forward up to the point where the pilot no longer has direct control of the swashplate collective in airplane configuration.

$$X_{COL} = X_{COL,gov} + X_{COL,pilot,\eta} \tag{4.10a}$$

$$X_{\text{COL,gov}} = \frac{\theta_{0,\text{gov}}}{\left(\frac{\partial\theta_0}{\partial X_{\text{COL}}}\Big|_{\eta=0}\right)} \tag{4.10b}$$

$$X_{COL,pilot,\eta} = X_{COL,pilot}\left(1 + \frac{2\eta}{\pi}\right) \tag{4.10c}$$

Differential Lateral Stick θ_0 Mixing and Phasing

The last term $\theta_{0,LAT,\eta}$ is defined in eq. (4.11a) and depends on the pilot lateral stick deflection X_{LAT} and the lateral-stick-to-swashplate-collective-gearing $\frac{\partial\theta_0}{\partial X_{LAT}}$ which is analytically approximated with eq. (4.11b). Here $\frac{\partial\theta_0}{\partial X_{LAT}}\Big|_{\eta=0}$ and $\frac{\partial\theta_0}{\partial X_{LAT}}\Big|_{\eta=-\pi/2}$ are the lateral-stick-to-swashplate-collective-gearing constant values in helicopter and airplane configuration respectively, provided in table A.13. A graphical comparison between the analytical approximation and GTRS gearing is also shown in fig. A.7. It can be seen that the gearing between the lateral stick and swashplate collective decreases sinusoidally from a value of $\frac{\partial\theta_0}{\partial X_{LAT}}\Big|_{\eta=0}$ in helicopter configuration, to a value of $\frac{\partial\theta_0}{\partial X_{LAT}}\Big|_{\eta=-\pi/2}$ in airplane mode, therefore the differential lateral stick to swashplate collective is not completely phased out in airplane configuration. Recalling eq. (4.6), this means that in helicopter configuration a lateral stick input results in one rotor producing more thrust than the other creating a moment imbalance making it possible for the tilt-rotor to roll. In airplane mode a lateral stick input also creates a moment imbalance, however since the nacelles are tilted forwards, the imbalance results in a yawing moment which aids the pilot in achieving a coordinated turn.

$$\theta_{0,LAT,\eta} = X_{COL,pilot}\frac{\partial\theta_0}{\partial X_{LAT}} \tag{4.11a}$$

$$\frac{\partial\theta_0}{\partial X_{LAT}} = \left(1 - \frac{\frac{\partial\theta_0}{\partial X_{LAT}}\Big|_{\eta=-\pi/2}}{\frac{\partial\theta_0}{\partial X_{LAT}}\Big|_{\eta=0}}\right)cos(\eta) + \frac{\frac{\partial\theta_0}{\partial X_{LAT}}\Big|_{\eta=-\pi/2}}{\frac{\partial\theta_0}{\partial X_{LAT}}\Big|_{\eta=0}} \tag{4.11b}$$

4.4.3. Commanded Engine Power R_{SHP}

The commanded engine power R_{SHP} control output is a non-linear function of the pilot collective stick as shown in eq. (4.12). This non-linear function represents an analytical approximation of the actual relationship between the collective stick and engine power that has been obtained by fitting the GTRS data provided in [6, p. B-94, p. B-111]. A graphical comparison between the analytical approximation and GTRS data is shown in fig. F.5. The implementation of the throttle lever in the 6DoF model is treated in more detail in section 7.3.5.

Note that the pilot collective stick also controls the throttle, therefore it may also be referred to as the collective-throttle stick. As a result the pilot collective stick deflection $X_{COL,pilot}$ is equal to the collective-throttle stick deflection $X_{COL,thr}$ as already indicated in eq. (4.12). It must be highlighted, however, that the $X_{COL,thr}$ is equal to the unmodified pilot collective stick deflection $X_{COL,pilot}$ and not the phased pilot collective stick input $X_{COL,pilot,\eta}$.

$$R_{\text{SHP}} = f(X_{COL,pilot} = X_{COL,thr}) =$$
$$= (0.2513)\,(X_{\text{COL,thr}})^4 + (4.822)\,(X_{\text{COL,thr}})^3 - (20.03)\,(X_{\text{COL,thr}})^2 + (121.7)\,(X_{\text{COL,thr}}) + 89.496 \tag{4.12}$$

4.4.4. Control Surfaces

This next section describes the relationship between the control inputs and the control surface deflections. It is appropriate to mention at this point that none of the control surfaces are subjected to control phasing, therefore their deflections do not depend on the nacelle tilt angle and the pilot has full control over them throughout the entire conversion range. Furthermore almost all control surfaces are controlled only by one control input with the exception of the flaperons which are treated first.

Flaperon Deflection δ_{ail}

As the name suggests, the flaperons behave as both ailerons and flaps, therefore their deflection δ_{ail} is affected by two control inputs, namely the pilot lateral stick deflection X_{LAT} and the flap lever deflection X_{FLA} as shown in eq. (4.13) for the left and right flaperons as indicated by the L and R subscripts. The only difference between these two relationships is the opposite sign in front of the $\frac{\partial \delta_{ail}}{\partial X_{LAT}}$ term which defines the lateral-stick-to-flaperon-deflection-gearing and makes it possible for the flaperons to generate a rolling body moment. The remaining $\frac{\partial \delta_{ail}}{\partial X_{FLA}}$ term defines the flap-lever-to-flaperon-deflection-gearing making it possible to increase the camber of the wing with the help of the flaperons. Both gearing terms are constant and are given in table A.13.

$$\delta_{ail,L} = X_{FLA}\frac{\partial \delta_{ail}}{\partial X_{FLA}} - X_{LAT}\frac{\partial \delta_{ail}}{\partial X_{LAT}} \tag{4.13a}$$

$$\delta_{ail,R} = X_{FLA}\frac{\partial \delta_{ail}}{\partial X_{FLA}} + X_{LAT}\frac{\partial \delta_{ail}}{\partial X_{LAT}} \tag{4.13b}$$

Elevator Deflection δ_{ele}

The elevator deflection δ_{ele} is affected only by one control input, namely the pilot longitudinal stick deflection X_{LON} as shown in eq. (4.14). Here $\frac{\partial \delta_{ele}}{\partial X_{LON}}$ is the longitudinal-stick-to-elevator-deflection-gearing which is constant and given in table A.13. The elevators of the left and right horizontal stabilizers deflect in the same direction therefore no distinction is made between the left and right elevator.

$$\delta_{ele} = X_{LON}\frac{\partial \delta_{ele}}{\partial X_{LON}} \tag{4.14}$$

Rudder Deflection δ_{rud}

The rudder deflection δ_{rud} is also affected only by one control input, namely the pilot pedal deflection X_{PED}, however a distinction between the left and right rudder must be made, as shown in eq. (4.15), where opposite signs are placed in front of $\frac{\partial \delta_{rud}}{\partial X_{PED}}$, i.e. the pedals-to-rudder-deflection-gearing which is constant and given in table A.13. The reason for the different signs is the opposite positive convention for the rudder deflection of the left and right (top) vertical stabilizer as has been shown in fig. 4.4.

$$\delta_{rud,L} = X_{PED}\frac{\partial \delta_{rud}}{\partial X_{PED}} \tag{4.15a}$$

$$\delta_{rud,R} = -X_{PED}\frac{\partial \delta_{rud}}{\partial X_{PED}} \tag{4.15b}$$

Flap Deflection δ_{fla}

The flap deflection δ_{fla} is also affected only by one control input, namely the pilot flap lever deflection X_{FLA} as shown in eq. (4.16). Here $\frac{\partial \delta_{fla}}{\partial X_{FLA}}$ is the flap-lever-to-flap-deflection-gearing which is constant and given in table A.13. The flaps of the left and right (flap) wing deflect in the same direction therefore no distinction is made between the left and right flap.

$$\delta_{fla} = X_{FLA}\frac{\partial \delta_{fla}}{\partial X_{FLA}} \tag{4.16}$$

4.4.5. Nacelle Tilt Rate $\dot{\eta}$

Finally the nacelle tilt rate $\dot{\eta}$ is also affected only by one control input, namely the pilot nacelle tilt switch deflection X_{TIL} as shown in eq. (4.17). Here $\frac{\partial \dot{\eta}}{\partial X_{TIL}}$ is the nacelle-tilt-switch-to-nacelle-tilt-rate-gearing which is constant and given in table A.13. Both the left and right nacelle tilts in the same direction therefore no distinction is made between the two.

$$\dot{\eta} = X_{TIL} \frac{\partial \dot{\eta}}{\partial X_{TIL}} \tag{4.17}$$

4.5. Model Parameters

Only the component geometric parameters and the input gearing ratios have been mentioned up to this point, however the 6DoF model requires several more constants in order to obtain a fully specified tilt-rotor model instance. This section summarizes all of the remaining constant parameters of the 6DoF model while the values of these parameters that have been used to obtain the XV-15 tilt-rotor implementation of this thesis work are given in appendix A. Most values are taken from external sources as indicated in the appendix, however in some cases the values are calculated and the methods of obtaining these calculated values are also described in this section.

This section starts by defining the general parameters that correspond to the tilt-rotor as a whole while the rest of the section is primarily structured according to the components of the 6DoF model with most of the parameters of the rotor, lifting surface, and lifting body treated separately. The parameters that define the position of all components with respect to the body, however, are treated collectively in a separate subsection. Lastly, special sign-change parameters that affect the signs of terms within the tilt-rotor expressions, depending on either the mounting position of a component or the direction of rotation of the rotor, are formally defined at the end. Note that references to these sign-change parameters are made throughout this section before this formal definition.

4.5.1. General

The general model parameters consist of the total body mass m, the I_{xx}, I_{yy}, and I_{zz} moments of inertia around the body X-, Y-, and Z-axes, and the body roll-yaw product of inertia I_{xz}. In addition the position of the body CoG defined in the aircraft station coordinate system used in [6] is also required in order to be able to later calculate the position of each component (i.e. the origin of each component reference frame) with respect to the body CoG. The longitudinal, lateral, and vertical positions of the body CoG are specified with the station line SL_{cg}, buttock line BL_{cg}, and water line WL_{cg} parameters. The 6DoF model XV-15 tilt-rotor implementation general parameters used in this thesis are provided in table A.1.

Note that the data provided in [6] specifies the positions of the tilt-rotor component also with respect to the aircraft station coordinate system which have to be converted to positions defined in the body frame before being supplied to the 6DoF model. The conversion of the component positions from these aircraft station coordinate system to the body axes are treated collectively in section 4.5.7.

4.5.2. Rotors

Apart from the geometric parameters already treated in section 4.2 (i.e. $\overline{a}_0$, c_{bl}, $\theta_{bl,g}$, $\theta_{bl,1}$, and R), the rotor component parameters additionally specify the number of blades per rotor N, the blade moment of inertia I_{bl} around the flapping hinge, the flapping spring stiffness K_β, the blade lift coefficient curve slope $C_{l_{\alpha,bl}}$, the blade drag coefficients $C_{d_{0,bl}}$, $C_{d_{1,bl}}$, and $C_{d_{2,bl}}$, and finally the maximum allowable flapping angle $\beta_{SP,absmax}$ defined with respect to the shaft plane (SP). These 6DoF model XV-15 tilt-rotor implementation rotor parameters used in this thesis are provided in table A.2.

Two additional rotor parameters must be calculated, however, namely the blade mass m_{bl} and first mass moment $M_{1,bl}$ which are derived from the blade moment of inertia I_{bl}. By assuming that the blade may be represented by a slender rod, the formula for the moment of inertia of a slender rod around one of its ends shown in eq. (4.18a) is rearranged to obtain the rod mass, or the blade mass as demonstrated in eq. (4.18b). In the former equation L is the rod length which is replaced by the blade length R, ρ is the rod density, s is the rod circular cross-sectional area, and m the rod mass.

$$I_{\text{slender rod end}} = \rho s \int_0^L x^2 dx = \frac{mL^2}{3} \quad (4.18a) \qquad m_{\text{blade}} = \frac{3I_{\text{bl}}}{R^2} \quad (4.18b)$$

Keeping the same slender rod assumption in mind, the formula for the first mass moment of a slender rod about one of its ends is shown in eq. (4.19a) and may be used to obtain the blade first mass moment around one of its ends (M_1) as demonstrated in eq. (4.19b).

$$M_{1,\text{ slender rod end}} = \rho s \int_0^L x dx = \frac{mL}{2} \quad (4.19a) \qquad M_{1,\text{ blade end}} = \frac{m_{bl}R}{2} \quad (4.19b)$$

The values of these calculated 6DoF model XV-15 tilt-rotor implementation rotor parameters used in this thesis are also provided in table A.2.

4.5.3. Tiltable Nacelles

The tiltable nacelle parameters consist of the nacelle pivot (np) position defined in the aircraft station coordinate system with the SL_{np}, BL_{np}, and WL_{np} parameters, and the nacelle length l_n. Three additional nacelle parameters must be calculated, however, namely the d_{xn}, d_{yn}, and d_{zn} which define the nacelle pivot position with respect to the body reference frame as shown in section 4.5.7. All of these nacelle parameters used in the 6DoF model XV-15 tilt-rotor implementation of this thesis are provided in table A.3.

4.5.4. Drivetrain

The drivetrain parameters consist of the maximum optimum engine power $HP_{RO,max}$, engine accessory power loss SHP_{acc}, transmission efficiency η_{XMSN}, rotor turbine gear ratio θ_{XPT}, and the maximum $\theta_{0,gov,max}$ and minimum $\theta_{0,gov,min}$ allowable collective governor swashplate collective deflections. The 6DoF model XV-15 tilt-rotor implementation drivetrain parameters used in this thesis are provided in table A.4.

4.5.5. Lifting Surfaces

Apart from the geometric parameters already treated in section 4.2 (i.e. $c_{r,ls}$, $c_{t,ls}$, $c_{rAC,ls}$, $b_{1/2,ls}$, Λ_{ls}, i_{ls}, and Γ_{ls}), the lifting surface component parameters additionally specify the profile lift coefficient curve slope $C_{l_\alpha,ls}$, maximum drag coefficient $C_{D,max,ls}$, pitching moment around the aerodynamic center coefficient $C_{M,AC,ls}$, and the zero lift angle of attack $\alpha_{0L,ls}$. Furthermore, if the lifting surface contains any control surfaces (cs), their nominal aerodynamic effectiveness $\partial C_{X,cls,nom}/\partial \delta_{cs}$ must also be provided. Here X should be replaced by the appropriate aerodynamic coefficient symbol, e.g. L in the case of the lift coefficient, cls by the complete lifting surface name (e.g. wing in the case of the wing segments), and cs by the appropriate control surface abbreviation. A summary of all the lifting surfaces, their abbreviations, the control surfaces that they contain, and the control surface abbreviations is presented in table 4.4 which should be used as a reference with the lifting surface parameter tables provided in appendix A.

Table 4.4: List of the 6DoF tilt-rotor model lifting surface components, their abbreviations, the control surfaces that they contain, and the control surface abbreviations.

Lifting Surface	LS Abbreviation	Control Surface	CS Abbreviation
free wing	frw	-	-
flap wing	flw	inboard flaps	fla
aileron wing	aw	outboard flaperons	ail
horizontal stabilizer	hs	elevator	ele
top vertical stabilizer	vst	rudder	rud
bot. vertical stabilizer	vsb	-	-

Several additional lifting surface parameters must be calculated, however, namely the maximum lift coefficient $C_{L,max,ls}$, control surface scaled aerodynamic effectiveness $\partial C_{X,ls}/\partial \delta_{cs}$, and the d_{xls}, d_{yls}, d_{zls} parameters which define the root AC position with respect to the body reference frame. The calculation of the AC position parameters is treated in section 4.5.7 where additional readily available lifting surface parameters necessary for these calculations are provided as well. The calculation of the maximum lift coefficient and scaled aerodynamic effectiveness is treated below.

The maximum lift coefficient of every lifting surface is assumed to be equal to its linear profile lift coefficient at an angle of attack 12 degrees, as shown in eq. (4.20), which roughly approximates the actual maximum lift coefficient for all lifting surfaces. In the future, however, more accurate values should be used such as the ones provided in the data tables of [6]. As a side note, the maximum drag coefficient of each lifting surface is taken to be equal to that of a flat plate, i.e. 1.8 [45, fig. 2], with the exception of the flap wing segment whose drag additionally depends on the flap deflection according to eq. (5.133).

$$C_{L,max,ls} = C_{l_\alpha,ls} \cdot 12/180 \cdot \pi \tag{4.20}$$

Unlike the rest of the control surfaces which span almost the entirety of their parent lifting surface, the flaps and flaperons only span a portion of the wing. Keeping in mind that the flap and flaperon (nominal) aerodynamic effectiveness provided in [6] is non-dimensionalized based on the whole wing area, once the wing is divided into segments in the 6DoF model, the nominal aerodynamic effectiveness must be scaled according to the new smaller segment surface area resulting in a larger aerodynamic effectiveness. Since the chord of the entire wing is constant, the scaling may be performed solely based on the span of each segment as shown in eq. (4.21). Here X should be replaced by the appropriate aerodynamic coefficient symbol, e.g. D in the case of the drag coefficient, ls is the lifting surface segment abbreviation, cls is the complete lifting surface (in this case the wing), cs is the control surface abbreviation, $b_{1/2,cls}$ is the half span of the complete lifting surface, and $b_{1/2ls}$ is the half span of appropriate the lifting surface segment.

$$\frac{\partial C_{X,ls}}{\partial \delta_{cs}} = \frac{\partial C_{X,cls,nom}}{\partial \delta_{cs}} \frac{b_{1/2,cls}}{b_{1/2,ls}} \tag{4.21}$$

Note that with the calculated scaled elevator effectiveness the 6DoF model has a too aggressive pitch response in airplane configuration (see fig. 8.39) resulting in a crash of the simulation caused by an unconverged rotor inflow solution. The reason for this is that the high agility makes it possible to flip the aircraft resulting in a flight condition in which the rotor experiences a very high air vector coming from below the rotor disk. Due to this rapid change the inflow solution moves too quickly away from the previous solution, or even out of the validity region of the momentum theory, resulting in a failed convergence of the iterative solver (see section 5.2.6 and fig. 5.15). As a consequence the calculated scaled elevator effectiveness is ultimately halved in the 6DoF Simulink model providing an approximately correct value for its effectiveness at high angles of attack and a stable simulation. A more detailed explanation of this adjustment is provided on page 267.

The values of these calculated 6DoF model XV-15 tilt-rotor implementation lifting surface parameters used in this thesis are also provided in appendix A.

4.5.6. Fuselage

Apart from the aforementioned equivalent flat plate drag A_{eq}, the fuselage parameters additionally consist of its aerodynamic center position defined by the d_{xfus}, d_{yfus}, and d_{zfus} parameters, and its orientation i_{fus} and Γ_{fus} with respect to the body frame of reference. For the sake of simplicity, the 6DoF model assumes that the fuselage axes are aligned with the ones of the body reference frame, and that the center of pressure coincides with the body frame origin. As a result the position and orientation parameters are all equal to zero as also indicated in table A.12 together with the value of the flat plate drag used in the 6DoF model XV-15 tilt-rotor implementation of this thesis. Note that in the case of the XV-15 tilt-rotor parameters shown in [6, p. B-11,B-12], the maximum possible difference between the position of the fuselage center of pressure and the body origin (CoG) is approximately 12 centimeters. It is assumed that aerodynamic moments generated as a result of this distance shall be insignificant in comparison to the other contributors, e.g. the tail.

4.5.7. Reference Frame Origin Disposition

The last set of model parameters corresponds to the calculated positions of the different components defined with respect to the body CoG, i.e. the body reference frame origin. These dispositions are calculated based on the difference between the component and body CoG coordinates defined in the aircraft station coordinate system provided in [6, app. B] with the use of the longitudinal station line (SL), lateral buttock line (BL), and vertical water line (WL) parameters. This section presents the calculation of the dispositions of the nacelle pivot point, free wing segment, flap wing segment, aileron wing segment, horizontal stabilizer, and both the top and bottom vertical stabilizers segments.

Note that some disposition parameters presented in this section are preceded with the d_{sgn} parameter meaning that the sign of their value depends on the side on which that component is mounted. A more detailed explanation of this sign-changing parameter is provided in section 4.5.8.

Nacelle Pivot Point

The disposition parameters of the nacelle pivot point are calculated according to eq. (4.22) where the subscripts np and cg refer to the nacelle pivot point and body CoG respectively. The aircraft station coordinate system parameters as well as the calculated nacelle pivot dispositions used in the 6DoF model XV-15 implementation of this thesis are provided in table A.3.

$$\begin{pmatrix} -d_{xn} \\ d_{sgn}d_{yn} \\ -d_{zn} \end{pmatrix} = \begin{pmatrix} -(SL_{np} - SL_{cg}) \\ d_{sgn}(BL_{np} - BL_{cg}) \\ -(WL_{np} - WL_{cg}) \end{pmatrix} \tag{4.22}$$

Free Wing Root AC

The disposition parameters of the root aerodynamic center (rAC) of the innermost free wing segment (frw) are calculated according to eq. (4.23). Here the subscripts cg, wte, and wcp refer to the body CoG, (complete) wing trailing edge, and (complete) wing center of pressure respectively. Furthermore the parameters $c_{r,w}$ and $c_{rAC,w}$ correspond the root chord length of the (complete) wing and the distance of the root profile aerodynamic center from the leading edge respectively. Typically the latter is equal to a quarter of the root chord length, i.e. $c_{rAC,w} = 0.25c_{r,w}$. The aircraft station coordinate system parameters and the complete wing chord lengths are given in table A.5 while the calculated free wing root AC dispositions used in the 6DoF model XV-15 implementation of this thesis are provided in table A.6.

$$\boldsymbol{s}_{wrAC|b} = \boldsymbol{s}_{frwrAC|b} = \begin{pmatrix} d_{xfrw} \\ d_{sgn}d_{yfrw} \\ -d_{zfrw} \end{pmatrix}^T \{\boldsymbol{E}_b\} = \begin{pmatrix} SL_{cg} - (SL_{wte} - (1 - \frac{c_{rAC,w}}{c_{r,w}})c_{r,w}) \\ 0 \\ -(WL_{wcp} - WL_{cg}) \end{pmatrix}^T \{\boldsymbol{E}_b\} \tag{4.23}$$

Note that the free wing root AC disposition vector is equated to the $\boldsymbol{s}_{wrAC|b}$ and $\boldsymbol{s}_{frwrAC|b}$ vector variables which correspond to the complete wing root AC position vector and the free wing root AC position vector respectively, indicating that root aerodynamic centers of the the complete wing and free wing coincide. The latter position vector is used in the calculation of the dispositions of the other two wing segments as presented next.

Flap Wing and Aileron Wing Root AC

The flap wing and aileron wing segments are positioned at a distance away from the plane of symmetry of the tilt-rotor, however their root aerodynamic centers lie on the locus of the wing profiles' aerodynamic centers. Therefore, given the geometry of the complete wing and the lateral distance between the wing root and roots of the segments, it is possible to calculate the disposition of the aerodynamic centers of the segments.

The first step consists of calculating the position vector $\boldsymbol{s}_{srAC|w}$ which spans from the wing root AC to the segment root AC and is defined in the wing reference frame $\{\boldsymbol{E}_w\}$. This position vector is obtained by defining a position vector that consists of only a lateral component equal to the spanwise distance between the wing root and segment root $b_{1/2,wr-sr}$, and transforming it through the wing sweep angle Λ_w with the use of the transformation matrix $\boldsymbol{T}_{\boldsymbol{\Lambda,w}}$, as shown in eq. (4.24). Here the subscripts wr and sr refer to the

wing root and segment root respectively. The formal definitions of the lifting surface reference frames and the shear transformation matrix are given in section 4.7.

$$\boldsymbol{s}_{srAC|w} = \begin{pmatrix} 0 & d_{sgn} b_{1/2,wr-sr} & 0 \end{pmatrix} \boldsymbol{T}_{\Lambda,w} \{\boldsymbol{E}_w\} \tag{4.24}$$

Next the $\boldsymbol{s}_{srAC|w}$ vector is transformed from the wing reference frame to the body reference frame $\{\boldsymbol{E}_b\}$ with the use of the $\boldsymbol{T}_{\boldsymbol{w|b}}$ transformation matrix which depends on the wing incidence i_w and dihedral Γ_w angles, as shown in eq. (4.25). However, since the resulting vector only provides the relative position of the segment root AC with respect to the wing root AC, the wing root AC position vector $\boldsymbol{s}_{wrAC|b}$ (defined in the body frame as shown in eq. (4.23)) must be finally added to the transformed vector yielding the position of the segment root AC defined in the body frame with respect to the body CoG. The formal definitions of the body reference frames and the wing-to-body transformation matrix are given in section 4.7.

$$\boldsymbol{s}_{srAC|b} = \begin{pmatrix} d_{xls} \\ d_{sgn} d_{yls} \\ d_{zls} \end{pmatrix}^T \{\boldsymbol{E}_b\} = \boldsymbol{s}_{srAC|w} \boldsymbol{T}_{w|b} \{\boldsymbol{E}_b\} + \boldsymbol{s}_{wrAC|b} \tag{4.25}$$

Supplying the wing parameters as well as the spanwise positions of the flap wing and aileron wing segments, and performing the transformations described above yields their root AC dispositions. The necessary wing parameters and the resulting root AC disposition vector components (i.e. d_{xls}, d_{yls}, and d_{zls}) of the flap wing and aileron wing segments of the 6DoF model XV-15 tilt-rotor implementation of this thesis are provided in table A.7 and table A.8 respectively.

Horizontal Stabilizer Root AC

The disposition parameters of the root aerodynamic center (rAC) of the horizontal stabilizer (hs) are calculated according to eq. (4.26). Here the subscripts $hsle$ and $hscp$ refer to the horizontal stabilizer (root) leading edge and horizontal stabilizer center of pressure respectively. Furthermore the parameter $c_{rAC,hs}$ corresponds to the distance of the (horizontal stabilizer) root profile aerodynamic center from the leading edge, typically equal to a quarter of the root chord length, i.e. $c_{rAC,hs} = 0.25 c_{r,hs}$. The aircraft station coordinate system parameters as well as the chord lengths and the calculated horizontal stabilizer root AC dispositions used in the 6DoF model XV-15 implementation of this thesis are provided in table A.9.

$$\begin{pmatrix} -d_{xhs} \\ d_{sgn} d_{yhs} \\ -d_{zhs} \end{pmatrix} = \begin{pmatrix} -((SL_{hsle} + c_{rAC,hs}) - SL_{cg}) \\ 0 \\ -(WL_{hscp} - WL_{cg}) \end{pmatrix} \tag{4.26}$$

Vertical Stabilizer Root AC

The last two segments to be treated are the top (vst) and bottom (vsb) vertical stabilizers (vs) whose root AC positions coincide, therefore only one set of calculations is needed to determine the disposition of their root aerodynamic centers as shown in eq. (4.27). Here the subscripts $vsle$ and $vscp$ refer to the vertical stabilizer (root) leading edge and vertical stabilizer center of pressure respectively. Furthermore the parameter $c_{rAC,vs}$ corresponds to the distance of the (vertical stabilizer) root profile aerodynamic center from the leading edge, typically equal to a quarter of the root chord length, i.e. $c_{rAC,vs} = 0.25 c_{r,vs}$. The aircraft station coordinate system parameters as well as the chord lengths and the calculated vertical stabilizer root AC dispositions used in the 6DoF model XV-15 implementation of this thesis are provided in table A.10.

$$\begin{pmatrix} -d_{xvst} \\ d_{sgn} d_{yvst} \\ -d_{zvst} \end{pmatrix} = \begin{pmatrix} -d_{xvsb} \\ d_{sgn} d_{yvsb} \\ -d_{zvsb} \end{pmatrix} = \begin{pmatrix} -((SL_{vsle} + c_{rAC,vs}) - SL_{cg}) \\ 0 \\ -(WL_{vscp} - WL_{cg}) \end{pmatrix} \tag{4.27}$$

4.5.8. Sign-Change Parameters

Apart from the physical parameters that have been described up to this point, the 6DoF tilt-rotor model also employs so-called sign-change parameters which serve the purpose of changing the sign of a term or

expression depending on either the mounting position of a component or the direction of rotation of the rotor. Using these sign-change-parameters makes it possible to derive a generic set of model expressions applicable to both left and right mounted components, and/or clockwise and counter-clockwise rotating rotors, instead of having to derive separate expressions for each component. The generic model expressions are then made component-specific by setting the sign-change parameters to their appropriate values. This approach also makes it possible to keep all component reference frames right-handed improving the consistency and clarity of the model and of the produced results.

To achieve the above, two sign-change parameters are introduced, namely the Omega-sign-change parameter Ω_{sgn} responsible for the distinction between clockwise and counter-clockwise rotating rotors (when viewed from above in helicopter mode), and the d-sign-change parameter d_{sgn} responsible for the distinction between left and right mounted components (when viewed from the aft of the aircraft). Both of these parameters may only be equal to either 1 or -1 and are defined according to eq. (4.28).

$$\Omega_{sgn} = \begin{cases} 1 & \text{if counter-clockwise} \\ -1 & \text{if clockwise} \end{cases} \qquad d_{sgn} = \begin{cases} 1 & \text{if right-mounted} \\ -1 & \text{if left-mounted} \end{cases} \tag{4.28}$$

The d_{sgn} parameter has already been mentioned in the sections above, while the Ω_{sgn} shall be first introduced in the definition of the rotor rotating frames described in the model reference frames section included at the end of this chapter.

4.6. Summary of Critical Assumptions and Simplifications

Before formally defining all of the reference frames, however, a summary of the most critical assumptions and simplifications applied throughout the 6DoF model derivation is presented first, listed in order of highest to lowest adverse-impact on the validity of the flight mechanics model as presented below. Future model revisions should attempt to remove the assumptions that affect the validity most severely first. Note that the flight mechanics model at hand aims at achieving accuracy in the domain of piloted and performance flight simulation. For this reason several assumptions (such as structural rigidity) are not considered critical nor of a high validity impact since they are not considered significant for piloted or performance flight simulation. Assumptions and simplifications are labeled with the following aspects which are believed to classify them as critical: serious violation of validity **V**; high influence on piloted flight fidelity **F**; and high impact on performance accuracy **A**. Where relevant, the source mentioning an impact of an assumption is provided next to the appropriate aspect of that assumption as well. The results of this thesis already verify some of the expected impacts, therefore in some cases the results section of this thesis is referenced. A complete list of all assumptions and simplifications applied to the 6DoF tilt-rotor model is provided in appendix B.

- **V[section 8.1.2] A** It is assumed that the tangential blade element velocity is much greater than its perpendicular counterpart.
- **V[section 8.1.2] A** The small angle approximation is used with the blade inflow angle.
- **V FA[5]** The rotor and wing ground effects are not modeled.
- **V F[5]** The mutual wake effect of the two rotors in proximity is neglected. In combination with ground effect the tilt-rotor may become very unstable near the ground, greatly affecting the handling quality.
- **F[5]** Due to the setup of the rotor wake calculation and the relative position of the horizontal stabilizer mean aerodynamic chord aerodynamic center the rotor wash is assumed to not affect the horizontal stabilizer.
- **F[29]** The main wing induced angle of attack at the horizontal tail is assumed to be zero. It is possible to specify a non-zero induced angle of attack however in the 6DoF model.
- **A[23][26]** The rotor-induced velocity is assumed to be uniform across the rotor disk and only consists of a single steady velocity component perpendicular to the disk plane.
- **F[27][5] A[23][26]** The quasi-static method is used to solve the flapping equation yielding only a steady-state solution in the form of a coning angle and disk tilt angles. The lack of any flapping dynamics results in a lack of stick input delay which is considered significant in piloted flight simulation.
- **A** The blade is assumed to only rotate around the shaft, feathering, and flapping axes. Lead/lag motion is not modeled.
- **A[26]** Mach effects on aerodynamic coefficients are not taken into account.
- **FA[23]** The flow reversal region is not taken into account.

- **A[23][5]** The tip loss factor is not taken into account.
- **A F** The fuselage is assumed to only produce drag and no lift or aerodynamic pitching moment.

4.7. Model Reference Frames

This model description chapter is concluded with the identification and definition of all of the 6DoF model reference frames used throughout the model derivation process which is treated in the next chapter. The model reference frames formally define the position vectors (i.e. the dispositions) and orientations of the model components relative to the body as well as the orientation of the reference frame axes which are oftentimes used to indicate the direction of action of model variables. Note that all reference frames are defined as right-handed orthogonal three-axes coordinate systems for the sake of consistency. As a reminder, the constant parameters used in the definition of the 6DoF model XV-15 implementation reference frames presented in this thesis work are provided in appendix A.

This section first presents the general aircraft reference frames, then treats the rotor-related reference frames, and concludes with the lifting surface reference frames.

Non-Rotating Flat Earth-Fixed Reference Frame $\{\boldsymbol{E}_C\}$

For simplicity purposes, the inertial frame of reference for this model is taken to be that of a non-rotating flat earth. Considering the applied simplifications and resulting inaccuracies of the presented model, neglecting the rotation and curvature of the Earth is thought to be permissible. The non-rotating flat Earth-fixed reference frame is defined by the Z_C-axis which points downwards, i.e. in the same direction as the gravitational acceleration vector, and the X_C and Y_C axes which are perpendicular to the Z_C-axis and each other. Coordinates within this reference frame are identified by being dot-multiplied with the column of unit vectors $\{\boldsymbol{E}_C\} = \begin{pmatrix} \boldsymbol{i}_c & \boldsymbol{j}_c & \boldsymbol{k}_c \end{pmatrix}^T$, where $\boldsymbol{i}_c$, $\boldsymbol{i}_c$, and $\boldsymbol{k}_c$ are aligned with the X_C, Y_C, and Z_C axes respectively. From this point on, any reference frame will be identified with its short notation for the column of units vectors, e.g. $\{\boldsymbol{E}_C\}$.
$\{\boldsymbol{E}_C\}$ is considered to be an inertial frame of reference.

Vehicle-Carried Normal-To-Earth Reference Frame $\{\boldsymbol{E}_E\}$

The vehicle-carried normal-to-Earth reference frame is defined by the X_E, Y_E, and Z_E axes which are parallel with and point in the same direction as the X_C, Y_C, and Z_C axes respectively, however the origin of $\{\boldsymbol{E}_E\}$ coincides with the CoG of the tilt-rotor. Therefore there is only a translational offset between $\{\boldsymbol{E}_E\}$ and $\{\boldsymbol{E}_C\}$ defined by the tilt-rotor CoG coordinates vector $\begin{pmatrix} x_{cg} & y_{cg} & z_{cg} \end{pmatrix}\{\boldsymbol{E}_C\}$.

Body Reference Frame $\{\boldsymbol{E}_b\}$

The body reference frame is fixed to the tilt-rotor airframe with its origin also located at the CoG of the aircraft and consists of the X_b, Y_b, and Z_b axes. The X_b-axis points in the direction of the nose along the plane of symmetry of the airframe, and is parallel with the ground when the empty-weight aircraft is standing on a flat horizontal surface. The Z_b-axis is perpendicular to the X_b-axis and points downwards along the same plane of symmetry towards the landing gear. The Y_b-axis points in the direction of the right wing (as viewed from the back) completing the orthogonal right-handed coordinate system. The orientation of these axes with respect to the tilt-rotor airframe have already been graphically shown in fig. 4.4.

The complete transformation from the $\{\boldsymbol{E}_E\}$ frame to the $\{\boldsymbol{E}_b\}$ is achieved through two intermediate rotational transformations. Henceforth, all rotations are defined positive according to the right-hand-rule unless stated otherwise. The first transformation is given by eq. (4.29) and involves the rotation of $\{\boldsymbol{E}_E\}$ around the Z_E-axis with the yaw angle ψ_b into the first intermediate reference frame $\{\boldsymbol{E}_{b'}\}$. The second transformation is given by eq. (4.30) and involves the rotation of $\{\boldsymbol{E}_{b'}\}$ around the $Y_{b'}$-axis with the pitch angle θ_b into the second intermediate reference frame $\{\boldsymbol{E}_{b''}\}$. The final transformation is given by eq. (4.31) and involves the rotation of $\{\boldsymbol{E}_{b''}\}$ around the $X_{b''}$-axis with the roll angle ϕ_b into the body reference frame $\{\boldsymbol{E}_b\}$. The complete transformation from the $\{\boldsymbol{E}_E\}$ frame to the $\{\boldsymbol{E}_b\}$ frame is given by eq. (4.32). Note that here the sine and cosine trigonometric functions have been abbreviated with S and C respectively, with the subscripts indicating the functions' argument. This shorthand notation will be used throughout the rest of this report where necessary.

In summary, a positive yaw, pitch, and roll angle results in a nose-right, nose-up, and right-wing-tip-down rotation respectively.

$$\{\boldsymbol{E}_E\} = \boldsymbol{T}_{E|b'}\{\boldsymbol{E}_{b'}\} = \begin{bmatrix} cos(\psi_b) & -sin(\psi_b) & 0 \\ sin(\psi_b) & cos(\psi_b) & 0 \\ 0 & 0 & 1 \end{bmatrix}\{\boldsymbol{E}_{b'}\} \tag{4.29}$$

$$\{\boldsymbol{E}_{b'}\} = \boldsymbol{T}_{b'|b''}\{\boldsymbol{E}_{b''}\} = \begin{bmatrix} cos(\theta_b) & 0 & sin(\theta_b) \\ 0 & 1 & 0 \\ -sin(\theta_b) & 0 & cos(\theta_b) \end{bmatrix}\{\boldsymbol{E}_{b''}\} \tag{4.30}$$

$$\{\boldsymbol{E}_{b''}\} = \boldsymbol{T}_{b''|b}\{\boldsymbol{E}_b\} = \begin{bmatrix} 1 & 0 & 0 \\ 0 & cos(\phi_b) & -sin(\phi_b) \\ 0 & sin(\phi_b) & cos(\phi_b) \end{bmatrix}\{\boldsymbol{E}_b\} \tag{4.31}$$

$$\begin{aligned} \{\boldsymbol{E}_E\} &= \boldsymbol{T}_{E|b}\{\boldsymbol{E}_b\} \\ &= \boldsymbol{T}_{E|b'}\boldsymbol{T}_{b'|b''}\boldsymbol{T}_{b''|b}\{\boldsymbol{E}_b\} \\ &= \begin{bmatrix} C_{\psi b}\,C_{\theta b} & C_{\psi b}\,S_{\theta b}\,S_{\phi b} - S_{\psi b}\,C_{\phi b} & C_{\phi b}\,C_{\psi b}\,S_{\theta b} + S_{\psi b}\,S_{\phi b} \\ S_{\psi b}\,C_{\theta b} & S_{\psi b}\,S_{\theta b}\,S_{\phi b} + C_{\phi b}\,C_{\psi b} & C_{\phi b}\,S_{\psi b}\,S_{\theta b} - C_{\psi b}\,S_{\phi b} \\ -S_{\theta b} & C_{\theta b}\,S_{\phi b} & C_{\theta b}\,C_{\phi b} \end{bmatrix}\{\boldsymbol{E}_b\} \end{aligned} \tag{4.32}$$

As an example, some vector $\boldsymbol{v} = \begin{pmatrix} v_x & v_y & v_z \end{pmatrix}$ defined in the $\{\boldsymbol{E}_E\}$ reference frame may be defined in the body reference frame $\{\boldsymbol{E}_b\}$ with the use of the transformation matrix $\boldsymbol{T}_{E|b}$ as shown in eq. (4.33). Note that the transpose of the final vector defined in the body reference frame is shown for improved readability.

$$\begin{aligned} \begin{pmatrix} v_x & v_y & v_z \end{pmatrix}\{\boldsymbol{E}_E\} &= \begin{pmatrix} v_x & v_y & v_z \end{pmatrix}\boldsymbol{T}_{E|b}\{\boldsymbol{E}_b\} \\ &= \begin{pmatrix} v_x\,C_{\psi b}\,C_{\theta b} + v_y\,C_{\theta b}\,S_{\psi b} - v_z\,S_{\theta b} \\ v_x\,C_{\psi b}\,S_{\theta b}\,S_{\phi b} + v_y\,S_{\psi b}\,S_{\theta b}\,S_{\phi b} - v_x\,C_{\phi b}\,S_{\psi b} + v_y\,C_{\phi b}\,C_{\psi b} + v_z\,C_{\theta b}\,S_{\phi b} \\ v_x\,C_{\phi b}\,C_{\psi b}\,S_{\theta b} + v_y\,C_{\phi b}\,S_{\psi b}\,S_{\theta b} + v_x\,S_{\psi b}\,S_{\phi b} - v_y\,C_{\psi b}\,S_{\phi b} + v_z\,C_{\phi b}\,C_{\theta b} \end{pmatrix}^T\{\boldsymbol{E}_b\} \end{aligned} \tag{4.33}$$

At this point it is most appropriate to mention that the tilt-rotor is assumed to be symmetrical in the X_b-Z_b plane.

Nacelle Pivot Reference Frame $\{\boldsymbol{E}_{np}\}$

The nacelle pivot reference frame is chosen to coincide with the nacelle pivot point located at the tip of each wing. Since there are two nacelles, one on each wing half, a distinction is made with the help of the d_{sgn} parameter which influences the lateral offset direction. Each $\{\boldsymbol{E}_{np}\}$ frame is defined by the X_{np}, Y_{np}, and Z_{np} axes which are parallel with and point in the same direction as the X_b, Y_b, and Z_b axes respectively. Therefore both reference frames have the same orientation and no rotational transformation is required going from the body reference frame to the $\{\boldsymbol{E}_{np}\}$ frame. The translational offset between $\{\boldsymbol{E}_{np}\}$ and $\{\boldsymbol{E}_b\}$ is defined by the vector $\boldsymbol{s}_{nO|b} = \begin{pmatrix} -d_{xn} & d_{sgn}d_{yn} & -d_{zn} \end{pmatrix}\{\boldsymbol{E}_b\}$. A schematic side view of the $\{\boldsymbol{E}_{np}\}$ reference frame with respect to the body is shown in fig. 4.5.

Nacelle Reference Frame $\{\boldsymbol{E}_n\}$

Again, two separate reference frames are defined for the two nacelles, however since the 6DoF model at hand does not take into account independent nacelle-tilt motion, both nacelle rotations may be described with one rotational transformation matrix. Each nacelle reference frame is fixed to the tiltable nacelle structure and is defined by the X_n, Y_n, and Z_n axes. Their origin is located at the nacelle pivot point and therefore coincides with the origin of the appropriate $\{\boldsymbol{E}_{np}\}$ frame. When in helicopter mode, the nacelle tilt angle

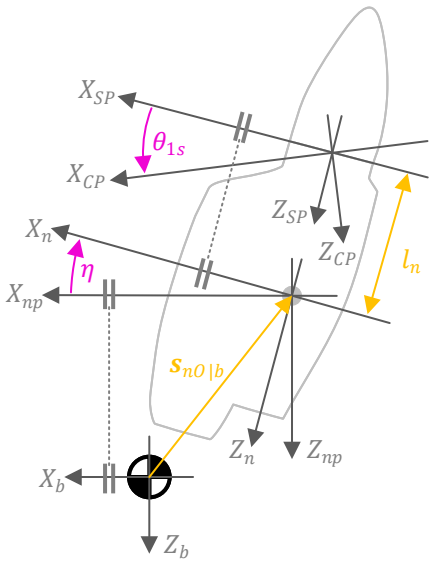

Figure 4.5: Schematic side view of a tilted nacelle and rotor hub with respect to the body CoG. Positive conventions of the nacelle tilt and control plane tilt angles are also shown.

η is 0°, and the nacelles' X_n, Y_n, and Z_n axes point in the same direction as the body X_b, Y_b, and Z_b axes respectively for both the left and right nacelle. The nacelle rotates around the Y_{np}-axis, defined positive according to the right-hand rule meaning that tilting the nacelle forwards corresponds with a negative tilt angle. Ultimately, airplane mode is achieved when $\eta = -90°$, the X_n-axes point in the direction of the body Z_b-axis, and the Z_n-axes point in the negative direction of the body X_b-axis. Again, the left and right nacelle reference frame have the same axis orientation. The rotational transformation matrix from $\{\boldsymbol{E}_b\}$ to $\{\boldsymbol{E}_n\}$ is given by eq. (4.34). A schematic side view of a tilted nacelle reference frame with respect to the body is shown in fig. 4.5, while the helicopter and airplane nacelle configurations have already been shown in fig. 4.4.

$$\{\boldsymbol{E}_{np}\} = \boldsymbol{T}_{np|n}\{\boldsymbol{E}_n\} = \begin{bmatrix} \cos(\eta) & 0 & \sin(\eta) \\ 0 & 1 & 0 \\ -\sin(\eta) & 0 & \cos(\eta) \end{bmatrix} \{\boldsymbol{E}_n\} \tag{4.34}$$

Shaft Plane Reference Frame $\{\boldsymbol{E}_{SP}\}$

The SP represents the plane that is perpendicular to the shaft and located at the hub of the rotor. It is assumed that the rotor shaft coincides with the nacelle Z_n-axis and tilts with the nacelle structure. The shaft plane reference frame is defined by the X_{SP}, Y_{SP}, and Z_{SP} axes which are parallel with and point in the same direction as the nacelle X_n, Y_n, and Z_n axes. Although there are two separate rotors, and thus two shaft planes may be defined, the orientation of the axes remains identical for both the left and right rotor. Moving forward, all following rotor-related reference frames will have an identical orientation for both the left and right rotor by default. The X_{SP}-Y_{SP} plane corresponds to the shaft plane. The origin of the shaft plane reference frame is located at the end of the nacelle mast, also referred to as the rotor hub. The translational offset between the $\{\boldsymbol{E}_n\}$ frame and $\{\boldsymbol{E}_{SP}\}$ frame is defined by the vector $\boldsymbol{s}_{\widehat{RO}|n} = \begin{pmatrix} 0 & 0 & -l_n \end{pmatrix}\{\boldsymbol{E}_n\}$. A schematic side view of the shaft plane and rotor hub with respect to the nacelle is shown in fig. 4.5.

Control Plane Reference Frame $\{\boldsymbol{E}_{CP}\}$

The CP is defined to be parallel to the swashplate of the rotor assembly and located at the hub of the rotor. The control plane reference frame is defined by the X_{CP}, Y_{CP}, and Z_{CP} axes with its origin coinciding with the origin of the shaft plane reference frame. The X_{CP}-Y_{CP} plane corresponds to the control plane. $\{\boldsymbol{E}_{CP}\}$ rotates around the Y_{SP}-axis with a negative longitudinal cyclic angle $-\theta_{1s}$ rad with respect to the shaft plane. The rotation is defined positive according to the right-hand rule therefore a positive longitudinal cyclic results in a downward motion of the fore section of the control plane as shown in fig. 4.5. When $\theta_{1s} = 0$ rad, the control plane coincides with the shaft plane. The tilt-rotor achieves lateral motion through differential

collective instead of lateral cyclic, therefore a lateral cyclic rotational transformation is not required. The rotational transformation matrix from $\{\boldsymbol{E}_{SP}\}$ to $\{\boldsymbol{E}_{CP}\}$ is given by eq. (4.35).

$$\{\boldsymbol{E}_{SP}\} = \boldsymbol{T}_{SP|CP}\{\boldsymbol{E}_{CP}\} = \begin{bmatrix} \cos(-\theta_{1s}) & 0 & \sin(-\theta_{1s}) \\ 0 & 1 & 0 \\ -\sin(-\theta_{1s}) & 0 & \cos(-\theta_{1s}) \end{bmatrix} \{\boldsymbol{E}_{CP}\} \tag{4.35}$$

Wind Axis Control Plane Reference Frame $\{\boldsymbol{E}_{\widehat{CP}}\}$

As shall be demonstrated later, the velocity and acceleration experienced by the rotor blades, as well as the forces and moments generated by them, must be defined with respect to a single common reference frame in order to be able to carry out the derivation in a clear and structured manner. The rotor model is then said to be derived in that reference frame. During the preliminary phase of this research, the rotor equations of the 3-DoF tilt-rotor model have been derived in the control plane reference frame described above, therefore the rotor equations of this 6-DoF tilt-rotor model could also be derived in the same frame for sake of consistency. It must be remembered, however, that the latter model may experience velocities in three-dimensional space, including lateral components which were not present in the 3-DoF model. It would therefore be convenient to be able to somehow remove the lateral component from the equations in order to obtain a 6-DoF model that has as much overlap with the 3-DoF model as possible making the 6-DoF derivation process more familiar and thus easier. One approach of doing so is to rotate the control plane reference frame around the Z_{CP}-axis such that its longitudinal axis X_{CP} is always aligned with the air velocity vector (projected onto the control plane). As a result the lateral velocity component would inherently always be zero, and all the rotor equations derived in this rotated control plane would be identical to the ones of a rotor that only experienced longitudinal motion, as was the case of the 3-DoF model rotor.

A reference frame that is rotated to be aligned with the velocity vector may be referred to as a wind axis reference frame, and in the case of the control plane, the resulting rotated frame may be referred to as the wind axis control plane reference frame. Due to the compelling convenience and ease of implementation of the wind axis approach it has been decided that the 6-DoF rotor model shall be derived in the wind axis control plane reference frame $\{\boldsymbol{E}_{\widehat{CP}}\}$. Note that the wind axis reference frame is distinguished from its non-wind-axis counterpart by a caret symbol ($\widehat{\ }$), and all future variables defined in the wind axis will also be indicated likewise.

The angle by which the control plane must be rotated is called the wind axis shift Δ and it is defined to be measured between the longitudinal air velocity vector V_{tc1} acting along the X_{CP}-axis and the total in-plane air velocity vector $\widehat{V}_{tc}$ projected onto the CP. Since the longitudinal axis of the wind axis control plane is rotated to be aligned with the total air velocity vector, $\widehat{V}_{tc}$ must act along the $X_{\widehat{CP}}$-axis. This is also the reason why a caret is placed atop this velocity vector. The formal definition of these velocity vectors is given by eqs. (5.19) and (5.21) in the model development chapter. A schematic depiction of the relationship between these velocity vectors, reference frame axes, and the wind shift angle is shown in fig. 4.6. The subscripts L and R refer to the left (clockwise rotating) and right (counter-clockwise rotating) rotors respectively.

The wind shift angle Δ is defined to be positive cw when looking from above the rotor for both cw and ccw rotating rotors, and may be obtained with eq. (4.36) where V_{tc2} is the air velocity vector acting along the Y_{CP}-axis (defined later in eq. (5.15)). A comparison between the wind axis control planes of a cw and ccw rotor is also shown in fig. 4.6. Note that all forces and moments derived in the wind axis control plane will also have to be transformed back into the non-wind-axis control plane with the same angle Δ in order for them to be ultimately incorporated in the force and moment vectors influencing the body motion of the tilt-rotor.

$$\Delta = \arctan\left(\frac{V_{tc2}}{V_{tc1}}\right) \tag{4.36}$$

In this wind-axis-shifted reference frame the blade azimuth angle ψ must be redefined such that the blade aligns with the negative wind axis control plane $X_{\widehat{CP}}$-axis when the wind axis blade azimuthal position $\widehat{\psi}$ is equal to zero. The relation between the nominal and the wind axis blade azimuth angle is given by eq. (4.37). Since the direction of rotor rotation has an effect on this relation, an Omega-sign-change parameter must

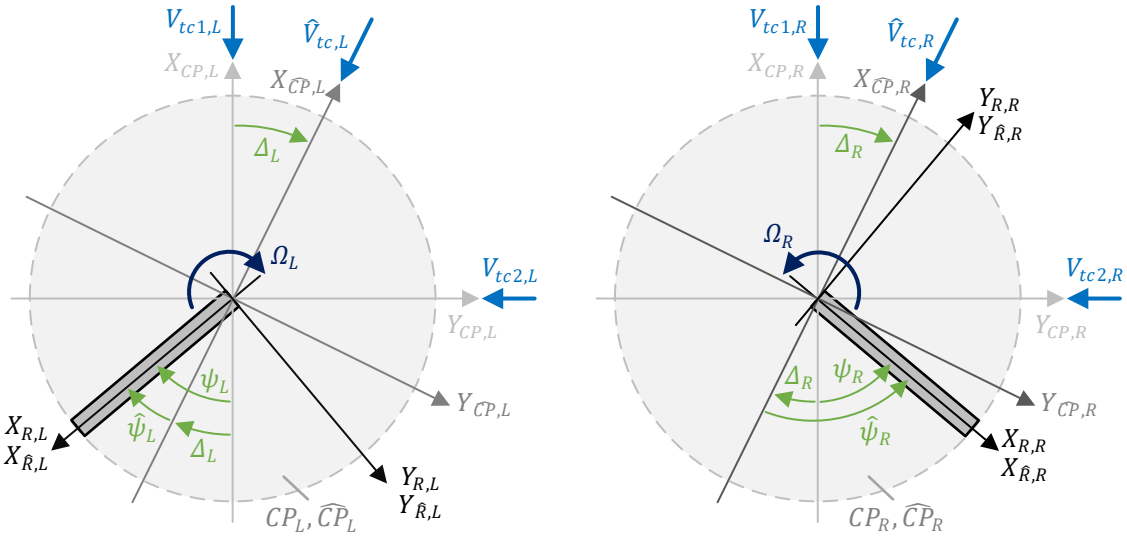

Figure 4.6: Schematic depiction of the wind axis control plane of a clockwise (left, L) and counterclockwise (right, R) rotating rotor with respect to the non-wind-axis control plane. Wind axis and non-wind-axis rotating frame axes also shown together with a schematic depiction of a single blade represented by the shaded rectangle. Velocity vectors indicate the direction of air flow.

be included. The relationship between ψ, $\widehat{\psi}$, and Δ is also presented graphically in fig. 4.6 for both a cw and ccw rotor where the X- and Y-axes with the subscripts R and $\widehat{R}$ correspond to the rotating and wind axis rotating frames (which share the same axes). The wind axis rotating frame shall be defined later, therefore at this point it must only be noted that the X-axes of both of these rotating frames are aligned with- and rotate together with- the rotor blade. To clarify, the non-wind-axis ψ is measured between the non-wind-axis control plane X_{CP}-axis and the blade (i.e. the X_R-axis), while the wind axis $\widehat{\psi}$ is measured between the wind shifted control plane $X_{\widehat{CP}}$-axis and the blade (i.e. the $X_{\widehat{R}}$-axis which coincides with the X_R-axis).

$$\psi = \widehat{\psi} - \Omega_{sgn}\Delta \tag{4.37}$$

By definition, the wind axis control plane is coplanar with the control plane with its axes only rotated around the Z_{CP}-axis with the wind shift angle Δ. The reference frame itself is defined by the $X_{\widehat{CP}}$, $Y_{\widehat{CP}}$, and $Z_{\widehat{CP}}$ axes with its origin coinciding with the origin of the control plane reference frame. The resulting wind shift rotational transformation from the $\{\boldsymbol{E}_{CP}\}$ frame to the $\{\boldsymbol{E}_{\widehat{CP}}\}$ frame is given by eq. (4.38). All wind and non-wind control plane axes of a cw and ccw rotating rotor are also shown in fig. 4.6.

$$\{\boldsymbol{E}_{CP}\} = \boldsymbol{T}_{CP|\widehat{CP}}\{\boldsymbol{E}_{\widehat{CP}}\} = \begin{bmatrix} cos(\Delta) & -sin(\Delta) & 0 \\ sin(\Delta) & cos(\Delta) & 0 \\ 0 & 0 & 1 \end{bmatrix} \{\boldsymbol{E}_{\widehat{CP}}\} \tag{4.38}$$

Wind Axis Disk Plane Reference Frame $\{\boldsymbol{E}_{\widehat{DP}}\}$

The wind axis DP is parallel to the plane formed by the tips of the rotating blades (i.e. the tip path plane described next) with its origin coincident with the rotor hub. The disk plane reference frame is defined by the $X_{\widehat{DP}}$, $Y_{\widehat{DP}}$, and $Z_{\widehat{DP}}$ axes which are parallel with the $X_{\widehat{CP}}$, $Y_{\widehat{CP}}$, and $Z_{\widehat{CP}}$ axes respectively in the nominal state of the DP. The origin of $\{\boldsymbol{E}_{\widehat{DP}}\}$ coincides with the origin of $\{\boldsymbol{E}_{\widehat{CP}}\}$.

The DP may rotate both longitudinally and laterally reflecting the possible tilting motion of the rotor disk. Therefore the complete transformation from the $\{\boldsymbol{E}_{\widehat{CP}}\}$ frame to the $\{\boldsymbol{E}_{\widehat{DP}}\}$ frame is achieved with the use of one intermediate rotational transformation. The intermediate transformation is given by eq. (4.39) and involves the rotation of $\{\boldsymbol{E}_{\widehat{CP}}\}$ around the $X_{\widehat{CP}}$-axis with the lateral disk tilt angle $\widehat{b}_1$ into the intermediate reference frame $\{\boldsymbol{E}_{\widehat{DP}'}\}$. The final transformation is given by eq. (4.40) and involves the rotation around the $Y_{\widehat{DP}'}$-axis with the longitudinal disk tilt angle $\widehat{a}_1$ into the wind axis disk plane reference frame $\{\boldsymbol{E}_{\widehat{DP}}\}$.

It must be highlighted that the orientation of the disk tilting motion is the same for a cw and ccw rotor. Also note that the longitudinal and lateral disk tilt angles are accompanied by a caret symbol since they act around the wind shifted reference frame axes. The complete transformation from the $\{\boldsymbol{E}_{\widehat{CP}}\}$ frame to the $\{\boldsymbol{E}_{\widehat{DP}}\}$ frame is given by eq. (4.41).

In summary, a positive lateral disk tilt angle results in a downward motion of the right side of the rotor disk (when viewed from the aft of the tilt-rotor), and a positive longitudinal disk tilt angle results in a downward motion of the aft of the rotor disk (disk blow-back). A graphical summary of these disk motions is shown in figs. 4.7 and 4.8 and described in the next section.

$$\{\boldsymbol{E}_{\widehat{CP}}\} = \boldsymbol{T}_{\widehat{CP}|\widehat{DP}'}\{\boldsymbol{E}_{\widehat{DP}'}\} = \begin{bmatrix} 1 & 0 & 0 \\ 0 & cos(\widehat{b}_1) & -sin(\widehat{b}_1) \\ 0 & sin(\widehat{b}_1) & cos(\widehat{b}_1) \end{bmatrix} \{\boldsymbol{E}_{\widehat{DP}'}\} \tag{4.39}$$

$$\{\boldsymbol{E}_{\widehat{DP}'}\} = \boldsymbol{T}_{\widehat{DP}'|\widehat{DP}}\{\boldsymbol{E}_{\widehat{DP}}\} = \begin{bmatrix} cos(\widehat{a}_1) & 0 & sin(\widehat{a}_1) \\ 0 & 1 & 0 \\ -sin(\widehat{a}_1) & 0 & cos(\widehat{a}_1) \end{bmatrix} \{\boldsymbol{E}_{\widehat{DP}}\} \tag{4.40}$$

$$\begin{aligned} \{\boldsymbol{E}_{\widehat{CP}}\} &= \boldsymbol{T}_{\widehat{CP}|\widehat{DP}}\{\boldsymbol{E}_{\widehat{DP}}\} \\ &= \boldsymbol{T}_{\widehat{CP}|\widehat{DP}'}\boldsymbol{T}_{\widehat{DP}'|\widehat{DP}}\{\boldsymbol{E}_{\widehat{DP}}\} \\ &= \begin{bmatrix} \cos(\widehat{a}_1) & 0 & \sin(\widehat{a}_1) \\ \sin(\widehat{b}_1)\sin(\widehat{a}_1) & \cos(\widehat{b}_1) & -\sin(\widehat{b}_1)\cos(\widehat{a}_1) \\ -\cos(\widehat{b}_1)\sin(\widehat{a}_1) & \sin(\widehat{b}_1) & \cos(\widehat{b}_1)\cos(\widehat{a}_1) \end{bmatrix} \{\boldsymbol{E}_{\widehat{DP}}\} \end{aligned} \tag{4.41}$$

Wind Axis Tip-Path-Plane Reference Frame $\{\boldsymbol{E}_{\widehat{TPP}}\}$

The wind axis tip path plane (TPP) represents the plane formed by the tips of the rotating blades. It is defined by the $X_{\widehat{TPP}}$, $Y_{\widehat{TPP}}$, and $Z_{\widehat{TPP}}$ axes which are parallel with the $X_{\widehat{DP}}$, $Y_{\widehat{DP}}$, and $Z_{\widehat{DP}}$ axes respectively at all times. For this reason no rotational transformation is required going from the wind axis disk plane to the wind axis tip path plane. The origin of $\{\boldsymbol{E}_{\widehat{TPP}}\}$ is located along the $Z_{\widehat{DP}}$-axis (typically) above the rotor hub with the height being dependent on the coning angle $\widehat{a}_0$. The translational offset between the origins of $\{\boldsymbol{E}_{\widehat{DP}}\}$ and $\{\boldsymbol{E}_{\widehat{TPP}}\}$ shall not be required in the derivation of the tilt-rotor model therefore its definition is not necessary.

A schematic view of the wind axis-control plane, -disk plane, and -tip path plane with respect to the nacelle is shown in fig. 4.7 and fig. 4.8 which provide a left-side view of the rotor-nacelle assemblies and an aft view of the left and right rotor-nacelle assemblies respectively. These figures also present the positive sign conventions of the disk tilt angles for a clockwise and counterclockwise rotor (in this case the left and right rotor respectively). In fig. 4.7 only one rotor-nacelle assembly is shown since the positive sign conventions of both the reference frames and disk tilt angles are identical for the left and right rotor.

Wind Axis Non-Rotating Reference Frame $\{E_{\widehat{NR}}\}$

The wind axis non-rotating reference frame is defined with respect to the wind axis control plane and represents the nominal position of the (later defined) rotating reference frame which has the $X-$ and $Z-$axes pointing in the opposite directions when compared to the axes of the $\{\boldsymbol{E}_{\widehat{CP}}\}$ frame. The $\{\boldsymbol{E}_{\widehat{NR}}\}$ frame itself is defined by the $X_{\widehat{NR}}$, $Y_{\widehat{NR}}$, and $Z_{\widehat{NR}}$ axes and the only rotational transformation from the wind axis control plane to the wind axis non-rotating reference frame is given by eq. (4.42). A schematic depiction of the w.a. non-rotating frame with respect to the w.a. control plane is shown in fig. 4.9.

$$\{\boldsymbol{E}_{\widehat{CP}}\} = \boldsymbol{T}_{\widehat{CP}|\widehat{NR}}\{\boldsymbol{E}_{\widehat{NR}}\} = \begin{bmatrix} cos(\pi) & 0 & sin(\pi) \\ 0 & 1 & 0 \\ -sin(\pi) & 0 & cos(\pi) \end{bmatrix} \{\boldsymbol{E}_{\widehat{NR}}\} = \begin{bmatrix} -1 & 0 & 0 \\ 0 & 1 & 0 \\ 0 & 0 & -1 \end{bmatrix} \{\boldsymbol{E}_{\widehat{NR}}\} \tag{4.42}$$

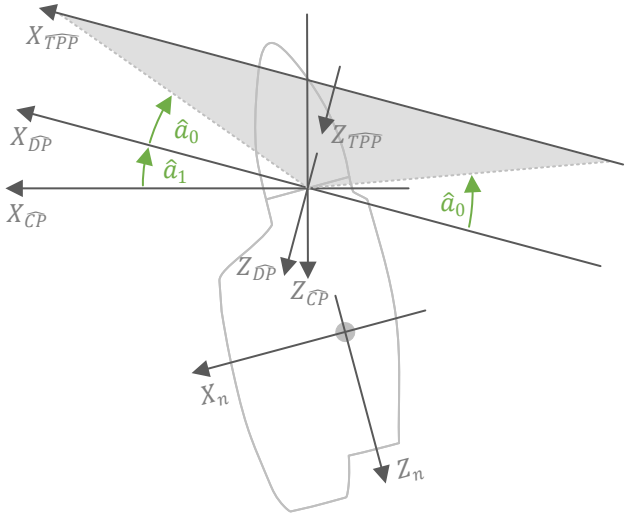

Figure 4.7: Left view of the rotor and nacelle assembly indicating the positive sign conventions of the coning and longitudinal disk tilt angles for both the left (cw.) and right (ccw.) rotor. The nacelle as well as the wind axis-control plane, -disk plane, and -tip path plane axes are also indicated.

Wind Axis Rotating Reference Frame $\{E_{\widehat{R}}\}$

The wind axis rotating reference frame is fixed to the azimuthal rotation of the rotor blade, but it does not flap, lead/lag, nor feather with the blade. It is defined by the $X_{\widehat{R}}$, $Y_{\widehat{R}}$, and $Z_{\widehat{R}}$ axes with the $X_{\widehat{R}}$-axis being aligned with the rotor blade azimuth angle. The transformation from the non-rotating to the rotating reference also requires only one rotational transformation matrix which is given by eq. (4.43) remembering that the wind shifted azimuthal angle $\widehat{\psi}$ must be used. Since the rotor rotational direction has an influence on the transformation, the Ω-sign-change parameter must be included. A schematic depiction of the w.a. rotating frame of a counter-clockwise rotating rotor with respect to the w.a. non-rotating frame is shown in fig. 4.9.

$$\{\boldsymbol{E}_{\widehat{NR}}\} = \boldsymbol{T}_{\widehat{NR}|\widehat{R}}\{\boldsymbol{E}_{\widehat{R}}\} = \begin{bmatrix} cos(\Omega_{sgn}\widehat{\psi}) & -sin(\Omega_{sgn}\widehat{\psi}) & 0 \\ sin(\Omega_{sgn}\widehat{\psi}) & cos(\Omega_{sgn}\widehat{\psi}) & 0 \\ 0 & 0 & 1 \end{bmatrix}\{\boldsymbol{E}_{\widehat{R}}\} = \begin{bmatrix} cos(\widehat{\psi}) & -\Omega_{sgn}sin(\widehat{\psi}) & 0 \\ \Omega_{sgn}sin(\widehat{\psi}) & cos(\widehat{\psi}) & 0 \\ 0 & 0 & 1 \end{bmatrix}\{\boldsymbol{E}_{\widehat{R}}\} \tag{4.43}$$

Wind Axis Blade Reference Frame $\{E_{\widehat{BL}}\}$

The wind axis blade reference frame is fixed to one of the rotor blades and, assuming there is no offset between the blade hinge point and hub, its origin is located at the rotor hub. It is very likely that the rotor assembly contains multiple blades, however it not necessary to define a separate reference frame for each blade in order to incorporate their effect in the simulation model. The blade reference frame is defined by the $X_{\widehat{BL}}$, $Y_{\widehat{BL}}$, and $Z_{\widehat{BL}}$ axes where the $X_{\widehat{BL}}$-axis points in the radial direction along the blade length, the $Y_{\widehat{BL}}$-axis coincides and points in the same direction as the $Y_{\widehat{R}}$-axis, and the $Z_{\widehat{BL}}$ is perpendicular to the $X_{\widehat{BL}}$ and $Y_{\widehat{BL}}$ axes completing the orthogonal right-handed coordinate system. It is assumed that the locus of the blade profile aerodynamic centers follow a straight line which coincides with the $X_{\widehat{BL}}$-axis.

The blade reference frame rotates together with the blade frame around the $Y_{\widehat{R}}$-axis, also referred to as the flapping axis, with the negative flapping angle $-\widehat{\beta}$ with respect to the wind axis rotating frame. Note that the flapping angle has a caret atop since it acts around a wind shifted axis. Lead/lag motion of the blade around the $Z_{\widehat{BL}}$-axis is not taken into account in this rotor model, while the cyclic feathering of the blade around the $X_{\widehat{BL}}$-axis is non-existent since the blade is defined with respect to the non-feathering control plane. The blade collective and geometric twist (also acting around the $X_{\widehat{BL}}$-axis), however, is included in the blade element reference frame described in the next section. The rotational transformation from $\{\boldsymbol{E}_{\widehat{R}}\}$ to $\{\boldsymbol{E}_{\widehat{BL}}\}$ is given by eq. (4.44).

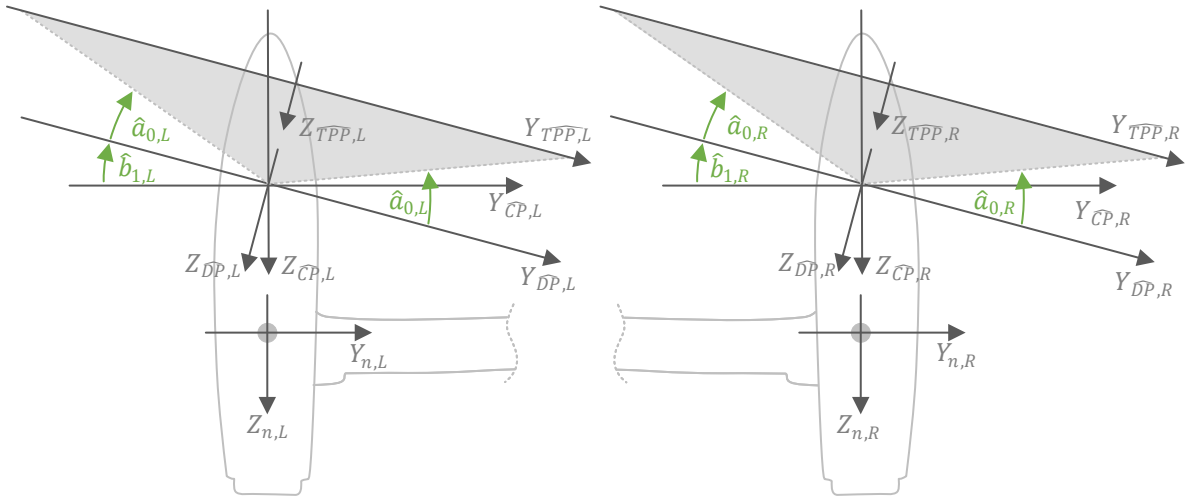

Figure 4.8: Aft view of the left (cw.) and right (ccw.) rotor and nacelle assemblies indicating the positive sign conventions of the coning and lateral disk tilt angles. The nacelle as well as the wind axis-control plane, -disk plane, and -tip path plane axes are also indicated.

$$\{\boldsymbol{E}_{\widehat{R}}\} = \boldsymbol{T}_{\widehat{R}|\widehat{BL}}\{\boldsymbol{E}_{\widehat{BL}}\} = \begin{bmatrix} \cos\left(-\widehat{\beta}\right) & 0 & \sin\left(-\widehat{\beta}\right) \\ 0 & 1 & 0 \\ -\sin\left(-\widehat{\beta}\right) & 0 & \cos\left(-\widehat{\beta}\right) \end{bmatrix} \{\boldsymbol{E}_{\widehat{BL}}\} = \begin{bmatrix} \cos\left(\widehat{\beta}\right) & 0 & -\sin\left(\widehat{\beta}\right) \\ 0 & 1 & 0 \\ \sin\left(\widehat{\beta}\right) & 0 & \cos\left(\widehat{\beta}\right) \end{bmatrix} \{\boldsymbol{E}_{\widehat{BL}}\} \quad (4.44)$$

Since the derivation of the rotor forces and moments will be performed in the wind axis control plane it is useful to show the w.a. blade reference frame in relation to the w.a.CP and the w.a. rotating frame as depicted in fig. 4.9 in three dimensions. In the figure the wind axis control plane is shown as a gray circular disk while the blade is represented with a dark shaded rectangle.

Blade Element Reference Frame $\{\boldsymbol{E}_{BE}\}$

The blade element reference frame is fixed to a cross-section of the blade located at a radial distance r_{BE} away from the rotor hub along the blade $X_{\widehat{BL}}$-axis. The cross-section of the blade corresponds to the airfoil of the blade at that radial position, and the blade element reference frame rotates around the $X_{\widehat{BL}}$-axis together with the airfoil according to the local geometric pitch of the blade θ_{BE} (which comprises the collective pitch and blade twist as defined by eq. (4.1)). The origin of $\{\boldsymbol{E}_{BE}\}$ is located at the aerodynamic center of the airfoil, hence it is assumed that the rotor blade pitches around the $X_{\widehat{BL}}$-axis.

The blade element reference frame is defined by the X_{BE}, Y_{BE}, and Z_{BE} axes where the X_{BE}-axis coincides and points in the same direction as the $X_{\widehat{BL}}$-axis, the Y_{BE}-axis is parallel to the blade chord and points in the direction of the leading edge of the blade on a ccw rotating rotor (while in the case of a cw rotor it points in the direction of the trailing edge), and the $Z_{\widehat{BL}}$ is perpendicular to the $X_{\widehat{BL}}$ and $Y_{\widehat{BL}}$ axes completing the orthogonal right-handed coordinate system.

As already mentioned, the blade element reference frame rotates around the $X_{\widehat{BL}}$-axis with the local geometric pitch of the blade. Since the reference frame orientation is identical for a cw. and ccw. rotating rotor, the direction of the pitch, i.e. the direction of rotation around the $X_{\widehat{BL}}$-axis, changes depending on the direction of rotation of the rotor. Therefore the blade element frame is rotated around the $X_{\widehat{BL}}$-axis with the angle $\Omega_{sgn}\theta_{BE}$ with the Ω_{sgn} parameter taking care of the direction of the blade pitch rotation. The resulting rotational transformation from $\{\boldsymbol{E}_{\widehat{BL}}\}$ to $\{\boldsymbol{E}_{BE}\}$ is given by eq. (4.45). The translational offset between the origins of $\{\boldsymbol{E}_{\widehat{BL}}\}$ and $\{\boldsymbol{E}_{BE}\}$ is defined by the vector $\boldsymbol{s}_{BE|\widehat{BL}} = \begin{pmatrix} r_{BE} & 0 & 0 \end{pmatrix}\{\boldsymbol{E}_{\widehat{BL}}\}$.

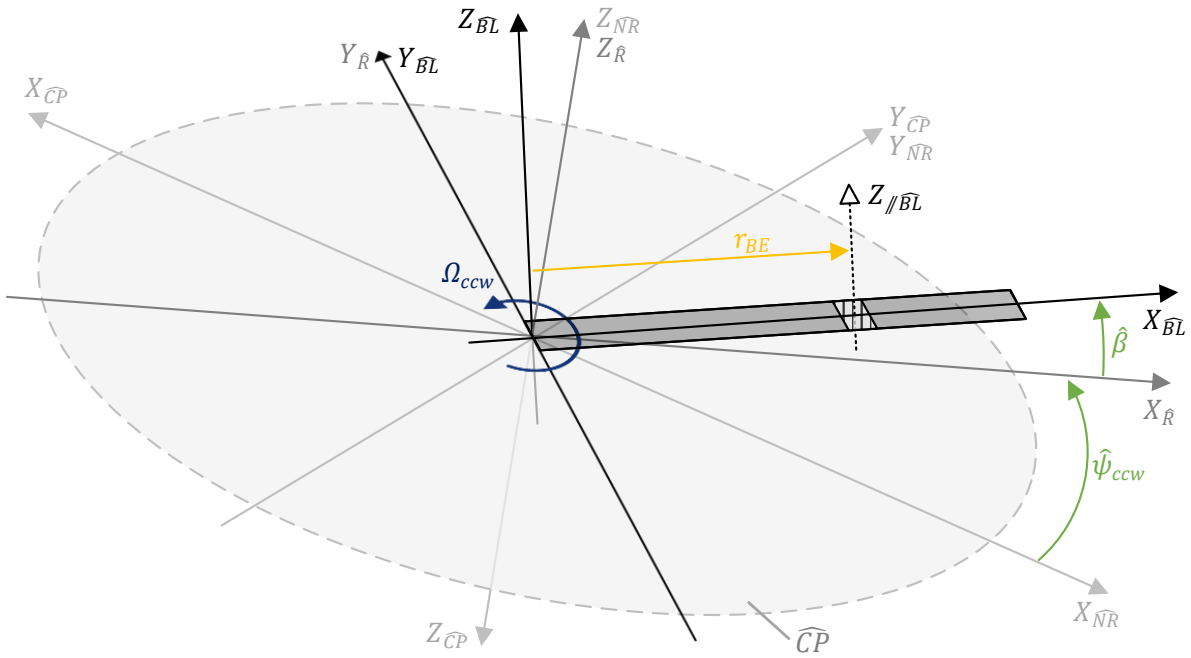

Figure 4.9: Depiction of the wind axis non-rotating, rotating, and blade reference frames of a ccw rotor with respect to the wind axis control plane reference frame. A single blade is shown, represented by the shaded rectangle. A blade element is also shown, represented by the striped box.

$$\begin{aligned}\{\boldsymbol{E}_{\widehat{BL}}\} = \boldsymbol{T}_{\widehat{BL}|\widehat{BE}}\{\boldsymbol{E}_{BE}\} &= \begin{bmatrix} 1 & 0 & 0 \\ 0 & cos(\Omega_{sgn}\theta_{BE}) & -sin(\Omega_{sgn}\theta_{BE}) \\ 0 & sin(\Omega_{sgn}\theta_{BE}) & cos(\Omega_{sgn}\theta_{BE}) \end{bmatrix}\{\boldsymbol{E}_{\widehat{BL}}\} \\ &= \begin{bmatrix} 1 & 0 & 0 \\ 0 & cos(\theta_{BE}) & -\Omega_{sgn}sin(\theta_{BE}) \\ 0 & \Omega_{sgn}sin(\theta_{BE}) & cos(\theta_{BE}) \end{bmatrix}\{\boldsymbol{E}_{\widehat{BL}}\}\end{aligned} \tag{4.45}$$

A three-dimensional depiction of the disposition of the blade element with respect to the wind axis blade reference frame has already been shown in fig. 4.9, while a two-dimensional view in-plane with the blade element airfoil showing the local geometric pitch of the blade element reference frame with respect to the wind axis blade frame of reference for both a clockwise (left) and counterclockwise (right) rotating rotor is shown in fig. 4.10.

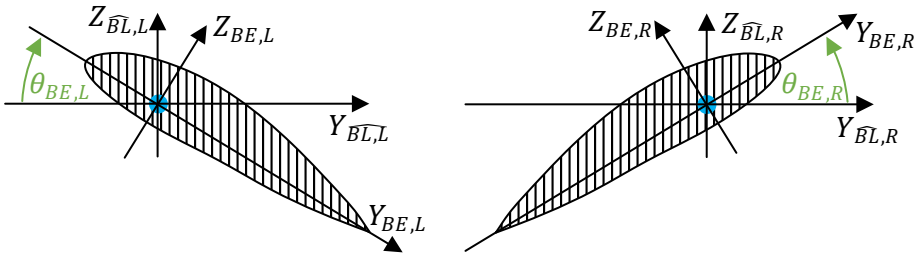

Figure 4.10: Schematic representation of a clockwise (left, L) and counterclockwise (right,R) blade element reference frame with respect to the the wind axis blade reference frame. Airfoil aerodynamic center indicated with blue dot.

Lifting Surface Root Aerodynamic Center Reference Frame $\{\boldsymbol{E}_{lsAC}\}$

Having defined all reference frames related to the rotor, the reference frames corresponding to the remaining subsystems must be defined, starting with the root of the lifting surfaces. As already mentioned in the

section treating the model components, the 6DoF tilt-rotor model consists of several instances of the generic lifting surface component which represent the main wing segments, as well as the tail stabilizers. As a result it is possible to describe a set of generic reference frames which may correspond to any desirable lifting surface instance given that the appropriate parameters are supplied. In this model only two generic reference frames are required to describe any lifting surface, the first being the lifting surface (ls) root aerodynamic center (AC) reference frame $\{\boldsymbol{E}_{lsAC}\}$ which specifies the position of the lifting surface with respect to the body, and the second being the lifting surface reference frame $\{\boldsymbol{E}_{ls}\}$ which defines the orientation of the lifting surface with respect to the body. In both cases the subscript ls may be replaced by the name or abbreviation of the desired lifting surface. A summary of the abbreviations used to reference to all the lifting surfaces of the 6DoF model implementation presented in this thesis work is shown in table 4.5. Note that a distinction between the left and right lifting surfaces is achieved by adding $,L$ or $,R$ to the subscripts which is not shown in the table.

Starting with the lifting surface root aerodynamic center reference frame $\{\boldsymbol{E}_{lsAC}\}$ whose origin is chosen to coincide with the aerodynamic center of the lifting surface root. Each $\{\boldsymbol{E}_{lsAC}\}$ frame is defined by the X_{lsaAC}-, Y_{lsAC}-, and Z_{lsAC}-axes which are parallel with and point in the same direction as the X_b, Y_b, and Z_b axes respectively (for both left and right mounted lifting surfaces). Therefore both reference frames have the same orientation and no rotational transformation is required going from the body reference frame to the $\{\boldsymbol{E}_{lsAC}\}$ frame.

The translational offset of the $\{\boldsymbol{E}_{lsAC}\}$ frame of each lifting surface from the body $\{\boldsymbol{E}_b\}$ frame origin (i.e. the body CoG) is defined by the generic position vector $\boldsymbol{s}_{lsrAC|b}$ where the subscript $lsrAC$ refers to the lifting surface (ls) root aerodynamic center (rAC). The position vector may be decomposed into three orthogonal components, namely d_{xls}, d_{yls}, and d_{zls}, which specify the translation magnitude along each of the body reference frame axes. The position vector symbol and the variables that represent its orthogonal components corresponding to each lifting surface of the 6DoF model implementation is summarized in table 4.5. Note that some variables are preceded by a minus sign meaning that their positive value indicates a translation in the opposite direction than the pointing direction of the appropriate body axis. Once again a distinction between the left and right lifting surface position vectors and variables is achieved by adding $,L$ or $,R$ to the subscripts which is not shown in the table. Furthermore the d_{sgn} parameter must be used in the case of the lateral translation components (i.e. d_{yls}) in order to indicate whether the lifting surface is mounted on the left or right side of the tilt-rotor.

Table 4.5: List of the 6DoF tilt-rotor model lifting surface names and subscript abbreviations, as well as root profile aerodynamic center position vectors defined in the body reference frame and the positive conventions of their X, Y, and Z component variables.

		Root AC Position Vector			
Lifting Surface	**Abbreviation**	**Symbol**	**X**	**Y**	**Z**
free wing	frw	$\boldsymbol{s_{frwrAC\|b}}$	$(d_{xfrw}$	$d_{sgn}d_{yfrw}$	$-d_{zfrw})$
flap wing	flw	$\boldsymbol{s_{flwrAC\|b}}$	$(d_{xflw}$	$d_{sgn}d_{yflw}$	$-d_{zflw})$
aileron wing	aw	$\boldsymbol{s_{awrAC\|b}}$	$(d_{xaw}$	$d_{sgn}d_{yaw}$	$-d_{zaw})$
horizontal stabilizer	hs	$\boldsymbol{s_{hsrAC\|b}}$	$(-d_{xh}$	$d_{sgn}d_{yh}$	$-d_{zh})$
top vertical stabilizer	vst	$\boldsymbol{s_{vstrAC\|b}}$	$(-d_{xvt}$	$d_{sgn}d_{yvt}$	$-d_{zvt})$
bot. vertical stabilizer	vsb	$\boldsymbol{s_{vsbrAC\|b}}$	$(-d_{xvb}$	$d_{sgn}d_{yvb}$	$-d_{zvb})$

Lifting Surface Reference Frame $\{\boldsymbol{E}_{ls}\}$

The generic lifting surface reference frame, on the other hand, is defined by the X_{ls}, Y_{ls}, and Z_{ls} axes. The origin of $\{\boldsymbol{E}_{ls}\}$ coincides with the origin of $\{\boldsymbol{E}_{lsAC}\}$. The X_{ls}-axis is defined to be parallel with the lifting surface root chord line and points in the direction of the leading edge of the lifting surface. The Y_{ls}-axis is defined to be perpendicular to the X_{ls}-axis, points to the right (for both left and right mounted lifting surfaces) when viewing the lifting surface from behind (looking at the trailing edge), and intersects the (possibly extended) lifting surface tip chord line. Finally the Z_{ls}-axis points in the downward direction completing the orthogonal right-handed system.

The complete transformation from the $\{\boldsymbol{E}_{lsAC}\}$ frame to the $\{\boldsymbol{E}_{ls}\}$ frame is achieved with the use of one intermediate rotational transformation. The intermediate transformation is given by eq. (4.46) and involves the rotation of $\{\boldsymbol{E}_{lsAC}\}$ around the Y_{lsAC}-axis with the lifting surface incidence angle i_{ls} into the intermediate reference frame $\{\boldsymbol{E}_{ls'}\}$. The final transformation is given by eq. (4.47) and involves the rotation around the $X_{ls'}$-axis with the lifting surface dihedral angle Γ_{ls} into the lifting surface reference frame $\{\boldsymbol{E}_{ls}\}$. Since the left and right mounted lifting surface reference frames are both right-handed and have an identical orientation, the aforementioned d-sign-change-parameter must be included in order for a positive dihedral angle to result in a lifting-surface-tip-up rotation for every lifting surface. The complete transformation from the $\{\boldsymbol{E}_{lsAC}\}$ frame to the $\{\boldsymbol{E}_{ls}\}$ frame is given by eq. (4.48).

In summary, a positive incidence and dihedral angle results in a lifting-surface-leading-edge-up and lifting-surface-tip-up rotation respectively as already shown in fig. 4.2 for a right-mounted lifting surface.

$$\{\boldsymbol{E}_{lsAC}\} = \boldsymbol{T}_{lsAC|ls'}\{\boldsymbol{E}_{ls'}\} = \begin{bmatrix} cos(i_{ls}) & 0 & sin(i_{ls}) \\ 0 & 1 & 0 \\ -sin(i_{ls}) & 0 & cos(i_{ls}) \end{bmatrix} \{\boldsymbol{E}_{ls'}\} \tag{4.46}$$

$$\{\boldsymbol{E}_{ls'}\} = \boldsymbol{T}_{ls'|ls}\{\boldsymbol{E}_{ls}\} = \begin{bmatrix} 1 & 0 & 0 \\ 0 & cos(-\Gamma_{ls}) & -d_{sgn}sin(-\Gamma_{ls}) \\ 0 & d_{sgn}sin(-\Gamma_{ls}) & cos(-\Gamma_{ls}) \end{bmatrix} \{\boldsymbol{E}_{ls}\} \tag{4.47}$$

$$\begin{aligned} \{\boldsymbol{E}_{lsAC}\} &= \boldsymbol{T}_{lsAC|ls}\{\boldsymbol{E}_{ls}\} \\ &= \boldsymbol{T}_{lsAC|ls'}\boldsymbol{T}_{ls'|ls}\{\boldsymbol{E}_{ls}\} \\ &= \begin{bmatrix} \cos(i_{ls}) & -d_{sgn}\sin(i_{ls})\sin(\Gamma_{ls}) & \sin(i_{ls})\cos(\Gamma_{ls}) \\ 0 & \cos(\Gamma_{ls}) & d_{sgn}\sin(\Gamma_{ls}) \\ -\sin(i_{ls}) & -d_{sgn}\cos(i_{ls})\sin(\Gamma_{ls}) & \cos(i_{ls})\cos(\Gamma_{ls}) \end{bmatrix} \{\boldsymbol{E}_{ls}\} \end{aligned} \tag{4.48}$$

The lifting surface sweep Λ_{ls} is treated as a shear transformation (performed in the lifting surface frame $\{\boldsymbol{E}_{ls}\}$) rather than a rotation, with the lifting surface chord lines remaining parallel with the body X_b-Z_b plane, therefore only two lifting surface rotational transformations are presented. The sweep transformation, however, may still be defined with a shear transformation matrix given by eq. (4.49). Again the d-sign-change-parameter must be included here in order for a positive sweep to result in a lifting-surface-tip-backward transformation for both left and right mounted lifting surfaces as already shown in fig. 4.2 for a right-mounted lifting surface.

$$\boldsymbol{T}_{\Lambda,ls}\{\boldsymbol{E}_{ls}\} = \begin{bmatrix} 1 & 0 & 0 \\ -d_{sgn}tan(\Lambda_{ls}) & 1 & 0 \\ 0 & 0 & 1 \end{bmatrix} \{\boldsymbol{E}_{ls}\} \tag{4.49}$$

The lifting surface abbreviations given in table 4.5 are applicable to the incidence, dihedral, and sweep parameters presented here as well, and the values corresponding to each lifting surface used in the 6DoF model implementation of this thesis are given in appendix A.

5

Model Development and Analysis

The main focus of this thesis work is the tilt-rotor model development which mostly involves the derivation of the expressions for the forces and moments generated by subsystems of the tilt-rotor. The different subsystems of the tilt-rotor have already been introduced in the model description chapter and consist of the wings, tail stabilizers, fuselage, and (most importantly) the rotors. The scope of the derivation is limited to forces and moments of aerodynamic origin for the most part, with the exception of the rotors which additionally incorporate loads generated as a result of acceleration in inertial space. A key characteristic of the rotor model developed in this thesis is the fact that it shall be derived analytically, yielding symbolic descriptions for the velocity and acceleration experienced by any point on the blades, the flapping equation, the rotor forces (including the thrust), and the rotor moments (including the torque). It shall then be possible to visually inspect and analyze these symbolic descriptions making it possible to address the research question concerned with the effect of the tiltable proprotor on the model equations.

The aerodynamic models of the remaining subsystems shall be relatively simple in comparison to the rotor model since they are not the focus of this thesis work. These models must be developed nonetheless since, together with the rigid body dynamics of the aircraft, they shall ultimately form the 6-DoF flight mechanics model of a tilt-rotor which shall be implemented in simulation enabling the generation of trim curves and flight data for the purpose of verification, validation, and further analysis of the tilt-rotor model. The latter is treated later, while this chapter is only concerned with the derivation of the force and moment expressions of the subsystems of this tilt-rotor model.

The structure of this chapter is as follows. First the rigid body dynamics describing the motion of the tilt-rotor presented in section 5.1, simultaneously introducing all the force and moment vectors of the subsystems that are derived in the subsequent sections, starting with the rotor model which is described and analyzed in section 5.2. Next the forces and moments generated by the wings and tail stabilizers are collectively treated in section 5.3, while the aerodynamics of the fuselage are briefly described in section 5.4. Finally the aerodynamic interaction between the rotor wash and the main wings is described in section 5.5 concluding the chapter.

5.1. Body Equations of Motion

The body equations of motion are limited to only describe the dynamics of the tilt-rotor as if it were a single point in space, which in this model has been chosen to coincide with the body CoG. The body motion is described by the linear velocities u_i, v_i, and w_i, and rotational velocities p_i, q_i, and r_i defined in the body frame of reference. The body acceleration is also defined in the same reference frame and is described by the time derivatives of these velocities, namely $\dot{u}_i$, $\dot{v}_i$, $\dot{w}_i$, $\dot{p}_i$, $\dot{q}_i$, and $\dot{r}_i$. Since the body reference frame is not inertial, apart from the the acceleration experienced as a result of any applied external force or moment, additional sources of acceleration perceived from within the body frame of reference emerge as a result of the motion of the body itself. The acceleration experienced by the body along and around the axes of the body frame of reference is given in eq. (5.1) (for derivation of equations see [46]). It must be remembered, however, that this set of equations of motion has been obtained with the assumption that the tilt-rotor is symmetrical in the $X_b - Z_b$ plane, and that the Earth is flat and may be considered an inertial frame of

reference. As a side note, the transformation of the body velocities into inertial space, and the obtention of the accompanying body position and attitude in the inertial non-rotating flat-Earth frame is treated in chapter 7 which, inter alia, covers the steps involved in the creation of the tilt-rotor Matlab-Simulink simulation.

Returning to eq. (5.1), here while F_{bx}, F_{by}, and F_{bz} are external forces acting along—and M_{bx}, M_{by}, and M_{bz} are external moments acting around—the X_b, Y_b, and Z_b axes respectively. Furthermore m is the tilt-rotor mass while I_{xx}, I_{yy}, I_{zz}, and I_{xz} are the three moments and one product of inertia of entire aircraft. A reminder of the positive sign conventions of the body velocities, and an added graphical summary of the positive sign conventions of the external forces and moments is shown in fig. 5.1.

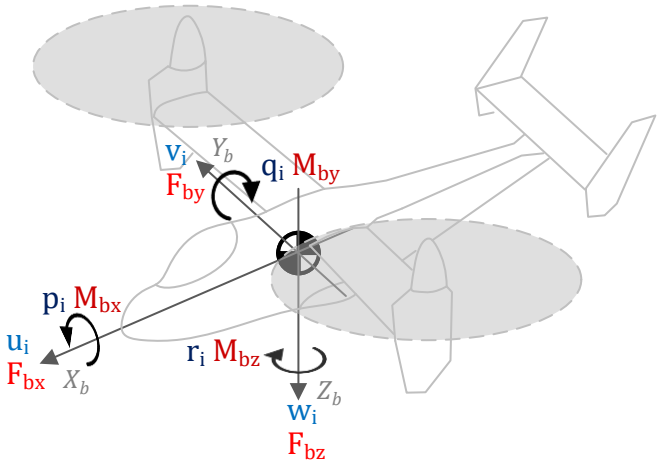

Figure 5.1: Positive sign conventions for the tilt-rotor body velocities, forces, and moments.

$$\dot{u}_i = \frac{F_{bx}}{m} - q_i w_i + r_i v_i \tag{5.1a}$$

$$\dot{v}_i = \frac{F_{by}}{m} - r_i u_i + p_i w_i \tag{5.1b}$$

$$\dot{w}_i = \frac{F_{bz}}{m} - p_i v_i + q_i u_i \tag{5.1c}$$

$$\dot{p}_i = \frac{I_{zz} M_{bx} + I_{xz} M_{bz} + (I_{xx} - I_{yy} + I_{zz})\, I_{xz} p_i q_i + (I_{yy} - I_{zz})\, I_{zz} - I_{xz}^2 q_i r_i}{I_{xx} I_{zz} - I_{xz}^2} \tag{5.1d}$$

$$\dot{q}_i = \frac{M_{by} + I_{xz}\left(r_i^2 - p_i^2\right) + (I_{zz} - I_{xx})\, p_i r_i}{I_{yy}} \tag{5.1e}$$

$$\dot{r}_i = \frac{I_{xz} M_{bx} + I_{xx} M_{bz} + (I_{xx} - I_{yy})\, I_{xx} + I_{xz}^2 p_i q_i + (-I_{xx} + I_{yy} - I_{zz})\, I_{xz} q_i r_i}{I_{xx} I_{zz} - I_{xz}^2} \tag{5.1f}$$

The previously mentioned external forces and moments acting on the body CoG are the summation of multiple contributions which, in the case of this model, are limited to the rotors (r), wings (w), horizontal stabilizers (hs), vertical stabilizers (vs), and fuselage (fus) only. For notation compactness the forces and moments are presented in vector form in eqs. (5.2) and (5.3) respectively. It can be seen that the total moment consists of pure moments and additional moments as a result of the generated forces acting at a distance from the CoG represented by the position vectors $\boldsymbol{s}$.

$$\begin{pmatrix} F_{bx} & F_{by} & F_{bz} \end{pmatrix} \{\boldsymbol{E}_b\} = \boldsymbol{F}_b = \boldsymbol{F}_r + \boldsymbol{F}_w + \boldsymbol{F}_{hs} + \boldsymbol{F}_{vs} + \boldsymbol{F}_{fus} \tag{5.2}$$

$$\begin{aligned} \begin{pmatrix} M_{bx} & M_{by} & M_{bz} \end{pmatrix} \{\boldsymbol{E}_b\} = \boldsymbol{M}_b = \boldsymbol{M}_r + \boldsymbol{M}_w + \boldsymbol{M}_{hs} + \boldsymbol{M}_{vs} + \boldsymbol{M}_{fus} \\ + \boldsymbol{s}_r \times \boldsymbol{F}_r + \boldsymbol{s}_w \times \boldsymbol{F}_w + \boldsymbol{s}_{hs} \times \boldsymbol{F}_{hs} + \boldsymbol{s}_{vs} \times \boldsymbol{F}_{vs} + \boldsymbol{s}_{fus} \times \boldsymbol{F}_{fus} \end{aligned} \tag{5.3}$$

The derivation of these force and moment contributions is treated in the sections below, starting with the rotor.

5.2. Rotor

The goal of the derivation of the rotor equations is to obtain expressions for the forces and moments generated by the rotor, preferably defined in a non-rotating frame, that can then be readily transformed into the body frame in order to determine the rotor's influence on the body dynamics. Since the blades of the rotor rotates, however, the derivation process of these forces and moments must begin in a rotating frame. Although multiple different options for the selection of a rotating frame exist (such as the rotating shaft plane, or the rotating disk plane), in this thesis work the wind axis rotating frame $\{\boldsymbol{E}_{\widehat{R}}\}$, coplanar with the wind axis control plane, has been chosen as the basis for the rotor equations. It is important to highlight at this point that the rotor equations are derived in a wind axis system with all wind axis reference frames and states indicated with a caret symbol ($\widehat{\ }$). A more elaborate explanation of the wind axis system and the decision for choosing it as the basis for the rotor equations is given in section 4.7. In short, however, employing the wind axis system removes the lateral velocity component in the wind axis control plane which simplifies the derivation process.

Since the rotor is modeled as an articulated type, only the feathering and flapping hinges need to be included in the expressions. Keeping in mind that the derivation is performed in the (wind axis) control plane, the definition of the blade pitch in this rotating frame shall consist of the collective swashplate input only since the cyclic pitch variation is, by definition, non-existent in the control plane (hence this frame is also referred to as the non-feathering plane). Furthermore, the blade flapping angle is defined to be measured between the wind axis blade $X_{\widehat{BL}}$-axis and the wind axis control plane, or to be more exact, between the wind axis blade $X_{\widehat{BL}}$-axis and the wind axis rotating frame $X_{\widehat{R}}$-axis.

The desired rotor forces and moments shall also be defined with respect to the wind axis control plane and shall be referred to as the H-, S-, and T-forces acting along - and the O-, P-, and Q-moments acting around - the negative $X_{\widehat{CP}}$-, $Y_{\widehat{CP}}$-, $Z_{\widehat{CP}}$-axes. A graphical summary of these forces and moments and their direction of action for the left and right rotor is shown in fig. 5.2. Notice that the orientation of the wind axis control plane frame axes (and thus also the directions of action of the forces and moments) of the left and right rotor are identical.

In order to obtain the expressions for the rotor forces and moments, first the blade forces and moments shall be derived in the (wind axis) rotating frame, expressed in terms of the wind axis azimuthal position $\widehat{\psi}$ and the wind axis flapping angle $\widehat{\beta}$. Next, these expressions shall be converted to the non-rotating (wind axis) control plane frame through the disk-tilt approximation and the corresponding wind axis disk-tilt angles $\widehat{a}_0$, $\widehat{a}_1$, and $\widehat{b}_1$. Combining the contribution of all the blades on the rotor shall finally yield the total forces and moments generated by the rotor.

The blade element method (BEM) shall be employed in this derivation which describes the blade with a two-dimensional airfoil section (also referred to as the blade element) that spans the blade length, "with the influence of the wake and the rest of the rotor contained entirely in an induced angle of attack at the section" [47, p45]. The geometric and aerodynamic characteristics of the blade are defined as a function of the radial position along the blade. In the case of this analytical rotor model, each blade element is of infinitesimal width therefore the contribution of all blade elements must be integrated symbolically to obtain the total loads generated by the entire blade. For this reason the derivation presented in this section begins with the definition of the velocity components experienced by the blade element defined in the (wind axis) blade frame of reference. These velocity components are then used in the derivation of the flapping equation which is required for the realization of the disk tilt approximation, enabling the definition of the blade forces and moments in the non-rotating frame. Next the derivation of each of the H-, S-, and T-forces and O-, P-, and Q-moments is treated in their own subsections which, in most cases, involves the blade element velocity components and the derivation of the forces and moments generated by the (infinitesimally wide) blade element.

5.2.1. Blade Element Velocity Components

The blade element velocity components are required for the determination of the flapping equation and the rotor forces and moments since these are derived according to the blade element method. It has been decided

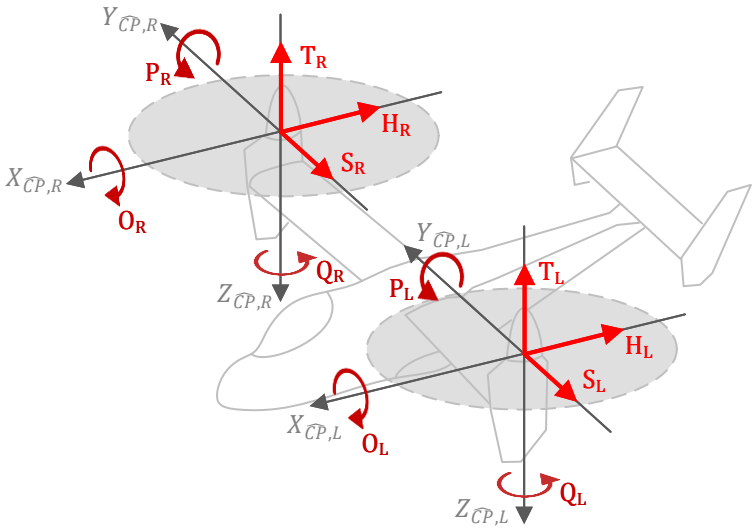

Figure 5.2: Positive sign conventions of the rotor forces and moments defined in the wind axis control planes of the left (cw.) and right (ccw.) rotor.

that these velocity components shall be defined in the (wind axis) blade reference frame and therefore the goal of the following derivation is to obtain the expressions for the velocity vector of the blade element decomposed along the $X_{\widehat{BL}}$-, $Y_{\widehat{BL}}$-, and $Z_{\widehat{BL}}$-axes. Ultimately these decomposed velocities shall be referred to as the radial U_R, tangential U_T, and perpendicular U_P blade element velocities respectively.

The blade element is part of not one, but multiple cascading frames that may be rotating and offset from one another, all contributing to the total velocity vector experienced by the blade element. Therefore the derivation of the total blade element velocity (and later blade element acceleration) is performed in multiple consecutive steps, each incorporating the contribution of an intermediate reference frame to the blade element velocity expressions. The tilt-rotor body is chosen as the basis frame of reference requiring a series of reference frame transformations to reach the blade element as depicted in fig. 5.3. The derivation of the blade element velocity components shall begin with the body linear and rotational velocities, and continue in an orderly manner to consecutively incorporate the rotational velocity contributions of the nacelle, rotor, and blade reference frames, and the linear velocities of the nacelle pivot point, rotor hub, and finally blade element as a result of their distance away from the point of rotation.

At this point it is most convenient to make the distinction between the different types of velocities used throughout the derivation of this tilt-rotor model. At the beginning of this chapter the body equations of motion given by eq. (5.1) are shown to depend on the body linear and rotational rates defined in inertial space, indicated by the subscript i. In the case of the derivation of the blade element velocity components ahead, however, the total aerodynamic velocity is of interest since the aerodynamic forces and moments generated by the blade element depend on the total aerodynamic velocity consisting of both the velocity with respect to inertia space, and the additional air velocity, also referred to as wind, gust, or wash velocity. For this reason a clear distinction is made between these three types of velocities with the help of subscripts, where a newly introduced subscript w shall correspond to body wash velocity components, while body velocities not accompanied by any subscript correspond to total aerodynamic velocities. The formal relationship between the three is given by eq. (5.4) where $\boldsymbol{V}_{b|b}$ and $\boldsymbol{\omega}_{b|b}$ are the linear and rotational body velocity vectors defined in the body reference frame. It is very important to note that the body wash velocity components are defined in the body frame of reference. Therefore, if an atmospheric wind model were to be used in combination with this tilt-rotor model, the wind velocity components would have to be first transformed to the body reference frame before being supplied to the tilt-rotor model. Furthermore, note that the wash velocity is subtracted from the body inertial velocity since the wash vector defines the movement direction *of* the air while the body velocity defines the movement direction of the body *through the air*, hence the difference in sign.

$$\boldsymbol{V}_{b|b} = \boldsymbol{V}_{b,i|b} - \boldsymbol{V}_{w|b} \tag{5.4a}$$

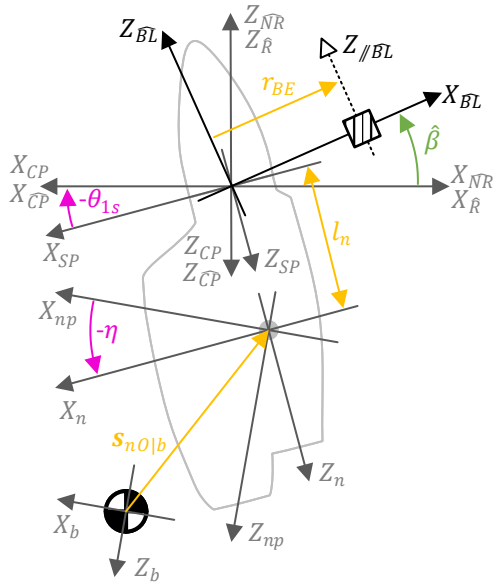

Figure 5.3: Schematic side-view of the cascaded reference frame transformations from the tilt-rotor body to the blade element. Wind shift angle Δ is set to zero and blade is positioned at $\psi = \widehat{\psi} = 0$. Blade element represented by striped box. Body CoG and nacelle outline shown in background.

$$\boldsymbol{\omega}_{b|b} = \boldsymbol{\omega}_{b,i|b} - \boldsymbol{\omega}_{w|b} \tag{5.4b}$$

Rotor Hub Velocity Derivation

The derivation starts with the linear and angular (total aerodynamic) body velocities as given by eq. (5.5) and eq. (5.6) respectively in the body reference frame (subscript $|b$). Here $\{\boldsymbol{E}_b\}$ represents the unit vectors in the body reference frame.

$$\boldsymbol{V}_{b|b} = \begin{pmatrix} u & v & w \end{pmatrix} \{\boldsymbol{E}_b\} \tag{5.5}$$

$$\boldsymbol{\omega}_{b|b} = \begin{pmatrix} p & q & r \end{pmatrix} \{\boldsymbol{E}_b\} \tag{5.6}$$

Next, in order to determine the velocity of the nacelle pivot point, its distance from the tilt rotor CoG (given by the position vector $\boldsymbol{s}_{nO}$) must be defined in the body reference frame as shown in eq. (5.7).

$$\boldsymbol{s}_{nO|b} = \begin{pmatrix} -d_{xn} & d_{sgn} d_{yn} & -d_{zn} \end{pmatrix} \{\boldsymbol{E}_b\} \tag{5.7}$$

The total linear velocity of the nacelle pivot point in the body frame is then given by eq. (5.8) and consists of the body linear velocity and additional linear velocity components as a result of the body angular velocity and the offset between the nacelle pivot point and the body CoG. In the case of the latter, the cross product with the body rates is replaced by dot multiplication with the matrix $[\boldsymbol{\omega}_{b|b}]_x$ given by eq. (5.9) for notation clarity. This type of notation replacement will be employed at multiple points later in this derivation for the same reason.

$$\boldsymbol{V}_{nO|b} = \boldsymbol{V}_{b|b} + \boldsymbol{\omega}_{b|b} \times \boldsymbol{s}_{nO|b} = \begin{pmatrix} u & v & w \end{pmatrix} \{\boldsymbol{E}_b\} + \begin{pmatrix} -d_{xn} & d_{sgn} d_{yn} & -d_{zn} \end{pmatrix} [\boldsymbol{\omega}_{b|b}]_x \{\boldsymbol{E}_b\} \tag{5.8}$$

$$[\boldsymbol{\omega}_{b|b}]_x = \begin{bmatrix} 0 & r & -q \\ -r & 0 & p \\ q & -p & 0 \end{bmatrix} \tag{5.9}$$

There exists only a translation from the body to the nacelle pivot reference frame $\{\boldsymbol{E}_{np}\}$, therefore $\{\boldsymbol{E}_{np}\} = \{\boldsymbol{E}_b\}$ and thus the pivot point velocity in the nacelle pivot reference frame (subscript $|np$) is given by eq. (5.10).

$$\boldsymbol{V}_{nO|np} = \begin{pmatrix} u - d_{sgn}d_{yn}r - d_{zn}q \\ v - d_{xn}r + d_{zn}p \\ w + d_{xn}q + d_{sgn}d_{yn}p \end{pmatrix}^T \{\boldsymbol{E}_{np}\} \tag{5.10}$$

Next the expression for the velocity of the rotor hub must be found. The rotor hub is located at a distance l_n along the negative Z_n-axis of the nacelle reference frame as given by eq. (5.11) defined in the nacelle reference frame.

$$\boldsymbol{s}_{hub|n} = \begin{pmatrix} 0 & 0 & -l_n \end{pmatrix} \{\boldsymbol{E}_n\} \tag{5.11}$$

The rotational velocity of the nacelle frame is given by eq. (5.12) and consists of not only the body angular velocities, but now also the angular velocity introduced by the tilting motion of the nacelle itself.

$$\boldsymbol{\omega}_n = \begin{pmatrix} p & q & r \end{pmatrix} \{\boldsymbol{E}_b\} + \begin{pmatrix} 0 & \dot{\eta} & 0 \end{pmatrix} \{\boldsymbol{E}_{np}\} \tag{5.12}$$

Since the nacelle rotates around the nacelle pivot frame Y_{np}-axis, a rotational transformation from the nacelle pivot frame to the nacelle frame is necessary, as has already been given by eq. (4.34). For notation compactness, however, this transformation matrix shall be referred to by the $[\eta]$ transformation as shown in eq. (5.13) where η is the nacelle tilt angle. As a reminder, in helicopter mode $\eta = 0$ and in airplane mode $\eta = -90°$, therefore a positive η angle tilts the nacelles backwards.

$$\{\boldsymbol{E}_{np}\} = \boldsymbol{T}_{np|n}\{\boldsymbol{E}_n\} = \begin{bmatrix} \cos(\eta) & 0 & \sin(\eta) \\ 0 & 1 & 0 \\ -\sin(\eta) & 0 & \cos(\eta) \end{bmatrix} \{\boldsymbol{E}_n\} = [\eta]\{\boldsymbol{E}_n\} \tag{5.13}$$

Using the above transformation matrix the total rotational velocity of the nacelle frame may be defined in the nacelle frame as demonstrated in eq. (5.14). The shorthand notation for the trigonometric functions is used where the sine and cosine of η is abbreviated with S_η and C_η respectively.

$$\boldsymbol{\omega}_{n|n} = \begin{pmatrix} p & q & r \end{pmatrix} [\eta]\{\boldsymbol{E}_n\} + \begin{pmatrix} 0 & \dot{\eta} & 0 \end{pmatrix} [\eta]\{\boldsymbol{E}_n\} = \begin{pmatrix} pC_\eta - rS_\eta \\ q + \dot{\eta} \\ pS_\eta + rC_\eta \end{pmatrix}^T \{\boldsymbol{E}_n\} \tag{5.14}$$

The total linear velocity of the rotor hub may be determined with eq. (5.15) where it can be seen to consist of the the pivot point total linear velocity and the linear velocity as a result of the total angular velocity of the nacelle frame and the distance between the pivot point and rotor hub. Again the cross product is replaced by dot multiplication with $[\omega_{n|n}]_x$ given by eq. (5.16).

$$\boldsymbol{V}_{hub} = \boldsymbol{V}_{nO|np} + \boldsymbol{\omega}_{n|n} \times \boldsymbol{s}_{hub|n} = \begin{pmatrix} u - d_{sgn}d_{yn}r - d_{zn}q \\ v - d_{xn}r + d_{zn}p \\ w + d_{xn}q + d_{sgn}d_{yn}p \end{pmatrix}^T \{\boldsymbol{E}_{np}\} + \begin{pmatrix} 0 \\ 0 \\ -l_n \end{pmatrix}^T [\boldsymbol{\omega}_{n|n}]_x \{\boldsymbol{E}_n\} \tag{5.15}$$

$$[\boldsymbol{\omega}_{n|n}]_x = \begin{bmatrix} 0 & pS_\eta + rC_\eta & -q - \dot{\eta} \\ -pS_\eta - rC_\eta & 0 & pC_\eta - rS_\eta \\ q + \dot{\eta} & -pC_\eta + rS_\eta & 0 \end{bmatrix} \tag{5.16}$$

Transformed into the nacelle reference frame, the total linear hub velocity is given by eq. (5.17).

$$\begin{aligned}\boldsymbol{V}_{hub|n} &= \begin{pmatrix} u - d_{sgn}d_{yn}r - d_{zn}q \\ v - d_{xn}r + d_{zn}p \\ w + d_{xn}q + d_{sgn}d_{yn}p \end{pmatrix}^T [\eta]\{\boldsymbol{E}_n\} + \begin{pmatrix} 0 \\ 0 \\ -l_n \end{pmatrix}^T [\boldsymbol{\omega}_{n|n}]_x \{\boldsymbol{E}_n\} \\ &= \begin{pmatrix} \left(-d_{sgn}\, d_{yn}\, r - d_{zn}\, q + u\right) C_\eta - \left(d_{sgn}\, d_{yn}\, p + d_{xn}\, q + w\right) S_\eta - l_n\ (\dot{\eta} + q) \\ \left(-l_n\, S_\eta - d_{xn}\right) r + \left(l_n\, C_\eta + d_{zn}\right) p + v \\ \left(d_{sgn}\, d_{yn}\, p + d_{xn}\, q + w\right) C_\eta - S_\eta\ \left(d_{sgn}\, d_{yn}\, r + d_{zn}\, q - u\right) \end{pmatrix}^T \{\boldsymbol{E}_n\} \end{aligned} \tag{5.17}$$

The flapping angle will be defined with respect to the (wind axis) control plane (so as not to have to include the longitudinal cyclic angle θ_{1s} in the blade pitch expression), therefore the hub velocity must be transformed into the control plane reference frame as well. First the velocity is transformed into the shaft plane frame $\boldsymbol{E}_{SP}$. There exists only a translation from the nacelle to shaft plane frame therefore $\{\boldsymbol{E}_{SP}\} = \{\boldsymbol{E}_n\}$. A rotational transformation from the shaft plane to the control plane around the negative Y_{SP}-axis with the angle θ_{1s} is present however, and has been already defined by eq. (4.35). Again, for notation compactness this transformation matrix shall be replaced by the $[-\theta_{1s}]$ transformation as shown in eq. (5.18) (remembering that the tilt-rotor does not have lateral cyclic). It should be mentioned at this point that the control plane reference frame should introduce a new rotational velocity component, namely $\dot{\theta_{1s}}$. For simplicity, however, it is neglected.

$$\{\boldsymbol{E}_{SP}\} = \boldsymbol{T}_{SP|CP}\{\boldsymbol{E}_{CP}\} = \begin{bmatrix} \cos(\theta_{1s}) & 0 & -\sin(\theta_{1s}) \\ 0 & 1 & 0 \\ \sin(\theta_{1s}) & 0 & \cos(\theta_{1s}) \end{bmatrix} \{\boldsymbol{E}_{CP}\} = [-\theta_{1s}]\{\boldsymbol{E}_{CP}\} \tag{5.18}$$

Rotor Hub Velocity Analysis

The rotor hub velocity defined in the control plane is then given by eq. (5.19) where the final components are substituted by single variable names for notation compactness.

A brief analysis of the hub velocity expression is performed to address the research sub-question concerned with determining the effect of the tilting proprotor on the velocity components experienced by the rotor hub. Visual inspection reveals that the presence of a tiltable proprotor affects all the terms within the longitudinal-tangential (V_{tc1}) and perpendicular (V_{pc}) velocity components, and almost all of the terms in the lateral-tangential velocity component (V_{tc2}), be it through a trigonometric function of the nacelle angle (e.g. S_η), the nacelle tilt rate $\dot{\eta}$, or the length of the tiltable nacelle l_n. As expected, the lateral-tangential velocity component V_{tc2} is not affected by the nacelle tilt rate while the opposite is true for the other two velocity components. Finally it must be highlighted that simply adding the nacelle tilt-rate to the body pitch rate q is only permissible in two cases, while all other instances of the body pitch rate are not accompanied by $\dot{\eta}$ due to the fact that the velocity experienced by the nacelle pivot point does not depend on the nacelle tilt rate. For this reason a simplified model derivation approach of simply adding the nacelle tilt-rate to all instances of the body pitch rate would not be valid.

$$\boldsymbol{V}_{hub|CP} = \begin{pmatrix} \left(-d_{sgn}\, d_{yn}\, r - d_{zn}\, q + u\right) C_\eta - \left(d_{sgn}\, d_{yn}\, p + d_{xn}\, q + w\right) S_\eta - l_n\ (\dot{\eta} + q) \\ \left(-l_n\, S_\eta - d_{xn}\right) r + \left(l_n\, C_\eta + d_{zn}\right) p + v \\ \left(d_{sgn}\, d_{yn}\, p + d_{xn}\, q + w\right) C_\eta - S_\eta\ \left(d_{sgn}\, d_{yn}\, r + d_{zn}\, q - u\right) \end{pmatrix}^T [-\theta_{1s}]\{\boldsymbol{E}_{CP}\}$$

$$= \begin{pmatrix} \left(-d_{sgn}\, d_{yn}\, r - d_{zn}\, q + u\right) C_\eta C_{\theta 1s} \\ -\left(d_{sgn}\, d_{yn}\, p + d_{xn}\, q + w\right) S_\eta C_{\theta 1s}\ - l_n\ (\dot{\eta} + q)\, C_{\theta 1s} \\ +\left(d_{sgn}\, d_{yn}\, p + d_{xn}\, q + w\right) C_\eta S_{\theta 1s} \\ -\left(d_{sgn}\, d_{yn}\, r + d_{zn}\, q - u\right) S_\eta S_{\theta 1s} \\ \hline \left(-l_n\, S_\eta - d_{xn}\right) r + \left(l_n\, C_\eta + d_{zn}\right) p + v \\ \hline \left(d_{sgn}\, d_{yn}\, r + d_{zn}\, q - u\right) C_\eta S_{\theta 1s} \\ +\left(d_{sgn}\, d_{yn}\, p + d_{xn}\, q + w\right) S_\eta S_{\theta 1s}\ + l_n\ (\dot{\eta} + q)\, S_{\theta 1s} \\ +\left(d_{sgn}\, d_{yn}\, p + d_{xn}\, q + w\right) C_\eta C_{\theta 1s} \\ -\left(d_{sgn}\, d_{yn}\, r + d_{zn}\, q - u\right) S_\eta C_{\theta 1s} \end{pmatrix}^T \{\boldsymbol{E}_{CP}\} = \begin{pmatrix} V_{tc1} \\ V_{tc2} \\ V_{pc} \end{pmatrix}^T \{\boldsymbol{E}_{CP}\} \tag{5.19}$$

Wind Axis System

As already mentioned, the derivation of the rotor equations will be performed in the wind axis system so that the lateral component of the rotor hub velocity does not have to be treated when determining the blade element velocity. Instead it is implicitly included in the wind axis shift Δ given by eq. (4.36), repeated below for clarity. The wind shift angle is defined to be cw when looking from above the rotor for both a cw and ccw rotating rotor.

$$\Delta = \arctan\left(\frac{V_{tc2}}{V_{tc1}}\right) \tag{4.36}$$

The transformation from the control plane to the wind axis control plane requires a rotation around the Z_{CP}-axis with the wind shift angle as has been introduced in eq. (4.38). Once again for notation compactness this transformation matrix shall be referred to by the $[\Delta]$ transformation as defined in eq. (5.20). It is not clear at the time of writing this report whether the wind axis shift transformation should introduce a new rotational velocity component, namely $\dot{\Delta}$, therefore it is not included in this derivation.

$$\{\boldsymbol{E}_{CP}\} = \boldsymbol{T}_{CP|\widehat{CP}}\{\boldsymbol{E}_{\widehat{CP}}\} = \begin{bmatrix} cos(\Delta) & -sin(\Delta) & 0 \\ sin(\Delta) & cos(\Delta) & 0 \\ 0 & 0 & 1 \end{bmatrix} \{\boldsymbol{E}_{\widehat{CP}}\} = [\Delta]\{\boldsymbol{E}_{\widehat{CP}}\} \tag{5.20}$$

In the wind axis control plane the blade azimuth angle and the rotor hub tangential and perpendicular velocity components are redefined according to eq. (4.37) (repeated below for clarity), eq. (5.21a), and eq. (5.21b) respectively, and can be easily identified with the caret symbol ($\widehat{\ }$) which will be applied to all following wind axis variables. The omega sign change parameter Ω_{sgn} is included in eq. (4.37) because it influences the the wind shift axis direction experienced by the azimuth angle $\widehat{\psi}$ depending on the direction of rotation of the rotor. It should be remembered that the wind shift angle is defined to act in the same direction irrespective of the rotational direction of the rotor.

$$\psi = \widehat{\psi} - \Omega_{sgn}\Delta \tag{4.37}$$

$$\widehat{V_{tc}} = \sqrt{V_{tc1}^2 + V_{tc2}^2} \tag{5.21a}$$

$$\widehat{V_{pc}} = V_{pc} \tag{5.21b}$$

The rotor hub velocity vector defined in the wind axis frame is then given by eq. (5.22). It should be noted that due to the definition of the wind shift angle Δ, the longitudinal component simplifies to $\widehat{V}_{tc}$ while the lateral component cancels out to zero as expected. It is also at this point that the rotor inflow velocity v_{in} is introduced into the velocity vector. Here it is assumed to be perpendicular to the control plane for simplicity, when in reality it should be perpendicular to the disk plane. This simplification removes the additional transformation of the inflow velocity from the disk plane to the control plane.

Note that a separate analysis of the effect of the tiltable proprotor on the rotor hub velocity expression defined in the wind axis frame shall not be performed since the only difference between eq. (5.22) and the non-wind axis rotor hub velocity is the wind shift angle Δ. Although this angle does contribute to the overall effect of the tiltable proprotor on the velocity experienced by the rotor hub in the wind axis frame, its contribution is indirect and limited as will be explained in more detail in the section analyzing the inertial flapping equation on page 136.

$$\boldsymbol{V}_{hub|\widehat{CP}} = \begin{pmatrix} V_{tc1} \\ V_{tc2} \\ V_{pc} - v_{in} \end{pmatrix}^T [\Delta]\{\boldsymbol{E}_{\widehat{CP}}\} = \begin{pmatrix} V_{tc1}C_\Delta + V_{tc2}S_\Delta \\ -V_{tc1}S_\Delta + V_{tc2}C_\Delta \\ V_{pc} - v_{in} \end{pmatrix}^T \{\boldsymbol{E}_{\widehat{CP}}\} = \begin{pmatrix} \widehat{V_{tc}} \\ 0 \\ \widehat{V_{pc}} - v_{in} \end{pmatrix}^T \{\boldsymbol{E}_{\widehat{CP}}\} \tag{5.22}$$

Blade Element Velocity Derivation

Before transforming the hub velocity into the rotating and blade reference frame, first a 180° rotation around the Y_{CP}-axis is performed into the non-rotating frame $E_{\widehat{NR}}$ as has been introduced in eq. (4.42). This transformation matrix shall also be referred to with the more compact notation $[\pi_Y]$ as defined in eq. (5.23).

$$\{\boldsymbol{E}_{\widehat{CP}}\} = \boldsymbol{T}_{\widehat{CP}|\widehat{NR}}\{\boldsymbol{E}_{\widehat{NR}}\} = \begin{bmatrix} cos(\pi) & 0 & sin(\pi) \\ 0 & 1 & 0 \\ -sin(\pi) & 0 & cos(\pi) \end{bmatrix}\{\boldsymbol{E}_{\widehat{NR}}\} = \begin{bmatrix} -1 & 0 & 0 \\ 0 & 1 & 0 \\ 0 & 0 & -1 \end{bmatrix}\{\boldsymbol{E}_{\widehat{NR}}\} = [\pi_Y]\{\boldsymbol{E}_{\widehat{NR}}\} \tag{5.23}$$

Next, the transformation from the non-rotating frame to the rotating frame $E_{\widehat{R}}$ has been given by eq. (4.43) where the rotating frame follows the azimuthal position of the blade, but does not flap, lead/lag, nor feather with the blade. Similar to the above, $[\widehat{\psi}]$ is used as a replacement for this transformation for notation compactness, and is defined in eq. (5.24). As a reminder, the Ω_{sgn} parameter must be used here as the direction of rotor rotation influences the sign of the angle in the transformation.

$$\begin{aligned} \{\boldsymbol{E}_{\widehat{NR}}\} = \boldsymbol{T}_{\widehat{NR}|\widehat{R}}\{\boldsymbol{E}_{\widehat{R}}\} &= \begin{bmatrix} cos(\Omega_{sgn}\widehat{\psi}) & -sin(\Omega_{sgn}\widehat{\psi}) & 0 \\ sin(\Omega_{sgn}\widehat{\psi}) & cos(\Omega_{sgn}\widehat{\psi}) & 0 \\ 0 & 0 & 1 \end{bmatrix}\{\boldsymbol{E}_{\widehat{R}}\} \\ &= \begin{bmatrix} C_{\widehat{\psi}} & -\Omega_{sgn}S_{\widehat{\psi}} & 0 \\ \Omega_{sgn}S_{\widehat{\psi}} & C_{\widehat{\psi}} & 0 \\ 0 & 0 & 1 \end{bmatrix}\{\boldsymbol{E}_{\widehat{R}}\} \\ &= [\widehat{\psi}]\{\boldsymbol{E}_{\widehat{R}}\} \end{aligned} \tag{5.24}$$

In addition, since the rotating frame introduces the blade rotational velocity Ω, the total rotational velocity of the rotating frame is given by eq. (5.25). Again the direction of rotor rotation influences the sign of Ω with respect to the other rotational velocity components, hence the Ω_{sgn} parameter. It must be highlighted that the blade rotational velocity Ω is defined to act around the $Z_{\widehat{NR}}$-axis which tilts together with the wind axis control plane, therefore this angular vector may no longer be aligned with the rotor shaft.

$$\begin{aligned}\boldsymbol{\omega}_{\widehat{R}} &= \begin{pmatrix} p & q & r \end{pmatrix} \{\boldsymbol{E}_b\} + \begin{pmatrix} 0 & \dot{\eta} & 0 \end{pmatrix} \{\boldsymbol{E}_{np}\} + \begin{pmatrix} 0 & 0 & \Omega_{sgn}\Omega \end{pmatrix} \{\boldsymbol{E}_{\widehat{NR}}\} \\ &= \begin{pmatrix} pC_\eta - rS_\eta \\ q + \dot{\eta} \\ pS_\eta + rC_\eta \end{pmatrix}^T \{\boldsymbol{E}_n\} + \begin{pmatrix} 0 & 0 & \Omega_{sgn}\Omega \end{pmatrix} \{\boldsymbol{E}_{\widehat{NR}}\} \end{aligned} \tag{5.25}$$

The transformation into the rotating frame is given by eq. (5.26).

$$\begin{aligned}\boldsymbol{\omega}_{\widehat{R}|\widehat{R}} &= \begin{pmatrix} pC_\eta - rS_\eta \\ q + \dot{\eta} \\ pS_\eta + rC_\eta \end{pmatrix}^T [-\theta_{1s}][\Delta][\pi_Y][\widehat{\psi}]\{\boldsymbol{E}_{\widehat{R}}\} + \begin{pmatrix} 0 & 0 & \Omega_{sgn}\Omega \end{pmatrix} [\widehat{\psi}]\{\boldsymbol{E}_{\widehat{R}}\} \\ &= \left(\begin{array}{l} \left(S_{\widehat{\psi}}\ (q+\dot{\eta})\,\Omega_{sgn} - \left(\left(p\,C_\eta - r\,S_\eta\right) C_{\theta 1s} + S_{\theta 1s}\ \left(p\,S_\eta + r\,C_\eta\right)\right) C_{\widehat{\psi}}\right) C_\Delta \\ -S_\Delta \left(\left(\left(p\,C_\eta - r\,S_\eta\right) C_{\theta 1s} + S_{\theta 1s}\ \left(p\,S_\eta + r\,C_\eta\right)\right) S_{\widehat{\psi}}\,\Omega_{sgn} + C_{\widehat{\psi}}\ (q+\dot{\eta})\right) \\ \hdashline \left(\left(\left(p\,C_\eta - r\,S_\eta\right) C_{\theta 1s} + S_{\theta 1s}\ \left(p\,S_\eta + r\,C_\eta\right)\right) S_{\widehat{\psi}}\,\Omega_{sgn} + C_{\widehat{\psi}}\ (q+\dot{\eta})\right) C_\Delta \\ -\left(-S_{\widehat{\psi}}\ (q+\dot{\eta})\,\Omega_{sgn} + \left(\left(p\,C_\eta - r\,S_\eta\right) C_{\theta 1s} + S_{\theta 1s}\ \left(p\,S_\eta + r\,C_\eta\right)\right) C_{\widehat{\psi}}\right) S_\Delta \\ \hdashline C_\eta\,S_{\theta 1s}\,p - S_\eta\,C_{\theta 1s}\,p - C_\eta\,C_{\theta 1s}\,r - S_\eta\,S_{\theta 1s}\,r + \Omega_{sgn}\,\Omega \end{array} \right)^T \{\boldsymbol{E}_{\widehat{R}}\} \\ &= \begin{pmatrix} \omega_{\widehat{R}|X\widehat{R}} & \omega_{\widehat{R}|Y\widehat{R}} & \omega_{\widehat{R}|Z\widehat{R}} \end{pmatrix} \{\boldsymbol{E}_{\widehat{R}}\} \\ &= \begin{pmatrix} \omega_{\widehat{R}|X\widehat{R}} & \omega_{\widehat{R}|Y\widehat{R}} & \Omega_{tot} \end{pmatrix} \{\boldsymbol{E}_{\widehat{R}}\} \end{aligned} \tag{5.26}$$

Finally, the transformation from the rotating frame to the blade frame $E_{\widehat{BL}}$ has been given by eq. (4.44) where the blade reference frame only follows the blade flapping motion around the negative $Y_{\widehat{R}}$-axis, but does not include the lead/lag motion. Once more, for notation compactness the $[-\widehat{\beta}]$ transformation shall be used instead as defined in eq. (5.27).

$$\{\boldsymbol{E}_{\widehat{R}}\} = \boldsymbol{T}_{\widehat{R}|\widehat{BL}}\{\boldsymbol{E}_{\widehat{BL}}\} = \begin{bmatrix} \cos\left(\widehat{\beta}\right) & 0 & -\sin\left(\widehat{\beta}\right) \\ 0 & 1 & 0 \\ \sin\left(\widehat{\beta}\right) & 0 & \cos\left(\widehat{\beta}\right) \end{bmatrix} \{\boldsymbol{E}_{\widehat{BL}}\} = [-\widehat{\beta}]\{\boldsymbol{E}_{\widehat{BL}}\} \tag{5.27}$$

The blade reference frame also introduces a rotational velocity component, namely $\dot{\widehat{\beta}}$ which also acts around the negative $Y_{\widehat{R}}$ axis. The resulting total rotational velocity of the blade frame is given by eq. (5.28).

$$\begin{aligned}\boldsymbol{\omega}_{\widehat{BL}} &= \begin{pmatrix} p & q & r \end{pmatrix} \{\boldsymbol{E}_b\} + \begin{pmatrix} 0 & \dot{\eta} & 0 \end{pmatrix} \{\boldsymbol{E}_{np}\} + \begin{pmatrix} 0 & 0 & \Omega_{sgn}\Omega \end{pmatrix} \{\boldsymbol{E}_{\widehat{NR}}\} + \begin{pmatrix} 0 & -\dot{\widehat{\beta}} & 0 \end{pmatrix} \{\boldsymbol{E}_{\widehat{R}}\} \\ &= \begin{pmatrix} pC_\eta - rS_\eta \\ q + \dot{\eta} \\ pS_\eta + rC_\eta \end{pmatrix}^T \{\boldsymbol{E}_n\} + \begin{pmatrix} 0 & 0 & \Omega_{sgn}\Omega \end{pmatrix} \{\boldsymbol{E}_{\widehat{NR}}\} + \begin{pmatrix} 0 & -\dot{\widehat{\beta}} & 0 \end{pmatrix} \{\boldsymbol{E}_{\widehat{R}}\} \end{aligned} \tag{5.28}$$

The transformation into the blade reference frame is given by eq. (5.29).

$$
\begin{aligned}
\boldsymbol{\omega}_{\widehat{BL}|\widehat{BL}} &= \begin{pmatrix} pC_\eta - rS_\eta \\ q + \dot{\eta} \\ pS_\eta + rC_\eta \end{pmatrix}^T [-\theta_{1s}][\Delta][\pi_Y][\widehat{\psi}][-\widehat{\beta}]\{\boldsymbol{E}_{\widehat{BL}}\} + \begin{pmatrix} 0 \\ 0 \\ \Omega_{sgn}\Omega \end{pmatrix}^T [\widehat{\psi}][-\widehat{\beta}]\{\boldsymbol{E}_{\widehat{BL}}\} + \begin{pmatrix} 0 \\ -\dot{\widehat{\beta}} \\ 0 \end{pmatrix}^T [-\widehat{\beta}]\{\boldsymbol{E}_{\widehat{BL}}\} \\
&= \left(\begin{array}{l}
-\left(\left(pC_\eta - rS_\eta\right) S_\Delta C_{\theta 1s} + \left(pS_\eta + rC_\eta\right) S_\Delta S_{\theta 1s} - (q + \dot{\eta})\, C_\Delta\right) \Omega_{sgn} S_{\widehat{\psi}} C_{\widehat{\beta}} \\
-\left(\left(pC_\eta - rS_\eta\right) C_\Delta C_{\theta 1s} + \left(pS_\eta + rC_\eta\right) C_\Delta S_{\theta 1s} + (q + \dot{\eta})\, S_\Delta\right) C_{\widehat{\psi}} C_{\widehat{\beta}} \\
-\left(-\Omega_{sgn}\Omega_r + \left(pS_\eta + rC_\eta\right) C_{\theta 1s} - \left(pC_\eta - rS_\eta\right) S_{\theta 1s}\right) S_{\widehat{\beta}} \\
\hdashline
\left(\left(\left(pC_\eta - rS_\eta\right) C_{\theta 1s} + S_{\theta 1s}\, \left(pS_\eta + rC_\eta\right)\right) S_{\widehat{\psi}}\, \Omega_{sgn} + (q + \dot{\eta})\, C_{\widehat{\psi}}\right) C_\Delta \\
+ (q + \dot{\eta})\, S_\Delta S_{\widehat{\psi}} \Omega_{sgn} - \left(\left(pC_\eta - rS_\eta\right) C_{\theta 1s} + \left(pS_\eta + rC_\eta\right) S_{\theta 1s}\right) C_{\widehat{\psi}} S_\Delta - \dot{\widehat{\beta}} \\
\hdashline
\left(\left(pC_\eta - rS_\eta\right) S_\Delta\, C_{\theta 1s} + \left(pS_\eta + rC_\eta\right) S_\Delta\, S_{\theta 1s} - (q + \dot{\eta})\, C_\Delta\right) \Omega_{sgn} S_{\widehat{\psi}} S_{\widehat{\beta}} \\
+ \left(\left(pC_\eta - rS_\eta\right) C_\Delta\, C_{\theta 1s} + \left(pS_\eta + rC_\eta\right) C_\Delta\, S_{\theta 1s} + (q + \dot{\eta})\, S_\Delta\right) C_{\widehat{\psi}} S_{\widehat{\beta}} \\
-\left(-\Omega_{sgn}\Omega_r + \left(pS_\eta + rC_\eta\right) C_{\theta 1s} - \left(pC_\eta - rS_\eta\right) S_{\theta 1s}\right) C_{\widehat{\beta}}
\end{array} \right)^T \{\boldsymbol{E}_{\widehat{BL}}\} \\
&= \begin{pmatrix} \omega_{\widehat{BL}|X\widehat{BL}} & \omega_{\widehat{BL}|Y\widehat{BL}} & \omega_{\widehat{BL}|Z\widehat{BL}} \end{pmatrix} \{\boldsymbol{E}_{\widehat{BL}}\}
\end{aligned}
\tag{5.29}
$$

Finally, finding the expression for the blade element velocity starts with the definition of the position of the blade element in the blade reference frame as shown in eq. (5.30) where the blade element is located at a distance r_{BE} from the rotor hub along the $X_{\widehat{BL}}$-axis as defined by the blade element position vector.

$$
\boldsymbol{s}_{BE|\widehat{BL}} = \begin{pmatrix} r_{BE} & 0 & 0 \end{pmatrix} \{\boldsymbol{E}_{\widehat{BL}}\} \tag{5.30}
$$

The total linear velocity of the blade element is given by eq. (5.31) and consists of the linear hub velocity defined in the wind axis control plane and the linear velocity as a result of the total angular velocity of the blade reference frame and the offset between the blade element and the rotor hub. Once again the cross product is replaced by dot multiplication with $[\omega_{\widehat{BL}|\widehat{BL}}]_x$ given by eq. (5.32).

$$
\boldsymbol{V}_{BE} = \boldsymbol{V}_{hub|\widehat{CP}} + \boldsymbol{\omega}_{\widehat{BL}|\widehat{BL}} \times \boldsymbol{s}_{BE|\widehat{BL}} = \begin{pmatrix} \widehat{V_{tc}} \\ 0 \\ \widehat{V_{pc}} - v_{in} \end{pmatrix}^T \{\boldsymbol{E}_{\widehat{CP}}\} + \begin{pmatrix} r_{BE} \\ 0 \\ 0 \end{pmatrix}^T [\boldsymbol{\omega}_{\widehat{BL}|\widehat{BL}}]_x \{\boldsymbol{E}_n\} \tag{5.31}
$$

$$
[\boldsymbol{\omega}_{\widehat{BL}|\widehat{BL}}]_x = \begin{bmatrix} 0 & \omega_{\widehat{BL}|Z\widehat{BL}} & -\omega_{\widehat{BL}|Y\widehat{BL}} \\ -\omega_{\widehat{BL}|Z\widehat{BL}} & 0 & \omega_{\widehat{BL}|X\widehat{BL}} \\ \omega_{\widehat{BL}|Y\widehat{BL}} & -\omega_{\widehat{BL}|X\widehat{BL}} & 0 \end{bmatrix} \tag{5.32}
$$

Transformed into the blade reference frame, the blade element total linear velocity is given by eq. (5.33). The expressions for the final blade element velocity components are substituted by the radial, tangential, and perpendicular velocity variables. It should be highlighted that the tangential component is additionally influenced by the Ω_{sgn} parameter in order for it to comply with the 'always positive' sign convention for the tangential blade element velocity component of a clockwise and counter-clockwise rotating rotor as presented graphically in fig. 5.5. Since the blade element velocity is derived in the wind axis blade reference frame (with the positive sign conventions of its components shown in fig. 5.4) which has its axes pointing in the same directions irrespective of the rotational direction of the rotor, in normal operation the expression for U_T would yield a positive value for a ccw-rotor, and a negative value for a cw-rotor. Since a positive value for the tangential velocity is expected by the 'always positive' sign convention, the expression for U_T must additionally be multiplied or divided by the Ω_{sgn} parameter in order to comply with the convention[1]. Note

[1]It should be noted that the division of U_T by the Ω_{sgn} parameter yields the same result as multiplying U_T with Ω_{sgn}. In this work, however, the division has been kept as it follows the course of the original discovery of the need for the Ω_{sgn} at this point in the derivation.

that the positive convention for the perpendicular velocity is the same for a cw and ccw rotor and therefore the Ω_{sgn} parameter is not needed for this component.

$$\begin{aligned}\boldsymbol{V}_{BE|\widehat{BL}} &= \begin{pmatrix} \widehat{V_{tc}} \\ 0 \\ \widehat{V_{pc}} - v_{in} \end{pmatrix}^T [\pi_Y][\widehat{\psi}][\widehat{\beta}]\{\boldsymbol{E}_{\widehat{BL}}\} + \begin{pmatrix} r_{BE} \\ 0 \\ 0 \end{pmatrix}^T [\boldsymbol{\omega}_{\widehat{BL}|\widehat{BL}}]_x \{\boldsymbol{E}_{\widehat{BL}}\} \\ &= \begin{pmatrix} \left(v_{in} - \widehat{V_{pc}}\right) S_{\widehat{\beta}} - C_{\widehat{\beta}} C_{\widehat{\psi}} \widehat{V_{tc}} \\ \Omega_{sgn} S_{\widehat{\psi}} \widehat{V_{tc}} \\ \left(v_{in} - \widehat{V_{pc}}\right) C_{\widehat{\beta}} + C_{\widehat{\psi}} S_{\widehat{\beta}} \widehat{V_{tc}} \end{pmatrix}^T \{\boldsymbol{E}_{\widehat{BL}}\} + \begin{pmatrix} 0 \\ r_{BE}\omega_{\widehat{BL}|Z\widehat{BL}} \\ -r_{BE}\omega_{\widehat{BL}|Y\widehat{BL}} \end{pmatrix}^T \{\boldsymbol{E}_{\widehat{BL}}\} \\ &= \begin{pmatrix} U_R \\ U_T/\Omega_{sgn} \\ U_P \end{pmatrix}^T \{\boldsymbol{E}_{\widehat{BL}}\} \end{aligned} \tag{5.33}$$

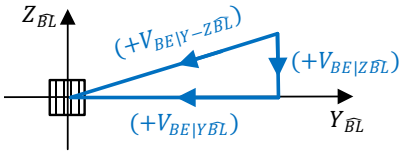

Figure 5.4: Positive sign conventions of the blade element velocity components along the $Y_{\widehat{BL}}$ and $Z_{\widehat{BL}}$ axes. Arrows indicate air velocity vectors.

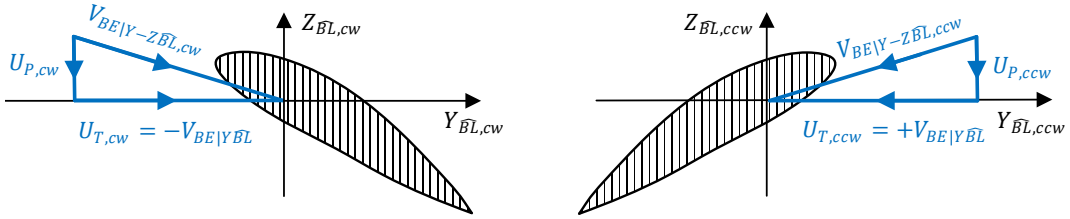

Figure 5.5: Positive sign conventions of the clockwise (cw) and counter-clockwise (ccw) rotating blade element tangential and perpendicular velocity components. Arrows indicate air velocity vectors.

Blade Element Velocity Analysis

The expanded radial U_R, tangential U_T, and perpendicular U_P velocity components experienced by the blade element are given by eq. (5.34a), eq. (5.34b), and eq. (5.34c) respectively. Although the radial component U_R shall not be used in the rotor derivation, a brief analysis reveals that it consists of a term that is multiplied by the cosine of the azimuthal position $\widehat{\psi}$ meaning that it periodically varies with the frequency of the rotating rotor, and an aperiodic term which does not vary as a function of the azimuthal position. The former consists of the tangential velocity experienced by the rotor hub, while the latter aperiodic term is a summation of the perpendicular rotor hub velocity and the rotor induced velocity. The entire expression does not depend on the radial position of the blade element which shall be shown not to be true for the tangential and perpendicular velocity components. In terms of the research question, the only effect of the tiltable nacelle is implicitly found within the rotor hub velocities as has already been described on page 121. It must also be noted that the radial component U_R does not include any Ω_{sgn} parameters therefore it is identical for both clockwise and counterclockwise rotating rotors which is not the case for the tangential and perpendicular components which shall be analyzed after the prior introduction of 'total' and 'effective' rates below which make performing the analysis easier.

$$U_R = \left(v_{in} - \widehat{V_{pc}}\right) S_{\widehat{\beta}} - \widehat{V_{tc}} C_{\widehat{\psi}} C_{\widehat{\beta}} \tag{5.34a}$$

$$
\begin{aligned}
U_T = \widehat{V_{tc}} S_{\widehat{\psi}} + r_{BE} \Big[& \Big(\Big[(pS_\eta + rC_\eta) S_{\theta 1s} + (pC_\eta - rS_\eta) C_{\theta 1s} \Big] S_\Delta - (q + \dot{\eta}) C_\Delta \Big) S_{\widehat{\psi}} S_{\widehat{\beta}} \\
& + \Omega_{sgn} \Big((q + \dot{\eta}) S_\Delta + \Big[(pS_\eta + rC_\eta) S_{\theta 1s} + (pC_\eta - rS_\eta) C_{\theta 1s} \Big] C_\Delta \Big) C_{\widehat{\psi}} S_{\widehat{\beta}} \\
& + \Big(\Omega + \Omega_{sgn} \Big[(pC_\eta - rS_\eta) S_{\theta 1s} - (pS_\eta + rC_\eta) C_{\theta 1s} \Big] \Big) C_{\widehat{\beta}} \Big]
\end{aligned}
\tag{5.34b}
$$

$$
\begin{aligned}
U_P = & \Big(v_{in} - \widehat{V_{pc}} \Big) C_{\widehat{\beta}} + \widehat{V_{tc}} C_{\widehat{\psi}} S_{\widehat{\beta}} \\
& + r_{BE} \Big[\dot{\widehat{\beta}} - \Omega_{sgn} \Big((q + \dot{\eta}) S_\Delta + \Big[(pS_\eta + rC_\eta) S_{\theta 1s} + (pC_\eta - rS_\eta) C_{\theta 1s} \Big] C_\Delta \Big) S_{\widehat{\psi}} \\
& \quad + \Big(\Big[(pS_\eta + rC_\eta) S_{\theta 1s} + (pC_\eta - rS_\eta) C_{\theta 1s} \Big] S_\Delta - (q + \dot{\eta}) C_\Delta \Big) C_{\widehat{\psi}} \Big]
\end{aligned}
\tag{5.34c}
$$

'Total' rates are defined to be instances where two rotational rates of independent origin act around the same axis and may be simply added together without invalidating the equations, allowing for the combination of these two rates to be substituted by a single 'total' rate variable improving the clarity of an expression. The only instances of 'total' rates in this tilt-rotor model are cases where the nacelle tilt rate $\dot{\eta}$ is directly added to the body pitch rate q, which are substituted by a single term referred to as the 'total' pitch rate q_{tot}. A similar substitution may also take place in the case of the nacelle tilt acceleration $\ddot{\eta}$ and body pitch acceleration $\dot{q}$ resulting in a 'total' pitch acceleration $\dot{q}_{tot}$, as shall be mentioned in the next section treating the derivation of the inertial terms of the flapping equation.

An 'effective' rate is the rotational rate experienced by the rotor from within its frame of reference, regardless of its current orientation with respect to the rest of the tilt-rotor body. For example an 'effective' roll rate p_{eff} experienced by an η-tilted rotor is equivalent to a non-tilted rotor (thus a rotor in helicopter configuration) experiencing a pure body roll rate p with the same magnitude. Therefore 'effective' rates correspond to relationships between body rates and trigonometric functions of the nacelle tilt angle η as seen in eq. (5.34) where the nacelle tilt angle can be observed to be the argument of trigonometric functions which serve the purpose of transforming the body roll and yaw angular rates into the shaft plane (which tilts together with the nacelle). As a result these rotational rates phase each other out as a function of η, e.g. $pcos(\eta) - rsin(\eta)$, however their combination yields an 'effective' roll rate p_{eff} as experienced by the rotor from within its tilting reference frame. Note that the rate multiplied by the cosine dictates the name of the effective rate since if η were set to zero (i.e. the rotor were in helicopter configuration), the trigonometric relationship would simplify to the roll rate p. The trigonometric relationship of such two rates may be substituted by a single 'effective' rate variable improving the clarity of an expression. A similar substitution may also take place in the case of trigonometric relationship between two rotational accelerations resulting in 'effective' accelerations. This too shall only be mentioned in the section treating the derivation of the inertial terms of the flapping equation.

Substituting all relevant combinations of body rates, the nacelle rate, and the nacelle tilt angle in eqs. (5.34b) and (5.34c) by single 'total' and 'effective' rates yields simplified (in notation) expressions for the tangential and perpendicular blade element velocity components, as given by eq. (5.35), which are analyzed below. Note that the annotations below some of the terms correspond to a later stage of expression notation simplification

and therefore should be ignored for now.

$$
\begin{aligned}
U_T = \widehat{V_{tc}} S_{\widehat{\psi}} + r_{BE} \Bigg[& \underbrace{\left(\underbrace{\left[r_{eff} S_{\theta 1s} + p_{eff} C_{\theta 1s} \right]}_{p_{eff,\theta 1s}} S_\Delta - q_{tot} C_\Delta \right)}_{-q_{toteff,\theta 1s,\Delta}} S_{\widehat{\psi}} S_{\widehat{\beta}} \\
& + \Omega_{sgn} \underbrace{\left(q_{tot} S_\Delta + \underbrace{\left[r_{eff} S_{\theta 1s} + p_{eff} C_{\theta 1s} \right]}_{p_{eff,\theta 1s}} C_\Delta \right)}_{p_{toteff,\theta 1s,\Delta}} C_{\widehat{\psi}} S_{\widehat{\beta}} \\
& + \left(\Omega + \Omega_{sgn} \underbrace{\left[p_{eff} S_{\theta 1s} - r_{eff} C_{\theta 1s} \right]}_{-r_{eff,\theta 1s}} \right) C_{\widehat{\beta}} \Bigg]
\end{aligned}
\tag{5.35a}
$$

$$
\begin{aligned}
U_P = & \left(v_{in} - \widehat{V_{pc}} \right) C_{\widehat{\beta}} + \widehat{V_{tc}} C_{\widehat{\psi}} S_{\widehat{\beta}} \\
& + r_{BE} \Bigg[\dot{\widehat{\beta}} - \Omega_{sgn} \underbrace{\left(q_{tot} S_\Delta + \underbrace{\left[r_{eff} S_{\theta 1s} + p_{eff} C_{\theta 1s} \right]}_{p_{eff,\theta 1s}} C_\Delta \right)}_{p_{toteff,\theta 1s,\Delta}} S_{\widehat{\psi}} \\
& + \underbrace{\left(\underbrace{\left[r_{eff} S_{\theta 1s} + p_{eff} C_{\theta 1s} \right]}_{p_{eff,\theta 1s}} S_\Delta - q_{tot} C_\Delta \right)}_{-q_{toteff,\theta 1s,\Delta}} C_{\widehat{\psi}} \Bigg]
\end{aligned}
\tag{5.35b}
$$

Starting with the visual inspection of the tangential blade element velocity component U_T it can be see that it consists of periodic and aperiodic terms, where the latter contains the rotor rotational rate Ω which indeed should not depend on the azimuthal position. The only radial-independent term in this expression is the rotor hub tangential velocity $\widehat{V}_{tc}$ while all other terms depend on the radial position of the blade element (r_{BE}) and consist of body effective rates, total pitch rates, and the rotor angular velocity Ω, all multiplied by one or more trigonometric function of the azimuthal position and flapping angle. Answering a portion of the research sub-question concerned with the effect of the tiltable proprotor on the blade element velocity components, two instances of the total pitch rate (i.e the nacelle tilt rate being simply added to body pitch rate) can be observed. Recalling that instances of the body pitch rate also exist within the tangential rotor hub velocity component, however, it may not be concluded that the body pitch rate and nacelle tilt rate may be simply added together in the entire U_T expression.

Visually inspecting the perpendicular blade element velocity component U_P it can be see that it also consists of periodic and aperiodic terms, where the latter consists of the rotor hub perpendicular velocity $\widehat{V}_{pc}$, the rotor induced velocity v_{in}, and the blade flapping rate $\dot{\widehat{\beta}}$. Apart from the perpendicular hub velocity, U_P also depends on the tangential hub velocity component $\widehat{V}_{tc}$ which has a periodic influence on U_P. Both rotor hub velocities as well as the rotor induced velocity are the only radial-independent terms, while all other terms depend on the radial position along the blade and consist of body effective rates and total pitch rates multiplied by trigonometric functions of the azimuthal position only (as opposed to the additional multiplication with trigonometric functions of $\widehat{\beta}$ in the case of U_T), and the mentioned aperiodic flapping

rate $\dot{\widehat{\beta}}$. Note that in contrast to the U_T expression, all radial-independent terms within U_P are multiplied by a trigonometric function of the flapping angle. It must be highlighted, however, that the rotor induced velocity was assumed to be perpendicular to the (wind axis) control plane therefore the only transformation that takes place is through the $\widehat{\beta}$ angle, hence it is only multiplied by the cosine of $\widehat{\beta}$. Finally, addressing the remaining portion of the research sub-question concerned with the effect of the tiltable proprotor on the blade element velocity components, two instances of the total pitch rate q_{tot} can be observed within U_P. Once again, however, it may not be concluded that the body pitch rate and nacelle tilt rate may be simply added together in the entire U_P expression due to the presence of the body pitch rate within the rotor hub velocity components.

Similarly to the effective rates which depend on the nacelle tilt angle, it is possible to further simplify the expressions in an analogous manner considering relationships between rotational rates as trigonometric functions of the control plane deflection angle θ_{1s} and the wind shift angle Δ. Referring back to the annotations below several of the terms in eq. (5.35), it can be seen that the effective roll and yaw rates phase each other out as a function of θ_{1s}, e.g. $r_{eff}sin(\theta_{1s}) + p_{eff}cos(\theta_{1s})$, and their combination may be replaced an augmented 'effective' roll rate $p_{eff,\theta 1s}$. Such an augmented 'effective' roll rate $p_{eff,\theta 1s}$ experienced by an η-tilted rotor rotated with the θ_{1s} angle is equivalent to a non-rotated (but still) η-tilted rotor (thus an η-tilted rotor with no longitudinal swash plate input) experiencing an 'effective' roll rate p_{eff} with the same magnitude. The scope of the augmented roll rate may be further expanded by considering the relationships between the rates as trigonometric functions of the wind shift angle Δ which, for example, give rise to $p_{eff,\theta 1s,\Delta}$ which is equivalent to $q_{tot}sin(\Delta) + p_{eff,\theta_{1s}}cos(\Delta)$ as indicated by the annotations in eq. (5.35). Note that 'effective' accelerations as well as 'total' rates and accelerations may be augmented in a similar fashion.

It is of high importance to reiterated that the augmented and non-augmented 'total' and 'effective' rates (and accelerations) are useful in expression analysis since their role in the tilt-rotor expressions is analogous to the role of their pure body rate and acceleration counterparts in helicopter expressions (under the simplifying condition that the swashplate input and wind shift angle are set to zero which shall be employed in the analysis of some of the rotor expressions derived later). It should be mentioned that the analyses of these rotor expressions derived later shall only make use of the non-augmented 'total' and 'effective' rates. Nonetheless, the notation of the tangential and perpendicular blade element velocity component expressions is simplified one last time with the use of the augmented 'effective' and 'total' rates for demonstration purposes only as shown in eq. (5.36).

As a result of the employment of augmented 'effective' and 'total' rates, eq. (5.36) may become representative of the tangential and perpendicular blade element velocity component expressions of a helicopter (in longitudinal flight with no swashplate input) if all augmented rates were to be replaced by their pure body rate counterparts. It can also be clearly seen now that the Ω_{sgn} parameter is only multiplied by the augmented 'effective' roll $p_{toteff,\theta 1s,\Delta}$ and yaw $r_{eff,\theta 1s}$ rates, while the augmented 'effective' pitch rate is left unaffected.

$$U_T = \widehat{V_{tc}}S_{\widehat{\psi}} + r_{BE}\left[\left(\Omega_{sgn}p_{toteff,\theta 1s,\Delta}C_{\widehat{\psi}} - q_{toteff,\theta 1s,\Delta}S_{\widehat{\psi}}\right)S_{\widehat{\beta}} + \left(\Omega - \Omega_{sgn}r_{eff,\theta 1s}\right)C_{\widehat{\beta}}\right] \tag{5.36a}$$

$$U_P = \left(v_{in} - \widehat{V_{pc}}\right)C_{\widehat{\beta}} + \widehat{V_{tc}}C_{\widehat{\psi}}S_{\widehat{\beta}} + r_{BE}\left[\dot{\widehat{\beta}} - \Omega_{sgn}p_{toteff,\theta 1s,\Delta}S_{\widehat{\psi}} - q_{toteff,\theta 1s,\Delta}C_{\widehat{\psi}}\right] \tag{5.36b}$$

Having derived the blade element velocity components, it is now possible to continue with the derivation of the rotor model, starting with the portion of the flapping equation dependent on the inertial loads.

5.2.2. Flapping Equation - Inertial Terms

The flapping equation describes the (dynamic) flapping motion of the blade as it revolves around the shaft and, in the case of this model, is influenced by an inertial $M'_{BL|Y\widehat{R},i}$, aerodynamic $M_{BL|-Y\widehat{R},a}$, and spring $M_{BL|Y\widehat{R},S}$ moment only. Other forcing sources which are considered outside of the scope of this study, such as structural blade loads, are not incorporated. Furthermore, gravitational acceleration is also not included since it is assumed negligible in comparison to the other loads. A graphical summary of the mentioned moments and their direction of action is shown in fig. 5.6. Equating these moments to the blade flapping angular

acceleration $\ddot{\widehat{\beta}}$ and inertia I_{bl}, as presented in eq. (5.37), should yield a non-linear differential equation describing the flapping motion of the blade in the rotating frame. In order to solve the differential equation in a relatively straightforward manner, however, additional simplifications are made throughout the derivation in order to obtain a flapping equation that should ultimately take the form of a linear differential equation as shown in eq. (5.38) with c representing the (aerodynamic) damping gain, k representing the (inertial and aerodynamic) spring gain, and M_{ext} representing the (inertial and aerodynamic) excitation moment. If these simplifications were not to be applied, the differential equation would additionally contain terms such as $\sin(\widehat{\beta})$, $\widehat{\beta}^2$, or $\widehat{\beta}\dot{\widehat{\beta}}$ making it more difficult to solve.

$$\begin{aligned} I_{bl}\ddot{\widehat{\beta}} &= \sum \overset{+}{M}_{(-Y\widehat{R})} \\ &= M_{BL|-Y\widehat{R},a} - M_{BL|Y\widehat{R},s} - M'_{BL|Y\widehat{R},i} \end{aligned} \tag{5.37}$$

$$I_{bl}\ddot{\widehat{\beta}} + c\dot{\widehat{\beta}} + k\widehat{\beta} = M_{ext} \tag{5.38}$$

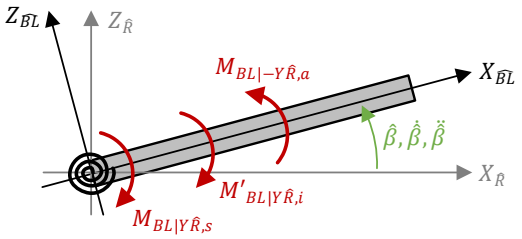

Figure 5.6: Direction of action of the inertial, aerodynamic, and spring moments on the flapping motion.

The flapping motion differential equation can be solved with the use of any appropriate technique used to solve these types of problems. In the case of this thesis work, only the averaged-per-revolution rotor forces and moments are desired, therefore only the steady state solution of the flapping equation is required for their determination (neglecting the transient flapping response and blade azimuth-varying rotor forces and moments). The disk tilt-approximation provides a compact solution for $\widehat{\beta}$ and therefore, considering that the analytical expressions for the rotor forces and moments are expected to already be extensive when defined in the rotating frame, it is chosen as the most appropriate solution option. A more elaborate explanation of the disk-tilt approximation and its implementation in the expressions is described later in its respective section. This section, on the other hand, describes the derivation of the inertial moment $M_{BL|Y\widehat{R},i}$, while the aerodynamic and spring flapping moments are also treated later. It should be noted that the inertial moment $M_{BL|Y\widehat{R},i}$ shall be derived such that it already contains $\ddot{\widehat{\beta}}$ and I_{bl}, therefore eq. (5.37) may be rearrange into the form of eq. (5.39).

$$-M_{BL|Y\widehat{R},i} = M_{BL|-Y\widehat{R},a} - M_{BL|Y\widehat{R},s} \quad \text{with} \quad M_{BL|Y\widehat{R},i} = -I_{bl}\ddot{\widehat{\beta}} - M'_{BL|Y\widehat{R},i} \tag{5.39}$$

Inertial Flapping Moment Expression Derivation

The inertial flapping moment $M_{BL|Y\widehat{R},i}$ is derived with Newtonian mechanics and obtained by integrating the inertial moment acting on the blade element ($dM_{BL|Y\widehat{R},i}$) around the $Y_{\widehat{R}}$-axis along the blade length as shown in eq. (5.40). Note that variables that correspond to inertial rates and accelerations are identified with the subscript i.

$$M_{BL|Y\widehat{R},i} = \int_0^R dM_{BL|Y\widehat{R},i}\, dr_{BE} \tag{5.40}$$

The inertial moment acting on the blade element is given by eq. (5.41). Here $d\boldsymbol{F}_{BL|\widehat{R},i}$ is the inertial force experienced by the blade element and $\boldsymbol{s}_{BE|\widehat{R}}$ is the position vector of the blade element, both defined in the wind axis rotating frame. The resulting differential inertial moment is the cross product between the position

vector and differential inertial load. The latter is given by eq. (5.42) where $\overline{m}$ is the distributed mass, i.e. the blade mass per length, and $\boldsymbol{a}_{BE|\widehat{R},i}$ is the acceleration of the blade element defined in the same rotating frame.

$$\begin{aligned} d\boldsymbol{M}_{BL|\widehat{R},i} &= \begin{pmatrix} dM_{BL|X\widehat{R},i} & dM_{BL|Y\widehat{R},i} & dM_{BL|Z\widehat{R},i} \end{pmatrix} \{\boldsymbol{E}_{\widehat{R}}\} \\ &= \boldsymbol{s}_{BE|\widehat{R}} \times d\boldsymbol{F}_{BL|\widehat{R},i} \\ &= \left[-\widehat{\beta}\right]^{-1} \boldsymbol{s}_{BE|\widehat{BL}} \quad \times \quad d\boldsymbol{F}_{BL|\widehat{R},i} \\ &= \begin{pmatrix} r_{BE}C_{\widehat{\beta}} & 0 & r_{BE}S_{\widehat{\beta}} \end{pmatrix} \{\boldsymbol{E}_{\widehat{R}}\} \times d\boldsymbol{F}_{BL|\widehat{R},i} \end{aligned} \tag{5.41}$$

$$d\boldsymbol{F}_{BL|\widehat{R},i} = \begin{pmatrix} dF_{BL|X\widehat{R},i} \\ dF_{BL|Y\widehat{R},i} \\ dF_{BL|Z\widehat{R},i} \end{pmatrix}^T \{\boldsymbol{E}_{\widehat{R}}\} = \overline{m}\,\boldsymbol{a}_{BE|\widehat{R},i} = \overline{m} \begin{pmatrix} a_{BE|X\widehat{R},i} \\ a_{BE|Y\widehat{R},i} \\ a_{BE|Z\widehat{R},i} \end{pmatrix}^T \{\boldsymbol{E}_{\widehat{R}}\} \tag{5.42}$$

The resulting expression for the differential blade inertial flapping moment is then given by eq. (5.43) and depicted in fig. 5.7. The differential flapping moment is defined to be positive along the $Y_{\widehat{R}}$-axis according to the right hand rule. As can be observed, the differential inertial flapping moment arises due to the longitudinal and vertical blade element inertial forces acting at a distance away from the flapping hinge. These inertial forces, in turn, are the result of the longitudinal and vertical acceleration of the blade element (when observed from the rotating frame $\{\boldsymbol{E}_{\widehat{R}}\}$), which in fact is the effect of the acceleration introduced by the rotating blade and the tilt-rotor body motion. In other words, the blade element may be considered a point (distributed) mass in inertial space, and its inertial force is the reaction to the change in its velocity vector caused by the motion of the rotor blade in inertial space. For this reason the inertial acceleration experienced by the blade element shall be derived next.

$$dM_{BL|Y\widehat{R},i} = r_{BE}\overline{m}\left(S_{\widehat{\beta}}a_{BE|X\widehat{R},i} - C_{\widehat{\beta}}a_{BE|Z\widehat{R},i}\right) \tag{5.43}$$

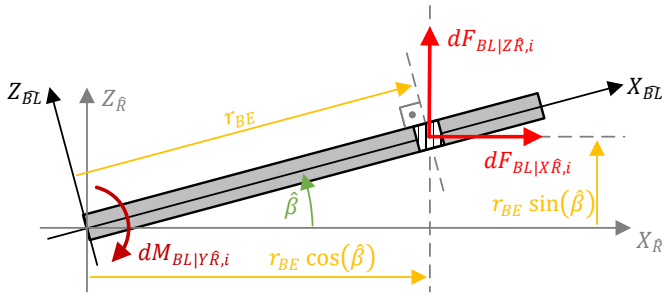

Figure 5.7: Contribution of the inertial forces acting on blade element to the inertial flapping moment.

The acceleration vector of the blade element will be derived in a cascaded manner, similarly to the blade element velocity and involving the same reference frames already depicted in fig. 5.3. The process consists of first obtaining the acceleration of the origin of a reference frame, and then obtaining the acceleration of a specific point in that reference frame. This cascaded process is summarized in eq. (5.44) where the subscript O refers to the origin of the reference frame indicated by the preceding letter in the subscript. All involved rotational transformations and offsets are indicated under the transformation arrows. It can be seen that the derivation will start with the acceleration of the body $\boldsymbol{a}_{bO,i}$ from which the acceleration of the nacelle pivot point $\boldsymbol{a}_{nO,i}$ will be found, first defined in the body frame, then transformed into the nacelle frame. Next the acceleration of the hub $\boldsymbol{a}_{\widehat{R}O,i}$ will be determined in the nacelle frame and transformed into the rotating wind axis frame to finally arrive at the acceleration of the blade element $\boldsymbol{a}_{BE,i}$ defined in the same rotating frame.

$$\boldsymbol{a}_{bO,i}\{\boldsymbol{E}_b\} \underset{\boldsymbol{s}_{nO|b}}{\rightarrow} \boldsymbol{a}_{nO,i}\{\boldsymbol{E}_b\} \underset{\eta}{\rightarrow} \boldsymbol{a}_{nO,i}\{\boldsymbol{E}_n\} \underset{l_n}{\rightarrow} \boldsymbol{a}_{\widehat{R}O,i}\{\boldsymbol{E}_n\} \underset{\theta_{1s},\Delta,\pi,\widehat{\psi}}{\rightarrow} \boldsymbol{a}_{\widehat{R}O,i}\{\boldsymbol{E}_{\widehat{R}}\} \underset{\boldsymbol{r}_{BE}}{\rightarrow} \boldsymbol{a}_{BE,i}\{\boldsymbol{E}_{\widehat{R}}\} \tag{5.44}$$

All of the involved reference frames are non-inertial and rotating, therefore eq. (5.45) must be used to obtain the expression for the acceleration of the points of interest in these rotating frames, defined in the rotating frame system. Here $\boldsymbol{s}$ is the position vector of the point of interest, defined in the rotating frame, and $\boldsymbol{\omega}_i$ is the pseudo-vector describing the inertial rotational velocity components of the rotating frame, also defined in the rotating frame.

$$\boldsymbol{a}_{\text{point,i}} = \ddot{\boldsymbol{s}}_{\text{point}} + 2\boldsymbol{\omega}_i \times \dot{\boldsymbol{s}}_{\text{point}} + \dot{\boldsymbol{\omega}}_i \times \boldsymbol{s}_{\text{point}} + \boldsymbol{\omega}_i \times (\boldsymbol{\omega}_i \times \boldsymbol{s}_{\text{point}}) + \boldsymbol{a}_{\text{origin,i}} \tag{5.45}$$

The tilt-rotor body acceleration, i.e. the acceleration of the body frame origin, will be calculated at every step of the simulation therefore the derivation may begin by determining the acceleration of nacelle frame origin $\boldsymbol{a}_{nO,i}$, i.e. the nacelle pivot point, defined in the body frame. The required position, rotational velocity, and acceleration vectors are given in eq. (5.46).

$$\boldsymbol{s}_{nO|b} = \begin{pmatrix} -d_{xn} & d_{sgn} d_{yn} & -d_{zn} \end{pmatrix} \{\boldsymbol{E}_b\} \tag{5.46a}$$
$$\dot{\boldsymbol{s}}_{nO|b} = \ddot{\boldsymbol{s}}_{nO|b} = \boldsymbol{0} \tag{5.46b}$$
$$\boldsymbol{\omega}_{b|b,i} = \begin{pmatrix} p_i & q_i & r_i \end{pmatrix} \{\boldsymbol{E}_b\} \tag{5.46c}$$
$$\dot{\boldsymbol{\omega}}_{b|b,i} = \begin{pmatrix} \dot{p}_i & \dot{q}_i & \dot{r}_i \end{pmatrix} \{\boldsymbol{E}_b\} \tag{5.46d}$$
$$\boldsymbol{a}_{bO|b,i} = \begin{pmatrix} \dot{u}_i & \dot{v}_i & \dot{w}_i \end{pmatrix} \{\boldsymbol{E}_b\} \tag{5.46e}$$

Plugging in the above position and angular velocity vectors, along with their derivatives and the acceleration of the origin into eq. (5.45) yields the worked out acceleration of the nacelle pivot point defined in the body frame as given by eq. (5.47). For notation compactness the components of this acceleration vector are replaced by single variable names representing the acceleration of the nacelle pivot point as denoted by the subscript *pvt*.

$$\begin{aligned} \boldsymbol{a}_{nO|b,i} &= \ddot{\boldsymbol{s}}_{nO|b} + 2\boldsymbol{\omega}_{b|b,i} \times \dot{\boldsymbol{s}}_{nO|b} + \dot{\boldsymbol{\omega}}_{b|b,i} \times \boldsymbol{s}_{nO|b} + \boldsymbol{\omega}_{b|b,i} \times (\boldsymbol{\omega}_{b|b,i} \times \boldsymbol{s}_{nO|b}) + \boldsymbol{a}_{bO|b,i} \\ &= \begin{pmatrix} -\dot{q}_i d_{zn} - \dot{r}_i d_{sgn} d_{yn} + q_i \left(p_i d_{sgn} d_{yn} + q_i d_{xn}\right) - r_i \left(p_i d_{zn} - r_i d_{xn}\right) + \dot{u}_i \\ \dot{p}_i d_{zn} - \dot{r}_i d_{xn} - p_i \left(p_i d_{sgn} d_{yn} + q_i d_{xn}\right) + r_i \left(-q_i d_{zn} - r_i d_{sgn} d_{yn}\right) + \dot{v}_i \\ \dot{p}_i d_{sgn} d_{yn} + \dot{q}_i d_{xn} + p_i \left(p_i d_{zn} - r_i d_{xn}\right) - q_i \left(-q_i d_{zn} - r_i d_{sgn} d_{yn}\right) + \dot{w}_i \end{pmatrix}^T \{\boldsymbol{E}_b\} \\ &= \begin{pmatrix} a_{\text{pvt}|Xb,i} & a_{\text{pvt}|Yb,i} & a_{\text{pvt}|Zb,i} \end{pmatrix} \{\boldsymbol{E}_b\} \end{aligned} \tag{5.47}$$

The next step is to determine the acceleration of the wind axis rotating frame origin $\boldsymbol{a}_{\widehat{RO},i}$, which coincides with the rotor hub and is defined in the nacelle frame. The required position, rotational velocity, and acceleration vectors which will be fed once again into eq. (5.45) are given in eq. (5.48). Note that eq. (5.48c) is a modified version of eq. (5.14) (introduced in the derivation of the blade element velocity components) where the total rotational body rates are substituted by their inertial counterparts. Also note that the nacelle origin acceleration vector must be first transformed from the body frame into the nacelle frame with the use of the $[\eta]$ transformation matrix as defined in eq. (5.13).

$$\boldsymbol{s}_{\widehat{RO}|n} = \begin{pmatrix} 0 & 0 & -l_n \end{pmatrix} \{\boldsymbol{E}_n\} \tag{5.48a}$$
$$\dot{\boldsymbol{s}}_{\widehat{RO}|n} = \ddot{\boldsymbol{s}}_{\widehat{RO}|n} = \boldsymbol{0} \tag{5.48b}$$
$$\boldsymbol{\omega}_{n|n,i} = \begin{pmatrix} p_i C_\eta - r_i S_\eta & q_i + \dot{\eta} & p_i S_\eta + r_i C_\eta \end{pmatrix} \{\boldsymbol{E}_n\} \tag{5.48c}$$
$$\dot{\boldsymbol{\omega}}_{n|n,i} = \begin{pmatrix} \dot{p}_i C_\eta - p_i \dot{\eta} S_\eta - \dot{r}_i S_\eta - r_i \dot{\eta} C_\eta & \dot{q}_i + \ddot{\eta} & \dot{p}_i S_\eta + p_i \dot{\eta} C_\eta + \dot{r}_i C_\eta - r_i \dot{\eta} S_\eta \end{pmatrix} \{\boldsymbol{E}_n\} \tag{5.48d}$$
$$\boldsymbol{a}_{nO|n,i} = \begin{pmatrix} a_{\text{pvt}|Xb,i} \\ a_{\text{pvt}|Yb,i} \\ a_{\text{pvt}|Zb,i} \end{pmatrix}^T [\eta] \{\boldsymbol{E}_n\} = \begin{pmatrix} a_{\text{pvt}|Xb,i} C_\eta - a_{\text{pvt}|Zb,i} S_\eta \\ a_{\text{pvt}|Yb,i} \\ a_{\text{pvt}|Xb,i} S_\eta + a_{\text{pvt}|Zb,i} C_\eta \end{pmatrix}^T \{\boldsymbol{E}_n\} \tag{5.48e}$$

Plugging in the above into eq. (5.45) yields the worked out acceleration of the rotor hub defined in the nacelle frame is given by eq. (5.49). Once again for the sake of notation compactness the acceleration components of the hub are replaced by single variable names with the use of the *hub* subscript.

$$\begin{aligned}\boldsymbol{a}_{\widehat{R}O|n,i} &= \ddot{\boldsymbol{s}}_{\widehat{R}O|n} + 2\boldsymbol{\omega}_{n|n,i} \times \dot{\boldsymbol{s}}_{\widehat{R}O|n} + \dot{\boldsymbol{\omega}}_{n|n,i} \times \boldsymbol{s}_{\widehat{R}O|n} + \boldsymbol{\omega}_{n|n,i} \times (\boldsymbol{\omega}_{n|n,i} \times \boldsymbol{s}_{\widehat{R}O|n}) + \boldsymbol{a}_{nO|n,i} \\ &= \begin{pmatrix} \left(-\dot{q}_i - \ddot{\eta} - {p_i}^2 C_\eta\, S_\eta - 2\, p_i\, r_i\, {C_\eta}^2 + {r_i}^2 C_\eta\, S_\eta + p_i\, r_i\right) l_n + C_\eta\, a_{\text{pvt}|Xb,i} - a_{\text{pvt}|Zb,i}\, S_\eta \\ \left(\dot{p}_i C_\eta - \dot{r}_i S_\eta - 2\,\dot{\eta}\, p_i\, S_\eta - 2\,\dot{\eta}\, r_i\, C_\eta - p_i\, q_i\, S_\eta - q_i\, r_i\, C_\eta\right) l_n + a_{\text{pvt}|Yb,i} \\ \left({p_i}^2 {C_\eta}^2 - 2\, p_i\, r_i\, C_\eta\, S_\eta - {r_i}^2 {C_\eta}^2 + \dot{\eta}^2 + 2\,\dot{\eta}\, q_i + {q_i}^2 + {r_i}^2\right) l_n + C_\eta\, a_{\text{pvt}|Zb,i} + a_{\text{pvt}|Xb,i}\, S_\eta \end{pmatrix}^T \{\boldsymbol{E}_n\} \\ &= \begin{pmatrix} a_{\text{hub}|Xn,i} & a_{\text{hub}|Yn,i} & a_{\text{hub}|Zn,i} \end{pmatrix} \{\boldsymbol{E}_n\}\end{aligned} \tag{5.49}$$

Finally it is possible to determine the acceleration of the blade element $\boldsymbol{a}_{BE,i}$ defined in the wind axis rotating frame. The required position, rotational velocity, and acceleration vectors are given in eq. (5.50). It should be mentioned at this point that the first and second derivatives of the blade element position, i.e. $\dot{\boldsymbol{s}}_{BE|\widehat{R}}$ and $\ddot{\boldsymbol{s}}_{BE|\widehat{R}}$, introduce the flapping rate $\dot{\widehat{\beta}}$ into the expression for the blade element acceleration. Interestingly, the flapping rate shall not have an effect on the inertial flapping moment as shall be shown later. Equation (5.50d) is a modified version of eq. (5.26) (also introduced in the derivation of the blade element velocity components) where, again, the total rotational body rates are substituted by their inertial counterparts. For the sake of notation compactness the components of the wind axis rotating frame angular velocity and angular acceleration pseudo-vectors have been replaced by single variable names (e.g. $\omega_{\widehat{R}|X\widehat{R},i}$). On that note, the angular velocity of the rotating frame around the $Z_{\widehat{R}}$-axis (i.e. $\omega_{\widehat{R}|Z\widehat{R},i}$) shall also be referred to as the total inertial rotor rotational rate $\Omega_{tot,i}$ with the hopes of improving clarity in the explanation of the obtention of the derivative of the blade azimuthal position as described next.

In the expression for the derivative of the rotational velocity, i.e. eq. (5.50e), the derivative of the blade azimuthal position $\dot{\widehat{\psi}}$ is not replaced by the nominal rotor rotational rate Ω but instead by $\Omega_{sgn}\Omega_{tot,i}$ since the derivative of the azimuthal blade position not only depends on the rotor rotational rate Ω, but also on the body rates as well. To possibly further clarify this, it should be remembered that the blade azimuthal position is not measured from an inertial frame, but from the $\{\boldsymbol{E}_{\widehat{NR}}\}$ frame which, despite its name, is in fact rotating together with the body. Only the resultant of the rotor rate Ω and the body rates shall yield the true derivative of the azimuthal blade position $\dot{\widehat{\psi}}$ with respect to inertial space. As an example a theoretical limit case may be considered where, in helicopter mode, the body yaw rate r_i is set equal in magnitude but opposite in direction to the rotor rotational rate Ω. In this case the resultant derivative of the azimuthal blade position $\dot{\widehat{\psi}}$ with respect to inertial space would be equal to zero, i.e. from the perspective of an inertial observer the blade would remain stationary.

Similarly to the case of the 'always positive' convention for the tangential blade element velocity, in normal operation $\dot{\widehat{\psi}}$ is also expected to be positive for both the clockwise and counter-clockwise rotating blade element. However, since the body rate $\Omega_{tot,i}$ is defined in the rotating frame $\{\boldsymbol{E}_{\widehat{R}}\}$ which has its axes pointing in the same direction irrespective of the direction of rotation of the rotor, the substitution $\dot{\widehat{\psi}} = \Omega_{tot,i}$ would yield a positive value for a ccw rotor, and a negative value for a cw rotor. Since a positive value for $\dot{\widehat{\psi}}$ is expected by the 'always positive' sign convention in this case as well, the expression for $\Omega_{tot,i}$ must additionally be multiplied (or divided) by the Ω_{sgn} parameter in order to comply with the convention.

Finally note that the acceleration vector of the rotating frame origin must first be transformed from the nacelle frame into the wind axis rotating frame with the use of the $[-\theta_{1s}]$, $[\Delta]$, $[\pi_Y]$, and $[\widehat{\psi}]$ transformation matrices defined in eqs. (5.18), (5.20), (5.23) and (5.24) respectively. The components of this acceleration vector have also been replaced by single variable names for notation compactness.

$$\boldsymbol{s}_{BE|\widehat{R}} = \begin{pmatrix} r_{BE} C_{\widehat{\beta}} & 0 & r_{BE} S_{\widehat{\beta}} \end{pmatrix} \{\boldsymbol{E}_{\widehat{R}}\} \tag{5.50a}$$

$$\dot{\boldsymbol{s}}_{BE|\widehat{R}} = \begin{pmatrix} -r_{BE}\dot{\widehat{\beta}} S_{\widehat{\beta}} & 0 & r_{BE}\dot{\widehat{\beta}} C_{\widehat{\beta}} \end{pmatrix} \{\boldsymbol{E}_{\widehat{R}}\} \tag{5.50b}$$

$$\ddot{\boldsymbol{s}}_{BE|\widehat{R}} = \begin{pmatrix} -r_{BE}\ddot{\widehat{\beta}}S_{\widehat{\beta}} - r_{BE}\dot{\widehat{\beta}}^2 C_{\widehat{\beta}} & 0 & r_{BE}\ddot{\widehat{\beta}}C_{\widehat{\beta}} - r_{BE}\dot{\widehat{\beta}}^2 S_{\widehat{\beta}} \end{pmatrix} \{\boldsymbol{E}_{\widehat{R}}\} \tag{5.50c}$$

$$\boldsymbol{\omega}_{\widehat{R}|\widehat{R},i} = \begin{pmatrix} \left(S_{\widehat{\psi}}\ (q_i + \dot{\eta})\,\Omega_{sgn} - \left(\left(p_i\,C_\eta - r_i\,S_\eta\right)C_{\theta 1s} + S_{\theta 1s}\ \left(p_i\,S_\eta + r_i\,C_\eta\right)\right)C_{\widehat{\psi}}\right)C_\Delta \\ -S_\Delta\left(\left(\left(p_i\,C_\eta - r_i\,S_\eta\right)C_{\theta 1s} + S_{\theta 1s}\ \left(p_i\,S_\eta + r_i\,C_\eta\right)\right)S_{\widehat{\psi}}\,\Omega_{sgn} + C_{\widehat{\psi}}\ (q_i + \dot{\eta})\right) \\ \hdashline \left(\left(\left(p_i\,C_\eta - r_i\,S_\eta\right)C_{\theta 1s} + S_{\theta 1s}\ \left(p_i\,S_\eta + r_i\,C_\eta\right)\right)S_{\widehat{\psi}}\,\Omega_{sgn} + C_{\widehat{\psi}}\ (q_i + \dot{\eta})\right)C_\Delta \\ -\left(-S_{\widehat{\psi}}\ (q_i + \dot{\eta})\,\Omega_{sgn} + \left(\left(p_i\,C_\eta - r_i\,S_\eta\right)C_{\theta 1s} + S_{\theta 1s}\ \left(p_i\,S_\eta + r_i\,C_\eta\right)\right)C_{\widehat{\psi}}\right)S_\Delta \\ \hdashline C_\eta\,S_{\theta 1s}\,p_i - S_\eta\,C_{\theta 1s}\,p_i - C_\eta\,C_{\theta 1s}\,r_i - S_\eta\,S_{\theta 1s}\,r_i + \Omega_{sgn}\,\Omega \end{pmatrix}^T \{\boldsymbol{E}_{\widehat{R}}\}$$

$$= \begin{pmatrix} \omega_{\widehat{R}|X\widehat{R},i} & \omega_{\widehat{R}|Y\widehat{R},i} & \omega_{\widehat{R}|Z\widehat{R},i} \end{pmatrix} \{\boldsymbol{E}_{\widehat{R}}\}$$

$$= \begin{pmatrix} \omega_{\widehat{R}|X\widehat{R},i} & \omega_{\widehat{R}|Y\widehat{R},i} & \Omega_{tot,i} \end{pmatrix} \{\boldsymbol{E}_{\widehat{R}}\} \tag{5.50d}$$

$$\dot{\boldsymbol{\omega}}_{\widehat{R}|\widehat{R},i} = \begin{pmatrix} \left[\left(\left(p_i\,C_\eta - r_i\,S_\eta\right)C_{\theta 1s} + S_{\theta 1s}\ \left(p_i\,S_\eta + r_i\,C_\eta\right)\right)\Omega_{tot,i} + \dot{q} + \dot{\eta}\right]S_{\widehat{\psi}}\,\Omega_{sgn}C_\Delta \\ +\Big[\ (q_i + \dot{\eta})\,\Omega_{tot,i} + \left(\left(\dot{\eta}\,r_i - \dot{p}\right)C_\eta + S_\eta\ \left(\dot{\eta}\,p_i + \dot{r}\right)\right)C_{\theta 1s} \\ -\left(\left(\dot{\eta}\,p_i + \dot{r}\right)C_\eta + S_\eta\ \left(-\dot{\eta}\,r_i + \dot{p}\right)\right)S_{\theta 1s}\Big]C_{\widehat{\psi}}C_\Delta \\ +S_{\widehat{\psi}}\Big[\ (q_i + \dot{\eta})\,\Omega_{tot,i} + \left(\left(\dot{\eta}\,r_i - \dot{p}\right)C_\eta + S_\eta\ \left(\dot{\eta}\,p_i + \dot{r}\right)\right)C_{\theta 1s} \\ -\left(\left(\dot{\eta}\,p_i + \dot{r}\right)C_\eta + S_\eta\ \left(-\dot{\eta}\,r_i + \dot{p}\right)\right)S_{\theta 1s}\Big]\Omega_{sgn}S_\Delta \\ -\Big[\left(\left(p_i\,C_\eta - r_i\,S_\eta\right)C_{\theta 1s} + S_{\theta 1s}\ \left(p_i\,S_\eta + r_i\,C_\eta\right)\right)\Omega_{tot,i} + \dot{q} + \ddot{\eta}\Big]C_{\widehat{\psi}}S_\Delta \\ \hdashline -\Big[\ (q_i + \dot{\eta})\,\Omega_{tot,i} + \left(\left(\dot{\eta}\,r_i - \dot{p}_i\right)C_\eta + S_\eta\ \left(\dot{\eta}\,p_i + \dot{r}_i\right)\right)C_{\theta 1s} \\ -\left(\left(\dot{\eta}\,p_i + \dot{r}_i\right)C_\eta + S_\eta\ \left(-\dot{\eta}\,r_i + \dot{p}_i\right)\right)S_{\theta 1s}\Big]S_{\widehat{\psi}}\Omega_{sgn}C_\Delta \\ +\Big[\left(\left(p_i\,C_\eta - r_i\,S_\eta\right)C_{\theta 1s} + S_{\theta 1s}\ \left(p_i\,S_\eta + r_i\,C_\eta\right)\right)\Omega_{tot,i} + \dot{q}_i + \ddot{\eta}\Big]\,C_{\widehat{\psi}}C_\Delta \\ +\Big[\left(\left(p_i\,C_\eta - r_i\,S_\eta\right)C_{\theta 1s} + S_{\theta 1s}\ \left(p_i\,S_\eta + r_i\,C_\eta\right)\right)\Omega_{tot,i} + \dot{q}_i + \ddot{\eta}\Big]S_{\widehat{\psi}}\,\Omega_{sgn}S_\Delta \\ +\Big[\ (q_i + \dot{\eta})\,\Omega_{tot,i} + \left(\left(\dot{\eta}\,r_i - \dot{p}_i\right)C_\eta + S_\eta\ \left(\dot{\eta}\,p_i + \dot{r}_i\right)\right)C_{\theta 1s} \\ -\left(\left(\dot{\eta}\,p_i + \dot{r}_i\right)C_\eta + S_\eta\ \left(-\dot{\eta}\,r_i + \dot{p}_i\right)\right)S_{\theta 1s}\Big]C_{\widehat{\psi}}S_\Delta \\ \hdashline \left(\left(-\dot{\eta}\,p_i - \dot{r}_i\right)C_\eta - S_\eta\ \left(-\dot{\eta}\,r_i + \dot{p}_i\right)\right)C_{\theta 1s} \\ +\left(\left(-\dot{\eta}\,r_i + \dot{p}_i\right)C_\eta - S_\eta\ \left(\dot{\eta}\,p_i + \dot{r}_i\right)\right)S_{\theta 1s} + \Omega_{sgn}\,\dot{\Omega} \end{pmatrix}^T \{\boldsymbol{E}_{\widehat{R}}\}$$

$$= \begin{pmatrix} \dot{\omega}_{\widehat{R}|X\widehat{R},i} & \dot{\omega}_{\widehat{R}|Y\widehat{R},i} & \dot{\omega}_{\widehat{R}|Z\widehat{R},i} \end{pmatrix} \{\boldsymbol{E}_{\widehat{R}}\} \tag{5.50e}$$

$$\boldsymbol{a}_{\widehat{R}O|\widehat{R},i} = \begin{pmatrix} a_{\text{hub}|Xn,i} & a_{\text{hub}|Yn,i} & a_{\text{hub}|Zn,i} \end{pmatrix} [-\theta_{1s}][\Delta][\pi_Y][\widehat{\psi}]\{\boldsymbol{E}_{\widehat{R}}\}$$

$$= \begin{pmatrix} \left(a_{\text{hub}|Yn,i}\,S_{\widehat{\psi}}\,\Omega_{sgn} - C_{\widehat{\psi}}\ \left(a_{\text{hub}|Xn,i}\,C_{\theta 1s} + a_{\text{hub}|Zn,i}\,S_{\theta 1s}\right)\right)C_\Delta \\ -\left(S_{\widehat{\psi}}\ \left(a_{\text{hub}|Xn,i}\,C_{\theta 1s} + a_{\text{hub}|Zn,i}\,S_{\theta 1s}\right)\Omega_{sgn} + a_{\text{hub}|Yn,i}\,C_{\widehat{\psi}}\right)S_\Delta \\ \hdashline \left(S_{\widehat{\psi}}\ \left(a_{\text{hub}|Xn,i}\,C_{\theta 1s} + a_{\text{hub}|Zn,i}\,S_{\theta 1s}\right)\Omega_{sgn} + a_{\text{hub}|Yn,i}\,C_{\widehat{\psi}}\right)C_\Delta \\ -S_\Delta\left(-a_{\text{hub}|Yn,i}\,S_{\widehat{\psi}}\,\Omega_{sgn} + C_{\widehat{\psi}}\ \left(a_{\text{hub}|Xn,i}\,C_{\theta 1s} + a_{\text{hub}|Zn,i}\,S_{\theta 1s}\right)\right) \\ \hdashline a_{\text{hub}|Xn,i}\,S_{\theta 1s} - a_{\text{hub}|Zn,i}\,C_{\theta 1s} \end{pmatrix}^T \{\boldsymbol{E}_{\widehat{R}}\} \tag{5.50f}$$

$$= \begin{pmatrix} a_{\text{hub}|X\widehat{R},i} & a_{\text{hub}|Y\widehat{R},i} & a_{\text{hub}|Z\widehat{R},i} \end{pmatrix} \{\boldsymbol{E}_{\widehat{R}}\}$$

The fully worked out expression for the acceleration of the blade element will not be shown due to its length, however it would be obtained with eq. (5.51) yielding the necessary $a_{BE|X\widehat{R},i}$ and $a_{BE|Z\widehat{R},i}$ acceleration

components mentioned in eq. (5.43) in order to obtain the differential inertial flapping moment. What is important to note is that the blade element acceleration does not contain any pure $\widehat{\beta}$ terms; instead only the flapping angular rate $\dot{\widehat{\beta}}$, acceleration $\ddot{\widehat{\beta}}$, and trigonometric functions of $\widehat{\beta}$ are present. This information shall aid the analysis of the inertial moment later.

$$\begin{aligned}\boldsymbol{a}_{BE|\widehat{R},i} &= \ddot{\boldsymbol{s}}_{BE|\widehat{R}} + 2\boldsymbol{\omega}_{\widehat{R}|\widehat{R},i} \times \dot{\boldsymbol{s}}_{BE|\widehat{R}} + \dot{\boldsymbol{\omega}}_{\widehat{R}|\widehat{R},i} \times \boldsymbol{s}_{BE|\widehat{R}} + \boldsymbol{\omega}_{\widehat{R}|\widehat{R},i} \times (\boldsymbol{\omega}_{\widehat{R}|\widehat{R},i} \times \boldsymbol{s}_{BE|\widehat{R}}) + \boldsymbol{a}_{\widehat{R}O|\widehat{R},i} \\ &= \begin{pmatrix} a_{BE|X\widehat{R},i} & a_{BE|Y\widehat{R},i} & a_{BE|Z\widehat{R},i} \end{pmatrix} \{\boldsymbol{E}_n\}\end{aligned} \tag{5.51}$$

As a reminder, the differential flapping moment is obtained with eq. (5.43). The resulting expression for the differential flapping moment is extensive therefore it shall not be shown here, however it can be generalized to the form given by eq. (5.52) where A and B are not functions of $\overline{m}$ nor r_{BE}. For this reason A and B may be left outside of the integral as shown in eq. (5.53). Solving the remaining integrals yields the blade moment of inertia I_{bl} and blade first mass moment M_1. It should be added that only A contains the term $\ddot{\widehat{\beta}}$, and neither A nor B contains any pure $\widehat{\beta}$ or $\dot{\widehat{\beta}}$ terms. Although the latter is present in the components (i.e. the blade element acceleration) that constitute $dM_{BL|Y\widehat{R},i}$, resolving the expression (eq. (5.43)) results in a (trigonometric) cancellation of all of the $\dot{\widehat{\beta}}$ terms meaning that they do not contribute to the inertial flapping moment being derived at hand. The lack of any pure $\widehat{\beta}$ terms, on the other hand, is explained by the fact that these terms do not exist in the components that constitute the $dM_{BL|Y\widehat{R},i}$ expression, i.e. pure $\widehat{\beta}$ terms shall not be found in the blade element position vector nor acceleration. Instead, $\widehat{\beta}$ is only present as the argument to trigonometric functions, e.g. $sin(\widehat{\beta})$. Applying the small angle approximation to $\widehat{\beta}$ changes this as shall be shown next. Finally it should be mentioned that B consists of the components of the hub acceleration $\boldsymbol{a}_{\widehat{R}O|\widehat{R},i}$ and if this acceleration vector were to be equal to zero (or if the hub acceleration were to be neglected), B would equal to zero.

$$dM_{BL|Y\widehat{R},i} = r_{BE}\overline{m}\left(S_{\widehat{\beta}}a_{BE|X\widehat{R},i} - C_{\widehat{\beta}}a_{BE|Z\widehat{R},i}\right) \tag{5.43}$$

$$dM_{BL|Y\widehat{R},i} = A \cdot \left(r_{BE}^2\overline{m}\right) + B \cdot \left(r_{BE}\overline{m}\right) \tag{5.52}$$

$$M_{BL|Y\widehat{R},i} = \int_0^R dM_{BL|Y\widehat{R},i}\, dr_{BE} = A\int_0^R \left(r_{BE}^2\overline{m}\right)\, dr_{BE} + B\int_0^R \left(r_{BE}\overline{m}\right)\, dr_{BE} = A\, I_{bl} + B\, M_1 \tag{5.53}$$

Inertial Flapping Moment Expression Analysis

The complete expression for the inertial flapping moment is too long to show here, however its generalization presenting collections of terms grouped according to the derivatives of $\widehat{\beta}$ is provided in eq. (5.54a) with $M'_{BL|Y\widehat{R},i}$ from eq. (5.39) being defined in eq. (5.54b). It is important to mention that the small angle approximation is applied to $\widehat{\beta}$ at this point enabling the future compilation of the complete flapping equation into the form of a linear differential equation.

$$\begin{aligned}M_{BL|Y\widehat{R},i} &= -I_{bl}\ddot{\widehat{\beta}} - \left(A_{\widehat{\beta}}I_{bl} + B_{\widehat{\beta}}M_{1,bl}\right)\widehat{\beta} + A_{ext}I_{bl} + B_{ext}M_{1,bl} \\ &= -I_{bl}\ddot{\widehat{\beta}} + M'_{BL|Y\widehat{R},i}\end{aligned} \tag{5.54a}$$

$$M'_{BL|Y\widehat{R},i} = -\left(A_{\widehat{\beta}}I_{bl} + B_{\widehat{\beta}}M_{1,bl}\right)\widehat{\beta} + A_{ext}I_{bl} + B_{ext}M_{1,bl} \tag{5.54b}$$

First of all it should be observed that a group of terms multiplied by a pure $\widehat{\beta}$ term has emerged as a result of the application of the small angle approximation to $\widehat{\beta}$. These terms can be further subdivided into $A_{\widehat{\beta}}$ and $B_{\widehat{\beta}}$ which are multiplied by the blade flapping inertia and first mass moment respectively. Furthermore, apart from the B_{ext} group (multiplied by $M_{1,bl}$) that has already been (partially) identified in eq. (5.53),

an additional excitation moment appears due to the application of the small angle approximation to $cos(\widehat{\beta})$ terms, namely A_{ext} which is multiplied by the blade flapping inertia.

Similarly to the B group, both $B_{\widehat{\beta}}$ and B_{ext} consist of hub acceleration terms, and in the case that the hub does not accelerate both would be equal to zero. $A_{\widehat{\beta}}$ and A_{ext}, on the other hand, depend on the blade azimuthal position $\widehat{\psi}$, however $A_{\widehat{\beta}}$ contains only second harmonics (i.e. $sin(2\widehat{\psi})$ and $cos(2\widehat{\psi})$) while A_{ext} contains only the first harmonic (i.e $sin(\widehat{\psi})$ and $cos(\widehat{\psi})$). As shall be explained later, all higher harmonics will be ultimately neglected in the disk tilt approximation, therefore removing the higher harmonics at this point is permissible and results in an $A_{\widehat{\beta}}$ group that is independent of the blade azimuthal position. Furthermore, $A_{\widehat{\beta}}$ only contains body angular rates, the nacelle tilt rate $\dot{\eta}$, and the rotor rotational rate Ω, while A_{ext} additionally contains body angular accelerations and the nacelle tilt acceleration $\ddot{\eta}$.

An expanded but partially simplified version of the linearized inertial flapping moment expression is shown in eq. (5.55) which shall be used to address the first half of the research sub-question concerned with determining the effect of the tilting proprotor on the inertial terms of the flapping equation, albeit superficially, through visual inspection. Again, it should be remembered that this expression is simplified after the prior application of the small angle approximation to $\widehat{\beta}$. Both sides of the expression have been multiplied by a negative sign as well in order to match the sign convention used in eq. (5.39) which presented the sum of moments around the flapping hinge.

In order to obtain this reduced expression first the hub acceleration is set to zero resulting in the disappearance of the B group. Next all higher harmonics of $\widehat{\psi}$ are removed which, as already described above, yields an $A_{\widehat{\beta}}$ group that is independent of the blade azimuth position. Finally, the control plane deflection θ_{1s}, which has been introduced at the point of transformation of the body angular rates from the nacelle frame into the rotating frame (eq. (5.26)), and the wind axis shift angle Δ are set to zero as well in order to improve the clarity of the expression.

The θ_{1s} and Δ angles are not unique to tilt-rotors therefore their inclusion is not considered essential in a tilt-rotor analysis. It must be remembered, however, that these angles may form augmented 'total' and 'effective' rates, e.g. $p_{eff}cos(\theta_{1s}) + r_{eff}sin(\theta_{1s}) = p_{eff,\theta,1s}$, which have already been described in great detail on page 129. Since these augmented rates are functions of the nacelle tilt angle (e.g. $p_{eff} = pcos(\eta) - rsin(\eta)$ in the example above), the inclusion of the control plane deflection and wind shift angles does contribute to answering the research question concerned with the effect of the nacelle tilt angle on the rotor expressions, albeit in an indirect manner. Since the contribution of θ_{1s} and Δ may be narrowed down to the 'effective' rates described in this paragraph, however, their inclusion in the simplified expressions presented for further analysis is not only considered unnecessary, but even hindering. For this reason the control plane deflection and wind shift angles will also not be included in any other rotor expressions analyzed in this chapter and the motivation behind this decision shall not be repeated for the sake of brevity.

Equation (5.55a) has been arranged into three distinct groups indicated by the right-hand-side annotations, namely the inertia, centrifugal spring, and Coriolis effect groups. The centrifugal spring group is equivalent to the $A_{\widehat{\beta}}$ term introduced in the generalized inertial moment expression shown in eq. (5.54a). On the other hand, apart from the flapping angular acceleration $\ddot{\widehat{\beta}}$, the inertia group additionally contains all the body angular acceleration terms which are part of the A_{ext} group, while the remaining terms form the Coriolis effect groups. The latter is subdivided into the roll-yaw, pitch-yaw, and tilt-yaw Coriolis sources.

In order to aid the inspection, eq. (5.55a) is further reduced by setting the nacelle tilt-angle η to zero and Ω_{sgn} to 1, yielding the inertial terms of the flapping equation that corresponds to a counter-clockwise rotating rotor of a the tilt-rotor in helicopter mode as is shown in eq. (5.56). This expression is assumed to be representative of the inertial portion of the flapping equation of a helicopter and thus shall be used in the determination of the effect of the tilting proprotor on the inertial flapping moment as described next.

$$
\begin{aligned}
-\frac{M_{BL|Y\widehat{R},i}}{I_{bl}} = {} & \ddot{\widehat{\beta}} - \Omega_{sgn}\left(\dot{p}_i C_\eta - \dot{r}_i S_\eta\right) S_{\widehat{\psi}} - \left(\dot{q}_i + \ddot{\eta}\right) C_{\widehat{\psi}} && \text{(inertia)} \\
& + \left(\Omega^2 - p_i^2\left(\frac{C_\eta^2}{2} - S_\eta^2\right) - \frac{(q_i + \dot{\eta})^2}{2} + \frac{r_i^2}{2}\left(3C_\eta^2 - 1\right) + A_{\widehat{\beta},\text{prod}}\right)\widehat{\beta} && \text{(centrifugal spring)} \\
& - \Omega_{sgn} 2\left(p_i C_\eta - r_i S_\eta\right)\left(\Omega - \Omega_{sgn}(p_i S_\eta + r_i C_\eta)\right) C_{\widehat{\psi}} && \text{(roll-yaw Coriolis)} \\
& + 2q_i\left(\Omega - \Omega_{sgn}(p_i S_\eta + r_i C_\eta)\right) S_{\widehat{\psi}} && \text{(pitch-yaw Coriolis)} \\
& + 2\dot{\eta}\left(\Omega - \frac{\Omega_{sgn}(p_i S_\eta + r_i C_\eta)}{2}\right) S_{\widehat{\psi}} && \text{(tilt-yaw Coriolis)}
\end{aligned}
\tag{5.55a}
$$

$$
A_{\widehat{\beta},\text{prod}} = 3p_i r_i S_\eta C_\eta - \Omega_{sgn} 2\left(p_i S_\eta + r_i C_\eta\right)\Omega \tag{5.55b}
$$

$$
\begin{aligned}
-\left.\frac{M_{BL|Y\widehat{R},i}}{I_{bl}}\right|_{\text{ccw. heli.}} = {} & \ddot{\widehat{\beta}} - \dot{p}_i S_{\widehat{\psi}} - \dot{q}_i C_{\widehat{\psi}} && \text{(inertia)} \\
& + \left(\Omega^2 - \frac{p_i^2}{2} - \frac{q_i^2}{2} + r_i^2 - 2r_i\Omega\right)\widehat{\beta} && \text{(centrifugal spring)} \\
& - 2p_i\left(\Omega - r_i\right) C_{\widehat{\psi}} && \text{(roll-yaw Coriolis)} \\
& + 2q_i\left(\Omega - r_i\right) S_{\widehat{\psi}} && \text{(pitch-yaw Coriolis)}
\end{aligned}
\tag{5.56}
$$

Starting with the inertia group, it can be seen that the nacelle tilt angle η appears as an angular acceleration term $\ddot{\eta}$ which is added to the body angular pitch acceleration resulting in a 'total' pitch acceleration experienced by the tilting rotor. In addition η can be observed to be the argument of trigonometric functions which serve the purpose of transforming the body roll and yaw angular accelerations into the shaft plane (which tilts together with the nacelle), yielding an 'effective' roll acceleration as experienced by the tilting rotor. Note that both the 'total' pitch acceleration as well as the 'effective' accelerations have already been described in great detail on page 127. When comparing with eq. (5.56) it can be seen that the 'total' pitch and 'effective' roll accelerations play an analogous role in the tilt-rotor expression as the body pitch and roll accelerations in the case of a helicopter. Finally it should be noted that the direction of rotation of the rotor influences the sign of the 'effective' roll rate.

In the centrifugal spring group, apart from the expected Ω^2 term, the squares of the body angular rates are also present, with the roll and yaw rates being additionally influenced by the sine and cosine of the nacelle tilt angle. As a side note, in the spring group the negative terms have a coning effect on the blade motion, i.e. they result in a larger flapping motion, while positive terms (such as Ω^2) have a flattening effect, i.e. they introduce a restoring flapping moment which reduces the flapping motion. Furthermore it should be noted that squared angular rates that are perpendicular to the rotor rotational rate have a coning effect, while squared angular rates that are aligned with the rotor rotational rate have a flattening effect. For this reason both the body pitch rate q_i and nacelle tilt rate $\dot{\eta}$ will always have a coning effect on the blade. As can also be observed, the nacelle tilt rate may be simply added to the body pitch rate to obtain a 'total' pitch rate. The body roll and yaw rate, on the other hand, swap their coning and flattening effect depending on the nacelle tilt angle, with the yaw rate having a flattening effect in helicopter mode and a coning effect in airplane mode, while the opposite is true for the roll rate. Note that squaring the body angular rates means that their coning or flattening effect is independent of the rotor rotation direction hence they are not multiplied by the Ω_{sgn} parameter. When comparing with eq. (5.56) it can be seen that the effect of the nacelle tilt rate disappears and the body roll and yaw rate do not swap their coning and flattening effects.

An additional term $A_{\widehat{\beta},\text{prod}}$ is also present in the spring group and contains several products of the body rates and rotor rate as shown in eq. (5.55b). Similarly to the 'effective' roll acceleration, the second product contains the multiplication of the rotor rate Ω with the 'effective' yaw rate which is a combination of the body roll and yaw rate that depends on the nacelle tilt angle, and whose sign depends on the rotor rotational

direction. It should be noted that the first product may only exist in conversion mode and thus is unique to a tilt-rotor since it contains η terms which, in pure helicopter or airplane modes, would collectively equal to zero. Unfortunately a more intuitive explanation for the origin of the products within the $A_{\widehat{\beta},\text{prod}}$ term has not been found. When comparing with eq. (5.56) it can be seen that the tilt-rotor-unique product is no longer present and only the product of the body yaw rate and rotor rotational rate remains.

Similarly to the $A_{\widehat{\beta},prod}$ term, the Coriolis effects also depend on 'effective' angular rates and arise due to the interaction between the 'effective' yaw rate and the: 'effective' roll rate; body pitch rate; and nacelle tilt rate. The 'effective' roll rate is a combination of the body roll and yaw rate similar to the 'effective' yaw rate, however with the trigonometric functions of η swapped. In all three cases the 'effective' yaw rate is subtracted from the rotor rotational rate Ω yielding the total inertia yaw rate $\Omega_{tot,i}$ (as defined in eq. (5.50d), with the exclusion of the θ_{1s} terms) which is then multiplied by the other perpendicular angular rates to obtain the Coriolis contribution to the flapping motion. A somewhat surprising and unexpected observation is that although the pitch rate and nacelle tilt rate act around the same axis, in the case of the tilt-yaw Coriolis effect the 'effective' yaw rate is halved while in the case of the pitch-yaw effect it is not. Hence, according to this, the nacelle tilt rate may not be simply added to the pitch rate when calculating the pitch-yaw Coriolis effect, as opposed to the inertia and centrifugal spring groups where analogous additions were permissible. This observation also contradicts the findings of Qi and Wenhai in [33] where the body and nacelle tilt rates are, in fact, simply added together to obtain the respective Coriolis effect. Unfortunately the derivation that leads to this result is not shown, and no other sources that explicitly show the inclusion of the nacelle tilt rate in the Coriolis effect have been found, therefore it is not clear at this point which version of the expression is correct. It is appropriate to mention at this point that if the rotor hub acceleration terms are to be included in the inertial flapping moment expression, the assumption that the nacelle tilt rate and acceleration may be simply added to the body pitch rate and acceleration in all cases is invalid nonetheless. This may be simply proven by recalling that the rotor hub acceleration (eq. (5.49)) partially depends on the nacelle pivot point acceleration (eq. (5.47)), where the latter depends on the body pitch rate and acceleration but not on the nacelle tilt rate and acceleration.

Finally, when comparing with eq. (5.56) it can be seen that the 'effective' roll and yaw rates play an analogous role in the tilt-rotor expression as the body roll and yaw rates in the case of a helicopter, while the tilt-yaw Coriolis effect completely disappears in the helicopter configuration.

Apart from inertial loads, the rotor additionally experiences aerodynamic forces which have an influence on the flapping motion of the blade. Therefore the derivation of the responsible aerodynamic moment is treated next.

5.2.3. Flapping Equation - Aerodynamic Terms

The aerodynamic moment $M_{BL|Y\widehat{BL},a}$ is derived in the wind axis blade frame $\boldsymbol{E}_{\widehat{BL}}$ according to the blade element method. Since the Y-axes of the blade and rotating frame coincide, this aerodynamic moment may be defined in the wind axis rotating frame without the need for any frame transformations and thus, for notation consistency with the inertial moment, it shall be referred to as $M_{BL|-Y\widehat{R},a}$ instead. The aerodynamic moment is the result of the total vertical blade force $F_{BL|Z\widehat{BL},a}$, parallel to the $Z_{\widehat{BL}}$-axis, acting at a radial distance r_{BE} away from the flapping hinge (which coincides with the rotor hub since this rotor model does not include a flapping hinge offset) as shown in fig. 5.8. The total of this force may be determined by taking the integral of the differential vertical blade force $dF_{BL|Z\widehat{BL},a}$ along the length of the blade R, which in turn depends on the blade differential lift dL_{BL} and drag dD_{BL} as shown in eq. (5.57) and depicted in fig. 5.9. Here the lift is perpendicular, and the drag is parallel, to the $V_{BE|Y-Z\widehat{BL}}$ velocity vector (formally defined later in eq. (5.60)). Also note that the tip-loss factor or flow reversal region have been omitted in the integration. The blade element (BE) inflow angle ϕ_{BE} is defined to be the angle between the total aerodynamic velocity $V_{BE|Y-Z\widehat{BL}}$ experienced by the blade element and the $Y_{\widehat{BL}}$-axis, both lying on the $Y_{\widehat{BL}}-Z_{\widehat{BL}}$ plane. The formal definition of the inflow angle is shown later in eq. (5.62).

$$\begin{aligned} M_{BL|-Y\widehat{R},a} &= \int_0^R r_{BE}\, dF_{BL|Z\widehat{BL},a} \\ &= \int_0^R r_{BE}(dL_{BL}cos(\phi_{BE}) - dD_{BL}sin(\phi_{BE})) \end{aligned} \tag{5.57}$$

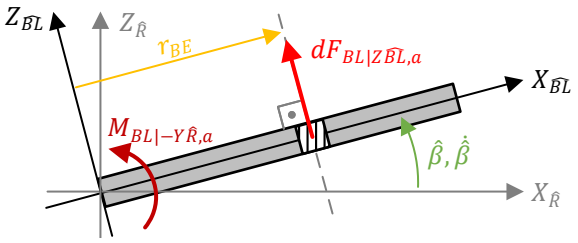

Figure 5.8: Schematic front/rear view of the rotor blade showing the contribution of the differential blade vertical force to the blade aerodynamic moment.

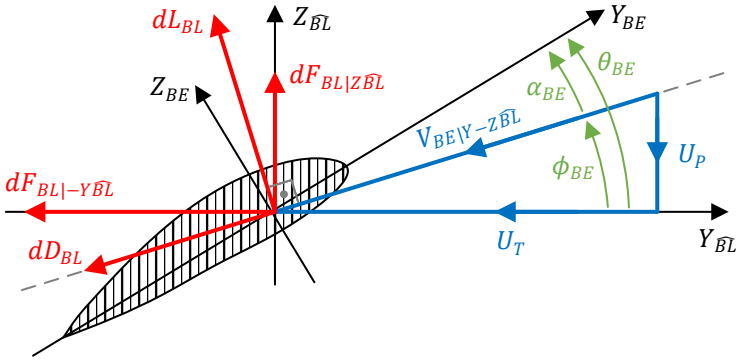

Figure 5.9: Schematic representation of the blade element in the wind axis blade element frame of reference. Velocity arrows indicate the direction of the airflow movement.

Assuming that the inflow angle ϕ_{BE} is small, and that the differential blade lift is much greater than the differential drag, eq. (5.57) may be reduced to the form shown in eq. (5.58). Although not recommended in literature, the small angle approximation is applied to the inflow angle of the tilt-rotor blades nonetheless in order to reduce the complexity of the equations. It should be greatly emphasized, however, that in the case of the tilt-rotor this small angle approximation may quickly become invalid during even standard operation such as the airplane configuration. Therefore, if this model were to be improved upon in the future, the removal of this simplification should be prioritized.

$$\text{if} \quad \phi_{BE} \ll 1 \quad \text{and} \quad dD_{BL} \ll dL_{BL} \quad \text{then} \quad M_{BL|-Y\hat{R},a} = \int_0^R r_{BE} dL_{BL} \tag{5.58}$$

The above assumptions remove the influence of the drag on the aerodynamic moment, therefore only the differential lift, as defined by eq. (5.59), must be derived. Here ρ is the air density, $V_{BE|Y-Z\widehat{BL}}$ is the total aerodynamic velocity experience by the blade element in the $Y_{\widehat{BL}} - Z_{\widehat{BL}}$ plane, $C_{l_\alpha,bl}$ is the lift curve slope of the blade airfoil, α_{BE} is the blade element angle of attack, c_{bl} is the blade chord length, and dr_{BE} is the blade element differential width. In this 6-DoF tilt-rotor model the lift curve slope and blade chord are assumed to be constants.

$$dL_{BL} = \frac{1}{2}\rho V^2_{BE|Y-Z\widehat{BL}} C_{l_\alpha,bl} \alpha_{BE} c_{bl} dr_{BE} \tag{5.59}$$

The square of the total aerodynamic velocity $V_{BE|Y-Z\widehat{BL}}$ in the $Y_{\widehat{BL}} - Z_{\widehat{BL}}$ plane is equal to the sum of the squares of the tangential and perpendicular velocity components experienced by the blade element as shown in eq. (5.60). These components have already been derived and are defined in eq. (5.34). A depiction of these components is also found in fig. 5.9.

$$V^2_{BE|Y-Z\widehat{BL}} = U_T^2 + U_P^2 \tag{5.60}$$

The blade element angle of attack depends on the blade element pitch angle θ_{BE} and the inflow angle as seen in eq. (5.61) and depicted in fig. 5.9. Here the blade element inflow angle is equal to the arctangent of

the ratio between the perpendicular and tangential blade element velocity component as shown in eq. (5.62). The blade element pitch angle, on the other hand, is measured between the Y-axes of the blade element frame and blade frame, where the latter is defined with respect to the rotating frame of reference $\{\boldsymbol{E}_{\widehat{R}}\}$. It is important to highlight that the rotating frame rotates around the $Z_{\widehat{CP}}$-axis and therefore it is coplanar with the control plane, also called the non-feathering plane. As a consequence the pitch angle of the blade element does not periodically vary with the swashplate cyclic angle but instead is only dependent on the total swashplate collective angle θ_0 and the local twist angle as shown in eq. (5.63). The latter is defined by the blade twist $\theta_{bl,1}$ (which is kept constant along the blade length in this model) and the blade element radial position.

$$\alpha_{BE} = \theta_{BE} - \phi_{BE} \tag{5.61}$$

$$\phi_{BE} = arctan\left(\frac{U_P}{U_T}\right) \tag{5.62}$$

$$\theta_{BE} = \theta_0 + \theta_{bl,1} r_{BE} \tag{5.63}$$

Since both the tangential and perpendicular velocity components contain $\widehat{\beta}$ terms, the expression for the inflow angle must be linearized in order to be able to ultimately obtain a linear differential equation for the flapping motion. The inflow angle is already assumed to be small (according to eq. (5.58)) and thus the arctangent may be replaced by its argument, however the only case where this is permissible is when the tangential blade element velocity component is assumed to be much greater than the perpendicular component. This latter assumption not only results in a linear inflow angle as shown in eq. (5.64), but also provides a simplified expression for the total velocity where the perpendicular component may be omitted as shown in eq. (5.65). This simplification is common in helicopter flight mechanics models, and therefore is sometimes also analogously employed when modeling tilt-rotors. It must be remembered, however, that tilt-rotors are capable of tilting their proprotors into a propeller-like configuration in which case the rotor may experience high perpendicular velocities grossly invalidating the assumption. This simplification is applied to the 6-DoF model at hand nonetheless as it greatly simplifies the derivation process. Future improvements to this model should prioritize replacing this simplification with a more valid assumption.

$$\text{if} \quad U_T \gg U_P \quad \text{then} \quad \phi_{BE} = \frac{U_P}{U_T} \tag{5.64}$$

$$\text{if} \quad U_T \gg U_P \quad \text{then} \quad V^2_{BE|Y-Z\widehat{BL}} = U_T^2 \tag{5.65}$$

Applying the simplifications to eq. (5.59) and expanding the expression for the angle of attack yields a simplified differential blade lift as seen in eq. (5.66). The simplified aerodynamic moment described by eq. (5.58) is then resolved in several steps. First the simplified differential lift is substituted into the simplified moment equation as shown in eq. (5.67). The expression is then expanded and rearranged to reveal three separate integrals containing the products of the blade element velocity components and the blade element radial position. These integrals are examples of common integrals (or CIs in short) which reappear throughout the derivation of the rotor forces and moments and are discussed in more detail in section 6.1. At this point they are only mentioned for the purposes of the expression analysis that is described below.

$$dL_{BL} = \frac{1}{2}\rho U_T^2 C_{l_\alpha,bl}\left(\theta_0 + \theta_{bl,1} r_{BE} - \frac{U_P}{U_T}\right) c_{bl} dr_{BE} \tag{5.66}$$

$$\begin{aligned} M_{BL|-Y\widehat{R},a} &= \int_0^R r_{BE} dL_{BL} = \int_0^R r_{BE} \frac{1}{2}\rho U_T^2 C_{l_\alpha,bl}\left(\theta_0 + \theta_{bl,1} r_{BE} - \frac{U_P}{U_T}\right) c_{bl} dr_{BE} \\ &= \frac{1}{2}\rho C_{l_\alpha,bl} c_{bl}\left(\theta_{bl,1} \underbrace{\int_0^R U_T^2 r_{BE}^2 dr_{BE}}_{CI_6} + \theta_0 \underbrace{\int_0^R U_T^2 r_{BE} dr_{BE}}_{CI_3} - \underbrace{\int_0^R U_P U_T r_{BE} dr_{BE}}_{CI_4}\right) \end{aligned} \tag{5.67}$$

After the common integrals are evaluated along the blade length, four non-dimensional terms are introduced, namely the blade lock number γ_{bl} which replaces the air density and several of the blade parameters (and introduces the blade moment of inertia I_{bl} into the expression which shall make the compilation of the complete flapping equation an easier task), the wind axis control plane advance ratio $\widehat{\mu}_{tc}$ and the wind axis control plane inflow ratio $\widehat{\lambda}_{pc}$ which non-dimensionalize the tangential and perpendicular rotor hub velocity components defined in the wind axis control plane, and the induced velocity inflow ratio λ_i which substitutes the rotor induced velocity v_{in}. These non-dimensional terms are defined in eqs. (5.68) to (5.71). Finally the small angle approximation is applied to $\widehat{\beta}$ where not only the trigonometric functions are simplified, but also all $\widehat{\beta}^2$ terms are set to zero. In addition all $\dot{\widehat{\beta}}^2$ and $\dot{\widehat{\beta}}\widehat{\beta}$ terms are also equated to zero under the assumption that $\dot{\widehat{\beta}}$ is also small which, most likely, is not the case during normal tilt-rotor operation, however it must be applied in order to linearize the aerodynamic moment with respect to $\widehat{\beta}$. Similarly to the inertial moment, the complete expression for the aerodynamic moment shall not be shown here due to its extensiveness, however a generalization is presented and analyzed in the following section.

$$\gamma_{bl} = \frac{\rho C_{l_\alpha,bl} c_{bl} R^4}{I_{bl}} \tag{5.68}$$

$$\widehat{\mu}_{tc} = \frac{\widehat{V}_{tc}}{\Omega R} \tag{5.69}$$

$$\widehat{\lambda}_{pc} = \frac{\widehat{V}_{pc}}{\Omega R} \tag{5.70}$$

$$\lambda_i = \frac{v_{in}}{\Omega R} \tag{5.71}$$

Aerodynamic Flapping Moment Expression Analysis

Equation (5.72) presents a generalization of the aerodynamic flapping moment expression where the terms are grouped according to the derivatives of $\widehat{\beta}$ once again. Furthermore an additional subdivision has been implemented grouping terms multiplied by the same power of the rotor rotational rate Ω which indicates the presence of the non-dimensional velocities defined in eqs. (5.69) to (5.71). The most significant observation that can be made based on this subdivision is the fact that groups that are not multiplied by Ω shall not contain any of these non-dimensional velocities. Finally it is important to highlight that the blade inertia is only present here due to the introduction of the blade lock number parameter γ_{bl}, and that the expression may take the form of a linear differential equation due to the application of the small angle approximation to $\widehat{\beta}$.

$$\begin{aligned}\frac{M_{BL|-Y\widehat{R},a}}{\gamma_{bl} I_{bl}} &= \left(D_{d\widehat{\beta},\Omega}\Omega + D_{d\widehat{\beta},\text{free}}\right)\dot{\widehat{\beta}} + \left(D_{\widehat{\beta},\Omega 2}\Omega^2 + D_{\widehat{\beta},\Omega}\Omega + D_{\widehat{\beta},\text{free}}\right)\widehat{\beta} + D_{ext,\Omega 2}\Omega^2 + D_{ext,\Omega}\Omega + D_{ext,\text{free}} \\ &= D_{d\widehat{\beta}}\dot{\widehat{\beta}} + D_{\widehat{\beta}}\widehat{\beta} + D_{ext}\end{aligned} \tag{5.72a}$$

$$D_{d\widehat{\beta}} = D_{d\widehat{\beta},\Omega}\Omega + D_{d\widehat{\beta},\text{free}} \tag{5.72b}$$

$$D_{\widehat{\beta}} = D_{\widehat{\beta},\Omega 2}\Omega^2 + D_{\widehat{\beta},\Omega}\Omega + D_{\widehat{\beta},\text{free}} \tag{5.72c}$$

$$D_{ext} = D_{ext,\Omega 2}\Omega^2 + D_{ext,\Omega}\Omega + D_{ext,\text{free}} \tag{5.72d}$$

The following analysis shall break down the contribution of each of the common integrals to the sub-groups, starting with the fourth common integral CI_4 which has the most widespread effect on the expression. Most importantly, this common integral brings the entire $D_{d\widehat{\beta}}$ group (which is multiplied by the flapping rate $\dot{\widehat{\beta}}$) into existence since the $\dot{\widehat{\beta}}$ term is only present in the perpendicular blade element velocity U_P. The evaluated integral yields terms multiplied by $\dot{\widehat{\beta}}$ that contain the first harmonics (i.e. $sin(\widehat{\psi})$ and $cos(\widehat{\psi})$), and terms that are independent of the blade azimuthal position (also referred to as azimuth-independent or 0^{th} harmonic terms). Following the small angle approximation and removing all the $\dot{\widehat{\beta}}\widehat{\beta}$ products, however,

leaves only one harmonic term that is multiplied by Omega, while all other terms are azimuth-independent. As a consequence the entire $D_{d\widehat{\beta},\text{free}}$ group is also azimuth-independent.

Once again the group of terms multiplied by a pure $\widehat{\beta}$ term, i.e. the $D_{\widehat{\beta}}$ group, only emerges as a result of the application of the small angle approximation to $\widehat{\beta}$. Applying the small angle approximation to the evaluated fourth common integral has the following contribution to the $D_{\widehat{\beta}}$ group. First of all this common integral introduced $\widehat{\beta}$ terms that are multiplied by Ω^2 with one term containing a first harmonic and one term containing a second harmonic. Again, higher harmonics shall ultimately be neglected nonetheless, therefore doing so at this step yields a contribution that consists of a single first harmonic term that depends on the longitudinal rotor hub velocity $\widehat{\mu}_{tc}$. Moreover, this shall be the only $\widehat{\beta}$ term that is multiplied by Ω^2 therefore the $D_{\widehat{\beta},\Omega 2}$ group entirely originates from the fourth common integral. Second of all, CI_4 introduces $\widehat{\beta}$ terms that are multiplied by Ω, some of which contain the first harmonics, while others contain the second harmonics. It is interesting to note that the latter terms are all multiplied by $\widehat{\beta}^2$, therefore by following the small angle approximation these terms may be removed yielding a contribution to the $D_{\widehat{\beta},\Omega}$ group consisting of first harmonic terms only. Thirdly the fourth common integral would have a large contribution to the $D_{\widehat{\beta},\text{free}}$ group, however all of these terms contain the second harmonics which, after their removal, results in CI_4 having no effective contribution to this group.

The fourth common integral also contributes to the aerodynamic excitation moment, i.e. the D_{ext} group, through nominally $\widehat{\beta}$-independent terms, and terms that become $\widehat{\beta}$-independent after the application of the small angle approximation to $\widehat{\beta}$. The nominally $\widehat{\beta}$-independent terms are all multiplied by Ω, some of which contain the second harmonics. Removing the latter results in azimuth-independent terms that contribute to the $D_{ext,\Omega}$ group. Applying the small angle approximation to terms multiplied with $cos(\widehat{\beta})$, on the other hand, yields a group that is multiplied by Ω^2, and another group that is multiplied by Ω, both containing terms that are azimuth-independent and terms that contain the first harmonics contributing to the D_{ext,Ω^2} and $D_{ext,\Omega}$ groups respectively. The employment of the small angle approximation also yields a group that is not multiplied by Ω at all contributing to the $D_{ext,\text{free}}$ group, however all of these terms contain the first harmonics only. It shall be seen later that the free excitation harmonic terms (i.e. the harmonic terms part of the $D_{ext,\text{free}}$ group) solely originate from the fourth common integral.

Since the third and sixth common integrals only differ by a power r_{BE}, the generalized contribution of these to the aerodynamic moment is identical therefore their analysis shall be treated simultaneously. It must be emphasized that only the generalized contribution is identical while the actual contributions to the expression does differ. As mentioned before, only the fourth common integral contributes to $D_{d\widehat{\beta}}$ group therefore the analysis of the contribution of CI_3 and CI_6 starts with the $D_{\widehat{\beta}}$ group. The application of the small angle approximation to the results of the common integrals three and six yields free $\widehat{\beta}$ terms and $\widehat{\beta}$ terms that are multiplied by Ω contributing to the $D_{\widehat{\beta},\text{free}}$ and $D_{\widehat{\beta},\Omega}$ groups respectively. The former contribution consists of first harmonic terms only, while the latter contribution consists of azimuth-independent terms and terms that contain the first and second order harmonics. Finally, azimuth-independent and second harmonic terms multiplied by $\widehat{\beta}^2$ also appear, however these may be neglected in accordance with the small angle approximation.

Common integrals three and six also have a contribution to the D_{ext} group through nominally $\widehat{\beta}$-independent terms, and terms that become $\widehat{\beta}$-independent after the application of the small angle approximation to $\widehat{\beta}$. The nominally $\widehat{\beta}$-independent terms are all multiplied by Ω^2, some of which contain the second harmonics. Removing the higher harmonics results in azimuth-independent terms that contribute to the $D_{ext,\Omega 2}$ group. Applying the small angle approximation to the $cos(\widehat{\beta})$-dependent terms, on the other hand, once again yields a group that is multiplied by Ω^2, and another group that is multiplied by Ω, both containing terms that are azimuth-independent and terms that contain the first harmonics contributing to the D_{ext,Ω^2} and $D_{ext,\Omega}$ groups respectively. The employment of the small angle approximation also yields another group that is not multiplied by Ω at all contributing to the $D_{ext,\text{free}}$ group, however all of these terms are azimuth-independent. As a result all harmonic terms in the $D_{ext,\text{free}}$ group originate from CI_4 (as has been stated above) while all azimuth-independent terms originated from CI_3 and CI_6.

A summary of the contribution of each common integral to the generalized terms of the aerodynamic flapping moment is shown in table 5.1.

An expanded but partially simplified version of the linearized aerodynamic flapping moment expression is shown in eq. (5.74) which shall be used to answer the remaining portion of the research sub-question

Table 5.1: Summarized contribution of common integrals three, four, and six to the generalized terms of the aerodynamic flapping moment.

	Common Integral Contribution	
Term	$\boldsymbol{CI_4}$	$\boldsymbol{CI_3}$, $\boldsymbol{CI_6}$
$D_{d\widehat{\beta},\Omega}$	0^{th} and 1^{st} harmonics only after small angle approximation of $S_{\widehat{\beta}}$ and $C_{\widehat{\beta}}$, and removal of $\dot{\widehat{\beta}}\widehat{\beta}$ terms	
$D_{d\widehat{\beta},\text{free}}$	azimuth-independent terms only after small angle approximation of $S_{\widehat{\beta}}$ and $C_{\widehat{\beta}}$, and removal of $\dot{\widehat{\beta}}\widehat{\beta}$ terms	
$D_{\widehat{\beta},\Omega 2}$	1^{st} harmonics only after small angle approximation of $S_{\widehat{\beta}}$ and $C_{\widehat{\beta}}$, and removal of 2^{nd} harmonics	
$D_{\widehat{\beta},\Omega}$	1^{st} harmonics only after small angle approximation of $S_{\widehat{\beta}}$ and $C_{\widehat{\beta}}$, and removal of $\widehat{\beta}^2$ terms	0^{th} and 1^{st} harmonics only after small angle approximation of $S_{\widehat{\beta}}$ and $C_{\widehat{\beta}}$, and removal of 2^{nd} harmonics
$D_{\widehat{\beta},\text{free}}$	none after small angle approximation of $S_{\widehat{\beta}}$ and removal of 2^{nd} harmonics	1^{st} harmonics only after small angle approximation of $S_{\widehat{\beta}}$ and $C_{\widehat{\beta}}$
$D_{ext,\Omega 2}$	0^{th} and 1^{st} harmonics only after small angle approximation of $C_{\widehat{\beta}}$	nominally $\widehat{\beta}$-independent azimuth-independent terms after removal of 2^{nd} harmonics; 0^{th} and 1^{st} harmonics only after small angle approximation of $C_{\widehat{\beta}}$
$D_{ext,\Omega}$	nominally $\widehat{\beta}$-independent azimuth-independent terms after removal of 2^{nd} harmonics; 0^{th} and 1^{st} harmonics only after small angle approximation of $C_{\widehat{\beta}}$	0^{th} and 1^{st} harmonics only after small angle approximation of $C_{\widehat{\beta}}$
$D_{ext,\text{free}}$	1^{st} harmonics only after small angle approximation of $C_{\widehat{\beta}}$	azimuth-independent terms only after small angle approximation of $C_{\widehat{\beta}}$

concerned with determining the effect of the tilting proprotor on the aerodynamic terms of the flapping equation. It must be emphasized again that this expression is simplified after the prior application of the small angle approximation to $\widehat{\beta}$ as has been described above. The aerodynamic moment is simplified in a similar fashion to the inertial flapping moment analysis, that is, both the control plane deflection and the wind axis shift angle are set to zero to improve readability (as explained on page 136). In addition all higher harmonics of $\widehat{\psi}$ are removed leaving only the first harmonics and azimuth independent terms. Furthermore the linearly varying blade twist parameter $\theta_{bl,1}$ is also set to zero, and the inflow ratio $\widehat{\lambda}_{pc}$ and induced velocity ratio λ_i are combined into a single total inflow ratio $\widehat{\lambda}_{tot}$, as shown in eq. (5.73), in order to improve the clarity of the expression.

$$\widehat{\lambda}_{tot} = \widehat{\lambda}_{pc} - \lambda_i \tag{5.73}$$

Equation (5.74) has been arranged into three main groups indicated by the right-hand-side annotations, namely the aerodynamic damping, aerodynamic spring, and aerodynamic excitation groups which correspond

to the terms that are multiplied by the flapping rate, flapping angle, and terms that do not depend on the flapping angle respectively. The aerodynamic damping group is representative of the $D_{d\widehat{\beta}}$ term introduced in the generalized aerodynamic moment expression shown in eq. (5.72) while the aerodynamic spring and excitation groups correspond to the $D_{\widehat{\beta}}$ and D_{ext} terms respectively. The latter two are further divided into sub-groups, however these do not relate to the sub-terms defined in the generalization. Instead they are grouped according to their periodicity (either periodic with $S_{\widehat{\psi}}$ or $C_{\widehat{\psi}}$, or constant) and the common terms multiplied by the advance ratio $\widehat{\mu}_{tc}$, total inflow ratio $\widehat{\lambda}_{tot}$, the blade collective angle θ_0, and effective pitch and roll rates (which shall be elaborated upon later) experienced by the rotor.

In order to aid the analysis, eq. (5.74) is further reduced to a counter-clockwise rotor of the tilt-rotor in a helicopter configuration by setting the nacelle tilt-angle η to zero and Ω_{sgn} to 1 as shown in eq. (5.75). This expression, too, is assumed to be representative of the aerodynamic portion of the flapping equation of a helicopter and thus shall be used in the determination of the effect of the tilting proprotor on the aerodynamic flapping moment as described next.
First of all it should be stated that all the Ω_{sgn} terms present in tilt-rotor expression have been introduced at the point of transforming the body angular rates into the rotating frame, therefore the sign change parameter is only present as a product with the body pitch or roll rates. It should also be reminded that the nacelle tilt angle also has an effect on the advance ratio $\widehat{\mu}_{tc}$ and inflow ratio $\widehat{\lambda}_{pc}$ since these depend on the tangential ($\widehat{V}_{tc}$) and perpendicular ($\widehat{V}_{pc}$) hub velocities (as defined in eqs. (5.69) and (5.70)), which in turn depend on the nacelle tilt rate and angle as demonstrated by eq. (5.22) and eq. (5.19). The effect of the tiltable nacelle on these rotor hub velocity components (to be more exact - their non-wind axis counterparts) has already been discussed within section 5.2.1 on page 121 and thus it shall not be repeated here.

Starting with the aerodynamic damping group it can be seen that the nacelle tilt angle η yields an 'effective' yaw rate in an almost identical manner as in the case of the inertial flapping expression, with the distinction that the 'effective' yaw rate here depends on the total (aerodynamic) angular rates and not just the inertial ones. Furthermore this 'effective' yaw rate is subtracted from the rotor rotational rate Ω yielding the total (aerodynamic) yaw rate Ω_{tot} (as defined in eq. (5.26), with the exclusion of the θ_{1s} terms). When comparing with eq. (5.75) it can be seen that the 'effective' yaw rate plays an analogous role in the tilt-rotor expression as the body yaw rate in the case of a helicopter. The damping term that includes the advance ratio, on the other hand, is identical for both the tilt-rotor and helicopter.

The aerodynamic spring group is divided into a periodic advance ratio group, periodic 'effective' roll group, periodic 'total' pitch group, and a constant aerodynamic spring group. When comparing to the helicopter expression, the 'effective' roll rate is equivalent to the body roll rate. The 'total' pitch rate is the sum of the body pitch rate and nacelle tilt rate and it should be highlighted that the effect of the tilting nacelle may be included through this simple summation. The 'total' pitch rate may also be observed in the constant aerodynamic spring group. In both cases, when comparing to eq. (5.75) the 'total' pitch rate of the tilt-rotor is equivalent to the body pitch rate of the helicopter. Similarly to the damping group, the nacelle angle also manifests itself in the 'effective' yaw rate which can be observed in all three periodic spring groups which is equivalent to the aerodynamic yaw rate in the helicopter expression.

Referring back to the flattening and coning effects introduced in the analysis of the inertial flapping expression, it should be noticed that the sign of the periodic advance ratio and 'total' pitch rate aerodynamic spring sub-groups is not influenced by the direction of rotation of the rotor. Therefore, in the case of a tilt-rotor with two counter-rotating rotors, the azimuthal flapping response as a result of these sub-groups should be symmetrical in the longitudinal plane ($X_b - Z_b$ plane) for both rotors. The same cannot be said about the periodic 'effective' roll sub-group which is multiplied by the Ω_{sgn} parameter and therefore contributes to an asymmetrical flapping response.

The excitation group is also divided into several sub-groups. Once again the nacelle angle appears in the 'effective' yaw rate which can be observed in both collective excitation groups, the constant inflow excitation group, and the 'effective' roll and pitch periodic excitation groups. In all cases the 'effective' yaw rate in the tilt-rotor expression is equivalent to the body yaw rate in the helicopter expression. As is the case in the spring group, the nacelle angle also yields the 'effective' roll and 'total' pitch rates which, again, are equivalent to the body roll and pitch rates when comparing to eq. (5.75). It should be highlighted that the effect of the nacelle tilt rate may be included through a simple summation with the body pitch rate in this case as well. Finally, the expression for the periodic inflow excitation moment is identical in both the tilt-rotor and helicopter expressions. Out of all excitation sub-groups, only the signs of the constant and

$$
\begin{aligned}
\frac{M_{BL|-Y\widehat{R},a}}{\gamma_{bl} I_{bl}} = &-\left[\frac{\Omega - \Omega_{sgn}\left(pS_\eta + rC_\eta\right)}{8} + \frac{\widehat{\mu}_{tc}}{6}\Omega S_{\widehat{\psi}}\right]\dot{\widehat{\beta}} && \text{aero. damping} \\
&-\left[\frac{\widehat{\mu}_{tc}}{6}\left(\Omega^2 - \Omega_{sgn}(pS_\eta + rC_\eta)\Omega\right) C_{\widehat{\psi}}\right. && \text{perio. adv. spring} \\
&- \Omega_{sgn}(pC_\eta - rS_\eta)\left(\frac{\theta_0}{4}\left(\Omega - \Omega_{sgn}(pS_\eta + rC_\eta)\right) + \frac{\widehat{\lambda}_{tot}}{6}\Omega\right) C_{\widehat{\psi}} && \text{perio. roll spring} \\
&+ (q + \dot{\eta})\left(\frac{\theta_0}{4}\left(\Omega - (pS_\eta + rC_\eta)\right) + \frac{\widehat{\lambda}_{tot}}{6}\Omega\right) S_{\widehat{\psi}} && \text{perio. pitch spring} \\
&\left. + \frac{\theta_0 (q + \dot{\eta})\widehat{\mu}_{tc}}{6}\Omega\right]\widehat{\beta} && \text{const. spring} \\
&+ \frac{\theta_0}{3}\left(\Omega^2 - \Omega_{sgn}(pS_\eta + rC_\eta)\Omega\right)\widehat{\mu}_{tc} S_{\widehat{\psi}} && \text{perio. col. ext.} \\
&+ \frac{\widehat{\lambda}_{tot}}{6}\left(\Omega^2 - \Omega_{sgn}(pS_\eta + rC_\eta)\Omega\right) && \text{const. infl. ext.} \\
&+ \frac{\widehat{\lambda}_{tot}}{4}\widehat{\mu}_{tc}\Omega^2 S_{\widehat{\psi}} && \text{perio. infl. ext.} \\
&+ \frac{\theta_0}{8}\left(\widehat{\mu}_{tc}^2\Omega^2 + \left(\Omega - \Omega_{sgn}(pS_\eta + rC_\eta)\right)^2\right) && \text{const. col. ext.} \\
&+ \Omega_{sgn}\frac{pC_\eta - rS_\eta}{8}\left(\Omega - \Omega_{sgn}(pS_\eta + rC_\eta)\right) S_{\widehat{\psi}} && \text{perio. roll ext.} \\
&+ \frac{q + \dot{\eta}}{8}\left(\Omega - \Omega_{sgn}(pS_\eta + rC_\eta)\right) C_{\widehat{\psi}} && \text{perio. pitch ext.} \\
&+ \Omega_{sgn}\frac{pC_\eta - rS_\eta}{12}\widehat{\mu}_{tc}\Omega && \text{const. roll ext.}
\end{aligned}
\tag{5.74}
$$

$$
\begin{aligned}
\left.\frac{M_{BL|-Y\widehat{R},a}}{\gamma_{bl} I_{bl}}\right|_{\text{ccw. heli.}} = &-\left[\frac{\Omega - r}{8} + \frac{\widehat{\mu}_{tc}}{6}\Omega S_{\widehat{\psi}}\right]\dot{\widehat{\beta}} && \text{aero. damping} \\
&-\left[\frac{\widehat{\mu}_{tc}}{6}\left(\Omega^2 - r\Omega\right) C_{\widehat{\psi}}\right. && \text{perio. adv. spring} \\
&- p\left(\frac{\theta_0}{4}\left(\Omega - r\right) + \frac{\widehat{\lambda}_{tot}}{6}\Omega\right) C_{\widehat{\psi}} && \text{perio. roll spring} \\
&+ q\left(\frac{\theta_0}{4}\left(\Omega - r\right) + \frac{\widehat{\lambda}_{tot}}{6}\Omega\right) S_{\widehat{\psi}} && \text{perio. pitch spring} \\
&\left. + \frac{\theta_0 q\widehat{\mu}_{tc}}{6}\Omega\right]\widehat{\beta} && \text{const. spring} \\
&+ \frac{\theta_0}{3}\left(\Omega^2 - r\Omega\right)\widehat{\mu}_{tc} S_{\widehat{\psi}} && \text{perio. col. ext.} \\
&+ \frac{\widehat{\lambda}_{tot}}{6}\left(\Omega^2 - r\Omega\right) && \text{const. infl. ext.} \\
&+ \frac{\widehat{\lambda}_{tot}}{4}\widehat{\mu}_{tc}\Omega^2 S_{\widehat{\psi}} && \text{perio. infl. ext.} \\
&+ \frac{\theta_0}{8}\left(\widehat{\mu}_{tc}^2\Omega^2 + \left(\Omega - r\right)^2\right) && \text{const. col. ext.} \\
&+ \frac{p_a}{8}\left(\Omega - r\right) S_{\widehat{\psi}} && \text{perio. roll ext.} \\
&+ \frac{q}{8}\left(\Omega - r\right) C_{\widehat{\psi}} && \text{perio. pitch ext.} \\
&+ \frac{p_a}{12}\widehat{\mu}_{tc}\Omega && \text{const. roll ext.}
\end{aligned}
\tag{5.75}
$$

periodic roll groups are affected by the rotational direction of the rotor meaning that only these sub-groups contribute to an asymmetrical aerodynamic excitation moment.

In summary, the effect of the tilting proprotor on the aerodynamic portion of the flapping equation can be observed in the expressions for the 'effective' and 'total' angular rates. Moreover, the nacelle tilt rate $\dot{\eta}$ may be simply added to the body pitch rate to incorporate this dynamic nacelle effect in the aerodynamic portion of the flapping equation.

5.2.4. Complete Flapping Equation

Having derived both the inertial and aerodynamic portions, it is finally possible to assemble the complete flapping equation as defined by eq. (5.39) which is repeated below. Due to its simplicity the expression for the spring moment $M_{BL|Y\widehat{R},s}$ does not require its own section and therefore it is introduced at this point. The flapping spring is modeled by a linear torsional spring with an angular offset from the un-flapped ($\widehat{\beta} = 0$) position, also referred to as the precone angle $\overline{a}_0$. The corresponding moment that it generates may be determined with eq. (5.76) where K_β is the torsional flapping spring constant. As a consequence the torsional spring shall introduce a flapping spring term and a precone excitation term into the flapping equation as shall be demonstrated next.

$$-M_{BL|Y\widehat{R},i} = M_{BL|-Y\widehat{R},a} - M_{BL|Y\widehat{R},s} \tag{5.39}$$

$$M_{BL|Y\widehat{R},s} = K_\beta(\widehat{\beta} - \overline{a}_0) \tag{5.76}$$

Substituting the derived expressions for the inertial, aerodynamic, and spring flapping moments into eq. (5.39) should form the complete flapping equation. For clarity purposes, however, only the simplified versions of the inertial and aerodynamic flapping moments shall be used here. Rearranging this expression into the form of a linear second order differential equation (with respect to $\widehat{\beta}$) yields a simplified flapping equation for a tilt-rotor as shown in eq. (5.77). The total damping and spring coefficients, as well as the forcing function may be identified for the flapping equation when presented in this form. Additionally all aerodynamic terms may be easily found as they are all multiplied by the blade lock number γ_{bl}. Finally the newly introduced flapping spring and precone excitation terms are indicated in text on the right hand side of eq. (5.77a).

A graphical analysis of the flapping equation is presented in chapter 8 together with the rest of the results of this study.

5.2.5. Disk Tilt Approximation

The flapping equation derived so far is defined in the rotating reference frame and is a function of the blade azimuthal position $\widehat{\psi}$. It shall also be shown later that the forces and moments generated by the rotor all depend on the flapping angle. It is possible to stop any further derivation of the flapping equation at this point and solve the differential equation numerically during the simulation, and perform numerical integration on the forces generated by the blade in order to obtain a resultant rotor force and moment acting on the tilt-rotor body. Both of these numerical solvers, however, may be computationally expensive and therefore may hinder the accuracy or performance of the model in real-time flight simulation. To tackle this problem, one option is to solve the flapping equation beforehand and to analytically integrate and transform the forces generated by the blade into a non-rotating reference frame. Fortunately the disk-tilt approximation provides the means to do so and therefore it shall be employed in this tilt-rotor model.

The disk-tilt approximation presumes a quasi-static solution for the flapping angle $\widehat{\beta}$ defined by constant and harmonic terms. For the purposes of this thesis the motion of the flapping blade is constrained to the first harmonics as shown in eq. (5.78a). If any higher harmonics shall appear in any rotor force or moment expressions before the application of the disk-tilt approximation, they shall be removed, i.e. $sin(n\widehat{\psi}) = cos(n\widehat{\psi}) = 0$ for $n > 1$ where $n \in \mathbb{N}$. Furthermore, it is assumed that the transient flapping response of the blade resolves relatively quickly (e.g. within one or two blade revolutions), therefore its effect of the tilt-rotor body motion dynamics shall also be neglected, permitting the sole use of the steady-state solution.

In eq. (5.78a) the non-harmonic term $\widehat{a}_0$ is referred to as the coning angle, $\widehat{a}_1$ is the longitudinal cone tilt, and $\widehat{b}_1$ is the lateral cone tilt. Similarly to $\widehat{\beta}$, the disk tilt angles are defined with respect to the (wind-axis)

$$
\begin{aligned}
&\ddot{\widehat{\beta}} + \gamma_{bl}\left[\frac{\Omega - \Omega_{sgn}\left(pS_\eta + rC_\eta\right)}{8} + \frac{\widehat{\mu}_{tc}}{6}\Omega S_{\widehat{\psi}}\right]\dot{\widehat{\beta}} && \text{(inertia \& aero. damping)} \quad (5.77a)\\
&+\left[\Omega^2 - p_i^2\left(\frac{C_\eta^2}{2} - S_\eta^2\right) - \frac{(q_i+\dot{\eta})^2}{2} + \frac{r_i^2}{2}\left(3C_\eta^2 - 1\right) + A_{\widehat{\beta},\text{prod}}\right. && \text{(centrifugal spring)}\\
&+\frac{\gamma_{bl}\widehat{\mu}_{tc}}{6}\left(\Omega^2 - \Omega_{sgn}(pS_\eta + rC_\eta)\Omega\right)C_{\widehat{\psi}} && \text{(aero. spring)}\\
&-\Omega_{sgn}\gamma_{bl}(pC_\eta - rS_\eta)\left(\frac{\theta_0}{4}\left(\Omega - \Omega_{sgn}(pS_\eta + rC_\eta)\right) + \frac{\widehat{\lambda}_{tot}}{6}\Omega\right)C_{\widehat{\psi}}\\
&+\gamma_{bl}(q+\dot{\eta})\left(\frac{\gamma_{bl}\theta_0}{4}\left(\Omega - (pS_\eta + rC_\eta)\right) + \frac{\widehat{\lambda}_{tot}}{6}\Omega\right)S_{\widehat{\psi}}\\
&+\left.\frac{\theta_0(q+\dot{\eta})\widehat{\mu}_{tc}}{6}\Omega + \frac{K_\beta}{I_{bl}}\right]\widehat{\beta} = && \text{(\& flapping spring)}\\
&\quad = \Omega_{sgn}\left(\dot{p}_i C_\eta + \dot{r}_i S_\eta\right)S_{\widehat{\psi}} - \left(\dot{q}_i + \ddot{\eta}\right)C_{\widehat{\psi}} && \text{(inertia ext.)}\\
&\quad + \Omega_{sgn}2(p_i C_\eta - r_i S_\eta)\left(\Omega - \Omega_{sgn}(p_i S_\eta + r_i C_\eta)\right)C_{\widehat{\psi}} && \text{(roll-yaw Coriolis)}\\
&\quad - 2q_i\left(\Omega - \Omega_{sgn}(p_i S_\eta + r_i C_\eta)\right)S_{\widehat{\psi}} && \text{(pitch-yaw Coriolis)}\\
&\quad - 2\dot{\eta}\left(\Omega - \frac{\Omega_{sgn}(p_i S_\eta + r_i C_\eta)}{2}\right)S_{\widehat{\psi}} && \text{(tilt-yaw Coriolis)}\\
&\quad + \frac{\gamma_{bl}\theta_0}{3}\left(\Omega^2 - \Omega_{sgn}(pS_\eta + rC_\eta)\Omega\right)\widehat{\mu}_{tc}S_{\widehat{\psi}} && \text{(aero. ext.)}\\
&\quad + \frac{\gamma_{bl}\widehat{\lambda}_{tot}}{6}\left(\Omega^2 - \Omega_{sgn}(pS_\eta + rC_\eta)\Omega\right)\\
&\quad + \frac{\gamma_{bl}\widehat{\lambda}_{tot}}{4}\widehat{\mu}_{tc}\Omega^2 S_{\widehat{\psi}}\\
&\quad + \frac{\gamma_{bl}\theta_0}{8}\left(\widehat{\mu}_{tc}^2\Omega^2 + \left(\Omega - \Omega_{sgn}(pS_\eta + rC_\eta)\right)^2\right)\\
&\quad + \Omega_{sgn}\gamma_{bl}\frac{pC_\eta - rS_\eta}{8}\left(\Omega - \Omega_{sgn}(pS_\eta + rC_\eta)\right)S_{\widehat{\psi}}\\
&\quad + \gamma_{bl}\frac{q+\dot{\eta}}{8}\left(\Omega - \Omega_{sgn}(pS_\eta + rC_\eta)\right)C_{\widehat{\psi}}\\
&\quad + \Omega_{sgn}\gamma_{bl}\frac{pC_\eta - rS_\eta}{12}\widehat{\mu}_{tc}\Omega + \frac{K_\beta\overline{a}_0}{I_{bl}} && \text{(\& precone ext.)}
\end{aligned}
$$

$$
A_{\widehat{\beta},\text{prod}} = 3p_i r_i S_\eta C_\eta - \Omega_{sgn}2\left(p_i S_\eta + r_i C_\eta\right)\Omega \qquad (5.77b)
$$

control plane and its axes. Therefore the longitudinal tilt $\widehat{a}_1$ rotates the rotor disk around the $Y_{\widehat{CP}}$-axis and defines the angle between the X-axes of the (wind axis) disk plane and control plane, while the lateral tilt $\widehat{b}_1$ rotates the disk around the $X_{\widehat{CP}}$-axis and defines the angle between the Y-axes of the same two planes. The coning angle $\widehat{a}_0$, on the other hand, defines the angle between the blade $Y_{\widehat{bl}}$-axis and the disk plane and therefore is a constant component that does not depend on the azimuthal position of the blade. It should be noted that the lateral cone tilt is multiplied by the Ω_{sgn} parameter in order for the positive convention of the lateral tilt to be irrespective of the rotational direction of the rotor. As a result the positive convention of all disk tilt angles are identical for both a clockwise and counter-clockwise rotating rotor as graphically shown in fig. 5.10. Here the longitudinal and lateral disk tilt angles for a cw. and ccw. rotor are shown on the left defined with respect to the wind axis control plane ($\widehat{CP}$), while the coning angle for both cw. and ccw. rotors is shown on the right defined with respect to the wind axis disk plane ($\widehat{DP}$). In the latter case the disk atop the rotor cone is referred to as the (wind axis) tip path plane ($\widehat{TPP}$). A formal description of the disk tilt angles and a clear graphical presentation of their effect on the rotor cone can be found in section 4.7 on page 108.

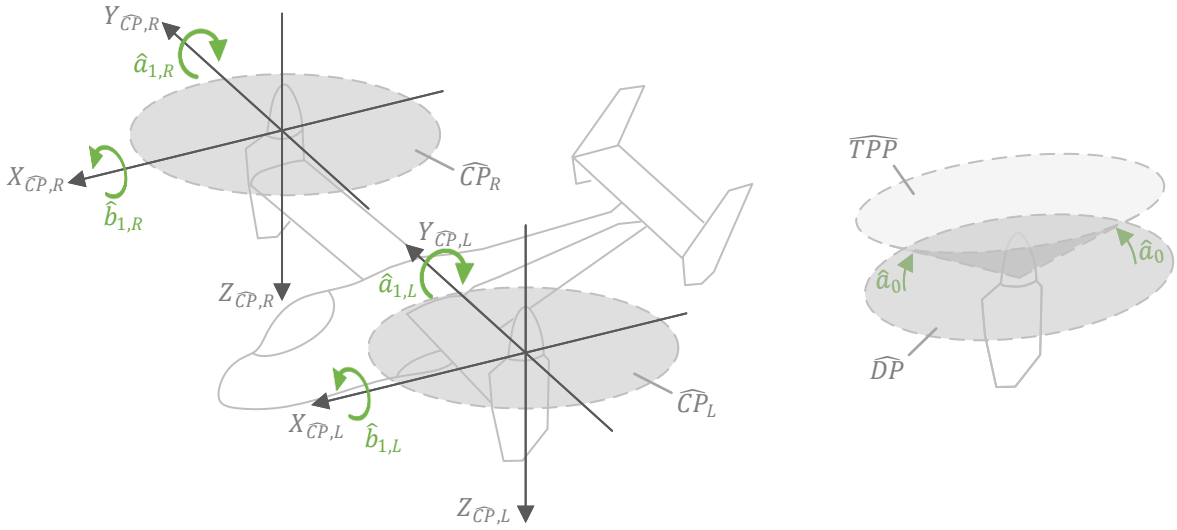

Figure 5.10: Positive sign conventions of longitudinal and lateral disk tilt angles (left), and the coning angle (right), for the left (cw.) and right (ccw.) rotor. The wind axis control plane ($\widehat{CP}$), disk plane ($\widehat{DP}$), and tip path plane ($\widehat{TPP}$) are also indicated.

Apart from the presumed solution for the flapping angle, the presumed solution for the flapping rate $\dot{\widehat{\beta}}$ and flapping acceleration $\ddot{\widehat{\beta}}$ must be found as well. These are determined by taking the time derivative of eq. (5.78a) as shown in eqs. (5.78b) and (5.78c), keeping in mind that $d\widehat{\psi}/dt = \Omega_{sgn}\Omega_{tot,i}$ as already explained in section 5.2.2 on page 133. As a consequence a squared Ω_{sgn} parameter appears in the expressions. It should be remembered, however, that this parameter may only take the value of 1 or -1, therefore squaring it will always yield a value of 1 and thus Ω_{sgn}^2 may be removed from the expressions. Note that the disk tilt angles $\widehat{a}_0$, $\widehat{a}_1$, and $\widehat{b}_1$ are assumed to be static and therefore their time derivatives are not taken into account. It is, however, recommended for a future revision of this model to allow for disk tilt dynamics as well.

$$\widehat{\beta} = \widehat{a}_0 - \widehat{a}_1 cos(\widehat{\psi}) - \Omega_{sgn}\widehat{b}_1 sin(\widehat{\psi}) \tag{5.78a}$$

$$\begin{aligned}\dot{\widehat{\beta}} &= \Omega_{sgn}\Omega_{tot,i}\widehat{a}_1 sin(\widehat{\psi}) - \Omega_{sgn}^2\Omega_{tot,i}\widehat{b}_1 cos(\widehat{\psi}) \\ &= \Omega_{sgn}\Omega_{tot,i}\widehat{a}_1 sin(\widehat{\psi}) - \Omega_{tot,i}\widehat{b}_1 cos(\widehat{\psi})\end{aligned} \tag{5.78b}$$

$$\begin{aligned}\ddot{\widehat{\beta}} &= \Omega_{sgn}^2\Omega_{tot,i}^2\widehat{a}_1 cos(\widehat{\psi}) + \Omega_{sgn}\Omega_{tot,i}^2\widehat{b}_1 sin(\widehat{\psi}) \\ &= \Omega_{tot,i}^2\widehat{a}_1 cos(\widehat{\psi}) + \Omega_{sgn}\Omega_{tot,i}^2\widehat{b}_1 sin(\widehat{\psi})\end{aligned} \tag{5.78c}$$

Substituting eqs. (5.78a) to (5.78c) into the complete flapping equation, removing any second or higher harmonics, and separating the cosine, sine, and aperiodic terms provides a system of three linear analytical equations for the disk tilt angles $\widehat{a}_0$, $\widehat{a}_1$, and $\widehat{b}_1$ which may be arranged in matrix form as shown in eq. (5.79). In eq. (5.79b) the top row corresponds to the collection of the aperiodic terms, the middle row to sine terms, and the bottom row to the cosine terms of the complete flapping equation. It must be remembered, however, that the system is only linear after the application of several simplifications such as the small angle approximation of $\widehat{\beta}$ or the removal of all non-linear flapping terms such as $\dot{\widehat{\beta}}^2$. Fortunately the system becomes even simpler after the application of an expression reduction scheme (described in great detail in section 6.3) which, in short, removes negligible terms from the expression. In the case of the tilt-rotor model implementation used in this thesis work, the expression reduction scheme has been setup such that the resulting reduced analytical expressions for the coning angle $\widehat{a}_0$ and the longitudinal disk tilt angle $\widehat{a}_1$ do not contain any lateral disk tilt terms since they are considered negligible within these expressions. The resulting system of equations reduces from a 3×3 to a 2×2 linear system which can be arranged into matrix form as shown in eq. (5.80a) which is analyzed next.

$$\boldsymbol{A}\widehat{\boldsymbol{a}} = \boldsymbol{B} \tag{5.79a}$$

$$\begin{bmatrix} A_{11} & A_{12} & 0 \\ A_{21} & A_{22} & 0 \\ A_{31} & A_{32} & A_{33} \end{bmatrix} \begin{pmatrix} \widehat{a}_0 \\ \widehat{a}_1 \\ \widehat{b}_1 \end{pmatrix} = \begin{pmatrix} B_1 \\ B_2 \\ B_3 \end{pmatrix} \tag{5.79b}$$

Disk Tilt Equation System Analysis

Solving for the two disk tilt angles may involve taking the inverse of the 2×2 $\boldsymbol{A}$ matrix as shown in eq. (5.80b). A brief investigation of the determinant of the inverted matrix, however, has shown that it is possible for the matrix to take a non-invertable form which, if the model were to be simulated, would result in a halt of the program. The investigation itself consisted of using the expression reduction scheme which, inter alia, provides information about the minimum and maximum values that an expression can taken. The reduction scheme has shown that the fraction $(A_{12}A_{21})/(A_{11}A_{22})$ may have a value that varies between -4.7 and $+4.7$ which means that potentially it is capable of taking on a value of 1 resulting in division by zero in eq. (5.80b). Emphasis should be put on the word *potentially*, however, since the reduction scheme does not guarantee that a variable is capable of taking all the values within its min-max range. For this reason this cause for concern is merely brought to attention while a more thorough investigation should be performed in the future to determine whether this problem may actually occur during simulation, and if so, what conditions facilitate its appearance and what solution should be put into place to alleviate the consequences.

The expression for the lateral disk tilt angle $\widehat{b}_1$ corresponds to the collection of cosine terms of the flapping equation only. Fortunately it is also linear with respect to the already known disk tilt angles $\widehat{a}_0$ and $\widehat{a}_1$ as shown in eq. (5.80c), and thus can be directly evaluated given that all other variables are known (it shall be later shown that one last unknown remains in the disk tilt expressions).

$$\begin{bmatrix} 1 & A_{12}/A_{11} \\ A_{21}/A_{22} & 1 \end{bmatrix} \begin{pmatrix} \widehat{a}_0 \\ \widehat{a}_1 \end{pmatrix} = \begin{pmatrix} B_1/A_{11} \\ B_2/A_{22} \end{pmatrix} \tag{5.80a}$$

$$\begin{pmatrix} \widehat{a}_0 \\ \widehat{a}_1 \end{pmatrix} = \begin{bmatrix} 1 & A_{12}/A_{11} \\ A_{21}/A_{22} & 1 \end{bmatrix}^{-1} \begin{pmatrix} B_1/A_{11} \\ B_2/A_{22} \end{pmatrix} = \frac{1}{1-\frac{(A_{12}A_{21})}{(A_{11}A_{22})}} \begin{bmatrix} 1 & -A_{12}/A_{11} \\ -A_{21}/A_{22} & 1 \end{bmatrix} \begin{pmatrix} B_1/A_{11} \\ B_2/A_{22} \end{pmatrix} \tag{5.80b}$$

$$\widehat{b}_1 = \frac{1}{A_{33}} \left(B_3 - A_{31}\widehat{a}_0 - A_{32}\widehat{a}_1 \right) \tag{5.80c}$$

The elements of the $\boldsymbol{A}$ and $\boldsymbol{B}$ matrices are expanded and shown in appendix C. It should be noted that these expressions have been simplified similarly to the flapping equation, as explained in the appendix, in order to

improve their clarity. Several interesting observations have been made however. First of all the nacelle tilt angle changes the 'effective' rotational rates experienced by the rotor in the same manner as described in the flapping equation analysis. Second, the reduction scheme removed all $\dot{\eta}$ terms from the aperiodic group (top row) as well as from the A_{21} and A_{22} elements meaning that the solution for $\widehat{a}_0$ does not contain any nacelle tilt rate ($\dot{\eta}$) terms. Furthermore, the A_{21} element does not contain any η terms at all therefore it is nacelle-tilt-independent and will remain identical in helicopter, conversion, and airplane modes. It should be mentioned that only the B_2 and B_3 elements contain $\dot{\eta}$ terms and only in the case of the B_2 term may the nacelle tilt rate be simply added to the body pitch rate. Thirdly, the effect of the flapping spring (the K_β term) may only be observed in the A_{11}, A_{32}, and B_1 elements meaning that the effect of the deformation of the flapping spring due to a lateral disk tilt may be considered negligible in this model. Finally, the most surprising observation is the appearance of pure aerodynamic rotational rate wash terms, p_w and r_w, which are contained within the A_{12} and A_{22} elements. The analytical expressions of the solved disk tilt angles (i.e. the elements of the inverse of matrix $\boldsymbol{A}$) shall not be presented, however, due to their extensiveness. It is believed that their presentation and analysis is considered unnecessary given that the flapping equation has already been analyzed thoroughly, adequately addressing the research question.

An interesting effect of the application of the ordering scheme is the fact that the expressions for the coning and longitudinal disk tilt angles become linear functions of the rotor inflow λ_i, while the expression for the lateral disk tilt becomes completely independent from it. As hinted above, the rotor inflow is the last unknown variable in the expressions, therefore a new system of linear equations may be formed, as presented in eq. (5.81), which accommodates the removal of the lateral disk tilt and the addition of the rotor inflow into the vector of unknowns[2]. The (simplified) expressions of the newly introduced elements of matrix $\boldsymbol{A_{2\times3}}$ and vector $\boldsymbol{B'}$ are also shown in appendix C.

$$\boldsymbol{A_{2\times3}}\widehat{\boldsymbol{a}}' = \boldsymbol{B'} \tag{5.81a}$$

$$\begin{bmatrix} A_{11} & A_{12} & A_{14} \\ A_{21} & A_{22} & A_{24} \end{bmatrix} \begin{pmatrix} \widehat{a}_0 \\ \widehat{a}_1 \\ \lambda_i \end{pmatrix} = \begin{pmatrix} B'_1 \\ B'_2 \end{pmatrix} \tag{5.81b}$$

$$B_1 = B'_1 - A_{14}\lambda_i \tag{5.81c}$$

$$B_2 = B'_2 - A_{24}\lambda_i \tag{5.81d}$$

The new system of equations is unfortunately underdetermined since there are more unknowns than equations, therefore it is not possible to solve for the disk tilt angles and rotor inflow with simple matrix inversion. Instead the problem may be solved by finding the expression for a general solution in the form of eq. (5.82a) which consists of a particular solution $\widehat{\boldsymbol{a}}'_{\text{part}}$ and a basis $\widehat{\boldsymbol{a}}'_{\text{basis}}$ multiplied by the free unknown variable, in this case λ_i. Both the particular solution and basis must satisfy the conditions presented in eq. (5.82b) and eq. (5.82c) respectively.

In practice the particular solution may be obtained by determining the nullspace of matrix $\boldsymbol{A_{2\times3}}$ while the basis may be found by calculating the least-square solution of the original system (eq. (5.81a)). Unfortunately these approaches have turned out to be computationally expensive. However, since the elements of matrix $\boldsymbol{A_{2\times3}}$ and vector $\boldsymbol{B'}$ are defined analytically, the underdetermined system may be rearranged by separating the rotor inflow from the unknown disk tilt angles and moving it and the elements multiplied by it (referred to as vector $\boldsymbol{A_{2\times3},:4}$) to the right hand side of the equation such that the rectangular $\boldsymbol{A_{2\times3}}$ matrix turns into the square $\boldsymbol{A_{2\times2}}$ matrix enabling its inversion as shown in eq. (5.82d). Presenting the matrices and vectors in compact single-variable notation shows the similarity between this system and the general solution to the underdetermined problem defined in eq. (5.82a). The approach of rearranging the system of equations yields the analytical expressions for the particular solution and basis shown in eq. (5.82e) and eq. (5.82f) respectively, without the need for any least-squares solutions, nor a numerical algorithm for the determination

[2]Note that the prime symbol above the $\widehat{\boldsymbol{a}}'$ and $\boldsymbol{B}'$ vectors serves the purpose of their distinction from their nominal forms, and does *not* indicate the transpose or derivative of these vectors.

of the nullspace of a matrix. Here the subscripts 1 : and 2 : refer to the first and second rows of the evaluated products between the brackets.

$$\widehat{\boldsymbol{a}}' = \widehat{\boldsymbol{a}}'_{\text{part}} + \widehat{\boldsymbol{a}}'_{\text{basis}}\lambda_i \tag{5.82a}$$

$$\boldsymbol{A_{2\times3}}\widehat{\boldsymbol{a}}'_{\text{part}} = \boldsymbol{B'} \tag{5.82b}$$

$$\boldsymbol{A_{2\times3}}\widehat{\boldsymbol{a}}'_{\text{basis}} = \boldsymbol{0} \tag{5.82c}$$

$$\begin{aligned}
\begin{bmatrix} A_{11} & A_{12} \\ A_{21} & A_{22} \end{bmatrix}\begin{pmatrix} \widehat{a}_0 \\ \widehat{a}_1 \end{pmatrix} &= \begin{pmatrix} B'_1 \\ B'_2 \end{pmatrix} + \begin{pmatrix} -A_{14} \\ -A_{24} \end{pmatrix}\lambda_i \\
\begin{pmatrix} \widehat{a}_0 \\ \widehat{a}_1 \end{pmatrix} &= \begin{bmatrix} A_{11} & A_{12} \\ A_{21} & A_{22} \end{bmatrix}^{-1}\begin{pmatrix} B'_1 \\ B'_2 \end{pmatrix} + \begin{bmatrix} A_{11} & A_{12} \\ A_{21} & A_{22} \end{bmatrix}^{-1}\begin{pmatrix} -A_{14} \\ -A_{24} \end{pmatrix}\lambda_i \\
&= \left(\boldsymbol{A_{2\times2}}^{-1}\boldsymbol{B'}\right) + \left(\boldsymbol{A_{2\times2}}^{-1}\boldsymbol{A_{2\times3,:4}}\right)\lambda_i \\
&\sim \widehat{\boldsymbol{a}}'_{\text{part}} + \widehat{\boldsymbol{a}}'_{\text{basis}}\lambda_i
\end{aligned} \tag{5.82d}$$

$$\widehat{\boldsymbol{a}}'_{\text{part}} = \begin{pmatrix} \left(\boldsymbol{A_{2\times2}}^{-1}\boldsymbol{B'}\right)_{1:} \\ \left(\boldsymbol{A_{2\times2}}^{-1}\boldsymbol{B'}\right)_{2:} \\ 0 \end{pmatrix} \tag{5.82e}$$

$$\widehat{\boldsymbol{a}}'_{\text{basis}} = \begin{pmatrix} \left(\boldsymbol{A_{2\times2}}^{-1}\boldsymbol{A_{2\times3,:4}}\right)_{1:} \\ \left(\boldsymbol{A_{2\times2}}^{-1}\boldsymbol{A_{2\times3,:4}}\right)_{2:} \\ 1 \end{pmatrix} \tag{5.82f}$$

At this point the rotor inflow still remains to be the free variable which means that λ_i may take any value and thus the system does not have a unique solution. For this reason a constraint must be imposed onto the system, as a consequence limiting the free variable to a single allowable value and thus yielding a unique solution to the system. A constraint that directly addresses the rotor inflow does not exist, however, and instead two different thrust equations dependent on the rotor inflow shall have to be introduced forming the necessary constraint which shall only be satisfied when the value of λ_i is chosen such that the two thrust equations yield the same result. Although these two equations supply only one additional unknown (the value of the thrust) and thus seemingly have the potential to provide the two missing linearly independent rows required to obtain an invertible $\boldsymbol{A}$ matrix, it is not advisable (in the case of the rotor model developed for this thesis work) to linearize one of the thrust expressions in order to form one of the missing rows. For this reason an iterative approach shall have to be employed in order to solve this problem, as is described in the section dealing with the derivation of the rotor thrust. The (inadvised) approach of linearizing all of the equations needed to form an invertible $\boldsymbol{A}$ matrix enabling the determination of the disk tilt angles, rotor inflow, and rotor thrust in one computation is, however, described and discussed in appendix C.2.

Before the expressions for the rotor thrust are presented, however, two brief topics concerned with the disk tilt approximation still remain to be discussed below.

Lateral Disk Tilt Angle Correction

The derived disk tilt angles are based on the assumption that the induced velocity is distributed uniformly across the rotor disk. As found during the literature study, a non-uniform distribution is highly recommended, especially since it has a significant effect on the lateral flapping angle in forward flight [48]. Although a non-uniform inflow distribution is not implemented in this model, an individual correction term for the lateral disk tilt has been included in order to emulate the effect of a non-uniform inflow. The correction term is added to $\widehat{b_1}$ yielding a corrected lateral disk tilt as shown in eq. (5.83a) where the correction factor K_{b1} is given by eq. (5.83b) [49]. Note that the correction term is nominally defined to increase the lateral disk tilt angle. Since the positive convention for the lateral disk tilt in this model is the same for a clockwise- and counterclockwise-rotating rotor, when one of the rotors has a positive lateral disk tilt, the other rotor will have a negative disk tilt (assuming identical flight conditions). For this reason the direction of rotation of the rotor must be taken into account in the correction term with the use of the Ω_{sgn} parameter since in the

case of one rotor the correction term must increase the lateral disk tilt towards a more positive value, while in the case of the other rotor it must increase the disk tilt towards a more negative value.

$$\widehat{b}_{1,corr} = \widehat{b}_1 + \Omega_{sgn} \frac{K_{b1} \lambda_i}{1 + \widehat{\mu}_{tc}^2/2} \tag{5.83a}$$

$$K_{b1} = \frac{1.33 \widehat{\mu}_{tc} / \left| \widehat{\lambda}_{tot} \right|}{1.2 + \widehat{\mu}_{tc} / \left| \widehat{\lambda}_{tot} \right|} \tag{5.83b}$$

Disk Tilt Angle Wind Axis Conversion

Finally it should be remembered that the presented disk tilt angles are defined in the wind axis control plane and thus their direction of deflection of the rotor disk depends on the current wind shift angle Δ. Therefore, for ease of interpretation, they may be transformed to the non-wind axis control plane as shown in eq. (5.84). Note that only the longitudinal and lateral disk tilt angles require a transformation since the coning angle $\widehat{a}_0$ is azimuth-independent. The expression for the non-wind axis flapping angle β is also shown as a function of the non-wind axis disk tilt angles.

$$a_0 = \widehat{a}_0 \tag{5.84a}$$

$$a_1 = \widehat{a}_1 cos(\Delta) + \widehat{b}_1 sin(\Delta) \tag{5.84b}$$

$$b_1 = \widehat{b}_1 cos(\Delta) - \widehat{a}_1 sin(\Delta) \tag{5.84c}$$

$$\beta = a_0 - a_1 cos(\psi) - \Omega_{sgn} b_1 sin(\psi) \tag{5.84d}$$

Summarizing this disk tilt approximation section, assuming that the rotor inflow is known, it is now possible to algebraically determine the flapping angle and rate (which are necessary for the calculation of the blade element velocity, which in turn is needed for the calculation of the rotor forces and moments as shall be shown next) based on the states and parameters of the tilt-rotor without the need for any numerical integration, which is especially desirable in real-time simulation. To do so, the coning angles should be evaluated with the help of eq. (5.82d) and substituted back into the presumed solution for $\widehat{\beta}$ and its rate, i.e. into eq. (5.78). However, since the rotor inflow is in fact not known yet, the next section commences the final phase of the rotor model development, namely the derivation of the rotor forces and moments, starting with the two thrust equations which shall enable the determination of the coning angles, induced velocity, and thrust, albeit in an iterative manner.

5.2.6. Solving for Thrust and Inflow

In order to be able to solve for the unknown disk tilt angles and rotor inflow, the rotor model developed for the purposes of this thesis makes use of the possibility to calculate the rotor thrust according to two different methods which impose the necessary constraint on the free inflow ratio variable λ_i providing a unique solution to the underdetermined problem. Other non-iterative methods of determining the rotor inflow do exist, however these may introduce a significant error into the model and thus have not been selected. This section begins with the thrust expression derived with the blade element method (BEM), then introduces the second thrust equation which is developed based on the momentum theory (mentioned in section 2.5), and finally concludes with a description of the inflow ratio constraint formed by the two thrust equations and the subsequent iterative process of converging onto a solution that satisfies that same constraint.

Blade Element Method Thrust (BEM Thrust)

As mentioned at the start of this section, almost all of the rotor forces and moments shall be derived using the blade element method (BEM), and all shall continue to be defined with respect to the wind axis control plane. The rotor thrust $\widehat{T}_{\text{BEM}}$ is derived in the wind axis rotating frame $\boldsymbol{E}_{\widehat{R}}$ and is defined to act along the Z-axis of the same frame. Since the Z-axes of the rotating frame and control plane coincide, however, the resulting thrust will simultaneously be aligned with the Z-axis of the control plane and thus no additional transformation will have to be performed (apart from a sign change due to the opposite pointing directions of the two axes) to obtain the desired expression for the thrust. The rotor thrust is the combined and averaged-over-one-rotor-revolution thrust of all the blades as given by eq. (5.85a) where N is the number of blades on the rotor, while $F_{BL|-Z\widehat{CP},a}$ is the blade thrust defined to be parallel to and pointing in the opposite direction as the $Z_{\widehat{CP}}$-axis. Note that the tip-loss factor and flow reversal region have been omitted in the integration, and this simplification shall be applied to all future rotor force and moment derivations. The blade thrust is obtained by integrating the differential blade perpendicular (to the wind axis control plane) force $dF_{BL|Z\widehat{R},a}$ which is equal to the projection of the vertical differential blade force $dF_{BL|Z\widehat{BL},a}$ (parallel to the $Z_{\widehat{BL}}$-axis) onto the $Z_{\widehat{R}}$-axis as given by eq. (5.85b) and depicted in fig. 5.11.

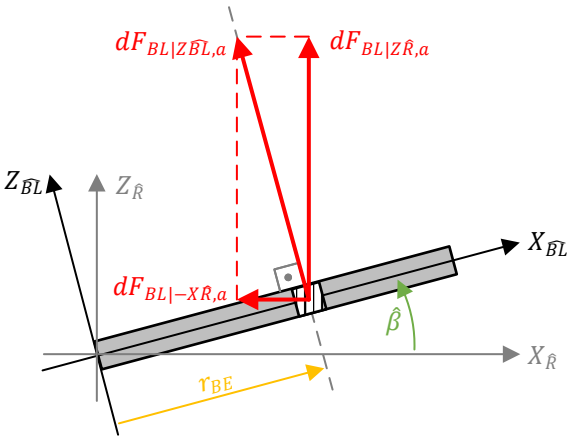

Figure 5.11: Schematic font/rear view (corresponding to a cw. and ccw. rotor respectively) of the rotor blade showing the decomposition of the differential blade vertical force into the differential blade perpendicular and radial components. Force arrows indicate the direction of action of the differential blade forces.

A three-dimensional depiction of the differential blade perpendicular force ($dF_{BL|Z\widehat{R},a}$) and the other projections of the differential blade forces and moment onto the remaining wind axis blade reference frame axes is shown in fig. 5.12. Here the differential blade perpendicular force may also be referred to as the blade element perpendicular force, while the other two may be called the blade element tangential ($dF_{BL|-Y\widehat{R},a}$) and radial ($dF_{BL|-X\widehat{R},a}$) forces acting along the negative $Y_{\widehat{R}}$- and $X_{\widehat{R}}$-axes respectively. The latter two, as well as the differential moment acting around the $Z_{\widehat{R}}$-axis ($dM_{BL|Z\widehat{R},a}$, also referred to as the blade element axial moment) shall be used in the derivation of the rotor hind force (H-force), side force (S-force), and torque (Q-moment). A similar depiction is shown in fig. 5.13 however here the blade element forces and moment are projected onto the axes of the wind axis control plane and may be referred to as the blade element thrust ($dF_{BL|-Z\widehat{CP},a}$), H-force ($dF_{BL|-X\widehat{CP},a}$), S-force ($dF_{BL|-Y\widehat{CP},a}$), and Q-moment ($dM_{BL|-Z\widehat{CP},a}$). References to these two figures shall be made in the sections treating the derivation of these rotor forces and moment.

The differential vertical blade force has already been defined in eq. (5.57) and is graphically presented in fig. 5.9. As a reminder it is assumed that both the inflow angle ϕ_{BE} and flapping angle $\widehat{\beta}$ are small, and that the differential blade lift is much greater than the differential blade drag. As a result the expression for the blade thrust simplifies to the form of eq. (5.85c) which only depends on the blade differential lift.

$$\widehat{T}_{\text{BEM}} = \frac{N}{2\pi}\int_0^{2\pi} F_{BL|-Z\widehat{CP},a}\, d\widehat{\psi} \tag{5.85a}$$

$$F_{BL|-Z\widehat{CP},a} = \int_0^R dF_{BL|Z\widehat{R},a} = \int_0^R cos(\widehat{\beta})\, dF_{BL|Z\widehat{BL},a} = \int_0^R cos(\widehat{\beta})(dL_{BL}cos(\phi_{BE}) - dD_{BL}sin(\phi_{BE}))$$

(5.85b)

If $\phi_{BE} \ll 1$, $dD_{BL} \ll dL_{BL}$, and $\widehat{\beta} \ll 1$ then:

$$F_{BL|-Z\widehat{CP},a} = \int_0^R dL_{BL} \tag{5.85c}$$

The expression for the (simplified) differential blade lift has already been derived and is given by eq. (5.66), repeated below for clarity. Substituting this lift into the blade thrust and rearranging yields eq. (5.86) which presents three common integrals (CIs in short, discussed in more detail in section 6.1) which form the basis of the rotor thrust expression.

$$dL_{BL} = \frac{1}{2}\rho U_T^2 C_{l_\alpha,bl}\left(\theta_0 + \theta_{bl,1} r_{BE} - \frac{U_P}{U_T}\right) c_{bl} dr_{BE} \tag{5.66}$$

$$\begin{aligned} F_{BL|-Z\widehat{CP},a} &= \int_0^R dL_{BL} = \int_0^R \frac{1}{2}\rho U_T^2 C_{l_\alpha,bl}\left(\theta_0 + \theta_{bl,1} r_{BE} - \frac{U_P}{U_T}\right) c_{bl} dr_{BE} \\ &= \frac{1}{2}\rho C_{l_\alpha,bl} c_{bl}\left(\theta_{bl,1}\underbrace{\int_0^R U_T^2 r_{BE} dr_{BE}}_{CI_3} + \theta_0 \underbrace{\int_0^R U_T^2 dr_{BE}}_{CI_1} - \underbrace{\int_0^R U_P U_T dr_{BE}}_{CI_2}\right) \end{aligned} \tag{5.86}$$

Similarly to the aerodynamic flapping moment, after the common integrals are evaluated along the blade length the same non-dimensional terms defined in eqs. (5.68) to (5.71) are introduced into the expressions, namely the blade lock number γ_{bl}, the wind axis control plane advance ratio $\widehat{\mu}_{tc}$, the wind axis control plane inflow ratio $\widehat{\lambda}_{pc}$, and the induced velocity inflow ratio λ_i. It must be remembered that at this point the solved integrals are still (non-linear) functions of the flapping angle $\widehat{\beta}$. Therefore first the small angle approximation is applied to $\widehat{\beta}$ simplifying the trigonometric functions and removing any powers or products of $\widehat{\beta}$ and its derivatives. Next, all instances of the flapping angle and its derivatives are replaced by the (wind axis) disk tilt quasi-static solution, as defined by eq. (5.78), which incorporates the disk tilt angles into the expressions, and simultaneously enables the future definition of the rotor thrust with respect to a non-rotating frame. The prior application of the small angle approximation to $\widehat{\beta}$ also ensures that the final expression is linear with respect to the disk tilt angles. It should be highlighted that the incorporation of the disk tilt approximation must be performed before taking the integral of the blade thrust around one blade revolution (eq. (5.85a)) since the disk tilt quasi-static solution is a function of the azimuth position $\widehat{\psi}$. Therefore, after the inclusion of the disk tilt angles, eq. (5.85a) may be finally evaluated yielding the analytical expression for the rotor thrust defined with respect to the (non-rotating) wind-axis control plane frame. Note that this thrust expression is accompanied by the subscript BEM which refers to the blade element method that has been used to obtain it. This distinction has been put in place due to the need for a second thrust expression which shall complete the system of equations necessary to solve for the unknown thrust, disk tilt angles, and rotor induced velocity. The derivation of this second thrust shall be treated later.

The complete expression for the BEM rotor thrust shall not be shown here due to its extensiveness, however a reduced and simplified version is presented and analyzed below.

BEM Thrust Expression Analysis

An expanded but partially simplified version of the BEM thrust expression is shown in eq. (5.87) which shall be used to answer a portion of the research sub-question concerned with determining the effect of the tilting proprotor on the rotor force expressions. The BEM thrust is initially supplied to the reduction scheme (described in great detail in section 6.3) which, in short, removes negligible terms from the expression. The obtained reduced expression is then further simplified in a similar fashion to the flapping moment expressions, that is, both the control plane deflection and the wind shift angle are set to zero to improve readability (as explained on page 136). Furthermore the linearly varying blade twist parameter $\theta_{bl,1}$ is also set to zero, while several linear and rotational rate combinations have been replaced by single variables for notation

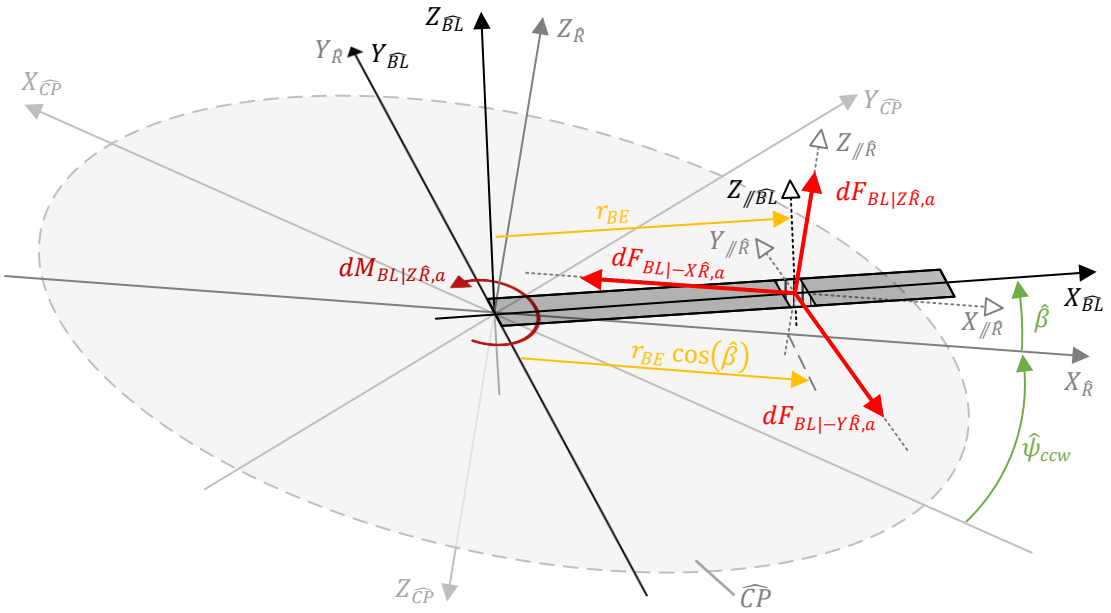

Figure 5.12: Schematic depiction of the forces and moment generated by the blade element, decomposed along and around the wind axis blade reference frame axes, corresponding to the blade element perpendicular, tangential, and radial forces, and blade axial moment. The gray rectangle aligned with the $X_{\widehat{BL}}$-axis represents a flapping blade of a counter-clockwise rotating rotor, while the striped portion of this rectangle represents the blade element.

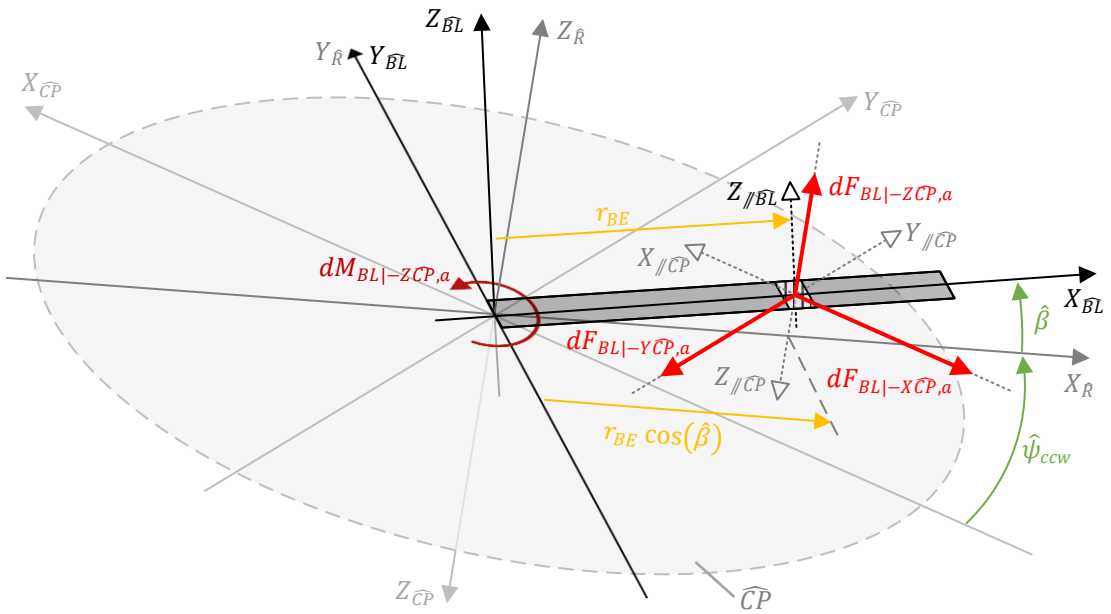

Figure 5.13: Schematic depiction of the differential forces and moment generated by the blade element, decomposed along and around the wind axis control plane reference frame axes, corresponding to the blade element thrust, H-force, S-force, and Q-moment. The gray rectangle aligned with the $X_{\widehat{BL}}$-axis represents a flapping blade of a counter-clockwise rotating rotor, while the striped portion of this rectangle represents the blade element.

compactness, including the total inflow ratio $\widehat{\lambda}_{tot}$ as already defined by eq. (5.73). In appendix C eq. (C.4) provides the expansion of the combined rotational rates while an overview and description of the subscripts of these combined terms is given in table C.1. For the sake of clarity, in summary the subscript eff refers to 'effective' rotational rates and tot refers to 'total' rotational rates, while the subscripts i and w refer to inertial and wash rates respectively which, when combined, yield aerodynamic rates which are not indicated by any subscripts. A detailed description of 'effective' and 'total' rates is provided on page 127, while the distinction between inertial, wash, and total rates is explained on page 118. The rotational rates have also been made non-dimensional, indicated with an overbar symbol ($\bar{}$), by dividing them by Ω making it possible to take Ω^2 outside of the brackets.

Equation (5.87) has been arranged into three main groups indicated by the right-hand-side annotations, namely the $\widehat{a}_1$-dependent group, and the free asymmetrical and symmetrical groups which correspond to the terms that are multiplied by the longitudinal disk tilt, Ω_{sgn}, and the remaining terms respectively. A separate expression corresponding to a counter-clockwise rotor in helicopter configuration shall not be presented since if all 'effective' rotational rates are replaced by their pure body rate counterparts, then eq. (5.87) becomes representative of the thrust expression corresponding to a helicopter.

$$\begin{aligned}\widehat{T}_{\text{BEM}} = \frac{I_{bl}\gamma_{bl}N\Omega^2}{R}\Bigg[& -\frac{\Omega_{sgn}}{6}\left(\overline{p}_{eff}\theta_0 - \frac{3\overline{r}_{w,eff}\widehat{\mu}_{tc}}{4} + \frac{3\overline{p}_{eff}\widehat{\lambda}_{pc}}{4}\right)\widehat{a}_1 && (\widehat{a}_1\text{-dependent}) \\ & + \frac{\theta_0}{6}\left(\overline{r}_{eff}^2 - \overline{r}^2 C_\eta^2 + \frac{3\widehat{\mu}_{tc}^2}{2} + 1\right) + \frac{\widehat{\lambda}_{tot}}{4} && (\text{free symmetrical}) \\ & - \frac{\Omega_{sgn}}{6}\left(2\theta_0\overline{r}_{eff} + \frac{3\overline{r}_{eff}\widehat{\lambda}_{tot}}{2} - \frac{3\overline{p}_{eff}\widehat{\mu}_{tc}}{4}\right)\Bigg] && (\text{free asymmetrical})\end{aligned} \tag{5.87}$$

First and foremost it should be noted that the BEM thrust depends on only one of the disk tilt angles, namely the longitudinal disk tilt angle $\widehat{a}_1$. The coning and lateral disk tilt angles are initially part of the expression for the thrust, however the reduction scheme deems these angles not significant enough to be included and thus the BEM thrust only depends on $\widehat{a}_1$. The reduction scheme also removes all $\dot{\eta}$ terms (originating from the tangential blade element velocity U_T) from the expression which are initially spread throughout the entire equation, all multiplied either by the disk tilt angles, the Ω_{sgn} parameter, or both. This means that the nacelle tilt rate is not considered a significant contributor to the rotor thrust. Although not shown in the simplified expression, the body pitch rate q is also part of the reduced expression, however all instances of it are multiplied by the sine of the wind shift angle implying that the body pitch rate is only considered significant when the rotor is in sideward flight. From the perspective of the wind-shifted rotor, in this condition the body pitch rate is interpreted as a body roll rate. This also explains why the body roll rate is present in the simplified expression while the body pitch rate is not.

Secondly, as already mentioned above, the nacelle tilt angle changes the 'effective' rotational rates and linear rates (i.e. $\widehat{\mu}_{tc}$, $\widehat{\lambda}_{pc}$, and $\widehat{\lambda}_{tot}$) experienced by the rotor in the same manner as described in the flapping equation analysis. It should be noted that any term that is not multiplied by an 'effective' rate is independent from the nacelle tilt angle. Several of such terms are present in the expression, one of which is the inflow ratio which is not explicitly dependent on the nacelle tilt angle as expected. Thirdly, the inertial rotational rates that are part of the aerodynamic rotational rates (e.g. $\overline{p}$ or $\overline{p}_{eff}$) have been introduced through the flapping rate part of the perpendicular blade element velocity component U_P, which in turn is contained within common integral 2 (CI_2). As a consequence, several inertial rates are subtracted from aerodynamic rates yielding pure wash rates which can be observed in the thrust expression (e.g. $\overline{r}_{w,eff}$). Lastly it should be highlighted that the presence of the $\widehat{a}_1$-dependent and asymmetrical groups (which are both multiplied by the Ω_{sgn} parameter) means that in certain flight conditions two counter-rotating rotors may produce a thrust-imbalance resulting in a rolling motion in helicopter configuration, yawing motion in airplane configuration, or a combined roll-yaw motion of the tilt-rotor in conversion mode.

Once again an interesting effect of the application of the ordering scheme is the fact that the BEM thrust expression becomes a linear functions of the rotor inflow λ_i (without the reduction, products of λ_i with $\widehat{a}_0$ and $\widehat{a}_1$ appear in the expression). As a result the elements of the BEM thrust expression may be rearranged according to eq. (5.88). Although in this form the BEM thrust expression may be appended to the system of linear equations containing the disk tilt angles and inflow ratio (i.e. eq. (5.81)), the system would still

be underdetermined (due to the introduction of a new unknown, i.e. the BEM thrust itself) and ultimately a roadblock would be encountered making it impossible to form an invertible system of linear equations without implementing additional simplifications. Keeping in mind the validity of the model, the latter is not desired and instead an iterative approach based on defining another equivalent thrust equation shall be employed to solve for the unknown disk tilt angles, inflow, and rotor thrust, as shall be described next. An attempt at forming an invertible system with the application of additional simplifications has been made nonetheless (as described in appendix C.2), hence the (simplified) expressions of the elements of eq. (5.88) are also defined in appendix C for the sake of completeness.

$$\widehat{T}_{\text{BEM}} = A_{42}\widehat{a}_1 + A_{44}\lambda_i - B_4 \tag{5.88}$$

Momentum Theory Thrust

As has already been stated, a second thrust expression is needed in order to constrain the free variable λ_i yielding a unique solution to the disk tilt approximation problem. Fortunately, apart from the blade element method, the thrust can also be determined with the use of the simplified momentum model, mentioned in section 2.5, which approximates the thrust based on the air mass flow ($\dot{m}_{\text{flow}}$) moving through the rotor disk and the rotor induced velocity. In the case of this rotor model, the momentum thrust shall be defined in the wind axis disk plane since it has been decided that the velocity components defined in the wind axis reference frame are to be used in order to be consistent with the BEM thrust derivation. A rearranged form of the (wind axis) momentum thrust $\widehat{T}_M$ is given by eq. (5.89) where $\|\boldsymbol{V}_{R|\widehat{DP}}\|$ is Euclidean norm of the resultant of the combined body and induced velocity, defined in the (wind axis) disk plane, given by eq. (5.90). Note that here the small angle approximation has been applied to the disk tilt angles when performing the transformation from the w.a. CP to the w.a. DP.

$$\widehat{T}_M = 2v_{in}(\dot{m}_{\text{flow}}) = 2v_{in}\left(\rho\pi R^2 \|\boldsymbol{V}_{R|\widehat{DP}}\|_2\right) \tag{5.89}$$

$$\begin{aligned}
\boldsymbol{V}_{R|\widehat{DP}} &= \boldsymbol{V}_{hub|\widehat{DP}} + \begin{pmatrix}0 & 0 & -v_{in}\end{pmatrix}\{\boldsymbol{E}_{\widehat{DP}}\} \\
&= \boldsymbol{V'}_{hub|\widehat{CP}}\boldsymbol{T}_{\widehat{CP}|\widehat{DP}} + \begin{pmatrix}0 & 0 & -v_{in}\end{pmatrix}\{\boldsymbol{E}_{\widehat{DP}}\} \\
&= \begin{pmatrix}\widehat{V}_{tc} & 0 & \widehat{V}_{pc}\end{pmatrix}\begin{bmatrix}1 & 0 & \widehat{a}_1 \\ \widehat{a}_1\widehat{b}_1 & 1 & -\widehat{b}_1 \\ -\widehat{a}_1 & \widehat{b}_1 & 1\end{bmatrix}\{\boldsymbol{E}_{\widehat{DP}}\} + \begin{pmatrix}0 & 0 & -v_{in}\end{pmatrix}\{\boldsymbol{E}_{\widehat{DP}}\} \\
&= \begin{pmatrix}\widehat{V}_{tc} - \widehat{a}_1\widehat{V}_{pc} \\ \widehat{b}_1\widehat{V}_{pc} \\ \widehat{a}_1\widehat{V}_{tc} + \widehat{V}_{pc} - v_{in}\end{pmatrix}^T\{\boldsymbol{E}_{\widehat{DP}}\} = \Omega R\begin{pmatrix}\widehat{\mu}_{tc} - \widehat{a}_1\widehat{\lambda}_{pc} \\ \widehat{b}_1\widehat{\lambda}_{pc} \\ \widehat{a}_1\widehat{\mu}_{tc} + \widehat{\lambda}_{tot}\end{pmatrix}^T\{\boldsymbol{E}_{\widehat{DP}}\}
\end{aligned} \tag{5.90}$$

In eq. (5.90) the rotor induced velocity (perpendicular to the disk plane) is added to the hub velocity $\boldsymbol{V}_{hub|\widehat{DP}}$ defined in the disk plane. The latter is obtained by transforming the hub velocity $\boldsymbol{V'}_{hub|\widehat{CP}}$ defined in the (wind axis) control plane into the disk plane with the use of $\boldsymbol{T}_{\widehat{CP}|\widehat{DP}}$ (previously defined by eq. (4.41)) which has been simplified by assuming that the longitudinal and lateral disk tilt angles are small. Note that a prime symbol has been placed above the hub velocity in order to distinguish it from the already defined hub velocity (i.e. eq. (5.22)) which already contains the rotor induced velocity, albeit defined perpendicular to the (wind axis) control plane. Since the simplified momentum model dictates that the induced velocity be perpendicular to the disk plane, v_{in} is first removed from $\boldsymbol{V}_{hub|\widehat{CP}}$ yielding $\boldsymbol{V'}_{hub|\widehat{CP}}$, which is then transformed into the disk plane in order to be able to (correctly) add the induced velocity to it. The linear velocity components in the final expression defining $\boldsymbol{V}_{R|\widehat{DP}}$ have been made non-dimensional according to eqs. (5.69) to (5.71) and (5.73) for sake of consistency as well.

The resulting Euclidean norm of the resultant velocity is given by eq. (5.91), while plugging this expression back into eq. (5.89) yields the definition of the momentum theory thrust with respect to the disk-tilt angles and inflow ratio as shown in eq. (5.92). To briefly address the research question, the effect of the tiltable nacelle only manifests itself through the rotor hub velocity components.

$$\|\boldsymbol{V}_{R|\widehat{DP}}\|_2 = \sqrt{\Omega^2 R^2 \left[(\widehat{\mu}_{tc} - \widehat{a}_1\widehat{\lambda}_{pc})^2 + (\widehat{b}_1\widehat{\lambda}_{pc})^2 + (\widehat{a}_1\widehat{\mu}_{tc} + \widehat{\lambda}_{tot})^2\right]} \tag{5.91}$$

$$\widehat{T}_M = 2\lambda_i \rho\pi R^4 \Omega^2 \sqrt{(\widehat{\mu}_{tc} - \widehat{a}_1\widehat{\lambda}_{pc})^2 + (\widehat{b}_1\widehat{\lambda}_{pc})^2 + (\widehat{a}_1\widehat{\mu}_{tc} + \widehat{\lambda}_{tot})^2} \tag{5.92}$$

It should be mentioned that when the ordering scheme was used on the momentum theory thrust in order to obtain a reduced expression, the iterative solver (that shall be described next) was not able to converge onto a solution. For this reason the original non-reduced momentum thrust equation is used in the tilt-rotor model of this thesis.

As a final note, according to [4] the momentum theory is only valid when the rotor is either in propeller state or in windmill brake state with an axial induction ratio a_{in} no greater than 0.5. In propeller state the rotor generates thrust in the opposite direction of the perpendicular airflow, while in windmill brake state the rotor generates thrust in the same direction as the perpendicular airflow, which may also be interpreted as the rotor generating drag. Note that in the latter case the rotor induced velocity attains a negative value. A graphical summary of these two states is shown in fig. 5.14 where T is the thrust, V_O is the (perpendicular) free stream velocity, v is the induced velocity, and a is the axial induction ratio. In the case of the rotor model developed for the purposes of this thesis, the free stream velocity is simplified to be equal to the velocity perpendicular to the (wind axis) control plane $\widehat{V}_{pc}$ resulting in the axial induction ratio being defined by eq. (5.93).

$$a_{in} = \frac{v_{in}}{\widehat{V}_{pc}} \quad \text{with} \quad a_{in} \leq 0.5 \tag{5.93}$$

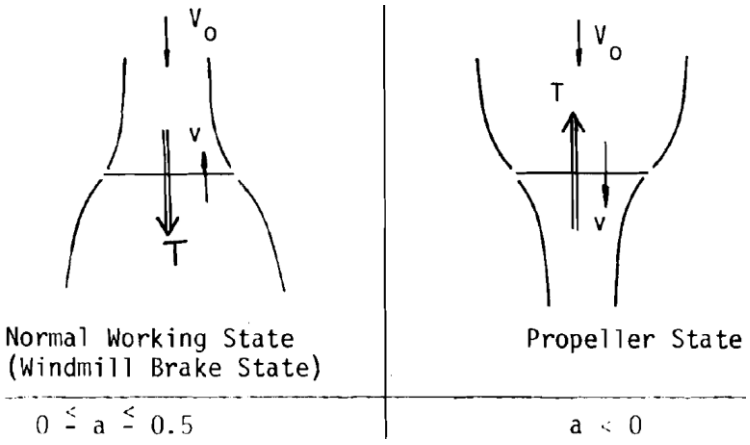

Figure 5.14: Schematic depiction of the windmill brake and propeller flow states of the rotor. Valid ranges of the axial induction ratio a for the two rotor flow states shown below the diagrams. Portion of FIGURE 2 taken from [4, p29].

Solving for the Unknowns

Recalling the underdetermined system defined by eq. (5.82), at this point it seems as if it is finally possible constrain the free variable λ_i by selecting a value for it such that the BEM thrust and momentum thrust are equal. It must be remembered, however, that these two forces and defined in two different reference frames, the former in the (wind axis) control plane while the latter in the (wind axis) disk plane. For this reason some transformation must first take place before the equivalence constraint may be imposed. It must be also remembered, however, that the BEM thrust is not the resultant force generated by the rotor. Instead, it is only one of the three orthogonal components that form the complete force vector $\boldsymbol{F}_{r|\widehat{CP}}$, the other two being the hind force $\widehat{H}_{\text{BEM}}$ and side force $\widehat{S}_{\text{BEM}}$ (also referred to as H- and S-forces in short, derived later), as shown in eq. (5.94). Note that the rotor forces point in the opposite direction to the (wind axis) control plane axes (as has been shown in fig. 5.2) hence the minus signs in front of $\widehat{H}_{\text{BEM}}$, $\widehat{S}_{\text{BEM}}$, and $\widehat{T}_{\text{BEM}}$. Transforming $\boldsymbol{F}_{r|\widehat{CP}}$

from the (wind axis) control plane into the (wind axis) disk plane yields the complete force vector defined in the disk plane $\boldsymbol{F}_{r|\widehat{DP}}$ (as shown in eq. (5.95a)). Once again the small angle approximation has been applied to the disk tilt angles when performing this transformation. The third component $\widehat{T}_{\text{BEM}|\widehat{DP}}$, which acts along the axis perpendicular to the disk plane and is defined in eq. (5.95b), may then be set equal to the thrust obtained with the momentum theory in order to form the constraint as formalized in eq. (5.96).

$$\boldsymbol{F}_{r|\widehat{CP}} = \begin{pmatrix} -\widehat{H}_{\text{BEM}} & -\widehat{S}_{\text{BEM}} & -\widehat{T}_{\text{BEM}} \end{pmatrix} \{\boldsymbol{E}_{\widehat{CP}}\} \tag{5.94}$$

$$\boldsymbol{F}_{r|\widehat{DP}} = \boldsymbol{F}_{r|\widehat{CP}} \boldsymbol{T}_{\widehat{CP}|\widehat{DP}} = \begin{pmatrix} -\widehat{H}_{\text{BEM}} & -\widehat{S}_{\text{BEM}} & -\widehat{T}_{\text{BEM}} \end{pmatrix} \begin{bmatrix} 1 & 0 & \widehat{a}_1 \\ \widehat{a}_1\widehat{b}_1 & 1 & -\widehat{b}_1 \\ -\widehat{a}_1 & \widehat{b}_1 & 1 \end{bmatrix} \{\boldsymbol{E}_{\widehat{DP}}\} = \begin{pmatrix} -\widehat{H}_{\text{BEM}|\widehat{DP}} \\ -\widehat{S}_{\text{BEM}|\widehat{DP}} \\ -\widehat{T}_{\text{BEM}|\widehat{DP}} \end{pmatrix}^T \tag{5.95a}$$

$$\widehat{T}_{\text{BEM}|\widehat{DP}} = \widehat{T}_{\text{BEM}} + \widehat{H}_{\text{BEM}}\widehat{a}_1 - \widehat{S}_{\text{BEM}}\widehat{b}_1 \tag{5.95b}$$

$$\text{find} \quad \lambda_i \quad \text{such that} \quad \widehat{T}_{\text{BEM}|\widehat{DP}} = \widehat{T}_M \tag{5.96}$$

Having defined a second thrust equation, the system is constrained and it is now possible to attempt to solve for the unknown disk tilt angles, inflow ratio, and thrust. As already stated, the iterative feedback method (mentioned in section 2.5) is employed which consists of initially guessing the value of λ_i and evaluating all the necessary equations in order to obtain a value for the BEM thrust and the momentum thrust separately. Since it is very unlikely that the initial guess for λ_i corresponds to the actual solution, the two thrust equations yield different results. This difference is then used to update the next estimate for the inflow ratio, and the procedure of evaluating all necessary equations to obtain updated thrust values is repeated until the difference between the two thrusts becomes acceptably small.

The procedure of evaluating all necessary equations starts with the determination of the particular disk tilt solution vector and the disk tilt basis vector according to eq. (5.82e) and eq. (5.82f) respectively. Next the current estimate for the inflow ratio is multiplied by the basis vector and the result is added to the particular solution in order to obtain the current estimate for the coning angle $\widehat{a}_0$ and longitudinal disk tilt angle $\widehat{a}_1$ according to eq. (5.82a). Next, this result is used to obtain an estimate for the lateral disk tilt $\widehat{b}_1$ with the use of eq. (5.80c), which is then corrected for the uniform inflow with the use of eq. (5.83) producing the current estimate for the corrected lateral disk tilt $\widehat{b}_{1,corr}$. Having determined the current estimates for all disk tilt angles and the rotor inflow ratio, it is possible to determine the current estimate for all the BEM forces with the use of eqs. (5.87), (5.107) and (5.113), and the momentum thrust with the use of eq. (5.92). The complete rotor force vector consisting of the BEM force estimates, as defined in eq. (5.94), is transformed from the control plane into the disk plane with the use of eq. (5.95a). The resulting disk plane BEM thrust estimate element $\widehat{T}_{\text{BEM}|\widehat{DP}}$ is extracted from the vector and the previously evaluated estimate for the momentum thrust is subtracted from it yielding an error ϵ_T as defined by eq. (5.97). Finally, this error is multiplied by a convergence-rate constant K_{ϵ_T} and the result is added to the current estimate for the inflow ratio yielding its updated value used in the next iteration as shown in eq. (5.98) where k is the current iteration number. Once the error between the two thrusts is smaller than a predefined threshold T_{ϵ_T}, the iterative process is stopped and the current estimate for the unknowns is accepted as the solution, as formalized by eq. (5.99). It may be the case that in some flight conditions no solution exists that satisfies the thrust constraint. For this reason a limit k_{max} is set on the number of allowed iterations, and when exceeded, the solver yields no solution which brings the simulation to a halt. A flow diagram of the entire procedure is shown in fig. 5.15 while the values of K_{ϵ_T}, T_{ϵ_T}, and k_{max} used in the tilt-rotor implementation of this thesis work are given in table A.15 in appendix A.

$$\epsilon_T = \widehat{T}_{\text{BEM}|\widehat{DP}} - \widehat{T}_M \tag{5.97}$$

$$\lambda_i^{k+1} = \lambda_i^k + K_{\epsilon_T}\epsilon_T \tag{5.98}$$

$$\epsilon_T \leq T_{\epsilon_T} \quad \text{and} \quad k \leq k_{max} \implies \text{solution found} \tag{5.99}$$

It should be highlighted that all expressions containing the later disk tilt $\widehat{b}_1$ use the corrected value $\widehat{b}_{1,corr}$ in order to incorporate the inflow distribution correction throughout the rotor model. Also, the expressions that are linear with respect to the unknowns have terms which do not change with every iteration step (i.e. all the elements of matrix $\boldsymbol{A}$ and vector $\boldsymbol{B'}$), therefore these may be evaluated only once (every simulation step) before the iterative process starts which improves the simulation performance. Finally, since the H- and S-forces have not been derived yet, it must be mentioned at this point that these forces are also functions of the disk tilt angles and rotor inflow, therefore they must be evaluated at every iteration as well. Hence the derivation of their expressions will be treated in the next section, starting with the H-force.

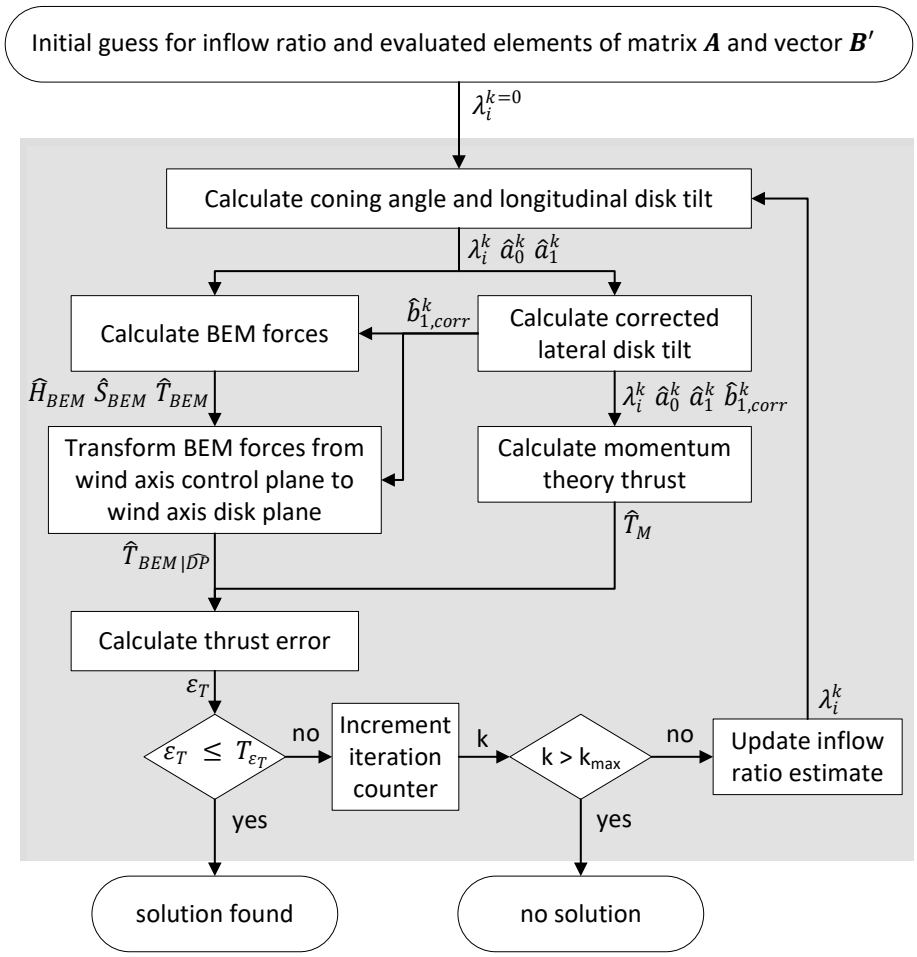

Figure 5.15: Flowchart showing the iterative procedure of determining the rotor disk tilt angles, inflow ratio, and orthogonal force components solution.

5.2.7. Blade Element Hind Force (H-Force)

The rotor hind force $\widehat{H}_{\text{BEM}}$ is derived with the blade element method in the wind axis rotating frame $\boldsymbol{E}_{\widehat{R}}$ and is defined to act along the negative $X_{\widehat{CP}}$-axis.[3] Once again the averaged-over-one-rotor-revolution contribution

[3]Although not necessary, the rotor hind force is also be accompanied by the subscript BEM for consistency purposes. It must be noted, however, that no other method shall be used to obtain an equivalent expression for the rotor hind force (as opposed to the thrust) hence the BEM subscript may be considered unnecessary. The same will apply to the rotor side force and torque.

of all the blades to the rotor H-force must be taken into account as given by eq. (5.100) where $F_{BL|-X\widehat{CP},a}$ is the blade hind force defined to be parallel to and pointing in the opposite direction as the $X_{\widehat{CP}}$-axis.

$$\widehat{H}_{\text{BEM}} = \frac{N}{2\pi}\int_0^{2\pi} F_{BL|-X\widehat{CP},a}\, d\widehat{\psi} \tag{5.100}$$

The blade hind force is composed of the projection of the blade tangential ($F_{BL|-Y\widehat{R},a}$) and radial ($F_{BL|-X\widehat{R},a}$) forces onto the $X_{\widehat{CP}}$-axis as given by eq. (5.101a). A depiction of the contribution of the differential blade tangential and radial forces to the differential hind force is also shown in fig. 5.16. Note that due to the 'always positive' sign convention of the blade azimuthal position $\widehat{\psi}$, the blade tangential force must be multiplied by the Ω_{sgn} parameter in order for the expression to hold for both a clockwise and counter-clockwise rotating rotor. A three-dimensional depiction of the direction of action of the differential blade tangential and radial forces - as well as of the differential hind force - with respect to the rotating and non-rotating frames has already been shown in figs. 5.12 and 5.13.

$$F_{BL|-X\widehat{CP},a} = \Omega_{sgn} F_{BL|-Y\widehat{R},a} sin(\widehat{\psi}) - F_{BL|-X\widehat{R},a} cos(\widehat{\psi}) \tag{5.101a}$$

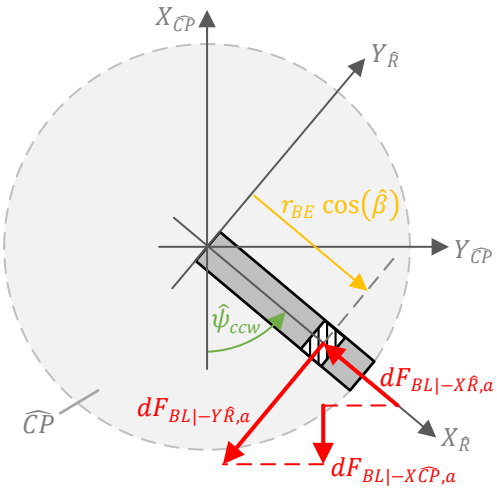

Figure 5.16: Schematic top view of a ccw. rotating rotor blade showing the contribution of the blade element radial and tangential forces to the blade element H-force.

The blade tangential force $F_{BL|-Y\widehat{R},a}$ is obtained by integrating the differential blade horizontal force $dF_{BL|-Y\widehat{BL},a}$ which consists of the blade differential lift dL_{BL} and drag dD_{BL} as given by eq. (5.101b) and as has been depicted in fig. 5.9, repeated below for clarity. Note that due to the 'always positive' convention of the tangential blade element velocity component U_T (as first mentioned on page 125), the direction of the lift and drag vectors will follow the 'always positive' airflow vector changing their positive sign convention direction depending on the direction of rotation of the rotor. Therefore, in order for the differential blade horizontal force $dF_{BL|-Y\widehat{BL},a}$ to always point in the negative direction of the $Y_{\widehat{BL}}$-axis, the lift and drag must be additionally multiplied by the Ω_{sgn} parameter. Recalling that the tangential blade force must also be multiplied by the Ω_{sgn} parameter in the expression for the rotor hind force (i.e. eq. (5.101a)), it shall be later demonstrated that the effects of both sign change parameters ultimately cancel.

$$\begin{aligned} F_{BL|-Y\widehat{R},a} &= \int_0^R dF_{BL|-Y\widehat{R},a} = \int_0^R dF_{BL|-Y\widehat{BL},a} \\ &= \int_0^R (\Omega_{sgn} dL_{BL} sin(\phi_{BE}) + \Omega_{sgn} dD_{BL} cos(\phi_{BE})) \\ &= \Omega_{sgn} \int_0^R (dL_{BL} sin(\phi_{BE}) + dD_{BL} cos(\phi_{BE})) \end{aligned} \tag{5.101b}$$

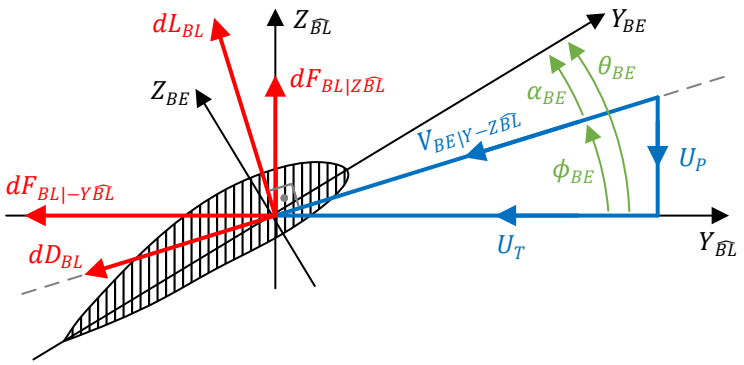

Figure 5.9: Schematic representation of the blade element in the wind axis blade element frame of reference. Velocity arrows indicate the direction of the airflow movement.

The blade radial force $F_{BL|-X\widehat{R},a}$, on the other hand, is obtained by integrating the blade element radial force $dF_{BL|-X\widehat{BL},a}$ which in turn equals to the projection of the differential blade vertical force $dF_{BL|Z\widehat{BL},a}$ onto the $X_{\widehat{R}}$-axis as given by eq. (5.101c) and as has already been shown in fig. 5.11.

$$\begin{aligned} F_{BL|-X\widehat{R},a} &= \int_0^R dF_{BL|-X\widehat{R},a} = \int_0^R sin(\widehat{\beta}) dF_{BL|Z\widehat{BL},a} \\ &= \int_0^R sin(\widehat{\beta})(dL_{BL}cos(\phi_{BE}) - dD_{BL}sin(\phi_{BE})) \end{aligned} \tag{5.101c}$$

Once again it is assumed that both the inflow angle ϕ_{BE} and flapping angle $\widehat{\beta}$ are small, and that the differential blade lift is much greater than the differential blade drag. As a result, the expressions for the blade tangential and radial forces simplify to the forms of eq. (5.101d) and eq. (5.101e). That is, if $\phi_{BE} \ll 1$, $dD_{BL} \ll dL_{BL}$, and $\widehat{\beta} \ll 1$ then:

$$F_{BL|-Y\widehat{R},a} = \Omega_{sgn} \int_0^R (dL_{BL}\phi_{BE} + dD_{BL}) \tag{5.101d}$$

$$F_{BL|-X\widehat{R},a} = \int_0^R \widehat{\beta} dL_{BL} \tag{5.101e}$$

Substituting the simplified expressions back into eq. (5.101a) yields the simplified expression for the blade hind force as given by eq. (5.101f). Notice that performing the substitution produces an Ω_{sgn}^2 term which always equates to 1 (since Ω_{sgn} may only take the value of ± 1), hence it can be removed from the expression simultaneously proving an earlier statement that the effect of the sign change parameter ultimately cancels out in this expression.

$$\begin{aligned} F_{BL|-X\widehat{CP},a} &= \Omega_{sgn} F_{BL|-Y\widehat{R},a} sin(\widehat{\psi}) - F_{BL|-X\widehat{R},a} cos(\widehat{\psi}) \\ &= \Omega_{sgn}^2 \int_0^R (dL_{BL}\phi_{BE} + dD_{BL}) sin(\widehat{\psi}) - \int_0^R \widehat{\beta} dL_{BL} cos(\widehat{\psi}) \\ &= sin(\widehat{\psi}) \int_0^R dL_{BL}\phi_{BE} + sin(\widehat{\psi}) \int_0^R dD_{BL} - \widehat{\beta} cos(\widehat{\psi}) \int_0^R dL_{BL} \end{aligned} \tag{5.101f}$$

It should be highlighted at this point that the blade tangential force $F_{BL|-Y\widehat{R},a}$ is the first rotor expression so far to depend on the blade drag. It is not obvious at this point, but it shall be shown that the inclusion of the blade drag significantly complicates the derivation process. For this reason the simplified expression for the blade hind force is divided into three differential H-force components as shown in eq. (5.102a), where $dH_{i,\phi}$ and $dH_{i,\widehat{\beta}}$ are referred to as lift-induced components while dH_0 is referred to as the drag-induced component. The definitions of these components are given in eqs. (5.102b) to (5.102d).

$$F_{BL|-X\widehat{CP},a} = dH_{i,\phi} + dH_0 - dH_{i,\widehat{\beta}} \tag{5.102a}$$

$$dH_{i,\phi} = sin(\widehat{\psi}) \int_0^R dL_{BL}\phi_{BE} \quad (5.102b) \qquad dH_{i,\widehat{\beta}} = \widehat{\beta}cos(\widehat{\psi}) \int_0^R dL_{BL} \quad (5.102c)$$

$$dH_0 = sin(\widehat{\psi}) \int_0^R dD_{BL} \quad (5.102d)$$

The expression for the (simplified) differential blade lift has already been derived and is given by eq. (5.66), repeated below for clarity. The differential blade drag dD_{BL}, however, has not been treated yet therefore it must be derived first before the derivation of the rotor hind force may continue.

$$dL_{BL} = \frac{1}{2}\rho U_T^2 C_{l_\alpha,bl}\left(\theta_0 + \theta_{bl,1}r_{BE} - \frac{U_P}{U_T}\right)c_{bl}dr_{BE} \quad (5.66)$$

Differential Blade Drag

The differential blade drag is defined by eq. (5.103a) where $C_{d,bl}$ is the drag coefficient of the blade airfoil. In contrast to the differential blade lift, the expression for the blade drag does not explicitly depend on the blade element angle of attack. Instead α_{BE} is implicitly included in the definition of the blade drag coefficient itself as given by eq. (5.103b). This definition is taken from literature (eq. (2.13) in section 2.5) and is repeated here with several of the subscripts changed for coherency purposes. It can be seen that the drag coefficient is a 2nd-degree polynomial as a function of the blade element angle of attack with three constant coefficients C_{d_0}, C_{d_1} and C_{d_2}. It should be mentioned that this definition of the blade drag coefficient is common in helicopter and tilt-rotor literature providing motivation to employ it in this tilt-rotor model as well.

$$dD_{BL} = \frac{1}{2}\rho V_{BE|Y-Z\widehat{BL}}^2 C_{d,bl}c_{bl}dr_{BE} \quad (5.103a)$$

$$C_{d,bl} = C_{d_0,bl} + C_{d_1,bl}\alpha_{BE} + C_{d_2,bl}\alpha_{BE}^2 \quad (5.103b)$$

The simplifications that have been used in the derivation of the differential blade lift are also employed in the case of the differential blade drag. In summary, the tangential blade element velocity component is assumed to be much larger than the perpendicular component resulting in the simplification of the total aerodynamic velocity $V_{BE|Y-Z\widehat{BL}}^2$, simultaneously making it possible to assume that the inflow angle ϕ_{BE} is small enabling its linearization. The definitions of the angle of attack and pitch of the blade element, as well as the simplified expressions for the blade element inflow angle and total aerodynamic velocity have already been given by eqs. (5.61) and (5.63) to (5.65), however they are repeated below for clarity.

$$\alpha_{BE} = \theta_{BE} - \phi_{BE} \quad (5.61) \qquad \theta_{BE} = \theta_0 + \theta_{bl,1}r_{BE} \quad (5.63)$$

$$\phi_{BE} = \frac{U_P}{U_T} \quad (5.64) \qquad V_{BE|Y-Z\widehat{BL}}^2 = U_T^2 \quad (5.65)$$

Applying the simplifications to eq. (5.103) and expanding the expression for the angle of attack yields a simplified differential blade drag as seen in eq. (5.104). At this point it becomes clear that the inclusion of the drag term in the rotor hind force expression increases the complexity of the derivation due to the much more extensive definition of the blade element drag when compared to the definition of the blade element lift. This is further demonstrated in the following section which continues with the derivation of the differential H-force components.

$$\begin{aligned} dD_{BL} =& \frac{1}{2}\rho U_T^2\left(C_{d_0,bl} + C_{d_1,bl}\alpha_{BE} + C_{d_2,bl}\alpha_{BE}^2\right)c_{bl}dr_{BE} \\ =& \frac{1}{2}\rho c_{bl}U_T^2\left(C_{d_0,bl} + C_{d_1,bl}\left(\theta_0 + \theta_{bl,1}r_{BE} - \frac{U_P}{U_T}\right) + C_{d_2,bl}\left(\theta_0 + \theta_{bl,1}r_{BE} - \frac{U_P}{U_T}\right)^2\right)dr_{BE} \end{aligned} \quad (5.104)$$

Differential H-Force Component Expansion

Having obtained (simplified) expressions for both the differential blade lift and drag it is now possible to substitute them back into the differential H-force components starting with the lift-induced $dH_{i,\widehat{\beta}}$ as shown in eq. (5.105a). Recalling the simplified blade thrust force (i.e. eq. (5.85c) repeated below), however, it can be seen that $dH_{i,\widehat{\beta}}$ contains the entirety of the blade thrust. Therefore instead of substituting the simplified lift and performing the expansion again, the result of the expansion of the blade thrust may be directly substituted into this lift-induced H-force component. As a consequence, the resulting expanded expressions are almost identical (with the exception of the product with $\widehat{\beta}cos(\widehat{\psi})$ outside of the integrals) since they depend on the same common integrals.

$$F_{BL|Z\widehat{R},a} = \int_0^R dL_{BL} \tag{5.85c}$$

$$\begin{aligned} dH_{i,\widehat{\beta}} &= \widehat{\beta}cos(\widehat{\psi}) \int_0^R dL_{BL} = \widehat{\beta}cos(\widehat{\psi}) F_{BL|Z\widehat{R},a} \\ &= \frac{1}{2}\rho C_{l_{\alpha,bl}} c_{bl} \widehat{\beta}cos(\widehat{\psi}) \left(\theta_{bl,1} \underbrace{\int_0^R U_T^2 r_{BE} dr_{BE}}_{CI_3} + \theta_0 \underbrace{\int_0^R U_T^2 dr_{BE}}_{CI_1} - \underbrace{\int_0^R U_P U_T dr_{BE}}_{CI_2} \right) \end{aligned} \tag{5.105a}$$

Inspecting the second lift-induced component $dH_{i,\phi}$ shown in eq. (5.105b) may lead to the conclusion that once again advantage may be taken of the similarity between the blade thrust and this differential H-force component to obtain an expanded expression. Unfortunately expanding the blade element inflow angle shows that it indirectly depends on the radial position through the blade element velocity components and therefore it may not be taken out of the integral. Therefore the expression must be expanded anew revealing that the second lift-induced component $dH_{i,\phi}$ now depends on two different common integrals, i.e. CI_4 and CI_5, the former having appeared already in the derivation of the aerodynamic flapping moment (i.e. eq. (5.67)) while the latter appearing for the first time.

$$\begin{aligned} dH_{i,\phi} &= sin(\widehat{\psi}) \int_0^R dL_{BL} \phi_{BE} \\ &= sin(\widehat{\psi}) \int_0^R \frac{1}{2}\rho U_T^2 C_{l_{\alpha,bl}} \left(\theta_0 + \theta_{bl,1} r_{BE} - \frac{U_P}{U_T} \right) c_{bl} dr_{BE} \frac{U_P}{U_T} \\ &= \frac{1}{2}\rho C_{l_{\alpha,bl}} c_{bl} sin(\widehat{\psi}) \int_0^R U_T U_P \left(\theta_0 + \theta_{bl,1} r_{BE} - \frac{U_P}{U_T} \right) dr_{BE} \\ &= \frac{1}{2}\rho C_{l_{\alpha,bl}} c_{bl} sin(\widehat{\psi}) \left(\theta_0 \underbrace{\int_0^R U_T U_P dr_{BE}}_{CI_2} + \theta_{bl,1} \underbrace{\int_0^R U_T U_P r_{BE} dr_{BE}}_{CI_4} - \underbrace{\int_0^R U_P^2 dr_{BE}}_{CI_5} \right) \end{aligned} \tag{5.105b}$$

Finally eq. (5.105c) presents the expansion of the drag-induced differential H-force component which is obtained after the substitution of the simplified differential blade drag expression (eq. (5.104)) into eq. (5.102d). The increased expression complexity brought by the inclusion of the drag may now be directly observed in the expanded expression which depends on three additional common integrals when compared to the previous differential H-force components, with common integral 6 making its first appearance in the rotor expressions.

$$
\begin{aligned}
dH_0 &= sin(\widehat{\psi}) \int_0^R dD_{BL} \\
&= sin(\widehat{\psi}) \int_0^R \frac{1}{2}\rho c_{bl} U_T^2 \left(C_{d_0,bl} + C_{d_1,bl}\left(\theta_0 + \theta_{bl,1} r_{BE} - \frac{U_P}{U_T}\right) + C_{d_2,bl}\left(\theta_0 + \theta_{bl,1} r_{BE} - \frac{U_P}{U_T}\right)^2 \right) dr_{BE} \\
&= \frac{1}{2}\rho c_{bl} sin(\widehat{\psi}) \Bigg(\left(C_{d_0,bl} + C_{d_1,bl}\theta_0 + C_{d_2,bl}\theta_0^2\right) \underbrace{\int_0^R U_T^2 dr_{BE}}_{CI_1} \\
&+ \left(C_{d_1,bl}\theta_{bl,1} + 2C_{d_2,bl}\theta_0\theta_{bl,1}\right) \underbrace{\int_0^R U_T^2 r_{BE} dr_{BE}}_{CI_3} + C_{d_2,bl}\theta_{bl,1}^2 \underbrace{\int_0^R U_T^2 r_{BE}^2 dr_{BE}}_{CI_6} \\
&- \left(C_{d_1,bl} + 2C_{d_2,bl}\theta_0\right) \underbrace{\int_0^R U_T U_P dr_{BE}}_{CI_2} - 2C_{d_2,bl}\theta_{bl,1} \underbrace{\int_0^R U_T U_P r_{BE} dr_{BE}}_{CI_4} + C_{d_2,bl} \underbrace{\int_0^R U_P^2 dr_{BE}}_{CI_5} \Bigg)
\end{aligned}
\tag{5.105c}
$$

Recalling eq. (5.100) and eq. (5.102a), the complete rotor H-force expression is obtained by solving eq. (5.106). Similarly to the rotor thrust, after all common integrals within the differential H-force components are evaluated along the blade length, the same non-dimensional terms defined in eqs. (5.68) to (5.71) are introduced into the expressions, namely the blade lock number γ_{bl}, the wind axis control plane advance ratio $\widehat{\mu}_{tc}$, the wind axis control plane inflow ratio $\widehat{\lambda}_{pc}$, and the induced velocity inflow ratio λ_i. Once again the solved integrals are still (non-linear) functions of the flapping angle $\widehat{\beta}$. Therefore first the small angle approximation is applied to $\widehat{\beta}$ simplifying the trigonometric functions and removing any powers or products of $\widehat{\beta}$ and its derivatives. Next, all instances of the flapping angle and its derivatives are replaced by the (wind axis) disk tilt quasi-static solution, as defined by eq. (5.78), which incorporates the disk tilt angles into the expressions, and simultaneously enables the future definition of the rotor hind force with respect to a non-rotating frame. The prior application of the small angle approximation to $\widehat{\beta}$ also ensures that the final expression is linear with respect to the disk tilt angles. It should be highlighted that the incorporation of the disk tilt approximation must be performed before taking the integral of the blade H-force around one blade revolution (eq. (5.102a)) since the disk tilt quasi-static solution is a function of the azimuth position $\widehat{\psi}$. After the inclusion of the disk tilt angles, eq. (5.106) may be finally evaluated yielding the analytical expression for the rotor hind force defined with respect to the (non-rotating) wind-axis control plane frame.

$$
\widehat{H}_{\text{BEM}} = \frac{N}{2\pi} \int_0^{2\pi} F_{BL|-X\widehat{CP},a} d\widehat{\psi} = \frac{N}{2\pi} \int_0^{2\pi} \left(dH_{i,\phi} + dH_0 - dH_{i,\widehat{\beta}} \right) d\widehat{\psi} \tag{5.106}
$$

The complete expression for the rotor hind force shall not be shown here due to its extensiveness, however a simplified version is presented and analyzed below.

BEM Hind Force Expression Analysis

An expanded but partially simplified version of the rotor H-force expression is shown in eq. (5.107) which shall be used to answer a portion of the research sub-question concerned with determining the effect of the tilting proprotor on the rotor force expressions. The rotor H-force is simplified in a similar fashion to the rotor thrust expression by first supplying it to the reduction scheme (described in great detail in section 6.3) removing all negligible terms. Next the linearly varying blade twist parameter $\theta_{bl,1}$, the control plane deflection, and the wind shift angle are all set to zero in order to improve readability (the motivation for the latter two is explained on page 136). Additionally the blade element drag coefficient $C_{d,bl}$ is simplified to only include the angle-of-attack-independent constant $C_{d_0,bl}$ while the other two constants are set to zero (i.e. $C_{d_1,bl} = C_{d_2,bl} = 0$), greatly reducing the expression length. It must be highlighted that the reduction scheme considers all three drag constants significant, therefore they appear in the reduced expression. In order to aid visual inspection of the expression, however, all terms multiplied by $C_{d_1,bl}$ and $C_{d_2,bl}$ are removed.

Several linear and rotational rate combinations have also been replaced by single variables for notation compactness, including the total inflow ratio $\widehat{\lambda}_{tot}$ as already defined by eq. (5.73). In appendix C eq. (C.4) provides the expansion of the combined rotational rates while an overview and description of the subscripts of these combined terms is given in table C.1. For the sake of clarity, in summary the subscript eff refers to 'effective' rotational rates and tot refers to 'total' rotational rates, while the subscript i refers to the inertial rates. Rates that are not indicated by any subscripts are total aerodynamic rates. A detailed description of 'effective' and 'total' rates is provided on page 127, while the distinction between inertial, wash, and total rates is explained on page 118. The rotational rates have also been made non-dimensional, indicated with an overbar symbol ($\bar{}$), by dividing them by Ω making it possible to take Ω^2 outside of the brackets.

Equation (5.107) has been arranged into five main groups indicated by the right-hand-side annotations, namely the $\widehat{a}_0$-dependent group, the symmetrical and asymmetrical $\widehat{a}_1$-dependent groups, and the free symmetrical and asymmetrical groups. The asymmetrical groups correspond to terms multiplied by the Ω_{sgn} parameter, while the symmetrical groups are rotor-rotation-independent. Note that this symmetry definition is only valid if the wind-shift angle Δ is zero or $180°$. A separate expression corresponding to a counter-clockwise rotor in helicopter configuration shall not be presented since if all effective rotational rates are replaced by their pure body rate counterparts, then eq. (5.107) becomes representative of the H-force expression corresponding to a helicopter.

$$
\begin{aligned}
\widehat{H}_{\text{BEM}} = \frac{\Omega^2 I_{bl}\gamma_{bl}N}{R}\Bigg[& \frac{3\theta_0\widehat{\lambda_{pc}} - 2}{24}\overline{q}\widehat{a}_0 && (\widehat{a}_0\text{-dependent}) \\
& + \Bigg(\frac{\overline{r}_{eff}^2 - \overline{r}^2 C_\eta^2 + \overline{r}_{eff}\overline{r}_{i,eff} + 2}{12}\theta_0 + \frac{3\widehat{\lambda_{tot}}}{8} && (\text{sym. } \widehat{a}_1\text{-dep.}) \\
& - \Omega_{sgn}\left\{ \frac{\overline{r}_{eff} + 2\overline{r}_{i,eff}}{8}\widehat{\lambda_{tot}} + \frac{3\overline{r}_{eff} + \overline{r}_{i,eff}}{12}\theta_0 + \frac{\overline{p}_{eff}\widehat{\mu}_{tc}}{32} \right\}\Bigg)\widehat{a}_1 && (\text{asym. } \widehat{a}_1\text{-dep.}) \\
& + \frac{\overline{p}_{eff}\overline{r}_{eff} - 3\widehat{\mu}_{tc}\widehat{\lambda}_{tot}}{12}\theta_0 + \frac{\widehat{\mu}_{tc}C_{d_0,bl}}{4C_{l_\alpha,bl}} && (\text{free symmetrical}) \\
& - \Omega_{sgn}\left(\frac{\theta_0}{12} + \frac{\widehat{\lambda}_{tot}}{4} \right)\overline{p}_{eff} \Bigg] && (\text{free asymmetrical})
\end{aligned}
\tag{5.107}
$$

Unlike the BEM thrust, the rotor H-force not only depends on the longitudinal disk tilt angle $\widehat{a}_1$, but also on the coning angle $\widehat{a}_0$. The lateral disk tilt angle $\widehat{b}_1$, however, is still not considered significant enough by the reduction scheme and therefore it is removed from the final H-force expression. Although the reduced H-force expression is linear with respect to these disk tilt angles, the same cannot be said for the inflow ratio λ_i. The full expression initially contains λ_i terms that are multiplied with $\widehat{a}_0$ and $\widehat{a}_1$. The reduction scheme does remove all products of λ_i with $\widehat{a}_0$, however several products with the longitudinal disk tilt are still considered significant enough to remain in the expression yielding the non-linearity. For this reason the rotor H-force expression may not be appended to the system of linear equations containing the disk tilt angles and inflow ratio (i.e. eq. (5.81)).

Although not shown in eq. (5.107), the nacelle tilt rate $\dot{\eta}$ does appear in the expression therefore it is considered a significant contributor to the H-force. The reduction scheme does, however, remove several instances of the tilt rate in terms where it is nominally directly added to the body pitch rate. This leads to the conclusion that in some cases the addition of the nacelle tilt rate to the body rate may be insignificant and therefore would (minimally yet still) unnecessarily increase the complexity of the expressions. Interestingly all remaining instances of $\dot{\eta}$ are always multiplied by the Ω_{sgn} parameter.

The tiltable nacelle also manifests itself in the 'effective' rotational rates and linear rates (i.e. $\widehat{\mu}_{tc}$, $\widehat{\lambda}_{pc}$, and $\widehat{\lambda}_{tot}$) experienced by the rotor in the same manner as described in the flapping equation analysis. It should be noted that any term that is not multiplied by an 'effective' rate is inherently independent from the nacelle tilt angle. Terms that only exist in conversion mode (and thus are unique to tilt-rotors) also appear in the expression, such as the result of the multiplication of the effective roll and yaw rates which contains products such as $sin(\eta)cos(\eta)$ which are non-zero only in conversion mode. Terms that do not depend on the nacelle tilt angle at all also appear in the expression, such as the symmetrical $\widehat{a}_1$ dependent θ_0 term.

It should be highlighted that the presence of the asymmetrical groups means that in certain flight conditions two counter-rotating rotors may produce a hind-force-imbalance resulting in a yawing motion in helicopter configuration, rolling motion in airplane configuration, or a combined roll-yaw motion of the tilt-rotor in conversion mode.

Lastly it should be noted that the rotor H-force expression shown above contains a ratio between the blade drag coefficient and blade lift coefficient, of which the latter does not appear explicitly in the BEM thrust equation. Instead the blade lift coefficient is implicitly contained within the blade lock number γ_{bl}. For sake of clarity and consistency, however, γ_{bl} is implemented into the H-force expression as well which unfortunately contains terms which do not contain the blade lift coefficient at all. For this reason if those terms are to be multiplied by γ_{bl}, they must also be divided by $C_{l_\alpha,bl}$ resulting in the mentioned ratio between the drag and lift coefficients.

5.2.8. Blade Element Side Force (S-Force)

The rotor side force $\widehat{S}_{\text{BEM}}$ is also derived with the blade element method in the wind axis rotating frame $\boldsymbol{E}_{\widehat{R}}$ and is defined to act along the negative $Y_{\widehat{CP}}$-axis. Once again the averaged-over-one-rotor-revolution contribution of all the blades to the rotor S-force must be taken into account as given by eq. (5.108) where $F_{BL|-Y\widehat{CP},a}$ is the blade side force defined to be parallel to and pointing in the opposite direction as the $Y_{\widehat{CP}}$-axis.

$$\widehat{S}_{\text{BEM}} = \frac{N}{2\pi}\int_0^{2\pi} F_{BL|-Y\widehat{CP},a}\, d\widehat{\psi} \tag{5.108}$$

Similarly to the blade hind force, the side force is also composed of the blade tangential ($F_{BL|-Y\widehat{R},a}$) and radial ($F_{BL|-X\widehat{R},a}$) forces, however in this case projected onto the $Y_{\widehat{CP}}$-axis as given by eq. (5.109a). A depiction of the contribution of the differential blade tangential and radial forces to the differential hind force is also shown in fig. 5.17. Note that due to the 'always positive' sign convention of the blade azimuthal position $\widehat{\psi}$, in the case of the side force the blade radial force must be multiplied by the Ω_{sgn} parameter (as opposed to the tangential force in the case of the hind force) in order for the expression to hold for both a clockwise and counter-clockwise rotating rotor. A three-dimensional depiction of the direction of action of the differential side force with respect to the rotating and non-rotating frames has also been already shown in fig. 5.13.

$$F_{BL|-Y\widehat{CP},a} = F_{BL|-Y\widehat{R},a}\cos(\widehat{\psi}) + \Omega_{sgn}F_{BL|-X\widehat{R},a}\sin(\widehat{\psi}) \tag{5.109a}$$

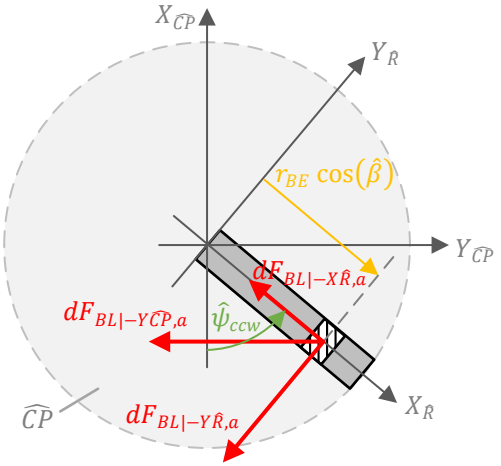

Figure 5.17: Schematic top view of a ccw. rotating rotor blade showing the contribution of the blade element radial and tangential forces to the blade element S-force.

The blade tangential and radial force have already been derived in the previous section treating the rotor hind force, therefore only the resulting simplified expressions for these blade forces given by eqs. (5.101d)

and (5.101e) are repeated below. As a reminder it is assumed that both the inflow angle ϕ_{BE} and flapping angle $\widehat{\beta}$ are small, and that the differential blade lift is much greater than the differential blade drag. Once again it should be noted that the blade tangential force is multiplied by the Ω_{sgn} parameter, however unlike in the blade hind force, in the case of the blade side force none of the Ω_{sgn} parameters shall cancel out therefore this effect of the rotation direction shall carry through to the final expression for the rotor side force.

$$F_{BL|-Y\widehat{R},a} = \int_0^R dF_{BL|-Y\widehat{R},a} = \Omega_{sgn} \int_0^R (dL_{BL}\phi_{BE} + dD_{BL}) \tag{5.101d}$$

$$F_{BL|-X\widehat{R},a} = \int_0^R dF_{BL|-X\widehat{R},a} = \int_0^R \widehat{\beta} dL_{BL} \tag{5.101e}$$

Substituting the simplified expressions back into eq. (5.109a) yields the simplified expression for the blade side force as given by eq. (5.109b). Referring back to the mentioned carried through effect of the rotation direction, notice that in the case of the blade side force both the blade tangential and radial forces are multiplied by Ω_{sgn}.

$$\begin{aligned} F_{BL|-Y\widehat{CP},a} &= F_{BL|-Y\widehat{R},a} cos(\widehat{\psi}) + \Omega_{sgn} F_{BL|-X\widehat{R},a} sin(\widehat{\psi}) \\ &= \Omega_{sgn} \int_0^R (dL_{BL}\phi_{BE} + dD_{BL}) cos(\widehat{\psi}) + \Omega_{sgn} \int_0^R \widehat{\beta} dL_{BL} sin(\widehat{\psi}) \\ &= \Omega_{sgn} cos(\widehat{\psi}) \int_0^R dL_{BL}\phi_{BE} + \Omega_{sgn} cos(\widehat{\psi}) \int_0^R dD_{BL} + \Omega_{sgn} \widehat{\beta} sin(\widehat{\psi}) \int_0^R dL_{BL} \end{aligned} \tag{5.109b}$$

Similarly to the blade hind force it can be seen that the blade side force also depends on the blade drag. Therefore, due to the increased complexity of the derivation, the simplified expression for the blade side force is divided into three differential S-force components as shown in eq. (5.110a), where $dS_{i,\phi}$ and $dS_{i,\widehat{\beta}}$ are referred to as lift-induced components while dS_0 is referred to as the drag-induced component. The definitions of these components are given in eqs. (5.110b) to (5.110d).

$$F_{BL|-Y\widehat{CP},a} = dS_{i,\phi} + dS_0 + dS_{i,\widehat{\beta}} \tag{5.110a}$$

$$dS_{i,\phi} = \Omega_{sgn} cos(\widehat{\psi}) \int_0^R dL_{BL}\phi_{BE} \tag{5.110b}$$

$$dS_0 = \Omega_{sgn} cos(\widehat{\psi}) \int_0^R dD_{BL} \tag{5.110c}$$

$$dS_{i,\widehat{\beta}} = \Omega_{sgn} \widehat{\beta} sin(\widehat{\psi}) \int_0^R dL_{BL} \tag{5.110d}$$

Although the expressions for the simplified differential blade lift and drag have already been derived and are given by eqs. (5.66) and (5.104) (repeated below for consistency), they are not necessary to obtain the expanded expressions of the differential S-force components as shall be demonstrated next.

$$dL_{BL} = \frac{1}{2}\rho U_T^2 C_{l_\alpha,bl} \left(\theta_0 + \theta_{bl,1} r_{BE} - \frac{U_P}{U_T}\right) c_{bl} dr_{BE} \tag{5.66}$$

$$dD_{BL} = \frac{1}{2}\rho c_{bl} U_T^2 \left(C_{d_0,bl} + C_{d_1,bl}\left(\theta_0 + \theta_{bl,1} r_{BE} - \frac{U_P}{U_T}\right) + C_{d_2,bl}\left(\theta_0 + \theta_{bl,1} r_{BE} - \frac{U_P}{U_T}\right)^2\right) dr_{BE} \tag{5.104}$$

Differential S-Force Component Expansion

Instead of substituting the simplified expressions for the differential blade lift and drag into the differential S-force components and carrying out the expansion as has been done in the case of the hind-force components, it is worthwhile to first inspect the integrals that are contained within these components. As it turns out, almost all of the steps involved in the expansion of the S-force components have already been carried out in the derivation of the rotor thrust and hind force. For this reason the simplified blade thrust $F_{BL|Z\widehat{R},a}$, lift-induced differential H-force $dH_{i,\phi}$, and drag-induced differential H-force dH_0 given by eqs. (5.85c), (5.102b) and (5.102d) respectively shall be repeated below for comparison with the differential S-force components.

Starting with the first lift-induced component $dS_{i,\widehat{\beta}}$ shown in eq. (5.111a) it can be seen that the integral along the blade length is equivalent to the simplified blade thrust given by eq. (5.85c). Hence $F_{BL|Z\widehat{R},a}$ may be directly substituted into eq. (5.111a) yielding the first expanded lift-induced S-force component. It is no surprise that this S-force component depends on the same common integrals as the expanded blade thrust (i.e. eq. (5.86)) and thus is almost identical to it with the exception of the product with $\Omega_{sgn}\widehat{\beta}sin(\widehat{\psi})$ outside of the integrals.

$$F_{BL|Z\widehat{R},a} = \int_0^R dL_{BL} \tag{5.85c}$$

$$\begin{aligned} dS_{i,\widehat{\beta}} &= \Omega_{sgn}\widehat{\beta}sin(\widehat{\psi}) \int_0^R dL_{BL} = \Omega_{sgn}\widehat{\beta}sin(\widehat{\psi})F_{BL|Z\widehat{R},a} \\ &= \Omega_{sgn}\frac{\rho C_{l_\alpha,bl} c_{bl}\widehat{\beta}sin(\widehat{\psi})}{2}\left(\theta_{bl,1}\underbrace{\int_0^R U_T^2 r_{BE} dr_{BE}}_{CI_3} + \theta_0 \underbrace{\int_0^R U_T^2 dr_{BE}}_{CI_1} - \underbrace{\int_0^R U_P U_T dr_{BE}}_{CI_2}\right) \end{aligned} \tag{5.111a}$$

Next, inspecting the second lift-induced component $dS_{i,\phi}$ shown in eq. (5.111b) it can be seen that the same integral along the blade length appears in the analogous differential lift-induced H-force component given by eq. (5.102b). Therefore $dH_{i,\phi}/sin(\widehat{\psi})$ may also replace the integral in eq. (5.111b) yielding the second expanded lift-induced S-force component. Once again this S-force component depends on the same common integrals as the expanded analogous H-force component (i.e. eq. (5.105b)) and thus is almost identical to it with the exception of the products outside of the integrals.

$$dH_{i,\phi} = sin(\widehat{\psi}) \int_0^R dL_{BL}\phi_{BE} \tag{5.102b}$$

$$\begin{aligned} dS_{i,\phi} &= \Omega_{sgn}cos(\widehat{\psi}) \int_0^R dL_{BL}\phi_{BE} = \Omega_{sgn}cos(\widehat{\psi})\frac{dH_{i,\phi}}{sin(\widehat{\psi})} \\ &= \Omega_{sgn}\frac{\rho C_{l_\alpha,bl} c_{bl} cos(\widehat{\psi})}{2}\left(\theta_0 \underbrace{\int_0^R U_T U_P dr_{BE}}_{CI_2} + \theta_{bl,1}\underbrace{\int_0^R U_T U_P r_{BE} dr_{BE}}_{CI_4} - \underbrace{\int_0^R U_P^2 dr_{BE}}_{CI_5}\right) \end{aligned} \tag{5.111b}$$

Finally, inspecting the drag-induced component dS_0 shown in eq. (5.111c) it can be seen that the same integral along the blade length appears in the analogous differential drag-induced H-force component given by eq. (5.102d). Therefore $dH_0/sin(\widehat{\psi})$ may replace the integral in eq. (5.111c) yielding the drag-induced S-force component. Again, this S-force component depends on the same common integrals as the expanded analogous H-force component (i.e. eq. (5.105c)) and thus is almost identical to it with the exception of the products outside of the integrals.

$$dH_0 = sin(\widehat{\psi}) \int_0^R dD_{BL} \tag{5.102d}$$

$$
\begin{aligned}
dS_0 &= \Omega_{sgn} cos(\widehat{\psi}) \int_0^R dD_{BL} = \Omega_{sgn} cos(\widehat{\psi}) \frac{dH_0}{sin(\widehat{\psi})} \\
&= \Omega_{sgn} \frac{\rho C_{l_\alpha,bl} c_{bl} cos(\widehat{\psi})}{2} \Bigg(\left(C_{d_0,bl} + C_{d_1,bl}\theta_0 + C_{d_2,bl}\theta_0^2\right) \underbrace{\int_0^R U_T^2 dr_{BE}}_{CI_1} \\
&+ \left(C_{d_1,bl}\theta_{bl,1} + 2C_{d_2,bl}\theta_0\theta_{bl,1}\right) \underbrace{\int_0^R U_T^2 r_{BE} dr_{BE}}_{CI_3} + C_{d_2,bl}\theta_{bl,1}^2 \underbrace{\int_0^R U_T^2 r_{BE}^2 dr_{BE}}_{CI_6} \\
&- \left(C_{d_1,bl} + 2C_{d_2,bl}\theta_0\right) \underbrace{\int_0^R U_T U_P dr_{BE}}_{CI_2} - 2C_{d_2,bl}\theta_{bl,1} \underbrace{\int_0^R U_T U_P r_{BE} dr_{BE}}_{CI_4} + C_{d_2,bl} \underbrace{\int_0^R U_P^2 dr_{BE}}_{CI_5} \Bigg)
\end{aligned}
\tag{5.111c}
$$

Recalling eqs. (5.108) and (5.110a), the complete rotor S-force expression is obtained by solving eq. (5.112). Similarly to the rotor thrust and hind force, after all common integrals within the differential S-force components are evaluated along the blade length, the same non-dimensional terms defined in eqs. (5.68) to (5.71) are introduced into the expressions, namely the blade lock number γ_{bl}, the wind axis control plane advance ratio $\widehat{\mu}_{tc}$, the wind axis control plane inflow ratio $\widehat{\lambda}_{pc}$, and the induced velocity inflow ratio λ_i. Once again the solved integrals are still (non-linear) functions of the flapping angle $\widehat{\beta}$. Therefore first the small angle approximation is applied to $\widehat{\beta}$ simplifying the trigonometric functions and removing any powers or products of $\widehat{\beta}$ and its derivatives. Next, all instances of the flapping angle and its derivatives are replaced by the (wind axis) disk tilt quasi-static solution, as defined by eq. (5.78), which incorporates the disk tilt angles into the expressions, and simultaneously enables the future definition of the rotor hind force with respect to a non-rotating frame. The prior application of the small angle approximation to $\widehat{\beta}$ also ensures that the final expression is linear with respect to the disk tilt angles. It should be highlighted that the incorporation of the disk tilt approximation must be performed before taking the integral of the blade S-force around one blade revolution (eq. (5.110a)) since the disk tilt quasi-static solution is a function of the azimuth position $\widehat{\psi}$. After the inclusion of the disk tilt angles, eq. (5.112) may be finally evaluated yielding the analytical expression for the rotor side force defined with respect to the (non-rotating) wind-axis control plane frame.

$$
\widehat{S}_{\text{BEM}} = \frac{N}{2\pi} \int_0^{2\pi} F_{BL|-Y\widehat{CP},a} d\widehat{\psi} = \frac{N}{2\pi} \int_0^{2\pi} \left(dS_{i,\phi} + dS_0 + dS_{i,\widehat{\beta}}\right) d\widehat{\psi} \tag{5.112}
$$

The complete expression for the rotor side force shall not be shown here due to its extensiveness, however a simplified version is presented and analyzed below.

BEM Side Force Expression Analysis

An expanded but partially simplified version of the rotor S-force expression is shown in eq. (5.113) which shall be used to answer a portion of the research sub-question concerned with determining the effect of the tilting proprotor on the rotor force expressions. The rotor S-force is simplified in the same manner as the rotor H-force expression by first supplying it to the reduction scheme (described in great detail in section 6.3) removing all negligible terms. Next the linearly varying blade twist parameter $\theta_{bl,1}$, the control plane deflection, and the wind shift angle are all set to zero in order to improve readability (the motivation for the latter two is explained on page 136). Additionally the blade element drag coefficient $C_{d,bl}$ is simplified to only include the angle-of-attack-independent constant $C_{d_0,bl}$ while the other two constants are set to zero (i.e. $C_{d_1,bl} = C_{d_2,bl} = 0$), greatly reducing the expression length. It must be highlighted that the reduction scheme considers the latter two drag constants significant, therefore they appear in the reduced expression. In order to aid visual inspection of the expression, however, all terms multiplied by $C_{d_1,bl}$ and $C_{d_2,bl}$ are removed.

Several linear and rotational rate combinations have also been replaced by single variables for notation compactness, including the total inflow ratio $\widehat{\lambda}_{tot}$ as already defined by eq. (5.73). In appendix C eq. (C.4)

provides the expansion of the combined rotational rates while an overview and description of the subscripts of these combined terms is given in table C.1. For the sake of clarity, in summary the subscript eff refers to 'effective' rotational rates and tot refers to 'total' rotational rates, while the subscript i refers to the inertial rates. Rates that are not indicated by any subscripts are total aerodynamic rates. A detailed description of 'effective' and 'total' rates is provided on page 127, while the distinction between inertial, wash, and total rates is explained on page 118. The rotational rates have also been made non-dimensional, indicated with an overbar symbol ($\bar{}$), by dividing them by Ω making it possible to take Ω^2 outside of the brackets.

Equation (5.113) has been arranged into eight main groups indicated by the right-hand-side annotations, namely the symmetrical and asymmetrical $\widehat{a}_0$-dependent groups, the symmetrical and asymmetrical $\widehat{a}_1$-dependent groups, the symmetrical and asymmetrical $\widehat{b}_1$-dependent groups, and the free symmetrical and asymmetrical groups. The definition of the S-force symmetry is not as straightforward as the one of the BEM thrust and H-force, therefore it is treated in the detailed expression analysis below eq. (5.113). A separate expression corresponding to a counter-clockwise rotor in helicopter configuration shall not be presented since if all effective rotational rates are replaced by their pure body rate counterparts, then eq. (5.113) becomes representative of the S-force expression corresponding to a helicopter.

$$
\begin{aligned}
\widehat{S}_{\text{BEM}} = \frac{\Omega^2 I_{bl}\gamma_{bl}N}{R}\Bigg[\Bigg(&\Omega_{sgn}\frac{3\theta_0 + 6\widehat{\lambda}_{tot}}{8}\widehat{\mu}_{tc} && \text{(sym. } \widehat{a}_0\text{-dep.)}\\
&+\frac{\overline{p}_{eff}}{12} - \frac{\overline{p}_{eff}\widehat{\lambda}_{tot} + 3\overline{r}_{eff}\widehat{\mu}_{tc}}{8}\theta_0\Bigg)\widehat{a}_0 && \text{(asym. } \widehat{a}_0\text{-dep.)}\\
&+\Bigg(-\Omega_{sgn}\frac{7(\overline{q}+\overline{\dot{\eta}})}{32}\widehat{\mu}_{tc} && \text{(sym. } \widehat{a}_1\text{-dep.)}\\
&+\frac{\overline{p}_{eff}\overline{q}\theta_0}{24}\Bigg)\widehat{a}_1 && \text{(asym. } \widehat{a}_1\text{-dep.)}\\
&\Bigg(-\frac{3\widehat{\mu}_{tc} + \overline{r}_{eff}\overline{r}_{i,eff} + 2}{12}\theta_0 - \frac{3\widehat{\lambda}_{tot}}{8} && \text{(sym. } \widehat{b}_1\text{-dep.)}\\
&+\Omega_{sgn}\left\{\frac{3\overline{r}_{eff} + \overline{r}_{i,eff}}{12}\theta_0 + \frac{8\overline{r}_{i,eff}\widehat{\lambda}_{tot} - 5\overline{p}_{eff}\widehat{\mu}_{tc} + 4\overline{r}_{eff}\widehat{\lambda}_{pc}}{32}\right\}\Bigg)\widehat{b}_1 && \text{(asym. } \widehat{b}_1\text{-dep.)}\\
&-\Omega_{sgn}\frac{(\overline{q}+\overline{\dot{\eta}})(\widehat{3\lambda}_{tot} + \theta_0)}{12} && \text{(free symmetrical)}\\
&+\frac{\overline{\dot{\eta}}\overline{p}S_\eta + \overline{r}_{eff}\overline{q}}{12}\theta_0\Bigg] && \text{(free asymmetrical)}
\end{aligned}
\tag{5.113}
$$

The S-force is the only rotor force that depends on all three disk tilt angles, even after all insignificant terms are removed by the reduction scheme. Although the reduced S-force expression is linear with respect to these disk tilt angles, the same cannot be said for the inflow ratio λ_i. The full expression contains λ_i terms that are multiplied with $\widehat{a}_0$ and $\widehat{b}_1$ and although some of these terms are removed, some instances of both products are still considered significant enough to remain in the expression resulting in the non-linearity. Similarly to the H-force, for this reason the rotor S-force expression may not be appended to the system of linear equations containing the disk tilt angles and inflow ratio (i.e. eq. (5.81)).

As can be observed in eq. (5.113), the nacelle tilt rate $\dot{\eta}$ appears in the expression therefore it is considered a significant contributor to the S-force. The reduction scheme does, however, remove several instances of the tilt rate in terms where it is nominally directly added to the body pitch rate. This leads to the conclusion that in some cases the addition of the nacelle tilt rate to the body rate may be insignificant and therefore would (minimally yet still) unnecessarily increase the complexity of the expressions. All remaining instances of $\dot{\eta}$ are either multiplied by $\widehat{a}_1$ or are part of the free groups.

The tiltable nacelle also manifests itself in the 'effective' rotational rates and linear rates (i.e. $\widehat{\mu}_{tc}$, $\widehat{\lambda}_{pc}$, and $\widehat{\lambda}_{tot}$) experienced by the rotor in the same manner as described in the flapping equation analysis. It should be noted that any term that is not multiplied by an 'effective' rate is inherently independent from the nacelle

tilt angle. Terms that only exist in conversion mode (and thus are unique to tilt-rotors) also appear in the expression, such as the result of the multiplication of the inertial and aerodynamic effective yaw rates which contains products such as $sin(\eta)cos(\eta)$ which are non-zero only in conversion mode. Terms that do not depend on the nacelle tilt angle at all also appear in the expression, such as the symmetrical $\widehat{b}_1$-dependent θ_0 term.

Since the S-force acts laterally, symmetry is only achieved if the left and right rotors (assumed to rotate in opposite directions) generate side forces pointing in opposite directions, thus have the opposite sign (remembering that the positive convention of the side force is identical for a cw. and ccw. rotating rotor). It must also be remembered, however, that the lateral disk tilt also acts laterally and thus in longitudinal operation the sign of this state is also opposite for the left and right rotor (due to its identical positive convention for cw. and ccw. rotating rotors). As a consequence the symmetrical groups correspond to terms multiplied either by the Ω_{sgn} parameter, or the lateral disk tilt $\widehat{b}_1$, while the asymmetrical groups correspond to terms either not multiplied by the Ω_{sgn} parameter nor $\widehat{b}_1$, or multiplied by both (i.e. $\Omega_{sgn}\widehat{b}_1$) since in this case the two opposite signs cancel each other out. Note that this symmetry definition is also only valid if the wind-shift angle Δ is zero or $180°$. Nonetheless, the presence of the asymmetrical groups means that in certain flight conditions two counter-rotating rotors may produce a side-force-imbalance resulting in a rolling and swaying motion in helicopter configuration, yawing and swaying motion in airplane configuration, or a combined roll-yaw-sway motion of the tilt-rotor in conversion mode.

Lastly it should be noted that the reduction scheme considers the angle-of-attack-independent drag constant $C_{d_0,bl}$ insignificant therefore it is not part of the reduced S-force expression. The other two drag coefficients are considered significant however they are not shown in eq. (5.113) due to the applied simplifications which improve expression clarity and aid visual inspection. Similarly to the H-force expression, however, ratios between these remaining drag coefficients and the lift coefficient also appear in the reduced S-force expression due to the blade lock number γ_{bl} placed outside of the square brackets. A more detailed explanation has already been made on page 167.

5.2.9. Blade Element Torque (Q-Moment)

The rotor torque $\widehat{Q}_{\text{BEM}}$ is also derived with the blade element method in the wind axis rotating frame $\boldsymbol{E}_{\widehat{R}}$ and is defined to act around the negative $Z_{\widehat{CP}}$-axis according to the right hand rule. Once again the averaged-over-one-rotor-revolution contribution of all the blades to the rotor Q-moment must be taken into account as given by eq. (5.114) where $M_{BL|-Z\widehat{CP},a}$ is the blade torque defined to also act around the negative $Z_{\widehat{CP}}$-axis.

$$\widehat{Q}_{\text{BEM}} = \frac{N}{2\pi}\int_0^{2\pi} M_{BL|-Z\widehat{CP},a}\, d\widehat{\psi} \tag{5.114}$$

The blade torque is obtained by integrating the differential blade axial moment $dM_{BL|Z\widehat{R},a}$ (acting around the (positive) Z-axis of the rotating frame), which in turn is equal to the blade element tangential force $dF_{BL|-Y\widehat{R},a}$ multiplied by the radial distance from the rotor hub to the blade element measured along the $Y_{\widehat{R}}$-axis as given by eq. (5.115a) and depicted in fig. 5.18. Note that a negative sign must be placed in front of the $dF_{BL|-Y\widehat{R},a}$ integral since the blade tangential force acts against the positive convention of the blade torque. A three-dimensional depiction of the direction of action of the differential blade axial moment - as well as of the differential blade torque - with respect to the rotating and non-rotating frames has already been shown in figs. 5.12 and 5.13.

$$M_{BL|-Z\widehat{CP},a} = \int_0^R dM_{BL|Z\widehat{R},a} = -\int_0^R dF_{BL|-Y\widehat{R},a} r_{BE} cos(\widehat{\beta}) \tag{5.115a}$$

The blade tangential force has already been derived in the hind force derivation, however unlike in the case of the side force, the non-simplified expression for the differential blade tangential force is extracted from eq. (5.101b) and repeated below. The non-simplified expression must be taken since the differential tangential force is now also multiplied by a trigonometric function of $\widehat{\beta}$ which affects how the blade torque changes after the application of the small angle to $\widehat{\beta}$. Note that the differential lift and drag terms are still multiplied by the Ω_{sgn} parameter as has already been explained on page 161. Similarly to the case of the side force, this direction of rotation effect shall carry through to the final expression for the rotor torque.

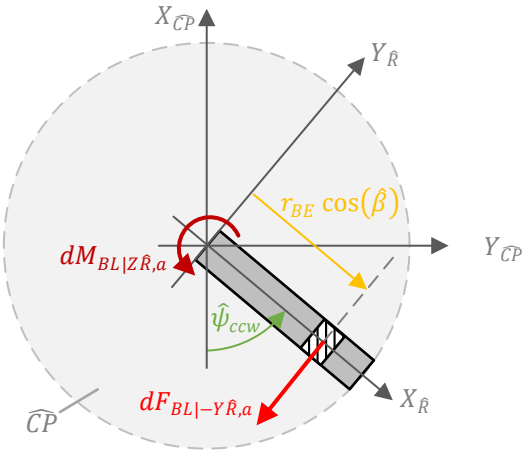

Figure 5.18: Schematic top view of a ccw. rotating rotor blade showing the contribution of the blade element tangential force to the blade element Q-moment.

Substituting the differential blade tangential force expressions back into eq. (5.115a) yields the expression for the blade torque as given by eq. (5.115b).

$$dF_{BL|-Y\widehat{R},a} = \Omega_{sgn} dL_{BL} sin(\phi_{BE}) + \Omega_{sgn} dD_{BL} cos(\phi_{BE}) \tag{5.101b}$$

$$\begin{aligned} M_{BL|-Z\widehat{CP},a} &= -\int_0^R dF_{BL|-Y\widehat{BL},a} r_{BE} cos(\widehat{\beta}) \\ &= -\int_0^R \left(\Omega_{sgn} dL_{BL} sin(\phi_{BE}) + \Omega_{sgn} dD_{BL} cos(\phi_{BE})\right) r_{BE} cos(\widehat{\beta}) \\ &= -\Omega_{sgn} \int_0^R r_{BE} cos(\widehat{\beta}) \left(dL_{BL} sin(\phi_{BE}) + dD_{BL} cos(\phi_{BE})\right) \end{aligned} \tag{5.115b}$$

Only at this point may the expression be simplified similarly to the rotor forces by applying the small angle approximation to the flapping angle $\widehat{\beta}$ and inflow angle ϕ_{BE}. Note that a third simplification was also applied to the rotor forces, namely the assumption that the differential blade lift is much greater than the differential blade drag. In the case of the blade torque, however, the differential lift is multiplied by the sine of the inflow angle. Recalling that the latter is considered small, the resulting product of the two may be of a similar order as the differential drag hence disregarding the drag may no longer be valid. Therefore, if $\phi_{BE} \ll 1$ and $\widehat{\beta} \ll 1$ only, then:

$$\begin{aligned} M_{BL|-Z\widehat{CP},a} &= -\Omega_{sgn} \int_0^R r_{BE} \left(dL_{BL} \phi_{BE} + dD_{BL}\right) \\ &= -\Omega_{sgn} \int_0^R r_{BE} dL_{BL} \phi_{BE} - \Omega_{sgn} \int_0^R r_{BE} dD_{BL} \end{aligned} \tag{5.115c}$$

Similarly to the blade hind and side forces, the blade torque also depends on the blade drag. Due to the resulting increased complexity of the derivation, the simplified expression for the blade torque is divided into two differential Q-moment components as shown in eq. (5.116), where dQ_i is the lift-induced component while dQ_0 is the drag-induced component. Their definitions are given by eqs. (5.116b) and (5.116c).

$$M_{BL|-Z\widehat{CP},a} = dQ_i + dQ_0 \tag{5.116a}$$

$$dQ_i = -\Omega_{sgn} \int_0^R r_{BE} dL_{BL} \phi_{BE} \qquad (5.116b) \qquad dQ_0 = -\Omega_{sgn} \int_0^R r_{BE} dD_{BL} \qquad (5.116c)$$

The expressions for the simplified inflow angle, differential blade lift, and differential drag have already been derived and are given by eqs. (5.64), (5.66) and (5.104), repeated below for clarity. These may then be substituted back into the differential Q-moment components which are expanded to reveal the common integrals as is shown next.

$$\phi_{BE} = \frac{U_P}{U_T} \qquad (5.64)$$

$$dL_{BL} = \frac{1}{2}\rho U_T^2 C_{l_\alpha,bl} \left(\theta_0 + \theta_{bl,1} r_{BE} - \frac{U_P}{U_T}\right) c_{bl} dr_{BE} \qquad (5.66)$$

$$dD_{BL} = \frac{1}{2}\rho c_{bl} U_T^2 \left(C_{d_0,bl} + C_{d_1,bl}\left(\theta_0 + \theta_{bl,1} r_{BE} - \frac{U_P}{U_T}\right) + C_{d_2,bl}\left(\theta_0 + \theta_{bl,1} r_{BE} - \frac{U_P}{U_T}\right)^2\right) dr_{BE} \qquad (5.104)$$

Differential Q-Moment Component Expansion

Starting with the lift-induced dQ_i shown in eq. (5.117a), after substituting the differential lift and rearranging it can be seen that the lift-induced differential torque consists of three common integrals, two of which have never been seen before, namely CI_7 and CI_8. The third common integral, CI_4 first appear in the derivation of the aerodynamic flapping moment (i.e. eq. (5.67)).

$$\begin{aligned} dQ_i &= -\Omega_{sgn} \int_0^R r_{BE} dL_{BL} \phi_{BE} \\ &= -\Omega_{sgn} \int_0^R r_{BE} \frac{1}{2}\rho U_T^2 C_{l_\alpha,bl} \left(\theta_0 + \theta_{bl,1} r_{BE} - \frac{U_P}{U_T}\right) c_{bl} dr_{BE} \frac{U_P}{U_T} \\ &= -\Omega_{sgn} \frac{\rho C_{l_\alpha,bl} c_{bl}}{2} \int_0^R U_T U_P r_{BE} \left(\theta_0 + \theta_{bl,1} r_{BE} - \frac{U_P}{U_T}\right) dr_{BE} \\ &= -\Omega_{sgn} \frac{\rho C_{l_\alpha,bl} c_{bl}}{2} \left(\theta_0 \underbrace{\int_0^R U_T U_P r_{BE} dr_{BE}}_{CI_4} + \theta_{bl,1} \underbrace{\int_0^R U_T U_P r_{BE}^2 dr_{BE}}_{CI_8} - \underbrace{\int_0^R U_P^2 r_{BE} dr_{BE}}_{CI_7}\right) \end{aligned} \qquad (5.117a)$$

Equation (5.105c), on the other hand, presents the expansion of the drag-induced differential Q-moment component which is obtained after the substitution of the simplified differential blade drag expression (eq. (5.104)) into eq. (5.116c). The increased expression complexity brought by the inclusion of the drag may again be observed in the expanded expression which not only depends on the two new common integrals introduced by the lift-induced Q-moment component, but also introduces the final common integral CI_9 which makes its first and last appearance in the rotor derivation. Due to the latter fact, this integral should not formally be classified as being common, however for the sake of completeness this formality is overlooked.

$$
\begin{aligned}
dQ_0 &= -\Omega_{sgn} \int_0^R r_{BE}\, dD_{BL} \\
&= -\Omega_{sgn} \int_0^R r_{BE} \frac{1}{2} \rho c_{bl} U_T^2 \left(C_{d_0,bl} + C_{d_1,bl} \left(\theta_0 + \theta_{bl,1} r_{BE} - \frac{U_P}{U_T} \right) + C_{d_2,bl} \left(\theta_0 + \theta_{bl,1} r_{BE} - \frac{U_P}{U_T} \right)^2 \right) dr_{BE} \\
&= -\Omega_{sgn} \frac{\rho c_{bl}}{2} \Bigg(\left(C_{d_0,bl} + C_{d_1,bl}\theta_0 + C_{d_2,bl}\theta_0^2 \right) \underbrace{\int_0^R U_T^2 r_{BE} dr_{BE}}_{CI_3} \\
&+ \left(C_{d_1,bl}\theta_{bl,1} + 2C_{d_2,bl}\theta_0\theta_{bl,1} \right) \underbrace{\int_0^R U_T^2 r_{BE}^2 dr_{BE}}_{CI_6} + C_{d_2,bl}\theta_{bl,1}^2 \underbrace{\int_0^R U_T^2 r_{BE}^3 dr_{BE}}_{CI_9} \\
&- \left(C_{d_1,bl} + 2C_{d_2,bl}\theta_0 \right) \underbrace{\int_0^R U_T U_P r_{BE} dr_{BE}}_{CI_4} - 2C_{d_2,bl}\theta_{bl,1} \underbrace{\int_0^R U_T U_P r_{BE}^2 dr_{BE}}_{CI_8} + C_{d_2,bl} \underbrace{\int_0^R U_P^2 r_{BE} dr_{BE}}_{CI_7} \Bigg)
\end{aligned}
\tag{5.117b}
$$

Recalling eq. (5.114) and eq. (5.116a), the complete rotor Q-moment expression is obtained by solving eq. (5.118). Similarly to the rotor BEM forces, after all common integrals within the differential Q-moment components are evaluated along the blade length, the same non-dimensional terms defined in eqs. (5.68) to (5.71) are introduced into the expressions, namely the blade lock number γ_{bl}, the wind axis control plane advance ratio $\widehat{\mu}_{tc}$, the wind axis control plane inflow ratio $\widehat{\lambda}_{pc}$, and the induced velocity inflow ratio λ_i. Once again the solved integrals are still (non-linear) functions of the flapping angle $\widehat{\beta}$. Therefore first the small angle approximation is applied to $\widehat{\beta}$ simplifying the trigonometric functions and removing any powers or products of $\widehat{\beta}$ and its derivatives. Next, all instances of the flapping angle and its derivatives are replaced by the (wind axis) disk tilt quasi-static solution, as defined by eq. (5.78), which incorporates the disk tilt angles into the expressions, and simultaneously enables the future definition of the rotor hind force with respect to a non-rotating frame. The prior application of the small angle approximation to $\widehat{\beta}$ also ensures that the final expression is linear with respect to the disk tilt angles. It should be highlighted that the incorporation of the disk tilt approximation must be performed before taking the integral of the blade Q-moment around one blade revolution (eq. (5.116a)) since the disk tilt quasi-static solution is a function of the azimuth position $\widehat{\psi}$. After the inclusion of the disk tilt angles, eq. (5.118) may be finally evaluated yielding the analytical expression for the rotor torque defined with respect to the (non-rotating) wind-axis control plane frame.

$$
\widehat{Q}_{\text{BEM}} = \frac{N}{2\pi} \int_0^{2\pi} M_{BL|-Z\widehat{CP},a}\, d\widehat{\psi} = \frac{N}{2\pi} \int_0^{2\pi} \left(dQ_i + dQ_0 \right) d\widehat{\psi} \tag{5.118}
$$

The complete expression for the rotor torque shall not be shown here due to its extensiveness, however a simplified version is presented and analyzed below.

BEM Torque Moment Expression Analysis

An expanded but partially simplified version of the rotor Q-moment expression is shown in eq. (5.119) which shall be used to answer a portion of the research sub-question concerned with determining the effect of the tilting proprotor on the rotor moment expressions. The rotor Q-moment is simplified in a similar fashion to the rotor H- and S-force expressions by first supplying it to the reduction scheme (described in great detail in section 6.3) removing all negligible terms. Next the linearly varying blade twist parameter $\theta_{bl,1}$, the control plane deflection, and the wind shift angle are all set to zero in order to improve readability (the motivation for the latter two is explained on page 136). Additionally the blade element drag coefficient $C_{d,bl}$ is simplified to only include the angle-of-attack-independent constant $C_{d_0,bl}$ while the other two constants are set to zero (i.e. $C_{d_1,bl} = C_{d_2,bl} = 0$), greatly reducing the expression length. It must be highlighted that the reduction scheme considers all three drag constants significant, therefore they appear in the reduced expression. In order to aid visual inspection of the expression, however, all terms multiplied by $C_{d_1,bl}$ and $C_{d_2,bl}$ are removed.

Several linear and rotational rate combinations have also been replaced by single variables for notation compactness, including the total inflow ratio $\widehat{\lambda}_{tot}$ as already defined by eq. (5.73). In appendix C eq. (C.4) provides the expansion of the combined rotational rates while an overview and description of the subscripts of these combined terms is given in table C.1. For the sake of clarity, in summary the subscript eff refers to 'effective' rotational rates and tot refers to 'total' rotational rates, while the subscripts i and w refer to inertial and wash rates respectively which, when combined, yield aerodynamic rates which are not indicated by any subscripts. A detailed description of 'effective' and 'total' rates is provided on page 127, while the distinction between inertial, wash, and total rates is explained on page 118. The rotational rates have also been made non-dimensional, indicated with an overbar symbol ($\overline{\ }$), by dividing them by Ω making it possible to take Ω^2 outside of the brackets.

Equation (5.119) has been arranged into four main groups indicated by the right-hand-side annotations, namely the symmetrical and asymmetrical $\widehat{a}_1$-dependent group, and the free symmetrical and asymmetrical groups. The symmetrical groups correspond to terms multiplied by the Ω_{sgn} parameter, while the asymmetrical groups are rotor-rotation-independent. This definition of symmetry shall be explained in the detailed expression analysis below eq. (5.119). A separate expression corresponding to a counter-clockwise rotor in helicopter configuration shall not be presented since if all effective rotational rates are replaced by their pure body rate counterparts, then eq. (5.119) becomes representative of the Q-moment expression corresponding to a helicopter.

$$
\begin{aligned}
\widehat{Q}_{\text{BEM}} = \Omega^2 I_{bl}\gamma_{bl}N\Bigg[\frac{1}{8}\Bigg(&\Omega_{sgn}\left(\overline{p}_{eff}\overline{r}_{i,eff} + 2\widehat{\mu}_{tc}\widehat{\lambda}_{tot}\right) && \text{(sym. } \widehat{a}_1\text{-dep.)} \\
&+\frac{2}{3}\left(\overline{r}_{w,eff}\widehat{\mu}_{tc} - \overline{p}_{eff}\widehat{\lambda}_{pc} + \overline{p}C_\eta\lambda_i\right)\theta_0 - \overline{p}_{eff}\Bigg)\widehat{a}_1 && \text{(asym. } \widehat{a}_1\text{-dep.)} \\
&+\Omega_{sgn}\left(\frac{\widehat{\lambda}_{tot}^2}{4} + \frac{\widehat{\lambda}_{tot}\theta_0}{6} + \frac{\overline{p}_{eff}^2}{16} - \frac{C_{d_0,bl}}{8C_{l_\alpha,bl}}\right) && \text{(free symmetrical)} \\
&+\frac{1}{12}\left(\overline{p}_{eff}\widehat{\mu}_{tc} - 2\overline{r}_{eff}\widehat{\lambda}_{tot}\right)\theta_0\Bigg] && \text{(free asymmetrical)}
\end{aligned}
\tag{5.119}
$$

Similarly to the BEM thrust, the rotor Q-moment only depends on the longitudinal disk tilt angle $\widehat{a}_1$. The coning and lateral disk tilt angles are initially part of the expression, however the reduction scheme deems these angles not significant enough to be included and thus the rotor torque only depends on $\widehat{a}_1$. Although the reduced Q-moment expression is linear with respect to $\widehat{a}_1$, the same cannot be said for the inflow ratio λ_i. The full expression contains λ_i terms that are either squared or multiplied with $\widehat{a}_1$ and $\widehat{b}_1$, and although some of these terms are removed (that includes all products with $\widehat{b}_1$), others are still considered significant enough to remain in the expression resulting in the non-linearity. Similarly to the H- and S-forces, for this reason the rotor Q-moment expression may not be appended to the system of linear equations containing the disk tilt angles and inflow ratio (i.e. eq. (5.81)). It must be highlighted, however, that the rotor torque is the only expression to contain a squared λ_i term which originates from CI_7. This is the only common integral that contains a squared blade element perpendicular velocity term U_P^2, which in turn contains the rotor induced velocity giving rise to the λ_i^2 term.

Interestingly the situation of the nacelle tilt rate and body rates within the torque expression is comparable to the one within the BEM thrust expression. That is, the reduction scheme also removes all $\dot{\eta}$ terms (originating from the tangential blade element velocity U_T) from the torque expression which are initially spread throughout the entire equation. This means that the nacelle tilt rate is not considered a significant contributor to the rotor torque. Furthermore, although not shown in the simplified expression, the body pitch rate q is also part of the reduced expression, however all instances of it are multiplied by the sine of the wind shift angle implying that the body pitch rate is only considered significant when the rotor is in sideward flight. From the perspective of the wind-shifted rotor, in this condition the body pitch rate is interpreted as a body roll rate. This also explains why the body roll rate is present in the simplified expression while the body pitch rate is not. Finally, the inertial rotational body rates that are part of the aerodynamic rotational rates (e.g. $\overline{r}$ or $\overline{r}_{eff}$) have been introduced through the flapping rate part of the perpendicular blade element velocity component U_P, which in turn is contained within common integrals 4, 7, and 8. As a consequence, several inertial rates are subtracted from aerodynamic rates yielding pure wash rates which can be observed in the torque expression (e.g. $\overline{r}_{w,eff}$).

The tiltable nacelle also manifests itself in the 'effective' rotational rates and linear rates (i.e. $\widehat{\mu}_{tc}$, $\widehat{\lambda}_{pc}$, and $\widehat{\lambda}_{tot}$) experienced by the rotor in the same manner as described in the flapping equation analysis. It should be noted that any term that is not multiplied by an 'effective' rate is inherently independent from the nacelle tilt angle. Terms that only exist in conversion mode (and thus are unique to tilt-rotors) also appear in the expression, such as the result of the multiplication of the inertial yaw rate with the aerodynamic roll rate which contains products such as $sin(\eta)cos(\eta)$ which are non-zero only in conversion mode. Terms that do not depend on the nacelle tilt angle at all also appear in the expression, such as the free symmetrical ratio between the blade drag coefficient and blade lift coefficient. On that subject, similarly to the H- and S-forces, the ratio between these coefficients appears in the reduced Q-moment expression due to the blade lock number γ_{bl} placed outside of the square brackets. A more detailed explanation has already been made on page 167.

The definition of symmetry for the torque is similar to the one corresponding to the side force since in order for there to be a torque balance (i.e. a net zero axial moment), the left and right rotor (assumed to rotate in opposite directions) must have torques of opposite signs. Fortunately the rotor Q-moment does not depend on the lateral disk tilt angle therefore the definition of symmetry only depends on the Ω_{sgn} parameter which, when multiplied by a term, ensures that that term contributes constructively to achieve the torque balance. As opposed to the hind and side forces, however, this symmetry definition remains valid for all wind-shift angles Δ. The presence of the asymmetrical groups means that in certain flight conditions two counter-rotating rotors may produce a torque-imbalance resulting in a yawing motion in helicopter configuration, rolling motion in airplane configuration, or a combined roll-yaw motion of the tilt-rotor in conversion mode. It must be noted that it is not uncommon for tilt-rotors to have the left and right rotor shafts interconnected (as is the case for the XV-15 tilt-rotor) resulting in the torque difference being balanced internally by the shaft. In this case a difference in the torques of the two rotors would not produce a non-zero net moment that would otherwise result in rotational motion of the tilt-rotor body.

Lastly it should be noted that, as opposed to the rotor forces, the terms outside the square brackets of the torque expression are not divided by the rotor radius R since eq. (5.119) defines a moment, not a force.

5.2.10. Rotor Hub Spring Reaction Moments

Up to this point the three orthogonal force components and one axial moment generated by the rotor blades that have been treated so far all originate from the aerodynamic interaction between the rotor blades and air, and are transmitted to the tilt-rotor body through the rotor hub. It seems that two additional orthogonal aerodynamic moment components still remain to be treated. It must be remembered, however, that the rotor blades are attached to the rotor hub with a flapping hinge, therefore one of the orthogonal aerodynamic moments acting around the flapping hinge (i.e. the aerodynamic flapping moment acting around the negative $Y_{\widehat{R}}$-axis that has already been treated in section 5.2.3) cannot be transmitted to the rotor hub. The remaining orthogonal aerodynamic moment acting around the blade-wise axis (i.e. the $X_{\widehat{BL}}$-axis) may be transmitted to the rotor hub, however it is assumed to be negligibly small therefore it is neglected. Any other contributions to the aerodynamic forces and moments generated by the blades and transmitted to the rotor hub are also assumed to be negligibly small and thus are neglected.

There is, however, one moment contribution that has not been treated yet in regards to the loads transmitted to the rotor hub, namely the hub spring (i.e. the flapping spring) reaction moment. Since the aerodynamic forces and moments are defined in the wind axis control plane, the same applies to the hub spring reaction moment which is decomposed into rolling ($M_{hub|-X\widehat{CP},s}$) and pitching ($M_{hub|-Y\widehat{CP},s}$) moments acting around the negative $X_{\widehat{CP}}$- and $Y_{\widehat{CP}}$-axes respectively. To be consistent with the rotor torque notation, these moments may also be referred to as the $\widehat{O}_s$- and $\widehat{P}_s$-moments. All spring-originating moments are indicated by the subscript s. The expressions for these rolling and pitching moments are derived below.

The rolling moment is obtained by projecting the hub spring reaction moment $M_{hub|-Y\widehat{BL},s}$ of each blade onto the negative $X_{\widehat{CP}}$-axis and taking the average-over-one-rotor-revolution as shown in eq. (5.120). Note that $M_{hub|-Y\widehat{BL},s}$ must be multiplied by the Ω_{sgn} parameter in order for it always act around the negative $X_{\widehat{CP}}$-axis irrespective of the direction of rotation of the rotor.

$$\widehat{O}_s = M_{hub|-X\widehat{CP},s} = \frac{N}{2\pi}\int_0^{2\pi} sin(\widehat{\psi})\Omega_{sgn}M_{hub|-Y\widehat{BL},s}d\widehat{\psi} \tag{5.120}$$

The hub spring reaction moment of a single blade $M_{hub|-Y\widehat{BL},s}$ acts around the negative $Y_{\widehat{BL}}$-axis and depends on the flapping angle, precone angle $\overline{a}_0$, and the flapping spring constant as shown in eq. (5.121). Note that because we are dealing with the spring reaction moment acting on the hub and not the blade, the positive convention of the moment points in the direction of the negative $Y_{\widehat{BL}}$axis (according to the right hand rule), as opposed to the case of the flapping equation where the spring moment was acting on the blade and thus the positive convention acted around the positive $Y_{\widehat{BL}}$-axis as was given by eq. (5.76).

$$M_{hub|-Y\widehat{BL},s} = \left(\widehat{\beta} - \overline{a}_0\right) K_\beta \tag{5.121}$$

In order to be able to resolve the spring reaction moment from the rotating frame into the non-rotating control plane frame, once again use is made of the wind axis disk tilt presumed solution for the flapping angle as defined by eq. (5.78a), repeated below for clarity.

$$\widehat{\beta} = \widehat{a}_0 - \widehat{a}_1 cos(\widehat{\psi}) - \Omega_{sgn}\widehat{b}_1 sin(\widehat{\psi}) \tag{5.78a}$$

Substituting the expression for $M_{hub|-Y\widehat{BL},s}$ back into eq. (5.120), replacing the flapping angle by the presumed solution, and evaluating the resulting equation yields the averaged-over-one-rotor-revolution contribution of all the blades to the rotor hub spring reaction roll moment as given by eq. (5.122). It must be highlighted that since the lateral disk tilt angle is also multiplied by the Ω_{sgn} parameter, the evaluation of the integral produces an Ω_{sgn}^2 term which always equates to 1, hence it may be removed from the expression meaning that the rolling spring reaction moment $\widehat{O}_s$ is not directly influenced by the direction of rotation of the rotor. Also note that the coning angle $\widehat{a}_0$ as well as the precone angle $\overline{a}_0$ do not have an effect on the averaged reaction moment since they acts homogeneously around a blade revolution.

$$\begin{aligned}
\widehat{O}_s &= \frac{N}{2\pi}\int_0^{2\pi} sin(\widehat{\psi})\Omega_{sgn} M_{hub|-Y\widehat{BL},s} d\widehat{\psi} \\
&= \Omega_{sgn}\frac{N}{2\pi}\int_0^{2\pi} sin(\widehat{\psi})\left(\widehat{\beta} - \overline{a}_0\right) K_\beta d\widehat{\psi} \\
&= \Omega_{sgn}\frac{NK_\beta}{2\pi}\int_0^{2\pi} sin(\widehat{\psi})\left(\widehat{a}_0 - \widehat{a}_1 cos(\widehat{\psi}) - \Omega_{sgn}\widehat{b}_1 sin(\widehat{\psi}) - \overline{a}_0\right) d\widehat{\psi} \\
&= -\Omega_{sgn}^2\frac{NK_\beta\widehat{b}_1}{2\pi} \\
&= -\frac{NK_\beta\widehat{b}_1}{2}
\end{aligned} \tag{5.122}$$

The pitching moment $\widehat{P}_s$ is obtained in a similar fashion to the rolling moment, however in this case the hub spring reaction moment $M_{hub|-Y\widehat{BL},s}$ has the same contribution to $\widehat{P}_s$ irrespective of the rotor rotation direction (thus it is not multiplied by the Ω_{sgn} parameter), and it is projected onto the negative $Y_{\widehat{CP}}$-axis instead of the $X_{\widehat{CP}}$-axis. Performing analogous substitutions of eqs. (5.78a) and (5.121) into eq. (5.123) yields the averaged-over-one-rotor-revolution contribution of all the blades to the rotor hub spring reaction pitch moment $\widehat{P}_s$. Similarly to the rolling moment, the pitching moment is also not directly influenced by the direction of rotation of the rotor.

$$\begin{aligned}
\widehat{P}_s &= M_{hub|-Y\widehat{CP},s} \\
&= \frac{N}{2\pi}\int_0^{2\pi} cos(\widehat{\psi}) M_{hub|-Y\widehat{BL},s} d\widehat{\psi} \\
&= \frac{N}{2\pi}\int_0^{2\pi} cos(\widehat{\psi})\left(\widehat{\beta} - \overline{a}_0\right) K_\beta d\widehat{\psi} \\
&= \frac{NK_\beta}{2\pi}\int_0^{2\pi} cos(\widehat{\psi})\left(\widehat{a}_0 - \widehat{a}_1 cos(\widehat{\psi}) - \Omega_{sgn}\widehat{b}_1 sin(\widehat{\psi}) - \overline{a}_0\right) d\widehat{\psi} \\
&= -\frac{NK_\beta\widehat{a}_1}{2}
\end{aligned} \tag{5.123}$$

5.2.11. Total Rotor Hub Forces and Moments

Having derived all the rotor forces and moments (considered within the scope of this thesis work) acting on the rotor hub it is finally possible to form force and moment vectors (still defined in the wind axis control plane reference frame). These may then be transformed into the body frame yielding the desired force and moment vectors defined in the body frame of reference, as shown in eqs. (5.124) and (5.125), concluding the derivation of the rotor equations. The transformed forces and moments can be directly substituted into the body equations of motion (eqs. (5.2) and (5.3)).

The last (transposed) vector in eqs. (5.124) and (5.125) contains the informal rotor force and moment notation which is equivalent to its formal counterpart and directly corresponds to the forces and moments that have been shown in fig. 5.2 at the beginning of this rotor derivation section (i.e. section 5.2). Note that a minus sign must be placed in front of all the forces and moments derived in this section since these have been defined to act along or around the negative axes of the wind axis control plane. Also note that since the positive convention of the forces and moments generated by the left and right rotor is identical, they may be simply added together to form the total rotor loads without having to worry about their disposition or direction of rotation (which have already been taken care of by the sign change parameters d_{sgn} and Ω_{sgn}).

$$\boldsymbol{F}_r = \begin{pmatrix} F_{r|X\widehat{CP}} \\ F_{r|Y\widehat{CP}} \\ F_{r|X\widehat{CP}} \end{pmatrix}^T \boldsymbol{T}_{\widehat{CP}|b}\{\boldsymbol{E}_b\} = -\begin{pmatrix} \widehat{H}_{\text{BEM},L} + \widehat{H}_{\text{BEM},R} \\ \widehat{S}_{\text{BEM},L} + \widehat{S}_{\text{BEM},R} \\ \widehat{T}_{\text{BEM},L} + \widehat{T}_{\text{BEM},R} \end{pmatrix}^T \boldsymbol{T}_{\widehat{CP}|b}\{\boldsymbol{E}_b\} = -\begin{pmatrix} H_L + H_R \\ S_L + S_R \\ T_L + T_R \end{pmatrix}^T \boldsymbol{T}_{\widehat{CP}|b}\{\boldsymbol{E}_b\} \tag{5.124}$$

$$\boldsymbol{M}_r = \begin{pmatrix} M_{r|X\widehat{CP}} \\ M_{r|Y\widehat{CP}} \\ M_{r|X\widehat{CP}} \end{pmatrix}^T \boldsymbol{T}_{\widehat{CP}|b}\{\boldsymbol{E}_b\} = -\begin{pmatrix} \widehat{O}_{s,L} + \widehat{O}_{s,R} \\ \widehat{P}_{s,L} + \widehat{P}_{s,R} \\ \widehat{Q}_{\text{BEM},L} + \widehat{Q}_{\text{BEM},R} \end{pmatrix}^T \boldsymbol{T}_{\widehat{CP}|b}\{\boldsymbol{E}_b\} = -\begin{pmatrix} O_L + O_R \\ P_L + P_R \\ Q_L + Q_R \end{pmatrix}^T \boldsymbol{T}_{\widehat{CP}|b}\{\boldsymbol{E}_b\} \tag{5.125}$$

5.3. Main Wing and Tail Stabilizers

Having described the forces and moments generated by the rotor, the next major contributors to the flight mechanics of the tilt-rotor are the main wing and the horizontal and vertical tail stabilizers. The equations describing the aerodynamics of these lifting surfaces are almost identical therefore they are all described together in this section. Note that advantage is taken of this commonality during the implementation of the tilt-rotor model and its FixedTrapezoidalLiftingSurface class (as described in section 7.2) which contains the aerodynamic equations of the mentioned lifting surfaces. These equations are presented and explained below.

As the name of the class suggests, all wings and stabilizers are treated geometrically as trapezoidal lifting surfaces which are characterized by root and tip chord lengths c_r and c_t respectively, a half-span $b_{1/2}$ (measuring from root to tip of the lifting surface), a root aerodynamic center (RAC) sweep angle Λ, an incidence angle i, and a dihedral angle Γ. As shall be shown later, several additional geometric parameters derived from the above will be needed, namely the surface area S, taper ratio λ, mean aerodynamic chord (MAC) length $\overline{C}$, and the MAC spanwise position $\overline{Y}$. The expressions for the obtention of these parameters are given by eqs. (5.126) to (5.129).

$$S = b_{1/2}\frac{c_r + c_t}{2} \tag{5.126}$$

$$\lambda = \frac{c_t}{c_r} \tag{5.127}$$

$$\overline{C} = \frac{2c_r(1 + \lambda + \lambda^2)}{3(1 + \lambda)} \tag{5.128}$$

$$\overline{Y} = \frac{b_{1/2}(1 + 2\lambda)}{3(1 + \lambda)} \tag{5.129}$$

In terms of aerodynamics, the lifting surfaces are treated as flat plates characterized by sinusoidally varying lift C_L, drag C_D, and pitching moment C_M coefficients as a function of the angle of attack [45]. The flat

plate model has been modified, however, to more closely fit some of the aerodynamic characteristics of the actual lifting surfaces, and to incorporate the effect of the control surfaces present on several of the lifting surfaces of the tilt-rotor. Therefore the largest deviations from the flat plate model are the inclusion of a zero-lift angle of attack parameter α_{0L} and, for simplicity's sake, the removal of a varying pitching moment coefficient which has been replaced by a constant value $C_{M,AC}$. The latter decision has been made due to the fact that the lifting surface forces and moments are calculated at the MAC AC ($\overline{AC}$ in short) where the pitching moment coefficient is assumed to be constant. The remaining flat plate model modifications are described together with the equations for the calculation of the aerodynamic coefficients presented below. Note that the 2-dimensional flat plate coefficients are immediately simplified to be equal to the 3-dimensional flat plate wing coefficients (e.g. $C_L = C_l$)), hence all coefficient subscripts are written in uppercase.

Aerodynamic Coefficients

Starting with eq. (5.130) the lift coefficient is almost identical to the expression for the lift coefficient of a flat plate where the sinusoidal variation depends on the angle of attack experienced by the lifting surface, here referred to as the local angle of attack α_{loc}, and a maximum lift coefficient $C_{L,max}$. As stated previously, however, this expression diverges from the standard flat plate model through the inclusion of a zero-lift angle of attack α_{0L} and a change in lift coefficient ΔC_L due to the deflection of control surfaces. It should be noted that the zero-lift angle of attack α_{0L} is additionally multiplied by the squared cosine of the local sideslip angle β_{loc} resulting in it being phased out towards $\pm 90°$ of sideslip. This has been implemented since it is assumed that at such high angles of sideslip the lifting surface no longer retains its airfoil characteristics and all the more starts to behave as a flat plate. The calculation of ΔC_L (also referred to as a control surface delta coefficient) shall be treated later. A graphical comparison between the lift coefficient curves of a flat plate (NFP), a flat plate with a change in lift coefficient due to a control surface deflection, and a flat plate with a control surface deflection and a zero-lift angle of attack parameter is shown in fig. 5.19. It can be seen that a positive ΔC_L value shift the entire curve upwards while a positive α_{0L} angle shifts the curve to the left. A notable effect of the vertical shift of the lift curve is an increase in the total zero-lift angle of attack which shall be treated formally in the next paragraph.

$$C_L = 2sin(\alpha_{loc} - \alpha_{0L}C^2_{\beta_{loc}})cos(\alpha_{loc} - \alpha_{0L}C^2_{\beta_{loc}})C_{L,max} + \Delta C_L \tag{5.130}$$

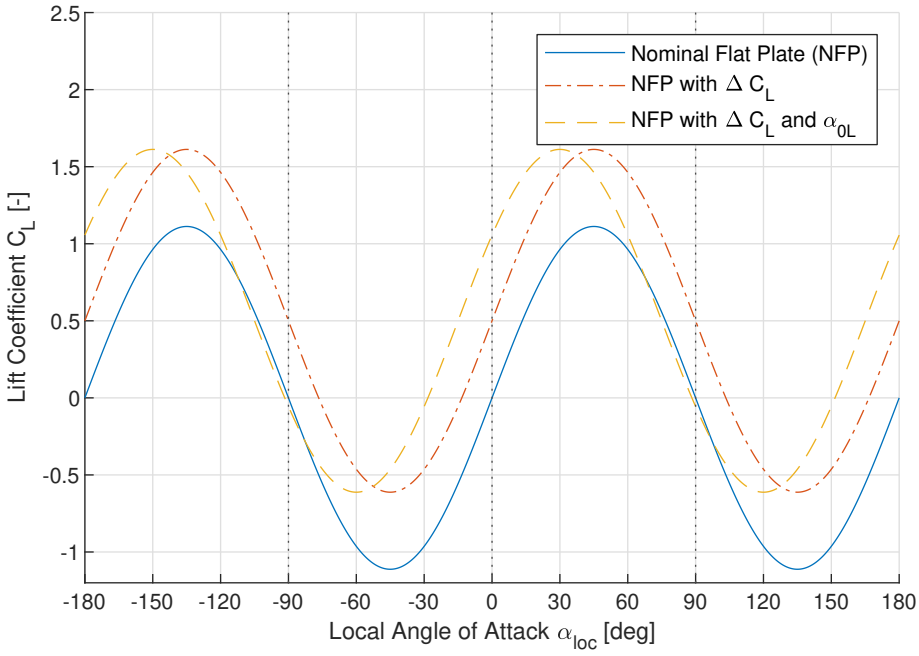

Figure 5.19: Modeled effect of control surface deflection and a zero-lift angle of attack parameter on the lift coefficient curve of a flat plate.

Similarly to the above, the drag coefficient expressions shown by eq. (5.131) also closely resembles that of a flat plate with the exception of a zero-lift angle of attack, and a change in drag coefficient ΔC_D due to the

deflection of control surfaces. It should be noted that apart from the airfoil zero-lift angle of attack α_{0L}, the drag curve is additionally shifted laterally as a result of a vertical shift of the lift curve due to the addition of ΔC_L, which in turn results in a new zero-lift angle of attack. The resulting change in α_{0L} is referred to as the zero-lift angle of attack delta $\Delta\alpha_{0L}$ and is determined by substituting $\Delta\alpha_{0L}$ as the trigonometric arguments in eq. (5.130), setting C_L to zero, and rearranging the expression to make $\Delta\alpha_{0L}$ the subject yielding eq. (5.132). A graphical comparison between the drag coefficient curves of a flat plate (NFP), a flat plate with a change in drag coefficient and zero-lift angle of attack due to a control surface deflection, and a flat plate with a control surface deflection and an explicit zero-lift angle of attack parameter is shown in fig. 5.20. It can be seen that a positive ΔC_D value shift the entire curve upwards while the increase in lift due to the control surface deflection introduces the zero-lift angle of attack delta which shifts the curve to the left. The inclusion of a positive α_{0L} angle shifts the curve to the left even more.

Note that the inclusion of a lift induced drag term in eq. (5.131) is questionable in the case of many of the lifting surfaces of a tilt-rotor due to factors that significantly alter the aerodynamic behavior at these surfaces' tips. The most notable example is the presence of rotors at the tips of the main wing which have a non-negligible effect on the wing tip vortices responsible for this source of drag. A different example are various tail configurations, such as an H-tail (present on the XV-15), which significantly alters the generation of wing tip vortices by these lifting surfaces. For this reason the induced drag is not included in the drag expression and is left as a recommendation for future research on this tilt-rotor model. As a result, the lifting surface aspect ratio and Oswald efficiency factor do not play a role in the aerodynamic calculations.

$$C_D = sin^2(\alpha_{loc} - \alpha_{0L} C^2_{\beta_{loc}} - \Delta\alpha_{0L}) C_{D,max} + \Delta C_D \tag{5.131}$$

$$\Delta\alpha_{0L} = \frac{1}{2} arcsin\left(\frac{-\Delta C_L}{C_{L,max}}\right) \tag{5.132}$$

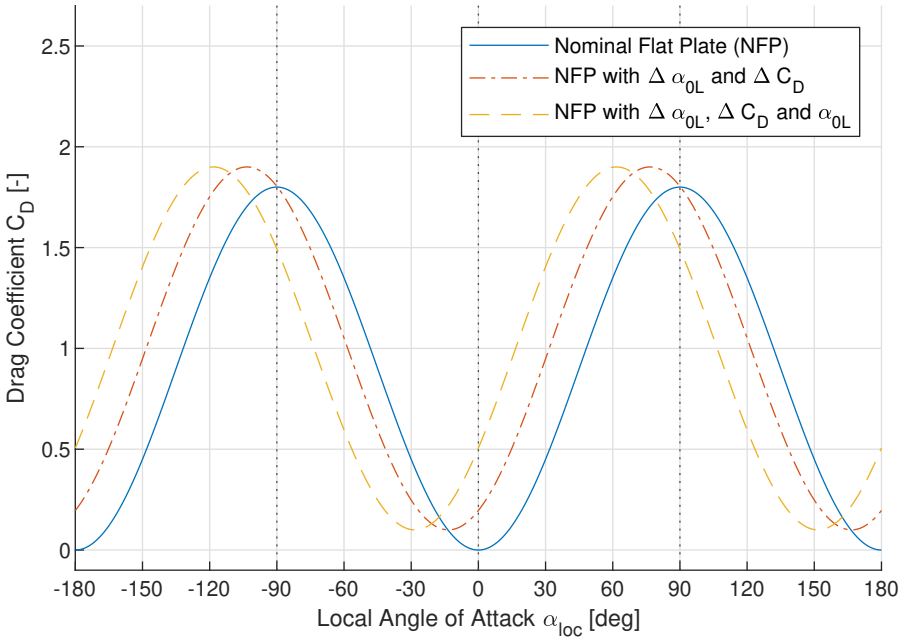

Figure 5.20: Modeled effect of control surface deflection and a zero-lift angle of attack parameter on the drag coefficient curve of a flat plate.

An exception has been made in the case of the flapped portion of the wings where instead of including the drag effect of the flaps in the ΔC_D variable, the flaps themselves are treated as separate flat plates. This has been done in order to ensure that the deflection of the flaps decreases the drag coefficient of the wing at angles of attack close to $\pm 90°$ which was not the case when the flaps were treated in the same way as the

other control surfaces. As a result the drag coefficient of the flapped portion of the wings is determined with eq. (5.133) where two sinusoidally varying drag terms can be observed. The first term corresponds to the fixed-wing portion of the flapped wing while the second term corresponds solely to the flap itself. These two terms are scaled by the flap-to-wing chord ratio ($R_{\text{flap:wing}}$) which is defined by eq. (5.134). Furthermore, the flap is assumed not to have a zero-lift angle of attack and the total angle of attack depends on the local angle of attack experienced by the flapped wing MAC AC (and not the MAC AC of the flap itself) α_{loc} and the flap deflection angle δ_{fla}. The contribution of the flap to the drag coefficient is then calculated by multiplying the squared sinus by the change in drag coefficient of the flapped wing as a function of flap deflection.

$$C_D = sin^2(\alpha_{loc} - \alpha_{0L} C^2_{\beta_{loc}} - \Delta\alpha_{0L}) C_{D,max}(1 - R_{\text{flap:wing}}) + sin^2(\alpha_{loc} + \delta_{fla}) \frac{\partial C_D}{\partial \delta_{fla}} (R_{\text{flap:wing}}) \quad (5.133)$$

$$R_{\text{flap:wing}} = \frac{c_{\text{flap}}}{c_{\text{flapped wing}}} \quad (5.134)$$

A graphical comparison between the drag coefficient curves of a flat plate (NFP), a flapped single flat plate, and a double flat plate is shown in fig. 5.21. The drag coefficient curve of the flapped single flat plate (NFP with $\Delta\alpha_{0L}$ and ΔC_D) is identical to the one of the flat plate with a control surface deflection presented in fig. 5.20 and only serves as a reference point for the comparison of the double flat plate curve. In fig. 5.21 it can be seen that the double flat plate curve is almost identical to the one of the (nominal) flat plate providing evidence that replacing a flapped flat plate with a double flat plate configuration may be considered equivalent. Deflecting the second flat plate (representing the flap) compresses the curve such that the drag coefficient becomes larger at angles of attack close to zero and $180°$ and becomes smaller at angles of attack close to $\pm 90°$. This characteristic agrees with the expected behavior of a tilt-rotor wing with a deflected flap, especially considering the situation where the tilt-rotor is in a helicopter configuration and the flaps are deployed to reduce the drag due to the download from the rotor wake. By contrast, in the case of the flapped single flat plate the drag coefficient at$\pm 90°$ is unchanged when compared to the nominal flat plate meaning that the deflection of the flap does not reduce the effect of the rotor downwash on the lifting surface. To combat this invalidity the double flat plate model has therefore been implemented for the flapped lifting surfaces of the tilt-rotor.

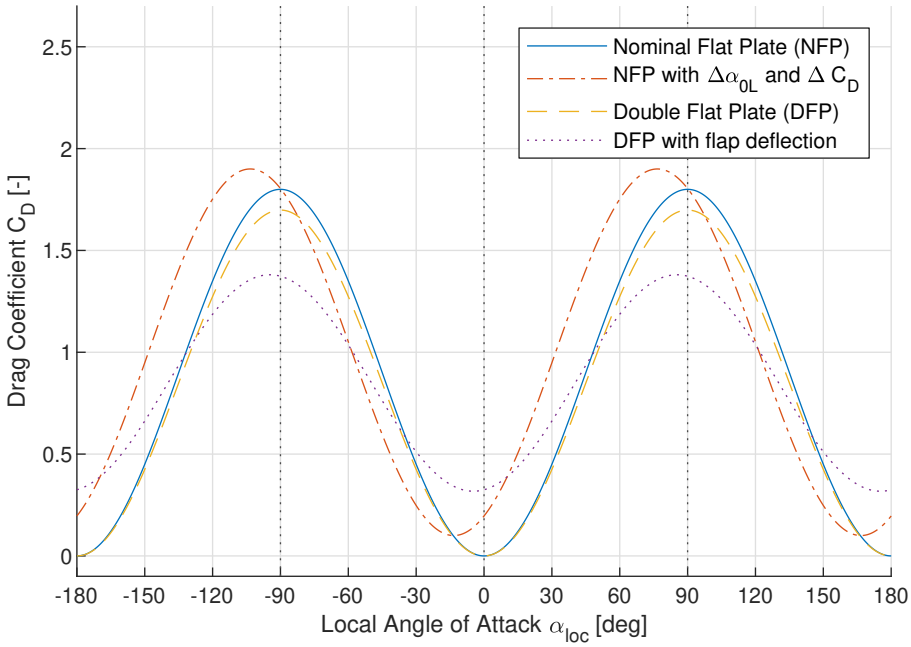

Figure 5.21: Comparison between the drag coefficient curves of a flapped flat plate and an equivalent double flat plate.

Finally, as already mentioned before, the pitching moment coefficient does not follow the characteristics of a flat plate and instead is simplified to be constant as seen in eq. (5.135), with a possible change in the pitching moment ΔC_M due to control surface deflection.

$$C_M = C_{M,AC} + \Delta C_M \tag{5.135}$$

As a final note, in the tilt-rotor model implementation used for this thesis work, only the flaps have an effect on the main wing drag coefficient, while all other control surfaces only modify the lifting surface lift coefficient. Furthermore, although the developed tilt-rotor model provides the possibility for control surfaces to modify the pitching moment of lifting surfaces, this feature is also not used in the final model implementation.

Control Surface Delta Coefficients

The calculation of the change in an aerodynamic coefficient as a result of a control surface depends on its angle of deflection and aerodynamic effectiveness, i.e. how much the control surface affects the coefficient of the lifting surface per angle of deflection. In this tilt-rotor model the aerodynamic effectiveness is kept constant and therefore the effect of a control surface on the coefficients of a lifting surface is linear. In hindsight, since several control surfaces of the tilt-rotor may experience very high angles of attack, it is very likely that their aerodynamic effectiveness may be much different in these extreme conditions. For this reason, as recommendations for the future, it is suggested that the aerodynamic effectiveness be a function of both the angle of attack and sideslip.

The relation for the control surface delta coefficient is given by eq. (5.136) where the subscript X may be substituted by the lift, drag, or moment coefficient. Here the first term on the right hand side of the expression (δ_{cs}) is the control surface (cs) deflection while the following fraction is the aerodynamic effectiveness parameter.

$$\Delta C_X = \delta_{cs} \frac{\partial C_X}{\partial \delta_{cs}} \tag{5.136}$$

The deflection of the control surface depends on the pilot input as shown in eq. (5.137) where X_{PIL} represents the deflection of a pilot (PIL) input while the subsequent fraction is referred to as the gearing ratio. The subscript should be substituted by the relevant input acronym such as LON in the case of the longitudinal stick input. Note that all pilot inputs have capitalized subscripts while control surface deflections do not. Substituting eq. (5.137) into eq. (5.136) yields eq. (5.138) where the control surface deflection may be canceled out. The resulting fraction $\partial C_X / \partial X_{PIL}$ is referred to as the control effectiveness of a control surface.

$$\delta_{cs} = X_{PIL} \frac{\partial \delta_{cs}}{\partial X_{PIL}} \tag{5.137}$$

$$\Delta C_X = X_{PIL} \frac{\partial \delta_{cs}}{\partial X_{PIL}} \frac{\partial C_X}{\partial \delta_{cs}} = X_{PIL} \frac{\partial C_X}{\partial X_{PIL}} \tag{5.138}$$

Since a single lifting surface may possess multiple control surfaces, the contributions of all relevant control surfaces to the change in a coefficient of a lifting surface must be added to obtain the final value of ΔC_X. For improved simulation performance advantage is taken of the linearity of the control effectiveness and instead of obtaining a delta coefficient individually for each control surface, the control effectiveness of each control surface on one lifting surface is first summed up to form the total lifting surface control effectiveness, as shown in eq. (5.139), and only then multiplied once by the pilot input. Once again, due to the linearity, matrix dot product may be employed as shown by the example in eq. (5.140) where the longitudinal (LON), lateral (LAT), collective (COL), pedal (PED), and flap (Fla) pilot inputs are multiplied by the lifting surface total control effectiveness parameters yielding the lift, drag, and pitching moment coefficient deltas.

$$\frac{\partial C_{X,tot}}{\partial X_{PIL}} = \sum_{cs} \frac{\partial C_X}{\partial X_{PIL}} \tag{5.139}$$

$$\begin{pmatrix}\Delta C_L\\ \Delta C_D\\ \Delta C_M\end{pmatrix}=\begin{bmatrix}\partial C_{L,tot}/\partial X_{LON} & \partial C_{L,tot}/\partial X_{LAT} & \partial C_{L,tot}/\partial X_{COL} & \partial C_{L,tot}/\partial X_{PED} & \partial C_{L,tot}/\partial X_{FLA}\\ \partial C_{D,tot}/\partial X_{LON} & \partial C_{D,tot}/\partial X_{LAT} & \partial C_{D,tot}/\partial X_{COL} & \partial C_{D,tot}/\partial X_{PED} & \partial C_{D,tot}/\partial X_{FLA}\\ \partial C_{M,tot}/\partial X_{LON} & \partial C_{M,tot}/\partial X_{LAT} & \partial C_{M,tot}/\partial X_{COL} & \partial C_{M,tot}/\partial X_{PED} & \partial C_{M,tot}/\partial X_{FLA}\end{bmatrix}\begin{pmatrix}X_{LON}\\ X_{LAT}\\ X_{COL}\\ X_{PED}\\ X_{FLA}\end{pmatrix} \tag{5.140}$$

Angles of Attack and Sideslip

The calculation of the local angle of attack and sideslip angle is treated next. Starting with the angle of attack in eq. (5.141) it can be seen that it consist of a summation of the angle of attack experienced by the mean aerodynamic chord aerodynamic center $\alpha_{\overline{AC}}$ and an induced angle of attack α_i. The former is calculated with eq. (5.142) where the arctangent of the ratio of the vertical velocity component to the total velocity experienced by the MAC AC ($w_{\overline{AC}}$ and $V_{\overline{AC}}$ respectively) is taken, while the source and calculation of the induced angle of attack α_i is treated later. The total velocity experienced by the MAC AC is obtained with eq. (5.143) where $u_{\overline{AC}}$ and $v_{\overline{AC}}$ are the remaining orthogonal longitudinal and lateral velocity components experienced by the MAC AC.

$$\alpha_{loc}=\alpha_{\overline{AC}}-\alpha_i \tag{5.141}$$

$$\alpha_{\overline{AC}}=arctan\left(\frac{w_{\overline{AC}}}{V_{\overline{AC}}}\right) \tag{5.142}$$

$$V_{\overline{AC}}=\sqrt{u_{\overline{AC}}^2+v_{\overline{AC}}^2+w_{\overline{AC}}^2} \tag{5.143}$$

The local sideslip angle β_{loc} is equivalent to the sideslip angle experienced by the MAC AC ($\beta_{\overline{AC}}$), and is also obtained with the use of the arctangent, as shown in eq. (5.144). In this case, however, the ratio between the lateral and longitudinal velocity components experienced by the MAC AC is used. It should be noted that the expressions used to obtain the angles of attack and sideslip differ from the ones that are commonly used in aerodynamic calculations. The expressions used here, however, provide the possibility to obtain a value for the angle of attack even at $\pm 90°$ of sideslip without having to additionally calculate the aerodynamic roll angle of the lifting surface. In order for this to be possible, the sideslip angle is also defined atypically where it behaves in the same way as the wind shift angle in the case of the rotor, following the total velocity vector. For this reason it is not comparable to the sideslip angle calculated for the body. These uncommon expressions, however, make it easier to obtain the forces and moments generated by the lifting surfaces when treated as flat plates.

$$\beta_{loc}=\beta_{\overline{AC}}=arctan\left(\frac{v_{\overline{AC}}}{u_{\overline{AC}}}\right) \tag{5.144}$$

Aerodynamic Velocity

The orthogonal components of the velocity experienced by the MAC AC are contained within the $\boldsymbol{V}_{\overline{AC}|ls}$ vector, as shown in eq. (5.145), which is defined in the lifting surface (ls) reference frame $\{\boldsymbol{E}_{ls}\}$. This velocity vector depends on the linear and rotational velocity of the tilt-rotor body, as well as the disposition of the lifting surface MAC AC with respect to the tilt-rotor center of gravity. As a result, a series of calculations must be performed in order to define $\boldsymbol{V}_{\overline{AC}|ls}$ as a function of the body velocity components, as is described next.

$$\boldsymbol{V}_{\overline{AC}|ls}=\begin{pmatrix}u_{\overline{AC}} & v_{\overline{AC}} & w_{\overline{AC}}\end{pmatrix}\{\boldsymbol{E}_{ls}\} \tag{5.145}$$

The $\boldsymbol{V}_{\overline{AC}|ls}$ vector is equal to the velocity vector of the MAC AC defined in the body frame ($\boldsymbol{V}_{\overline{AC}|b}$), multiplied by a transformation matrix from the body to the lifting surface frame $\boldsymbol{T}_{b|ls}$ as shown in eq. (5.146). This transformation matrix contains the rotations trough the incidence and dihedral angles of the lifting surface and has already been defined for each lifting surface type in section 4.7. As a reminder, wing sweep is considered a shear transformation therefore the sweep angle is not included in this transformation matrix. It shall be, however, used in the calculation of the position vector of $\overline{AC}$, i.e. $\boldsymbol{s}_{\overline{AC}}$.

$$\boldsymbol{V}_{\overline{AC}|ls} = \boldsymbol{V}_{\overline{AC}|b}\boldsymbol{T}_{b|ls}\{\boldsymbol{E}_{ls}\} \tag{5.146}$$

The $\boldsymbol{V}_{\overline{AC}|b}$ vector, on the other hand, is defined by eq. (5.147) where it can be seen that it depends on the aerodynamic velocity vector ($\boldsymbol{V}_{b|b}$) and a cross product between the rotational velocity vector of the body ($\boldsymbol{\omega}_{b|b}$) and the position vector of the lifting surface MAC AC ($\boldsymbol{s}_{\overline{AC}|b}$) with respect to the tilt-rotor center of gravity, all three defined in the body reference frame. Paraphrasing what has been already introduced on page 118, the aerodynamic linear velocity vector is a combination of the body linear inertial velocity and a linear wash velocity (indicated by the subscripts i and w respectively) as given by eq. (5.4a) and repeated below for clarity. Recall that the wash velocity is subtracted from the body velocity since the wash vector defines the movement direction *of* the air while the body velocity defines the movement direction of the body *through* the air, hence the difference in sign. The determination of the linear wash velocity vector (of rotor origin) acting on the lifting surfaces shall be treated in section 5.5 while the body linear and angular velocity vectors have already been defined in eqs. (5.5) and (5.6).

$$\boldsymbol{V}_{\overline{AC}|b} = \boldsymbol{V}_{b|b} + \boldsymbol{\omega}_{b|b} \times \boldsymbol{s}_{\overline{AC}|b} \tag{5.147}$$

$$\boldsymbol{V}_{b|b} = \boldsymbol{V}_{b,i|b} - \boldsymbol{V}_{w|b} \tag{5.4a}$$

The mentioned position vector $\boldsymbol{s}_{\overline{AC}|b}$ is a summation of the position vector $\boldsymbol{s}_{ls,RAC|b}$ defined from the tilt-rotor center of gravity to the the lifting surface root aerodynamic center (RAC), with the position vector $\boldsymbol{s}_{\overline{AC}-RAC|b}$ defined from the RAC to the MAC AC (both defined in the body frame), as shown in eq. (5.148). The latter position vector is presented in eq. (5.149) where it can be seen that it is equal to an analogous position vector $\boldsymbol{s}_{\overline{AC}-RAC|ls}$ defined in the lifting surface frame multiplied by a transformation matrix from the lifting surface frame to the body frame $\boldsymbol{T}_{ls|b}$ (which is the inverse of the already defined $\boldsymbol{T}_{b|ls}$ matrix).

$$\boldsymbol{s}_{\overline{AC}|b} = \boldsymbol{s}_{ls,RAC|b} + \boldsymbol{s}_{\overline{AC}-RAC|b} \tag{5.148}$$

$$\boldsymbol{s}_{\overline{AC}-RAC|b} = \boldsymbol{s}_{\overline{AC}-RAC|ls}\boldsymbol{T}_{ls|b}\{\boldsymbol{E}_b\} \tag{5.149}$$

Finally, the $\boldsymbol{s}_{\overline{AC}-RAC|ls}$ vector is defined in eq. (5.150) where it can be seen that it depends on the MAC spanwise position $\overline{Y}$ and incorporates the wing sweep shear transformation. Note that the sign of the lateral component of this position vector depends on the d_{sgn} parameter since $\overline{Y}$ is a scalar and thus is positive for both the left and right lifting surfaces.

$$\boldsymbol{s}_{\overline{AC}-RAC|ls} = \begin{pmatrix} -|\overline{Y}|tan(\Lambda_{AC}) & d_{sgn}\overline{Y} & 0 \end{pmatrix}\{\boldsymbol{E}_{ls}\} \tag{5.150}$$

Aerodynamic Forces and Moments

After having determined the aerodynamic coefficients of a lifting surface at a particular angle of attack and sideslip, it is possible to calculate the aerodynamic forces and moments generated by that surface. For simplicity's sake only it is assumed that the lifting surface only generates lift, drag, and a pitching moment while the lateral force and the other two moments are neglected. Compressibility effects are also not taken into account. For this reason the expressions for determining the lift L_{ls}, drag D_{ls}, and pitching moment M_{ls} of the lifting surface are simple and are presented in eqs. (5.151) to (5.153) where ρ is the air density.

$$L_{ls} = \frac{1}{2}\rho V_{\overline{AC}}^2 S C_L \quad (5.151) \qquad D_{ls} = \frac{1}{2}\rho V_{\overline{AC}}^2 S C_D \quad (5.152)$$

$$M_{ls} = \frac{1}{2}\rho V_{\overline{AC}}^2 S C_M \quad (5.153)$$

It should be remembered that these forces and moment are aligned with the local wind reference frame and therefore need to be first transformed into the lifting surface frame before finally being transformed into the body frame to able to perform force and moment summation on the tilt-rotor body. Recalling that the angle of attack and sideslip are not equivalent to the typical definition of these angles, the standard transformation from the aerodynamic reference frame to the body frame cannot be used. Instead, in the case of the lift and drag, first a longitudinal force F_{lon} aligned with the aerodynamic velocity vector is calculated according to eq. (5.154) and then decomposed into the longitudinal $F_{ls|Xls}$ and lateral $F_{ls|Yls}$ force components along the X- and Y-axes of the lifting surfaces with the use of the sideslip angle, as shown in eqs. (5.155) and (5.156). The vertical force component $F_{ls|Zls}$ is calculated in an analogous manner as the longitudinal force as shown in eq. (5.157). Note that the sideslip rotation happens around the axis of action of the vertical force component and therefore it is not present in the expression. A force vector may then be formed and transformed into the body frame yielding the desired force vector defined in the body frame of reference, as shown in eq. (5.158), which can be directly substituted into the body equations of motion force summation (eq. (5.2)). Note that since the positive convention of the forces generated by each lifting surface is identical, no conditional minus signs have to be included in eq. (5.158) since the effect of the disposition of a lifting surface has already been taken care of by the sign change parameter d_{sgn}.

$$F_{lon} = L_{ls}sin(\alpha_{loc}) - D_{ls}cos(\alpha_{loc}) \quad (5.154) \qquad F_{ls|Xls} = F_{lon}cos(\beta_{loc}) \quad (5.155)$$

$$F_{ls|Yls} = F_{lon}sin(\beta_{loc}) \quad (5.156) \qquad F_{ls|Zls} = -L_{ls}cos(\alpha_{loc}) - D_{ls}sin(\alpha_{loc}) \quad (5.157)$$

$$\boldsymbol{F}_{ls} = \begin{pmatrix} F_{ls|Xls} & F_{ls|Yls} & F_{ls|Zls} \end{pmatrix} \boldsymbol{T}_{ls|b}\{\boldsymbol{E}_b\} \quad (5.158)$$

The tilt-rotor model implementation presented in this thesis work contains several different lifting surfaces which together form the force vectors shown in eq. (5.2) that act on the body. Recalling the model description in section 4.2, the force vector of the wings (w) consists of the contribution of the left (L) and right (R) wing halves which are further divided into the free (frw), flap (flw), and aileron (aw) segments as given by eq. (5.159a). The horizontal stabilizer (hs) vector only consists of the left and right horizontal stabilizer lifting surfaces as shown in eq. (5.159b), while in the case of the vertical stabilizer (vs) an additional division into top (vst) and bottom (vsb) segments is employed, given by eq. (5.159c).

$$\boldsymbol{F}_w = \boldsymbol{F}_{frw,L} + \boldsymbol{F}_{flw,L} + \boldsymbol{F}_{aw,L} + \boldsymbol{F}_{frw,R} + \boldsymbol{F}_{flw,R} + \boldsymbol{F}_{aw,R} \quad (5.159a)$$

$$\boldsymbol{F}_{hs} = \boldsymbol{F}_{hs,L} + \boldsymbol{F}_{hs,R} \quad (5.159b)$$

$$\boldsymbol{F}_{vs} = \boldsymbol{F}_{vst,L} + \boldsymbol{F}_{vsb,L} + \boldsymbol{F}_{vst,R} + \boldsymbol{F}_{vsb,R} \quad (5.159c)$$

The pitching moment acts around the lateral wind axis and may be decomposed into a longitudinal $M_{ls|Xls}$ and lateral $M_{ls|Yls}$ moment component in the lifting surface frame with the use of the sideslip angle as

presented in eqs. (5.160) and (5.161). The pitching moment acts around an axis orthogonal to the vertical wind axis therefore no moment is assumed to exist around the vertical axis. For this reason the angle of attack is also not used in any transformation of the moment into the lifting surface frame. These moments may also be arranged into vector form and transformed into the body frame yielding the desired moment vector defined in the body frame of reference, as shown in eq. (5.162), which can be directly substituted into the body equations of motion moment summation (eq. (5.3)). Note that in eq. (5.3) the lifting surface forces also generate moments as a result of an offset of the force from the center of gravity of the tilt-rotor. In this case the position vectors $\boldsymbol{s}_{ls}$ are equal to the position vector of the lifting surface MAC AC (i.e. $\boldsymbol{s}_{\overline{AC}|b}$ from eq. (5.148)) since the calculated forces are assumed to act at this point. Similarly to the force vector, no conditional minus signs have to be included in eq. (5.162) since the effect of the disposition of a lifting surface has already been taken care of by the sign change parameter d_{sgn}.

$$M_{ls|Xls} = -M_{ls}sin(\beta_{loc}) \tag{5.160}$$

$$M_{ls|Yls} = M_{ls}cos(\beta_{loc}) \tag{5.161}$$

$$\boldsymbol{M}_{ls} = \begin{pmatrix} M_{ls|Xls} & M_{ls|Yls} & 0 \end{pmatrix} \boldsymbol{T}_{ls|b}\{\boldsymbol{E}_b\} \tag{5.162}$$

Similarly to the force vector, the pure moment vector that acts on the body (shown in eq. (5.3)) also consists of the same segment contributions as given by eq. (5.163).

$$\boldsymbol{M}_w = \boldsymbol{M}_{frw,L} + \boldsymbol{M}_{flw,L} + \boldsymbol{M}_{aw,L} + \boldsymbol{M}_{frw,R} + \boldsymbol{M}_{flw,R} + \boldsymbol{M}_{aw,R} \tag{5.163a}$$

$$\boldsymbol{M}_{hs} = \boldsymbol{M}_{hs,L} + \boldsymbol{M}_{hs,R} \tag{5.163b}$$

$$\boldsymbol{M}_{vs} = \boldsymbol{M}_{vst,L} + \boldsymbol{M}_{vsb,L} + \boldsymbol{M}_{vst,R} + \boldsymbol{M}_{vsb,R} \tag{5.163c}$$

Note that the focus of the tilt-rotor model derivation in this thesis work has been set on the rotor equations therefore only the simplest lifting surface aerodynamics have been implemented. Attempts at implementing more sophisticated approaches of approximating aerodynamic coefficients at high angles of attack led to problems when generating trim curves where the results would greatly deviate from validation data and thus were considered incorrect. Although effort was put into understanding and solving these issues, ultimately the aerodynamic model was reverted to the simpler approach described above. Due to this no attempt was made at using a more accurate model for the fuselage aerodynamics and therefore a very simple approach was implemented as shall be briefly described in the following section.

5.4. Fuselage

The calculation of the forces and moments generated by the fuselage somewhat overlaps with the method of obtaining these values for the lifting surfaces described above. The commonality appears in the calculation of the angle of attack and sideslip as well as the transformation of the forces from the wind frame to the fuselage frame. There are major differences, however, such as the simplification that the fuselage only generates drag while the lift and pitching moment are omitted. Furthermore the fuselage is not characterized by a sinusoidally varying drag coefficient but instead an equivalent flat plate area parameter (A_{eq}) is used to calculate the drag force, as shown in eq. (5.164). The most significant consequence of this simplification is that the drag only depends on the total velocity and not the angle of attack and sideslip of the fuselage. Since the fuselage reference frame coincides with the body reference frame, there is no need to perform any velocity or forces transformations between the two. Therefore the velocity used in eq. (5.164) is equal to the body velocity which is obtain with eq. (5.165). In addition, the center of gravity of the tilt-rotor is assumed to be the point of action of the fuselage drag force and the fuselage is assumed not to be affected by any wash effects.

$$D_{fus} = \frac{1}{2}\rho V_b^2 A_{eq} \quad (5.164) \qquad V_b = \sqrt{u^2 + v^2 + w^2} \quad (5.165)$$

For the purpose of completeness, the fuselage forces and moments are presented in vector form in eqs. (5.166) and (5.167) which may be directly substituted into eqs. (5.2) and (5.3). Here the angle of attack and sideslip are defined by eqs. (5.168) and (5.169).

$$\boldsymbol{F}_{fus} = \begin{pmatrix} -D_{fus}cos(\alpha_{loc})cos(\beta_{loc}) & -D_{fus}cos(\alpha_{loc})sin(\beta_{loc}) & -D_{fus}sin(\alpha_{loc}) \end{pmatrix} \{\boldsymbol{E}_b\} \quad (5.166)$$

$$\boldsymbol{M}_{fus} = \begin{pmatrix} 0 & 0 & 0 \end{pmatrix} \{\boldsymbol{E}_b\} \quad (5.167)$$

$$\alpha_{loc} = arctan\left(\frac{w}{V_b}\right) \quad (5.168) \qquad \beta_{loc} = arctan\left(\frac{v}{u}\right) \quad (5.169)$$

5.5. Rotor Wash Effect on Lifting Surfaces

As mentioned in the section treating the angle of attack, the local angle of attack not only depends on the velocity of the point of interest, but also on any local effects that induce a velocity in the vicinity of the point of interest. In this tilt-rotor model only one such source has been implemented, namely the rotor wash effect on the lifting surfaces as described below. As a side note, an attempt has been at implementing the effect of the main wing downwash on the tail, however the results appeared to be invalid at high angles of attack and therefore the wing induced angle of attack has been set to zero effectively removing this aerodynamic interaction from the model.

The rotor is assumed to induce a linear velocity in a cylindrical volume below its disk (for simplicity's sake) while the magnitude of the induced velocity follows the "contracted stream-tube" model [29, p6] as shown in eq. (5.170). Here V_{rw} is the rotor wash (rw) velocity determined at a perpendicular distance z_{rw} away from the rotor disk. As a reminder R is the rotor radius while v_{in} is the induced velocity directly at the rotor disk. The rotor is assumed not to induce any angular wash velocity components.

$$V_{rw} = v_{in}\left(1 + \frac{z_{rw}/R}{\sqrt{1 + (z_{rw}/R)^2}}\right) \quad (5.170)$$

The effect of the rotor wash does not directly provide a value for an induced angle of attack, instead the induced velocity is added to the velocity experienced by the point of interest implicitly affecting its local angle of attack while also changing the magnitude of the total aerodynamic velocity. If the point of interest is outside of the cylindrical area below the rotor, the induced velocity is no longer added. Since the rotor wash is modeled to only affect lifting surfaces, the point of interest is always going to be the MAC AC of a lifting surface.

The induced velocity addition is performed in the body frame of reference, and since the rotor is typically not aligned with the body axes, a transformation from the rotor disk frame to the body frame must be performed as shown in eq. (5.171) where $\boldsymbol{T}_{CP|b}$ is the transformation matrix from the rotor (control plane) to the body frame[4]. This transformed rotor wash yields the wash velocity vector $\boldsymbol{V}_{w|b}$ which may then be added to the body velocity vector to form the aerodynamic velocity as already shown in eq. (5.4a).

$$\boldsymbol{V}_{w|b} = \begin{pmatrix} 0 & 0 & V_{rw} \end{pmatrix} \boldsymbol{T}_{CP|b} \{\boldsymbol{E}_b\} \quad (5.171)$$

Recalling, the wash velocity is added to the body velocity only when the point of interest, i.e. the MAC AC, is within the cylindrical volume below the rotor disk. To determine whether this is true, two conditions

[4] Although the correct approach is to transform from the disk plane, in actuality the induced velocity is assumed to be perpendicular to the control plane removing the extra transformation and thus improving simulation speed.

must be satisfied, namely the MAC AC must be below the rotor disk, and the MAC AC must lie within the projection of the rotor disk along the Z_{CP}-axis. To be able to verify these conditions, the position vector between the MAC AC and rotor hub must be determined and transformed into the control plane (since the wake is assumed to be perpendicular to the CP). To do so, first the position vector of the rotor hub is determined in the body frame as shown in eq. (5.172) where the contribution of the tilting rotor mast (or nacelle) length l_n is added to the position vector of the nacelle pivot point $\boldsymbol{s}_{np|b}$ also defined in the body frame. Note that only a rotation through the nacelle tilt angle η is necessary since the nacelle rotation is assumed to be aligned with the body Y-axis.

$$\boldsymbol{s}_{hub|b} = \boldsymbol{s}_{np|b} + \begin{pmatrix} -l_n sin(\eta) & 0 & -l_n cos(\eta) \end{pmatrix} \{\boldsymbol{E}_b\} \tag{5.172}$$

Next the mentioned position vector $\boldsymbol{s}_{\overline{AC}-hub|b}$, spanning between the MAC AC and rotor hub, may be determined in the body frame by subtracting the MAC AC position vector $\boldsymbol{s}_{\overline{AC}|b}$ (already defined in eq. (5.148)) from the hub position vector as shown in eq. (5.173). Finally $\boldsymbol{s}_{\overline{AC}-hub|b}$ must be transformed from the body into the control plane reference frame with the transformation matrix $\boldsymbol{T}_{b|CP}$ as shown in eq. (5.174). The resulting vector $\boldsymbol{s}_{\overline{AC}-hub|CP}$ consists of three scalar values, namely x_{rw}, y_{rw}, and z_{rw} which correspond to the distance between the MAC AC and the rotor hub decomposed along the axis of the control plane reference frame.

$$\boldsymbol{s}_{\overline{AC}-hub|b} = \boldsymbol{s}_{hub|b} - \boldsymbol{s}_{\overline{AC}|b} \tag{5.173}$$

$$\boldsymbol{s}_{\overline{AC}-hub|CP} = \boldsymbol{s}_{\overline{AC}-hub|b} \boldsymbol{T}_{b|CP} \{\boldsymbol{E}_{CP}\} = \begin{pmatrix} x_{rw} & y_{rw} & z_{rw} \end{pmatrix} \{\boldsymbol{E}_{CP}\} \tag{5.174}$$

These decomposed distances may then be used to determine whether the MAC AC is within the rotor wash as shown with the two inequalities in eq. (5.175). The first inequality verifies that the in-plane distance between the MAC AC and rotor hub is less than the rotor radius, i.e. that the MAC AC lies within the projection of the rotor disk. The second inequality ensures that the perpendicular distance is positive and thus that the MAC AC lies (on or) below the rotor disk. If both inequalities are true then the lifting surface is considered to be wholly affected by the rotor wash. This last assumption may not be accurate for all tilt-rotor configurations especially if a large portion of the lifting surface lies outside of the rotor wake in reality. For this reason it is suggested to divide such a lifting surface into two separate entities, one being 'free' and the other 'wetted' by the rotor wake. This workaround has been employed for the tilt-rotor implementation of this thesis as has been described in section 4.2. In summary, each main wing half is divided into three segments, two of which are affected by the rotor wake, namely the *flap wing* and *aileron wing* segments. It is appropriate to mention at this point that each horizontal stabilizer half has not been subdivided. As a result the MAC AC of each half lies just outside of the rotor wake cylinder meaning that the horizontal stabilizer is completely unaffected by the rotor wake. One of the recommended modeling elements is to incorporate the rotor wake effect on the tail therefore this shortcoming of the present 6DoF model should be addressed in the future.

$$\sqrt{x_{rw}^2 + y_{rw}^2} \leq R \quad \text{and} \quad z_{rw} \geq 0 \tag{5.175}$$

The approach of incorporating the rotor wash effect on the lifting surfaces described above has a notable shortcoming, namely the assumption that the entire lifting surface within the rotor wake is at a mostly uniform distance away from the rotor disk. In other words, it is assumed that the perpendicular distance (z_w) from the rotor disk is the same for all points on the lifting surface, therefore the induced velocity is the same across the entire lifting surface area. An example where this would not be true would be the case of a tilt-rotor main wing with a high dihedral angle where the tip of the wing could be considerably closer to the rotor disk than the root. Although using the induced velocity at the wing MAC AC would provide an averaged value that could be somewhat representative of the integrated effect of the varying rotor wash across the lifting surface, its accuracy would be questionable especially considering the non-linearity of the variation of the induced velocity as a function of perpendicular distance. Therefore it is recommended that the presented approach be expanded in the future to incorporate the effect of a varying induced velocity

along the span of the lifting surface. Such an improvement to the model would also allow for a seamless inclusion of the effect of a non-uniform rotor wake distribution, providing all the more motivation for this recommendation.

6

Derivation Execution in Practice

Obtaining the rotor equations presented in the previous chapter has proven to be quite the logistical challenge due to the extensive nature of analytical expressions. This chapter describes the approach that has been taken in executing this derivation process in practice. Section 6.1 starts with describing the general derivation methodology and the choice of dividing the rotor equations into more manageable segments. The relationships between these segments is then outlined in section 6.2 and illustrated in appendix D. Finally section 6.3 explains the need for a method to reliably simplify the extensive rotor expressions and presents a scheme that has been specifically developed for the purpose of this thesis in order to achieve this goal. This section is also supported by appendix E.

6.1. Derivation Methodology and Common Integrals

Apart from several exceptions, the equations describing the flight dynamics of the 6DoF tilt-rotor model have been mostly derived analytically with the use of Maple [18], a symbolic manipulating and computing environment. An analytical approach has been chosen over a numerical one since it is believed that the former provides more understanding and direct insight into the equations, the model behavior, and most importantly, the effects of each state and parameter on the model dynamics. Furthermore, since the integrals in the equations are performed before the simulation, and not during as in the case of the numerical approach, it is expected that an analytical model can either provide a higher model accuracy at the same computational cost, or the same accuracy at a lower computational cost as compared to a numerical simulation.

The integrals mentioned above are in fact the basis of the flight dynamics model. This is because a signification portion of the derivation consists of equations related with the dynamics and aerodynamics of the rotor, which in turn depend on the combined effect of the rotor blades. In order to obtain this combined effect, each blade is divided into an infinite amount of blade elements which generate a unique lift and drag force that can be obtained with simple two-dimensional airfoil aerodynamics. Next, these forces are integrated along the length of the blade to obtain the forces generated by the entire blade. Finally the force contributions of all the blade must be combined in order to obtain a resultant force and moment generated by the complete rotor.

Instead of performing a direct derivation, it is more convenient to derive the orthogonal components of this resultant force and moment first, and later combine the effects of these components. Such a decomposition also aids in result interpretation and analysis. In the case of this 6DoF model it has been decided that the most convenient option will be to perform such a decomposition in the wind axis control plane. The corresponding three forces along the X_{CP}-, Y_{CP}-, and Z_{CP}-axes are declared as H, S, and T respectively. Analogously, the moments around these respective axes are O, P, and Q. The derivation of each of these components begins with an aerodynamic description of the already mentioned blade element and its contribution to the particular rotor force or moment component. For this reason it is no surprise that some common expressions will exist among the decomposed forces and moments, and in this work these common expressions will be referred to as common integrals.

It is of paramount importance to identify and take advantage of these reappearing expressions as it provides the opportunity to solve an integral only once, and use the result at multiple occasions later in the derivation.

This is only amplified when dealing with an extensive analytical derivation such as the one corresponding to this 6DoF model. In addition, if a similar but not identical common integral is found, it may be possible to only alter a previous solution without having to solve the newly found integral. Again this reduces the amount of work and time that needs to be put into the derivation of the equations, or the re-derivation in the case that a change must be made or a mistake fixed.

To provide a tangible example, the first steps of the derivation of the wind axis rotor thrust T and longitudinal force H are shown below. Equation (6.1) shows the simplified expression for the rotor thrust, inter alia containing the integral of the blade element lift dL_{BL} over the span of the rotor blade. On the other hand, eq. (6.2) presents the simplified expression for the rotor longitudinal force which consists of multiple integrals, one of which is identical to the one found in the expression for the thrust. At this point one could consider $\int_0^R dL_{BL}$ a common integral, however it is possible to expand this expression further into more fundamental integrals containing the blade element velocity components and possibly a power of the radial position of the blade element only, as shown in eq. (6.3). These more fundamental integrals could have also been expanded further, however with each expansion the result of the integral becomes more abstract and it's interpretation in the physical world more difficult. For example, the result of the initial integral contain the differential blade element lift (eq. (6.3)) yields the lift generated by the entire blade which is readily understandable, while the integrals in eq. (6.4) already lose their physical interpretation. The only interpretation that can be performed is by either looking at the units, or by describing these integrals as some part of the lift generated by the blade that, for example, depends on the squared tangential velocity of the blade element (as is the case for the first integral in eq. (6.4)). For this reason it has been decided that further expansion is unnecessary and all common integrals shall only contain the blade element velocity components and a power of the blade element radial position.

Returning to the initial example, since the three integrals shown in eq. (6.4) fit the common integral (CI) description stated above, and are found in both the thrust and H-force equations, they are considered common integrals (CIs) and therefore they should only be solved for once in the derivation process. A complete list of all common integrals identified in the derivation of the rotor equations of this 6DoF tilt-rotor model, as well as an indication of their presence (shown with the symbol 'x') within the blade lift (BL Lift), drag (BL Drag), and aerodynamic flapping moment (BL AFM) expressions, as well as within the rotor longitudinal H-force, lateral S-force, vertical thrust, and axial torque expressions is presented in table 6.1. The expressions for the rolling and pitching moment of the rotor have been derived based on the results of the disk-tilt approximation therefore no common integrals are involved. As a final note, three integrals that satisfy the common integral description have been identified in the derivation of the rotor torque, however they do not appear in the derivations of the other forces and moments. Two of them do, however, appear twice in the derivation of the torque itself, namely CI_7 and CI_8, hence they may still be referred to as common integrals since solving them once yields results that may be used at two different points in the derivation. The last integral CI_9, however, only appears once in the derivation therefore it should not be formally classified as a common integral. Nonetheless it has been included in the table for the sake of completeness and is indicated with the tilde symbol (~).

$$\widehat{T}_{BEM} = \frac{N}{2\pi} \int_0^{2\pi} \int_0^R dL_{BL} d\widehat{\psi} \tag{6.1}$$

$$\widehat{H}_{BEM} = \frac{N}{2\pi} \int_0^{2\pi} \left(sin(\widehat{\psi}) \int_0^R \phi_{BE} dL_{BL} - \widehat{\beta} cos(\widehat{\psi}) \int_0^R dL_{BL} + sin(\widehat{\psi}) \int_0^R dD_{BL} \right) d\widehat{\psi} \tag{6.2}$$

$$\int_0^R dL_{BL} = \frac{\rho c_{bl} C_{l_\alpha,bl}}{2} \left(\theta_0 \int_0^R U_T^2 dr_{BE} + \theta_{bl,1} \int_0^R U_T^2 r_{BE} dr_{BE} - \int_0^R U_T U_P dr_{BE} \right) \tag{6.3}$$

$$\text{common integrals: } \int_0^R U_T^2 dr_{BE} \quad , \quad \int_0^R U_T^2 r_{BE} dr_{BE} \quad , \quad \int_0^R U_T U_P dr_{BE} \tag{6.4}$$

Table 6.1: Presence of common integrals in the different derivation groups.

	Derivation Group						
Common Integral	**BL Lift**	**BL Drag**	**BL AFM**	**H-force**	**S-force**	**Thrust**	**Torque**
$CI_1 = \int_0^R U_T^2 dr_{BE}$	×	×		×	×	×	
$CI_2 = \int_0^R U_T U_P dr_{BE}$	×	×		×	×	×	
$CI_3 = \int_0^R U_T^2 r_{BE} dr_{BE}$	×	×	×	×	×	×	×
$CI_4 = \int_0^R U_T U_P r_{BE} dr_{BE}$		×	×	×	×		×
$CI_5 = \int_0^R U_P^2 dr_{BE}$		×		×	×		
$CI_6 = \int_0^R U_T^2 r_{BE}^2 dr_{BE}$		×	×	×	×		×
$CI_7 = \int_0^R U_P^2 r_{BE} dr_{BE}$							×
$CI_8 = \int_0^R U_T U_P r_{BE}^2 dr_{BE}$							×
$CI_9 = \int_0^R U_T^2 r_{BE}^3 dr_{BE}$							~

6.2. Derivation Relationship Diagram

As mentioned in the previous section, taking advantage of the common integrals involves solving an integral only once and using the result at multiple points in the derivation. For this reason many Maple files depend on other files which contain the solutions to a common integral. Due to the extensiveness of the 6DOF rotor equations a plethora of dependencies exists. In order to improve the clarity of the derivation at hand, multiple Maple file relationship diagrams have been created showing the file names and their inputs and outputs consisting of shared integral solutions. Each diagram presents a collection of Maple files which belong to a particular portion of the complete derivation, such as the derivation of the blade element lift, or the derivation of the rotor thrust. There also exist relationships between these collections of files and these too are indicated in the diagrams. Again, to improve clarity, a diagram showing an overview of the relationships between these collections has been created, however the specific shared solutions are not indicated here.

All diagrams and tables are included in appendix D where fig. D.1 presents the general overview of the collections' relationships while figs. D.2 to D.4 present the relationships between the files in the derivations of the rotor hub velocity components in the wind axis control plane, rotor hub velocity components in the wind axis disk plane, and the blade element velocity components derived in the wind axis control plane respectively. Next, fig. D.5 shows the diagram corresponding to the derivation of the rotor thrust according to the Glauert momentum theory defined in the wind axis disk plane while fig. D.6 corresponds to the derivation of the rotor thrust according to the blade element method defined in the wind axis control plane. Figures D.7 to D.9 show the derivation diagrams of the blade element aerodynamic flapping moment, lift, and drag respectively, all defined in the wind axis control plane, while figs. D.10 to D.12 show the diagrams for the rotor torque, H-force, and S-force respectively, all derived according to the blade element method in the wind axis control plane. Finally fig. D.13 presents the relationship diagram for the derivation of the blade element inertial flapping moment and flapping equation, together with the acquisition of the disk tilt angles. In addition table D.1 acts as a legend to these relationship diagrams explaining the meaning behind all diagram elements, while table D.2 briefly rationalizes the convention used in the naming of the Maple files.

Due to the existence of the dependencies, the execution of all the files must follow a coherent order. For this reason all the files involved in the derivation of the rotor equations are organized in the suggested execution order and are listed in table D.3.

Apart from providing better understanding of the derivation, an additional purpose of these relationship diagrams and execution order list is to aid in any future alteration to the model, be it due to a mistake that needs to be fixed or a desired feature that has not been implemented in the model at this stage. By following

the relationship diagrams it is possible to track all the files that are affected by a change in an 'upstream' expression, with the execution order list then indicating the order in which these files should be changed. These tools have already been taken advantage of during the derivation of the 6DoF model at hand when mistakes had to be fixed, and it is hoped that they shall continue to provide a more efficient and reliable model alteration process in the future as well.

6.3. Order Reduction

The end-result of the rotor equations' derivation yields expressions containing many terms, not all being of equal importance however. Keeping all terms would indeed provide the most accurate model (limited by the validity of the assumptions and parameters), but it is possible for some terms to have such a minute contribution to the results, that it would be permissible to completely neglect them without meaningfully affecting the accuracy of the model. Removing such terms would not only reduce the computational complexity, but would also increase the clarity of the model - a trait crucial to reaching the goal of this study and answering the research question.

6.3.1. Nominal Ordering Scheme

The determination of the importance of the terms may be carried out with the use of an ordering scheme such as the one used in [32, p. 41]. In short, it is assumed that all relevant expressions can be represented by a polynomial with terms separated by an addition or subtraction operator, while each term may consist of the product of multiple variables, each having their own order based on their minimum and maximum values which have to be identified beforehand. The polynomial can be simplified by calculating the order of each term to determine its importance within the polynomial, and subsequently removing any terms that are not significant, i.e. are small and thus have an order that is higher than some specified threshold. The final reduced-order polynomial then only contains large terms that have an order equal to or lower than the threshold while all higher order terms are neglected.

For the purposes of this thesis the nomenclature of the ordering scheme has been set as follows. The polynomial shall be referred to as the Sum of Terms (SoTs), the polynomial terms shall be refereed to as the Products of Terms (PoTs), and the variables shall be referred to as terms (Ts). The formal definition of these two expressions is given in eq. (6.5) and eq. (6.6) respectively where i indicates the relevance to the i^{th} term, NoT is the Number of Terms, sgn indicates the sign in front of the term (either a plus or minus), and pow indicates the power the term is raised to.

$$\mathrm{SoT} = \sum_{i=1}^{\mathrm{NoT}} \mathrm{sgn}_i \mathrm{T}_i \tag{6.5}$$

$$\mathrm{PoT} = \prod_{i=1}^{\mathrm{NoT}} \mathrm{T}_i^{\mathrm{pow}_i} \tag{6.6}$$

As an example consider eq. (6.7) which shows an arbitrary sum of terms SoT consisting of three terms. In this case the term parameters would be as follows: $\mathrm{NoT}_{SoT} = 3$; $\mathrm{sgn}_1 = (+)$; $\mathrm{sgn}_2 = (+)$; and $\mathrm{sgn}_3 = (-)$. To complete the example, consider eq. (6.8) which shows the first term T_1 which in actuality is a product of terms on its own consisting of three terms. In this case the term parameters would be as follows: $\mathrm{NoT}_{T,1} = 3$; $\mathrm{pow}_{1,1} = 1$; $\mathrm{pow}_{1,1} = 2$; $\mathrm{pow}_{1,3} = -3$.

$$\mathrm{SoT} = \mathrm{T}_1 + \mathrm{T}_2 - \mathrm{T}_3 \tag{6.7}$$

$$\mathrm{T}_1 = \frac{T_{1,1} T_{1,2}^2}{T_{1,3}^3} \tag{6.8}$$

The order of a term is also formally defined according to the O-notation shown in eq. (6.9a) where y represents the term, O is shorthand for Order, ϵ is the order basis, and n indicates the actual order. The order and basis must be chosen such that eq. (6.9b) is satisfied. In that case it may be said that term y has an order of n with basis ϵ. Since ϵ is less than 1, terms that are smaller (in the absolute sense) are assigned a higher order while terms that are absolutely larger are assigned a lower order.

$$y = O(\epsilon^n) \quad \text{with} \quad 0 < \epsilon < 1 \quad \text{and} \quad n \in \mathbb{Z} \tag{6.9a}$$

$$|y| \leq \epsilon^n \tag{6.9b}$$

As an example consider the term $T_{1,1}$ which has a minimum value of -3 and a maximum value of 2. If a basis of 0.5 is chosen ($\epsilon = 0.5$), according to eq. (6.9) the order of $T_{1,1}$ should be -2 as demonstrated in eq. (6.10).

$$\begin{aligned} |T_{1,1}| &\leq 3 \\ &\leq 0.5^{-2} \\ &= O(\epsilon^{-2}) \quad \text{with } \epsilon = 0.5 \end{aligned} \tag{6.10}$$

It is also possible to demonstrate that the collective order of a product of terms is equal to the sum of the products of each term's order and the power that the term has been raised to in the PoT, as shown in eq. (6.11). A formula for the collective order of a sum of products can be derived as well, however it shall not be shown since

$$\begin{aligned} \mathrm{PoT} &= \prod_{i=1}^{\mathrm{NoT}} \mathrm{T}_i^{\mathrm{pow}_i} \\ &\leq \prod_{i=1}^{\mathrm{NoT}} \left(\epsilon_i^{n_i}\right)^{\mathrm{pow}_i} \\ &\leq \epsilon^{\left(\sum_{i=1}^{\mathrm{NoT}} n_i \mathrm{pow}_i\right)} \\ &= O\left(\epsilon^{\left(\sum_{i=1}^{\mathrm{NoT}} n_i \mathrm{pow}_i\right)}\right) \end{aligned} \tag{6.11}$$

6.3.2. Shortcomings

The nominal ordering scheme described above is capable of simplifying a long expression, leaving only the most significant terms. Unfortunately several shortcomings have been identified that are briefly explained below.

First of all, the selection of ϵ and the significance threshold is considered arbitrary.

Second of all, the error introduced by ordering scheme is only known after the ordering scheme is performed and compared with the full expression. This requires one to execute the ordering scheme in an iterative manner until the accuracy of the reduced expression is satisfactory, which may become very time consuming in the case of extremely long expressions.

Thirdly, although eq. (6.11) is simple to use, it is not the only approach of calculating the order of a product of terms, and it is not applicable in the calculation of the order of a sum of products. The latter means that any SoTs that could have otherwise been represented by one convenient term, would have to be expanded to expose all fundamental terms.

Fourthly, the order of a PoT obtained with eq. (6.11) may be unnecessarily overestimated as shall be demonstrated in the following subsection.

For these reasons an extension to the nominal ordering scheme has been developed for the purposes of this study which addresses the shortcomings mentioned above.

6.3.3. Extended Ordering Scheme

As a first step in the description of the extended ordering scheme, a generalization of the calculation of an (exact) order of a value X (in short notation: O_X) has been formulated for the purposes of this thesis and is given by eq. (6.12) where the result may be non-integer. In order to convert this result to an integer the order must be rounded down to the nearest integer with a floor function ($\lfloor . \rfloor$) as shown in eq. (6.13). In both cases new notation for the order power (O^X) is also introduced for later use.

$$O_{X,exact} = O\left(\epsilon^{\log_\epsilon(X)}\right) \quad \text{with} \quad O^{X,exact} = \log_\epsilon(X) \tag{6.12}$$

$$O_{X,int} = O\left(\epsilon^{\lfloor \log_\epsilon(X) \rfloor}\right) \quad \text{with} \quad O^{X,int} = \lfloor \log_\epsilon(X) \rfloor \tag{6.13}$$

Additionally, a new parameter is introduced, namely Δ_O which is the difference between the highest order power that should be considered significant (Highest Significant Order - HSO), and the smallest order power present in a given expression (Smallest Present Order - SPO), formulized in eq. (6.14). For example if $\Delta_O = 3$, then terms that are 3 orders higher than the smallest present order are desired to be kept. In this case if the smallest present order power is equal to -2 (or $O(\epsilon^{-2})$) then the highest significant order power is equal to 1 (or $O(\epsilon^1)$) as shown in eq. (6.15). Any terms with an order power higher than 1 would be considered insignificant and thus should be removed from the reduced expression. At this point it may seem that the significance threshold of the nominal ordering scheme is replaced by another parameter which is just as arbitrary and would require an iterative process to determine the correct value in order to achieve a desired reduction accuracy. It shall be later shown, however, that this parameter will not have to be chosen arbitrarily, nor iteratively.

$$\Delta_O = HSO - SPO \tag{6.14}$$

$$\text{HSO} = \Delta_O + \text{SPO} = 3 + (-2) = 1 \tag{6.15}$$

Solution to First and Second Shortcoming - Introduction

The first step in addressing the first two shortcomings is to identify the effect of the choice of the order basis. The order basis ϵ determines how many higher order terms are equivalent to a single lower order term (later referred to as the basis equivalence number), with a smaller basis requiring more higher order terms to achieve equivalence. For example if $\epsilon = 0.1$, then ten $O(\epsilon^0)$ terms are equivalent to one $O(\epsilon^{-1})$ term as shown in eq. (6.16a), while with a basis of $\epsilon = 0.5$ only two $O(\epsilon^0)$ terms are equivalent to one $O(\epsilon^{-1})$ term as shown in eq. (6.16b). A generalized rule is given in eq. (6.16c) for any (valid) basis and difference between the orders of the considered terms, while the last (highlighted) row in table 6.2 shows the basis equivalence number for a basis-difference of 1 across a range of bases rounded to the nearest tenth. The order basis will remain an ordering scheme parameter which unfortunately will have to be chosen in a somewhat arbitrary manner, however later it shall become apparent that a smaller basis results in a more conservative order reduction scheme that is lenient towards keeping more terms in an expression since more terms will be grouped under a single order than in the case of a larger basis.

$$(10)O(\epsilon^0) = (10)(0.1^0) = (10)(1) = 10 = (1)(0.1^{-1}) = (1)O(\epsilon^{-1}) \tag{6.16a}$$

$$(2)O(\epsilon^0) = (2)(0.5^0) = (2)(1) = 2 = (1)(0.5^{-1}) = (1)O(\epsilon^{-1}) \tag{6.16b}$$

$$(\epsilon^{-N})O(\epsilon^p) = (1)O(\epsilon^{p-N}) \tag{6.16c}$$

Returning to the example of eq. (6.15), by removing the higher order terms (ones that are larger than $O(\epsilon^1)$) the final result of the reduced expression may be different from the result of the nominal expression. If $O(\epsilon^1)$ is to be considered the highest significant order, then the largest allowable error that should be introduced by removing the higher order terms should be less than a single term of the highest significant order, i.e. the error should have an order of at most $O(\epsilon^1)$ or have a value that is less than ϵ^1. Otherwise it would mean

that, collectively, the higher order terms (which have been removed) are more significant than the terms with the highest allowable significant order (which have been kept) - which is contradictory. Unfortunately, if a fixed significance threshold is used (as is done in the nominal ordering scheme), this paradox may occur and there is no guarantee that the reduction error will satisfy the inequality.

It would be convenient, however, to be able to select a tailored significance threshold before executing the ordering scheme, such that if a single lower order term is decided to be kept, and if there is a large enough number of higher order terms such that collectively they have an equivalent significance, then these higher order terms should also be kept. To clarify this, eq. (6.17) presents an example of a sum of terms consisting of one low order term, and 100 higher order terms. If the basis is chosen to be $\epsilon = 0.1$ then one such low order term is 100 times larger than one of the higher order terms and thus one may find it acceptable to neglect the higher order terms supporting their decision with the large difference in the order of magnitude between the two. However, according to eq. (6.16c), 100 of these higher order terms are equivalent to one such low order term and therefore if one decides to keep the low order term, then it is only logical to also keep the 100 higher order terms since collectively they have an equivalent importance in the SoT.

$$\text{SoT} = (1)O(0.1^{-2}) + (100)O(0.1^{0}) \tag{6.17}$$

The mentioned tailored significance threshold has been derived with the use of a reverse-engineering approach and an example as is shown below. In short, it is considered tailored to a specific expression since it depends on the mean of the orders of the terms in an expression and a threshold extension variable that only depends on the selected ϵ and Δ_O parameters.

Solution to First and Second Shortcoming - Extended Significance Threshold

Consider a sum of terms consisting of one low order term and ten higher order terms as given by eq. (6.18), where the order has been determined with a basis of $\epsilon = 0.1$. If an ordering scheme were to be applied to this expression with the desire to only keep the lowest four orders (i.e. $\Delta_O = 4$), then the significance threshold would be equal to the highest significant order, i.e. $O(\epsilon^{(-2)+4}) = O(\epsilon^2)$, and thus the ten $O(\epsilon^3)$ terms would be considered insignificant. However, since $\epsilon = 0.1$, the ten $O(\epsilon^3)$ terms are considered equivalent to one $O(\epsilon^2)$ term and therefore they too should be kept in the expression. In order for this to happen, however, the nominal significance threshold (eq. (6.19)) has to be extended to encompass these ten higher order terms as well. If the expression in eq. (6.18) can be considered a limit case in which the number of individually insignificant higher order terms is just enough for them to be considered collectively significant, then it can be concluded that the new tailored significance threshold should equal to $O(\epsilon^3)$ or, in new notation, $T_{tail} = 3$ as given in eq. (6.20). In addition, if basis equivalence is to be taken into account, then the maximum allowable value error (e_{EOS}) that would be introduced by neglecting higher order terms would be no greater than a single term with the highest significant order as shown in eq. (6.21a), with the maximum allowable fractional error (E_{EOS}) equal to 0.1^4 as shown in eq. (6.21b).

$$\text{SoT} = (1)O(0.1^{-2}) + (10)O(0.1^{3}) \tag{6.18}$$

$$O_{\text{thr,nom}} = O(0.1^2) \quad or \quad O^{\text{thr,nom}} = T_{\text{nom}} = 2 \tag{6.19}$$

$$O_{\text{thr,tail}} = O(0.1^3) \quad or \quad O^{\text{thr,tail}} = T_{\text{tail}} = 3 \tag{6.20}$$

$$e_{\text{EOS}} < \left(\text{SoT}_{\text{complete}} - \text{SoT}_{\text{reduced}}\right) = \left((1)(0.1^{-2}) + (10)(0.1^{3})\right) - (1)(0.1^{-2}) = 0.1^2 = \epsilon^{HSO} \tag{6.21a}$$

$$E_{\text{EOS}} < \frac{e_{\text{EOS}}}{\text{SoT}_{\text{reduced}}} = \frac{0.1^2}{(1)(0.1^{-2})} = 0.1^4 \tag{6.21b}$$

Since this is a limit case, and since this example has been chosen specifically to simplify the problem, it was trivial to deduce that the tailored threshold should equal to 3 and that the difference between the

nominal and tailored threshold is equal to 1. If a much longer expression were to be considered, however, the determination of the tailored threshold would no longer be a quick and easy task, and some algorithm would have to be employed to determine this new threshold, taking into account the orders of the terms and how many of them there are in an expression. Fortunately, taking the arithmetic mean of the evaluated orders (M_O) already provides much of the functionality of such an algorithm as it outputs a single value which takes into account both the order values and their quantity. To clarify this concept eq. (6.22) presents the calculation of the mean of the evaluated orders of the SoT given in eq. (6.18) with NoT being the number of terms and pow being the term order power. If one desires to obtain a new significance threshold, then the order of this mean must be taken with eq. (6.12) as shown in eq. (6.23) (rounded to 4 significant figures).

$$M_{\mathsf{SoT}} = \frac{\sum_{i=1}^{\mathsf{NoT}} \epsilon^{\mathsf{pow}_i}}{\mathsf{NoT}} = \frac{(1)(0.1^{-2}) + (10)(0.1^{3})}{11} = 9.09\overline{18} \tag{6.22}$$

$$O^{M,\mathsf{SoT}} = \log_{\epsilon}\left(M_{\mathsf{SoT}}\right) = \log_{0.1}\left(9.09\overline{18}\right) = -0.9587 \tag{6.23}$$

Unfortunately the above result is far from the desired significance threshold of 3. If, however, it is assumed that the order of the arithmetic mean will remain representative of some portion of the desired significance threshold, then the next step is to find the remaining portion, in this case equal to $3 - (-0.9587) = 3.9587$. To do so, an attempt is made to generalize the above scenario as shown in eq. (6.24a) where T_{ext} is the still undefined threshold extension parameter (which in this case should eventually equate to 3.9587). Since the goal is to define the threshold extension parameter, the generalized expression is rearranged appropriately as shown in eq. (6.24b). After some thought and trial and error, a generalized definition of the value of T_{tail} can also be found as shown in eq. (6.24c) remembering that SPO is the power of the smallest present order, in this case -2. Substituting the latter into eq. (6.24b) yields a partially generalized definition for the threshold extension parameter (eq. (6.24d)).

$$T_{tail} = O^{M,\mathsf{SoT}} + T_{ext} \tag{6.24a}$$
$$T_{ext} = T_{tail} - O^{M,\mathsf{SoT}} \tag{6.24b}$$
$$T_{tail} = \mathsf{SPO} + \Delta_O + 1 = (-2) + (4) + (1) = 3 \tag{6.24c}$$
$$T_{ext} = (\mathsf{SPO} + \Delta_O + 1) - O^{M,\mathsf{SoT}} \tag{6.24d}$$

The next step is to generalize the method of obtaining the order power of the mean of the sum of terms, i.e. obtaining $O^{M,SoT}$, starting with the sequence of steps taken to generalize the arithmetic mean as shown in eq. (6.25). Note that the following generalization only applies to the limit case, while the generalized formula for the arithmetic mean of any sum of terms is mentioned in eq. (6.22).

$$\begin{aligned} M_{\mathsf{SoT}} &= \frac{\text{sum of terms in expression}}{\text{number of all terms}} \\ &= \frac{(\text{value of smallest present order}) + (\text{collective value of the just-insignificant terms})}{1 + \text{basis equivalence number}} \\ &= \frac{\epsilon^{\mathsf{SPO}} + (\text{basis equivalence number})(\text{value of one just-insignificant term})}{1 + \epsilon^{-1}} \\ &= \frac{\epsilon^{\mathsf{SPO}} + \left(\epsilon^{-1}\right)\left(\epsilon^{HSO+1}\right)}{1 + \epsilon^{-1}} \end{aligned} \tag{6.25}$$

...and since $\mathsf{HSO} = \Delta_O + \mathsf{SPO}$ (according to eq. (6.14)) then:

$$\begin{aligned} &= \frac{\epsilon^{\mathsf{SPO}} + \left(\epsilon^{-1}\right)\left(\epsilon^{(\Delta_O+\mathsf{SPO})+1}\right)}{1 + \epsilon^{-1}} \\ &= \frac{\epsilon^{\mathsf{SPO}} + \epsilon^{(\Delta_O+\mathsf{SPO})+\cancel{1}-\cancel{1}}}{1 + \epsilon^{-1}} \end{aligned} \tag{6.25 cont.}$$

$$= \frac{\epsilon^{\text{SPO}} + \left(\epsilon^{\text{SPO}}\right)\left(\epsilon^{\Delta_O}\right)}{1+\epsilon^{-1}}$$
$$= \frac{\epsilon^{\text{SPO}}\left(1+\epsilon^{\Delta_O}\right)}{1+\epsilon^{-1}}$$

Having the generalized formula for the arithmetic mean of the limit case, it is possible to determine the generalized formula for the order power of the mean of the sum of terms (in alignment with eq. (6.12)) as shown in eq. (6.26).

$$\begin{aligned} O^{M,\text{SoT}} &= \log_\epsilon\left(M_{\text{SoT}}\right) \\ &= \log_\epsilon\left(\frac{\epsilon^{\text{SPO}}\left(1+\epsilon^{\Delta_O}\right)}{1+\epsilon^{-1}}\right) \\ &= log_\epsilon\left(\epsilon^{\text{SPO}}\right) + \log_\epsilon\left(\frac{1+\epsilon^{\Delta_O}}{1+\epsilon^{-1}}\right) \\ &= \text{SPO} + \log_\epsilon\left(\frac{1+\epsilon^{\Delta_O}}{1+\epsilon^{-1}}\right) \end{aligned} \tag{6.26}$$

Plugging the above result into the partially generalized definition for the threshold extension parameter (eq. (6.24d)) yields the fully generalized definition as shown in eq. (6.27). It is critical to notice that by performing this substitution, the only expression-dependent term, i.e. the smallest present order power SPO, is canceled out meaning that no information about the to-be-reduced-expression is needed to obtain the threshold extension parameter.

$$\begin{aligned} T_{ext} &= (\text{SPO} + \Delta_O + 1) - O^{M,\text{SoT}} \\ &= (\text{SPO} + \Delta_O + 1) - \left(\text{SPO} + \log_\epsilon\left(\frac{1+\epsilon^{\Delta_O}}{1+\epsilon^{-1}}\right)\right) \\ &= (\Delta_O + 1) + \cancel{\text{SPO}} - \cancel{\text{SPO}} - \log_\epsilon\left(\frac{1+\epsilon^{\Delta_O}}{1+\epsilon^{-1}}\right) \\ &= (\Delta_O + 1) - \log_\epsilon\left(\frac{1+\epsilon^{\Delta_O}}{1+\epsilon^{-1}}\right) \end{aligned} \tag{6.27}$$

Additionally, returning to the example of eq. (6.18), it may be shown that the generalized formula for the maximum allowable fractional error introduced by the extended ordering scheme will always be less than the order basis raised to the power of Δ_O as shown in eq. (6.28) (keeping in mind that this derivation is based on the limit case). Again, notice that the fractional error is expression-independent as well.

$$E_{\text{EOS}} < \frac{e_{\text{EOS}}}{\text{SoT}_{\text{reduced}}} = \frac{\epsilon^{HSO}}{\epsilon^{SPO}} = \frac{\epsilon^{\Delta_0+SPO}}{\epsilon^{SPO}} = \epsilon^{\Delta_0+\cancel{SPO}-\cancel{SPO}} = \epsilon^{\Delta_0} \tag{6.28}$$

These final generalized results show some of the elegant feature of extended ordering scheme. Since both the threshold extension parameter and the maximum introduced error are expression-independent, they may be calculated beforehand without any information about the to-be-reduced-expression. This means that by choosing a specific combination of ϵ and Δ_O it is possible to determine the maximum fractional error that may arise in the results of the expressions reduced by the extended ordering scheme. This relation may be rearranged such that a requirement for a desired maximum error is defined first, and with the selection of a basis, the necessary value of Δ_O may be determined. This directly addresses the first and second shortcomings of the nominal ordering scheme removing the necessity of executing the ordering scheme in an iterative manner to achieve a desired allowable error. In addition, the extended ordering scheme guarantees that the introduced fractional error will be below a specific value ensuring that the error is bound.

Table 6.2 has been created specifically for the purpose of presenting the mentioned relationship between ϵ, Δ_O, and the fractional error E_{EOS}. Several of the expressions of the 6DoF tilt-rotor model derived in

this thesis have been reduced by the extended ordering scheme. For this purpose a basis of 0.5 and a maximum fractional error of 0.0625 (or and error of 6.25%) have been chosen requiring a value of 4 for the Δ_O parameter, as indicated by the highlighted table cells. It must be pointed out, however, that the selection of the basis has remained quite arbitrary. The maximum allowable error has been chosen to roughly match the (subjectively estimated) error introduced by the other inaccuracies and uncertainties of the model.

Table 6.2: Relation between the maximal possible fractional error introduced by the extended ordering scheme and the choice of the ϵ and Δ_O parameters.

	ϵ								
Δ_O	**0.1**	**0.2**	**0.3**	**0.4**	**0.5**	**0.6**	**0.7**	**0.8**	**0.9**
5	0.00001	0.00032	0.00243	0.0102	0.0313	0.0778	0.168	0.328	0.591
4	0.0001	0.0016	0.0081	0.0256	0.0625	0.130	0.240	0.410	0.656
3	0.001	0.008	0.027	0.064	0.125	0.216	0.343	0.512	0.729
2	0.01	0.04	0.09	0.16	0.25	0.36	0.49	0.64	0.81
1	0.1	0.2	0.3	0.4	0.5	0.6	0.7	0.8	0.9
0	1	1	1	1	1	1	1	1	1
-1	10	5	3.33	2.5	2	1.67	1.43	1.25	1.11

In summary, given an expression consisting of a sum of terms varying in orders of magnitude, it is possible to determine which terms should be considered significant and kept in the expression with the use of the extended ordering scheme (EOS). Once the EOS parameters ϵ, Δ_O, and E_{EOS} have been selected, if a term has an order power that is less than or equal to the significance threshold (as shown in eq. (6.29)), it is considered significant, either on its own or due to an abundance of other terms of similar magnitude, and thus is kept in the reduced expression. The fractional error introduced by this expression-reduction process is guaranteed to be less than ϵ^{Δ_O}.

$$O^X \leq T_{\text{tail}} \implies \text{term } X \text{ is considered significant} \tag{6.29}$$

Solution to Third and Fourth Shortcoming

To solve the third shortcoming a different approach has been proposed and selected for the determination of the collective order of a product of terms. Namely, instead of determining the orders of individual terms, first all terms in the product are substituted by their appropriate values, next the product of terms is evaluated to obtain the largest possible PoT value, and finally the order of this result is calculated to obtain the maximum order of the PoT. This approach does involve several extra steps when compared to the nominal approach, however it is more robust as it can also be used to calculate the order of a sum of terms. It is possible to derive a similarly elegant expression as eq. (6.11) for the calculation of the order of a SoT, however it is longer and unnecessarily complex considering the conceptual simplicity of the more robust approach. With this approach not all expressions have to be fully expanded to expose all fundamental terms, and those SoTs that are more conveniently presented as single terms may remain unexpanded.

In addition it has been decided that each PoT and SoT shall be described by not one, but two orders. The first order corresponds to the maximum value, while the second order corresponds to the minimum value that the PoT or SoT may attain. This approach solves the fourth shortcoming as is demonstrated below with an example.

Minimum and Maximum Orders Example - Product of Terms

Consider a PoT that consists of three terms (as shown in eq. (6.30)) with the minimum and maximum values of these terms indicated in table 6.3. Using eq. (6.11) the absolute largest order of this PoT is found to be $O(\epsilon^{-5})$ as shown in eq. (6.31) (with $\epsilon = 0.5$). On the other hand, using the proposed approach of determining the order of the maximum ($O_{\text{PoT,max}}$) and minimum value ($O_{\text{PoT,min}}$) of the PoT separately,

the absolute largest order of this PoT is found to be $O(\epsilon^{-4})$ as shown in eq. (6.32). Hence the nominal approach yields an overestimated order which may result in this PoT unnecessarily remaining in a sum of terms in the case that the significance threshold is set to $O(\epsilon^{-5})$.

Note that in the calculation of the minimum and maximum orders of the PoT, an optimization scheme had to be employed to determine whether the minimum or maximum value of a particular term needs to be taken. Therefore, to determine the maximum order of the PoT the minimum value of all terms had to be taken. Also, if the minimum value of T_3 would be negative, then it would be possible for this term to, at some point, be equal to zero. In that case the maximum possible value for the corresponding PoT would be infinite, meaning that it would be infinitely more significant than the other non-infinite terms and thus it would break the ordering scheme. Furthermore, this would mean that the expression containing this term could also approach infinity which may also break the simulation. Expressions with division by a potential zero should therefore be avoided.

$$\text{PoT} = \frac{T_1 T_2}{T_3} \tag{6.30}$$

Table 6.3: Minimum and maximum values of arbitrary terms used in an example of the minimum and maximum order of a product of terms.

Term	Minimum Value	Maximum Value	Absolute Maximum Value
T_1	-5	1	5
T_2	-3	2	3
T_3	1	4	4
$1/T_3$	0.25	1	1

$$\begin{aligned} O_{\text{PoT,abs}} &= O_{T1,\text{absmax}}\, O_{T2,\text{absmax}}\, O_{(1/T3),\text{absmax}} \\ &= O(\epsilon^{-3})O(\epsilon^{-2})O(\epsilon^{0}) \\ &= O(\epsilon^{-3-2+0}) \\ &= O(\epsilon^{-5}) \end{aligned} \tag{6.31}$$

$$\text{PoT}_{\text{min}} = \frac{T_{1,\text{min}} T_{2,\text{max}}}{T_{3,\text{min}}} = \frac{(-5)(2)}{(1)} = -10 \tag{6.32a}$$

$$\text{PoT}_{\text{max}} = \frac{T_{1,\text{min}} T_{2,\text{min}}}{T_{3,\text{min}}} = \frac{(-5)(-3)}{(1)} = 15 \tag{6.32b}$$

$$O_{\text{PoT,min}} = O_{10} = O(\epsilon^{-4}) \tag{6.32c}$$

$$O_{\text{PoT,max}} = O_{15} = O(\epsilon^{-4}) \tag{6.32d}$$

$$O_{\text{PoT,abs}} = O(\epsilon^{-4}) \tag{6.32e}$$

Minimum and Maximum Orders Example - Sum of Terms

Another example is provided to not only show the application of the proposed method to the sum of terms, but also to highlight the repeated necessity for an optimization scheme in order to determine whether a minimum or maximum value of a term needs to be taken in the calculation of the order of a product or sum.

Consider a SoT that consists of three terms (as shown in eq. (6.33)) with the minimum and maximum values of these terms indicated in table 6.4. Using the proposed approach of determining the order of the maximum ($O_{\text{SoT,max}}$) and minimum value ($O_{\text{SoT,min}}$) of the SoT separately, the absolute largest order of this SoT is found to be $O(\epsilon^{-3})$ as shown in eq. (6.34). An optimization scheme has to be employed here as well when selecting the minimum or maximum value of a term. Otherwise, if only the absolutely largest values of the terms were to be only taken, and the sign in front of the terms would be neglected, the order of this SoT

would be found to be $O(\epsilon^{-4})$ (as shown in eq. (6.35)) which is again an overestimated result. Again, it may be the case that if an optimization scheme would have not been employed, this SoT might have remained in an expression despite it actually being insignificant.

Note that in the calculation of the maximum value of the SoT, the minimum value of T_3 had to be taken, and vice versa, due to the presence of a minus sign in front of T_3, hence the optimization scheme must take these arithmetic signs into account.

$$\mathrm{SoT} = T_1 + T_2 - T_3 \tag{6.33}$$

Table 6.4: Minimum and maximum values of arbitrary terms used in an example of the minimum and maximum order of a sum of terms.

Term	Minimum Value	Maximum Value	Absolute Maximum Value
T_1	-4	3	4
T_2	1	2	2
T_3	3	4	4

$$\mathrm{SoT}_{\mathrm{min}} = T_{1,min} + T_{2,min} - T_{3,max} = (-4) + (1) - (4) = -7 \tag{6.34a}$$
$$\mathrm{SoT}_{\mathrm{max}} = T_{1,max} + T_{2,max} - T_{3,min} = (3) + (2) - (3) = 2 \tag{6.34b}$$
$$O_{\mathrm{SoT,min}} = O_7 = O(\epsilon^{-3}) \tag{6.34c}$$
$$O_{\mathrm{SoT,max}} = O_2 = O(\epsilon^{-1}) \tag{6.34d}$$
$$O_{\mathrm{SoT,abs}} = O(\epsilon^{-3}) \tag{6.34e}$$

$$\mathrm{SoT}_{\mathrm{abs}} = T_{1,absmax} + T_{2,absmax} + T_{3,absmax} = (4) + (2) + (4) = 10 \tag{6.35a}$$
$$O_{\mathrm{SoT,abs}} = O_{10} = O(\epsilon^{-4}) \tag{6.35b}$$

6.3.4. Automatic Ordering Scheme

Executing the extended ordering scheme manually would be an endeavor, therefore it has been automated with the use of the Python programming language [50]. The extended ordering scheme has been implemented exactly as described by the formulas presented in this section with one exception, namely the threshold extension parameter which is additionally multiplied by a Rounding Factor (RF) as shown in eq. (6.36). This parameter extends the threshold even further ensuring that, even in a limit case, all terms that should be kept, will be kept despite any numerical rounding errors introduced by the Python implementation. Although this conservative approach will result in more terms being kept in the reduced expression than necessary, this option is considered safer than removing too many terms which would yield a reduced expression that could possibly violate the maximum allowable error guarantee. For the purpose of this thesis, this parameter has been set to a value of 1.01 allowing for a 1% numerical rounding error.

$$T_{\mathrm{ext}} = RF\left[\Delta_O + 1 - \log_\epsilon\left(\frac{1+\epsilon^{\Delta_O}}{1+\epsilon^{-1}}\right)\right] \tag{6.36}$$

A flow diagram of the implementation of the extended ordering scheme is presented in fig. 6.1. The process starts with reading the to-be-reduced expression which is assumed to be a sum of terms. In the case of this work, this expression was in the form of a saved Maple expression file with the extension (.mpl). This expression is then divided into separate terms that may be individual variables or products of terms, however for clarity purposes these terms will be referred to as PoTs from this point forwards. The arithmetic sign

(either a plus or minus) in front of each PoT is stored as it plays a key part in the determination of the maximum and minimum order of the complete expression.

Next a looped process is started which repeats the same steps for each PoT, starting with the determination of the minimum and maximum value of the current PoT with the use of an optimization scheme. A custom optimization scheme has been developed for the purposes of this thesis, however any other suitable optimization algorithm may be also used here. In both cases the minimum and maximum values of each term within the PoT have to be read from an outside spreadsheet which has been prepared beforehand and shall be briefly described in the next subsection. Returning to the evaluated minimum and maximum values of the PoT, if either one of these contains a division by zero or a complex number, the automatic ordering scheme (AOS) is stopped with an error since such results are not supported. Otherwise, the program continues with the calculation of the integer order powers of these minimum and maximum values of the PoT with the use of eq. (6.12) and eq. (6.13). Simultaneously, the minimum and maximum value of the PoT is either added to or subtracted from the minimum and maximum complete expression values based on the previously identified arithmetic sign in front of it.

Once the algorithm loops over all PoTs, the integer order powers of the minimum and maximum values of the complete expression are calculated with the two equations mentioned in the previous paragraph yielding the total minimum and maximum order of the unreduced expression. This order may then be used to represent the treated expression in a different sum of terms without having to expand the initial expression to expose the fundamental variables. In order for this to happen, however, this minimum and maximum order would have to be first included in the parameter spreadsheet.

In parallel, all order powers that are positive-infinite, i.e. correspond to a minimum or maximum PoT value that is equal to zero, are removed since they are considered infinitely insignificant. Next, two mean order powers are calculated for the remaining PoTs (with the use of eq. (6.22) and eq. (6.23)), one for the minimum orders, and one for the maximum orders. These, together with the threshold extension parameter which (using eq. (6.36)) has been calculated beforehand based on the selected EOS parameters (which have been also specified in the parameter spreadsheet), are then used to calculate two tailored significance thresholds (with eq. (6.24a)): one for the minimum PoT orders; and one for the maximum PoT orders.

Next, another looped process is started which decides whether or not a PoT is to be kept in the reduced expression according to eq. (6.29). If either the minimum PoT order power is less than or equal to the minimum tailored significance threshold, or the maximum PoT order power is less than or equal to the maximum tailored significance threshold, then the PoT is kept in the reduced equation. It is important to note that in order for a PoT to be considered insignificant, both the minimum and maximum PoT orders have to be considered insignificant when compared to their respective minimum and maximum peers.

The final result of the automated ordering scheme is the reduced expression which satisfies the maximum error bound given by eq. (6.28).

An example of one of the expressions of the 6DoF tilt-rotor model being reduced with the automatic ordering scheme is provided in appendix E. A summary of the parameters of the AOS applied to the tilt-rotor model implementation of this thesis, however, is given in appendix A in table A.16.

6.3.5. Minimum and Maximum Values

As mentioned in the previous subsection, a spreadsheet containing all the relevant term names and their minimum and maximum values has to be prepared beforehand and later supplied to the automated ordering scheme in order to be able to reduce expressions. The minimum and maximum values of these terms should be chosen to match the experienced conditions and limits of the modeled aircraft as much as possible in order to obtain a flight mechanics model that is reduced to a degree that is only as conservative as necessary. Expanding the parameter ranges any further would possibly yield expressions containing negligible terms which unnecessarily increase the complexity of the model. Since one of the goals of this work is to develop a clear model, advantage should be taken of the opportunity to reduce the model complexity whenever it arises. It must be highlighted, however, that modeling a different aircraft necessitates the reduction of the model expressions anew, given the different limitations of the each aircraft, yielding a flight mechanics model that is tailored specifically to it.

The terms that constitute the 6DoF tilt-rotor expressions are either aircraft parameters, environmental variables, or trigonometric functions. A list of the term names and values contained in the spreadsheet

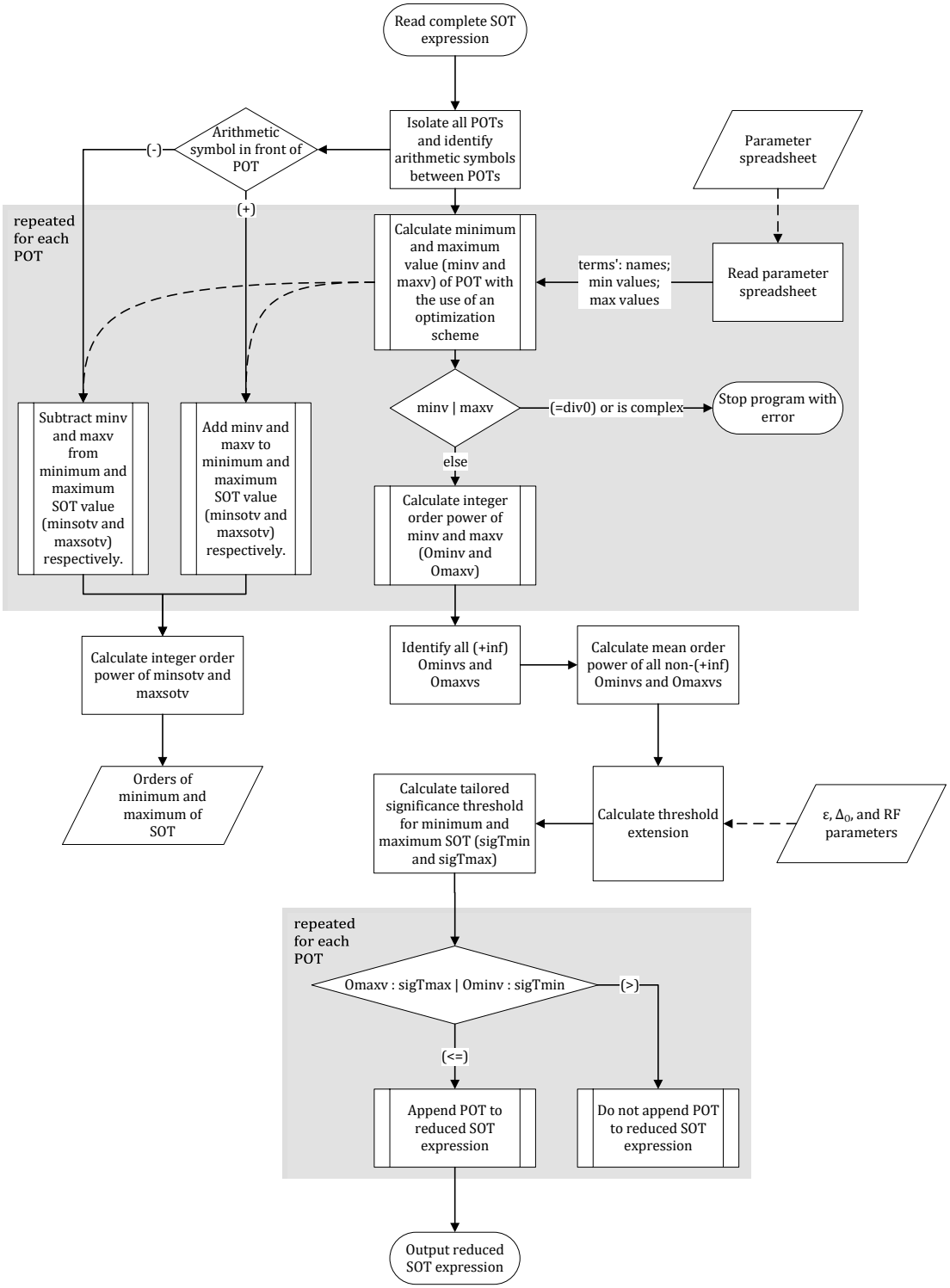

Figure 6.1: Automatic ordering scheme flow diagram.

that has been prepared for the reduction of the expressions corresponding to the XV-15 tilt-rotor model is presented in table A.17.

The determination of the minimum and maximum values of several terms has proven to be somewhat problematic therefore, in these cases, a small description of the approach of determining these values is provided below.

Blade Collective and Cyclic Pitch

The minimum and maximum values for the blade collective pitch at the blade root have been determined by finding the minimum and maximum value of the combined contributions to the collective pitch. In the case of the XV-15 tilt-rotor, the total blade root pitch θ_0 depends on the geometric blade root pitch $\theta_{bl,g}$, the global pitch modifier $\theta_{0,LL,mod,\eta}$, the control-phased lateral stick differential collective $\theta_{0,\mathrm{LAT},\eta}$, the control-phased pilot collective stick collective $\theta_{0,pilot,\eta}$, and the collective governor input $\theta_{0,gov}$ as shown in eq. (6.37a). The limit case for the minimum blade root pitch is when the tilt-rotor is in helicopter mode, and therefore the corresponding minimum $\theta_{0,LL,mod,\eta}$, $\theta_{0,\mathrm{LAT},\eta}$, and $\theta_{0,pilot,\eta}$ values are substituted in, along with the minimum possible contribution from the collective governor as shown in eq. (6.37b). The limit case for the maximum blade root pitch is when the tilt-rotor is in airplane mode and the maximum value can be found analogously as shown in eq. (6.37c). The geometric blade root pitch as well as the gearing ratios and minimum and maximum pilot and governor inputs may be found in appendix A.

$$\theta_0 = \theta_{bl,g} + \theta_{0,LL,mod,\eta} + \theta_{0,\mathrm{LAT},\eta} + \theta_{0,pilot,\eta} + \theta_{0,gov} \tag{6.37a}$$

$$\begin{aligned}\theta_{0,min} &= \theta_{bl,g} + \theta_{0,LL,mod,heli.} + \left(\left.\frac{\partial\theta_0}{\partial X_{LAT}}\right|_{heli.}\right) X_{LAT,min} + \left(\left.\frac{\partial\theta_0}{\partial X_{COL}}\right|_{\eta=0}\right) X_{COL,pilot,heli.,min} + \theta_{0,gov,min} \\ &= (40.9) + (-8.675) + (0.625)(-4.8) + (1.6)(0) + (-5) \\ &= 24.225^\circ\end{aligned} \tag{6.37b}$$

$$\begin{aligned}\theta_{0,max} &= \theta_{bl,g} + \theta_{0,LL,mod,arpln} + \left(\left.\frac{\partial\theta_0}{\partial X_{LAT}}\right|_{arpln}\right) X_{LAT,max} + \left(\left.\frac{\partial\theta_0}{\partial X_{COL}}\right|_{\eta=0}\right) X_{COL,pilot,arpln,max} + \theta_{0,gov,max} \\ &= (40.9) + (14.93) + (0.121)(4.8) + (1.6)(0) + (33.5) \\ &= 89.9108^\circ\end{aligned} \tag{6.37c}$$

The minimum and maximum values for the longitudinal cyclic may also be found by determining the maximum and minimum value of the appropriate combined contributions, which in this case are the phased longitudinal stick $\theta_{1s,LON,\eta}$, pedals $\theta_{1s,PED,u\eta}$, and stick-invariant offset $\theta_{1s,offset,\eta}$ as shown in eq. (6.38a). Here, however, the limit case for both the minimum and maximum values corresponds to the tilt-rotor in helicopter mode and substituting the appropriate values yields the minimum and maximum values for the longitudinal cyclic as shown in eq. (6.38b). The gearing ratios, minimum and maximum pilot inputs, and the cyclic offset in helicopter configuration in hover (i.e. $u = 0$) may also be found in appendix A.

$$\theta_{1s} = \theta_{1s,LON,\eta} + \theta_{1s,PED,u\eta} + \theta_{1s,offset,\eta} \tag{6.38a}$$

$$\begin{aligned}\pm\theta_{1s,max} &= \pm\left[\left(\left.\frac{\partial\theta_{1s}}{\partial X_{LON}}\right|_{heli.}\right) X_{LON,max} + \left(\left.\frac{\partial\theta_{1s}}{\partial X_{PED}}\right|_{heli.,u=0}\right) X_{PED,max}\right] + \theta_{1s,offset,heli.} \\ &= \pm\left[(2.1)(4.8) + (1.6)(2.5)\right] + (0) \\ &= \pm 14.08^\circ\end{aligned} \tag{6.38b}$$

Custom Limitation and Preliminary Results

Several terms have a minimum and/or maximum value that is not supported by any source and instead a custom limitation has been set upon these terms. In these cases, the minimum and maximum values simply define the range of validity for the model and may be changed in the future as seen appropriate.

Other terms' minimum and maximum values are indicated as being supported by preliminary results. This means that the values have been determined based on the results of the 3-DoF tilt-rotor model developed during the preliminary phases of this thesis. It is suggested that these values are to be revisited in the future and adjusted according to the results of the present version of the 6DoF tilt-rotor model.

It should be noted that the inflow velocity limits have also been determined based on preliminary results. Since the preliminary model did not support negative inflow velocities, the minimum inflow velocity is set to a positive value whilst the 6DoF model has been derived such that it is possible for it to enter a rotor windmill state where the inflow velocity is negative. Therefore it should be a priority to adjust this value in the future to ensure that the validity of the model is not compromised by an incorrect setup of the ordering scheme.

Automatic Ordering Scheme Result

Finally, a handful of terms shown in table A.17 are in actuality either products of terms or sums of products and therefore it is possible to employ the automatic ordering scheme to obtain their minimum and maximum values. In these cases the source of the values is indicated as AOS.

7

Model Implementation, Simulation, and Trimming

The analytical expressions governing the flight mechanics of the tilt-rotor, derived in chapter 5, provide full insight into the workings of the model, however performing this assessment is not very intuitive. Converting these expressions to some sort of visual form, however, would provide much more understanding. For this reason the analytical expressions have been collected and implemented in the Matlab programming language yielding the nominal 6DoF tilt-rotor Matlab model which has the primary capability of calculating the state derivatives of a complete tilt-rotor configuration. Furthermore this Matlab model has been incorporated into a simulation environment with the use of Simulink in order to be able to generate a time history of the variation of the states of the tilt-rotor model. An extra step has also been taken to connect this Simulink simulation with the graphical flight simulator FlightGear.

This chapter starts with section 7.1 which explains the need for a description of the tilt-rotor body position and orientation in inertial space, and presents the suggested solution to this problem which is employed in the Matlab implementation described in section 7.2. Next the incorporation of the Matlab model in the Simulink simulation environment is treated in section 7.3, while section 7.4 describes the method used to trim the model which, apart from being a convenience when setting up a simulation run, also provides crucial data used in the verification and validation of the model. Finally section 7.5 briefly discusses the methods employed in the optimization of the Matlab model allowing for real-time simulation - an unavoidable requirement for this model which is ultimately intended for piloted flight simulation as stated in the objective of this thesis.

7.1. Body Position and Orientation in Inertial Space

The dynamics of the tilt-rotor model are nominally presented in the body reference frame with linear and rotational accelerations defined along the body axes. Although this does not hinder the model analysis process in any way, it may be beneficial to additionally transform these accelerations into inertial space in order to obtain a more intuitive representation of the motion in the form of a time history of the position, height, and Euler attitude. In fact, if one desires to later connect the model to a graphical flight simulator, this step may be inevitable.

The body accelerations defined in the inertial space may be integrated twice in order to obtain the inertial position and Euler attitude of the tilt-rotor body. It is more convenient, however, to first integrate the body accelerations (defined in the body frame) to obtain the body rates (which are nonetheless required for the calculations of the flight dynamics) and then transform these into inertial space yielding the inertial-space velocity $V_{b|C,i}$ and Euler rates ω_e. These can then be integrated again to obtain the body inertial position and attitude.

The transformation of the body linear velocity from the body frame to the inertial frame may be achieved with the $\boldsymbol{T}_{b|C}$ matrix which transforms vectors from the body frame $\{\boldsymbol{E}_b\}$ to the non-rotating flat Earth-fixed reference frame $\{\boldsymbol{E}_C\}$. This transformation involves going through an intermediate reference frame, namely

the vehicle-carried normal-to-Earth reference frame $\{\boldsymbol{E}_E\}$. However, since no rotational transformation is required from the inertial frame to the vehicle-carried frame, the inertial frame may be directly substituted by the vehicle carried frame, i.e. $\{\boldsymbol{E}_C\} = \{\boldsymbol{E}_E\}$. Therefore the transformation from $\{\boldsymbol{E}_b\}$ to $\{\boldsymbol{E}_C\}$ can be achieved with the $\boldsymbol{T}_{b|E}$ matrix, or with its equivalent, the inverse of the $\boldsymbol{T}_{E|b}$ matrix that was introduced in eq. (4.32), as shown in eq. (7.2).

$$\boldsymbol{V}_{b|C,i} = \boldsymbol{V}_{b|b,i}\boldsymbol{T}_{E|b}^{-1} = \begin{pmatrix} u_i & v_i & w_i \end{pmatrix} \begin{bmatrix} C_{\psi b}C_{\theta b} & S_{\psi b}C_{\theta b} & -S_{\theta b} \\ -S_{\psi b}C_{\phi b} + C_{\psi b}S_{\theta b}S_{\phi b} & C_{\psi b}C_{\phi b} + S_{\psi b}S_{\theta b}S_{\phi b} & C_{\theta b}S_{\phi b} \\ S_{\psi b}S_{\phi b} + C_{\psi b}S_{\theta b}C_{\phi b} & -C_{\psi b}S_{\phi b} + S_{\psi b}S_{\theta b}C_{\phi b} & C_{\theta b}C_{\phi b} \end{bmatrix} \tag{7.1}$$

The transformation of the rotational rates can be achieved with the use of the inverse of the transformation matrix $[\boldsymbol{E}]$ shown in eq. (7.2). Unlike in the case of the linear rates, this is not the same as transforming the body rates from the body frame to the inertial frame, i.e. decomposing the body rates into the inertial frame axes. Therefore the matrix describing the transformation from the body frame to the inertial frame is not used in this case. These Euler rates can then be integrated to obtain the body attitude which is typically described with the Euler angles ϕ_b, θ_b, and ψ_b which represent the roll, pitch, and heading angles of the tilt-rotor body respectively.

$$\boldsymbol{\omega}_e = \boldsymbol{\omega}_{b|C,i} = \boldsymbol{\omega}_{b|b,i}[\boldsymbol{E}]^{-1} = \begin{pmatrix} p_i & q_i & r_i \end{pmatrix} \begin{bmatrix} 1 & 0 & 0 \\ sin(\phi_b)tan(\theta_b) & cos(\phi_b) & sin(\phi_b)/cos(\theta_b) \\ cos(\phi_b)tan(\theta_b) & -sin(\phi_b) & cos(\phi_b)/cos(\theta_b) \end{bmatrix} \tag{7.2}$$

The use of Euler angles and rates seems to be the most appropriate approach, but it unfortunately also has several drawbacks. First of all this approach is sensitive to a too large of a simulation step size which manifests itself in a quickly growing accumulated integration error. Second of all, pitch angles of ± 90 degrees result in division by zero in parts of the transformation matrix resulting in incorrectly calculated Euler rates nearing infinity. This situation is sometimes referred to as gimbal lock. Although pitch angles of ± 90 degrees may be outside of the flight envelope of a tilt-rotor, it may still be desired to correctly predict the behaviour of a tilt-rotor in such states, therefore a more robust approach of determining the orientation should be employed.

One alternative is to use quaternions in which case the body rotational rates are used to determine the derivative of a 4-value quaternion $\boldsymbol{q}_4$ describing the magnitude and axis of rotation in three-dimensional inertial space as defined in eq. (7.3). The definition of the differential quaternion in terms of body rates is given by eq. (7.4) where an additional "constraint equation c"[23, p41] is introduced and is defined by eq. (7.5) (the necessity for this constraint equation is explained later). The differential quaternion is then integrated to obtain the quaternion description of the rotational orientation of the tilt-rotor body. For a more intuitive understanding, the Euler representation for the orientation of the tilt-rotor may then be extracted from the quaternion with the use of eq. (7.6).

$$\boldsymbol{q}_4 = \begin{pmatrix} e_0 & e_1 & e_2 & e_3 \end{pmatrix}^T \tag{7.3}$$

$$\dot{\boldsymbol{q}}_4 = \begin{Bmatrix} \dot{e_0} \\ \dot{e_1} \\ \dot{e_2} \\ \dot{e_3} \end{Bmatrix} = \frac{1}{2} \begin{bmatrix} c & -p_i & -q_i & -r_i \\ p_i & c & r_i & -q_i \\ q_i & -r_i & c & p_i \\ r_i & q_i & -p_i & c \end{bmatrix} \begin{Bmatrix} e_0 \\ e_1 \\ e_2 \\ e_3 \end{Bmatrix} \tag{7.4}$$

$$c = K_c\left(1 - \boldsymbol{q}_4^T\boldsymbol{q}_4\right) \quad \text{with} \quad K_c > 0 \tag{7.5}$$

$$\phi_b = \arctan\left(\frac{2(e_0e_1 + e_2e_3)}{e_0^2 - e_1^2 - e_2^2 + e_3^2}\right) \tag{7.6a}$$

$$\theta_b = \arcsin(2e_0e_2 - 2e_1e_3) \quad \text{ensuring that} \quad -1 \leq (2e_0e_2 - 2e_1e_3) \leq 1 \tag{7.6b}$$

$$\psi_b = \arctan\left(\frac{2(e_0e_3 + e_1e_2)}{e_0^2 + e_1^2 - e_2^2 - e_3^2}\right) \tag{7.6c}$$

The main advantage of quaternions is the absence of gimbal lock. Furthermore quaternion integration is less sensitive to integration step size and thus introduces much less integration error in comparison to Euler rate integration. A potential division by zero is still present in the conversion from quaternion to Euler angles, however it occurs within an arctangent function and therefore does not result in a divergence towards infinity but instead towards $\pm\pi$.

One disadvantage is the need for quaternion normalisation which may be computationally expensive. This can be circumvented, however, with feedback error correction which implicitly normalises the quaternion. In the case of the quaternion implementation for the 6DoF tilt-rotor model at hand, this error correction is achieved with the constraint equation c mentioned above and shown in eq. (7.5). The term K_c is a positve gain that controls the error correction rate and nominally equals to 1, however, for this thesis work a value of 32 has been chosen. Care should be taken when selecting this gain since a too low value could yield inaccurate results, while a too high value may lead to a too-aggressive error correction process resulting in quaternion divergence. It should be noted that if the quaternion is normalised, the constraint equation c equals to zero. Although this approach does introduce integration errors due to a lag in the quaternion normalisation process, the errors are still much smaller than in the case of Euler angle integration.

Finally, it may be necessary to convert the inertial position to a latitude, longitude, and altitude value when connecting the model to a graphical flight simulator. In the case of this thesis, the tilt-rotor model has been implemented in Matlab and Simulink and therefore advantage has been taken of the built-in Flat Earth to LLA block (part of the Aerospace Blockset) to perform this conversion as shall be described in section 7.3. This was a necessary step when connecting the Matlab/Simulink model with the open-source graphical flight simulator FlightGear.

7.2. Matlab Model Implementation

All the equations that define the flight characteristic model of the 6DoF tilt-rotor as presented in chapter 5 have been implemented in Matlab[19] giving rise to the nominal 6DoF tilt-rotor Matlab model. It has been decided that the model implementation design shall follow an object oriented programming (OOP) organization structure mainly due to OOP being widely known and providing more approachable code that is easier to decipher and expand in the future. Although this approach is not ideal when dealing with the Matlab programming language (as discussed in section 7.5), it allows for an easier conversion process to a different, more suitable and efficient programming language if that need arises in the future.

Model Class Structure Description

The model inputs, outputs, states, and parameters are already listed and explained in chapter 4 and thus this shall not be repeated here. A graphical description of the model class structure, however, is provided in appendix F in fig. F.1 which presents the relationships between the Matlab classes, the Simulink environment, and supplementary Matlab scripts.

To briefly summarize, the tilt-rotor model is distributed among several classes. All tilt-rotor elements are brought together in the `TiltRotorModel` class which determines the correct order of calculation of all the forces and moments acting on the body, and calculates the nacelle-tilt state derivative. The methods for the calculation of the remaining body state derivatives (as described in section 5.1) and the quaternion body attitude derivative (as described in section 7.1) is inherited from the `Vehicle` class. All force and moment generating tilt-rotor components that are desired to be modeled must be defined beforehand with the use of specialized classes. In the case of this tilt-rotor model implementation, separate classes for the rotors, lifting surfaces, and the fuselage have been defined only, and are as follows: the `ArticulatedRotor` class; the `FixedTrapezoidalLiftingSurface` class; and the `LiftingBody` class respectively. These classes are mainly responsible for the calculation of the forces and moments generated by a single component (defined in that components reference frame), and thus primarily contain the expressions derived in chapter 5. In addition the transformation matrices from the body frame to the component frame (based on the transformation matrices presented in section 4.7), and vice versa, are also included as (either constant or varied) attributes of these

classes. These three component classes also inherit methods from the ForceMomentComponent class for the calculation of the velocity vector at the component origin defined in the component frame, the calculation of the moment generated at the body CoG as a result of the component force acting at a distance from the body CoG, and for the transformation of the component forces from the component frame to the body frame.

Ultimately, the tilt-rotor model should be instantiated with a script that first creates instances of the ArticulatedRotor, FixedTrapezoidalLiftingSurface, and LiftingBody classes which are then supplied to the TiltRotorModel class as force-moment components. In the case of this implementation, a script containing all the necessary tilt-rotor parameters is called separately when creating an instance of the tilt-rotor. Furthermore, this instance is created directly in Simulink at the beginning of each simulation run.

Model State Derivatives Calculation

The main goal of the tilt-rotor model is to calculate the state derivatives based on the previous state of the tilt-rotor and the environmental conditions. A simplified top level flow diagram of the calculation process of these states derivatives performed within the TiltRotorModel class (also referred to as the TiltRotorModel.calcStateDerivatives() method) is presented in fig. 7.1. The process starts with the determination of the mixed and phased pilot inputs, as well as the resulting left and right rotor longitudinal and collective swashplate angles, with the doControlMixing() method of the TiltRotorModel class. The preceding obj. in the diagram indicates that the method, or attribute, belongs to the TiltRotorModel class. Next the value of the air density is taken from an external source, and together with the previous states and state derivatives, the calcForceMomentSum() method is called which determines the combined contribution of all force-moment components to the total force and moment vectors acting on the body. The internals of this method are treated in more detail below. Together with an externally sourced value for the gravitational acceleration, this resultant force and moment are supplied to the calcStateDerivatives() method of the Vehicle class to determine the body state derivatives[1]. To complete the state derivative output, the value of the nacelle tilt rate $\dot{\eta}$ is determined based on the X_{TIL} input.

As mentioned above, the internal flow diagram of the calcForceMomentSum() method is presented in fig. 7.2. With the use of the inputs supplied to this method, it can be seen that the calculation of the force and moment contributions from the different force-moment components is executed in a cascaded manner rather than in parallel. The forces and moments generated by the rotors are calculated first with the calcForcesAndMomentsOnBody() method of the ForceMomentComponent class, additionally outputting parameters that describe the corresponding rotor wake which has an effect on the main wings and stabilizers. Once this calculation is repeated for all rotors, a collection of these wake parameters is then passed onto the same calcForcesAndMomentsOnBody() method, however this time corresponding to the main wing components that are part of the tilt-rotor instance. It should be mentioned at this point that although the calcForcesAndMomentsOnBody() has the same name in both the rotor and wing instances, its internal functionality differs depending on the class of the inheriting component. Therefore, apart from the forces and moments generated by the main wings, this main wing method also outputs the wing downwash angles which will have an additional effect on the down-wind stabilizers. Once this calculation is repeated for all main wing components, a collection of the downwash angles and rotor wake parameters is passed onto the calcForcesAndMomentsOnBody() method corresponding to the horizontal and vertical stabilizers, ultimately yielding the forces and moments generated by these lifting surfaces. One calculation may be performed in parallel, namely the determination of the forces and moments generated by the fuselage, again with the use of the same calcForcesAndMomentsOnBody() method which corresponds to the fuselage instance. This final calculation may be done in parallel since it is assumed that no aerodynamic effect exists between the fuselage and the other force-moment components. The resulting forces and moments are then combined to produce the final output of the calcForceMomentSum() method.

7.3. Simulink Simulation Implementation

The Matlab model has been incorporated into a simulation environment with the use of Simulink. Apart from providing an overview of the general structure of this simulation, additional model elements which are not part of the Matlab code and instead were implemented directly in the Simulink environment are also

[1]The state derivatives in the diagram are indicated using Lagrange's prime-mark notation instead of Newton's dot notation.

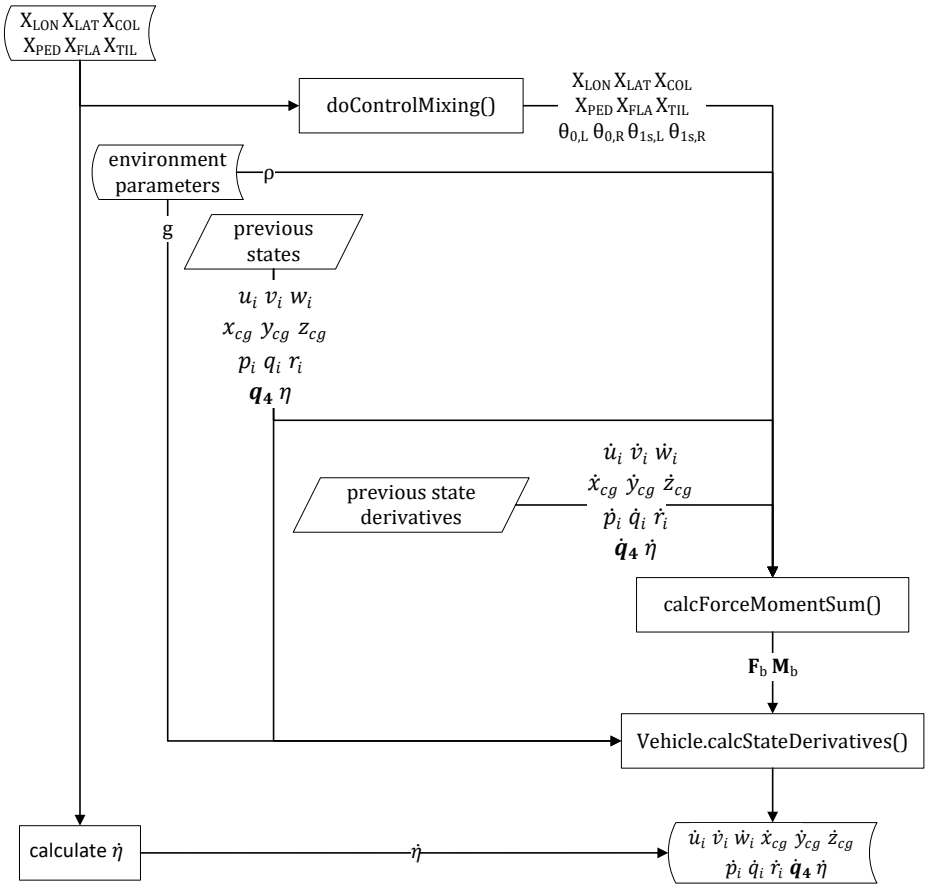

Figure 7.1: Simplified top level flow diagram of the calcStateDerivatives() method of the TiltRotorModel class.

described below. These elements only affect the dynamic response of the model, and since the dynamic analysis of the model is performed with Simulink, it is sufficient for the purposes of this study to only implement these elements in Simulink alone. In the future, however, it is recommended to perform this implementation in the Matlab code itself.

7.3.1. General Overview

Since object oriented programming has been used to develop the Matlab model, at the beginning of each simulation an instance of the tilt-rotor has to be created. This brings the advantage of being able to call methods and attributes of the model instance at any point in the simulation, making for a cleaner structure in Simulink. After the model is instantiated the simulation may be run according to fig. 7.3 which presents the top level block diagram corresponding to the implementation of the tilt-rotor simulation in Simulink. As can be observed, the 6DoF tilt-rotor Matlab model is only one of the multiple elements that comprise the entire simulation. This block internally consists of the TiltRotorModel.calcStateDerivatives() method (called from the tilt-rotor instance created at the beginning of the simulation) which calculates the state derivatives of the 6DoF model. This method is already explained in section 7.2 and therefore it shall not be treated again in this section. The remaining block elements exclusive to the Simulink implementation, however, are described below.

Pilot Inputs, Drivetrain, Rotor RPM dynamics, and the Collective Governor Model Block

Starting from the left, the first block deals with the pilot inputs, drivetrain, rotor RPM dynamics, and the collective governor model. The last three are treated in greater detail in their own sections below, however it is appropriate to highlight at this point that these elements require the current left and right rotor rotational rates Ω_L and Ω_R, as well as the current left and right rotor torques Q_L and Q_L, which are object attributes that are read every simulation loop form the instantiated tilt-rotor model. In addition, the rotor RPM dynamics need the value of the initial rotational rate of rotors $\Omega_{L,0}$ and $\Omega_{R,0}$ which is taken from the initial states block

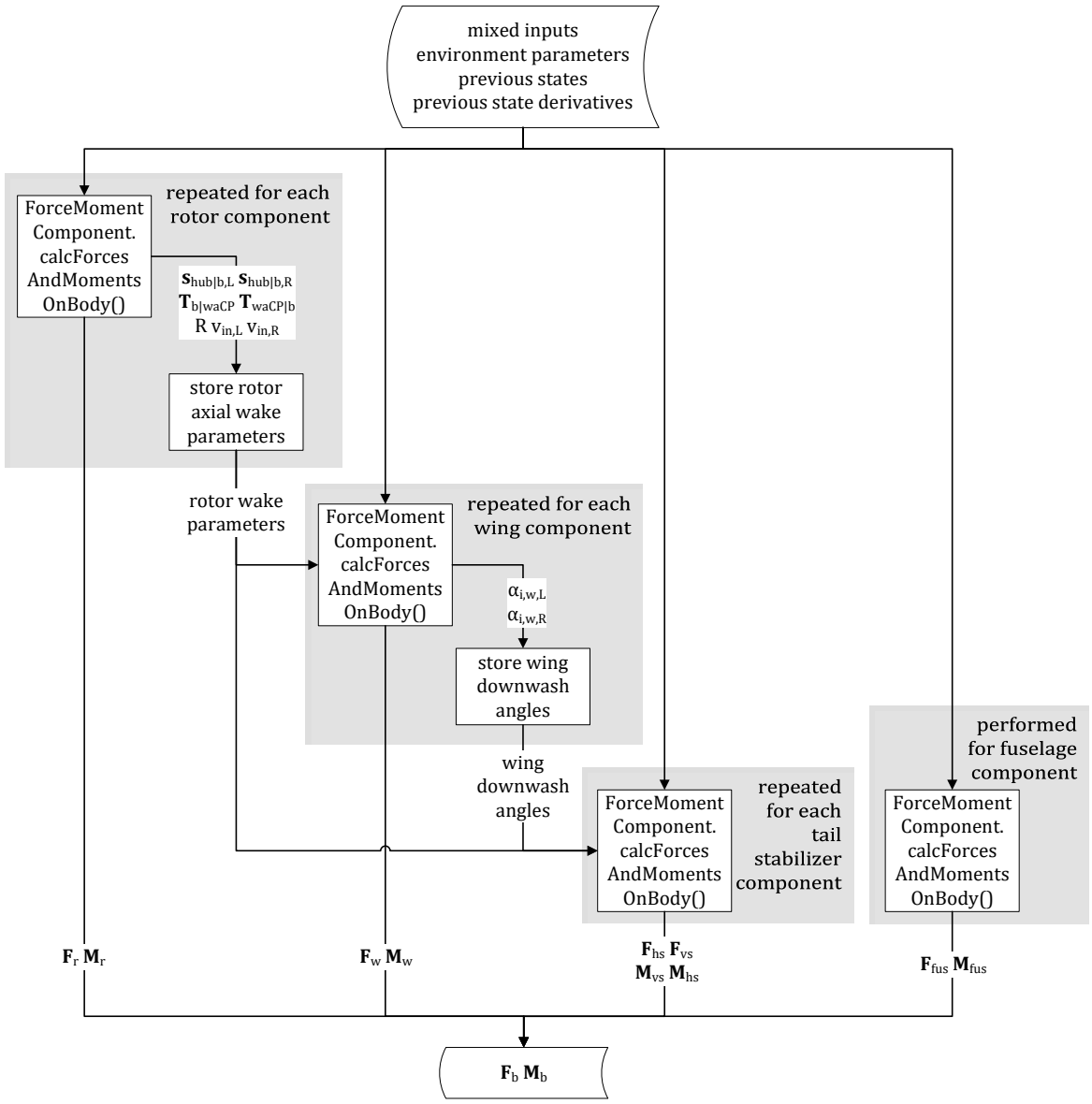

Figure 7.2: Simplified flow diagram of the $\mathrm{calcForceMomentSum}()$ method of the $\mathrm{TiltRotorModel}$ class.

treated later. The pilot inputs consist of a combination of manual (or scheduled) joystick inputs, preset constant inputs, and trim values.

The joystick inputs are ones that may originate from an externally connected physical joystick, or a scheduled control input implemented in Simulink. These control the longitudinal, lateral, and collective stick, as well as the pedals, and are referred to as the pilot deflections X_{LON}, X_{LAT}, $X_{\mathrm{COL,pilot}}$, and X_{PED} respectively.

The preset constant inputs are values that are set before the simulation is started and, in the case of this Simulink implementation, define the flap position X_{FLA}, the nacelle tilt toggle status X_{TIL}, the variable RPM toggle status $\mathrm{VRPM}_{\mathrm{toggle}}$, the governor toggle status $\mathrm{GOV}_{\mathrm{toggle}}$, and the desired operating rotor speed $\mathrm{RPM}_{\mathrm{SEL}}$. The last three pertain to the variable RPM implementation and the collective governor model and thus are treated in more detail in their respective sections. Ideally these preset inputs should neither be constants, nor preset variables, allowing the pilot to alter their values during the simulation. This is not strictly necessary for the purposes of this study, however, and therefore these variables have been implemented as constants for simplicity reasons.

Finally, the trim values are constants that are also set beforehand, and are added to the pilot stick and pedal inputs, as well as the collective governor output. If these values are chosen in accordance with the

trim solution corresponding to the set initial flight condition in the simulation, the simulated tilt-rotor flight should being in a trimmed state without the need for any corrective input from the pilot, nor the governor. Again, the possibility to change these trim values during simulation would be a welcome addition to the Simulink implementation, however this is not necessary for the purposes of this study.

The final output of this block consists of: the updated left and right rotor rotational rates Ω_L and Ω_R; the trimmed pilot outputs X_{LON}, X_{LAT}, and X_{PED}; the constant present outputs X_{FLA} and $\text{TILT}_{\text{toggle}}$; and the combined pilot and governor collective stick-deflection-equivalent output X_{COL}. The latter is elaborated in the collective governor section. These final outputs are then supplied to the Matlab model block in order for it to be able to calculate the state derivatives. It should be mentioned that Ω_L and Ω_R are not supplied to the model as inputs, but instead advantage is taken of the OOP implementation and the model rotor rotational rate object attributes are overwritten by the updated rotor rotational rate values.

The block diagram describing the internals of this first simulation element is shown in fig. F.2 in appendix F.

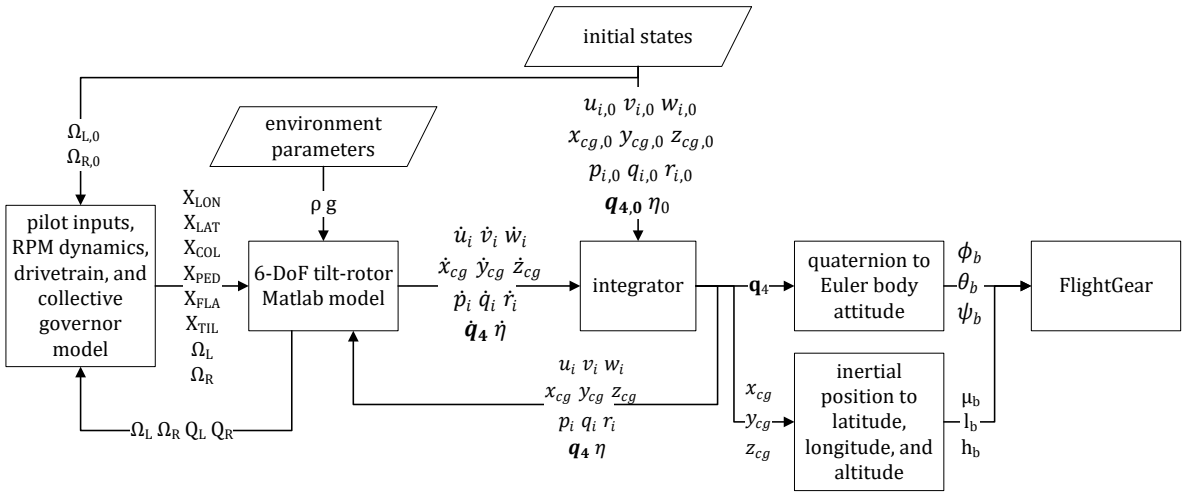

Figure 7.3: Top level block diagram of the Simulink simulation implementation.

Environment Parameters, Initial States, and Integrator Blocks

In order for the simulation to run as desired, the 6DoF model requires the value of several environmental parameters, and the state integrator requires the definition of the initial condition. The environment parameters and initial states blocks both consist of constant preset values. In the current form, the Matlab model only depends on the air density and gravitational acceleration when considering environmental parameters, therefore only these are defined. In the future, however, it is recommended for these parameters to be dynamically calculated and dependent on the altitude of the aircraft providing a more complete simulation. The initial states block does not need much explanation as it only contains the starting values for the states of the tilt-rotor. At the beginning of the simulation these values are supplied to the state integrator block which allows for an external definition of the initial condition. The state integrator itself is a built-in Simulink block that performs continuous-time integration of the state derivatives that are output by the 6DoF tilt-rotor model block every simulation cycle. The resulting integrated states are fed back to the 6DoF model, and at the same time, passed onto the next blocks responsible for the proper connection with FlightGear, as is described next.

FlightGear Connection

In order to be able to connect the Simulink model with FlightGear[51], several of the tilt-rotor states have to be converted into a form that is accepted by FlightGear. First, the quaternion description for the attitude of the tilt-rotor needs to be converted to Euler angles with the *quaternion to Euler body attitude* block. It has been decided that the equations described in section 7.1 shall be used to perform this conversion instead of any appropriate built-in Simulink blocks. Second, the inertial position of the tilt-rotor needs to be converted to a latitude μ_b, longitude l_b, and an altitude h_b. In this case the built-in Simulink Flat Earth to LLA block is used to perform this conversion. All of these converted states are finally supplied to the FlightGear block which is required to complete the connection between Simulink and the FlightGear software.

7.3.2. Variable RPM

After running the Simulink simulation without the implementation of the Simulink-exclusive elements described here it quickly becomes apparent that there is an issue with the model. To be more precise, a step input on the longitudinal stick, for example, results in a near-first-order lag response of the longitudinal body velocity and pitch angle instead of the expected phugoid oscillatory motion. By temporarily removing the rotors from the model and giving the same input, the phugoid motion can be observed hinting at the possibility that the rotors introduce a large amount of damping resulting in an overdamped phugoid motion. Due to a suspicion that the culprit may be the constant RPM, the variable RPM rotor dynamics were implemented as described below. In the end this suspicion turned out to be correct.

The rotor RPM dynamics are implemented based on the GTRS model described in [6], with no major deviations from the equations presented in this document therefore the reader is referred to page A-270 in [6] for the exact implementation. It should be noted that the torque generated by each rotor is taken to be the Q-moment in the equations derived in section 5.2 (keeping in mind the necessary conversion from metric to imperial units). Furthermore, the rotor RPM dynamics of [6] require some value for the torque generated by the engines. Therefore a portion of the drivetrain has also been implemented in the Simulink simulation.

For added functionality it is possible to enable and disable the portion of the simulation responsible for the variable RPM with the $\text{VRPM}_{\text{toggle}}$ switch.

7.3.3. Drivetrain

Similarly to the RPM dynamics, the drivetrain is also based on the GTRS model, however only the minimally required portions of the full drivetrain have been implemented in Simulink for simplicity reasons. Therefore the implementation starts with the total engine power HP_{ENG} (fig. A18-1, Note 10 in [6, A-265]) which is simplified to be equal to the commanded engine horsepower R_{SHP} (fig. A18-1, Note 3 in [6, A-262]) that directly depends on the throttle position X_{thr} (or the collective-throttle stick deflection $X_{\text{COL,thr}}$ treated later) as shown in eq. (7.7a). The relation between the engine power and throttle position $f(X_{\text{thr}})$ is treated in the section on the throttle lever implementation. The engine dynamics, atmospheric effects, and RAM effect that constitute the portion of the drivetrain model between R_{SHP} and HP_{ENG} are neglected. The engine accessory power loss SHP_{ACC} and the transmission efficiency η_{XMSN} are then taken into account to obtain the available engine power HP_{AV} (eq. (7.7b)). This can then be used to determine the torque available at the engine shaft Q_{KPT} (as shown in eq. (7.7c)) and the torque available at the rotor shaft Q_{AV} (as shown in eq. (7.7d)), where θ_{XPT} is the rotor turbine gear ratio and the (1.356) factor converts the result from $ft\text{-}lb$ to Nm. Although modeled in the GTRS program, the jet thrust is not implemented in this thesis work.

$$HP_{\text{ENG}} = R_{\text{SHP}} = f(X_{\text{thr}}) = f(X_{\text{COL,thr}}) \tag{7.7a}$$

$$HP_{\text{AV}} = (HP_{\text{ENG}} - SHP_{\text{ACC}})(\eta_{\text{XMSN}}) \tag{7.7b}$$

$$Q_{\text{KPT}} = (1.356)\frac{(550)HP_{\text{AV}}}{\Omega\theta_{\text{XPT}}} \tag{7.7c}$$

$$Q_{\text{AV}} = Q_{\text{KPT}}\theta_{\text{XPT}} \tag{7.7d}$$

The block diagram relationship between the drivetrain and the variable RPM dynamics is shown in fig. F.3 in appendix F.

For the purpose of checking whether a trim solution (for the XV-15 tilt-rotor model realization) is realistic considering power management, the determination of the maximum torque available at the rotor shaft starts with the maximum optimum engine power $HP_{RO,\text{max}}$ (fig. A18-1, Note 8 in [6, A-264]). Assuming that the optimum engine power equals the total engine power HP_{ENG} (eq. (7.8a)), and by taking into account the engine accessory power loss SHP_{ACC} and the transmission efficiency η_{XMSN} again, the maximum available engine power amounts to $HP_{AV,\text{max}}$ as shown in eq. (7.8b). This too can be converted to a maximum torque

available at the engine shaft $Q_{KPT,\max}$ (as shown in eq. (7.8c)) and the maximum torque available at the rotor shaft $Q_{AV,\max}$ (as shown in eq. (7.8d)). In both expressions it can be observed that it is not possible to provide a single value for the maximum available torque as it depends on the current rotational rate of the rotor Ω. The values of $HP_{RO,\max}$ and $HP_{AV,\max}$, however, are constant and provided in table A.4.

$$HP_{\mathrm{ENG,max}} = HP_{\mathrm{RO,max}} \tag{7.8a}$$

$$HP_{\mathrm{AV,max}} = (HP_{\mathrm{ENG,max}} - SHP_{\mathrm{ACC}})(\eta_{\mathrm{XMSN}}) \tag{7.8b}$$

$$Q_{KPT,\max} = (1.356)\frac{(550)HP_{AV,\max}}{\Omega\theta_{XPT}} \tag{7.8c}$$

$$Q_{AV,\max} = Q_{KPT,\max}\theta_{XPT} \tag{7.8d}$$

It should be remembered that since the Matlab model does not allow for the dynamic change in rotor RPM, a change in the flight conditions as a result of a perturbation results in a change in the torque generated by the rotor. If the RPM were to be kept constant, the engine would have to supply enough torque to meet the demand of the rotor, possibly leading to a situation where the maximum available torque provided by the engine is exceeded. For this reason it is crucial that the variable RPM dynamics and the drivetrain are included in the model when performing dynamic analysis.

7.3.4. Collective Governor

The nominal Matlab model does not include the collective governor since it is assumed that the engine can supply enough torque to meet the demands of the rotor and, as a consequence, the rotor rotational rate is assumed to be constant. The implementation of the variable RPM in the Simulink simulation, however, results in large variations of the rotor RPM during even small perturbations. Since this is not representative of the typical operational conditions of a real tilt-rotor, it was decided that the collective governor should also be implemented in the Simulink simulation. This is only enforced by the fact that in reality, the collective governor is always active during normal operation and therefore its inclusion is considered important as well when performing a dynamic analysis of the model.

The collective governor is also based on the GTRS model, however not all of its elements are transferred to this Simulink implementation. Only the minimally-required elements of the primary system described in [6, A-254, fig.A17-1] are implemented, meaning that all failure monitors have been neglected. For this reason all the expressions starting on page A-250 in [6] are implemented with the exception of the calculation of the RPM error ϵ_{RPM2} for system 2 which is only activated when one of the failure monitors is triggered.

The output of the collective governor is the collective governor deflection angle $\theta_{0,gov}$ which must be converted to the collective governor stick-deflection-equivalent $X_{\mathrm{COL,gov}}$ by dividing it by the collective-stick-to-collective-swashplate gearing ratio in helicopter mode as shown in eq. (7.9). This must be done in order for it to be suppliable to the Matlab model which expects a collective stick input. A more detailed explanation of the need for this inconvenient conversion is provided in section 7.4 which describes the trimming routine.

$$X_{\mathrm{COL,gov}} = \frac{\theta_{0,\mathrm{gov}}}{\left(\frac{\partial\theta_0}{\partial X_{\mathrm{COL}}}\Big|_{\eta=0}\right)} \tag{7.9}$$

This collective governor implementation also entails a new pilot input, namely the operating rotor speed $\mathrm{RPM_{SEL}}$, and a new trim input in the form of the trimmed collective governor deflection angle. The determination of the latter is also treated in the trimming routine section. The governor may also be toggled on and off with the $\mathrm{GOV_{toggle}}$ switch. The top level block diagram of this simplified collective governor

model is shown in fig. F.4 in appendix F, while the relationship between the variable RPM dynamics and the collective governor model can be observed in fig. F.3 in the same appendix.

As a final note, several expressions in the collective governor model require the determination of the sign of a calculated value resulting in a signal that may abruptly change its value from a 1 to -1, and vice versa. This may result in Simulink not being able to solve the arisen algebraic loop in the model, consequently terminating the simulation prematurely. Therefore, in order to solve this, a first order lag (with a time constant of 0.01s) has been introduced into these abruptly changing signals such that they can vary in a smoother fashion.

7.3.5. Throttle Lever Implementation

The throttle lever is completely neglected in the nominal Matlab model due to the assumption that the engine can supply the required torque at all times and therefore the drivetrain is also not included in the Matlab model. However, since the drivetrain is a necessity in the dynamic simulation, the throttle lever must also be implemented as an additional control input in Simulink since a value for the throttle position X_{thr} is required for the calculation of the commanded engine power R_{SHP} (as mentioned in eq. (7.7a)). Following the construction of the XV-15 tilt-rotor, a separate throttle lever is not implemented and instead the position of the collective stick determines the throttle position. This throttle position is then used to determine the commanded engine power which, ultimately, allows for the calculation of the torque available at the rotor shaft.

The relation between the collective-throttle stick displacement $X_{\text{COL,thr}}$ and the throttle position X_{thr}, as well as the relation between the throttle position and the commanded engine horsepower R_{SHP}, are given in [6, tab. 8a-VI] and [6, tab. 18-I] respectively, both corresponding to the XV-15 tilt-rotor. Curve fitting has been employed to obtain a single continuous function for the direct relationship between the collective-throttle stick displacement $X_{\text{COL,thr}}$ and the commanded engine horsepower R_{SHP} mentioned in eq. (7.7a), with the result being a fourth order polynomial as shown in eq. (4.12). A graphical representation of this relationship is also shown in fig. F.5 in appendix F.

$$\begin{aligned} R_{\text{SHP}} &= f(X_{\text{COL,thr}}) = \\ &= (0.2513)\,(X_{\text{COL,thr}})^4 + (4.822)\,(X_{\text{COL,thr}})^3 - (20.03)\,(X_{\text{COL,thr}})^2 + (121.7)\,(X_{\text{COL,thr}}) + 89.496 \end{aligned} \tag{4.12}$$

As shall be described in more detail in the section on the trimming routine (section 7.4), the nominal Matlab model does not include the collective governor and instead incorporates its effect into the pilot collective stick. For this reason the collective stick must be representative of the contribution of the collective governor in all flight phases. In reality, however, the collective stick is phased out as the nacelles tilt forward, meaning that in airplane mode the pilot has no control over the collective swashplate and only the collective governor may adjust the blade collective pitch. Since it has been decided that the collective governor is necessary in the Simulink implementation it is possible to reintroduce the pilot collective stick phasing into the Simulink simulation as well.

For this reason the pilot collective stick input is split into two signals, one being the collective-throttle stick deflection $X_{\text{COL,thr}}$ described above, and the second being the pilot collective stick deflection $X_{\text{COL,pilot}}$ as shown in eq. (7.10). $X_{\text{COL,pilot}}$ is then multiplied by a phasing gain which yields the phased collective stick deflection $X_{\text{COL,pilot},\eta}$ as has already been shown in eq. (4.10c), repeated below for clarity (remembering that in airplane mode $\eta = -\pi/2$).

$$X_{\text{COL,thr}} = X_{\text{COL,pilot}} \tag{7.10}$$

$$X_{\text{COL,pilot},\eta} = X_{\text{COL,pilot}} \left(1 + \frac{2\eta}{\pi}\right) \tag{4.10c}$$

To obtain the total collective stick deflection X_{COL} that should be fed into the Matlab model, the phased pilot collective stick deflection $X_{\text{COL,pilot},\eta}$ must be added to the collective governor stick-deflection-equivalent $X_{\text{COL,gov}}$ already shown in eq. (4.10a), repeated below for clarity.

$$X_{\text{COL}} = X_{\text{COL,gov}} + X_{\text{COL,pilot},\eta} \tag{4.10a}$$

7.4. Trimming Routine

One method of verifying and validating a tilt-rotor model involves the inspection and comparison of it's trim curves. These trim curves present the variation of the pilot inputs, control system inputs, and states of the tilt-rotor as a function of the velocity, nacelle angle, and possibly other trim conditions such as the climb angle. The model can then be roughly verified by inspecting the trim curves and confronting them with prior knowledge and expectations for their shape. If the trim curves grossly deviate from the expectations, then it is possible for the model to be erroneous. If, however, the trim curves have a correct-looking shape, they may be compared with the trim curves obtained in other studies or through experiment, making it possible to validate the model. This section presents the approach of trimming the Matlab model which is necessary to be able to generate the trim curves. It should be noted that the trim routine used to generate trim curves for the 6DoF model differs from the one used in the generation of the preliminary results due to a number of reasons including computation time and the new requirement for determining the trim state in non-symmetric flight. It must be highlighted that the Matlab model alone is used in the trimming procedure, while the Simulink implementation is not used for this purpose at all.

Trim Conditions and Variables

The tilt-rotor is said to be in trimmed condition if an equilibrium is achieved in the resultant forces and moments acting on the body. Although the following is not universal for all trimmed conditions, for the purposes of this thesis trimming has been limited to conditions where the tilt-rotor experiences a zero net linear and rotational acceleration. It is possible to trim the tilt-rotor in other conditions, however with the mentioned limitation the obtention of a trimmed state in this thesis work is only possible for linear un-accelerated flight with the added option of defining a climb angle and an angle of sideslip. Neither are bound, however, therefore it is possible to attempt to trim the tilt-rotor model in, for example, vertical climbing flight, sideward flight, or even in rearward flight. Trimming in other flight conditions, such as a steady turn, has not been implemented mainly due to the fact that such data is scarce in literature and thus this extra effort would not benefit the validation of the model.

To summarize the inputs and outputs of the trimming routine developed for this study, the trim condition is described by the total aerodynamic body velocity V_b, the nacelle tilt angle η, the body flight path angle γ_b, the body angle of sideslip β_b, and the flap settings X_{FLA}, while the trimming routine yields values for the trim variables required to achieved the desired trim condition, i.e. the deflections of the longitudinal stick X_{LON}, lateral stick X_{LAT}, collective stick X_{COL}, and pedals X_{PED}, together with the body angle of attack α_b and roll angle ϕ_b .

It should be mentioned that the flap setting has been decided to be part of the trim routine input rather than the output since in the latter case the trim routine would always produce trim results with the flaps either fully deflected, or almost not deflected at all. This behaviour is not surprising considering that the flap deflection primarily has an effect on the generated wing lift which is also affected by the body angle of attack. Since the body angle of attack is already an independent variable that is adjusted to achieve the necessary lift for a given trim condition, providing the trimming routine with another variable that has an almost identical contribution to the problem only makes the trimming task more complex. At most this additional trim variable may potentially reveal trim conditions that would have otherwise been considered impossible, however this has not been observed in practice.

It should also be mentioned that the contribution of the collective governor has been implicitly incorporated into the pilot collective stick giving rise to the combined pilot and governor collective stick-deflection-equivalent X_{COL} (also referred to as the collective quasi-stick), with the quasi-stick limits appropriately adjusted to enable full governor contribution. This has been done for a similar reason as the one mentioned with the flap settings, namely the true pilot collective stick (also referred to as the collective-throttle stick since the same stick controls both the collective and throttle) and collective governor control the same actuator, i.e. the collective swashplate. Separating the two in the trim routine is not necessary. Instead, after the trim condition is achieved, the required total collective quasi-stick deflection X_{COL} is distributed among the phased pilot collective stick deflection $X_{\text{COL,pilot},\eta}$ and the collective governor stick-deflection-equivalent

$X_{\text{COL,gov}}$ as shown in eq. (7.11a), with the pilot stick deflection being based on the required shaft torque (indicated with the subscript SP) of the left and right rotor (eq. (7.11b)). It must be highlighted that the phased pilot collective stick deflection must be used in eq. (7.11a) in order to include the effect of collective stick control phasing since this is not incorporated in the nominal Matlab model. The actual required governor swashplate deflection is then obtained by multiplying the collective stick-deflection-equivalent deflection by the collective-stick-to-collective-swashplate gearing ratio in helicopter mode as shown in eq. (7.11c). Equations (7.11a) and (7.11c) are treated in more detail in section 4.4 while the relation between the pilot collective stick deflection (or to be more precise the collective-throttle deflection) and the rotor torques from eq. (7.11b) (i.e. $f(Q_L, Q_R)$) is described below.

$$X_{\text{COL,gov}} = X_{\text{COL}} - X_{\text{COL,pilot},\eta} \tag{7.11a}$$

$$X_{\text{COL,pilot},\eta} = \frac{X_{\text{COL,thr}}}{1 + 2\eta/\pi} = \frac{f(Q_{SP,L}, Q_{SP,R})}{1 + 2\eta/\pi} \tag{7.11b}$$

$$\theta_{0,\text{gov}} = X_{\text{COL,gov}} \left(\frac{\partial \theta_0}{\partial X_{\text{COL}}}\bigg|_{\eta=0} \right) \tag{7.11c}$$

The calculation of the collective-throttle stick deflection $X_{\text{COL,thr}}$ required for trim (i.e. the relation previously referred to as $f(Q_{SP,L}, Q_{SP,R})$) is performed in the reverse order of the calculation of the commanded engine horsepower as described with eq. (7.7) and eq. (4.12) in section 7.3. First, the required average torque at one of the rotor shafts Q_{REQ} is obtained by subtracting the right rotor shaft torque $Q_{SP,R}$ from the left rotor torque $Q_{SP,L}$ and dividing by two as shown in eq. (7.13a). The right torque is being subtracted since it is nominally negative due to the right rotor rotating in the counterclockwise direction, while the opposite is true for the left rotor. In addition, the average of the two torques may be taken in this simple manner since the left and right rotor shafts are interconnected and therefore, for simplicity's sake, it is assumed that the total torque that needs to be provided by each engine will be equal.

Before continuing, it must be highlighted that the shaft torques indicated with the SP subscript act around the Z-axis of the shaft plane reference frame, while the rotor torques derived in section 5.2, i.e. $\widehat{Q}_{BEM,R}$ and $\widehat{Q}_{BEM,L}$, are defined to act around the Z-axis of the wind axis control plane. Therefore the rotor moment vector (which also includes the two other orthogonal spring reaction moments $\widehat{O}_s$ and $\widehat{P}_s$) must first be transformed from the wind axis control plane into the control plane reference frame, and then transformed once again from the control plane to the shaft plane in order to obtain the rotor moment vector defined in the shaft plane as shown in eq. (7.12). The z-component of this vector may then be extracted to obtain the shaft torque of the left and right rotor $Q_{SP,L}$ and $Q_{SP,R}$.

$$\begin{pmatrix} O_{SP} \\ P_{SP} \\ Q_{SP} \end{pmatrix}^T \{\boldsymbol{E}_{SP}\} = \begin{pmatrix} \widehat{O}_s \\ \widehat{P}_s \\ \widehat{Q}_{\text{BEM}} \end{pmatrix}^T \boldsymbol{T}_{\overline{CP}|SP} \{\boldsymbol{E}_{SP}\} \tag{7.12}$$

Returning to the calculation of the collective-throttle stick deflection $X_{\text{COL,thr}}$ required for trim, the torque required at one of the engine shafts $Q_{\text{KPT,REQ}}$ is obtained with eq. (7.13b) which can then be converted to the power required at the engine output HP_{REQ} with eq. (7.13c). The transmission efficiency and accessory power loss then dictates the total required engine power $HP_{\text{ENG,REQ}}$ (as shown in eq. (7.13d)) which is assumed to be equal to the required commanded engine horsepower $R_{\text{SHP,REQ}}$ (eq. (7.13e)). Finally, eq. (7.13f) (the inverse counterpart of eq. (4.12)) is used to determine the collective-throttle stick deflection required to satisfy the torque required by the rotors in a given trimmed state. A graphical representation of this last relationship is also shown in fig. F.6 in appendix F.

$$Q_{\text{REQ}} = \frac{Q_{SP,L} - Q_{SP,R}}{2} \tag{7.13a}$$

$$Q_{\mathrm{KPT,REQ}} = \frac{Q_{\mathrm{REQ}}}{\theta_{\mathrm{XPT}}} \tag{7.13b}$$

$$HP_{\mathrm{REQ}} = \frac{1}{1.356}\frac{Q_{\mathrm{KPT,REQ}}\Omega\theta_{\mathrm{XPT}}}{550} \tag{7.13c}$$

$$HP_{\mathrm{ENG,REQ}} = \frac{HP_{\mathrm{REQ}}}{\eta_{\mathrm{XMSN}}} + SHP_{\mathrm{ACC}} \tag{7.13d}$$

$$R_{\mathrm{SHP,REQ}} = HP_{\mathrm{ENG,REQ}} \tag{7.13e}$$

$$\begin{aligned} X_{\mathrm{COL,thr}} = {} & (1.3\mathrm{e}{-12})\left(R_{\mathrm{SHP,REQ}}\right)^4 - (2.5\mathrm{e}{-9})\left(R_{\mathrm{SHP,REQ}}\right)^3 \\ & - (2.5\mathrm{e}{-6})\left(R_{\mathrm{SHP,REQ}}\right)^2 + (0.0119)\left(R_{\mathrm{SHP,REQ}}\right) - 1.1199 \end{aligned} \tag{7.13f}$$

Trim Limits

Every trim variable mentioned above has a bound set upon it, be it a pilot input travel range, the collective governor minimum and maximum swashplate deflections, or a practical bound of $\pm\pi/2$ and $\pm\pi$ on the angle of attack and roll angle respectively (apart from the last two, the limits of these trim variables are given in tables A.4, A.14 and A.17). Although these limits exist in reality, they do not have to exist in simulation and therefore the trim routine is setup such that it is allowed to exceed these bounds and search for unrealistic solutions. If such a solution is found, the trim routine still returns the values of the trim variables, but in addition it specifies by how much each trim variable has been exceeded and that the solution is unrealistic. These unrealistic solutions are excluded from the trim curves, and only serve the purpose of indicating the factor that limits the trimmed-flight-envelope of the tilt-rotor for that given flight condition.

It should be mentioned that in the case of the collective quasi-stick limits, only the total collective quasi-stick variable X_{COL} is checked for exceeded limits, while the governor and throttle collective deflections are not inspected individually. The latter has been implemented, but unfortunately the resulting trim curves and conversion corridor were greatly underestimated leading to the suspicion that the method of dividing the total collective quasi-stick deflection among the two, as presented in eq. (7.11a), is not completely correct. Therefore it has been decided that the individual limits of the collective-throttle-stick and the collective governor will not decide whether a trim solution is realistic, while the total required collective quasi-stick will. The limits of the latter are defined in eq. (7.14). The erroneous collective-throttle-stick and collective governor contributions are, however, used as trim inputs in the Simulink simulation and therefore will be shown in the results section nonetheless.

$$X_{\mathrm{COL,max}} = X_{\mathrm{COL,pilot},\eta,\mathrm{max}} + X_{\mathrm{COL,gov,max}} \tag{7.14a}$$

$$X_{\mathrm{COL,min}} = X_{\mathrm{COL,gov,min}} \tag{7.14b}$$

Apart from trim variable limits, the trim routine also takes into account flapping angle limits (defined with respect to the non-wind axis shaft plane SP, hence θ_{1s} must be subtracted from a_1) informally defined by eq. (7.15), and the maximum available torque at the rotor shaft. Note that the calculation must be performed in a non-wind axis frame since the rotation of the control plane θ_{1s} occurs around the non-wind-axis Y_{CP}-axis, therefore the non-wind axis disk tilt angles already defined by eq. (5.84) must be used. The calculation of the available torque is already treated in section 7.3.

$$\max\left(\mathrm{abs}\left(a_0 - (a_1 - \theta_{1s})\cos(\psi) - b_1\sin(\psi)\right)\right) \leq \beta_{SP,absmax} \quad \forall\,\psi \in [0, 2\pi] \tag{7.15}$$

Trim Routine Implementation

Although the 6DoF tilt-rotor model at hand is derived analytically and therefore all equations are available in their full symbolic form, due to the complexity of the model it is decided that a numerical approach shall be employed to determine the trim solution instead of an analytical one. This has already been the case during the generation of the preliminary results where the built-in Matlab variable-precision arithmetic solve function *vpasolve* was used to solve a system of non-linear equations formed by the body equations of motion and the thrust-induced-velocity relation. However, for the purpose of trimming the 6DoF model, this solver has been replaced by a different Matlab function, namely *fmincon* due to better performance and a higher chance of convergence. Since *fmincon* is an optimization scheme with the goal to find the minimum of a multivariable non-linear function, when compared to the preliminary analysis, the trimming procedure changes from an unsolved system of non-linear equations to an optimization problem.

As with every optimization problem, the trimming routine must be appropriately described in order for *fmincon* to find the desired trim solution. In this case the m decision variables, i.e. the unknowns to be determined, are defined to be non-integer and to consist of the pilot stick and pedal inputs, the body angle of attack, and the body roll angle, as shown in eq. (7.16) with $\boldsymbol{x}$ being an $m \times 1$ vector. These decision variables may be subject to multiple constraint types, however in the case of finding a trim solution only the equality constraints $\boldsymbol{b}_{eq}$ must be formally defined as shown in eq. (7.17) where $\boldsymbol{A}_{eq}$ is the equality constraint $n \times m$ matrix which dictates these constraints, with n being the number of constraints. The $\boldsymbol{A}_{eq}$ matrix may be left with all its elements equal to zero, however in some trim conditions where some decision variables are expected to be equal to zero, it may be beneficial to employ constraints to reflect this, possibly resulting in a faster and more successful trimming procedure. For example if the trim condition consists of longitudinal symmetric flight only, all lateral decision variables may be set to zero as shown in eq. (7.18). Since this is the only case when the equality constraints are employed, the $\boldsymbol{b}_{eq}$ will always be left with its elements equal to zero.

$$\boldsymbol{x} = \begin{pmatrix} X_{\mathrm{LON}} & X_{\mathrm{LAT}} & X_{\mathrm{COL}} & X_{\mathrm{PED}} & \alpha_b & \phi_b \end{pmatrix}^T \tag{7.16}$$

$$\boldsymbol{A}_{eq}\boldsymbol{x} = \boldsymbol{b}_{eq} \tag{7.17}$$

$$\begin{bmatrix} 0 & 1 & 0 & 0 & 0 & 0 \\ 0 & 0 & 0 & 1 & 0 & 0 \\ 0 & 0 & 0 & 0 & 0 & 1 \end{bmatrix} \begin{Bmatrix} X_{\mathrm{LON}} \\ X_{\mathrm{LAT}} \\ X_{\mathrm{COL}} \\ X_{\mathrm{PED}} \\ \alpha_b \\ \phi_b \end{Bmatrix} = \begin{Bmatrix} 0 \\ 0 \\ 0 \end{Bmatrix} \tag{7.18}$$

The *fmincon* function allows for the informal definition of upper and lower bounds for the decision variables and therefore advantage was taken of this luxury when setting up this optimization problem. While trimming the XV-15 model these upper and lower bounds have been set to values approximately 10 times larger than their realistic counterparts given in appendix A. A factor of ten has been chosen as a compromise between an expanded solution space providing more information about why certain solutions become no longer realistic, and a not-too-encumbered performance of the optimization scheme caused by this larger search space.

The description of the optimization problem may be finalized with the definition of an objective function Z, whose single-value result needs to be minimized. The only formal requirement for the objective function is for it to be (directly or indirectly) dependent on the decision variables, while its practical formulation may be chosen freely. It should be kept in mind, however, that a poorly defined objective function may not only hinder the chance of finding the minimum of the non-linear function, but it may also produce solutions that are, in fact, not the ones that are sought for.

As mentioned at the beginning of this section, the trim conditions treated in this work are defined by a tilt-rotor that is in unaccelerated flight. For this reason, and for simplicity's sake, the objective function defined

for the trimming problem at hand is defined informally in eq. (7.19) as equal to the largest absolute body acceleration determined with the function to calculate the state derivatives of the 6DoF tilt-rotor model. An alternative objective function has been experimented with, namely taking the sum of these absolute body acceleration, however the objective function presented below performed better.

$$Z = \max\left(\text{abs}\left(\{\dot{u}, \dot{v}, \dot{w}, \dot{p}, \dot{q}, \dot{r}, \}\right)\right) \tag{7.19}$$

For the sake of completeness and repeatability the exact settings used in the *fmincon* algorithm are provided in table A.19.

Trim Curves, Trim-Sweep, and the Conversion Corridor

In order to generate the trim curves for the tilt-rotor, the *fmincon* function has to be run again for every desired trim point. A collection of all desired trim points, or trim solutions, may then be referred to as the trim set. Typically the trim set is plotted against the velocity for a single nacelle tilt angle, yielding a single trim curve, while the other trim curves would then correspond to other nacelle tilt angles. In such a case the nacelle tilt angle may be referred to as the primary independent variable while the velocity may be referred to as the secondary independent variable. This is not the only method of generating trim curves, however, and it is possible for, for example, a single trim curve to correspond to a single velocity while the trim set is varied across a range of sideslip angles. Here the primary variable would be the velocity while the secondary variable would be the sideslip angle. Both types of trim curves are presented and explained in more detail in the results chapter (chapter 8). In order to improve the chance of finding the complete trim curve, however, a 'trim-sweeping' procedure has been employed during the generation of the trim curves as described below.

First an initial guess of zero is used for the unknown decision variables producing a trim curve for one primary variable value - referred to as the first primary variable. This trim curve is visually verified, and in the case that it does not resemble the expected shape, it is inspected for a single point on the trim curve that seems to be realistic. This trim solution is then used as the initial guess for an adjacent second trim point. This second solution is then used for the following third adjacent trim point, and the process is repeated in order to generate the entire desired trim curve for one primary variable value.

Apart from using the previous trim solution as an initial guess for the decision variables for the following trim point, the rotor coning angles and induced velocity solutions also had to be supplied to the trimming routine due to the presence of the thrust-induced-velocity relationship which is iteratively solved every time the state derivatives of the complete model need to be determined. Not providing the previous solution to this internal solver often led to an unconverged solution which resulted in an incorrectly determined trim condition.

In order to generate the trim curve for a second primary variable value, the secondary variable closest-to-zero trim solution of the trim curve of the first primary variable is used as an initial guess for the secondary variable closest-to-zero trim solution of the second primary variable value. The entire trim curve for the second primary variable value may be then determined in the same manner as the trim curve of the first primary variable value. The secondary variable closest-to-zero trim solution of the second trim curve is then used as the initial guess for the next primary variable value, and this process is repeated for the remaining desired primary variable values yielding a trim curve for every primary variable value.

This 'trim-sweeping' procedure is only effective at increasing the chance of finding a new solution under the condition that the primary and secondary variable increments are small enough. This condition should ensure that the solutions of adjacent trim points are 'close' to each other, motivating the use of adjacent solutions as initial guesses, which should increase the chance of finding the trim solution.

Finally, acknowledging the vagueness of the *small enough increment* condition, it can at least be said that increments below 1m/s for the total velocity V, 1° for the sideslip angle β_b, and 30° for the nacelle tilt angle η are suitable as these were the increments used in the generation of the the trim curves in this study. This statement may not be universal, however, since the 'closeness' of adjacent solutions also depends on the steepness of the trim curve, which in turn depends on the flight characteristics of the specific tilt-rotor. Therefore the mentioned maximum increments should be treated as a rule of thumb.

Once all the trim curves are generated for a particular trim condition, it is possible to construct the corresponding conversion corridor. The conversion corridor indicates the minimum and maximum velocity that the tilt-rotor may operate at in a trimmed state, plotted across the entire tilt range of the nacelle. Therefore only trim curves where the primary variable is the nacelle tilt angle, and the secondary variable is the velocity, may be used to generate a conversion corridor. Together with the trim curves, the conversion corridor may also be used to validate the model.

7.5. Simulation Optimization

The objective of this thesis work was to develop a tilt-rotor flight mechanics model suitable for, inter alia, piloted flight simulation. For this reason it is not only required that the model runs in real-time, but also that it does so with an acceptable accuracy. Part of the accuracy depends on the simulation time step, therefore it was crucial to optimize the model implementation such that the simulation could be run in real time with the time step being sufficiently small. Since no structural dynamics are included in the presented model, the highest expected dynamics frequency corresponds to the rotor disk tilt which, in reality, achieves a steady state solution in approximately one rotor revolution. If the highest rotational rate that the rotor is expected to achieve is 61.7 rad/s (according to table A.17), and if the sampling theorem is taken into account, the minimum required simulation frequency is double that of the highest expected frequency, i.e. $(2)(61.7)/(2\pi) \approx 20$ Hz. It should be noted that since the disk tilt approximation dynamics depend on the simulation frequency, the model flight dynamic characteristics are only accurate if the simulation frequency is equal to the rotor frequency, otherwise the disk tilt steady state assumption is invalidated. This dependency of the rotor equations on the simulation frequency is a shortcoming of this model and therefore shall be discussed in more detail in chapter 10 which treats future recommendations. If this dependency would not exist, however, it would be desirable to have the simulation frequency be as high as possible. This would facilitate future expansion of the model which could potentially require more computational power that would lower the simulation frequency, or which could introduce higher frequency dynamics which would require a smaller simulation step size.

At the current stage of model implementation, the simulation has been optimized such that real time simulation may be achieved with a maximum simulation frequency of at least 200Hz on a competent mobile workstation laptop.[2] The optimization approaches taken to achieve this are described below.

The first step in the optimization process was to use the Matlab profiler to determine the computation time of every function in the model. The functions that took the longest time to compute were inspected and, if possible, appropriately changed in order to decrease this time. The change that made the largest impact on the performance was to identify pieces of code that were incorrectly placed within a loop when in reality it was either sufficient to perform the calculations only once, or when it was more efficient to perform the calculations within their own loop with the result then passed onto other looped functions which previously unnecessarily repeated the same calculations multiple times on their own.

Since object oriented programming (OOP) was used to implement the tilt-rotor model in Matlab, initially all functions took advantage of the high accessibility of the object attributes and thus all necessary parameters and states were read in this manner. Unfortunately it seems that Matlab is not optimized for OOP and it was more efficient to read all these object attributes to temporary variables once at the beginning of each simulation loop, and these temporary variables were then passed onto functions as function inputs instead. Employing this change also had a high impact on the simulation performance.

Several of the model classes use the built-in Matlab input parser which enables variable-length input argument verification allowing for better model expansion flexibility. Unfortunately the input parser is quite computationally expensive and therefore its use has been reduced throughout the model, while using it in internally looped functions has been eliminated. Similar to the previous two approaches, this too significantly improved the simulation performance.

Two final approaches have been employed in the hopes of reducing the computational load of the model. Firstly, heavy use was made of the structure array data type (struct in short) throughout the model as it provides a convenient way of passing a large number of named variables from one function to another. It

[2] In practice a simulation frequency of 300Hz was achieved on a HP ZBook 15 G5 with an Intel i7-8750H CPU @3.91GHz boosted clock speed.

was suspected that using these structs was computationally expensive and therefore, in many instances, they have been replaced by an ordered list of variable values instead. Secondly, the rotor expressions often contain variables which are repeatedly raised to a power or are the argument of a trigonometric function. As means of optimization, these types of common variables were therefore pre-calculated once and their result was then supplied to all appropriate functions. Both approaches did improve the overall performance, however their impact was at most marginal.

Optimization techniques that are expected to positively impact the performance, but have not been implemented in the model, are described in chapter 10 together with the other recommendations for the future.

8

Simulation Results

Having implemented the 6DoF tilt-rotor model in Matlab and Simulink, it is finally possible to simulate static and dynamic flight providing data which can then be presented graphically enabling a more intuitive method of analyzing and validating the developed tilt-rotor model.

This chapter is organized into three main segments with the first segment concerned with the analysis and verification of the flapping equation and blade element states presented in section 8.1.

The second segment treats static trimmed flight presented in the form of trim curves, conversion corridors, and Haffner diagrams. The first set of trim curves is treated in section 8.2 and corresponds to longitudinal and level trimmed flight used to validate the 6DoF model and its subsystems. Recording the limits of the 6DoF model longitudinal and level flight trim curves enables the generation of a conversion corridor which is validated against the real XV-15 conversion corridor and analyzed with regards to the bounding factors in section 8.3. The next set of trim curves is treated in section 8.4 and corresponds to longitudinal climbing and descending trimmed flight used to generate Haffner diagrams. These, in turn, are used to verify the rotor model and are analyzed with regard to their variation as a function of nacelle tilt angle. The third and fourth set of trim curves correspond to level yet non-longitudinal trimmed flight with section 8.5 validating the sideward flight trim curves of the tilt-rotor in helicopter configuration while section 8.6 validates the trim curves of the tilt-rotor in airplane configuration in sideslip flight concluding the second static trimmed flight segment.

The third and last segment deals with dynamic flight which is validated and analyzed in the time domain in section 8.7, presenting the responses of the tilt-rotor in helicopter and airplane configuration to longitudinal and lateral pilot step inputs.

8.1. Flapping Equation Analysis and Verification

The first set of simulation results presents an analysis of the complete flapping equation in the time domain, as well as the variation of the aerodynamic states experienced by the rotor blade across the entire rotor disk. These results serve as the starting point for the verification of the rotor model which shall also be validated in later sections.

8.1.1. Flapping Response Analysis and Verification in the Time Domain

The flapping equation corresponding to this tilt-rotor rotor model has been derived analytically in section 5.2 yielding a differential equation describing the flapping motion of the blade as a function of time, with a simplified version of this equation given by eq. (5.77). Note that this equation does not depend on time explicitly, instead it is a function of the azimuthal position of the blade $\widehat{\psi}$ defined with respect to the wind axis (non-rotating) reference frame. In order to be able to solve this differential equation in the time domain, the azimuthal position must first be replaced by its time-dependent function given by eq. (8.1) where t represents the time variable while $\Omega_{tot,i}$ is the total rotor axial rotational rate defined in inertial space. In this case the total inertial rate $\Omega_{tot,i}$ must be used instead of the nominal rotor axial rotational rate Ω for

the same reason as why $\dot{\widehat{\psi}}$ is replaced by $\Omega_{tot,i}$ which has already been explained in the derivation of the inertial flapping equation on page 133.

$$\widehat{\psi} = \Omega_{sgn}\Omega_{tot,i}t \tag{8.1}$$

Performing the above substitution yields a time-dependent ordinary differential equation with the flapping angle $\widehat{\beta}$ (also defined in the wind axis reference frame) being the unknown variable and time being the independent variable. It should be noted that apart from the blade azimuthal position, other variables within the flapping equation also may depend on time such as the tilt-rotor body rates. In order to isolate the dynamics of the whole tilt-rotor model from the rotor model, however, all other time dependent variables within the flapping equation are set to constant values. It has been decided that these constant values shall correspond to the states of the tilt-rotor in a trim condition.

For the purpose of verification the differential flapping equation is solved numerically with the use of the Matlab *ode45* solver since the flapping equation is not expected to be stiff. The output of this solver consists of the time variation of the flapping angle $\widehat{\beta}$ and flapping rate $\dot{\widehat{\beta}}$ which is visually inspected for different flight conditions in order to determine whether the flapping equation has been derived correctly and thus produces results in alignment with the chosen flapping motion model.

The flapping equation is first verified in trimmed undisturbed flight conditions corresponding to the tilt-rotor in helicopter configuration both in hover and forward flight, as well as the tilt-rotor in forward flight in conversion and airplane configuration. The time variation of the numerically solved flapping angle is compared to the presumed disk tilt approximation solution given by eq. (5.78a) for these different flight conditions and in all cases both solutions are (almost) identical with the exception for minute errors introduced by the numerical solver verifying the correct derivation and implementation of the disk tilt approximation. Since the differential equation initial conditions correspond to a trimmed state, the flapping angle time responses correspond to a steady state solution from the start yielding either a constant flapping angle in the case of hover, or a sinusoidally varying flapping angle (with a frequency equal to the rotational rate of the rotor) in the case of forward flight. The latter result verifies that the simplification of the flapping equation to only include the first harmonic has been performed correctly. The written analysis of these overlapping responses is considered sufficiently descriptive and therefore their plots are not shown in this report to conserve space.

It must be highlighted that the presumed solution, consisting of the coning angle $\widehat{a}_0$ and disk tilt angles $\widehat{a}_1$ and $\widehat{b}_1$, is directly taken from the trimmed tilt-rotor model. Recalling that a lateral disk tilt correction factor (i.e. eq. (5.83a)) is employed only in the disk tilt approximation, in order to be able to compare the differential equation solution to the presumed solution, this correction factor must be temporarily disabled in the tilt-rotor model. For this reason the flapping presumed solutions shown in this section differ from the ones shown in the trim curves presented later in this chapter where the correction factor is enabled.

Having treated the steady state solutions, the next set of tests consists of inspecting the transient flapping response to different disturbances in different flight conditions. In the first test the tilt-rotor is hovering in helicopter configuration and at time $t = 0$ the rotor hub is accelerated upwards with a constant value of 9.81 m/s^2 resulting in a disturbance to the steady state solution as shown in fig. 8.1 where both the initial steady state solution and the numerically solved transient solutions are plotted. Note that the horizontal time axis has been replaced by the the azimuthal position of one of the blades passing the $\widehat{\psi} = 0$ position at time $t = 0$ making it possible to assess the duration of the response in terms of rotor revolutions. Also note that the hub acceleration has been specifically set to equal gravitational acceleration to simulate the effect of gravity on the blades which has been deliberately not included in the model under the assumption that it is not significant. Observing the plot it can be seen that the effect of the simulated gravity reduces the coning angle by about 2% which is below the 6.25% significance threshold of the ordering scheme (see table 6.2) therefore the mentioned assumption is considered verified. Furthermore, the transient response exhibits a one-per-revolution frequency, and settles to within 5% of the final value in under two revolutions, verifying the assumption that the transient flapping response resolves within two blade revolutions.

The next test consists of the tilt-rotor in helicopter configuration once again, however it is now trimmed in forward flight and disturbed by a positive 5° swashplate collective θ_0 step input resulting in a transient response as shown in fig. 8.2. As expected the mean flapping angle, i.e. the coning angle, increases as a result of the step input verifying the effect of the collective on the flapping response. After the transient

response dissipates a new steady state solution is reached as expected. A similar test conducted with the tilt-rotor trimmed in airplane configuration yields similar results as shown in fig. 8.3.

8.1.2. Variation of Blade Element Aerodynamic States Across the Rotor Disk

In order to verify other key assumptions that have been throughout the rotor derivation, several figures presenting the variation of various aerodynamic states experienced by the blade element across the entire rotor disk have been generated. Since the rotor derivation has been performed in the wind axis control plane, the location of effect of the aerodynamic states shall be given with respect to the wind axis control plane axes. Two flight conditions have been selected to generate two sets of data, the first condition consisting of the tilt-rotor in helicopter configuration (with 40° of flap deflection) in trimmed forward level flight at 40 knots, and the second condition consisting of the tilt-rotor in airplane configuration in trimmed forward level flight at 225 knots (with 20° of flap deflection). In both cases the rotor rotational rate Ω is set to 589 RPM. The former flight condition is selected since it corresponds to a rotor disk with a high in-plane to axial velocity ratio, while the latter condition corresponds to the opposite, i.e. a high axial to in-plane velocity ratio.

The first set of plots shows the variation of the blade element angle of attack α_{BE} for the helicopter and airplane configuration as shown in fig. 8.4 and fig. 8.5 respectively. Although no key assumptions have been made involving the angle of attack, it is useful to analyze the distributions as shall be demonstrated later. In the case of the helicopter configuration it can be seen that the distribution is mostly uniform across the disk with the exception of the area close to the rotor hub where on the blade advancing side a region of large positive angles of attack can be observed, while a region of highly negative angles of attack can be seen on the retreating side. The outer regions of the rotor disk also experience slightly negative angles of attack. In contrast, the disk distribution corresponding to the airplane configuration only shows negative angles of attack near the rotor hub while the remainder of the distribution is positive and circumferentially uniform. The angle of attack is largest at a radius of approximately half the length of a blade.

The next set of plots presents the variation of the blade element (nonlinear) inflow angle ϕ_{BE} (calculated with eq. (5.62), repeated below for clarity) which has been assumed to be small and therefore its linearization was considered permissible. Inspecting the disk distribution corresponding to the airplane configuration as shown in fig. 8.6 it can be seen that this assumption is grossly violated across the entire disk with the smallest inflow angle being equal to 26°. Addressing this assumption violation is left as a important recommendation for the future. In the case of the helicopter configuration the assumption is also violated however to a lesser degree and only near the rotor hub, therefore it is not show here to preserve space, however it is shown in appendix G in fig. G.1.

$$\phi_{BE} = arctan\left(\frac{U_P}{U_T}\right) \tag{5.62}$$

One of the conditions for the inflow angle to be considered small is the additional assumption that the blade element tangential velocity U_T is much greater than the perpendicular velocity U_P. As a result the non-linear inflow angle may be replaced by its linear counterpart given by eq. (5.64), also repeated below for clarity. Considering the degree to which the small inflow angle assumption has been violated, however, an additional set of disk distributions has been generated quantifying the percentage difference between the non-linear and linear inflow angle magnitudes in order to verify the made assumptions. Figure 8.7 presents the variation of this difference across the rotor disk for the airplane configuration and it is clear that the simplifying assumptions introduce an error that is larger than the significance threshold set by the ordering scheme across the entire disk, with the error rapidly growing towards the rotor hub. Once again the ill-effects of these assumptions in the case of the helicopter configuration are much less severe and limited to the region close to the rotor hub. Nonetheless the distribution is shown in appendix G in fig. G.2.

$$\text{if} \quad U_T \gg U_P \quad \text{then} \quad \phi_{BE} = \frac{U_P}{U_T} \tag{5.64}$$

A follow-up set of plots also address another consequence of the aforementioned blade element velocity assumption, namely the simplification of the total longitudinal blade element velocity $V^2_{BE|Y-Z\widehat{BL}}$ being equal

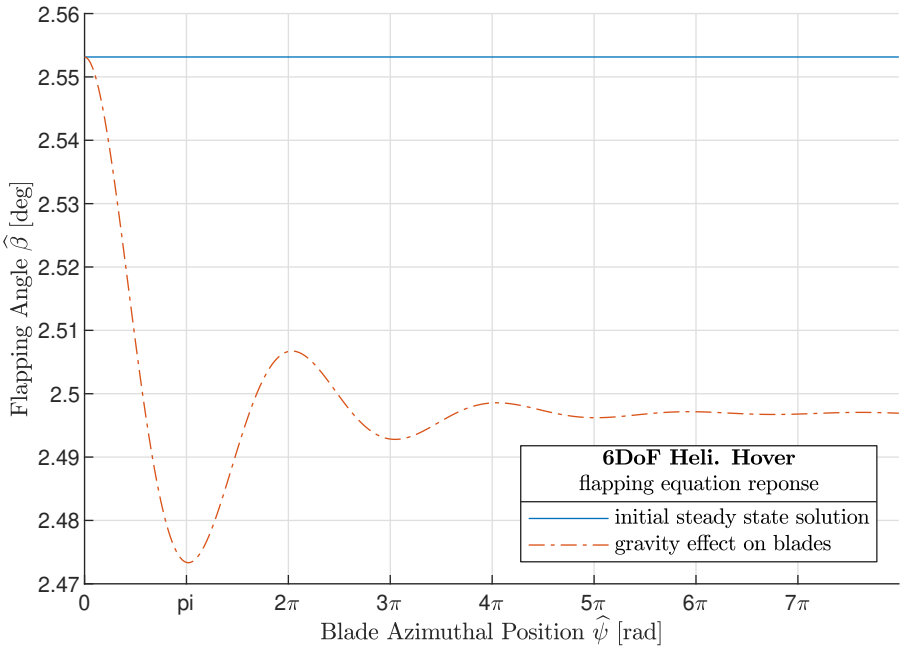

Figure 8.1: Time domain comparison between the 6DoF model rotor flapping equation steady state solution in helicopter hover and the transient response to an upward rotor hub acceleration simulating the effect of gravity on the rotor blades.

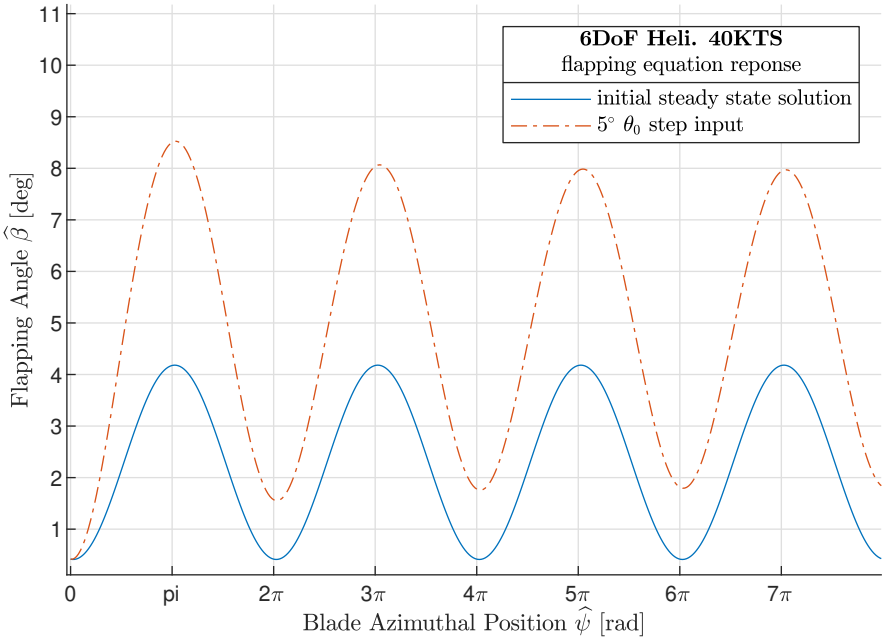

Figure 8.2: Time domain comparison between the 6DoF model rotor flapping equation steady state solution in helicopter level forward flight (40 knots) and the transient response to a 5° step swashplate collective input.

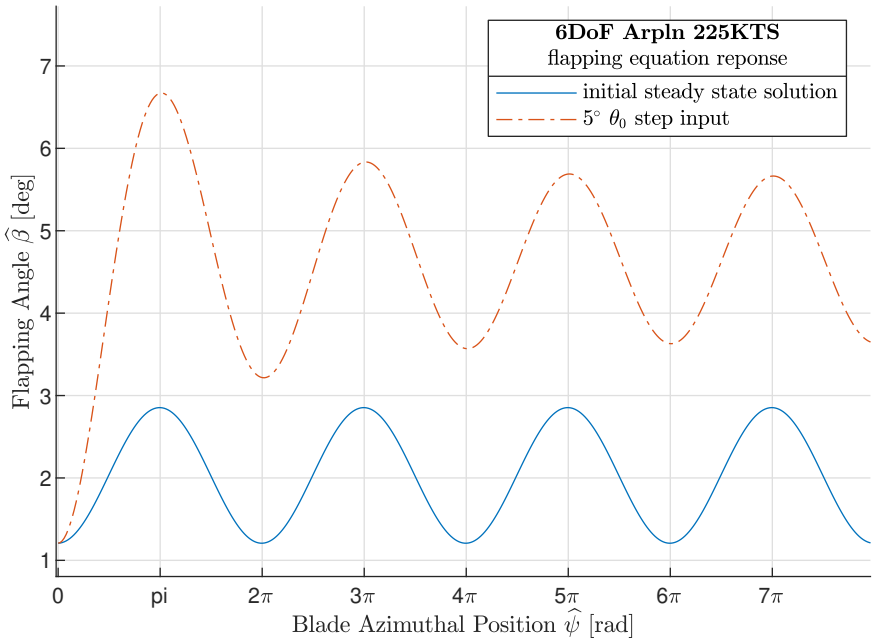

Figure 8.3: Time domain comparison between the 6DoF model rotor flapping equation steady state solution in airplane level flight (225 knots) and the transient response to a 5° step swashplate collective input.

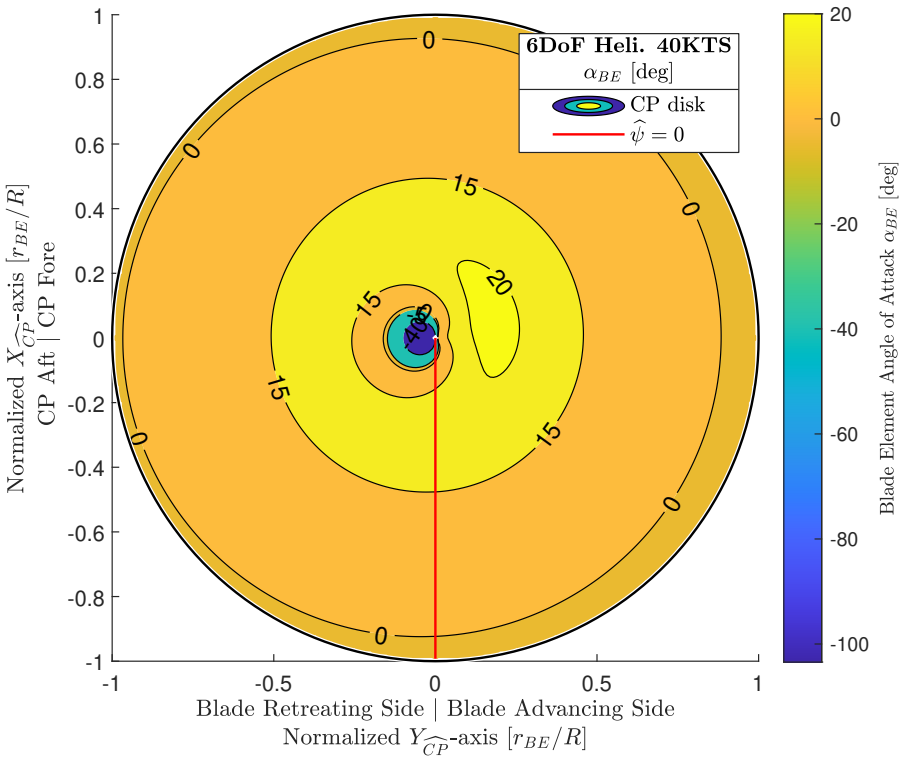

Figure 8.4: Variation of the blade element angle of attack across the rotor disk of the 6DoF tilt-rotor model in helicopter forward flight (40 knots).

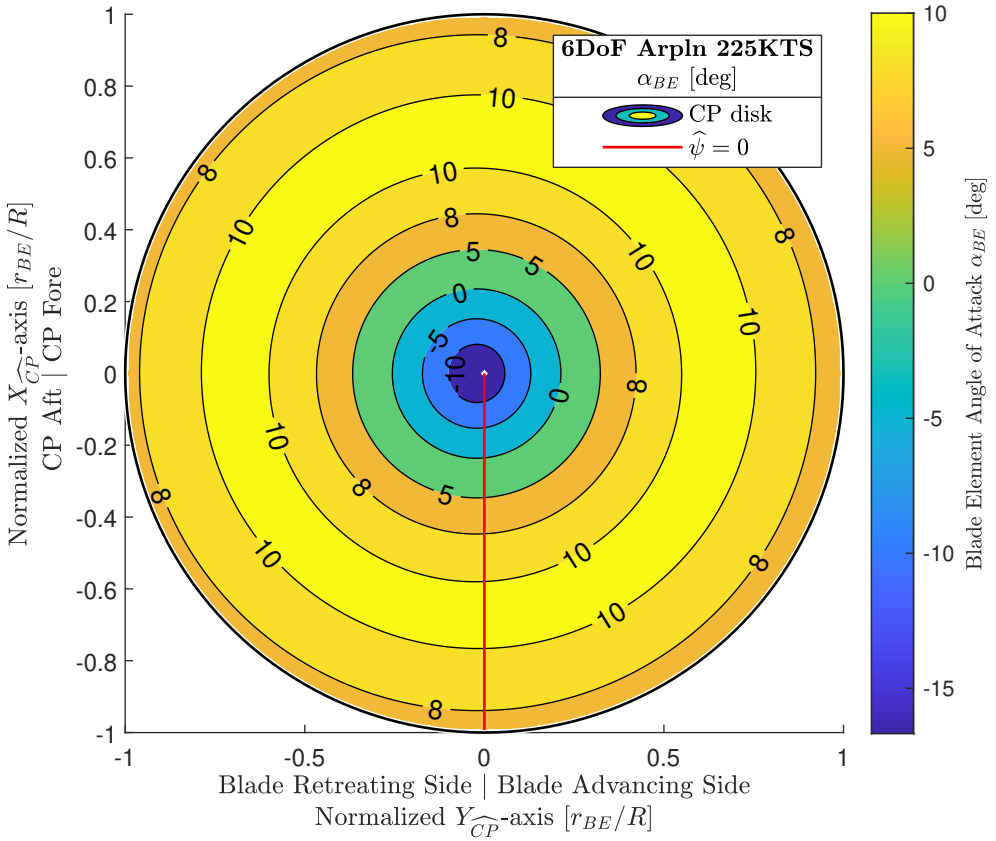

Figure 8.5: Variation of the blade element angle of attack across the rotor disk of the 6DoF tilt-rotor model in airplane level flight (225 knots).

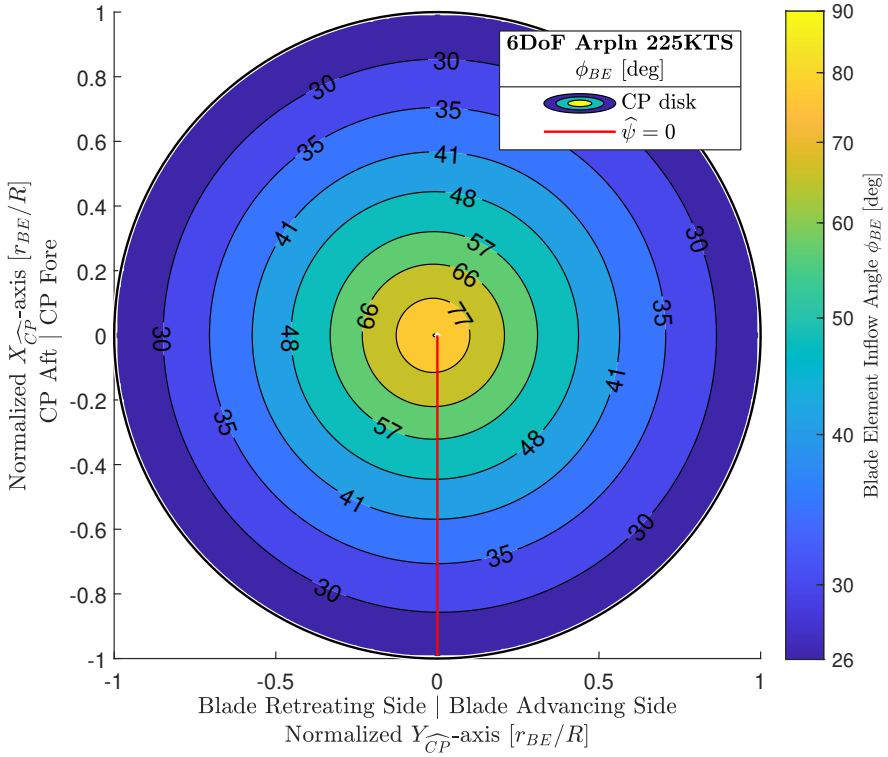

Figure 8.6: Variation of the blade element inflow angle across the rotor disk of the 6DoF tilt-rotor model in airplane level flight (225 knots).

to the squared tangential velocity while neglecting the perpendicular component as given by eq. (5.65) and repeated below for clarity. A similar absolute difference plot has been generated quantifying the percentage difference between the complete and simplified total velocity magnitudes in order to verify the made assumptions. Figure 8.8 presents the variation of this difference across the rotor disk for the airplane configuration and it can be seen that the simplifying assumption introduces a considerable error that grows towards the rotor hub. In the case of the helicopter configuration the percentage difference is much smaller and limited to the region close to the rotor hub as shown in appendix G in fig. G.3.

$$\text{if} \quad U_T \gg U_P \quad \text{then} \quad V^2_{BE|Y-Z\widehat{BL}} = U_T^2 \tag{5.65}$$

The last set of plots address the last key assumption, namely the simplification that the blade element lift is much greater than the blade element drag making it possible to omit the latter in several expressions such as the aerodynamic flapping moment (i.e. eq. (5.58)). These disk distributions present the percentage ratio between the blade element drag and lift, with a low percentage indicating that indeed the lift is much greater than the drag. Fortunately, in both the helicopter and airplane configuration the drag to lift ratio is small across most of the rotor disk with the exception of the regions where the angle of attack is close to zero as shown in fig. G.4 and fig. G.5 respectively in appendix G. Since the blade element drag additionally contains a zero-angle-of-attack component, in the regions where the angle of attack is close to zero the blade element lift also tends to zero, while the drag tends to the zero-angle-of-attack value resulting in a quickly growing drag to lift ratio. Since these regions are very narrow, however, the assumption is considered permissible.

8.2. Trimmed Longitudinal and Level Flight Analysis and Validation

The next set of results present the trim curves of the tilt-rotor model developed for the purposes of this thesis (referred to as the 6DoF model) which are compared to the trim data corresponding to the Generic Tilt-Rotor Simulation (GTRS) provided in appendix A of [5] in order to assess the validity of the 6DoF model. Note that the positive sign conventions of the GTRS model variables, taken from [6, p.A-13] and [52, p.18], are different from the 6DoF model is several cases. For sake of report consistency, the GTRS data is adjusted to be in accordance with the positive conventions of the 6DoF model. The parameters of both the 6DoF and GTRS model implementations have been set to match the XV-15 tilt-rotor aircraft and the trim routines of both models have been set to find the trim values of the tilt-rotor in longitudinal and level flight. The GTRS has been extensively validated against real flight data of the XV-15 in [5] showing a high correlation between the model and reality. For this reason, and due to the better availability of simulated data over real flight data, it has been decided that it is acceptable to validate the 6DoF model against the GTRS data treating the latter as if it represented reality.

Each trim plot in this section contains multiple trim curves showing the variation of a single tilt-rotor state or variable as a function of velocity, with each trim curve corresponding to a different nacelle tilt angle. Referring to the formal definition of trim curves given in section 7.4, in this case the nacelle tilt angle is the primary independent variable while the velocity is the secondary independent variable. The trim curves corresponding to the 6DoF model are represented by line patters of different color while trim curves of the GTRS are represented by shapes of different color connected with gray lines in order to improve readability of the sparse data. The nacelle tilt and flap deflection angles corresponding to a particular trim curve are indicated in the legend of each plot. Note that only one flap angle is indicated which corresponds to the deflection of the inboard flaps. The XV-15 additionally has outboard flaperons which follow the flap deflection of the inboard flaps linearly with a ratio of $8:5$, i.e. for every 8 degrees of inboard deflection, the outboard flaperons deflect by 5 degrees. Since the deflection of the flaperons may be easily extrapolated, its value is not shown in the legend to preserve plot space.

The trim curve validation process is divided into three parts, namely whole-model validation, subsystem trim curve trend validation, and subsystem validation. The first part serves the purpose of assessing both the relative (i.e. trim curve trend) and absolute accuracy of the model as a whole where all of the 6DoF trim curves are generated using the nominal trimming routine described in section 7.4. Trim curves obtained in this manner are referred to as nominal trim curves. A quick inspection of the nominal body angle of attack and pilot/governor input trim curves, however, shows a significant absolute divergence between the

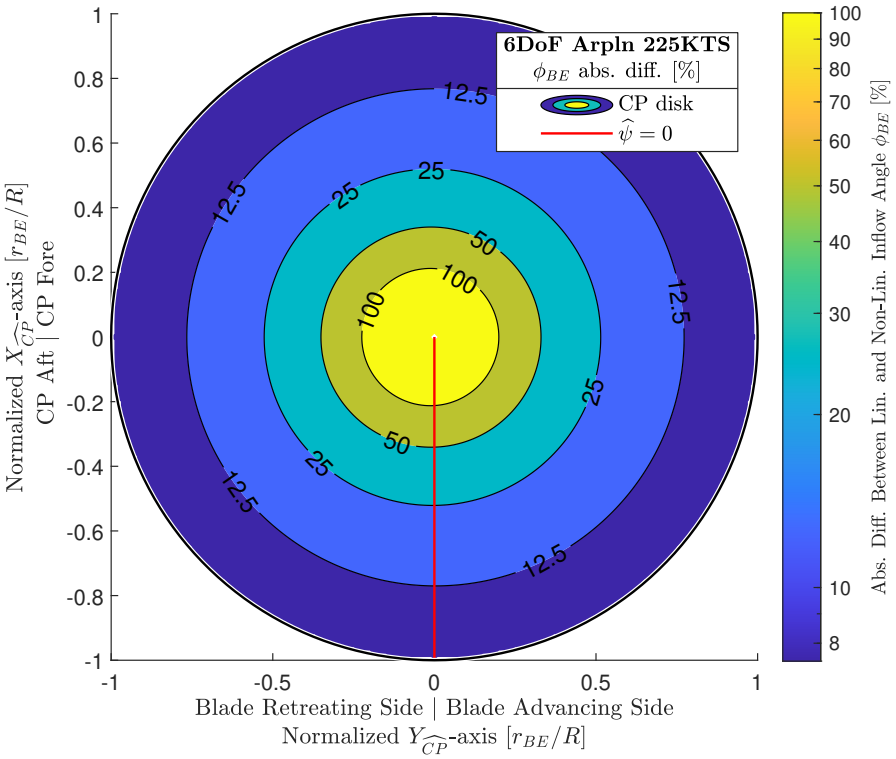

Figure 8.7: Variation of the percentage difference between the non-linear and linearized blade element inflow angle across the rotor disk of the 6DoF tilt-rotor model in airplane level flight (225 knots).

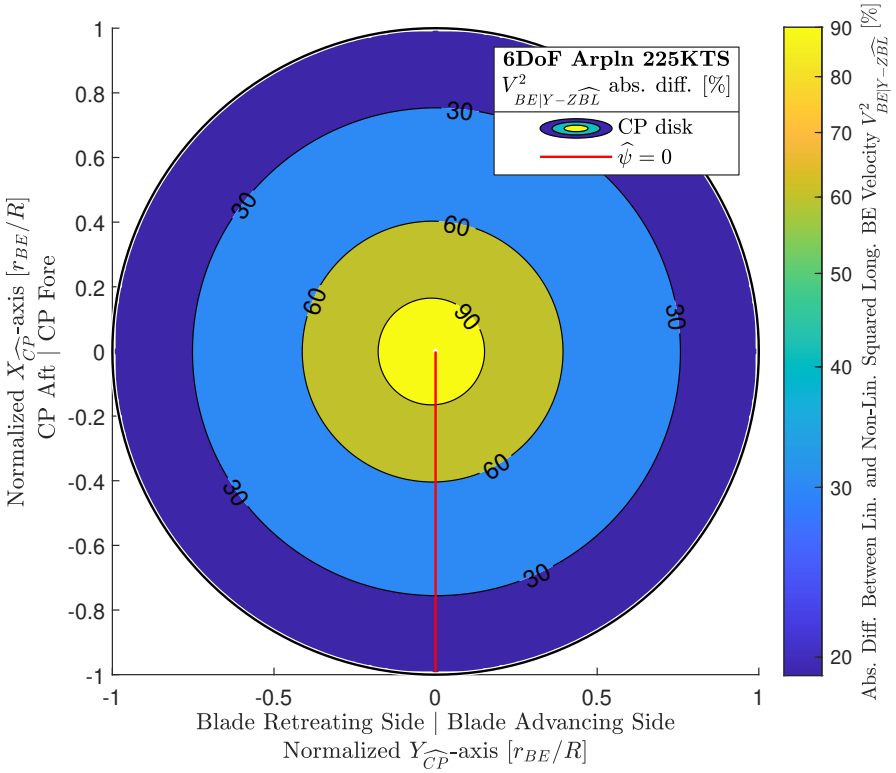

Figure 8.8: Variation of the percentage difference between the complete and simplified blade element total longitudinal velocity across the rotor disk of the 6DoF tilt-rotor model in airplane level flight (225 knots).

6DoF model and the GTRS as shall be presented later. Since the trim curves of all other model subsystems largely depend on the body angle of attack and pilot inputs, the mentioned divergence carries through to the remaining trim curves making it difficult to accurately assess the validity of each subsystem independently. For this reason the whole-model validation section shall focus only on the validation of the trim variables consisting of the body angle of attack and pilot inputs. The subsystem trim curve trend validation section shall then only inspect the trends of the remaining subsystem trim curves and compare them to the ones of the GTRS in order to assess whether the 6DoF model correctly estimates the relative variation of the subsystem states necessary to achieve trimmed flight as a function of velocity and nacelle tilt. The subsystem validation section, on the other hand, shall replace the whole-model trim variables (i.e. the body angle of attack and pilot inputs) with the ones of the GTRS in order to generate new subsystem trim curves, also referred to as pseudo trim curves. In this manner the 6DoF subsystems shall experience the same flight conditions as the ones of the GTRS making it possible to determine the absolute accuracy (validity) of each 6DoF model subsystem independently with respect to the XV-15 tilt-rotor (represented by the GTRS data). It must be highlighted, however, that the 6DoF model trim curves obtained in this manner do not represent the variation of the variables of a tilt-rotor in trimmed state. Instead they indicate the value of those variables in flight conditions experienced by the GTRS. For this reason they are referred to as pseudo trim curves and are only used to assess the similarity in magnitude between the two models and not the similarity in trends.

8.2.1. Whole-Model Validation

The whole-model validation section shall present the 6DoF model and GTRS trim curves corresponding to the trim variables, namely the pilot longitudinal and collective quasi-stick inputs, as well as the body angle of attack. Recalling from section 7.4, the collective quasi-stick input trim variable (X_{COL}) combines the pilot collective stick deflection ($X_{\text{COL,pilot}}$) with the governor stick-deflection-equivalent ($X_{\text{COL,gov}}$). Since the data provided in [5] does not provide such a combined equivalent stick deflection, the resulting total swashplate collective deflection θ_0 (which depends on both the pilot and governor inputs) shall be compared between the two models instead. The approach of distributing the total swashplate deflection among the pilot and governor contributions shall be validated in the subsystem validation section. Note that the lateral pilot stick inputs and body roll angle are all equal to zero in longitudinal flight, therefore they shall not be shown.

Body Angle of Attack Trim Curves

The whole-model validation begins with the comparison between the body angle of attack trim curves of the 6DoF tilt-rotor model and the GTRS as shown in fig. 8.9. The trend of the trim curves of the models is quite similar in two regards. First of all, the variation of the body angle of attack as a function of the total velocity for each nacelle tilt angle is almost identical, neglecting the glaring offset between the curves, and may be compared to a cubic function where initially the body angle of attack increases and later decreases as a function of the total velocity. In general the tilt-rotor nose points more upwards at lower velocities and tends towards pointing downwards as the velocity increases. The characteristic inflection point is most visible in the $\eta = -15^\circ$ trim curve of the GTRS model and in the $\eta = -30^\circ$ trim curve of the 6DoF model. The largest difference in trim curve shapes can be observed in the case of the helicopter mode where the curvature of the 6DoF model is significantly larger while the trim curve of the GTRS is almost linear at velocities above 20 knots. Furthermore the 6DoF helicopter curve shows a kink near hover where the body angle of attack initially decreases and at around 3 knots the slope of the trim curve abruptly changes from a negative to a positive value. A detailed view of the same trim curve plotted with a higher velocity step resolution near hover is shown in fig. G.6 (in appendix G) demonstrating that the trim curve remains smooth even near this abrupt change in slope. This behavior is not seen in the GTRS trim curve, but it must be highlighted that the data points of the GTRS trim curve are sparse and therefore such a detailed variation in the body angle of attack would never appear nonetheless. For this reason it is not clear whether the shape of the 6DoF trim curve in helicopter mode near hover accurately approximates reality. The cause of this kink has not been investigated, leaving it for future research.

The second similarity between the trim curve trends of the two models may be observed in the translation of the trim curves as a function of the nacelle tilt angle. In both models it can be seen that the trim curves are translated upwards, i.e. the nose of the tilt-rotor points more upwards as the proprotors tilt more towards airplane mode meaning that trimmed flight at the same velocity is achieved at a higher body angle of attack for more horizontal (more negative) nacelle tilt angles. A slight leftward translation of the trim curves may

also be observed, however it is negligible in comparison to the vertical translation. Although the general trend of translation is similar for the two models, the difference in the magnitudes of the translations is significantly large and increases towards airplane mode indicating a growth in the overall 6DoF model invalidity. At this point it is not clear whether this invalidity stems from the governing equations or a difference in the model parameters (such as wing lift coefficients).

It must be highlighted that the 6DoF model body angle of attack variation does seem to remain relatively valid in helicopter mode and up to conversion angles of $\eta = -15^\circ$ for most of the velocity range as suggested by the small differences between the respective trim curves of the two models. The high similarity in the trends of the curves also suggests that the model accurately estimates the body angle of attack required for trimmed flight of a generic tilt-rotor almost across the entire velocity and nacelle tilt range with the exception of low velocity flight close to helicopter configuration.

Longitudinal Stick Deflection Trim Curves

The next trim curves to be inspected are shown in fig. 8.10 and correspond to the variation of the longitudinal stick deflection as a function of velocity for both the 6DoF and GTRS models. Once again a similarity in the translation of the trim curves as a function of the nacelle tilt angle may be observed for both models, where the trim curves appear to be translated downwards, i.e. towards a greater nose-down stick deflection, as the nacelles tilt towards airplane mode. Although the trend of the translation is similar for the two models, the difference in magnitude is also significant and generally increases towards airplane configuration simultaneously reducing the validity of the model. The closest overlap may be observed in the case of a conversion angle of $\eta = -15^\circ$, while the largest differences occur in both airplane and helicopter configurations.

This leads to the second observation of the variation of the stick deflection as a function of velocity of both models. For the most part this trend is very similar for both the 6DoF and GTRS model and may be described as an almost linear function at a nacelle tilt angle of $\eta = -15^\circ$ which transitions into a trim curve resembling a logarithmic function towards airplane mode. In general less nose-up and more nose-down stick deflection is required as velocity increases. Unfortunately a great dissimilarity between the two models may be observed in helicopter configuration where in the case of the 6DoF model the trim curve remains relatively linear while in the case of the GTRS the trim curve has a somewhat sinusoidal variation near hover before approaching a linear trend at higher velocities. The initial stick deflection in hover is also significantly different with the 6DoF model requiring an aft stick deflection to achieve a trimmed state, while the GTRS requires a fore stick deflection. Since the parameters of the 6DoF model have been set to match the ones of the GTRS, including the position of the center of gravity, from a perspective of moment balance around the CoG the deflection of the 6DoF model longitudinal stick in hover is expected to almost coincide with the one of the GTRS. It seems, however, that the interaction between the rotor and wing (which is modeled to a greater extent in the case of the GTRS) has a large impact on the trim curves, especially in helicopter mode close to hover where the majority of the aerodynamic velocity experienced by the wing stems from the rotor wake. This would explain why the largest deviation occurs in helicopter mode at low velocities, and why this difference fades at higher velocities and closer to airplane mode where the rotor wake no longer is the largest contributor to the velocity vector near the wing.

In general the longitudinal stick deflection variation is relatively valid for conversion angles between $\eta = -15^\circ$ and $\eta = -60^\circ$ across most of the velocity range. The model also approximates trimmed flight of a generic tilt-rotor most accurately in conversion and airplane configuration flight, while the same cannot be said for flight near helicopter configuration.

Swashplate Collective Trim Curves

The final trim curves used to assess the validity of the model as a whole are shown in fig. 8.11 and present the variation of the swashplate collective angle as a function of velocity for the 6DoF and GTRS models. It can be clearly seen that the trim curves of both models are very similar in terms of their variation as a function of the velocity and as a function of the nacelle tilt angle. In the former case both models show an initially higher required collective angle in hover which slightly dips at intermediate velocities, only to increase again in a roughly linear fashion at higher velocities. The 6DoF model expects the required collective to increase at a higher rate than the GTRS, however, as indicated by the steeper slope of the curve in airplane mode.

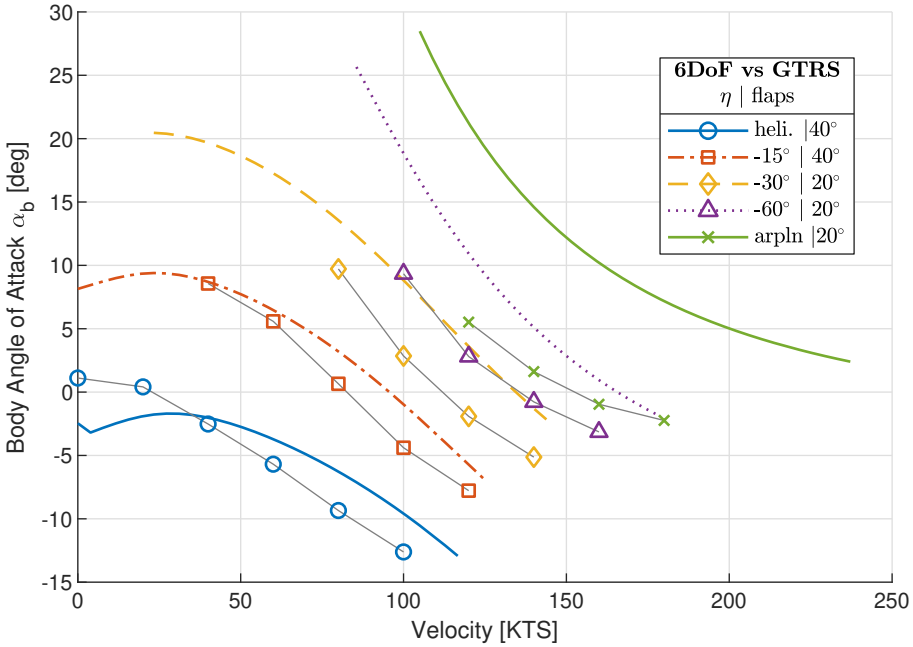

Figure 8.9: Comparison between the body angle of attack trim curves of the 6DoF tilt-rotor model and the GTRS. Color line patterns correspond to the 6DoF model while shapes connected with gray lines correspond to the GTRS data[5, app. A]. Nacelle tilt η and flap deflection angles indicated in legend.

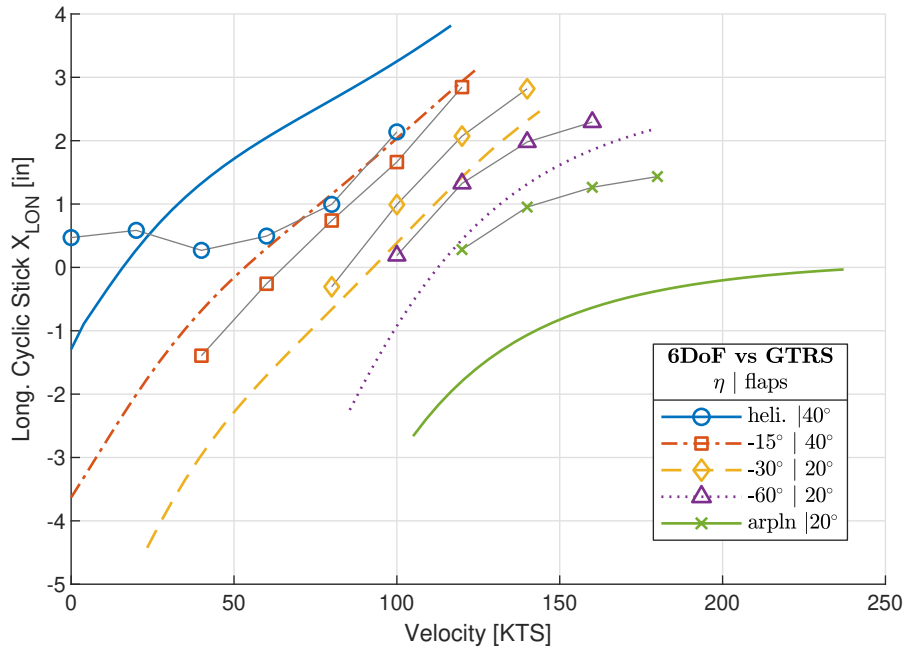

Figure 8.10: Comparison between the longitudinal stick deflection trim curves of the 6DoF tilt-rotor model and the GTRS. Color line patterns correspond to the 6DoF model while shapes connected with gray lines correspond to the GTRS data[5, app. A]. Nacelle tilt η and flap deflection angles indicated in legend.

The trim curves don't appear to significantly change as a function of the nacelle tilt angle between helicopter mode and $\eta = -30°$, however a clear upward translation of the trim curves, i.e. a larger required collective angle, does start to appear as the nacelle tilt tends towards airplane mode. A less evident downward translation of the trim curves may still be observed near helicopter mode at intermediate velocities. The upward translation is more pronounced in the 6DoF model while the downward translation is more noticeable in the case of the GTRS.

The overlap between the two models is greatest in airplane configuration, and gradually decreases towards helicopter configuration where the 6DoF model underestimates the required collective angle by about 4 degrees. The discrepancies near helicopter configuration are hypothesized to be caused by differences in the rotor downwash effect on the wing between the two models, which diminishes as the wing experiences less of a perpendicular downwash towards airplane mode. In general, however, the swashplate collective variation may be considered mostly valid for all nacelle tilt angles and velocities, especially when compared to the previous two trim variables.

8.2.2. Subsystem Trim Curve Trend Validation

The subsystem trim curve trend validation section shall present the 6DoF model and GTRS trim curves of the rotor, main wing, horizontal stabilizers, and fuselage subsystems which have been generated using the nominal trimming routine described in section 7.4. The trim curves of the vertical stabilizers shall not be shown in this section, however they will be briefly discussed. Since this section is only concerned with the validation of the subsystem trim curve trends, the trim curves shall be analyzed with regard to their similarity in shape only, while the assessment of how well they overlap (in magnitude) is left to the subsystem validation section. Note that the subsystem trim curve trend validation may also be referred to as relative validation.

Rotor

The rotor subsystem trim curve trends are validated by analyzing the trim curves of the induced velocity, disk tilt angles, and of the rotor-generated forces and torque defined in the shaft plane. Since the required engine power is proportional to the rotor torque, analyzing it here is considered unnecessary, however its calculation shall be verified later in the subsystem validation section.

The rotor subsystem relative validation starts with the comparison between the induced velocity trim curves of the 6DoF tilt-rotor model and the ones of the GTRS as shown in fig. 8.12. It can be seen that the trim curves of both models are very similar and follow the same trends in their variation as a function of velocity and nacelle tilt angle. In the former case the curves follow an almost sinusoidal function near helicopter configuration and tend towards an asymptote for all nacelle angles at higher velocities. The similarity in this trend is greatest near helicopter mode and weakens towards airplane mode where the trim curves of the GTRS become almost completely linear while the 6DoF model still shows significant curvature towards higher induced velocities at lower flight velocities. It is speculated, however, that the curvature would also appear in the GTRS trim curve if more trim points at lower velocities were available. The effect of the tiltable proprotor on the induced velocity is also very similar for both models where the trim curves appear to be translated downward, i.e. the rotor generates a lower induced velocity, as the nacelles tilt towards airplane mode. Near hover the curves seem to be unaffected by the nacelle tilt angle.

The next rotor trim curves to be analyzed correspond to the disk tilt angles defined in the shaft plane (referred to as the mast axis system in the validation data source [5]). Note that the 6DoF model disk tilt angles must first be transformed from the wind axis control plane to the non-wind axis shaft plane in order to enable the validation of these angles. The relative validation starts with the coning angle a_0 trim curves of the 6DoF and GTRS models as shown in fig. 8.13. Although the trim curves of the two models clearly do not overlap, a similarity in trends may be observed. The variation of the trim curves as a function of velocity is very similar for both models and can be approximated by a sinusoidal function where the rotor experiences a higher coning angle near hover which dips at moderate velocities and increases again at higher velocities. This trend is similar for both models for almost all nacelle tilt angles with the exception of airplane mode where the GTRS shows an almost linear variation while the 6DoF model indicates a quadratic variation of the coning angle. The variation of the trim curves as a function of the nacelle tilt is also very similar where the trim curves are translated downward and rightward, i.e. indicating a lower coning angle at higher velocities, as the nacelle tilts towards airplane mode. The trim curve corresponding to the airplane configuration shows

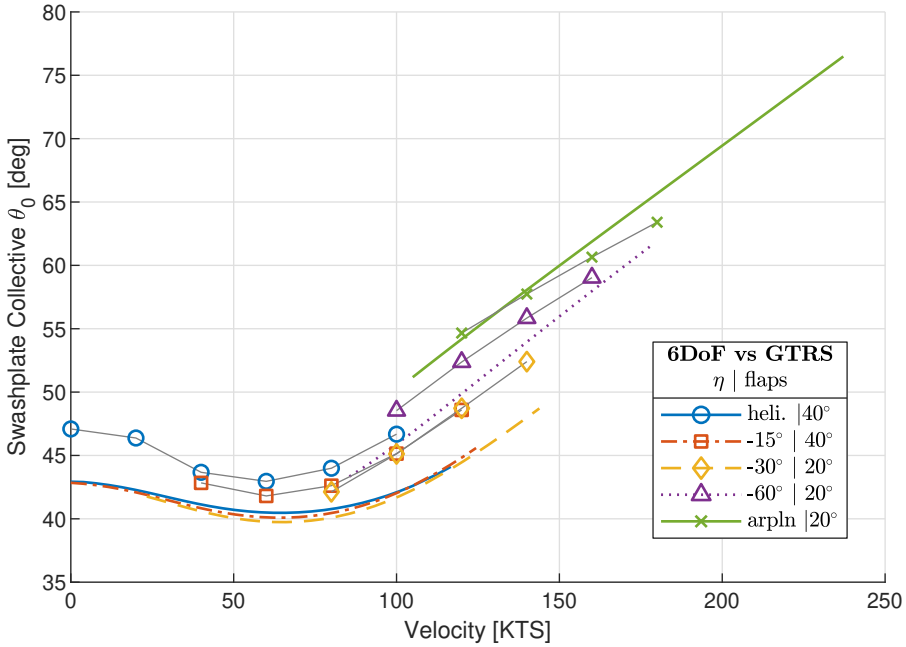

Figure 8.11: Comparison between the swashplate collective trim curves of the 6DoF tilt-rotor model and the GTRS. Color line patterns correspond to the 6DoF model while shapes connected with gray lines correspond to the GTRS data[5, app. A]. Nacelle tilt η and flap deflection angles indicated in legend.

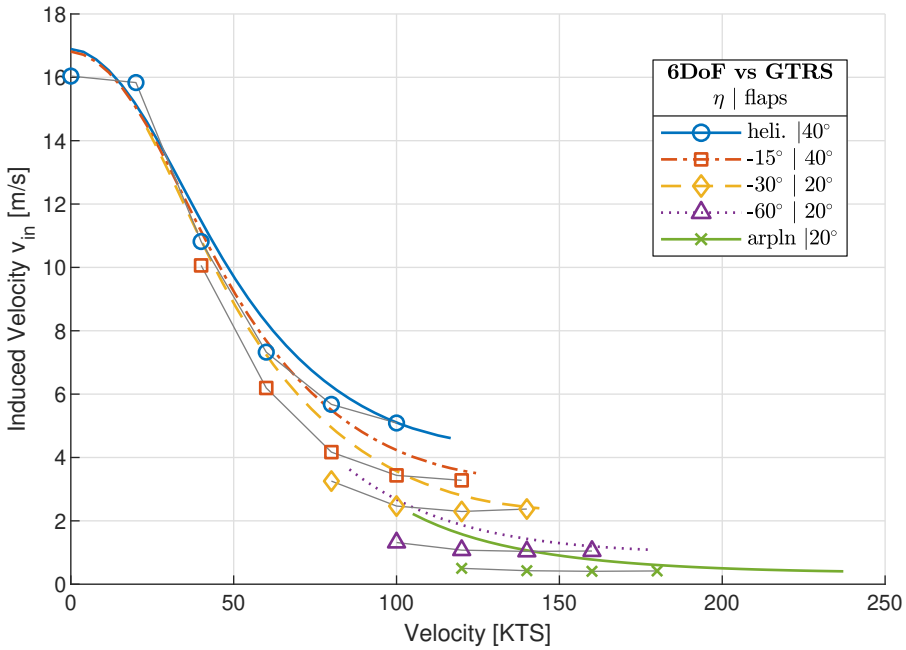

Figure 8.12: Comparison between the rotor induced velocity trim curves of the 6DoF tilt-rotor model and the GTRS. Color line patterns correspond to the 6DoF model while shapes connected with gray lines correspond to the GTRS data[5, app. A]. Nacelle tilt η and flap deflection angles indicated in legend.

a significant divergence from this trend where instead of translating downwards, the trim curve translates upwards with respect to the $\eta = -60°$ trim curve. This is surprising considering the trends of the other trim variables that the coning angle depends on (i.e. the body angle of attack, induced velocity, longitudinal disk tilt angle, and rotor forces) largely agree with the ones of the GTRS. Further investigation into this anomaly is left as a recommendation for future research.

The longitudinal disk tilt angle a_1 is validated next where the corresponding trim curves of both models are shown in fig. 8.14. At first glance the two trim curve sets seem to differ greatly, however some similarity in the trends may still be noticed. The variation in a_1 as a function of velocity is similar for both models near airplane mode and be may approximated by an almost linear relation where in airplane mode the longitudinal disk tilt angle decreases as velocity increases, while the opposite holds in the case of $\eta = -60°$. A similar trend may be observed for the remaining nacelle tilt angles where the disk tilt generally increases with velocity, however the trim curves of the GTRS resemble a quadratic function while the trim curves of the 6DoF model exhibit cubic characteristics which includes an inflection point which cannot be observed in the GTRS trim curves. For this reason the largest divergence between the two models exists at lower velocities. The trend of the variation of the trim curves as a function of the nacelle tilt angle, on the other hand, is similar for both models and may be generalized (for the most part) to a leftward translation and a decrease in the slope of the curves resulting in a lower longitudinal disk tilt at the same velocity as the nacelle tilts towards airplane mode. The trim curves are not affected by the nacelle tilt angle near hover.

The lateral disk tilt angle $b_{1,R}$ corresponding to the right counter-clockwise rotating rotor (indicated with the subscript R) is the last disk tilt angle to be validated where the appropriate trim curves of the 6DoF model and GTRS are shown in fig. 8.15. Note that the trim curves of the left clockwise rotating rotor are identical to the trim curves of the right rotor mirrored about the $b_{1,r} = 0$-axis. Returning to the lateral disk tilt angle, apart from the clear absolute difference, the trends of the trim curves are similar for both models. In the case of the velocity variation, both models show an initial spike in the later disk tilt at moderate velocities which then gradually reduces as the velocity increases. Both models show an almost linear variation in b_1 in airplane mode. The trim curves of the 6DoF model all seem to reach an asymptote at higher velocities while in the case of the GTRS the trim curves either start to increase again (in helicopter and conversion configuration) or continue to decrease (in airplane configuration). The asymptotic characteristic of the trim curves was not observed in the results of the preliminary 3DoF model shown in fig. 3.3 which did not include the lateral disk tilt correction described by eq. (5.83). Instead, the trim curves of the 3DoF model showed an increasing b_1 angle in helicopter and conversion mode, and a continued decreasing b_1 angle in airplane mode similarly to the GTRS model. For this reason the discrepancy between the 6DoF model and the GTRS is attributed to a too large of a influence of the lateral disk tilt correction at higher velocities which should be amended in future iterations of this rotor model. The variation of the trim curves as a function of the nacelle tilt, on the other hand, is similar for both models and may be summarized by a general downward translation, i.e. a lower lateral disk tilt at the same velocity, as the nacelles tilt towards airplane mode. The magnitude of this translation decreases at lower velocities for the 6DoF model to the point of the nacelle tilt having no effect on the trim curves near hover. Unfortunately the same cannot be observed in the trim curves of the GTRS due to the lack of data at these lower velocities.

The next group of rotor trim curves trends to be validated are the rotor forces, also defined in the shaft plane (indicated with the SP subscript), which once again must first be transformed from the wind-axis control plane to the non-wind axis shaft plane in the case of the 6DoF model. The relative validation starts with the rotor thrust trim curves of the 6DoF and GTRS models as shown in fig. 8.16. Recalling the analysis of the thrust equation (eq. (5.87)), the rotor thrust is not directly influenced by the coning angle a_0 since the reduction scheme considers its explicit contribution insignificant. However, a large similarity between the trim curves of the thrust and coning angle may be observed hinting that a_0 is correlated with the thrust, albeit implicitly through the iterative rotor solver (graphically summarized by fig. 5.15). For this reason the conclusions about the coning angle trim curve trend accuracy largely apply to the validation of the thrust trim curve trends. In summary, the variation of the trim curves as a function of velocity is very similar for both models and can be approximated by a sinusoidal function where the rotor produces more thrust near hover which dips at moderate velocities and increases again at higher velocities. The similarity in this trend applies to almost all trim curves with the exception of the airplane configuration where the 6DoF model indicates a quadratic variation of the thrust instead of a linear one as in the case of GTRS, and at lower velocities in helicopter configuration where a distinct dip in thrust is not clearly observable. The variation of the trim curves as a function of the nacelle tilt is also very similar where the trim curves are translated downward and

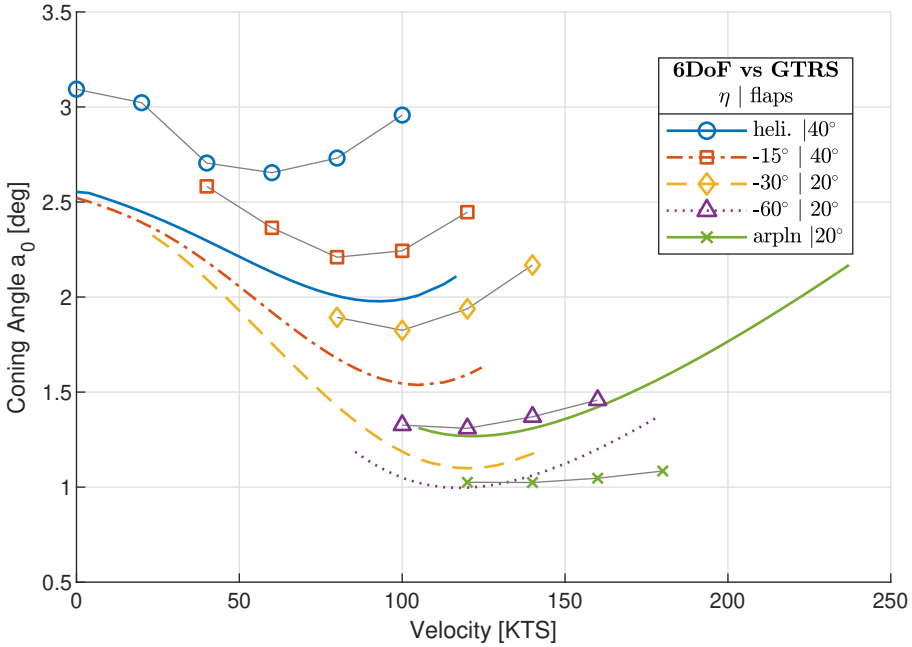

Figure 8.13: Comparison between the shaft plane coning angle trim curves of the 6DoF tilt-rotor model and the GTRS. Color line patterns correspond to the 6DoF model while shapes connected with gray lines correspond to the GTRS data[5, app. A]. Nacelle tilt η and flap deflection angles indicated in legend.

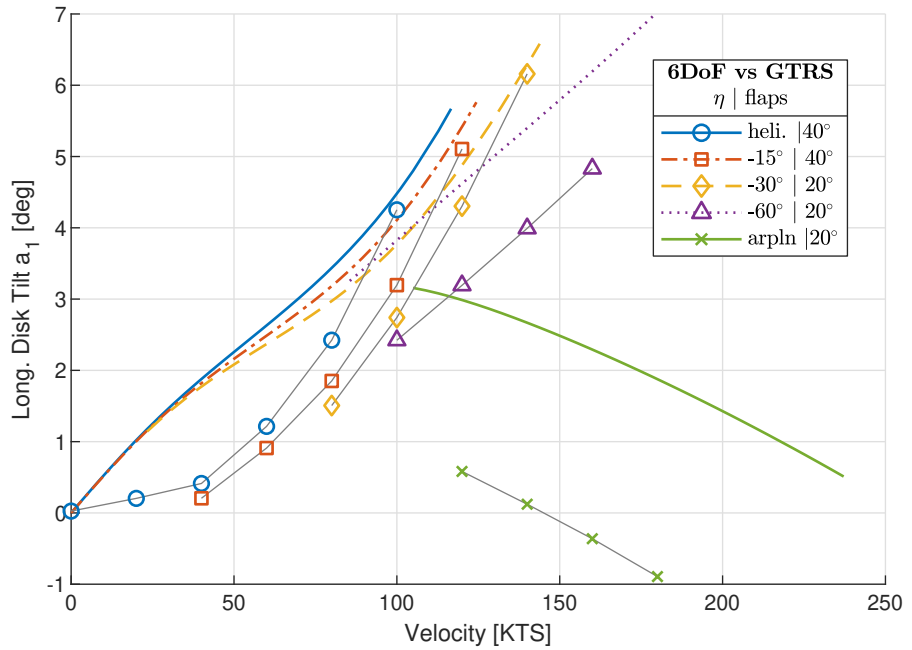

Figure 8.14: Comparison between the shaft plane longitudinal disk tilt angle trim curves of the 6DoF tilt-rotor model and the GTRS. Color line patterns correspond to the 6DoF model while shapes connected with gray lines correspond to the GTRS data[5, app. A]. Nacelle tilt η and flap deflection angles indicated in legend.

rightward, i.e. indicating a lower thrust at higher velocities, as the nacelle tilts towards airplane mode. This trend applies to all nacelle angles, even airplane mode, which was not the case for the coning angle a_0 trim curves.

The rotor side force $S_{SP,R}$ corresponding to the right counter-clockwise rotating rotor (indicated with the subscript R) is validated against the GTRS next where the corresponding trim curves of both models are shown in fig. 8.17. Analogously to the rotor thrust and coning angle, a correlation between the side force and lateral disk tilt may also be observed, albeit a weaker one. The variation of the side force as a function of velocity shows a familiar (negative) spike at moderate velocities which gradually wanes as the side force becomes positive at higher velocities. This trend seems to stop at a nacelle angle of $-60°$ in the case of the 6DoF model, and in airplane configuration for the GTRS where instead of becoming more positive, the side force once again tends towards a negative value. Assuming that the $\eta = -30°$ trim curve of the 6DoF model is correct, however, the velocity trend seems to resemble a sinusoidal function with a negative peak at lower velocities and a positive peak at higher velocities. Keeping this in mind, the largest discrepancy between the two models observed at $\eta = -60°$ may be attributed to the 6DoF model reaching the positive peak sooner than the GTRS resulting in a negative slope of the trim curve as opposed to a positive slope in the case of the GTRS trim curve. In this case the calculation of the side force is not necessarily grossly inaccurate and may be instead caused by a difference in parameters between the two models which shall be discussed in the subsystem validation section. In terms of the variation of the trim curves as a function of the nacelle tilt angle, both models show an upward curve translation at intermediate velocities, and a downward translation at higher velocities, the latter being more pronounced, as the nacelle tilts towards airplane mode. This means that in general the rotor shall produce a smaller in (absolute) magnitude side force as the nacelle tilts forwards, with the exception of the 6DoF trim curve at $\eta = -60°$ which does not follow this generalization at higher velocities. The tillable nacelle does not seem to have an effect on the side force at velocities close to hover based on the 6DoF model data. Unfortunately the same cannot be observed in the trim curves of the GTRS due to the lack of data at these lower velocities.

The final rotor force to be validated is the hind force H_{SP} where the corresponding trim curves of the 6DoF model and GTRS are shown in fig. 8.18. The variation of the hind force as a function of the velocity is somewhat similar for both models which can be generalized to a quadratic function for nacelle tilt angles ranging from helicopter mode up to $\eta = -30°$, with an almost-linearly increasing hind force at $\eta = -60°$ and an almost-linearly decreasing hind force in airplane mode. The largest difference between the two models may be observed in helicopter mode where the GTRS trim curve resembles a sinusoidal function with the hind force rate of increase being negative as opposed to a positive one in the case of the 6DoF model. The variation of the trim curves as a function of the nacelle tilt angle of both models is similar to a greater extent where an upward translation of the curves, i.e. a higher hind force, is seen for conversion angles ranging from $0°$ to $-60°$. At some point during conversion the hind force starts to decrease at the same velocity as the nacelle tilts towards airplane mode as suggested by the downwards-translated $\eta = -90°$ trim curve.

The last rotor variable to be validated is the rotor torque $Q_{SP,R}$ corresponding to the right counter-clockwise rotating rotor (also defined in the shaft plane, thus acting around the shaft axis), with the trim curves of the 6DoF model and GTRS shown in fig. 8.19. Before the relative validatory analysis is performed it must be highlighted that the entire trim set is negative, therefore any mention of the magnitude of torque shall refer to its absolute value, i.e. lower values shall be found at the top of the plot, while greater ones at the bottom. Returning to the analysis, the variation of the rotor torque as a function of velocity is very similar for both models which is characterized by a dip in torque at intermediate velocities which rises again at higher velocities. The fall and rise of the torque is more abrupt for nacelle tilt angles close to helicopter mode and becomes more gradual near airplane mode. The difference in the airplane trim curves is attributed to a narrower velocity range of the GTRS data and it is believed that the GTRS trim curve would continue to follow a similar trend if more data were available. The variation of the trim curves as a function of the nacelle tilt is also mostly similar for both models where the trim curves are translated rightward and upwards as the nacelle tilts towards airplane mode. The vertical translation means that the rotor generates a lower torque at the same velocity, while an analogous generalization may not be made about the lateral translation due to the dip in the curves. The largest discrepancy between the two models may be observed at a nacelle angle of $-60°$ and in airplane mode where instead of translating upwards, the 6DoF model trim curves are translated downwards resulting in a greater torque. The cause of this divergence is not clear at this point and further investigation is left as a recommendation for the future.

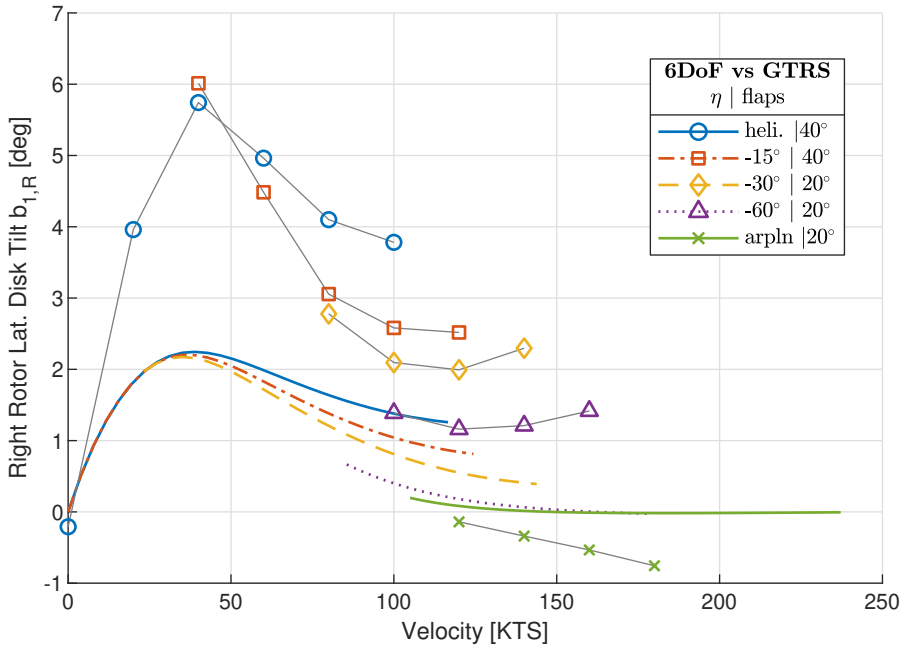

Figure 8.15: Comparison between the right counter-clockwise rotating rotor shaft plane lateral disk tilt angle trim curves of the 6DoF tilt-rotor model and the GTRS. Color line patterns correspond to the 6DoF model while shapes connected with gray lines correspond to the GTRS data[5, app. A]. Nacelle tilt η and flap deflection angles indicated in legend.

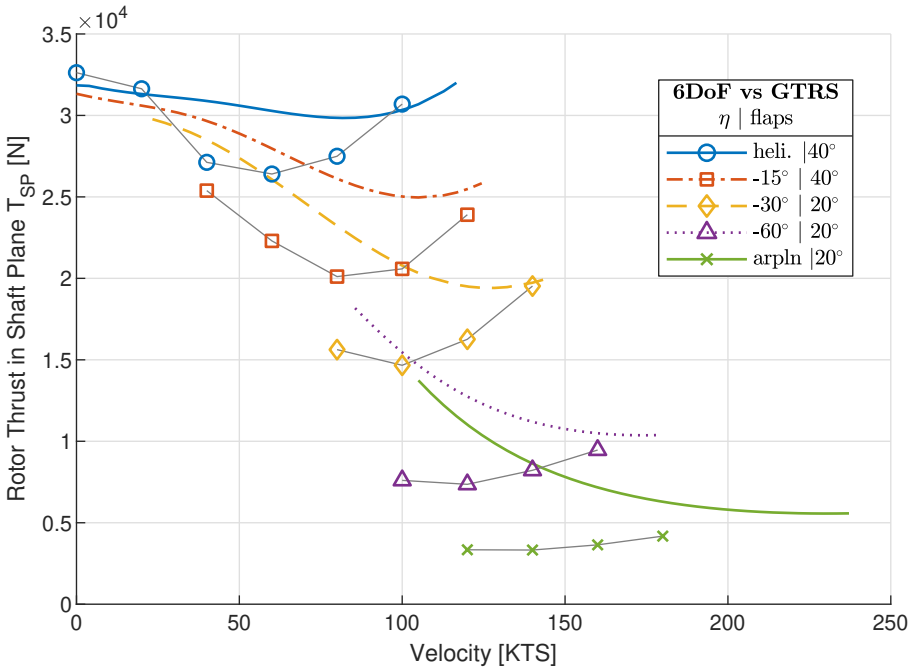

Figure 8.16: Comparison between the shaft plane rotor thrust trim curves of the 6DoF tilt-rotor model and the GTRS. Color line patterns correspond to the 6DoF model while shapes connected with gray lines correspond to the GTRS data[5, app. A]. Nacelle tilt η and flap deflection angles indicated in legend.

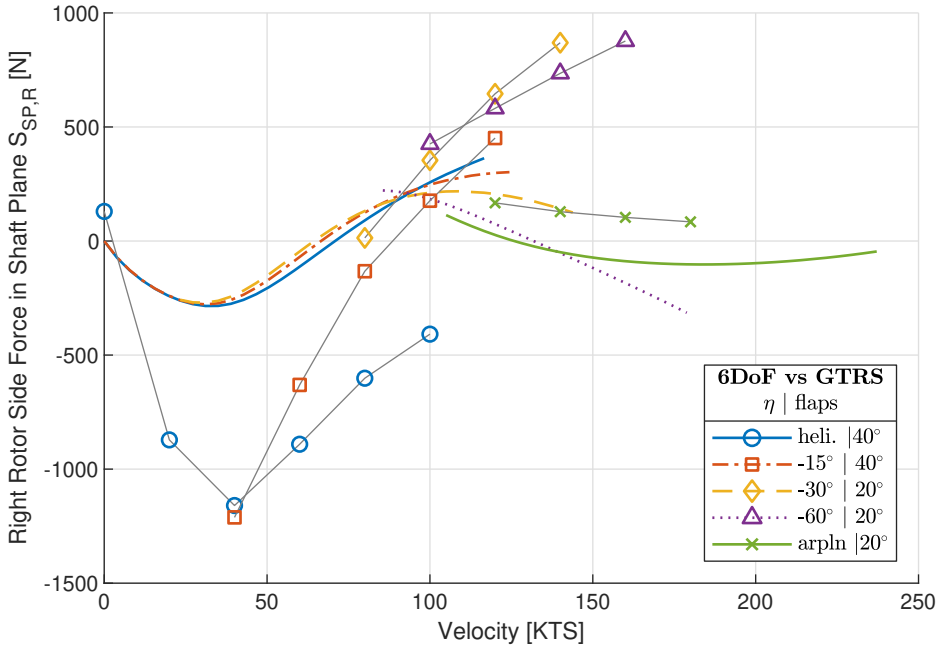

Figure 8.17: Comparison between the right counter-clockwise rotating rotor shaft plane side force trim curves of the 6DoF tilt-rotor model and the GTRS. Color line patterns correspond to the 6DoF model while shapes connected with gray lines correspond to the GTRS data[5, app. A]. Nacelle tilt η and flap deflection angles indicated in legend.

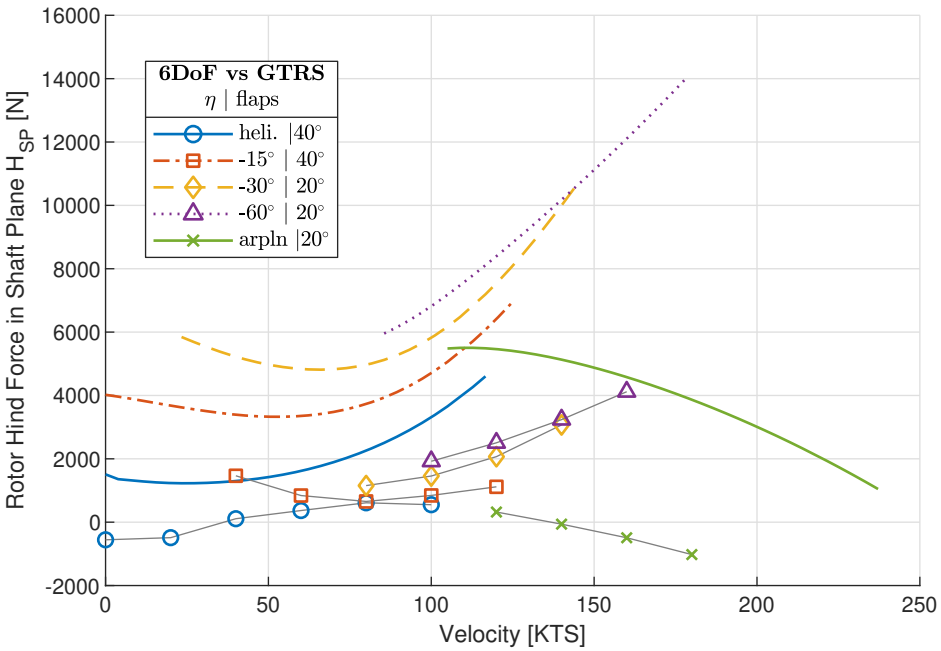

Figure 8.18: Comparison between the shaft plane rotor hind force trim curves of the 6DoF tilt-rotor model and the GTRS. Color line patterns correspond to the 6DoF model while shapes connected with gray lines correspond to the GTRS data[5, app. A]. Nacelle tilt η and flap deflection angles indicated in legend.

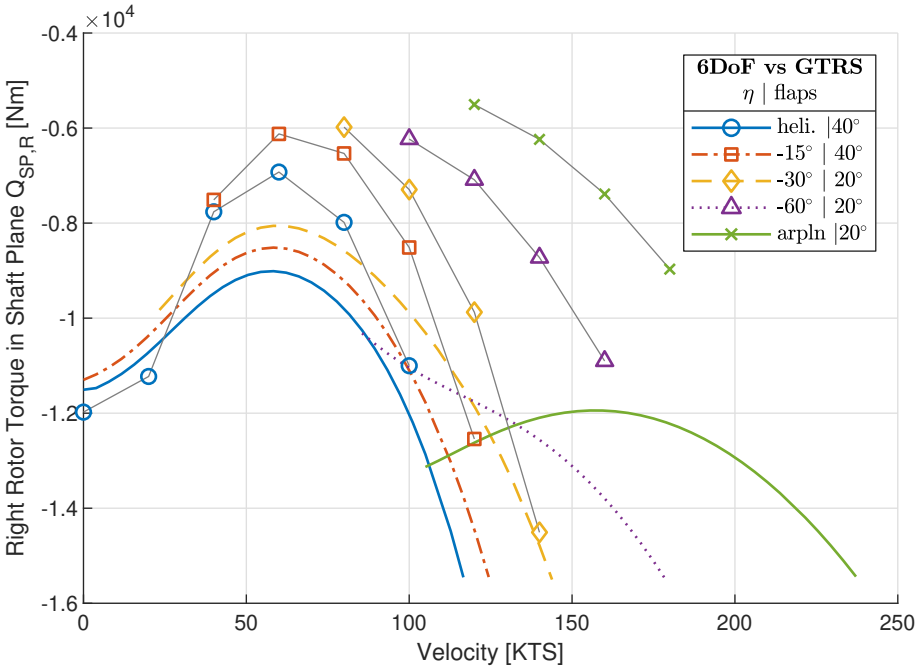

Figure 8.19: Comparison between the right counter-clockwise rotating rotor shaft plane torque trim curves of the 6DoF tilt-rotor model and the GTRS. Color line patterns correspond to the 6DoF model while shapes connected with gray lines correspond to the GTRS data[5, app. A]. Nacelle tilt η and flap deflection angles indicated in legend.

The required engine power is proportional to the rotor torque therefore the same conclusions about the validity of the torque trim curve trends may be applied to the trends of the engine power. For this reason the required engine power shall not be discussed here, however it is shown in fig. G.7 in appendix G for the interested reader. Similarly, the swashplate longitudinal cyclic deflection is largely proportional to the longitudinal stick deflection hence its analysis is unnecessary considering that the longitudinal stick trim curve has already been analyzed. Nonetheless, the swashplate longitudinal cyclic deflection trim curves are shown in fig. G.8 in appendix G. The implementation of the gearing between the longitudinal stick and longitudinal cyclic swashplate deflection shall, however, be verified in the subsystem validation section where the nominal longitudinal stick trim curve shall be replaced by the one of the GTRS providing more comparable data.

The trim curves of the two remaining rotor moments, O and P, acting on the rotor hub shall not be shown here since no other sources providing such data for a tilt-rotor have been found in literature, however they are shown in appendix G and shall be briefly analyzed here. Figure G.9 presents the (right) rotor spring reaction rolling moment $O_{SP,R}$ while fig. G.10 presents the rotor spring reaction pitching moment P_{SP}, both defined in the shaft plane. Recalling eq. (5.123), the P moment (defined in the wind axis control plane) is proportional to the $\widehat{a}_1$ disk tilt angle, and this proportionality may also be observed between the rotor pitching moment and longitudinal disk tilt angle defined in the non-wind axis shaft plane as demonstrated by the similarity between the two trim curve sets (i.e. fig. 8.14 and fig. G.10). The P moment is also not affected by the nacelle tilt near hover. The same cannot be said for the rolling moment and lateral disk tilt angle defined in the non-wind axis shaft plane as demonstrated by the clear differences between fig. G.9 and fig. 8.15 despite a similar proportionality existing between the O rolling moment (defined in the wind axis control plane) and $\widehat{b}_1$ disk tilt angle as given by eq. (5.122). The reason for this is that the transformation from the control plane to the shaft plane involves a rotation around the Y_{SP}-axis with the θ_{1s} angle which significantly affects the rolling moment. As a result the downward translation of the θ_{1s} trim curves as a function of nacelle tilt (shown in fig. G.8) can also be seen in the trim curves of the rolling moment. Note that the wind-axis control plane pitching moment P acts around an axis that is almost coincident with the Y_{SP}-axis therefore the θ_{1s} rotational transformation affects it to a much lesser degree resulting in a higher correlation between the P_{SP} moment $\widehat{a}_1$ angle.

Main Wing

The next subsystem to be validated is the main wing which consists of both wing halves of the tilt-rotor. As a result, in the case of the 6DoF model, the main wing comprises the forces and moments of all wing segments, namely the left and right free wing, flap wing, and aileron wing segments. The relative validation of this subsystem shall analyze the trim curve trends of the longitudinal and vertical forces acting along the X_b- and Z_b-axes respectively, as well as the total pitching moment acting at the body CoG around the Y_b-axis, all defined in the body reference frame.

Note that since most effort was put into the development of the rotor subsystem, the validation of the remaining subsystems, including the main wing, shall be less detailed. As a result, the validity of each subsystem is only be briefly discussed in this chapter while the trim plots are included in appendix G. Any differences between the trim curves of the two models are left to be investigated in a future research project.

Returning to the main wing subsystem, the variation of both the 6DoF model's longitudinal and vertical forces as a function of the velocity and nacelle tilt angle is generally in good agreement with the GTRS as shown in figs. G.11 and G.12. Both trim curves are almost entirely negative therefore references to magnitude shall refer to their absolute values. In summary, the longitudinal force becomes larger (in absolute terms) as the velocity increases and the trim curves are translated rightwards, i.e. a more 'dragging'[1] force is generated at the same velocity, as the nacelles tilt towards airplane mode. A familiar kink near hover in helicopter mode may be observed, similar to the one seen in the body angle of attack trim curve (fig. 8.9). The vertical force, on the other hand, experiences a peak at varying intermediate velocities (with the exception of airplane mode where the force linearly increases with velocity), while the trim curves are translated downward and to the right, the former meaning that a larger 'lifting' force is generated at the same velocity, as the nacelles tilt towards airplane mode. At velocities close to hover the nacelle tilt does not seem to have an effect on the trim curves.

The variation of the pitching moment as a function of both velocity and nacelle tilt angle is also mostly similar with the pitching moment peaking at various intermediate velocities in conversion and airplane mode as seen in fig. G.13. In helicopter configuration the pitching moment fluctuates around a constant value at low velocities, and clearly dips to negative values at higher velocities. The largest discrepancy may be observed in airplane mode, however, where the 6DoF trim curve does not have a peak. The variation of the trim curves as a function of the nacelle tilt is also similar for both models near helicopter configuration where the trim curves are translated upwards and to the right, the former meaning a more nose-up pitching moment is generated at the same velocity, as the nacelles tilt forwards. A significant divergence between the two models appear at nacelle tilt angles closer to airplane mode where in the case of the 6DoF model the trim curves continue to be translated upwards, while in the case of the GTRS the trim curves begin to translate downwards.

Horizontal Stabilizers

The next subsystem to be validated are the left and right horizontal stabilizers which are combined into one collective lifting surface. Similarly to the main wing, the relative validation of this subsystem shall analyze the trim curve trends of the longitudinal and vertical forces acting along the X_b- and Z_b-axes respectively, as well as the pitching moment acting at the body CoG around the Y_b-axis, all defined in the body reference frame.

Starting with the longitudinal force shown in fig. G.14, it appears that the trim curves of the 6DoF model and GTRS share little in common, especially considering the variation of this force as a function of velocity. The trim curves of the GTRS show a dip at intermediate velocities and a rise at higher velocities, while most of the 6DoF trim curves only show a decreasing tendency. The variation of the trim curves as a function of the nacelle tilt, however, is similar for both the 6DoF and GTRS model where the trim curves are translated rightward, i.e. a lower absolute 'dragging' force is generated at the same velocity, as the nacelles tilt towards airplane mode.

The majority of the pitching moment generated by the horizontal stabilizers originates from its vertical force acting at a considerable distance away from the body CoG. AS a result the vertical force and pitching moment trim curves, shown in figs. G.15 and G.16, are almost identical in shape for both the 6DoF model and GTRS,

[1] 'Dragging' is put between quotation marks since the longitudinal force is not aligned with the velocity vector and therefore it cannot be formally referred to as drag. Analogous reasoning applies to the 'lifting' force which is not perpendicular to the velocity vector.

demonstrating that this correlation has been implemented accurately in the 6DoF model. Furthermore, the effect of the nacelle tilt angle on both 6DoF trim curves is in good agreement with the effect observed in the trim curves of the GTRS, namely that the trim curves are translated downwards as the nacelle tilts forward with the exception of conversion angles very close to airplane mode in which case the trim curves are translated back upwards. This means that as the tilt-rotor begins converting from helicopter to airplane mode, the amount of 'lifting' force and nose-down pitching moment generated by the horizontal stabilizers increases until airplane mode is reached at which point the horizontal stabilizer starts to produce less 'lift' and a more nose-up moment. Finally, it must be noted that in both models the nacelle tilt has a negligible effect on the trim curves at velocities near hover. Similarly to the longitudinal force, the variation of the pitching moment and vertical force as a function of velocity appears to differ greatly between the two models due to the fact that the GTRS trim curves show a dip at intermediate velocities and a significant rise at higher velocities, while the same may only be observed in the airplane trim curve of the 6DoF model. The remaining trim curves only show a decreasing tendency.

At this point it is not clear whether the inaccuracies in the variation of the forces and moment as a function of velocity stem from the model equations or wrongly set parameters.

Vertical Stabilizers

In the 6DoF model the vertical stabilizers experience a local angle of attack which is equal to zero, hence the trim curves of the longitudinal force, pitching moment, and yawing moment all equal to zero. On the other hand, in the case of the GTRS the vertical stabilizers produce non-zero values which is suspected to be caused by the rotor and main wing wake effects at the tail which are not included in the 6DoF mode, however further investigation into the reasons behind this is left as a recommendation for the future. Since the 6DoF trim curves are all equal to zero, they do not provide any information for a meaningful discussion about the accuracy of the model. They validation trim curves are, however, shown in appendix G (figs. G.39 to G.41) and further discussed in the subsystem validation section where a brief analysis of the magnitude impact shall be performed. The only conclusion that may be made here is that the 6DoF model lacks some fundamental elements such as the rotor and wing wake effects at the tail which affect the forces and moments generated by the vertical stabilizer, which in turn may be a significant contributors to the flight mechanics of a tilt-rotor.

Fuselage

The fuselage is the final subsystem to be validated, however only the trim curve trends of the longitudinal force acting along the X_b-axis are analyzed in this section. Recalling section 5.4, the fuselage is modeled to only produce drag acting at the body CoG, and both the lift and pitching moment are assumed to be zero. As a result the total pitching moment of the fuselage is zero in all conditions, while the only vertical force that appear is a small component of the drag. For this reason the vertical force and pitching moment trim curves shall not be analyzed here, however the impact of the implemented fuselage simplifications on the whole model shall be discussed in the subsystem validation section. Nonetheless, these two trim curve sets are shown together with the appropriate GTRS validation data in figs. G.18 and G.19 in appendix G.

The longitudinal fuselage force mostly consists of the fuselage drag which is not dependent on the angle of attack (also see section 5.4), only on the total velocity. As a result the longitudinal force trim curves, shown in fig. G.17, corresponding to different nacelle tilt angles do not translate as a function of η since the total velocity is the same for all conversion angles. The GTRS fuselage drag, on the other hand, depends on the angle of attack, and since the body angle of attack trim curves translate as a function of nacelle angle, the fuselage longitudinal force trim curves also translate in a similar fashion. Apart from this discrepancy, the variation of the fuselage longitudinal forces as a function of velocity is similar for both models resembling a quadratic increase in the 'dragging' force of the fuselage as the velocity increases.

8.2.3. Effect of Nacelle Tilt Rate on Handling and Performance

Before continuing to the subsystem validation section, additional nominal trim curve plots have been generated for longitudinal and level flight showing the effect of the nacelle tilt rate $\dot{\eta}$ on the handling and performance of the tilt-rotor. The trim curves presented up to this point correspond to trim conditions where the nacelle tilt rate is set to zero. However, during converting flight the nacelles do not change their tilt angle instantaneously and instead they introduce an additional rotational rate which is experienced by

the rotor for the duration of the conversion. The effect of this additional rotational rate is non negligible and therefore must be taken into account in order to perform conversion flight in a controlled manner.

The effect of the nacelle tilt rate on handling and performance is chosen to be represented by the change in the trim curves of the longitudinal stick deflection and required engine power respectively in helicopter and airplane configurations. For sake of conciseness only the most affected trim curve is shown in this section, namely the required power engine in airplane configuration (fig. 8.20), while the airplane longitudinal stick trim curve (fig. G.22) as well as the helicopter power (fig. G.20) and longitudinal stick (fig. G.21) trim curves are shown in appendix G.

In summary, when compared to the non-conversion flight trim curves, converting from helicopter to airplane mode requires more power as the total velocity increases throughout the entire conversion process. Furthermore, more nose down longitudinal stick deflection is required in helicopter mode which gradually changes to more nose up longitudinal stick deflection while increasing velocity and nearing airplane mode. On the other hand, when converting from airplane to helicopter mode less power is required as the total velocity increases throughout the entire conversion process. In addition more nose up longitudinal stick deflection is required in helicopter mode which gradually changes to more nose down longitudinal stick deflection while increasing velocity and nearing airplane mode.

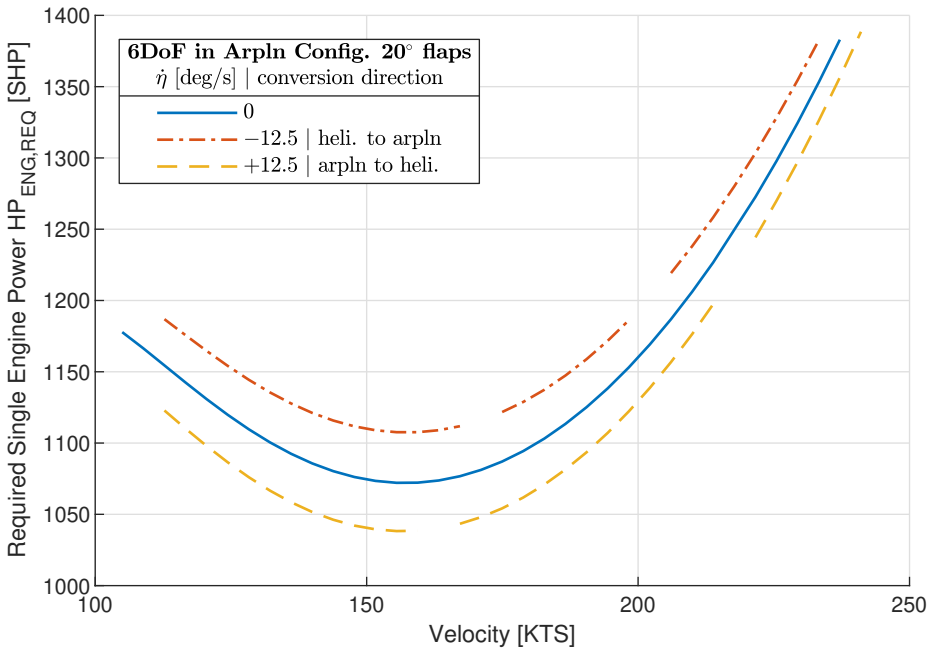

Figure 8.20: Effect of nacelle tilt rate on the required single engine power trim curves of the 6DoF tilt-rotor model in airplane configuration. Nacelle tilt rate $\dot{\eta}$ indicated in legend.

8.2.4. Subsystem Validation

The subsystem validation section shall compare the 6DoF model pseudo trim curves to the trim curves of the GTRS of the rotor, main wing, horizontal stabilizers, vertical stabilizers, fuselage, pilot throttle, and collective governor subsystems where the 6DoF model pseudo trim curves have been generated using the body angle of attack, longitudinal stick input, and swashplate collective trim solutions of the GTRS model already presented in the preceding sections. As a result the subsystems of the 6DoF model shall experience the same flight conditions and receive the same inputs as the ones of the GTRS model enabling a more accurate assessment of the validity of each subsystem. It must be recalled, however, that using the trim solution of the GTRS as input to the 6DoF model means that the latter will no longer be in trimmed flight yielding pseudo trim curves that may exhibit unexpected trends. For this reason the validation process shall only focus on comparing the similarity in magnitude between the trim curves of the two models, starting with the rotor subsystem. Also note that for the sake of brevity, the 6DoF model pseudo trim curves shall be sometimes simply referred to as trim curves.

Rotor

The rotor subsystem is validated by analyzing the trim curves of the induced velocity, disk tilt angles, and of the forces and torque defined in the shaft plane. The correct implementation of the gearing between the longitudinal stick and longitudinal swashplate deflection shall also be demonstrated at the end. Since the required engine power is proportional to the rotor torque, validating it here is considered unnecessary. However, the implementation of the calculation of the required engine power shall be verified later together with the validation of the distribution of the swashplate collective among the pilot and governor contributions where the rotor torque (and later also throttle deflection) trim solution of the GTRS shall be additionally used to calculate these three dependent variables.

The rotor subsystem validation starts with the comparison between the induced velocity trim curves of the 6DoF tilt-rotor model and the GTRS as shown in fig. 8.21. Although the rotors of both models experience the same flight conditions and receive the same swashplate inputs, their induced velocity trim curves are significantly different in magnitude, especially at lower velocities near helicopter configuration. This is all the more surprising considering that the nominal 6DoF induced velocity trim curves show a very good overlap with the validation data as has been shown in fig. 8.12. The pseudo trim curves slightly over estimate the induced velocity for almost all nacelle tilt angles, with the exception of airplane mode where at higher velocities the rotor enters the windmill brake state, depicted in fig. 5.14. In this state, instead of producing thrust, it starts to generate drag (see the thrust pseudo trim curve shown in fig. G.26), hence the induced velocity becomes negative, i.e. the air traveling through the rotor disk is not accelerated but slowed down, and the rotor extracts energy from the airflow (also see the reversal of torque sign shown in fig. G.29). The overestimation is greatest at lower velocities for all nacelle tilt angles, however the greatest divergence in comparison to the GTRS is present in helicopter mode.

Considering that the difference in magnitude between the induced velocity 6DoF model pseudo trim curves and GTRS trim curves is significant, and that the pseudo trim curves of the remaining rotor variables are dependent on the induced velocity, the remaining validation analysis shall be kept succinct and a more thorough analysis of an improved and more valid version of this rotor model is left as a recommendation for the future. For this reason all remaining rotor validation plots are also moved to appendix G to improve the readability of this chapter.

Returning to the rotor variable analysis, the disk tilt angle pseudo trim curves are compared next starting with the coning angle a_0 show in fig. G.23. The coning angle pseudo trim curves are overestimated for nacelle tilt angles closer to helicopter mode, and underestimated for nacelle angles closer to airplane mode. Similarly to the induced velocity, the greatest overestimation appears in helicopter mode while the greatest underestimation occurs in airplane configuration. The magnitude of the divergence is also highest for low and high velocities, while it is lowest at intermediate velocities. The longitudinal disk tilt a_1 pseudo trim curves shown in fig. G.24, on the other hand, are significantly overestimated almost for the entire nacelle tilt range, with the exception of airplane mode where the curves of the 6DoF model and GTRS almost completely overlap. The magnitude of the overestimation is mostly similar across the entire velocity range for all trim curves. Finally, the (right rotor) lateral disk tilt $b_{1,R}$ pseudo trim curves shown in fig. G.25 are significantly underestimated for almost all nacelle tilt angles except for airplane mode where the 6DoF model trim curves appear to reach an asymptote again (as was already pointed out in the subsystem trim curve trend validation section), while the GTRS trim curve continues to decrease. As a result the 6DoF model always seems to underestimate the magnitude (in absolute terms) of $b_{1,R}$. The largest underestimation occurs at lower velocities where the trim curves exhibit their distinct peaks.

The pseudo trim curves of the rotor forces are validated next, starting with the rotor thrust shown in fig. G.26. The thrust pseudo trim curves are significantly overestimated for almost the entire nacelle tilt range with the exception of airplane mode where at higher velocities the thrust is underestimated. Recalling that in airplane mode the induced velocity is also underestimated, this does not come as a surprise. It can also be seen that at higher velocities the 6DoF model thrust is negative meaning that the rotor effectively generates drag, still keeping in mind that the pseudo trim curves do not represent variables necessary to achieve a trimmed state with the 6DoF model. The magnitude of the overestimation is mostly consistent across the entire velocity range with the exception of conversion angles close to airplane mode where the overestimation decreases towards higher velocities. The overestimation and underestimation of the side force, on the other hand, fluctuates at different nacelle tilt angles and velocities, however the side force is generally underestimated in magnitude with some exceptions in conversion flight at intermediate velocities. The largest discrepancy

between the 6DoF and GTRS side forces occurs at lower velocities where the trim curves peak and at higher velocities with the nacelle tilt angle close to $-60°$. Unfortunately the rotor hind force is grossly overestimated for almost all conversion angles except for airplane mode, with the discrepancy quickly growing as velocity increases. Surprisingly, in airplane mode the trim curves of both models are not much different in magnitude with the 6DoF model hind force being overestimated (in the absolute sense) at higher velocities.

The only rotor moment to be validated is the rotor torque since validation data for the rotor pitching and rolling moments is not (explicitly) available in [5]. The torque pseudo trim curves are shown in fig. G.29 where it can be seen that the rotor torque magnitude is overestimated (in the absolute sense) for almost all conversion angles with the exception of airplane mode where at higher velocities the magnitude is underestimated. It must be remembered, however, that the airplane mode pseudo trim curve corresponds to a rotor that generates drag and extracts energy from the airflow, therefore at higher velocities the rotor torque changes sign meaning that the rotor starts to supply torque to the drivetrain. The large deviation of the torque close to airplane mode at high velocities may also be attributed to the small inflow angle assumption (i.e. $\phi_{BE} \ll 1$) which might be grossly violated in these flight conditions. The magnitude of overestimation is mostly consistent across the entire velocity range for each trim curve with the exception of conversion angles close $-60°$ where the magnitude decreases.

The required engine power is proportional to the rotor torque therefore comparing it here is considered unnecessary, however the calculation of the required engine power shall be later verified together with the distribution of the swashplate collective among the pilot collective stick deflection and collective governor contribution when the rotor torque trim solution of the GTRS will be used to calculate these three torque-dependent variables.

The final rotor subsystem pseudo trim curves to be inspected are the ones corresponding to the longitudinal swashplate cyclic deflection θ_{1s} shown in fig. G.32. It can be seen that the pseudo trim curves of the 6DoF model completely overlap with the ones of the GTRS, and recalling from section 4.4 that θ_{1s} depends on the pilot longitudinal stick deflection which has been set to equal to the trim solution of the GTRS, it can be concluded that the control mixing and phasing of the longitudinal stick has been implemented correctly. Note that despite the longitudinal stick deflection not being constant, in airplane mode the longitudinal swashplate cyclic is constant since all pilot control input is phased out by a constant non-zero value.

Before the other subsystems are validated in an analogous manner to the rotor, the rotor is additionally validated by plotting the (left) rotor torque as a function of the rotor thrust instead of the velocity, yielding a correlation plot. Again, both the thrust and torque must be transformed into the shaft plane in order to be able to compare the data with the one of the GTRS model. It is important to highlight that these torque and thrust values are not taken from the nominal nor pseudo trim data presented up to this point. Instead, the trim routine is modified such that the tilt-rotor (in helicopter configuration) is not able to move and the pilot collective-throttle stick input is varied from its minimal (0 inches) to its maximal (10 inches) deflection, effectively simulating a tie-down thrust test. In order to be able to use this data to validate the rotor model, it must first be non-dimensionalized by dividing the thrust by $\rho\pi\Omega^2R^4$ and the torque by $\rho\pi\Omega^2R^5$ yielding the thrust C_T and torque C_Q coefficients which may be plotted on top of the thrust-torque correlation plot of the GTRS model as shown in fig. 8.22.

Inspecting fig. 8.22 it can be seen that both the rotors of both the 6DoF and GTRS models show a positive nonlinear correlation resembling a parabolic function, however the slope of the correlation trend of the GTRS model is steeper. As a result the 6DoF model over predicts the torque at lower thrust magnitudes and under predicts it at higher thrust magnitudes. The only region where the ratio between the thrust and torque is similar for both models is in the mid-range of the thrust magnitude. The different slope of the trend of the 6DoF model may be caused by a mismatch of the drag coefficient of the blade which is a parabolic function of the blade angle of attack, which in turn depends on the pilot collective deflection. Keeping in mind that the trend of the correlation resembles a parabolic function as well, it is hypothesized that adjusting the blade drag coefficients may improve the overlap between the two correlation data sets and thus improve the validity of the rotor model. For this reason it is also believed that the derived rotor thrust and torque expressions are not at fault and thus they are considered valid at least for a generic tilt-rotor model. Nonetheless an investigation into the correct selection of the rotor blade drag coefficients and confirmation of the above hypothesis is left as a recommendation for the future.

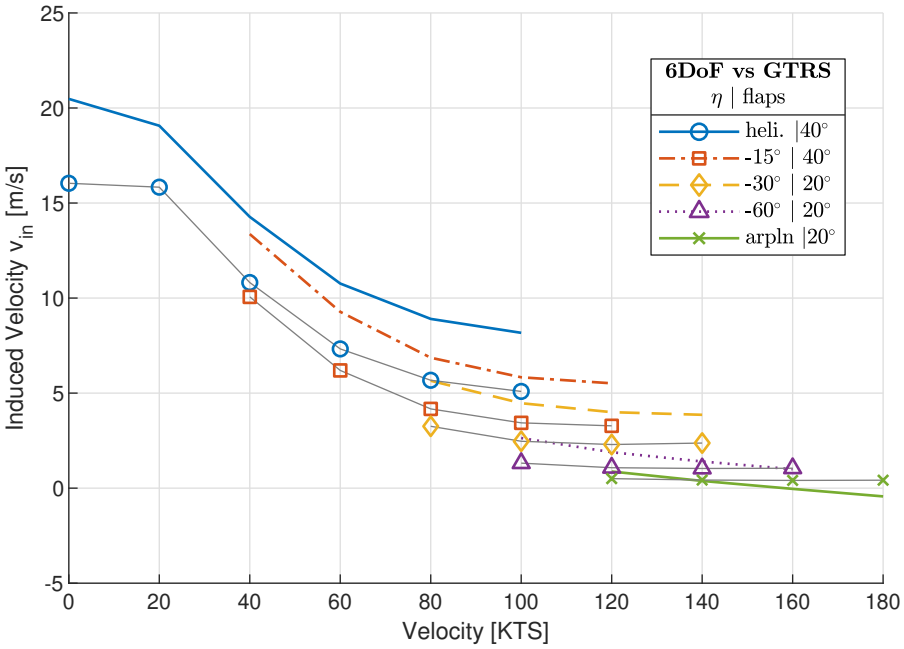

Figure 8.21: Comparison between the rotor induced velocity pseudo trim curves of the 6DoF tilt-rotor model and the GTRS. Color line patterns correspond to the 6DoF model while shapes connected with gray lines correspond to the GTRS data[5, app. A]. Nacelle tilt η and flap deflection angles indicated in legend.

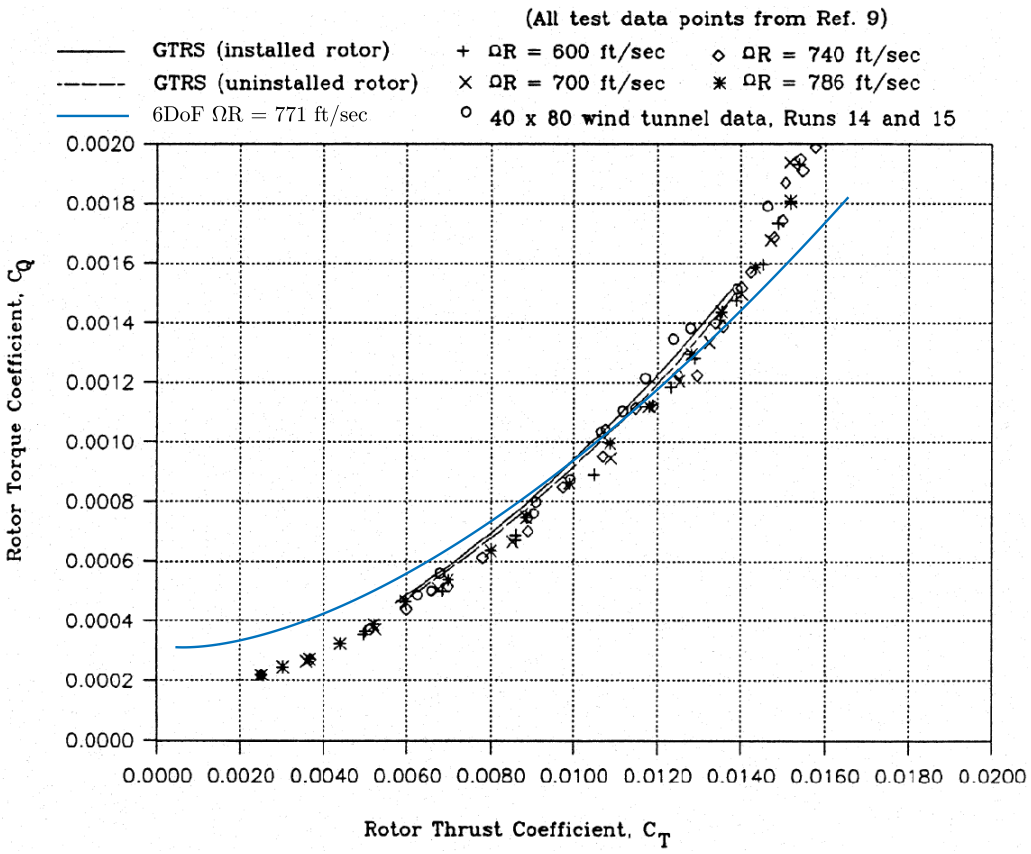

Figure 8.22: 6DoF tilt-rotor model left clockwise-rotating rotor thrust-torque correlation in a tie-down hover test plotted against the rotor thrust-torque correlation data of the GTRS model and real XV-15 tilt-rotor[5, p. 14 fig. 3].

Main Wing

The next subsystem to be validated is the combined main wing consisting of all wing segments as already explained in the trend validation section. The validation of this subsystem shall analyze the pseudo trim curves of the longitudinal and vertical forces acting along the body X_b- and Z_b-axes, as well as the total pitching moment acting at the body CoG around the Y_b-axis. Once again, since the current and the remaining subsystems were not the primary focus of the model development process, their pseudo trim curves are not shown here and instead are included in appendix G to improve the readability of this chapter.

The pseudo trim curves of the wing longitudinal force are shown in fig. G.33 where it can be seen that the 6DoF model force is underestimated, i.e. a less 'dragging' force is indicated, for almost all velocities and nacelle tilt angles with the discrepancy increasing with velocity for each conversion angle. Near airplane mode at lower velocities, however, the wing longitudinal force is overestimated. The wing vertical force shown in fig. G.34 is also significantly underestimated, i.e. less 'lifting' force is indicated, with a similar magnitude across the entire velocity range of each nacelle tilt angle. The underestimation does grow, however, as the nacelles tilt toward airplane mode. Finally the wing pitching moment is shown in fig. G.35 where it can be seen that it is also underestimated, i.e. a more nose down pitching moment is indicated, for helicopter mode and most of the conversion nacelle tilt angles, while near airplane mode the pitching moment is overestimated, i.e. a more nose-up pitching moment is indicated. Given that the wing aerodynamic center is in front of and above the body CoG, and that the majority of wing pitching moment acting on the body originates from the vertical and longitudinal forces, the 6DoF pitching moment is expected to continue to be underestimated in airplane mode since both the longitudinal and vertical forces of the 6DoF model are underestimated in airplane mode. Investigating why this is not the case is left as a recommendation for the future.

Horizontal Stabilizers

The combined horizontal stabilizers are validated next where the pseudo trim curves of the longitudinal and vertical forces, as well as the pitching moment acting at the body CoG, all defined in the body axes, are compared against the GTRS.

The horizontal stabilizer vertical force and pitching moment pseudo trim curves are shown in fig. G.37 and fig. G.38 respectively, where it can be seen that they are almost identical since most of the pitching moment is generated by the vertical force acting at a significant distance away from the body CoG. The missing model elements suggested in the subsystem trim curve trend validation section that result in a discrepancy in the trim curves (e.g. the effect of the rotor wash at the tail) have little impact near hover, however the magnitude of the difference does grow considerably at higher velocities and at nacelle angles closer to airplane mode. In airplane mode, where the magnitude of this difference is largest, the vertical force produced by the wings is almost an order of magnitude larger than the one produced by the horizontal stabilizer, therefore the suspected missing model elements do not significantly affect the tilt-rotor as a whole in this regard. In the same flight condition, however, the horizontal stabilizers are the largest contributors to the total body pitching moment[2] and therefore a discrepancy in the calculation of the pitching moment significantly affects the validity of the entire tilt-rotor flight mechanics model. For this reason it is highly recommended for the horizontal stabilizer model to be improved in the future. The horizontal stabilizer longitudinal force, on the other hand, has good overlap with the GTRS at lower and intermediate velocities, however it is grossly overestimated, i.e. a larger 'dragging' force is indicated, at higher velocities. However, given that the horizontal stabilizers are a minor contributor to the total body longitudinal force in comparison to the other subsystems, this deficiency in the model is not as crucial as the one related with the invalidity of the pitching moment.

Vertical Stabilizers

The next subsystem to be validated are the vertical stabilizers where the validation data given in [5] provides separate data for the left and right vertical stabilizer. Since the tilt-rotor is trimmed in longitudinal flight, the left and right vertical stabilizer data is symmetrical (in the $X_b - Z_b$ plane) therefore it is sufficient to only analyze one of the two stabilizers. In this case the data of the right vertical fin is analyzed. In contrast to the other subsystems, only the longitudinal force of the vertical stabilizer shall be analyzed since the vertical force trim solution is zero for the GTRS, while apart from the pitching moment, the yawing moment shall

[2] The combined left and right rotor pseudo trim curves of the pitching moment acting at the body CoG (which are not validated) are shown in fig. G.31 in appendix G to support this argument.

be additionally analyzed since it is not zero for the GTRS. Once again the force and moments are defined in the body frame of reference, and act at the body CoG. The pseudo trim curves of the vertical stabilizer force and moments are shown in figs. G.39 to G.41[3].

Before proceeding with the analysis it must be highlighted that the vertical stabilizers of the 6DoF model are aligned with the body axes therefore they experience a local angle of attack which is equal to zero in longitudinal flight. As a result the trim curves of the longitudinal force, pitching moment, and yawing moment all equal to zero. In the case of the GTRS, however, the vertical stabilizers produce non-zero values for unclear reasons. Therefore the validation of the vertical stabilizers only focuses on the impact of the magnitude of the differences between the two models on the overall validity of the model relative to the contributions of the other subsystems.

Returning to the analysis, in longitudinal flight the vertical stabilizer longitudinal force (fig. G.39) and pitching moment (fig. G.40) of the GTRS are minute in comparison to the other contributors[4]. The yaw moment, shown in fig. G.41, is of a similar order of magnitude to the pitching moment, however it has not been compared to the other subsystems therefore it is difficult to assess the importance of its validity in the model as a whole. It must be remembered, however, that in longitudinal flight the vertical stabilizers do not play as big of a role as they do in, for example, sideward flight, therefore the assessment of the impact of the difference between the 6DoF model and GTRS is greatly limited here. For this reason a more thorough investigation into the validity of the vertical stabilizers is left as a recommendation for the future, whilst a brief comparison between the 6DoF model and GTRS sideward flight trim curves shall be presented later serving as a rough and implicit assessment of the vertical stabilizer validity in this thesis.

Fuselage

The fuselage is validated next, however only the longitudinal force pseudo trim curves is shown since the other two trim sets corresponding to the fuselage vertical force and pitching moment do not change (noticeably) with respect to the nominal 6DoF model trim curves. Furthermore the GTRS validation data of these two trim variables has already been shown for the purposes of subsystem trim curve trend validation and can be found in figs. G.18 and G.19 in appendix G.

Inspecting the longitudinal force pseudo trim curves shown in fig. G.42 it can be seen that the magnitude of the 6DoF model force is underestimated, i.e. a smaller 'dragging' force is indicated', for all nacelle tilt angles across most of the velocity range. The underestimation grows as the velocity increases, however in the case of intermediate nacelle tilt angles the longitudinal force is slightly overestimated at lower velocities. Although the growth of the difference between the models is mostly the same for all nacelle tilt angles, the largest discrepancy appears at high velocities in helicopter configuration. The fuselage is not the most greatest contributor to the longitudinal force in the whole tilt-rotor model, however it is significant therefore it is suggested for the fuselage model to be revisited in the future.

Looking at the fuselage vertical force validation trim curves shown in fig. G.18 it can be seen that the 6DoF model underestimates the magnitude of the negative vertical force, i.e. indicating a smaller 'lifting' force. The underestimation quickly grows as the nacelles tilt towards airplane mode where the difference is largest. The magnitude of overestimation becomes more constant as a function of velocity towards airplane mode, while it varies significantly for the remaining nacelle tilt angles. At higher velocities in helicopter configuration where the GTRS vertical force is positive the 6DoF model overestimates the 'lifting' force. Considering the effect of the main wings, however, the fuselage is not considered a significant contributor to the vertical force in the whole tilt-rotor model therefore modeling its lift in the 6DoF model is not considered a priority.

Finally, keeping in mind that the 6DoF fuselage pitching moment is always equal to zero, inspecting the fuselage pitching moment validation trim curves shown in fig. G.19 it can be seen that for every nacelle angle at lower velocities the GTRS model indicates a nose up moment, while at higher velocities a nose down pitching moment. The magnitude of the difference between the 6DoF model and GTRS varies linearly at higher velocities. Relative to the other subsystems the fuselage is a significant contributor to the total body pitching moment, therefore revising the assumption that the aerodynamic center of the fuselage coincides

[3]Recalling section 4.2, the 6DoF model additionally segments the vertical stabilizer into a top and bottom half. For the purposes of this analysis the forces and moments generated by both halves are combined therefore the vertical plot label includes the word 'Combined'.

[4]The combined left and right rotor pseudo trim curves of the longitudinal force and pitching moment acting at the body CoG (which are not validated) are shown in fig. G.30 and fig. G.31 respectively in appendix G to support this argument.

with the body CoG, and expanding the fuselage model by a pitching moment is considered critical and thus left as a recommendation for the future.

Rotor Torque Dependent Subsystems Verification

This validation section is paradoxically concluded with the verification of the implementation of the rotor torque dependents subsystems consisting of the drivetrain power, the throttle stick, and collective governor. In order to be able to verify the correct implementation of these subsystems, apart from the trim variables, the rotor torque trim solution of the 6DoF model is additionally replaced by the trim solution of the GTRS in order to generate new pseudo trim curves, hence this verification subsection is included in the validation section.

Starting with the required engine power (related to the rotor torque through eq. (7.13)), the pseudo trim curves of the 6DoF model completely overlap the ones of the GTRS, as shown in fig. G.43 in appendix G, meaning that the calculation of the required engine power of the GTRS described in section 7.4 has been correctly implemented in the 6DoF model. Since this portion of the drivetrain is correctly implemented, it is possible to directly (without any additional trim solution substitution) inspect the throttle stick curves of the two models which depend on the required engine power.

Inspecting the the throttle stick deflection pseudo trim curves shown in fig. 8.23 it can be seen that the throttle deflection is slightly overestimated (with respect to the GTRS trim curves) for all nacelle tilt angles and the magnitude of this difference is mostly constant with a slight growth at higher velocities for each trim curve. The offset between the 6DoF and GTRS throttle curves exists probably due to the simplification made in eq. (7.13) where the commanded engine horsepower R_{SHP} is simplified to be equal to the total engine power HP_{ENG}. This is not the case in the GTRS model where instead the commanded engine power is a function of the velocity and nacelle tilt angle, among others. As a result, supplying this erroneous R_{SHP} value to the throttle stick function (eq. (7.13f)) yields an erroneous stick deflection. The correcting expansion of the drivetrain model is left as a recommendation for the future however.

The pseudo trim curves of the collective governor are treated last. It should be recalled, however, that the governor collective deflection is the difference between the required blade pitch (θ_0 which has already been set to the trim solution of the GTRS for the purposes of subsystem validation) and the blade pitch obtained from the deflection of the collective-throttle pilot lever, as already defined by eq. (7.11). Since the throttle stick pseudo trim curves do not overlap with the ones of the GTRS, the collective governor pseudo trim curves will also not coincide. Implementing the correcting expansion of the drivetrain should correct the discrepancy between the collective governor implementations, however when additionally replacing the 6DoF throttle stick deflection by the trim solution of the GTRS, a discrepancy between the collective governor trim curves of the two models still remains as shown in fig. 8.24. Surprisingly, the difference between the two models only exists in early conversion flight where the governor collective deflection is slightly underestimated in the 6DoF model, while in helicopter and close to airplane mode the trim curves coincide. Further investigation into this issue is also left as a recommendation for the future however.

8.3. Conversion Corridor Validation and Analysis

To conclude the trimmed longitudinal and level flight results, the XV-15 tilt-rotor implementation of the 6DoF model is once again trimmed in level flight, however this time the nacelle tilt angle is varied by 5° throughout the entire conversion range. Recording the lowest and highest velocity of each trim curve makes it then possible to generate a conversion corridor which shows the feasible trim region of the tilt-rotor plotted as a function of the total velocity and nacelle tilt angle. The conversion corridor of the 6DoF model shall be validated against the real XV-15 tilt-rotor and later analyzed indicating the limiting factors that bound the conversion corridor based on the trimming routine results.

Conversion Corridor Validation

Two conversion corridors have been generated for the 6DoF model. The first one corresponds to the XV-15 6DoF model implementation with the flap schedule presented in the trim validation data of [5], i.e. an inboard flap deflection of 40° for nacelle angles ranging from 5° up to (but not including) −30°, while the remainder of the conversion (including $\eta = -30°$) is performed with an inboard flap deflection of 20°. The second conversion corridor is generated for the same tilt-rotor implementation, however in this case the flap

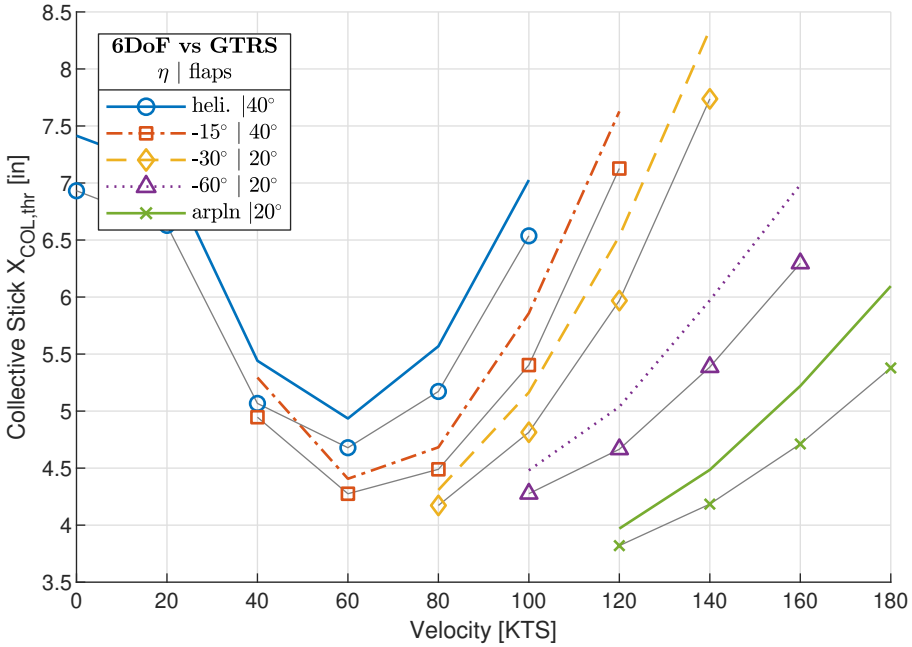

Figure 8.23: Comparison between the pilot throttle stick deflection pseudo trim curves of the 6DoF tilt-rotor model and the GTRS. Color line patterns correspond to the 6DoF model while shapes connected with gray lines correspond to the GTRS data[5, app. A]. Nacelle tilt η and flap deflection angles indicated in legend.

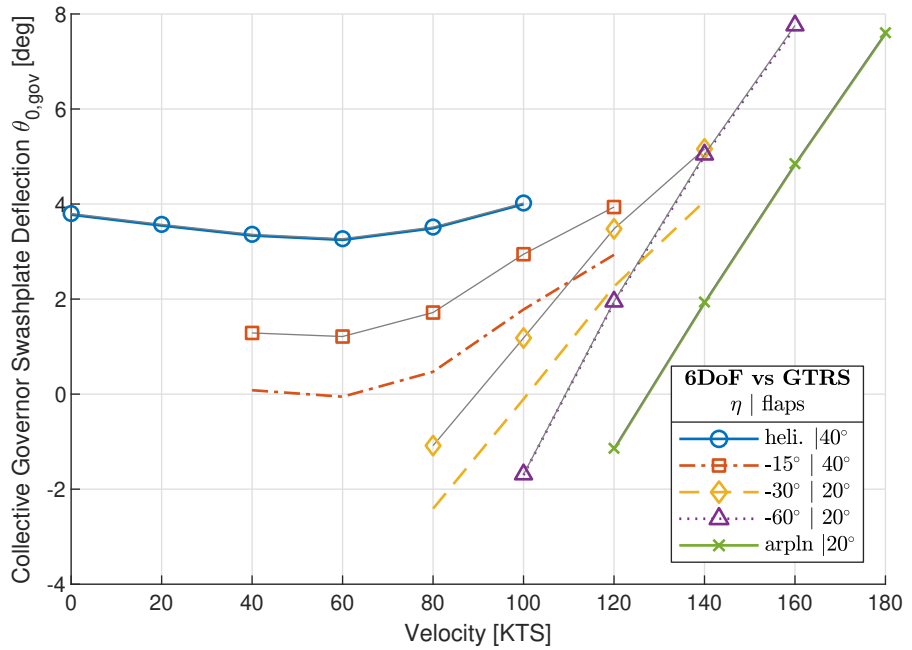

Figure 8.24: Comparison between the collective governor swashplate deflection pseudo trim curves of the 6DoF tilt-rotor model and the GTRS. Color line patterns correspond to the 6DoF model while shapes connected with gray lines correspond to the GTRS data[5, app. A]. Nacelle tilt η and flap deflection angles indicated in legend.

deflection is set to $0°$ for all conversion angles. Both of these conversion corridors are plotted together with the actual XV-15 conversion corridor taken from [2, p. 124], and the conversion corridor of the preliminary 3DoF tilt-rotor model, as shown in fig. 8.25.

Observing fig. 8.25 it can be seen that both 6DoF model conversion corridors cover similar regions with the flapped corridor being slightly narrower at higher velocities. Nonetheless, both of these estimate the higher velocity limits close to helicopter mode and lower velocity limits close to airplane mode quite well when compared to the real XV-15 conversion corridor. However, the 6DoF model significantly underpredicts the lower velocity limits for nacelle angles ranging between $-10°$ and $-45°$, while greatly overpredicting the upper velocity limits for nacelle angles ranging between $-60°$ and airplane mode. Note that in airplane mode the real XV-15 conversion corridor extends up to approximately 275 knots which is similar to the trim limits indicated by the 6DoF model. For this reason it is believed that the upper limits of the real XV-15 conversion corridor for nacelle angles ranging between $-60°$ and airplane mode are limited by model factors that are outside of the scope of this research project, such as diverging aeroelasticity, exceeded structural loads, or operational safety. The latter may also explain why the 6DoF model underpredicts the lower limit at nacelle tilt angles ranging between $-10°$ and $-45°$ where the body pitch angle required for trim is above $10°$ which may hinder pilot vision and thus be considered unsafe. On the other hand the conversion corridor predicted by the 6DoF model indicates the feasible trim region which is bounded by limits regarding pilot and governor inputs, blade flapping magnitude, and required engine power only. In general, however, the conversion corridor of the 6DoF model is considered mostly valid.

As a quick note, comparing the conversion corridors of the 3DoF and latest 6DoF model shows that the improvements and modifications made to the tilt-rotor model after the preliminary research phase resulted in the expansion of the conversion corridor in conversion flight at moderate velocities and near airplane mode, while the upper limits for conversion flight near helicopter configuration have been slightly reduced.

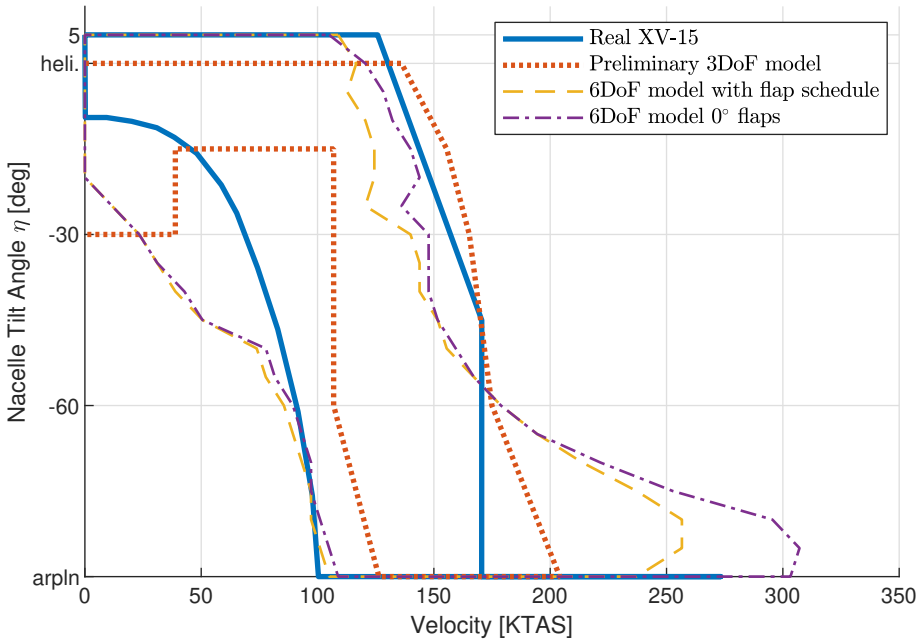

Figure 8.25: Comparison between the conversion corridors of the preliminary 3DoF tilt-rotor model, latest 6DoF tilt-rotor model with and without flap deflection, and the real XV-15 tilt-rotor.

Conversion Corridor Limits

A feature of the trimming routine described in section 7.4 is the capability to trim the tilt-rotor model outside the limits imposed by the real XV-15 tilt-rotor mentioned above, such as the pilot stick deflection limits. As a result it is possible to generate an augmented conversion corridor which shows the nominal feasible trim region and identifies all infeasible regions indicating the limits that are exceeded in those regions, as shown in fig. 8.26. Here the nominal feasible conversion corridor (corresponding to the 6DoF model without the

flap schedule) is bounded by a red border, while all other regions, indicated with different colors, outside of the border are infeasible. Each infeasible region is labeled with a single or several letters, with each letter corresponding to a different exceeded limit consisting of the pilot throttle (T) and longitudinal stick (L) deflections, total swashplate collective (C), flapping angle magnitude $|\beta|$ (B), and required engine power (P). The white regions indicate velocities for which the trimming routine did not find any solution.

Inspecting fig. 8.26 it can be seen that almost the entire upper velocity boundary of the feasible region is bounded by the power limit meaning that, primarily, it is not possible to achieve trimmed flight at higher velocities due to a lack of engine power indicated by the **P** belt. One exception is trimmed flight at a nacelle angle of $-85°$ where the conversion corridor is bounded by a maxed-out swash plate collective deflection indicated by the **C** region. It is no surprise that the power limit is accompanied next by the throttle deflection limit at even higher velocities for almost the entire conversion corridor indicated by the **PT** belt. However, if the engine power were to be increased, the next boundaries encountered by the tilt-rotor would consist of an exceeded flapping angle (indicated by the **PTB** region) at moderate conversion angles, and/or a maxed-out swashplate collective closer to airplane configuration (indicated by the **PC**, **PTC**, and **PTBC** regions). At conversion angles close to helicopter configuration the next limiting factor of the maximal trim velocity appears to be an insufficient longitudinal stick deflection range, however the trim data in this region is sparse thereby rendering this conclusion unreliable. The same applies to the limiting factors of the lower trim velocity boundary where at conversion angles closer to helicopter configuration the lower velocity is limited by the flapping magnitude and/or longitudinal stick deflection range (indicated by the **L** and **BL** regions). A small infeasible yet theoretically possible region corresponding to the tilt-rotor close to airplane configuration at very low velocities indicates that a trim solution is not feasible due to exceeded power, throttle, swashplate collective, and/or longitudinal stick deflection limits. In theory, however, the lower left corner of fig. 8.26 suggests that it would be possible to trim the tilt-rotor in airplane configuration in hover ignoring the exceeded limits.

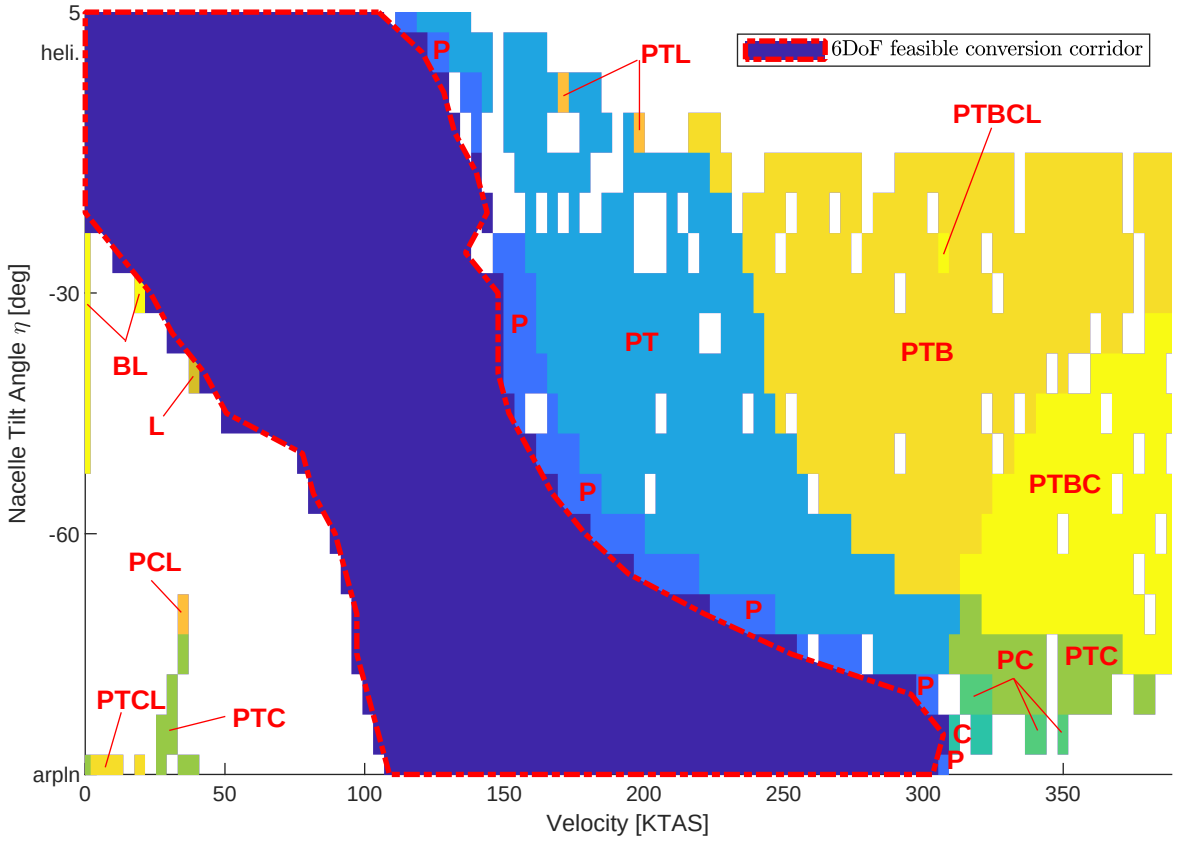

Figure 8.26: 6DoF tilt-rotor model (without flap deflection) conversion corridor additionally indicating infeasible regions with exceeded limits consisting of the pilot throttle (T) and longitudinal stick (L) deflections, total swashplate collective (C), flapping angle magnitude $|\beta|$ (B), and required engine power (P).

The conversion corridor section concludes the longitudinal and level trimmed flight results, while the next section treats longitudinal non-level trimmed flight.

8.4. Trimmed Climbing Flight and Haffner Diagrams

Apart from level flight, it is worthwhile exploring trimmed longitudinal climbing flight in which the trim conditions are adjusted such that the flight path angle γ_b no longer is equal to zero but instead varies across a desired range. Although such trimmed climbing flight data may provide useful predictions about the performance limits of the tilt-rotor, in this thesis report focus is put on the Haffner diagrams which may be derived from the same trim data. Haffner diagrams present the variation of the rotor induced velocity as a function of in-plane and axial velocities experienced by the rotor disk plane. Once such a diagram is generated, it provides a quick method of determining the induced velocity for different forward flight velocities without the need for an inflow solver such as the one presented in fig. 5.15.

The Haffner diagram of an isolated rotor based on the momentum theory, such as the one part of the 6DoF model, may be generated by solving for the induced velocity $\overline{v}_i$ in the Glauert expression defined in terms of the velocity components experienced by the rotor disk plane as given by eq. (8.2a). All velocities with an overbar symbol have been non-dimensionalized through a division by the rotor induced velocity in hover v_{ih} defined by eq. (8.2b) where W is the tilt-rotor weight which must be halved since the tilt-rotor has two rotors. As a result the non-dimensional induced velocity is given by eq. (8.2c). Although the non-dimensional total longitudinal velocity $\overline{V}$ and the disk plane angle of attack α_{DP} are part of the expression, they shall not be defined here since their combined product shall later be substituted by other already defined terms.

$$\overline{v}_i^2 = \frac{1}{\left(\overline{V}cos\left(\alpha_{DP}\right)\right)^2 + \left(\overline{V}sin\left(\alpha_{DP}\right) + \overline{v}_i^2\right)^2} \tag{8.2a}$$

$$v_{ih} = \sqrt{\frac{W/2}{2\rho\pi R^2}} \tag{8.2b}$$

$$\overline{v}_i = \frac{v_{in}}{v_{ih}} \tag{8.2c}$$

Returning to the Glauert expression, $\overline{V}cos\left(\alpha_{DP}\right)$ is the non-dimensional longitudinal in-plane airflow velocity defined positive coming from the front of the rotor disk and is given by eq. (8.2d). On the other hand $\overline{V}sin\left(\alpha_{DP}\right)$ is the non-dimensional axial airflow velocity defined positive coming from above the rotor disk and is given by eq. (8.2e). Both of these velocity components are defined in the disk plane reference frame and may be determined by transforming the longitudinal tangential V_{t1} and perpendicular V_{pc} control plane velocity components already defined by eq. (5.19) in the model development chapter. This simple transformation is only possible under the condition that the wind shift angle Δ is equal to zero. Note that the transformation from the control plane to the disk plane involves the longitudinal non-wind axis disk tilt angle a_1.

$$\overline{V}cos\left(\alpha_{DP}\right) = \frac{V_{tc1}cos(a_1) - V_{pc}sin(a_1)}{v_{ih}} \tag{8.2d}$$

$$\overline{V}sin\left(\alpha_{DP}\right) = \frac{-V_{tc1}sin(a_1) - V_{pc}cos(a_1)}{v_{ih}} \tag{8.2e}$$

Solving the Glauert expression and plotting the resulting $\overline{v}_i$ against the tangential velocity $\overline{V}cos\left(\alpha_{DP}\right)$ on the x-axis and the axial velocity $\overline{V}sin\left(\alpha_{DP}\right)$ on the y-axis produces a contour plot with mostly circular contours. Trimming the isolated 6DoF rotor model in forward flight for different flight path angles (ranging from vertical climbing to vertical descending) generates the data (i.e. the induced velocity, longitudinal disk tilt angle, and velocity components experienced by the disk plane) required to generate a model-specific Haffner

diagram. Plotting both the Glauert and model-specific Haffner diagrams together as shown in fig. 8.27 it can be seen that they overlap (almost) completely. This is expected since the 6DoF rotor model induced velocity solver is based on the momentum theory, therefore this result verifies the correct implementation of the momentum theory in the rotor model. Note that the trim data of the isolated rotor is obtained with the nominal trimming routine described in section 7.4, however in this case the primary independent variable is the flight path angle while the velocity continues to be the secondary independent variable. As a result the nacelle tilt angle becomes a trim condition which is constant for all trim curves.

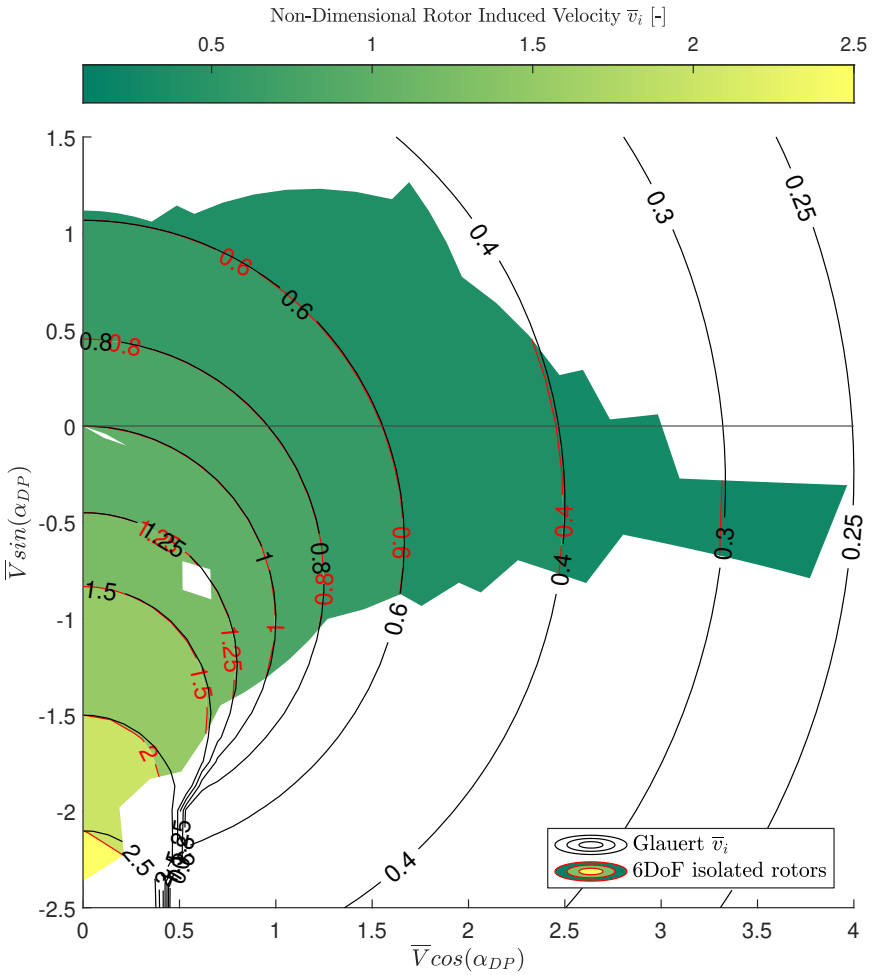

Figure 8.27: Haffner diagram corresponding to the isolated 6DoF rotor model plotted against the Glauert Haffner contours.

Unfortunately the Haffner diagram of a rotor installed on a tilt-rotor changes as a result of the aerodynamic effects of the other subsystems and, more so, as a function of the nacelle tilt angle, therefore each tilt-rotor configuration produces a unique Haffner diagram. For this reason several Haffner diagrams shall be presented corresponding to different configurations highlighting the effect of the tiltable proprotor on the Haffner diagram.

Similarly to the isolated rotor, however, in order to generate the Haffner diagrams, the tilt-rotor must first be trimmed in forward flight for flight path angles ranging from vertical climb to vertical descent. Once again the trim curves are obtained with the nominal trimming routine with the flight path angle being the primary independent variable while the nacelle tilt is a trim condition that changes depending on the tilt-rotor configuration. The resulting trim curves may be plotted against the Glauert Haffner diagram presenting the trimmed climbing and descending flight envelope of the 6DoF model XV-15 implementation as shown in fig. 8.28. Here each group of trim curves of the same color correspond to a single nacelle tilt angle, while each trim curve within the same color group corresponds to a different flight path angle. It must be highlighted, however, that the trimmed rotor induced velocities corresponding to those trim curves do not

coincide with the ones indicated by the Glauert Haffner diagram. The difference between the Glauert and configuration-specific Haffner diagrams clearly demonstrate this as is shown next.

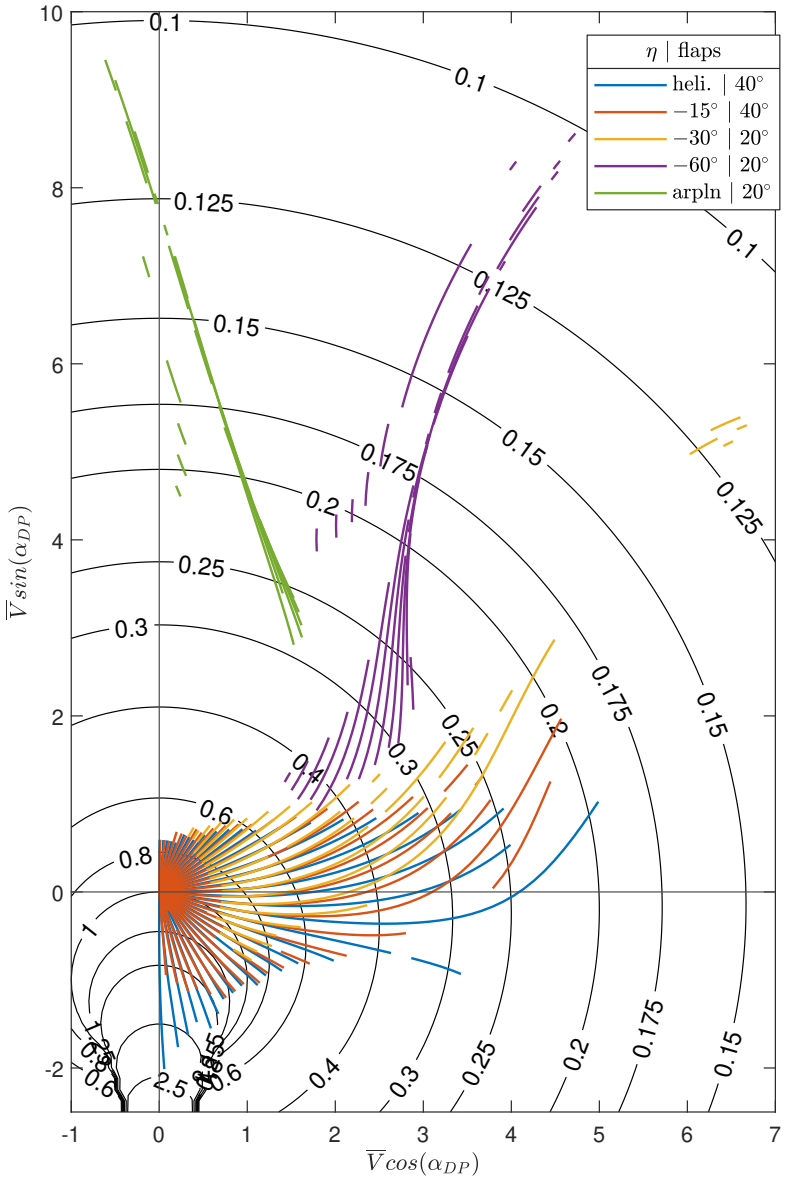

Figure 8.28: Climbing and descending flight trim curves of the 6DoF tilt-rotor model plotted against the Glauert Haffner contours. Nacelle tilt η and flap deflection angles indicated in legend.

Figure 8.29 compares the Haffner diagram of the tilt-rotor in helicopter configuration to the Glauert Haffner diagram. Before inspecting the plot it must be noted that the induced velocity in hover of the tilt-rotor in helicopter configuration is slightly higher than the one of the uninstalled rotor since the effect of the rotor wake on the wing introduces a downward force which must be compensated by an increased thrust. As a result the presented tilt-rotor Haffner diagram is generated using the higher induced velocity taken from the trim routine instead of the one calculated with eq. (8.2b). Furthermore, since not all tilt-rotor configurations are capable of hovering flight, for sake of consistency the same induced velocity in hover of the tilt-rotor in helicopter configuration is used to generate the Haffner diagrams corresponding to the other configurations. Returning to fig. 8.29 it can be seen that the two contour plots only closely overlap near hover and at low in-plane velocities. As the in-plane velocity increases the the tilt-rotor Haffner diagram indicates lower induced velocities than the Glauert expression. This trend is further amplified as the axial velocity becomes more negative, i.e. the rotor experiences descending flight, while the opposite is true for ascending flight.

Nonetheless, for almost the entire flight envelope in helicopter configuration the Glauert Haffner diagram overestimates the induced velocity.

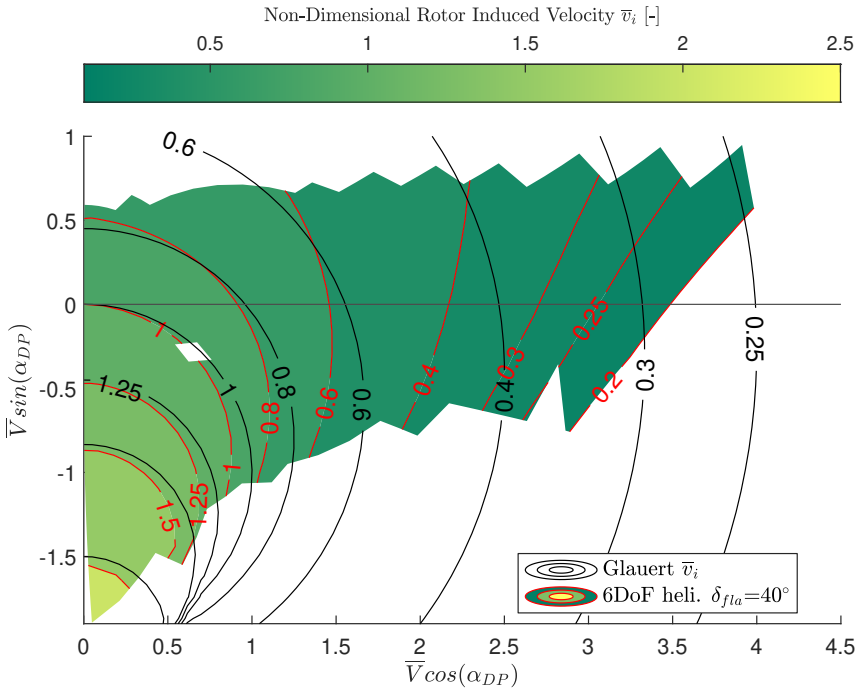

Figure 8.29: Haffner diagram corresponding to the 6DoF tilt-rotor in helicopter configuration plotted against the Glauert Haffner contours. Flap deflection angle indicated in legend.

The Haffner diagrams of the tilt-rotor in conversion flight with nacelle tilt angles set to $-15°$, $-30°$, and $-60°$ are shown in figs. G.44 to G.46 in appendix G to preserve report space. In general the same trends that have been observed in the helicopter configuration Haffner diagram apply to the Haffner diagrams corresponding to the remaining tilt-rotor configurations, including the most important conclusion which is the fact that the Glauert Haffner diagram overestimates the induced velocity for all configurations. The overestimation appears to grow as the tilt-rotor converts from helicopter to airplane mode.

The airplane configuration Haffner data is unfortunately too sparse to produce a readable contour plot therefore it is not shown in this report, however in this configuration the Glauert Haffner diagram also overestimates the induced velocity. It must also be added that in several descending flight conditions the tilt-rotor is capable of achieving trimmed flight with the rotors in windmill brake state, i.e. the rotors effectively generate drag to slow down the tilt-rotor, as has been explained with fig. 5.14. In this state the rotor induces a negative velocity which is not shown in the Glauert Haffner diagram.

8.5. Trimmed Sideward Flight in Helicopter Configuration Validation

After having treated trimmed longitudinal flight the next and final set of static flight results corresponds to non-longitudinal trimmed flight starting with level sideward flight in helicopter configuration. The 6DoF model may be trimmed in sideward flight using the nominal trimming routine described in section 7.4 with the sideslip trim condition β_b set to 90° to simulate sideward flight. Note that in order to be able to trim the 6DoF tilt-rotor in sideward flight, all trim decision variables (see eq. (7.16)) must not be constrained to equal to zero. This includes the lateral pilot inputs and body roll angle which may be and has been constrained (with the use of eq. (7.18)) when trimming in longitudinal symmetrical flight. The total velocity remains to be the secondary independent variable while, for the purposes of validation, the primary independent variable has been chosen to be the flap deflection angle which alternates between 0° and 40°. This has been done since it is not clear from the validation data provided in [5] whether the actual and simulated XV-15 tilt-rotor has its flaps deflected or not.

The sideward flight trim curves of three trim variables are plotted against the available validation data of the GTRS model provided in [5], namely the body roll angle ϕ_b, lateral pilot stick deflection (X_{LAT}), and pilot pedals deflection (X_{PED}) as shown in figs. 8.30 to 8.32 respectively. The validation data provides the trim curves of the GTRS model as well as the trim points measured during real XV-15 test flights as indicated in the legends of the plots. For sake of consistency the 6DoF model shall only be compared to the GTRS model, leaving the comparison with real flight data up to the reader.

Inspecting fig. 8.30 it can be seen that the 6DoF model body roll trim curves generally mostly overlap the ones of the GTRS with the 6DoF 0° flap deflection trim curve showing better overlap. The similarity between the two models is highest at lower velocities, however the 6DoF model begins to slightly underestimate the body roll angle magnitude as the sideward velocity increases (in absolute terms). Nonetheless both models show similar trim curve trends with the GTRS model exhibiting a more non-linear relationship between the roll angle and velocity.

6DoF tilt-rotor model body roll angle trim curves in helicopter sideward flight plotted against the rotor thrust-torque correlation data of the GTRS model and real XV-15 tilt-rotor[5, p. 14 fig. 3].
Looking at the lateral pilot stick deflection trim curves shown in fig. 8.31 it can be seen that a larger discrepancy exists between the 6DoF and GTRS models both in terms of magnitude and trend. In general the 6DoF model underestimates the magnitude of the lateral stick deflection required to achieve trim for all velocities when compared to the GTRS. The deflection of the flaps does not appear to have a significant effect on the trim curves. Furthermore the 6DoF trim curve is completely linear while the GTRS trim curves is piecewise linear with a kink at a velocity of around 20 knots. It is hypothesized that this behavior may be the result of some control phasing related to the differential rotor thrust that has been missed during the development stage of the 6DoF model. An investigation into this unknown is left as a recommendation for the future however. Note that the positive conventions of the lateral stick and pedal deflections of the GTRS are different from the ones of the 6DoF model. For sake of report consistency, all validation data is adjusted to be in accordance with the positive conventions of the 6DoF model therefore the vertical axes of the lateral stick and pedal trim plots are flipped.

Finally, inspecting the pedal deflection trim curves shown in fig. 8.32 it can be seen that once again both the 6DoF and GTRS models have closely overlapping trim curves with the 6DoF model slightly overestimating the required pedal input at higher sideward velocities. Furthermore the GTRS trim curve has a more linear trend than the trend of the trim curves of the 6DoF model. The flap deflection does not appear to have a significant effect on the trim curves.

In general the 6DoF tilt-rotor model in helicopter configuration in sideward flight is considered mostly valid with the exception of the lateral stick deflection which needs to be revised in a future iteration of the model.

8.6. Trimmed Sideslip Flight in Airplane Configuration Validation

The next set of non-symmetrical trimmed flight results corresponds to level flight in airplane configuration with a non-zero sideslip angle. Once again the 6DoF model is trimmed in slipping flight using the nominal trimming routine described in section 7.4, however in contrast to the constant value set in sideward flight, in this case the sideslip trim condition β_b is varied across a desired range. Moreover, the sideslip trim condition is set to be the secondary independent trim variable while velocity becomes the primary independent variable. As a result each trim curve shows the variation of a tilt-rotor state as a function of sideslip for a given fixed total velocity making it possible to validate the 6DoF model against the available GTRS sideslip data provided in [5]. Again it is not clear what the flap deflection is in the validation data therefore the 6DoF model presents trim curves corresponding to flap deflections alternating between 0° and 40°.

The sideslip flight trim curves of four trim trim variables are plotted, namely the body roll angle ϕ_b, lateral pilot stick deflection (X_{LAT}), pilot pedals deflection (X_{PED}), and pilot longitudinal stick deflection (X_{LON}) as shown in figs. 8.33 to 8.36 respectively. The validation data provides the trim curves of the GTRS model as well as the trim points measured during real XV-15 test flights at two different longitudinal velocities, i.e. 167 knots and 188 knots, as indicated in the legends of the plots. For sake of consistency the 6DoF model shall only be compared to the GTRS model, leaving the comparison with real flight data up to the reader.

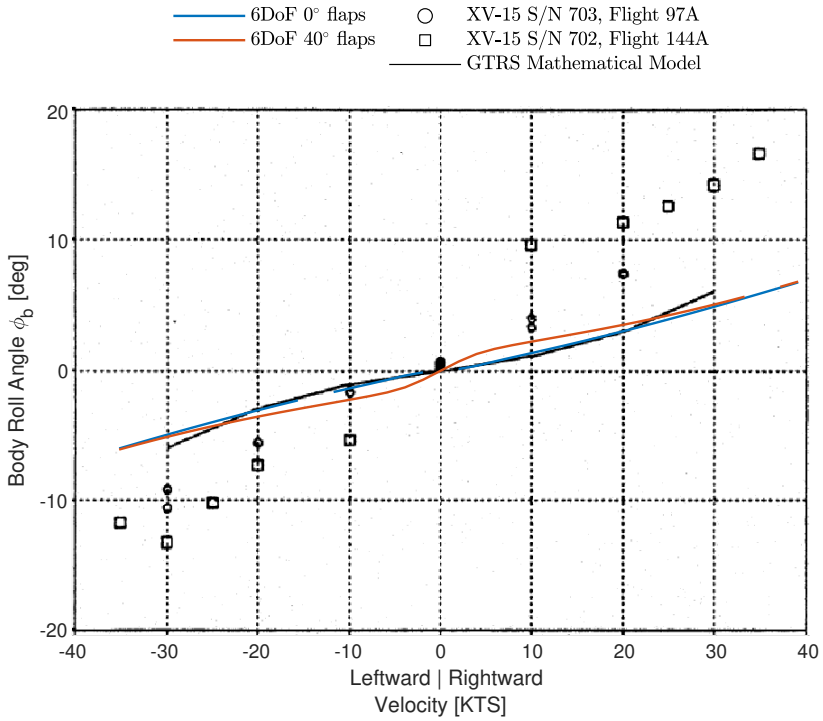

Figure 8.30: Comparison between the body roll angle trim curves of the 6DoF tilt-rotor model, GTRS model, and real XV-15 tilt-rotor in trimmed helicopter sideward flight[5, p. 26 fig. 9]. 6DoF model flap deflection angles indicated in legend.

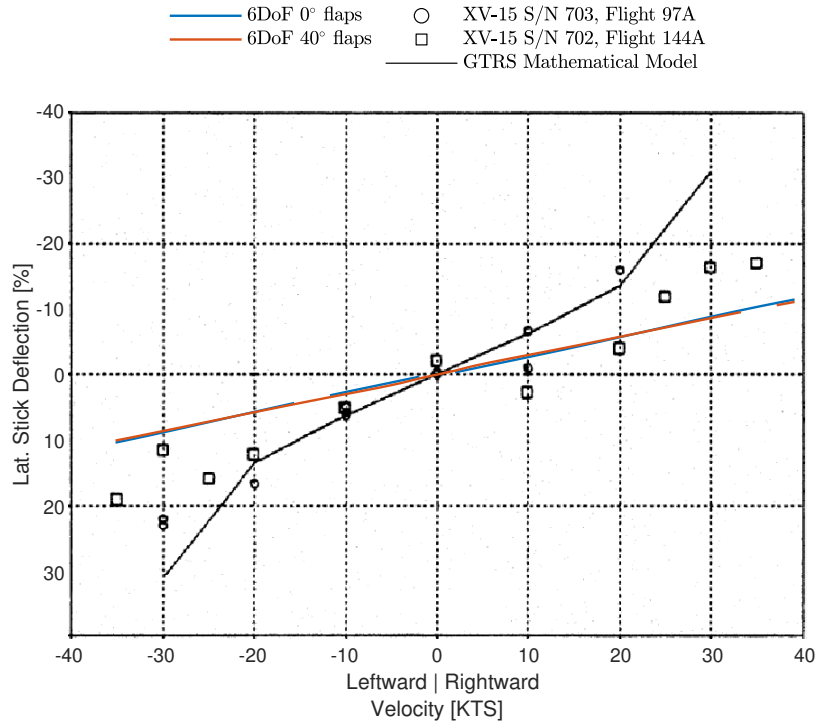

Figure 8.31: Comparison between the lateral stick deflection trim curves of the 6DoF tilt-rotor model, GTRS model, and real XV-15 tilt-rotor in trimmed helicopter sideward flight[5, p. 26 fig. 9]. 6DoF model flap deflection angles indicated in legend.

Inspecting fig. 8.33 it can be seen that the trim curves of the 6DoF model have a similar trend to the GTRS where the body roll angle increases linearly as the angle of sideslip increases, and the magnitude of the roll angle at the same angle of sideslip grows as a function of velocity. Nonetheless, the 6DoF model slightly underpredicts the body roll angle when compared to the GTRS model. The effect of the flap deflection is observable yet considered insignificant in comparison to the effect of the velocity.

Looking at the lateral pilot stick deflection trim curves shown in fig. 8.34 it can be seen that once again a larger discrepancy exists between the 6DoF and GTRS models both in terms of magnitude. In general the 6DoF model greatly overestimates the magnitude of the lateral stick deflection required to achieve trim when compared to the GTRS, however both models show the same negative linear correlation (note the flipped vertical axis) between the lateral stick deflection and angle of sideslip. A surprising observation is the fact that the slope of the linear correlation increases as a function of velocity in the case of the 6DoF model while the trim curves of the GTRS are unaffected by the total velocity. Due to the large discrepancy between the trim curves of the two models an investigation into the deficiencies of lateral stick input in sideslip flight in airplane mode is left as a recommendation for the future. Finally the deflection of the flaps has a minute effect on the 6DoF trim curves. Note that once again the vertical axes of the lateral stick and pedal deflection trim plots has been flipped due to a difference in positive pilot input conventions between the 6DoF and GTRS model.

Inspecting the pedal deflection trim curves shown in fig. 8.35 it can be seen that both the 6DoF and GTRS models have almost completely overlapping trim curves with linear trends. The slope of the GTRS trim curves increases as a function of the total velocity while the 6DoF trim curves appear to be unaffected. As a result the 6DoF model overestimates the pedal deflection required for trim at lower velocities. The flap deflection does not appear to have a significant effect on the 6DoF trim curves.

Finally, observing the longitudinal stick deflection trim curves shown in fig. 8.36 it can be seen that a large discrepancy in magnitude exists between the 6DoF model and GTRS with the 6DoF model requiring a more nose-up stick deflection for both velocities. However this discrepancy has already been discussed in section 8.2 therefore only the variation of the longitudinal stick as a function of sideslip angle shall be addressed here. It can be seen that the GTRS model shows a somewhat convex trim curve requiring more nose-down stick deflection as the angle of sideslip increases, while the opposite is shown by the concave 6DoF model trim curves indicating a more nose-up stick deflection as the sideslip angle increases. Furthermore the curvature of the GTRS trim curves does not appear to change as a function of total velocity while in the case the of the 6DoF model the trim curves corresponding to the lower velocity appear to be curved more. The effect of the flap deflection is also significant, however it acts against expectations since the trim curves indicate that more nose-down stick deflection is required with the flaps deflected which is contradictory to the expectation that the flaps introduce a more nose-down pitching moment which would require a more nose-up stick deflection to counter the nose-down pitching moment. Investigation into this anomaly and possible invalidity of the wing model is left as a recommendation for the future.

In general the body roll angle and pedal deflection required for trimmed sideslipping flight in airplane configuration prediction made by the 6DoF tilt-rotor model is considered valid, however the same cannot be said for the lateral and longitudinal stick deflection predictions which need to be investigated and revised in a future iteration of the tilt-rotor model.

8.7. Dynamic Analysis and Validation in the Time Domain

The sideslip trim curves conclude the static validation of the tilt-rotor, however the last set of simulation results presented in this thesis work corresponds to dynamic flight and its analysis and validation in the time domain. These results consist of simulating the responses of the 6DoF tilt-rotor model to step pilot inputs with the use of the Simulink simulation described in section 7.3. All simulation runs begin with 6DoF model in a trimmed state which is determined with the use of the trimming routine described in section 7.4 with the flight conditions set to the ones corresponding to the validation data provided in [5] which presents the step inputs and responses of the GTRS model as well as real flight data of the inputs and responses of the actual XV-15 model. All validation data has been obtained or generated with the tilt-rotor Stability and Control Augmentation System (SCAS) turned off. For sake of brevity and consistency the step inputs are based on the (smoother) GTRS inputs and the 6DoF model responses are only compared to the responses of the GTRS model, leaving the comparison with real flight data up to the reader.

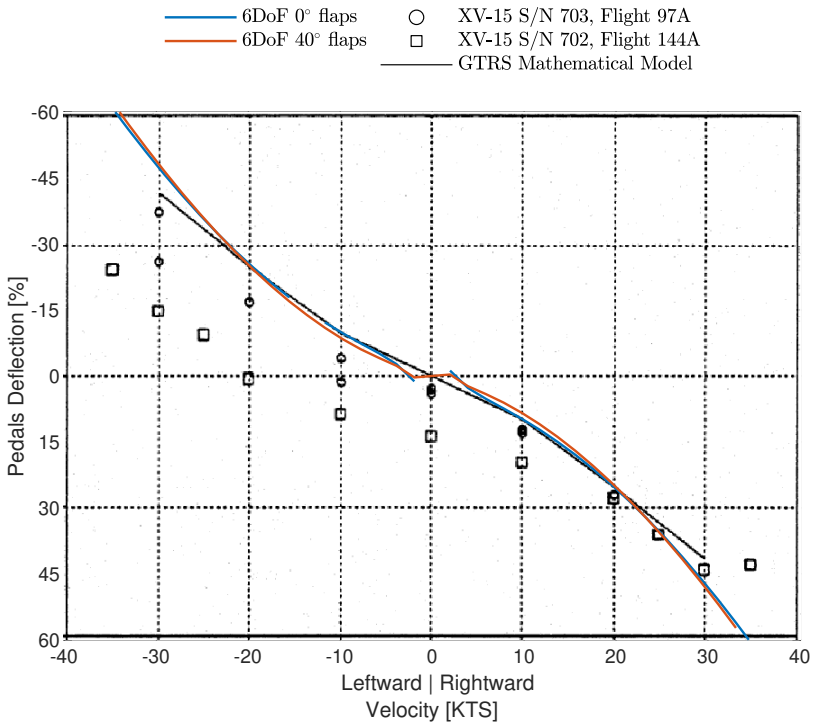

Figure 8.32: Comparison between the pedals deflection trim curves of the 6DoF tilt-rotor model, GTRS model, and real XV-15 tilt-rotor in trimmed helicopter sideward flight[5, p. 26 fig. 9]. 6DoF model flap deflection angles indicated in legend.

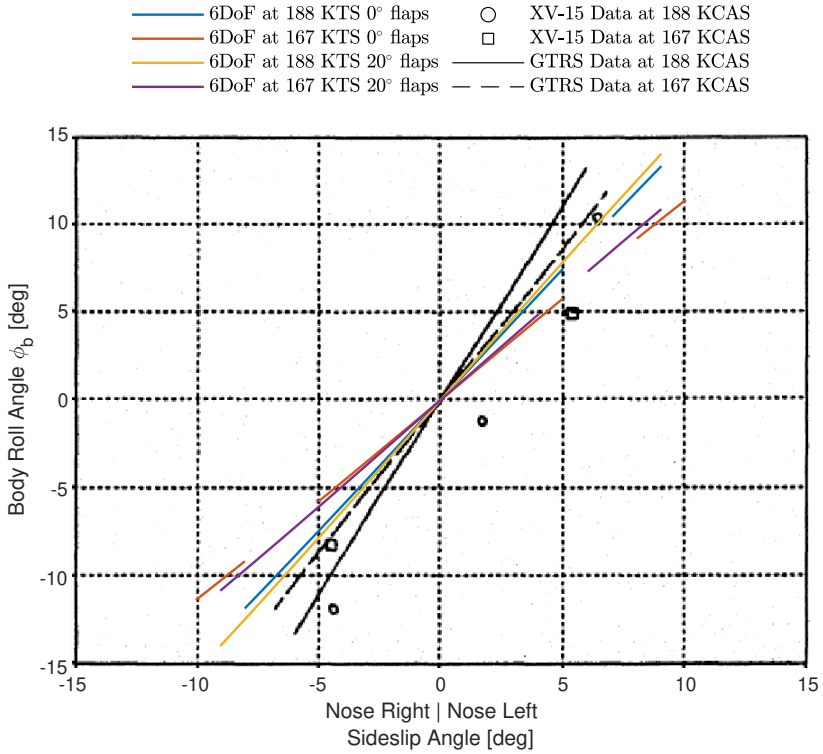

Figure 8.33: Comparison between the body roll angle trim curves of the 6DoF tilt-rotor model, GTRS model, and real XV-15 tilt-rotor in trimmed airplane sideslipping flight[5, p. 45 fig. 19]. 6DoF model flap deflection angles indicated in legend.

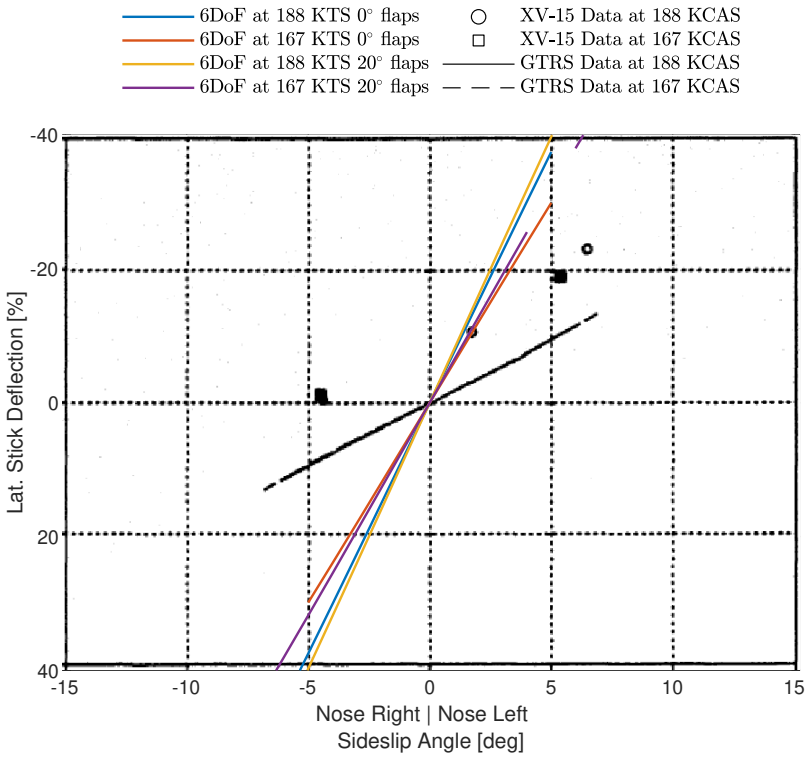

Figure 8.34: Comparison between the lateral stick deflection trim curves of the 6DoF tilt-rotor model, GTRS model, and real XV-15 tilt-rotor in trimmed airplane sideslipping flight[5, p. 45 fig. 19]. 6DoF model flap deflection angles indicated in legend.

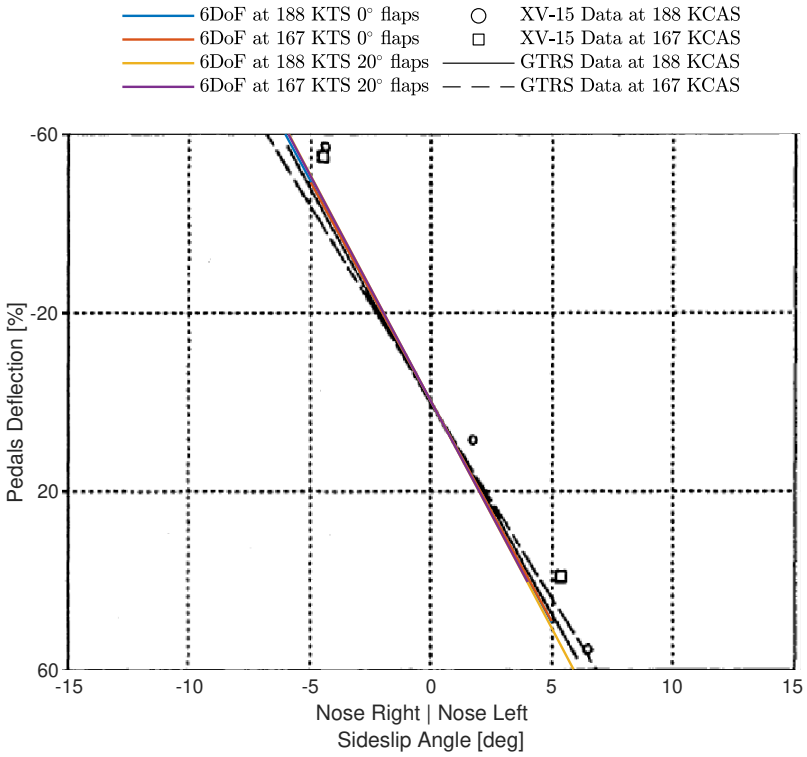

Figure 8.35: Comparison between the pedals deflection trim curves of the 6DoF tilt-rotor model, GTRS model, and real XV-15 tilt-rotor in trimmed airplane sideslipping flight[5, p. 45 fig. 19]. 6DoF model flap deflection angles indicated in legend.

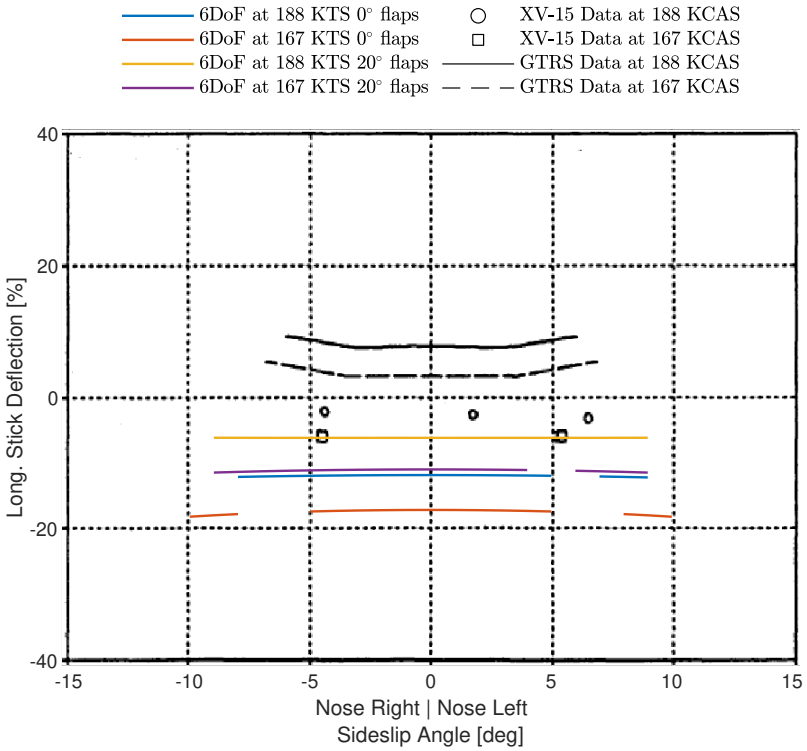

Figure 8.36: Comparison between the longitudinal stick deflection trim curves of the 6DoF tilt-rotor model, GTRS model, and real XV-15 tilt-rotor in trimmed airplane sideslipping flight[5, p. 45 fig. 19]. 6DoF model flap deflection angles indicated in legend.

In total the responses to five step inputs are presented. The first two simulations consist of the responses of the tilt-rotor in helicopter configuration in trimmed hover to step inputs of the longitudinal stick and pedals. The remaining three simulations consist of the responses of the tilt-rotor in airplane configuration in longitudinal trimmed level flight to step inputs of the longitudinal and lateral stick, as well as the pedals.

Longitudinal Stick Step Input in Hover

A combined chart of the longitudinal stick step input as well as the body pitch attitude θ_b and rate $\dot{\theta}_b$ responses is presented in fig. 8.37 with all three plots sharing a common horizontal time axis. Since the GTRS step input is terminated at around the 6 second mark, the corresponding attitude and rate responses shall only be compared up to that point in time. Note that the 6DoF model longitudinal step input curve is shifted downwards to match the stick deflection required to achieve trim in hover.

Apart from the steady state offset between the GTRS and 6DoF model attitude caused by a difference in trim solution, inspecting the pitch attitude and rate responses it can be seen that the 6DoF model has a slightly milder response with respect to the GTRS model achieving a smaller change in pitch and a smaller in magnitude pitch rate in the 6 second time frame. Since the tilt-rotor is in hover, one of the culprits of the difference between the responses may be the 6DoF rotor model. However the initial pitch rate response between the 3 and 4 second mark shows good overlap while the difference increases as the pitch rate increases. This may hint that instead of the rotor model being at fault, other subsystems that take effect only when the rotational rate of the body is higher, such as the horizontal tail stabilizer, may be the cause of the discrepancy. For this reason an investigation into this issue is left as a recommendation for the future while the pitch response of the 6DoF model in helicopter configuration in hover is considered only somewhat valid until then.

Pedal Step Input in Hover

The next time simulation corresponds to a pedal step input in helicopter configuration in hover with the combined chart of the input as well as the body yaw attitude ψ_b and rate $\dot{\psi}_b$ responses is presented in fig. 8.38 with all three plots sharing a common horizontal time axis. In this case the GTRS step input is

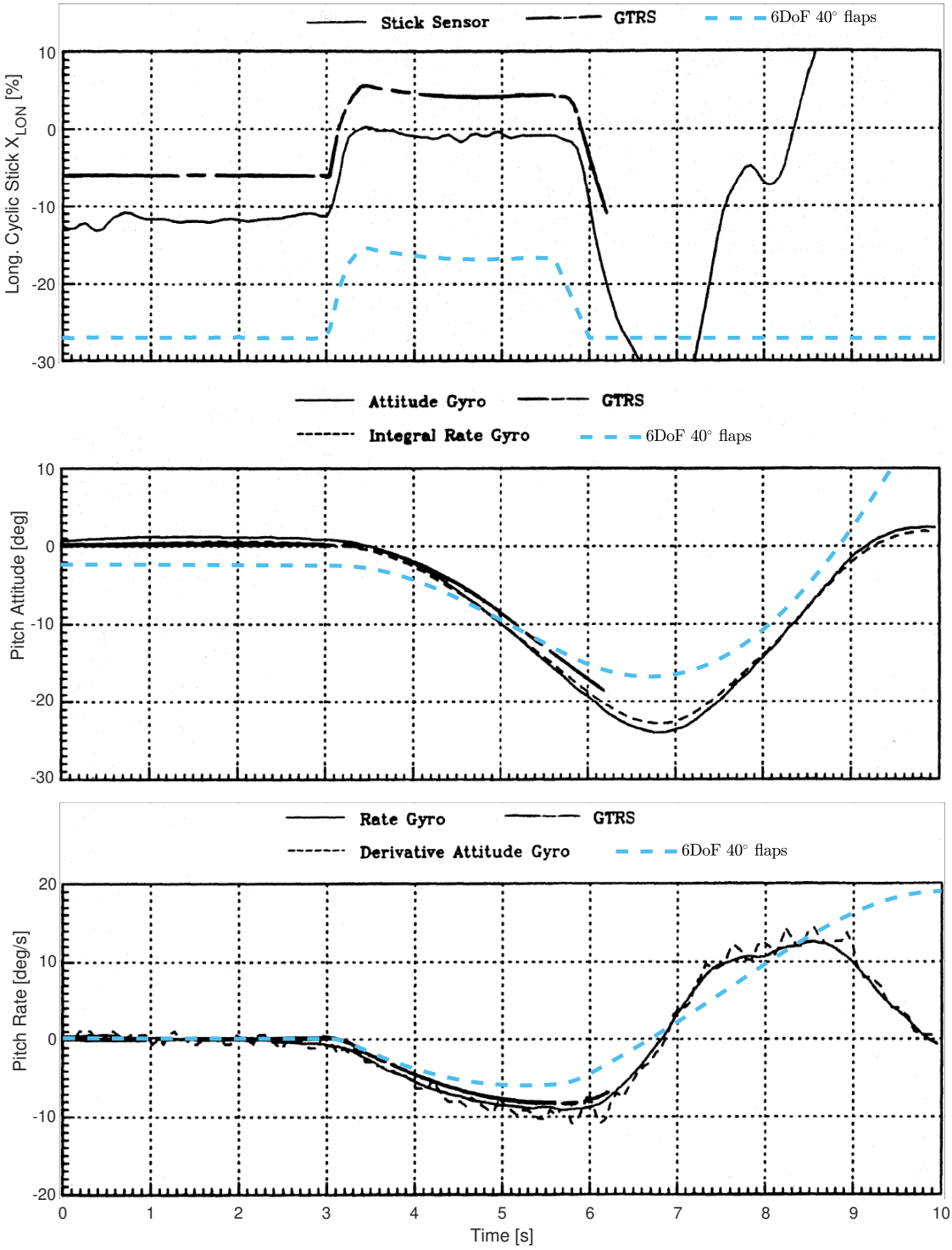

Figure 8.37: Comparison between the pitch responses of the 6DoF tilt-rotor model, GTRS model, and actual XV-15 tilt-rotor in helicopter configuration in hover to a longitudinal stick step input. 6DoF model flap deflection indicated in the legend.

terminated at around the 8 second mark, therefore the corresponding attitude and rate responses shall only be compared up to that point in time.

Inspecting the yaw attitude and rate responses it can be seen that the 6DoF model almost completely overlaps the response of the GTRS model with a small non-linearly growing underestimation of both states with time. Once again since the discrepancy grows in a non-linear fashion it is hypothesized that the differences in responses arise due to the invalidity of subsystems other than the rotor, such as the vertical tail stabilizer. In general, however, the yaw response of the 6DoF model in helicopter configuration in hover is considered mostly valid (within the yaw rate range presented in the plots).

Longitudinal Stick Step Input in Airplane Configuration

The third time simulation corresponds to the response of the tilt rotor in airplane mode trimmed in level flight at 175 knots to a longitudinal stick step. The combined chart of the input as well as the body pitch attitude θ_b and rate $\dot{\theta}_b$ responses is presented in fig. 8.39 with all three plots sharing a common horizontal time axis. In this case the GTRS step input is terminated at around the 8 second mark, therefore the corresponding attitude and rate responses shall only be compared up to that point in time.

Apart from the steady state offset between the GTRS and 6DoF model attitude caused by a difference in trim solution, inspecting the pitch attitude and rate responses it can be seen that the 6DoF model has a significantly more aggressive response with respect to the GTRS model. Before the results are analyzed any further, it must be noted that the elevator aerodynamic effectiveness in the 6DoF model is constant and does not depend on the angle of attack of the control surface, while according to [6, fig. 15] the effectiveness significantly drops at higher angles of attack of the horizontal stabilizer resulting in a lifting force that is roughly half of what is predicted with the nominal constant control effectiveness. For this reason the aerodynamic effectiveness of the elevator is temporarily halved to approximate the actual aerodynamic impact of the elevator in high speed airplane flight enabling a more accurate validation process of this dynamic motion of the 6DoF model.

Figure 8.40 presents the same longitudinal stick step input response as before, however in this case the elevator aerodynamic effectiveness $\partial C_{L,hs}/\partial \delta_e$ is halved as indicated in the plot legends. Although the adjusted model is less aggressive, the responses still do not overlap well. Looking at the pitch rate it can be seen that the amplitude of the short period mode is similar for both models, however the 6DoF response frequency is observably lower and the oscillations are less damped with the pitch rate returning to an almost zero value. For this reason the 6DoF model short period motion is considered only somewhat valid.

The phugoid motion of the GTRS may be already observed in the pitch attitude response while the same cannot be observed in the response of the 6DoF mode. Since the dynamic validation of the 6DoF model presented in this thesis is limited to the time domain only, at this point it is not possible to assess the validity of the phugoid mode of the 6DoF model. However, a similar longitudinal stick step input response (without the termination of the input) is plotted for a longer period of time as shown in fig. 8.41, providing evidence that the 6DoF model does exhibit phugoid mode motion. Here two responses are shown, one corresponding to the 6DoF model with the collective governor turned on, while in the second response the governor is turned off. Note that the 6DoF responses shown up until this point, including the previous response shown in fig. 8.40, correspond to the model with the governor turned on. Returning to fig. 8.41, the phugoid motion can be clearly observed in the response with the collective governor turned off, in which case the rotational rates of the rotors are free to vary and the collective pitch remains constant (given that the pilot collective input does not change). On the other hand, turning the collective governor on greatly influences the longitudinal response, not only heavily dampening the phugoid motion, but also distorting it from the damped sinusoidal shape. Unfortunately the validity of this result is not investigated in this report, leaving this task to a future research project instead.

Lateral Stick Step Input in Airplane Configuration

The next time simulation corresponds to a lateral stick step input in airplane configuration trimmed in level flight at 178 knots with the combined chart of the input as well as the body roll attitude ϕ_b and rate $\dot{\phi}_b$ responses presented in fig. 8.42. Again, all three plots share a common horizontal time axis. In this case the GTRS step input is terminated at around the 7 second mark, therefore the corresponding attitude and rate responses shall only be compared up to that point in time.

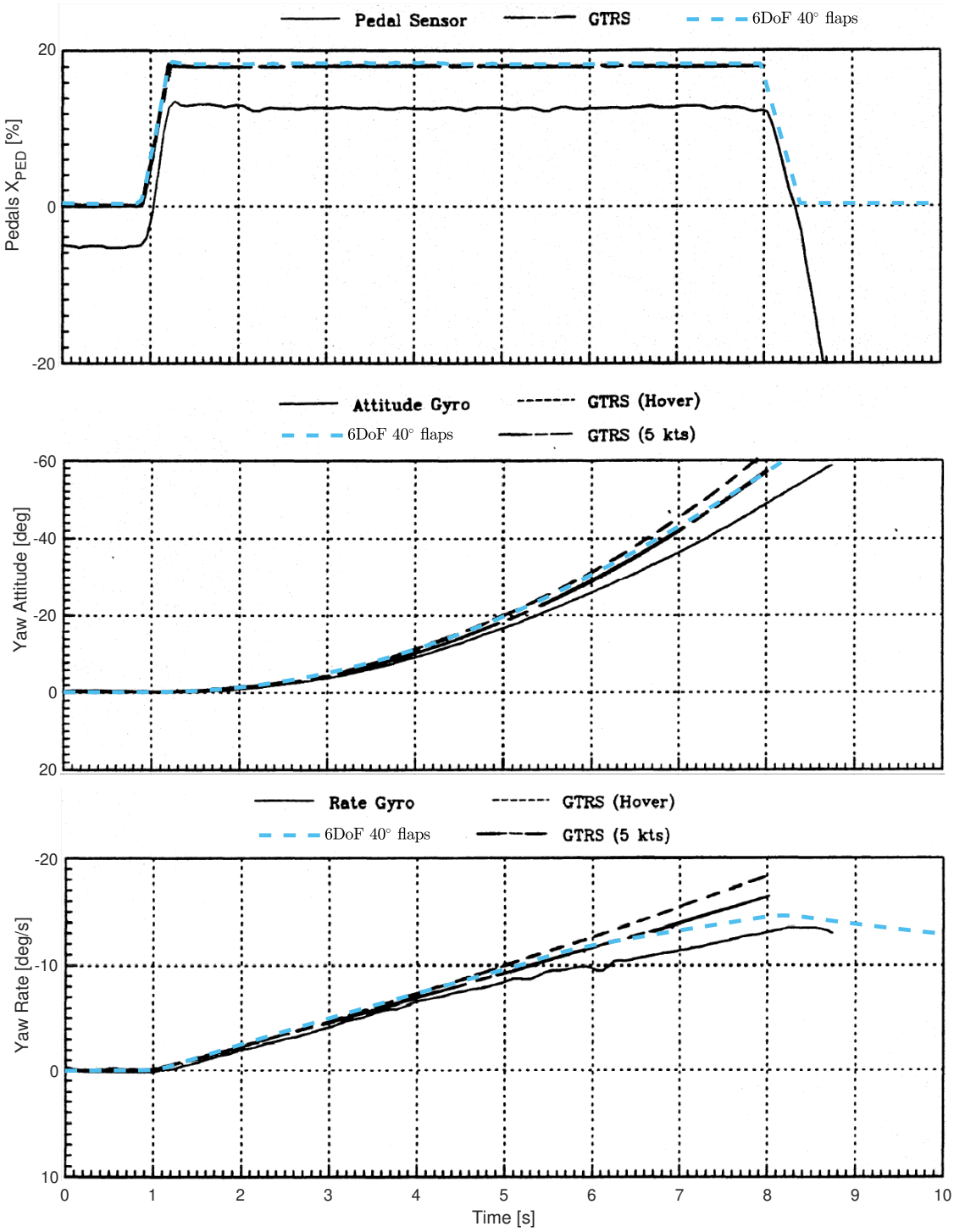

Figure 8.38: Comparison between the yaw responses of the 6DoF tilt-rotor model, GTRS model, and actual XV-15 tilt-rotor in helicopter configuration in hover to a pedals step input. 6DoF model flap deflection indicated in the legend.

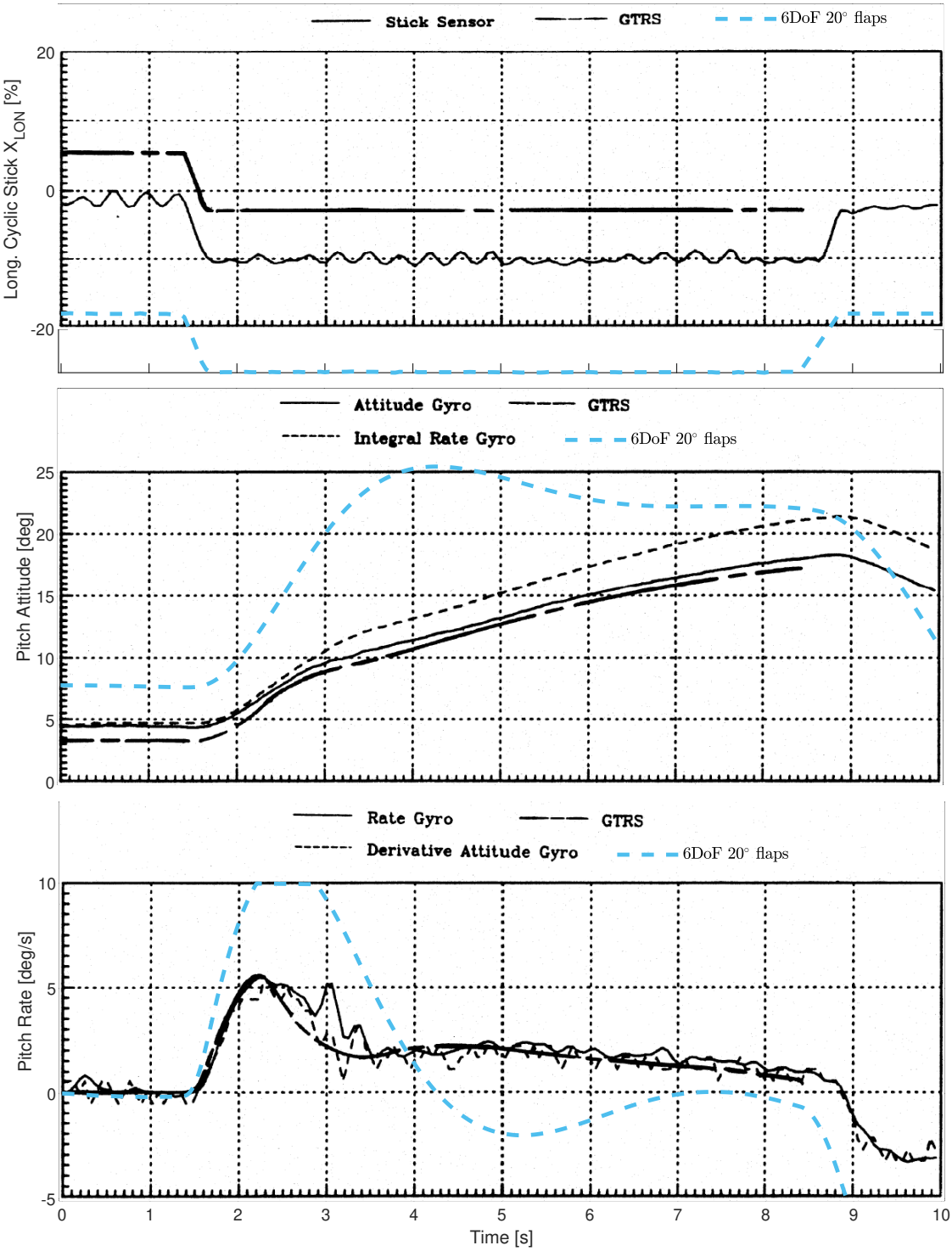

Figure 8.39: Comparison between the pitch responses of the 6DoF tilt-rotor model, GTRS model, and actual XV-15 tilt-rotor in airplane configuration to a longitudinal stick step input. 6DoF model flap deflection indicated in the legend.

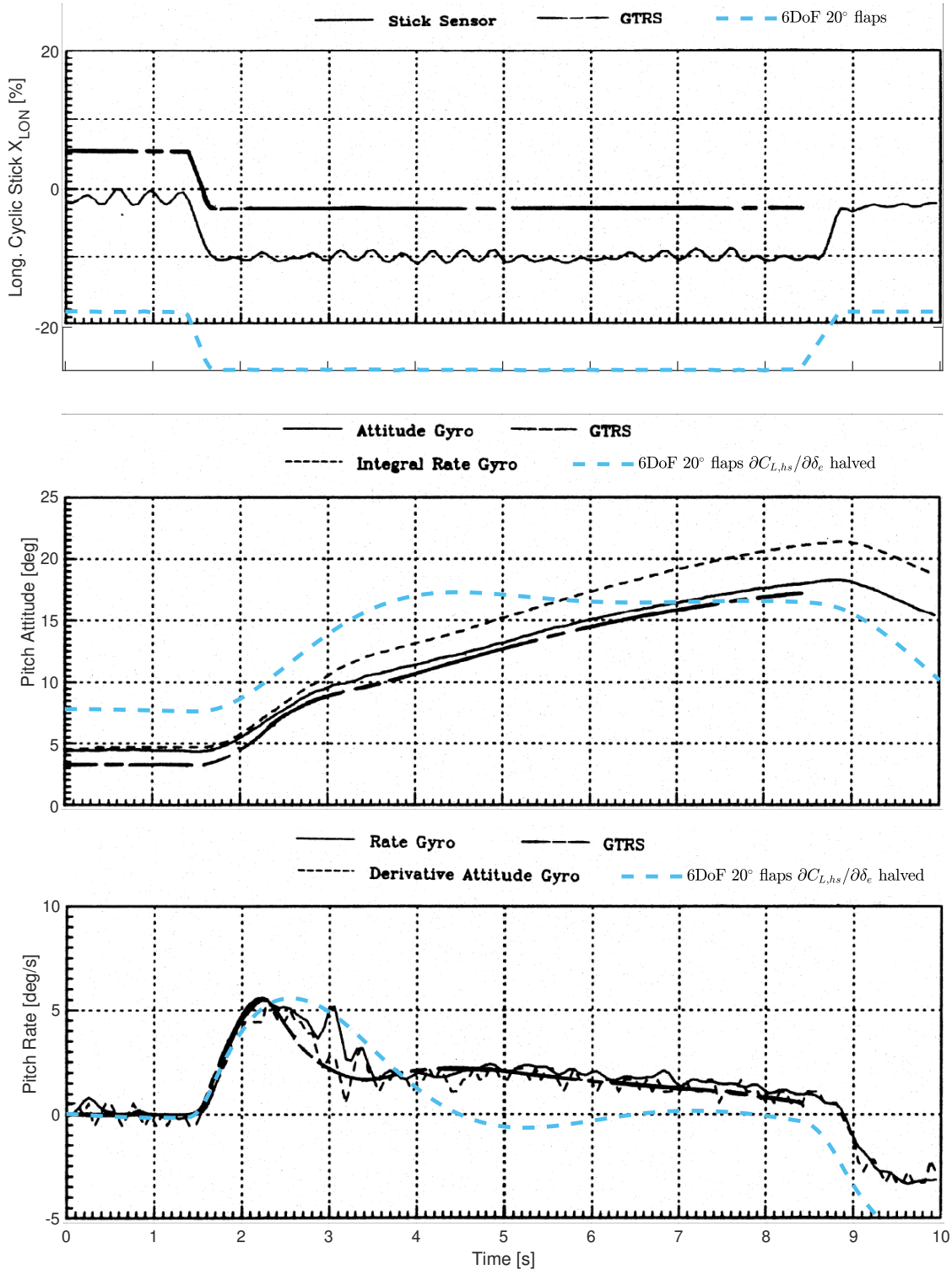

Figure 8.40: Comparison between the pitch responses of the adjusted 6DoF tilt-rotor model, GTRS model, and actual XV-15 tilt-rotor in airplane configuration to a longitudinal stick step input. Adjusted 6DoF model flap deflection and elevator effectiveness indicated in the legend.

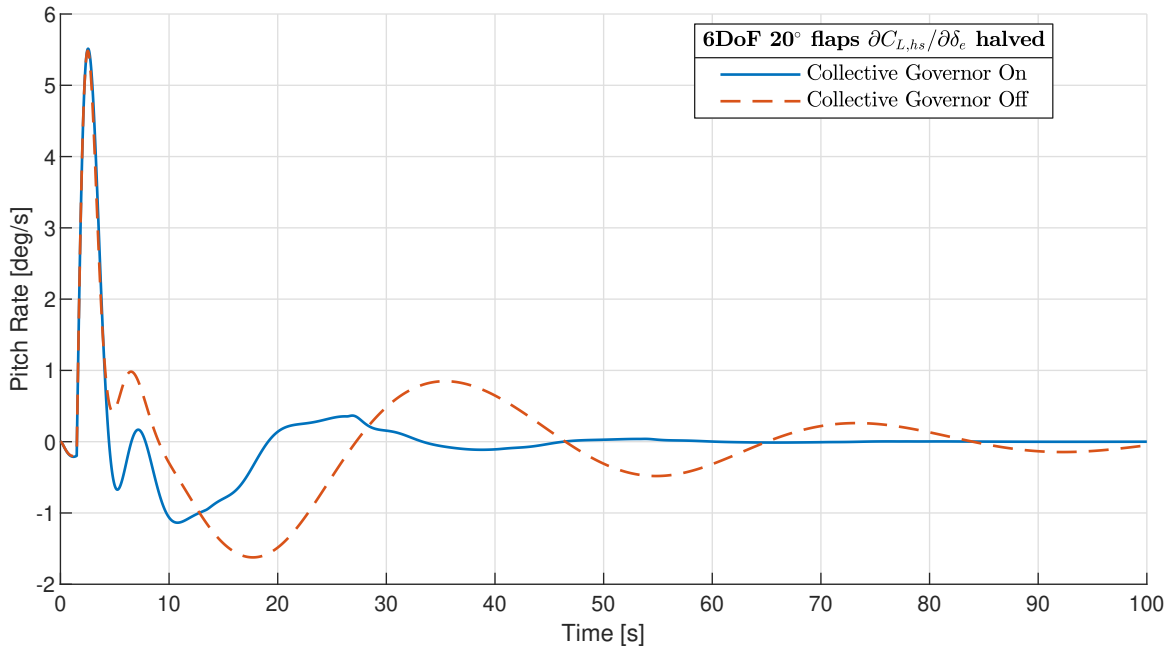

Figure 8.41: Comparison between the phugoid motion of the adjusted 6DoF tilt-rotor model in airplane configuration with the collective governor turned on and off.

Looking at the pitch rate first, the asymmetric highly damped aperiodic motion may be observed in the responses of both models with the roll rate reaching a plateau and the roll angle increasing (approximately) linearly due to the damping of the wings at higher rolling rates. The GTRS reaches the plateau faster than the 6DoF model however, hinting that the damping provided by the wings is not sufficiently large. Both models also show a stable damped spiral mode which can be observed in a slight decline of the roll rate plateau. Nonetheless, the 6DoF model response is significantly milder in comparison to the GTRS, reaching a lower pitch rate and roll angle at the end of the response. Since the 6DoF model has a less damped roll rate than the GTRS, the resulting less aggressive response is most likely caused by a too low aileron effectiveness. Furthermore, in airplane mode the rotors do not have any body roll control (only some yaw control through the lateral stick), therefore the rotor model is also not suspected as the culprit of this discrepancy between the two models. In general the roll response of the 6DoF model to a lateral stick input is therefore considered only partially valid.

Pedal Step Input in Airplane Configuration

The final time simulation corresponds to a pedal step input in airplane configuration trimmed in level flight at 176 knots with the combined chart of the input as well as the body yaw attitude ψ_b and rate $\dot{\psi}_b$ responses presented in fig. 8.43. All three plots share a common horizontal time axis. Note that the 6DoF pedal input axis is shifted downwards, as indicated with the vertical axis on the right hand side of the plot, in order for it to fit within the plotting area. This is caused by the fact that the initial pedal deflection of the 6DoF model is equal to zero in trimmed flight, while the GTRS input is non-zero (for unclear reasons).

Inspecting the yaw attitude and rate it can be seen that the responses of the 6DoF and GTRS models are similar in trend and magnitude. Looking at the yaw rate it can be seen that the responses of both models oscillate with a similar magnitude and are clearly damped tending towards a stable non-zero yaw rate at the end of the response. Nonetheless, the response of the 6DoF model appears to have a lower frequency resulting in the only visible difference between the responses of the two models. Based on the shown data it is not clear whether this difference in frequency is caused by the rotors (which have been shown to have the capability of significantly affecting the dynamics of the tilt-rotor, such as the phugoid mode) or the other subsystems such as the vertical tail stabilizer or fuselage. For this reason an investigation into this discrepancy is left as a recommendation for the future. In general, however, the yaw response of the 6DoF model in airplane configuration is considered mostly valid.

As a final note, during the pedal step input response simulation additional data consisting of the body roll angle and rate has been generated in hopes of observing the Dutch-roll mode of the tilt-rotor. Unfortunately the phase difference between the roll and yaw responses was not larger enough to clearly observe this eigenmotion therefore it appears that the 6DoF tilt-rotor model is not yet suitable to determine the safe flight envelope of tilt-rotors which was one of the main motives for this research project. Nonetheless, the presented 6DoF model is considered an adequate first attempt at modeling the flight mechanics of a tilt-rotor which is expected to be improved and expanded in future research works in the hopes of it ultimately being able to predict unsafe flight conditions before they are accidentally entered during real-world flight.

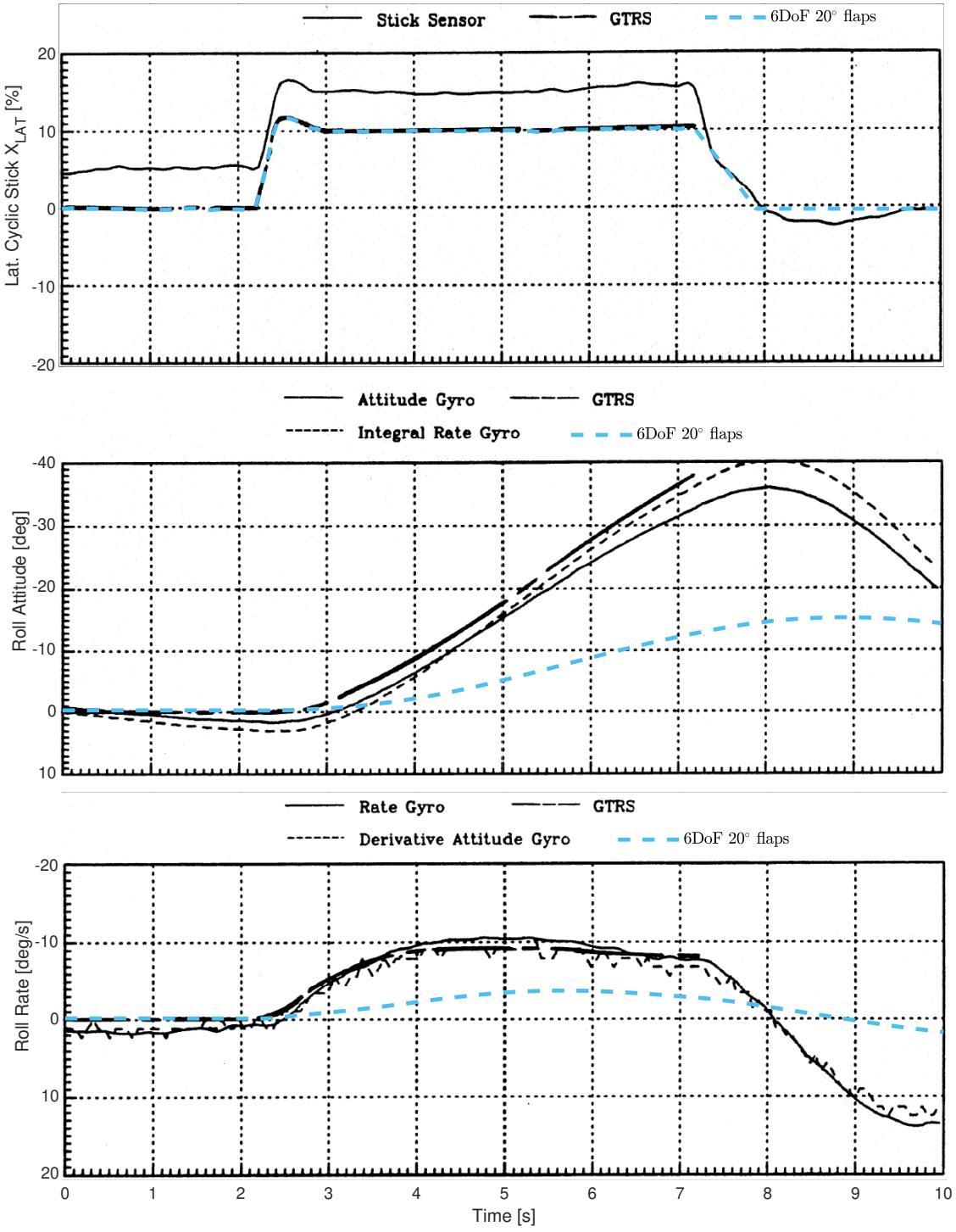

Figure 8.42: Comparison between the roll responses of the 6DoF tilt-rotor model, GTRS model, and actual XV-15 tilt-rotor in airplane configuration to a lateral stick step input. 6DoF model flap deflection indicated in the legend.

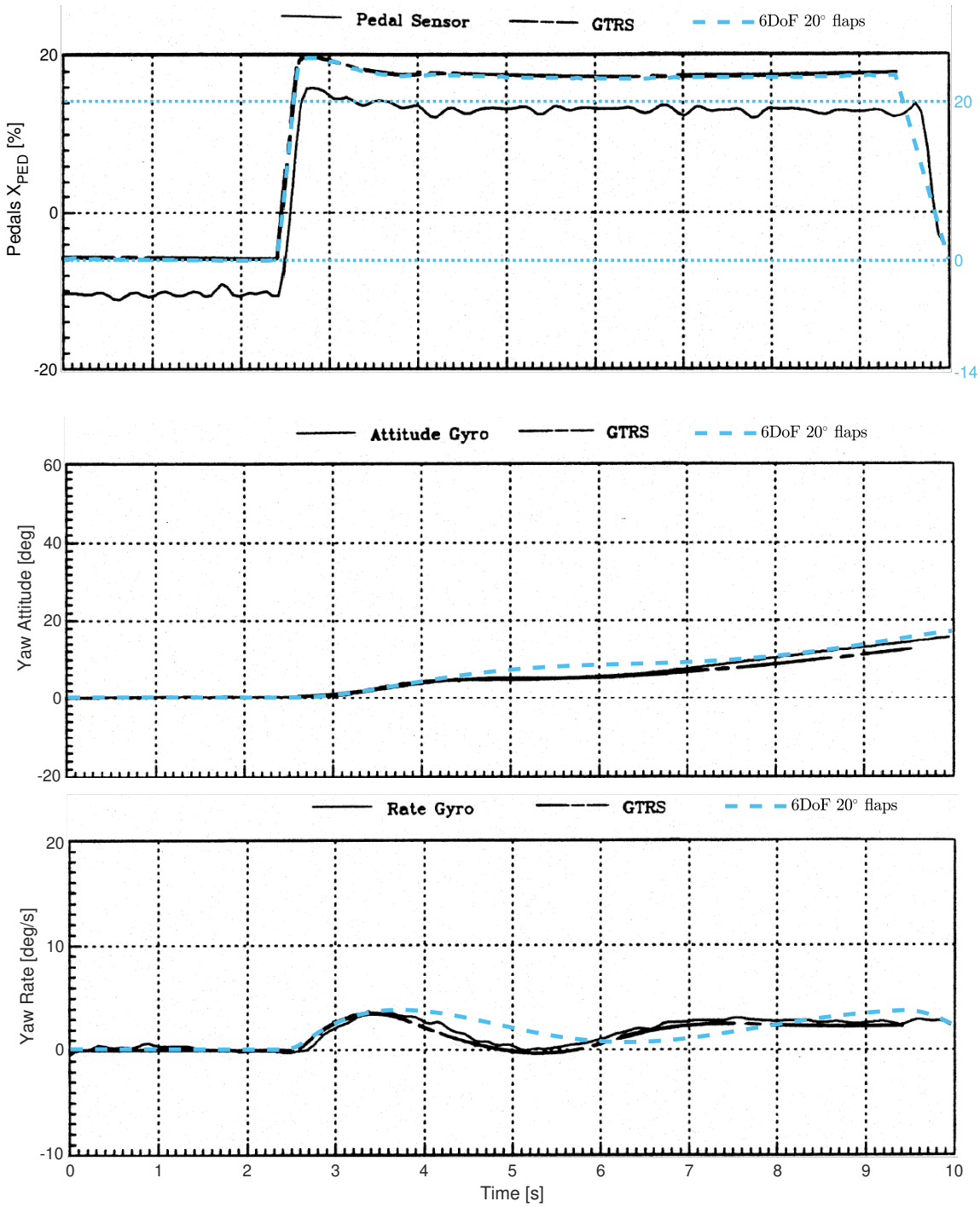

Figure 8.43: Comparison between the yaw responses of the 6DoF tilt-rotor model, GTRS model, and actual XV-15 tilt-rotor in airplane configuration to a pedals step input. 6DoF model flap deflection indicated in the legend.

9

Conclusions

The objective of this thesis work was to develop a tilt-rotor flight mechanics model capable of performance and piloted flight simulation. The obtained tilt-rotor model has six degrees of body motion freedom (hence it is referred to as the 6-degrees-of-freedom model, or 6DoF model in short) and thus is capable of three-dimensional flight simulation. It consists of tiltable simplified articulated rotors, trapezoidal planform lifting surfaces that mostly exhibit flat plate aerodynamics, and a fuselage model that only produces drag. The tiltable rotor model was derived analytically based on the blade element method (BEM) with the use of Maple, a symbolic manipulation program. The 6DoF model was then implemented in simulation with the use of Matlab and Simulink. The parameters of the 6DoF model were then set to those corresponding to the real-life XV-15 tilt-rotor aircraft in order to generate simulation results and validate the model. Note that the rotors of the 6DoF model tilt together with the nacelles with the angle η and tilt rate $\dot{\eta}$. In helicopter configuration the nacelles are orientated vertically and the nacelle angle η is equal to 0, while in airplane configuration the nacelles are tilted forward and the nacelle angle is equal to -90° (note the negative sign).

The main research question of this thesis project is concerned with the effect of the tiltable proprotor on the tilt-rotor flight mechanics, and has been divided into literature- and thesis work-related sub-questions. The literature-related sub-questions are concerned with the general workings of a tilt-rotor aircraft, and the methods of modeling a tilt-rotor for the purposes of performance and piloted flight simulation as documented in literature. The thesis work-related sub-questions, on the other hand, are concerned with the effect of the tiltable proprotor on the analytical rotor expressions and the simulation results. This chapter presents the thesis work-related sub-question conclusions only.

The thesis work-related research sub-questions were addressed through the visual inspection and discussion of the analytical rotor expressions, as summarized in section 9.1, and the analysis of the simulation results summarized in section 9.2. Apart from the research questions, two additional steps have been taken in the 6DoF model development process in order to satisfy the objective of this thesis work. First, several rotor assumptions have been challenged, as summarized in section 9.3, by verifying whether the simulation results do not violate them. Second, the simulation results have been compared to those corresponding to the real-life XV-15 tilt-rotor in order to assess the validity of the 6DoF model which is summarized in section 9.4. Finally the general validity of the 6DoF model is summarized in section 9.5.

9.1. Effect of Tiltable Proprotor on the Analytical Rotor Expressions

This first set of conclusions addresses the research sub-questions concerned with the effect of the nacelle tilt angle η and tilt rate $\dot{\eta}$ on the analytical rotor expressions starting with the effect on the rotor hub velocity components. The remainder of this section follows the order of the derivation therefore the effect of the tiltable proprotor on the blade element velocity components is next, followed by the inertial and aerodynamic flapping moment expressions, the disk tilt angles, and ends with the effect on the rotor forces and moments.

Rotor Hub Velocity Components

Almost all terms within the rotor hub velocity components' expressions are affected by either a trigonometric function of the nacelle tilt angle η, the nacelle tilt rate $\dot{\eta}$, or the length of the tiltable nacelle l_n. The lateral-tangential velocity component V_{tc2} is not affected by the nacelle tilt rate at all while the longitudinal-tangential V_{tc1} and perpendicular V_{pc} components are. Simply adding the nacelle tilt-rate to the (total aerodynamic) body pitch rate q is not permissible in some cases due to the fact that the velocity experienced by the nacelle pivot point does not depend on the nacelle tilt rate.

Blade Element Velocity Components

All three blade element velocity components, i.e. the radial U_R, tangential U_T, and perpendicular U_P components, are affected by the nacelle tilt angle, however not all influences are explicit. The radial component is affected only implicitly through the rotor hub velocity, while the tangential and perpendicular components additionally include explicit instances of the nacelle tilt angle giving rise to so-called 'effective' and 'total' rates.

'Effective' rates are defined to be the combination of two orthogonal body rotational rates that phase each other out as a trigonometric function of the nacelle tilt angle, while the 'total' rate corresponds to the combined nacelle tilt rate and body pitch rate. Both of these definitions are applicable to rotational accelerations which are then referred to as 'effective' and 'total' accelerations.

Although 'total' rates appear in both tangential and perpendicular velocity components, in several cases simply adding the nacelle tilt rate $\dot{\eta}$ to the body pitch rate q is not permissible due to the presence of the nacelle pivot velocity terms (which do not depend on the nacelle tilt rate) within the rotor hub velocities.

Inertial Flapping Moment

Analogously to the blade element velocity components, instances of 'effective' and 'total' rates and accelerations appear in the inertial flapping moment $M_{BL|Y\widehat{R},i}$ expression. To be more precise, the nacelle tilt acceleration $\ddot{\eta}$ may be added to the (inertial, indicated with the i subscript) body pitch acceleration $\dot{q}_i$ when calculating the inertial effect of angular acceleration on the flapping motion, and the nacelle tilt rate may be simply added to the body pitch rate q_i in the centrifugal spring portion of the inertial flapping moment. However, the nacelle tilt rate may not be added to the body pitch rate when calculating the pitch-yaw Coriolis effect contradicting what is found in literature. Furthermore the nacelle tilt rate and acceleration may not be simply added to the body pitch rate and acceleration in the rotor hub acceleration components since these contain the pivot acceleration terms that only depend on the body rates and accelerations and not on the nacelle tilt rate and acceleration.

Regarding the flapping motion of the blade, the nacelle tilt rate always increases the flapping angle β, and the nacelle tilt angle swaps the effect of the body roll and yaw rate on the flapping angle where the yaw rate decreases the flapping angle in helicopter mode and increases the flap angle in airplane mode, while the opposite is true for the roll rate.

The inertial flapping moment also contains terms that are only present in conversion mode and thus are unique to the tiltable proprotors, one of which is the tilt-yaw Coriolis effect.

Aerodynamic Flapping Moment

The aerodynamic flapping moment $M_{BL|Y\widehat{R},a}$ expression also contains 'effective' and 'total' rates which consist of explicit instances of the nacelle tilt angle and rate. Specifically, the nacelle tilt angle swaps the effect of the body roll and yaw rate on the aerodynamic damping term in the aerodynamic flapping moment, and the nacelle tilt rate may be simply added to the body pitch rate in both the aerodynamic spring and excitation terms of the aerodynamic moment. The nacelle tilt is also implicitly present in the rotor hub linear velocity terms.

Disk Tilt Angles

The coning $\widehat{a}_0$, longitudinal $\widehat{a}_1$, and lateral $\widehat{b}_1$ disk tilt angles are also affected by the tiltable proprotor, however only the significant effects (as determined by an automated ordering scheme) are summarized here. The resulting reduced expressions of all three disk tilt angles continue to contain 'effective' rates and rotor hub linear velocities which implicitly contain the nacelle tilt angle and rate. However, the coning angle $\widehat{a}_0$ is not affected by the nacelle tilt rate at all, while there is only one occurrence of the tilt rate in each of the

longitudinal and lateral disk tilt angle expressions. In the latter case the nacelle tilt rate may be simply added to the body pitch rate providing the only instance of a 'total' rate among all disk tilt angle expressions.

Rotor Thrust

Similarly to the disk tilt angles, the rotor thrust $\widehat{T}_{BEM}$ expression obtained with the use of the blade element method (BEM) has been reduced with the automated ordering scheme leaving only the terms that are considered significant. Therefore only the significant effects of the tiltable proprotor on the BEM thrust are mentioned here. This also applies to the H- and S- forces, as well as the Q-moment treated later.

The BEM thrust also contains 'effective' rates and is implicitly affected by the nacelle tilt angle and rate through the rotor hub linear velocities. However, the reduction scheme does not consider the (explicit) nacelle tilt rate to be a significant contributor to the BEM thrust therefore this expression does not contain any explicit $\dot{\eta}$ terms.

The thrust expression obtain with the use of the momentum theory is also implicitly affected by the tiltable proprotor through the rotor hub linear velocities.

Rotor H- and S-Forces

Almost identical conclusions may be made about the effect of the tiltable proprotor on the (reduced) rotor hind H-force ($\widehat{H}_{BEM}$) and side S-force ($\widehat{S}_{BEM}$). First of all instances of 'effective' rates are present in both expressions, and the nacelle tilt angle and rate has an implicit effect through the rotor hub velocity components. The nacelle tilt rate may be simply added to the body pitch rate in some cases giving rise to 'total' rates, however in other cases $\dot{\eta}$ is considered insignificant leaving sole q terms. Finally both H- and S-force expressions contain terms that only exist in conversion configuration making them unique to tiltable proprotors.

Rotor Torque Q-Moment

The (reduced) rotor torque Q-moment ($\widehat{Q}_{BEM}$) also contains 'effective' rates and rotor hub velocity terms presenting both explicit and implicit effects of the tiltable proprotor. However, the explicit instances of the nacelle tilt rate are not considered significant at all therefore the Q-moment expression does not have any explicit $\dot{\eta}$ terms. Finally the rotor torque expression also contains terms that only exist in conversion configuration making them unique to tiltable proprotors.

Rotor Hub Spring Reaction Moments

The last analytical rotor expressions that have been analyzed with regards to the effect of the tiltable proprotor on them are the rolling O ($\widehat{O}_s$) and pitching P ($\widehat{P}_s$) hub spring reaction moments which are only implicitly affected by the nacelle tilt through the lateral $\widehat{b}_1$ and longitudinal $\widehat{a}_1$ disk tilt angles respectively.

9.2. Effect of Tiltable Proprotor on the Simulation Results

The second set of conclusions addresses the research sub-questions concerned with the effect of the tiltable proprotor on the 6DoF model trim curves which present the variation of different aircraft variables as a function of the total velocity and the nacelle tilt angle for the tilt-rotor in a trimmed state. In this case most of the trim curves correspond to an unaccelerated, longitudinal, and level flight trim condition with the exception of the Haffner diagram trim curves which correspond to climbing (and descending) flight conditions instead of level ones.

This section begins with the effect of the tiltable proprotor on the general body and control trim curves, and continues with its effect on the rotor, main wing, and tail stabilizer trim curves. A portion of this section then summarizes the effect of the nacelle rate on the handling and performance of the tilt-rotor, and concludes with the effect of the nacelle tilt on the Haffner diagrams.

Body and Control Trim Curves

As the proprotor tilts towards airplane configuration, the body angle of attack α_b trim curves are translated upwards, i.e. more nose-up pitch attitude is required for trim, while the longitudinal stick X_{LON} trim curves are translated downwards meaning that a greater nose-down stick deflection is required for trim as the proprotor tilts towards airplane mode. Near helicopter configuration the swashplate collective θ_0 trim curves

are slightly translated downwards, i.e. less collective is required as the nacelles tilt forwards, however closer to airplane mode the trim curves are clearly translated upwards requiring a larger collective angle towards airplane mode. Near hover θ_0 is not affected by the nacelle tilt angle.

The fuselage longitudinal force $F_{fus|Xb}$ trim curves of the 6DoF model, however, are (almost) completely not affected by the nacelle tilt which contradicts the results found in literature. This is explained by the fact that the 6DoF model fuselage force does not depend on the angle of attack of the body which does vary with the nacelle tilt angle, while the fuselage forces of models found in literature do depend on the angle of attack.

Rotor Trim Curves

The effect of the tiltable proprotor on the induced velocity, disk tilt angles, and rotor forces and moments trim curves is summarized below.

The induced velocity v_{in} trim curves appear to be translated downward, i.e. the rotor generates a lower induced velocity at the same flight speed, as the nacelles tilt towards airplane mode. Near hover the induced velocity is not affected by the nacelle tilt angle.

The non-wind axis disk tilt angles are also affected by the nacelle tilt angle, starting with the coning angle a_0 trim curves which are translated downward and rightward, i.e. indicating a lower coning angle at higher velocities, as the nacelle tilts towards airplane mode. This trend is reversed in airplane mode, however, which contradicts the results found in literature and thus further investigation is left as a recommendation for the future. The longitudinal disk tilt a_1 trim curves are translated rightward, i.e. a lower required longitudinal disk tilt at the same velocity, and the gradient of the curves changes from a positive to a negative value as the nacelle tilts towards airplane configuration. Near hover a_1 is not affected by the nacelle tilt angle. The lateral disk tilt b_1 trim curves exhibit a general downward translation, i.e. a lower required lateral disk tilt at the same velocity, as the nacelles tilt towards airplane mode. The magnitude of this translation decreases at lower velocities for the 6DoF model to the point of the nacelle tilt having no effect on the trim curves near hover.

The effect of the nacelle tilt on the rotor forces defined in the shaft plane is described next, starting with the thrust T_{SP} which is affected in a similar manner as the coning angle a_0, i.e. the trim curves are translated downward and rightward as the nacelle tilts towards airplane mode, indicating a lower thrust is required for trim at higher velocities. This trend also applies to the tilt-rotor in airplane configuration which is not the case for a_0 however. On the other hand, the side force S_{SP} varies as a function of the nacelle tilt similarly to the lateral disk tilt angle b_1, i.e. the rotor produces a smaller in (absolute) magnitude side force as the nacelle tilts forwards, with the exception of the trim curve corresponding to $\eta = -60^\circ$ which does not follow this generalization at higher velocities. The tillable nacelle does not seem to have an effect on the side force at velocities close to hover. Finally the hind force H_{SP} trim curves show an upward translation, i.e. a higher hind force, for η angles ranging from 0° to -60° and a downward translation, i.e. a lower hind force, towards airplane mode.

The nacelle tilt also has an effect on the rotor moments defined in the shaft plane, starting with the rotor torque Q_{SP} trim curves which are translated rightward and upwards as the nacelle tilts towards airplane mode. The vertical translation means that the rotor generates a lower torque at the same velocity. At a nacelle angle of -60° and in airplane mode, however, instead of translating upwards, the 6DoF model trim curves are translated downwards resulting in a greater required torque which contradicts the results found in literature. The trim curves of the rotor hub spring reaction rolling moment O_{SP} are generally translated downwards, i.e. towards a more negative rolling moment, as the proprotors tilts towards airplane mode, albeit near airplane mode this translation becomes less pronounced. The rotor hub spring reaction pitching moment P_{SP}, on the other hand, is affected by the nacelle tilt in an identical way as the a_1 trim curves.

Main Wing Trim Curves

The main wing longitudinal force $F_{w|Xb}$ trim curves are translated rightwards, i.e. a more 'dragging' force is generated at the same velocity, as the nacelles tilt towards airplane mode. The vertical force $F_{w|Zb}$ trim curves are translated downward and to the right, the former meaning that a larger 'lifting' force is generated at the same velocity, as the nacelles tilt towards airplane mode. At velocities close to hover the nacelle tilt does not seem to have an effect on the $F_{w|Xb}$ and $F_{w|Zb}$ trim curves. Finally the pitching moment $M_{w|Yb}$ trim curves are translated upwards and to the right, the former meaning a more nose-up pitching moment is generated at the same velocity, as the nacelles tilt forwards.

Tail Stabilizer Trim Curves

The horizontal stabilizer (h-stab) longitudinal force $F_{hs|Xb}$ trim curves are translated rightward, i.e. a lower absolute 'dragging' force is generated at the same velocity, as the nacelles tilt towards airplane mode. The h-stab pitching moment $M_{hs|Yb}$ (acting at the body CoG) is mostly generated by the h-stab vertical force $F_{hs|Zb}$ therefore the trim curves of these two variables look very similar and thus are described collectively. Both sets of trim curves are translated downwards as the nacelle tilts forward indicating a higher 'lifting' force and more nose-down pitching moment. The only exception are the trim curves very close to airplane mode which are translated back upwards indicating a lower 'lifting' force and more nose-up moment. The nacelle tilt has a negligible effect on all three trim curve sets at velocities near hover however.

The vertical stabilizer trim curves are all equal to zero for the 6DoF model since they experience a zero angle of attack (as measured from their rotated frame of reference) in longitudinal flight. The results found in literature that correspond to the same flight conditions show non-zero values however.

Effect of Nacelle Tilt Rate on Handling and Performance

An additional set of longitudinal and level flight trim curves has been generated where the instantaneous nacelle tilt rate $\dot{\eta}$ is set to its maximum forward- and backward-tilting values in order to determine the effect of the nacelle tilt rate on the tilt-rotor handling and performance. These two effects are assessed based on the variation of the longitudinal stick X_{LON} and required engine power $HP_{ENG,REQ}$ trim curves as a function of $\dot{\eta}$. The results show that the nacelle tilt rate affects the performance of the tilt-rotor more than its handling characteristics. When compared to the $\dot{\eta} = 0$ flight trim curves, converting from helicopter to airplane mode requires more power as the total velocity increases throughout the entire conversion process. Furthermore, more nose down longitudinal stick deflection is required in helicopter mode which gradually changes to more nose up longitudinal stick deflection while increasing velocity and nearing airplane mode. On the other hand, when converting from airplane to helicopter mode less power is required as the total velocity increases throughout the entire conversion process. In addition more nose up longitudinal stick deflection is required in helicopter mode which gradually changes to more nose down longitudinal stick deflection while increasing velocity and nearing airplane mode.

Haffner Diagrams

Apart from level flight, additional longitudinal climbing flight trim curves at different flight path angles have been generated in order to create Haffner diagrams corresponding to the tilt-rotor at different conversion stages, including the tilt-rotor in helicopter configuration and airplane configuration. Haffner diagrams may be used to quickly estimate the induced velocity of a (typically helicopter) rotor in forward flight without the need for a (computationally expensive) rotor inflow solver. The obtained 6DoF model Haffner diagrams are compared to a standard helicopter Haffner diagram generated according to the momentum theory, also referred to as the Glauert Haffner diagram.

In summary the Haffner diagram of a tilt-rotor drastically changes when converting from helicopter to airplane mode resulting in induced velocities that are much lower than the ones calculated with the momentum theory for an isolated rotor. As a result if the Glauert Haffner diagram were to be used to approximate the induced velocity of a tilt-rotor, the approximated induced velocity would be increasingly overestimated as the tilt-rotor converts from helicopter to airplane mode.

9.3. Assumption Verification

Apart from addressing the result-related research questions, several assumptions made throughout the rotor expression derivations have been challenged by generating appropriate results as summarized below.

Based on the numerically obtained flapping response (in the time domain) to a vertical rotor hub acceleration, the effect of the gravitational acceleration on the flapping equation is verified to be negligible resulting in only a 2% difference in steady state solution. Furthermore the transient response settles to within 5% of the final value in under two revolutions, verifying the assumption that the transient flapping response resolves within two blade revolutions.

Based on the simulated variation of the blade element aerodynamic states across the rotor disk the assumption that the blade element lift is much greater than blade element drag is considered verified for critical flight conditions, and thus is considered acceptable. However, several assumptions have been shown to be violated

and thus are due for a revision in future iterations of the 6DoF model. First of all, the the small inflow angle assumption is grossly violated in airplane mode as expected, while in helicopter mode it is only violated near the rotor hub. Moreover, linearizing the inflow angle introduces large errors across the entire rotor disk in airplane mode, while in helicopter mode significant errors once again only appear near the rotor hub. Finally, simplifying the total longitudinal velocity experienced by the blade element to equal to its tangential component only also introduces considerable errors across entire disk in airplane mode. In helicopter configuration mode the error is much smaller and confined to the rotor hub region.

9.4. Model Validity Against the GTRS

The generated results have been additionally used to validate the 6DoF model against the Generic Tilt-Rotor Simulation (GTRS) which has been extensively validated against the real flight data of the real-life XV-15 tilt-rotor model showing a high correlation between model and reality. For this reason, and due to the better availability of simulate data over real flight data, the GTRS is used to validate the 6DoF model. One exception is the conversion corridor which is directly validated against the real-life XV-15 tilt-rotor. A brief comparison between the 6DoF model and the GTRS is presented in table 9.1.

This section begins with the conclusions made about the validity of the 6DoF model conversion corridor, continues with the static flight validation based on trim curves, and concludes with the time-domain dynamic flight validation.

Table 9.1: Summarized comparison of model characteristics between 6DoF model and GTRS.

Model Characteristic	**6DoF Model**	**GTRS**
DoFs	7 total: 6 body motion + 1 combined rotors' RPM	11 total: 6 body motion + 1 combined rotor's RPM + 2×2 flapping
rotor	derived in wind-axis control plane (no feathering plane); first-harmonic quasi-static flapping; static, uniform, and axial induced velocity	derived in wind-mast axis system (shaft plane); first-harmonic, first order dynamic flapping; static, non-uniform and axial induced velocity with side-by-side rotor and ground effects
collective governor	partial implementation of GTRS collective governor	complete; includes failure monitors
drivetrain	simplified implementation of GTRS drivetrain	complete; includes temperature and compressibility effects, and turbine dynamics
main wing and tail stabilizers	flat plate aerodynamics	based on wind-tunnel data; includes Mach effects
control surfaces	linear aerodynamics; exception: flaps treated as flat plates	based on wind-tunnel data
fuselage aerodynamics	produces drag only; modeled by equivalent flat plate area	based on wind-tunnel data
nacelle aerodynamics	no	based on wind-tunnel data
aerodynamic interactions	rotor wake effect on wing; wing downwash on tail	rotor wake effect on wing, tail, and ground; airframe effect on tail
controls	control phasing	control phasing and Stability and Control Augmentation System

9.4.1. Conversion Corridor

The conversion corridor of the 6DoF model is generated based on the unaccelerated, longitudinal, and level flight limits. In general the 6DoF conversion corridor is considered mostly valid, predicting the higher velocity limits close to helicopter mode, and lower velocity limits close to airplane mode, quite well when compared to the real XV-15 conversion corridor. However, the 6DoF model significantly underpredicts the lower velocity limits for nacelle angles ranging between $-10°$ and $-45°$, while greatly overpredicting the upper velocity

limits for nacelle angles ranging between $-60°$ and airplane mode. The real XV-15 conversion corridor is hypothesized to be additionally limited by model factors that are outside of the scope of this research project, such as diverging aeroelasticity, exceeded structural loads, or operational safety, resulting in the large differences between the 6DoF model and real life conversion corridors at lower velocities in conversion flight and higher velocities near airplane mode.

The trimming routine used to generate the conversion corridor additionally outputs data about the factors that bound the feasible region of flight of the 6DoF model. It has been found that the upper velocity limit of the 6DoF model conversion corridor is bounded by insufficient engine power and throttle range, with the next limiting factor being either the flapping magnitude, a maxed-out swashplate collective angle, or a combination of both. Sparse data is available for the limiting factors of the lower velocity range, however close to helicopter configuration the conversion corridor is limited by an exceeded flapping angle.

9.4.2. Static Flight Validity

The static flight validity is assessed based on the similarity between the variation of the tilt-rotor variables as a function of the nacelle tilt and velocity (i.e. the trim curve trends), and based on the similarity between the magnitudes of those variables. The trends are assessed by comparing the nominal trim curves of the 6DoF model to the ones of the GTRS. The similarity between the magnitudes of the variables, however, is assessed by generating new so-called pseudo trim curves and comparing those to the GTRS model.

Pseudo trim curves are generated by supplying specific portions of the GTRS trim solution to the 6DoF model trimming routine such that the subsystems of the 6DoF model receive the same control inputs and experience the same aerodynamic conditions yielding pseudo trim curves that are believed to be better suited for magnitude comparisons. These pseudo trim curves do not correspond to a trimmed 6DoF model, however, therefore they cannot be used to assess the validity of the trim curve trends.

The validity of the general body and control is summarized first, followed by the rotor, rotor torque dependent subsystems, main wing, and tail stabilizers. The static flight validation is then concluded with an assessment of sideward and sideslip flight trim curves.

Body and Controls

In terms of the body angle of attack α_b, the 6DoF model becomes less representative of the XV-15 tilt-rotor towards airplane mode, but remains valid in helicopter mode and up to conversion angles of $\eta = -15°$. The model also accurately represents the angle of attack of a generic tilt rotor almost across the entire velocity and nacelle tilt range with the exception of low velocity flight close to helicopter configuration. The longitudinal stick deflection variation is relatively valid for conversion angles between $\eta = -15°$ and $\eta = -60°$ across most of the velocity range. It is approximated most accurately in conversion and airplane configuration flight, while the same cannot be said for flight near helicopter configuration. The swashplate collective prediction may be considered mostly valid for all nacelle tilt angles and velocities, with the greatest overlap being in airplane mode.

The fuselage longitudinal force $F_{fus|Xb}$ is only valid in terms of its variations as a function of velocity, while the variation as a function of the nacelle tilt angle is non-existent in the 6DoF model rendering it grossly invalid. The pseudo trim curves underpredict the fuselage 'dragging' force with the largest discrepancy appearing at high velocities in helicopter configuration. The vertical force $F_{fus|Zb}$ is also underestimated by the 6DoF model however the fuselage is not a significant contributor to the total vertical body force making this invalidity non-critical. Finally the 6DoF model fuselage pitching moment $M_{fus|Yb}$ is always zero which is not the case for the GTRS model rendering the 6DoF model grossly invalid in this aspect, especially considering that the fuselage is a significant contributor to the total body pitching moment.

Rotor

The rotor induced velocity v_{in} trim curves of the 6DoF and GTRS are very similar and follow the same trends in their variation as a function of velocity and nacelle tilt angle with the highest similarity near helicopter mode. The pseudo trim curves slightly over estimate the induced velocity for almost all nacelle tilt angles with the greatest divergence present in helicopter mode.

The variation of the coning angle a_0 trim curves as a function of velocity and nacelle tilt angle is very similar for both models with some divergence towards airplane configuration. Pseudo trim curves overestimate a_0

for nacelle tilt angles closer to helicopter mode, and underestimated it for nacelle angles closer to airplane mode with the magnitude of divergence highest for low and high velocities.

The longitudinal disk tilt angle a_1 trim curve velocity and nacelle angle trends are generally similar for both models with the exception of the velocity trend which diverges towards helicopter configuration. The pseudo trim curves significantly overestimate a_1 almost for the entire nacelle tilt range, with the exception of airplane mode where the curves of the two models almost completely overlap.

The variation of the lateral disk tilt b_1 trim curves as a function of velocity and nacelle tilt is similar for both models, however the 6DoF velocity trends exhibit asymptotic characteristics, which are not observed in the GTRS model, and are hypothesized to be caused by a too large of a influence of the lateral disk tilt correction at higher velocities. The pseudo trim curves indicate that b_1 is always underestimated (in the absolute magnitude) by the 6DoF model.

The variation of the rotor thrust T_{SP} as a function of velocity and nacelle angle is generally similar for both models with the exception of the velocity trends in airplane configuration and at lower velocities in helicopter configuration. The pseudo trim curves significantly overestimate T_{SP} for almost entire nacelle tilt range with exception of airplane mode where at higher velocities the thrust is underestimated.

The variation of the rotor side force S_{SP} as a function of velocity and nacelle tilt angle similar for the 6DoF and GTRS model, although a larger discrepancy between the two models is observed at $\eta = -60°$ hypothesized to be be caused by a difference in the model parameters. The pseudo trim curves mostly underestimate the magnitude of S_{SP} with the largest discrepancy occurring at lower velocities where the trim curves have their distinct peak, and at higher velocities with the nacelle tilt angle close to $-60°$.

The variation of the rotor hind force H_{SP} as a function of the nacelle tilt angle is similar for both models, while the velocity trend is only partially similar with the largest discrepancy existing in helicopter mode. The pseudo trim curves grossly overestimate H_{SP} for almost all conversion angles except for airplane mode.

The rotor torque Q_{SP} velocity and nacelle angle trends are very similar for both models with the exception of the 6DoF model at a nacelle angle of $-60°$ and in airplane mode where the nacelle trend differs from the one of the GTRS resulting in the torque being overpredicted by the 6DoF model. The pseudo trim curves overestimate (in the absolute sense) Q_{SP} for almost all conversion angles. The large deviation of the 6DoF rotor torque from the GTRS close to airplane mode at high velocities may also be attributed to the small inflow angle assumption employed in the 6DoF model which is grossly violated in these flight conditions.

The θ_{1s} pseudo trim curves of the 6DoF model completely overlap the trim curves of the GTRS meaning that the control mixing and phasing of the longitudinal stick has been implemented correctly.

Finally, the relation between the rotor thrust and torque of both the 6DoF and GTRS models show positive parabolic correlation, however the 6DoF model over predicts the torque at low thrust, and under predicts it at high thrust. This discrepancy is attributed to a mismatch of the blade drag coefficients while the expressions for the rotor thrust and torque are considered valid for a generic tilt-rotor.

Rotor Torque Dependent Subsystems

The rotor torque-dependent subsystems are validated with the use of pseudo trim curves which additionally use the GTRS rotor torque trim solution simulating the condition where the rotors of the 6DoF model require the same amount of torque as the ones of the GTRS. As a result the 6DoF model pseudo trim curves of the required engine power $HP_{ENG,REQ}$ completely overlap the ones of the GTRS meaning that the calculation of the required engine power of the GTRS has been correctly implemented in the 6DoF model.

The pseudo trim curves slightly overestimate the throttle stick deflection $X_{COL,thr}$ for all nacelle tilt angles and this offset is hypothesized to exists due to the simplification made in the implementation of the drivetrain where the commanded engine horsepower R_{SHP} is set to be equal to the total engine power HP_{ENG}.

Finally, the governor collective deflection $\theta_{0,gov}$ depends on the collective-throttle pilot deflection $X_{COL,thr}$, and since the $X_{COL,thr}$ pseudo trim curves do not overlap with the ones of the GTRS, the collective governor pseudo trim curves will also not coincide. When additionally replacing the 6DoF throttle stick deflection by the trim solution of the GTRS, a discrepancy between the collective governor trim curves of the two models still remains, however only exists in early conversion flight where the governor collective deflection is slightly underestimated in the 6DoF model, while in helicopter and near airplane mode the trim curves coincide.

Main Wing

The variation of the 6DoF model main wing longitudinal force $F_{w,X|b}$ and vertical force $F_{w,Z|b}$ as a function of velocity and nacelle tilt angle is generally in good agreement with the GTRS. The pseudo trim curves underestimate the 'dragging' and 'lifting' forces for almost all velocities and nacelle tilt angles with the discrepancy being largest at higher velocities for each conversion angle. The 'lifting' force similarity additionally diverges towards airplane mode.

The variation of the wing pitching moment $M_{w|Yb}$ as a function of both velocity and nacelle tilt angle is also mostly similar with the largest discrepancy being in airplane mode. The pseudo trim curves overestimate the nose down pitching moment for the nacelle tilt angles closer to helicopter configuration, while near airplane mode the pitching moment is underestimated.

Tail Stabilizer

The horizontal stabilizer (h-stab) longitudinal force $F_{hs|Xb}$ trim curves of the 6DoF model and GTRS generally share little in common, however the nacelle trend is similar for both models. The pseudo trim curves of $F_{hs|Xb}$ have good overlap at lower and intermediate velocities, however the 6DoF model grossly overestimates the h-stab 'dragging' force at higher velocities. Given that the h-stabs are a minor contributor to the long force in comparison to the other subsystems, this deficiency in the model is not crucial.

The h-stab pitching moment $M_{hs|Yb}$ is mostly generated by the vertical h-stab force $F_{hs|Zb}$ therefore trim curves of these two variables look very similar, which is also the case in the GTRS demonstrating good model correlation. The effect of the nacelle tilt angle on both $M_{hs|Yb}$ and $F_{hs|Zb}$ is in good agreement with the GTRS model, however their variation as a function of velocity appears to differ greatly between the two models. The pseudo trim curves of the 6DoF vertical force and pitching moment show a growing difference in magnitude when compared to the GTRS as the velocity increases near airplane configuration. In airplane mode the horizontal stabilizers are the largest contributors to the total body pitching moment and therefore a discrepancy in the calculation of the pitching moment significantly affects the validity of the entire tilt-rotor flight mechanics model.

The trim curves of the 6DoF model vertical stabilizer (v-stab) are all equal to zero while the GTRS trim curves are non-zero hinting that the 6DoF model lacks some fundamental elements such as the rotor and wing wake effects at the tail which affect the forces and moments generated by the vertical stabilizer in longitudinal symmetrical flight.

Sideward and Sideslip Flight

In general the 6DoF tilt-rotor model in helicopter configuration in sideward flight is considered mostly valid with the exception of the lateral stick deflection which needs to be revised in a future iteration of the model. The lateral stick input required for trim is significantly underestimated and does not follow the piecewise linear trend of the validation data.

The body roll angle and pedal deflection required for trimmed sideslipping flight in airplane configuration, on the other hand, is considered valid. The same cannot be said for the lateral and longitudinal stick deflection predictions, however, which need to be investigated and revised in a future iteration of the tilt-rotor model. The lateral stick input required for trim is significantly overestimated, however it does follow the same linear trend as the GTRS. The longitudinal stick deflection trim has a concave shape indicating a more nose-up stick deflection as the sideslip angle increases, while the opposite is indicated by the GTRS trim curves.

9.4.3. Dynamic Flight Validity

Finally the dynamic flight of the 6DoF model is validated by comparing its time-responses to various inputs with the ones of the GTRS model. The pitch and yaw response validity of the 6DoF model in helicopter configuration is summarized first, followed by the pitch, roll, and yaw response validity in airplane configuration.

The pitch response of the 6DoF model in helicopter configuration in hover is considered only somewhat valid due to a milder response which is hypothesized to be caused by a deficiency of the horizontal tail stabilizer which overdamps the pitch response. The initial pitch response, however, hints that the rotor pitch effectiveness is valid. The yaw response of the 6DoF model in the same conditions is considered mostly valid with a small non-linearly growing underestimation of the yaw angle and rate hypothesized to be caused by the invalidity of the vertical tail stabilizers.

In airplane configuration the elevator aerodynamic effectiveness $dC_{L,ele}/d\delta_e$ must be halved in order to come close to a somewhat valid pitch response in airplane mode. For this adjusted 6DoF model the amplitude of the short period mode is similar to the one of the GTRS, however the 6DoF response frequency is observably lower and the oscillations are less damped. For this reason the 6DoF model short period motion is considered only somewhat valid. The 6DoF model is also shown to exhibit phugoid motion with the collective governor turned on and off, however the collective governor greatly influences the longitudinal response, not only heavily dampening the phugoid motion, but also distorting it from the damped sinusoidal shape.

The roll response of the 6DoF model to a lateral stick input in airplane configuration is considered only partially valid due to a significantly milder response in comparison to the GTRS. The asymmetric highly damped aperiodic motion and the (stable) spiral motion is observed in the response of the 6DoF model.

Lastly, the yaw response of the 6DoF model in airplane configuration is considered mostly valid, however the oscillatory response of the 6DoF model has a lower frequency than the one of the GTRS. It is unclear whether this is caused by an invalid rotor model or other subsystem model such as the vertical tail stabilizer or fuselage. A clear Dutch-roll mode of the tilt-rotor has not been observed in the response however.

9.5. Final Validity Conclusions

In general the developed 6DoF tilt-rotor model shows good flight mechanics characteristics that are representative of a generic tilt-rotor aircraft as demonstrated by the high similarity in trim curve trends and dynamic modes when compared to the GTRS model. The 6DoF model does not predict the flight characteristics of the specific XV-15 aircraft well enough for it to be considered valid for performance and piloted flight simulation, however, as demonstrated by the pseudo trim curves and the magnitudes and frequencies of the dynamic responses. It is hypothesized that this specific validity may be considerably improved by selecting more accurate model parameters without changing or re-deriving the governing equations.

In order to improve the generic validity of the model, however, several assumptions demonstrated to be grossly violated will have to be addressed, most likely requiring a re-derivation of the governing equations. The implementation of missing model elements recommended in literature is also expected to improve the generic validity of the 6DoF model.

10

Recommendations for Future Work

A number of recommendations for the future regarding the 6DoF tilt-rotor model have been identified throughout this research project and suggested within this thesis report. A summary of these recommendations is presented below. Note that the critical assumptions listed in section 4.6 are not treated here, however they are also considered model elements that should be investigated for their validity and potentially revised in the future.

General Recommendations

The general recommendations are concerned with the overall deficiencies of the 6DoF tilt-rotor model as follows. It is recommended that the nacelle tilt angle influences the general tilt-rotor center of gravity and inertia. An investigation into the dynamic responses of the 6DoF model is also recommended in order to determine the cause of a milder pitch response in helicopter configuration in hover, and a difference in frequency of the yaw response in airplane mode when compared to the GTRS model. Finally the validity of the phugoid mode with the collective governor turned on and off, and the validity of the Dutch-roll mode, or lack thereof, should also be determined in the future.

Rotor Model

The rotor recommendations are concerned with the rotor expressions and simulation results as follows. First of all it is recommended to expand the rotor theory to encompass axial induction ratios larger than 0.5, i.e. enable the modeling of the turbulent wake, vortex ring, and propeller brake states. It is also recommended to include rotor disk tilt dynamics and inflow dynamics. A conceptual analysis of whether the wind axis shift angle should introduce an angular velocity into the blade element velocity and acceleration expressions should be performed as well. Solving for the coning $\widehat{a}_0$ and longitudinal disk tilt $\widehat{a}_1$ angles involves the inversion of a matrix that may potentially be non-invertible. The likeliness of this happening and the potentially required solution should be investigated. Finally the rotor derivation should incorporate a tip loss factor and flow reversal region.

Regarding the results, the coning angle a_0 in airplane mode does not follow the nacelle tilt angle trend of the GTRS and is greater than expected, therefore further investigation into this anomaly is suggested. The divergence of the 6DoF model lateral disk tilt b_1 velocity trend from the GTRS trend at higher velocities is hypothesized to be caused by the lateral disk tilt correction which should be adjusted in the future to improve the model validity. The rotor torque Q_{SP} nacelle angle trend also diverges near airplane configuration and is inexplicably greater than expected, therefore further investigation is left as a recommendation for the future. The mismatch of the blade drag coefficients is thought to hinder the validity of the correlation between the rotor thrust and torque, therefore a more accurate selection of these coefficients is suggested for the future. Finally the gearing between the lateral stick to differential rotor thrust in helicopter configuration appears to hinder the validity of the tilt-rotor in sideward flight, therefore it is suggested for it to be investigated and possibly revised in the future.

On the subject of lateral stick control, additionally an investigation into any deficiencies of the lateral stick input is recommended in order to improve the validity of the 6DoF model in airplane configuration in trimmed flight with sideslip.

Lifting Surface Model

The lifting surface recommendations are concerned with the deficiencies of the main wing segments and tail stabilizers as follows. It is recommended for more sophisticated airfoil models to be used which could include the effects of the laminar drag bucket or the non-linear behavior in the stall region. Furthermore three-dimensional effects are also suggested to be included in the lifting surface model, as well as an improved sideslip model and the influence of wing shape on the lift induced drag. The control surface aerodynamic effectiveness should also be a function of the angle of attack and sideslip in the future. Finally, similarly to the main wing, the horizontal stabilizer should also be divided into segments in the future in order for the rotor wake to have an effect on the tail.

Regarding the results, an investigation should be carried out in order to establish why the vertical stabilizer trim curves of the GTRS model in longitudinal flight are non-zero, while the ones of the 6DoF model are zero. A more elaborate investigation into the validity of the 6DoF vertical stabilizer should be carried out as well. The contradicting trends of the wing pitching moments of the GTRS and 6DoF model in airplane configuration should be investigated as well. Finally, the results indicate that more nose-down stick deflection is required when the flaps of the 6DoF model are deflected in trimmed longitudinal flight. This contradicts the expectation that the flaps introduce a more nose-down pitching moment requiring a more nose-up stick deflection to counter the nose-down pitching moment, therefore an investigation into this anomaly is left as a recommendation for the future.

Lifting Body Model

It is suggested that the fuselage drag model be revised, and the lift and pitching moment model be introduced since the fuselage is a significant contributor to the longitudinal force and pitching moment of the whole tilt-rotor model. Secondly the assumption that the aerodynamic center of the fuselage coincides with the body center of gravity should be removed.

Aerodynamic Interaction

Two recommendations regarding the aerodynamic interactions have also been mentioned. First of all the rotor wash effect on the wing should be revised to incorporate the effect of a non-uniform rotor inflow distribution. Secondly, the wing downwash effect on the tail should also be revised such that it produces valid results even at high angles of attack.

Drivetrain Model

A recommendation relevant to the drivetrain model has also been mentioned and consists of employing the complete throttle-lever-to-engine-horsepower drivetrain instead of simplifying the commanded engine horsepower to be equal to the total engine power. This should be done to achieve a valid distribution of the swashplate collective deflection among the pilot collective stick input and governor collective input.

Automatic Ordering Scheme

The minimum and maximum values based on the 3DoF model which were supplied to the automatic ordering scheme should be adjusted based on the minimum and maximum values observed during the simulation of the 6DoF model.

Simulation Computation Performance

The last set of recommendations is concerned with the optimization of the 6DoF model simulation and thus reduction of its computational cost. Firstly, all automatically-reduced expressions should be simplified within Maple before being implemented in Matlab, shortening the lengths of the expressions and reducing the number of repeated calculations. Secondly, when solving for inflow it might not be necessary to transform the thrust, hind, and side forces from the wind axis control plane to the wind axis disk plane in order to compare the thrust in the disk plane with the Glauert momentum theory thrust. Instead, the previous solution for the disk tilt may be used saving computational power that would be used to recalculate the transformation matrix at every inflow-solver iteration. In order for this to be accurate, however, some sort of disk plane dynamics (e.g. first order lag) should be implemented, otherwise the disk plane may radically change its tilt angle from one simulation step to another completely invalidating the previous transformation matrix from the wind axis control plane to the wind axis disk plane. A different option would be to use the linearized inflow solver as described in appendix C.2, however the validity of this approach should be additionally investigated.

Bibliography

[1] VFS, "Transcendental Model 1-G - Vertical Flight Society." [Online]. Available: https://gallery.vtol.org/image/tjqS

[2] D. C. Dugan, R. G. Erhart, and L. G. Schroers, "The XV-15 Tilt Rotor Research Aircraft," NASA ARC, Moffett Field, CA, USA, Tech. Memo. 81244, 1980.

[3] P. Sokolowski, "Tilt-Rotor Simulation Literature Study," Master's thesis literature study, Delft University of Technology, 2020.

[4] F. S. Stoddard, "Discussion of Momentum Theory for Windmills," *Wind Energy Center Reports*, no. 20, pp. Appendix IV, 28–35, 1976.

[5] S. W. Ferguson, "Development and Validation of a Simulation for a Generic Tilt-Rotor Aircraft," Systems Tech., Inc., Mountain View, CA, USA, Contractor Rep. CR-166537, 1989.

[6] ——, "A Mathematical Model for Real Time Flight Simulation of a Generic Tilt-Rotor Aircraft, Rev. A," Systems Tech., Inc., Mountain View, CA, USA, Contractor Rep. CR-166536, 1988.

[7] M. D. Maisel, D. J. Giulianetti, and D. C. Dugan, "The History of The XV-15 Tilt Rotor Research Aircraft: From Concept to Flight," *NASA Special Publication 4517*, 2000.

[8] M. Maisel et al., "Tilt Rotor Research Aircraft Familiarization Document," NASA ARC, Moffett Field, CA, USA, Tech. Memo. TM X-62, 407, Jan. 1975.

[9] J. A. Weiberg and M. D. Maisel, "Wind-Tunnel Tests of the XV-15 Tilt Rotor Aircraft," NASA ARC, Moffett Field, CA, USA, Tech. Memo. 81177, Apr. 1980.

[10] G. B. Churchill and D. C. Dugan, "Simulation of the XV-15 Tilt Rotor Research Aircraft," NASA ARC, Moffett Field, CA, USA, Tech. Memo. 84222, Mar. 1982.

[11] Bell Helicopter Company, "Advancement of Proprotor Technology - Task 2: Wind-Tunnel Test Results," Bell Helicopter Company, Fort Worth, TX, USA, Contractor Rep. CR114363, Sep. 1971.

[12] M. D. Betzina, "Rotor Performance of an Isolated Full-Scale XV-15 Tiltrotor in Helicopter Mode," *Am. Helicopter Soc. Aerodyn. Acoust. Test Eval. Tech. Spec. Meet.*, pp. 1–12, Jan. 2002.

[13] F. Felker, L. E. Young, and D. Signor, "Performance and Loads Data from a Hover Test of a Full-Scale Advanced Technology XV-15 Rotor," NASA ARC, Moffett Field, CA, USA, Tech. Memo. 86854, Jan. 1986.

[14] R. A. Ormiston, "Revitalising Advanced Rotorcraft Research - and the Compound Helicopter," *Aeronaut. J.*, vol. 120, no. 1223, pp. 83–129, 2016, doi: 10.1017/aer.2015.5.

[15] W. Johnson, G. K. Yamauchi, and M. E. Watts, "Designs and Technology Requirements for Civil Heavy Lift Rotorcraft," presented at the AHS Vert. Lift Aircraft Des. Conf., San Francisco, CA, USA, Jan. 18-20, 2006, Paper 1.

[16] Mark Huber, "AW609 Final Accident Report Issued ," *AINonline*. [Online]. Available: https://www.ainonline.com.[Accessed:Jan.31,2020]

[17] Italy. Italian Civil Aviation Safety Investigation Authority, "Accident Occurred to the AugustaWestland AW609 Aicraft Registration Marks N609AG, in Toronzano Vercellese (VC), on the 30th of October 2015," *ANSV - Agenzia Nazionale per la Sicurezza del Volo*. [Online]. Available: http://www.ansv.it.[Accessed:Jan.31,2020]

[18] *Maple*. (2020.1). Maplesoft.

[19] *Matlab*. (R2020a). MathWorks.

[20] R. A. Ormiston, W. G. Warmbrodt, D. H. Hodges, and D. A. Peters, "Survey of Army/NASA Rotorcraft Aeroelastic Stability Research," NASA ARC, Moffett Field, CA, USA, Tech. Memo. 101026, Oct. 1988.

[21] W. A. Decker, "Handling Qualities Evaluation of XV-15 Noise Abatement Landing Approaches Using a Flight Simulator," presented at the AHS 57th Annual Forum, Washington, DC, USA, May 9-11, 2001, pp. 1211–1220.

[22] D. F. Kimball, "Recent Tilt Rotor Flight Control Law Innovations," *J. Am. Helicopter Soc.*, vol. 32, no. 3, pp. 33–42, 1987, doi: 10.4050/jahs.32.33.

[23] M. E. Dreier, *Introduction to Helicopter and Tiltrotor Simulation*. Reston, VA, USA: AIAA, Inc., 2007.

[24] W. Johnson, "Dynamics of Tilting Proprotor Aircraft in Cruise Flight," NASA, Moffett Field, CA, USA, Tech. Note TN D-7677, May 1974.

[25] ——, "Analytical Modeling Requirements for Tilting Proprotor Aircraft Dynamics," NASA, Moffett Field, CA, USA, Tech. Note TN D-8013, Jul. 1975.

[26] ——, "An Assessment of the Capability to Calculate Tilting Prop-Rotor Aircraft Performance, Loads, and Stability," NASA ARC, Moffett Field, CA, USA, Tech. Paper 2291, Mar. 1984.

[27] R. K. Heffley and M. A. Mnich, "Minimum-Complexity Helicopter Simulation Math Model," Manudyne Systems, Inc., Los Altos, CA, USA, Contractor Rep. CR177476, Apr. 1988.

[28] R. T. N. Chen, "A Survey of Nonuniform Inflow Models for Rotorcraft Flight Dynamics and Control Applications," NASA ARC, Moffett Field, CA, USA, Tech. Memo. 102219, Nov. 1989.

[29] W. Appleton, A. Filippone, and N. Bojdo, "Aeromechanics Modelling of Tiltrotor Aircraft," presented at the 45th ERF, Warsaw, Poland, Sep. 17-20, 2019, Paper 118.

[30] P. B. Harendra, M. J. Joglekar, T. M. Gaffey, and R. L. Marr, "V/STOL Tilt Rotor Study - Volume V: A Mathematical Model for Real Time Flight Simulation of the Bell Model 301 Tilt Rotor Research Aircraft," Bell Helicopter Company, A Textron Company, Fort Worth, TX, USA, Contractor Rep. CR114614, Apr. 1973.

[31] F. Barra, S. Godio, and G. Guglieri, "Implementation of a Comprehensive Mathematical Model for Tilt-Rotor Real-Time Flight Simulation," presented at the 45th ERF, Warsaw, Poland, Sep. 17-20, 2019, Paper 20.

[32] K. M. Kleinhesselink, "Stability and Control of Modeling of Tiltrotor Aircraft," Master's thesis, University of Maryland, 2007.

[33] W. Qi and W. Wenhai, "Modelling and Analysis of Tiltrotor Aircraft for Flight Control Design," *Inf. Technol. J.*, vol. 13, no. 5, pp. 885–894, 2014, doi: 10.3923/itj.2014.885.894.

[34] W. Johnson, "Analytical Model for Tilting Proprotor Aircraft Dynamics, Including Blade Torsion and Coupled Bending Modes, and Conversion Mode Operation," NASA, Moffett Field, CA, USA, Tech. Memo. TM X-62, 369, Aug. 1974.

[35] O. Gur and A. Rosen, "Comparison Between Blade-Element Models of Propellers," *Aeronaut. J.*, vol. 112, no. 1138, pp. 689–704, 2008.

[36] M. Miller and J. Narkiewicz, "Tiltrotor Modelling for Simulation in Various Flight Conditions," *J. Theor. Appl. Mech.*, vol. 44, no. 4, pp. 881–906, 2006.

[37] G. D. Klein, "Linear Modeling of Tiltrotor Aircraft (in Helicopter and Airplane Modes) for Stability Analysis and Preliminary Design," Ph.D. dissertation, Nav. Postgraduate School, Monterey, CA, USA, 1996.

[38] D. A. Peters and N. HaQuang, "Dynamic Inflow for Practical Applications," *J. Am. Helicopter Soc.*, vol. 33, no. 4, pp. 64–68, 1988.

[39] A. Gessow and G. C. Myers Jr., *Aerodynamics of the Helicopter*. New York, NY, USA: Fredderick Ungar Publishing Co., 1952.

[40] A. Gessow and A. D. Crim, "An Extension of Lifting Rotor Theory to Cover Operation at Large Angles of Attack and High Inflow Conditions," NACA, Washington, DC, USA, Tech. Note TN 2665, Apr. 1952.

[41] R. T. N. Chen, "A Simplified Rotor System Mathematical Model for Piloted Flight Dynamics Simulation," NASA ARC, Moffett Field, CA, USA, Tech. Memo. 78575, May 1979.

[42] D. A. Spera, "Models of Lift and Drag Coefficients of Stalled and Unstalled Airfoils in Wind Turbines and Wind Tunnels," Jacobs Technology, Inc., Cleveland, OH, USA, Contractor Rep. CR-2008-215434, October 2008.

[43] W. W. McCormick Jr., *Aerodynamics of V/STOL Flight*. Mineola, NY, USA: Dover Publications, Inc., 1999.

[44] E. B. Carlson and Y. J. Zhao, "Prediction of Tiltrotor Height-Velocity Diagrams Using Optimal Control Theory," *J. Aircr.*, vol. 40, no. 5, pp. 896–905, 2003.

[45] W. R. Skrzypinski, F. Zahle, and C. Bak, "Parametric Approximation of Airfoil Aerodynamic Coefficients at High Angles of Attack," *Proceedings of EWEA 2014 European Wind Energy Association (EWEA)*, 2014.

[46] J. e. a. Mulder, *Lecture Notes AE3202, Flight Dynamics*. Delft, Netherlands: TU Delft, March 10, 2013.

[47] W. Johnson, *Helicopter Theory*. New York, NY, USA: Dover Publications, Inc., 1994.

[48] A. R. S. Bramwell, G. Done, and D. Blamford, *Bramwell's Helicopter Dynamics*, 2nd ed. Oxford, UK: Butterworth-Heinemann, 2001.

[49] R. Van Aalst and M. D. Pavel, "On the Question of Adequate Modelling of Steady-State Rotor Disc-Tilt for Helicopter Manoeuvring Flight," *29th European Rotorcraft Forum 2002, ERF 2002*, 2002.

[50] *Python*. (3.8.6). python.org.

[51] *FlightGear*. (2020.3). https://www.flightgear.org/.

[52] H. Gregory D. and F. Samuel W., "Generic Tilt-Rotor Simulation (GTRSIM) User's and Prorammer's Guide, Volume 1: User's Guide, Rev. A," Systems Tech., Inc., Moffett Field, CA, USA, Contractor Rep. CR-166535, 1988.

[53] Aero Toolbox, "Standard Atmosphere Calculator." [Online]. Available: https://aerotoolbox.com/atmcalc

Part IV

Appendices

A

Implementation Parameters

This appendix presents the values of the parameters used in the 6DoF model XV-15 tilt-rotor implementation which has been used to generate the simulation results, and figures comparing the 6DoF model analytical approximations of parameter relationships to the GTRS model. This appendix is structured as follows. First the XV-15 aircraft parameters are presented consisting of the general, rotor, nacelle, drivetrain, wing, tail stabilizers', fuselage, and control parameters. Next the parameters used in the iterative inflow solver are shown, followed by the automatic ordering scheme and the simulation parameters. The appendix is concluded with the trimming routine parameters.

A.1. XV-15 Aircraft Parameters

A.1.1. General

Table A.1: 6DoF model XV-15 tilt-rotor implementation general parameters.

Parameter	Value	Units	Source
m	5897	kg	[6, p. B-10]
I_{xx}	71580	kgm^2	[6, p. B-10]
I_{yy}	28960	kgm^2	[6, p. B-10]
I_{zz}	89940	kgm^2	[6, p. B-10]
I_{xz}	1673	kgm^2	[6, p. B-10]
SL_{cg}	7.575	m	[6, p. B-10]
BL_{cg}	0	m	[6, p. B-10]
WL_{cg}	1.869	m	[6, p. B-10]

A.1.2. Rotor Parameters

Table A.2: 6DoF model XV-15 tilt-rotor implementation rotor parameters.

Parameter	Value	Units	Source
$\overline{a}_0$	$2.5\pi/180$	rad	[6, p. B-17]
c_{bl}	0.3557	m	[6, p. B-16]
$\theta_{bl,g}$	$40.9\pi/180$	rad	[6, p. B-16]
$\theta_{bl,g,0.75R}$	$6.375\pi/180$	rad	[6, p. B-16]
$\theta_{bl,1}$	$-40.9\pi/180/R$	rad/m	linear twist fig. A.1
R	3.81	m	[6, p. B-16]
N	3	–	[6, p. B-16]
I_{bl}	139.0	kgm^2	[6, p. B-13]
K_β	17480	Nm/rad	[6, p. B-17]
$C_{l_\alpha,bl}$	6.56	$1/rad$	[26, p. 6 fig. 5]
$C_{d_0,bl}$	0.015	–	[6, p. B-17]
$C_{d_1,bl}$	−0.068	$1/rad$	[6, p. B-17]
$C_{d_2,bl}$	0.81	$1/rad^2$	[6, p. B-17]
$\beta_{SP,absmax}$	$12\pi/180$	rad	[6, p. B-13]
m_{bl}	28.73	kg	eq. (4.18b)
$M_{1,bl}$	54.73	kgm	eq. (4.19b)

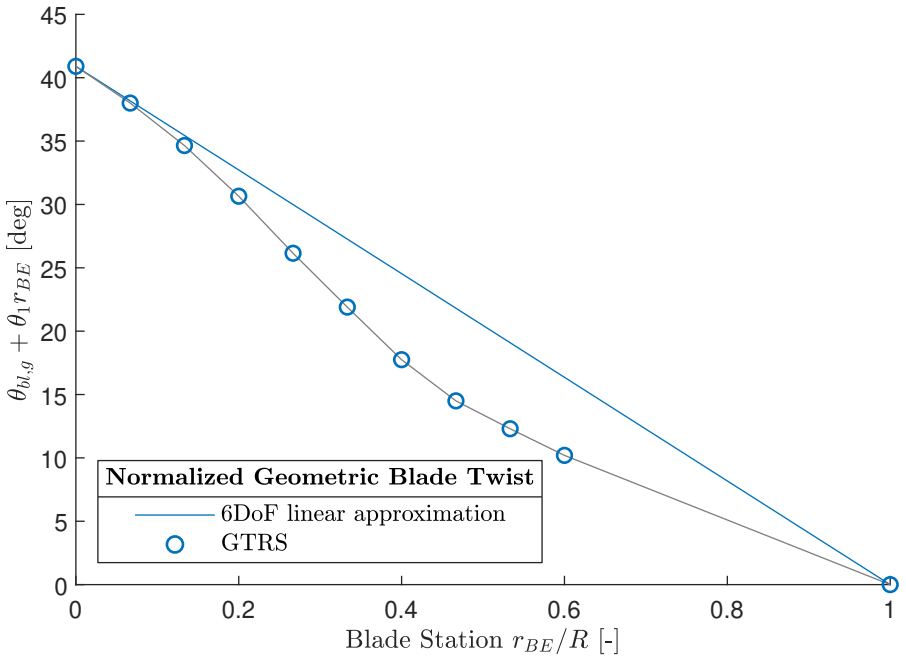

Figure A.1: Comparison between the 6DoF model linear blade twist approximation and the GTRS blade twist[6, p. B-16].

A.1.3. Nacelle/Pylon Parameters

Table A.3: 6DoF model XV-15 tilt-rotor implementation (right) tiltable nacelle parameters.

Parameter	Value	Units	Source
SL_{np}	7.62	m	[6, p. B-13]
BL_{np}	4.902	m	[6, p. B-13]
WL_{np}	2.54	m	[6, p. B-13]
l_n	1.423	m	[6, p. B-13]
d_{xn}	0.04056	m	eq. (4.22)
d_{yn}	4.902	m	eq. (4.22)
d_{zn}	0.6709	m	eq. (4.22)
$\eta_{min.}$	$-90/180\pi$	rad	[6, p. B-14]
$\eta_{max.}$	$5/180\pi$	rad	[6, p. B-14]

A.1.4. Drivetrain Parameters

Table A.4: 6DoF model XV-15 tilt-rotor implementation drivetrain parameters.

Parameter	Value	Units	Source
$HP_{RO,max}$	1400	SHP	coefficient K_{18} in [6, p. B-110]
$HP_{AV,max}$	1293	SHP	eq. (7.8b)
SHP_{acc}	10	SHP	[6, p. B-110]
η_{XMSN}	0.93	–	[6, p. B-110]
θ_{XPT}	35.133	–	θ_{RPT_1} in [6, p. B-115]
$\theta_{0,gov,max}$	33.5	deg	[6, p. B-108]
$\theta_{0,gov,min}$	-5	deg	[6, p. B-108]

A.1.5. Wing Parameters

Table A.5: 6DoF model XV-15 tilt-rotor implementation complete (right) wing and common (right) wing segments' parameters.

Parameter(s)	Value	Units	Source
$c_{r,w}$, $c_{r,frw}$, $c_{r,flw}$, $c_{r,aw}$	1.593	m	[6, p. B-31]
$c_{t,w}$, $c_{t,frw}$, $c_{t,flw}$, $c_{t,aw}$	1.593	m	[6, p. B-31]
$c_{rAC,w}$, $c_{rAC,frw}$, $c_{rAC,flw}$, $c_{rAC,aw}$	$0.25c_{r,w}$	m	simplification
Λ_w, Λ_{frw}, Λ_{flw}, Λ_{aw}	$-6.5\pi/180$	rad	[6, p. B-31]
i_w, i_{frw}, i_{flw}, i_{aw}	0	rad	[32, p. 150]
Γ_w, Γ_{frw}, Γ_{flw}, Γ_{aw}	$2\pi/180$	rad	[23, p. 131]
$C_{l_\alpha,w}$, $C_{l_\alpha,frw}$, $C_{l_\alpha,flw}$, $C_{l_\alpha,aw}$	5.31	$1/rad$	[32, p. 150]
$C_{D,max,w}$, $C_{D,max,frw}$, $C_{D,max,flw}$, $C_{D,max,aw}$	1.8	–	[45, fig. 2]
$C_{M,AC,w}$, $C_{M,AC,frw}$, $C_{M,AC,flw}$, $C_{M,AC,aw}$	−0.02	–	[32, p. 150]
$\alpha_{0L,w}$, $\alpha_{0L,frw}$, $\alpha_{0L,flw}$, $\alpha_{0L,aw}$	$-4.02\pi/180$	rad	[32, p. 150]
$C_{L,max,w}$, $C_{L,max,frw}$, $C_{L,max,flw}$, $C_{L,max,aw}$	1.112	–	eq. (4.20)
$b_{1/2,w}$	9.805/2	m	[6, p. B-31]
SL_{wte}	8.590	m	[6, p. B-31]
WL_{wcp}	2.435	m	[6, p. B-31]
$\frac{\partial C_{L,w,nominal}}{\partial \delta_{fla}}$	0.34	$1/rad$	[32, p. 150]
$\frac{\partial C_{D,w,nominal}}{\partial \delta_{fla}}$	0.304	$1/rad$	[32, p. 150]
$\frac{\partial C_{L,w,nominal}}{\partial \delta_{ail}}$	0.00316[a]	$1/rad$	for X_{FL1} in [6, p. B-54]

[a]Corrigendum: in [6, p. B-54] this value is provided in degrees (i.e. 0.00316 $1/deg$) which has not been converted to radians (i.e. $0.00316/(\pi/180)$ = 0.181 $1/rad$) before supplying it to the 6DoF model which expects the value to be provided in radians. As a result the supplied aileron aerodynamic effectiveness is approximately 57 times smaller than it should be. This should be corrected in the next 6DoF model iteration.

Table A.6: 6DoF model XV-15 tilt-rotor implementation unique (right) free wing segment parameters.

Parameter	Value	Units	Source
$b_{1/2,frw}$	1.09	m	graphically determined from [8, p. 3 fig. 2.1]
d_{xfrw}	0.1797	m	eq. (4.23)
d_{yfrw}	0	m	eq. (4.23)
d_{zfrw}	0.5659	m	eq. (4.23)

Table A.7: 6DoF model XV-15 tilt-rotor implementation unique (right) flap wing segment parameters.

Parameter	Value	Units	Source
$b_{1/2,flw}$	1.07	m	graphically determined from [8, p. 3 fig. 2.1]
$b_{1/2,wr-flw}$	$b_{1/2,frw} + b_{1/2,flw}$	m	graphically determined from [8, p. 3 fig. 2.1]
$c_{\text{flapped wing}}$	$c_{r,flw}$	m	[6, p. B-31]
c_{flap}	$0.25c_{r,flw}$	m	graphically determined from [8, p. 3 fig. 2.1]
d_{xflw}	0.3039	m	eq. (4.25)
d_{yflw}	1.0893	m	eq. (4.25)
d_{zflw}	−0.6040	m	eq. (4.25)
$\frac{\partial C_{L,flw}}{\partial \delta_{fla}}$	1.5578	$1/rad$	eq. (4.21)
$\frac{\partial C_{D,flw}}{\partial \delta_{fla}}$	1.3929	$1/rad$	eq. (4.21)

Table A.8: 6DoF model XV-15 tilt-rotor implementation unique (right) aileron wing segment parameters.

Parameter	Value	Units	Source
$b_{1/2,aw}$	2.74	m	graphically determined from [8, p. 3 fig. 2.1]
$b_{1/2,wr-aw}$	$b_{1/2,wr-flw} + b_{1/2,aw}$	m	graphically determined from [8, p. 3 fig. 2.1]
d_{xaw}	0.4258	m	eq. (4.25)
d_{yaw}	2.1587	m	eq. (4.25)
d_{zaw}	−0.6413	m	eq. (4.25)
$\frac{\partial C_{L,aw}}{\partial \delta_{ail}}$	0.0057	$1/rad$	eq. (4.21)

A.1.6. Horizontal Stabilizer Parameters

Table A.9: 6DoF model XV-15 tilt-rotor implementation (right) horizontal stabilizer segment parameters.

Parameter	Value	Units	Source
$c_{r,hs}$	1.2	m	[6, p. B-12]
$c_{t,hs}$	1.2	m	[6, p. B-12]
$c_{rAC,hs}$	$0.25c_{r,hs}$	m	simplification
Λ_{hs}	0	rad	graphically determined from [8, p. 3 fig. 2.1]
i_{hs}	0	rad	[6, p. B-56]
Γ_{hs}	0	rad	simplification
$C_{l_\alpha,hs}$	4.03	$1/rad$	[6, p. 36]
$C_{D,max,hs}$	1.8	–	[45, fig. 2]
$C_{M,AC,hs}$	0	–	simplification
$\alpha_{0L,hs}$	0	rad	[32, p. 151]
$C_{L,max,hs}$	0.844	–	eq. (4.20)
$b_{1/2,hs}$	3.91/2	m	[6, p. B-12]
SL_{hsle}	13.926	m	[6, p. B-12]
WL_{hscp}	2.616	m	[6, p. B-12]
d_{xhs}	6.651	m	eq. (4.26)
d_{yhs}	0	m	eq. (4.26)
d_{zhs}	0.7469	m	eq. (4.26)
$\frac{\partial C_{L,hs}}{\partial \delta_{ele}}$	2.29	$1/rad$	graphically determined from linear region in [6, p. 36 fig. 15]

A.1.7. Vertical Stabilizer Parameters

Table A.10: 6DoF model XV-15 tilt-rotor implementation top (right) vertical stabilizer segment and common bottom vertical stabilizer segment parameters.

Parameter	Value	Units	Source
$c_{r,vs}$, $c_{r,vst}$, $c_{r,vsb}$	1.24	m	graphically determined from [8, p. 3 fig. 2.1]
$c_{rAC,vs}$	$0.25c_{r,vs}$	m	simplification
i_{vst}, i_{vsb}	0	rad	[6, p. B-69]
$C_{l_\alpha,vst}$, $C_{l_\alpha,vsb}$	3.06	$1/rad$	[32, p. 150]
$C_{D,max,vst}$, $C_{D,max,vsb}$	1.8	–	[45, fig. 2]
$C_{M,AC,vst}$, $C_{M,AC,vsb}$	0	–	simplification
$\alpha_{0L,vst}$, $\alpha_{0L,vsb}$	0	rad	[32, p. 150]
$C_{L,max,vst}$, $C_{L,max,vsb}$	0.6409	–	eq. (4.20)
SL_{vsle}	13.88	m	[6, p. B-13]
WL_{vscp}	2.61	m	[6, p. B-12]
d_{xvst}, d_{xvsb}	6.6151	m	eq. (4.27)
d_{yvst}, d_{yvsb}	1.96	m	eq. (4.27)
d_{zvst}, d_{zvsb}	0.7409	m	eq. (4.27)
$c_{t,vst}$	0.714	m	graphically determined from [8, p. 3 fig. 2.1]
Λ_{vst}	$32.4\pi/180$	rad	graphically determined from [8, p. 3 fig. 2.1]
Γ_{vst}	$90\pi/180$	rad	simplification
$b_{1/2,vst}$	1.49	m	graphically determined from [8, p. 3 fig. 2.1]
$\frac{\partial C_{L,vst}}{\partial \delta_{rud}}$	−1.15	$1/rad$	[32, p. 150]

Table A.11: 6DoF model XV-15 tilt-rotor implementation unique (right) bottom vertical stabilizer segment parameters.

Parameter	Value	Units	Source
$c_{t,vsb}$	0.709	m	graphically determined from [8, p. 3 fig. 2.1]
Λ_{vsb}	$6.74\pi/180$	rad	graphically determined from [8, p. 3 fig. 2.1]
Γ_{vsb}	$-90\pi/180$	rad	simplification
$b_{1/2,vstb}$	0.87	m	graphically determined from [8, p. 3 fig. 2.1]

A.1.8. Fuselage Parameters

Table A.12: 6DoF model XV-15 tilt-rotor implementation fuselage parameters.

Parameter	Value	Units	Source
A_{eq}	0.1487	m^2	[32, p. 149]
d_{xfus}	0	m	simplification
d_{yfus}	0	m	simplification
d_{zfus}	0	m	simplification
i_{fus}	0	rad	simplification
Γ_{fus}	0	rad	simplification

A.1.9. Controls, Mixing, and Phasing

Analytical Approximation Comparison Figures

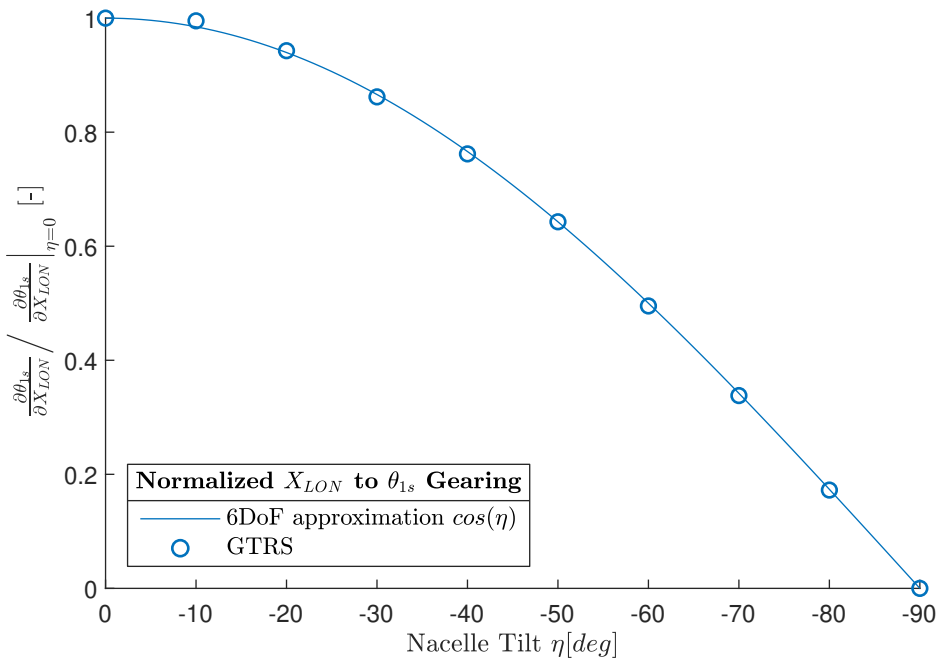

Figure A.2: Comparison of the 6DoF model analytical approximation of the longitudinal-stick-to-longitudinal-cyclic control phasing with the GTRS control phasing[6, p. B-89].

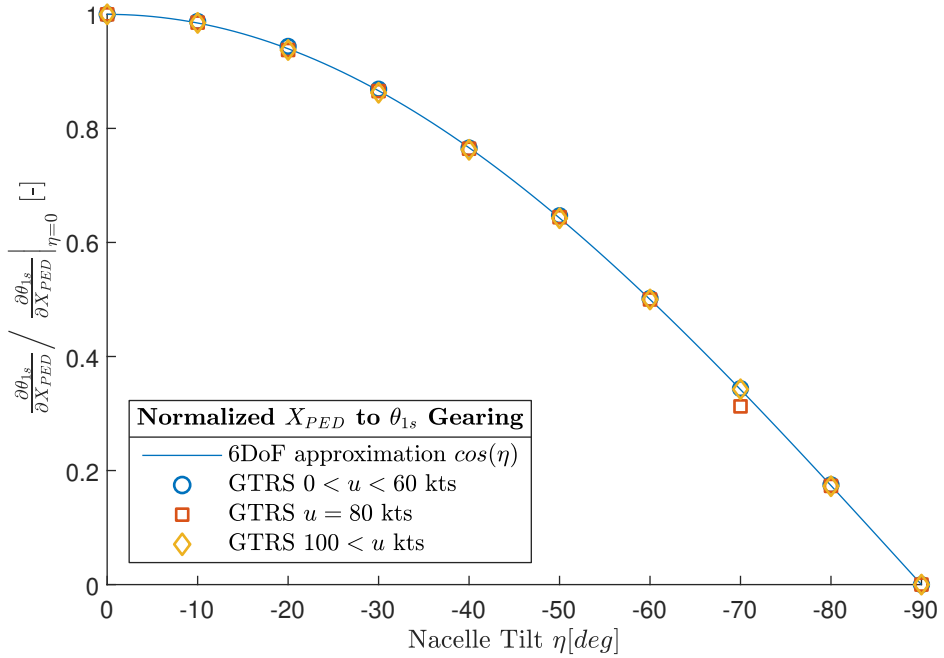

Figure A.3: Comparison of the 6DoF model analytical approximation of the pedals-to-longitudinal-cyclic control η-phasing with the GTRS control phasing for different longitudinal velocities[6, p. B-90].

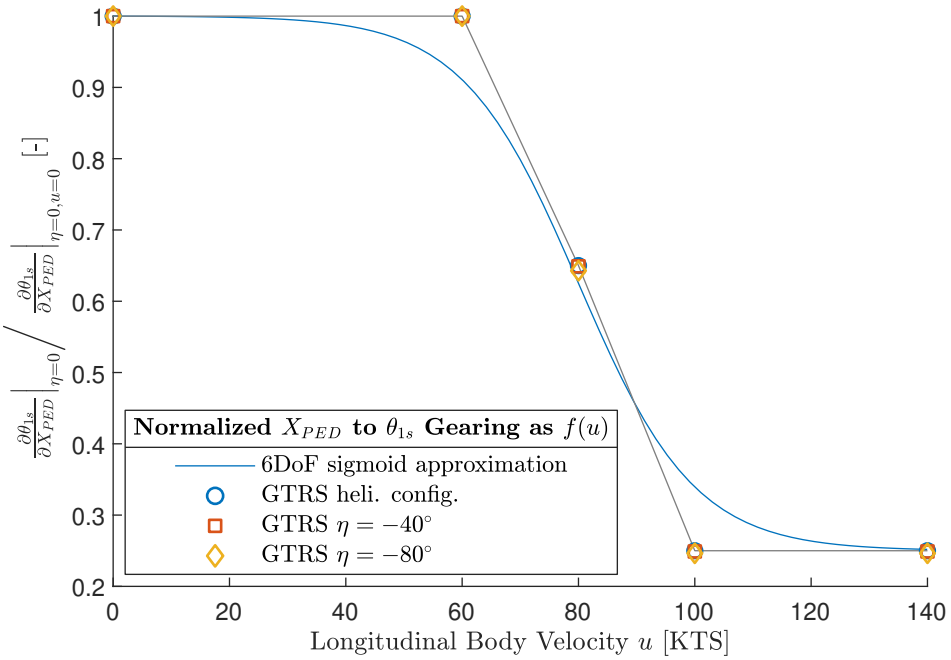

Figure A.4: Comparison of the 6DoF model analytical approximation of the pedals-to-longitudinal-cyclic control velocity-phasing with the GTRS control phasing for different nacelle tilt angles[6, p. B-90].

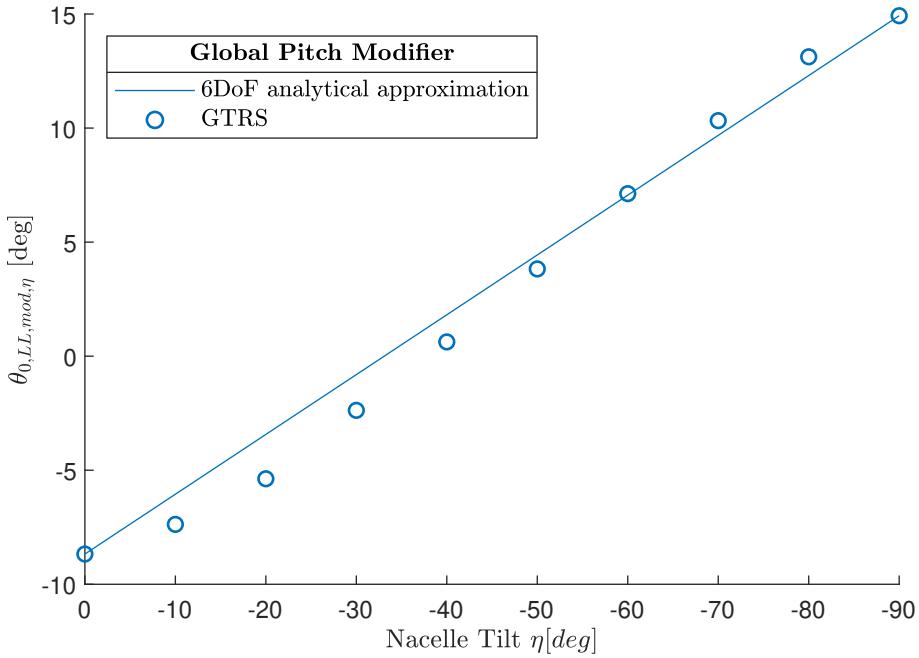

Figure A.5: Comparison of the 6DoF model analytical approximation of the global blade pitch modifier with the GTRS modifier[6, p. B-92].

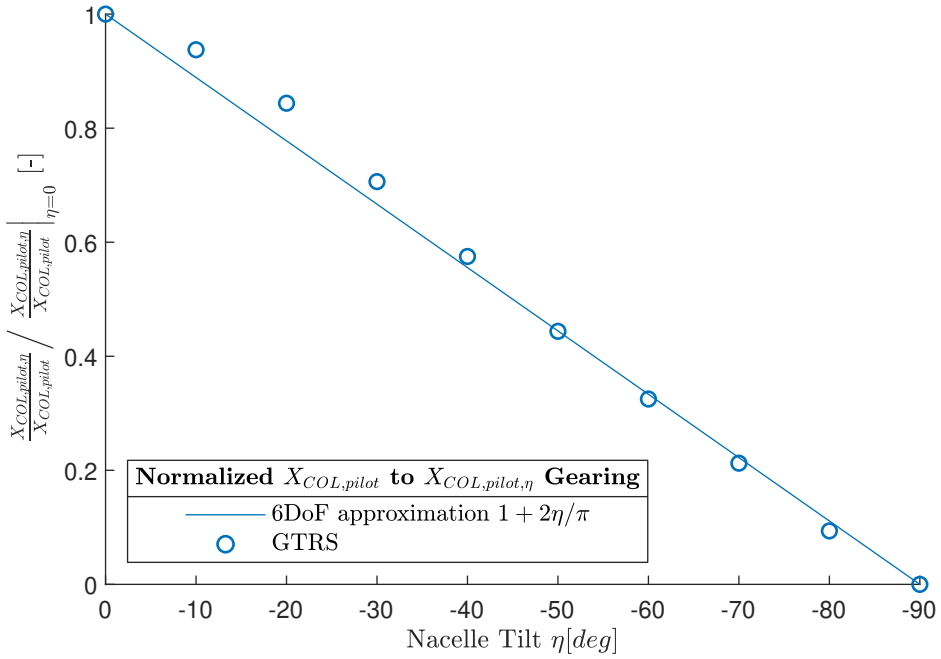

Figure A.6: Comparison of the 6DoF model analytical approximation of the collective-stick-to-swashplate-collective control phasing with the GTRS control phasing[6, p. B-92].

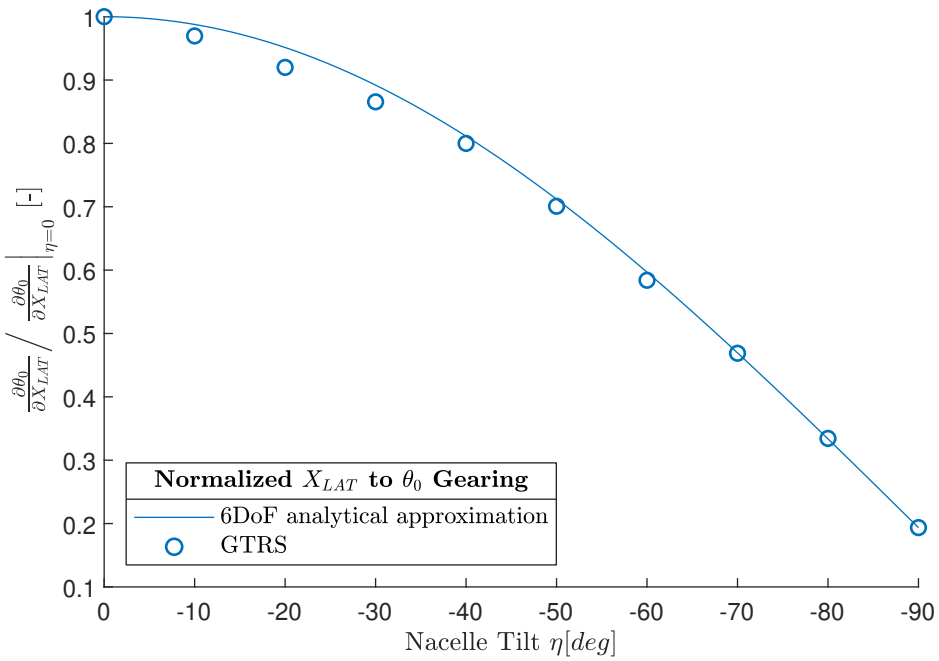

Figure A.7: Comparison of the 6DoF model analytical approximation of the lateral-stick-to-swashplate-collective control phasing with the GTRS control phasing[6, p. B-91].

Constant Parameters

Table A.13: 6DoF model control phasing and mixing constant parameters.

Parameter	Value	Units	Source
δ_{B1}	1.5	deg	[6, p. B-88]
$\frac{\partial\theta_{1s}}{\partial X_{LON}}\Big\vert_{\eta=0}$	2.1	deg/in	[6, p. B-88]
$\frac{\partial\theta_{1s}}{\partial X_{PED}}\Big\vert_{\eta=0,u=0}$	1.6	deg/in	[6, p. B-90]
$\frac{\partial\theta_{1s}}{\partial X_{PED}}\Big\vert_{\eta=0,u=100kts}$	0.4	deg/in	[6, p. B-90]
S_{inflex}	$80 \cdot 0.51444$	m/s	[6, p. B-90]
S_{slope}	0.1/0.51444	(deg/in)/(m/s)	fitted
$\theta_{0,LL,0.75R,heli}$	-2.3	deg	[6, p. B-92]
$\theta_{0,LL,0.75R,arpln}$	21.3	deg	[6, p. B-92]
$\frac{\partial\theta_0}{\partial X_{COL}}\Big\vert_{\eta=0}$	1.6	deg/in	[6, p. B-92]
$\frac{\partial\theta_0}{\partial X_{LAT}}\Big\vert_{\eta=0}$	0.625	deg/in	[6, p. B-91]
$\frac{\partial\theta_0}{\partial X_{LAT}}\Big\vert_{\eta=-\pi/2}$	0.121	deg/in	[6, p. B-91]
$\frac{\partial\delta_{ail}}{\partial X_{LAT}}$	3.93	deg/in	[6, p. B-88]
$\frac{\partial\delta_{ail}}{\partial X_{FLA}}$	47	deg/1	max flaperon deflection [6, p. A-133]
$\frac{\partial\delta_{ele}}{\partial X_{LON}}$	4.167	deg/in	[6, p. B-88]
$\frac{\partial\delta_{rud}}{\partial X_{PED}}$	8	deg/in	[6, p. B-88]
$\frac{\partial\delta_{fla}}{\partial X_{FLA}}$	75	deg/1	max flap deflection [6, p. A-133]
$\frac{\partial\dot{\eta}}{\partial X_{TIL}}$	90/12	deg/s	conversion in 12 seconds [7, p. 85]

Table A.14: 6DoF model control input limits.

Parameter	Min. Value	Max. Value	Units	Source
X_{LON}	-4.8	4.8	in	[6, p. B-15]
X_{LAT}	-4.8	4.8	in	[6, p. B-15]
$X_{COL,pilot}$	0	10	in	[6, p. B-15]
X_{PED}	-2.5	2.5	in	[6, p. B-15]
X_{FLA}	0	1	–	6DoF model
X_{TIL}	-1	1	–	6DoF model
RPM_{SEL}	601	433	RPM	[6, p. A-255]

A.2. Iterative Rotor Disk Tilt Angle, Inflow Ratio, and Thrust Solver

Table A.15: Parameters used in the iterative rotor disk tilt angle, inflow ratio, and thrust solver implementation.

Parameter	Value
K_{ϵ_T}	0.5
T_{ϵ_T}	$1e-6$
k_{max}	1000

A.3. Automatic Ordering Scheme Parameters

Table A.16: Summary of the parameters used in the setup of the automatic ordering scheme applied to the tilt-rotor model of this thesis.

AOS Parameter	Implemented Value
ϵ	0.5
E_{EOS}	0.0625
Δ_O	4
RF	1.01

Table A.17: List of minimum and maximum values of all fundamental terms and products of terms used in the reduction of the 6-DoF tilt-rotor model rotor expressions.

Term	Min.	Max.	Units	Source
ρ	0.4271	1.225	kg/m^3	min.: sea level max.: 110% service ceiling, i.e. 9.7km [source] standard atmosphere calculator [53]
Ω	54.1	61.7	rad	min.: airplane RPM max.: helicopter RPM [6, B-13]
$\overline{\omega}_{\widehat{R}\|z\widehat{R},i}$	-1.062	1.062	-	AOS
R	3.81	3.81	m	[6, B-13]
c_{bl}	0.3557	0.3557	m	[6, B-13]
K_{beta}	17480	17480	Nm/rad	[6, B-13]
N	3	3	-	[6, B-13]
$C_{l_\alpha,bl}$	6.56	6.56	rad^{-1}	[26, p6, fig.5]
$C_{d,0}$	0.015	0.015	-	[6, C-2]
$C_{d,1}$	-0.068	-0.068	rad^{-1}	[6, C-2]
$C_{d,2}$	0.81	0.81	rad^{-2}	[6, C-2]
I_{bl}	139.0	139.0	kgm^2	[6, B-13]
m_{bl}	28.73	28.73	kg	section 4.5
$M_{1,bl}$	54.71	54.71	kgm	section 4.5
γ_{bl}	1.511	4.334	-	AOS
θ_0	0.4228	1.569	rad	section 6.3
$\theta_{bl,1}$	-0.3491	0	rad/m	ranges between actual XV-15 twist and no twist
θ_{1s}	-0.2457	0.2457	rad	section 6.3
$\hat{V}_{tcr}$	0	65	m/s	min.: hover max.: max. heli. mode vel. [7, p124, fig.A-7]
$\hat{V}_{pcr}$	-20	170	m/s	custom limitation
v_{ir}	0.1	20	m/s	preliminary results
$\widehat{\mu}_c$	0	0.2765	-	calculated
$\widehat{\lambda}_c$	-0.08508	0.7232	-	calculated
$\widehat{\lambda}_i$	0.0004254	0.08508	-	calculated
Ω_{sgn}	-1	1	-	-
d_{sgn}	-1	1	-	-
l_n	1.423	1.423	m	[6, B-13]
BL_{nO}	4.902	4.902	m	[6, B-13]
d_{xn}	-0.03048	0.2108	m	calculated [6, B-11,B-13]
d_{yn}	4.902	4.902	m	calculated [6, B-11,B-13]
d_{zn}	0.4661	0.4661	m	calculated [6, B-11,B-13]
$\dot{\eta}$	-0.1309	0.1309	rad/s	90° in 12 seconds [7, p85]
$\overline{\dot{\eta}}$	-0.002122	0.002122	-	calculated
$\ddot{\eta}$	0	0	rad/m	simplification: neglect nacelle tilt jolt

(continued on next page)

Table A.17: List of minimum and maximum values of all fundamental terms and products of terms used in the reduction of the 6-DoF tilt-rotor model rotor expressions.
(concluded)

Term	Min.	Max.	Units	Source
a_0	0.0001745	0.02618	rad	preliminary results
a_1	-0.1745	0.1745	rad	preliminary results
b_1	-0.008727	0.008727	rad	preliminary results
S_η	-0.08716	-1	-	calculated
C_η	0	1	-	calculated
$S_{\theta,1s}$	-0.2433	0.2433	-	calculated
$C_{\theta,1s}$	0.9700	0.9700	-	calculated
S_Δ	-1	1	-	calculated
C_Δ	-1	1	-	calculated
$S_{\widehat{\psi}}$	-1	1	-	calculated
$C_{\widehat{\psi}}$	-1	1	-	calculated
u	-20	170	m/s	min.: custom limitation max.: never exceed velocity [source]
v	-20	20	m/s	custom limitation
w	-20	20	m/s	custom limitation
$\overline{u}$	-0.08508	0.7232	-	calculated
$\overline{v}$	-0.08508	0.08508	-	calculated
$\overline{w}$	-0.08508	0.08508	-	calculated
$\dot{u}_i$	-15	20	m/s^2	preliminary results
$\dot{v}_i$	10	10	m/s^2	custom limitation
$\dot{w}_i$	-20	40	m/s^2	preliminary results
$a_{hub\|Xn,i}$	-91.8	123.1	m/s^2	AOS
$a_{hub\|Yn,i}$	-33.4	53.4	m/s^2	AOS
$a_{hub\|Zn,i}$	-90	117.5	m/s^2	AOS
$\overline{p}_i$	-0.03241	0.03241	-	custom limitation
$\overline{q}_i$	-0.01621	0.01621	-	preliminary results
$\overline{r}_i$	-0.02107	0.02107	-	custom limitation
$\overline{p}_w$	-0.01621	0.01621	-	custom limitation
$\overline{q}_w$	-0.01621	0.01621	-	custom limitation
$\overline{r}_w$	-0.01621	0.01621	-	custom limitation
$\overline{p}$	-0.04862	0.04862	-	calculated
$\overline{q}$	-0.03241	0.03241	-	calculated
$\overline{r}$	-0.03728	0.03728	-	calculated
$\dot{p}_i$	-3.9	3.9	rad/m	custom limitation
$\dot{q}_i$	-3	3	rad/m	preliminary results
$\dot{r}_i$	-0.75	0.75	rad/m	custom limitation

A.4. Simulation Parameters

Table A.18: Quaternion constraint equation parameters.

Parameter	Value	Units
ρ	1.225	kg/m^3
g	9.81	m/s^2
K_c	32	–

A.5. Trimming Routine Parameters

Table A.19: Options used with the *fmincon* Matlab function in the trimming routine.

Option	Value
'Algorithm'	'sqp'
'ObjectiveLimit'	5e−5
'MaxFunctionEvaluations'	1e+3

B

6DoF Model Assumptions and Simplifications

The following is a list of the assumptions and simplifications employed in the 6DoF tilt-rotor model, grouped by subsystem.

General Assumptions and Simplifications

- All tilt-rotor structural elements are assumed to be rigid.
- The rate of change of the mass and moment of inertia of the tilt-rotor has no effect on the flight mechanics model, however these values may be changed during simulation.
- The tilt-rotor airframe geometry and mass distribution is assumed to be symmetrical in the surge-heave (X_b-Z_b) plane.
- The simulation environment is defined by a flat, non-rotating Earth which is considered an inertial frame of reference.
- Gravity is assumed to be uniform therefore the center of mass coincides with the center of gravity (CoG).
- The rotor and wing ground effects are not modeled.
- Mach effects on aerodynamic coefficients are not taken into account.
- The nacelle tilting motion does not have an effect on the body dynamics, and vice versa.
- The nacelle tilt position does not alter the overall inertia of the tilt-rotor.

Rotor Assumptions and Simplifications

- Effect of gravitational acceleration on blades is assumed negligible.
- In accordance with the limitations of the blade-element theory mentioned in [47], the blade aspect ratio is assumed to be high and air is assumed to be incompressible.
- The rotor-induced velocity is assumed to be uniform across the rotor disk and only consists of a single steady linear velocity component perpendicular to the disk plane.
- In the derivation of the velocities experienced by the blade element, it is assumed that the induced velocity is perpendicular to the control plane instead of the disk plane.
- Is is assumed that the tangential blade element velocity is much greater than its perpendicular counterpart.
- It is assumed that the blade element lift component is much greater than its drag component.
- The blade is assumed to have a constant cross-sectional shape and area, and the twist angle is defined by a linearly varying component.
- The blade is assumed to be rigid.
- The blade is treated as a slender rod in terms of mass moment of inertia.
- The lift coefficient of the blade element is assumed to vary linearly with the blade element angle of attack, and it is assumed that the zero-lift angle of attack is equal to zero.
- The drag coefficient of the blade element is assumed to vary according to a second-degree polynomial as a function of the blade element angle of attack with a zero-angle-of-attack component.

- The pitching moment of the blade element is assumed to be negligible and therefore it is not included in the model.
- The flow reversal region is not taken into account.
- The tip loss factor is not taken into account.
- The aerodynamic center of the blade profile is assumed to lie at its quarter-chord point.
- The blade feathering axis is assumed to coincide with the blade quarter-chord point.
- The blade is assumed to only rotate around the shaft, feathering, and flapping axes. Lead/lag motion is not modeled.
- The rate of change of the longitudinal cyclic $\dot{\theta}_{1s}$ is assumed to have a negligible effect on the aerodynamics of the rotor and therefore it is also not included in the calculation of the velocities experienced by the blade element.
- The rate of change of the wind shift angle $\dot{\Delta}$ is not included in the calculation of the velocities experienced by the blade element.
- The first harmonic quasi-static method is used to solve the flapping equation yielding only a steady-state solution in the form of a coning angle and disk tilt angles.
- The small angle approximation is used with the flapping, longitudinal cyclic, and blade inflow angles.
- Any non-linear flapping angle terms (e.g. $\widehat{\beta^2}$) are removed from the flapping equation and the rotor force and moment expressions defined in the rotating frame.
- Rotor forces and moments acting on the rotor hub are averaged over one revolution. Any force or moment variation throughout one revolution is therefore neglected.
- The mutual wake effect of the two rotors in proximity is neglected.

Nacelle Assumptions and Simplifications

- The nacelle is assumed to only rotate in pure tilting motion, i.e. around the axis parallel to the Y_b body axis. Any lateral angular deviation as part of the tilting motion is not modeled.

Wing and Tail Lifting Surface Assumptions and Simplifications

- The main wing induced angle of attack at the horizontal tail is assumed to be zero. It is possible to specify a non-zero induced angle of attack however in the 6DoF model.
- Due to the setup of the rotor wake calculation and the relative position of the horizontal stabilizer mean aerodynamic chord aerodynamic center the rotor wash is assumed to not affect the horizontal stabilizer.
- The lifting surfaces are assumed to be rigid.
- The lift and drag coefficients of the lifting surfaces are modeled by a flat plate with the possibility to have a non-zero angle of attack and control surfaces that may influence the aerodynamic coefficients.
- The pitching moment coefficients around the aerodynamic centers of the lifting surfaces are assumed to be constant which may be affected by control surface deflections.
- The lifting surface aerodynamic coefficients are assumed to be equal to the aerodynamic coefficients of their profiles, ignoring all three-dimensional aerodynamic effects.
- Control surface aerodynamic effectiveness is assumed to be constant.
- The lift, drag, and pitching moment of a lifting surfaces is assumed to act at the aerodynamic center of the mean aerodynamic chord of the lifting surface.
- The aerodynamic center of a lifting surface profile is assumed to lie at the quarter-chord point of the profile.
- The lifting surfaces are assumed to be trapezoidal in shape.

Fuselage Assumptions and Simplifications

- The fuselage is assumed to only produce drag and no lift or aerodynamic pitching moment.
- The effect of rotor wash on the fuselage is assumed to be negligible.

C

Disk Tilt Rotor Equations

This appendix presents the elements of the 6DoF model disk tilt approximation expressions, and shows the derivation of a linearized thrust and inflow solver. The linearized solver is compared to the non-linear iterative solver in order to assess the error introduced by the linearization process.

C.1. Disk Tilt Approximation Matrix Elements

This section presents the analytical expressions of the elements of the $\boldsymbol{A}$ and $\boldsymbol{B}$ matrices that form the system of linear equations of the disk tilt angles and BEM thrust, where the generalized description is introduced in section 5.2 with eq. (5.79), appended with the inflow ratio unknown as shown in eq. (5.81), and expanded by the BEM thrust expression given by eq. (5.88) ultimately forming the linear system shown in eq. (C.1). The elements of the $\boldsymbol{A_{4\times4}}$ matrix are given by eq. (C.2) while the elements of the $\boldsymbol{B'}$ matrix are given by eq. (C.3). The definitions of the two elements of the original $\boldsymbol{B}$ matrix (i.e. eq. (5.79)) are given by eqs. (5.81c) and (5.81d) and are repeated below as well for clarity. Equation (C.4) provides the expansion of several combined rotational rates that have been introduced into the two previous equations for notation compactness and improved readability. The rotational rates have also been made non-dimensional, indicated with an overbar symbol ($\bar{}$), by dividing them by Ω for improved readability and consistency with the rotor force and moment expressions. An overview and description of the subscripts of these non-dimensional and combined terms is given in table C.1.

The matrix elements presented below are not the complete expressions corresponding to the tilt-rotor model. Instead, for the purpose of their presentation in this thesis work, they have been simplified in a similar fashion as the flapping equation (presented in section 5.2) in order to improve their readability and aid analysis. The following simplifications have been applied. First of all, the original system of equations has been supplied to the automatic ordering scheme (described in section 6.3) yielding a set of reduced expressions containing only the terms that are considered significant according to the set threshold (a summary of the AOS parameters determining the threshold is provided in appendix E). Next, the reduced expressions have been simplified by setting the linear hub acceleration terms, the control plane deflection θ_{1s}, the wind shift angle Δ, and the linearly varying blade twist parameter $\theta_{bl,1}$ to zero. Finally, the inflow ratio $\widehat{\lambda}_{pc}$ and induced velocity ratio λ_i are again combined into a single total inflow ratio $\widehat{\lambda}_{tot}$ in accordance with eq. (5.73) which is repeated below for clarity.

$$\boldsymbol{A_{4\times4}}\widehat{\boldsymbol{a}}' = \boldsymbol{B'} \tag{C.1a}$$

$$\begin{bmatrix} A_{11} & A_{12} & 0 & A_{14} \\ A_{21} & A_{22} & 0 & A_{24} \\ A_{31} & A_{32} & A_{33} & 0 \\ 0 & A_{42} & 0 & A_{44} \end{bmatrix} \begin{pmatrix} \widehat{a}_0 \\ \widehat{a}_1 \\ \widehat{b}_1 \\ \lambda_i \end{pmatrix} = \begin{pmatrix} B_1{}' \\ B_2{}' \\ B_3 \\ B_4 \end{pmatrix} \tag{C.1b}$$

$$\widehat{\lambda}_{tot} = \widehat{\lambda}_{pc} - \lambda_i \tag{5.73}$$

$$A_{11} = \Omega^2 \left(\Omega_{sgn} - \overline{r}_{i,eff}\right)^2 I_{bl} + K_\beta \tag{C.2a}$$

$$A_{12} = \Omega_{sgn} \frac{I_{bl}\gamma_{bl}\Omega^2}{12} \left(\overline{p}_{eff}\left(\widehat{\lambda}_{pc} + \frac{3\theta_0}{2}\right) - \overline{r}_{w,eff}\widehat{\mu}_{tc}\right) \tag{C.2b}$$

$$A_{14} = \frac{I_{bl}\gamma_{bl}\Omega^2}{6}\left(\Omega_{sgn}\overline{r}_{eff} - 1\right) \tag{C.2c}$$

$$A_{21} = \frac{I_{bl}\gamma_{bl}\Omega^2}{4}\theta_0\overline{q} \tag{C.2d}$$

$$A_{22} = \frac{I_{bl}\gamma_{bl}\Omega^2}{16}\left(\left(2 - \widehat{\mu}_{tc}\right) + \Omega_{sgn}\frac{4}{3}\left(\overline{p}_{eff}\theta_0\widehat{\mu}_{tc} + \frac{3}{2}\overline{r}_{w,eff}\right) + 2\overline{r}_{eff}\overline{r}_{i,eff}\right) \tag{C.2e}$$

$$A_{24} = -\frac{I_{bl}\gamma_{bl}\Omega^2}{4}\widehat{\mu}_{tc} \tag{C.2f}$$

$$A_{31} = \frac{I_{bl}\gamma_{bl}\Omega^2}{6}\left(\widehat{\mu}_{tc} - S_\eta\overline{p}\widehat{\mu}_{tc} - \Omega_{sgn}\left(\widehat{\lambda}_{pc} + \frac{3\theta_0}{2}\right)\overline{p}_{eff}\right) \tag{C.2g}$$

$$A_{32} = \frac{I_{bl}\Omega^2}{12}\left(9\overline{p}_i^2 C_\eta^2 - \gamma_{bl}\theta_0\overline{q}\widehat{\mu}_{tc} - 18\overline{r}_{i,eff}\overline{r}_i C_\eta\right) - K_\beta \tag{C.2h}$$

$$A_{33} = \frac{I_{bl}\gamma_{bl}\Omega^2}{8}\left(\Omega_{sgn} - \overline{r}_{i,eff}\right) \tag{C.2i}$$

$$A_{42} = -\Omega_{sgn}\frac{I_{bl}\gamma_{bl}\Omega^2 N}{6R}\left(\overline{p}_{eff}\theta_0 - \frac{3\overline{r}_{w,eff}\widehat{\mu}_{tc}}{4} + \frac{3\overline{p}_{eff}\widehat{\lambda}_{pc}}{4}\right) \tag{C.2j}$$

$$A_{44} = \frac{I_{bl}\gamma_{bl}\Omega^2 N}{4R}\left(\Omega_{sgn}\overline{r}_{eff} - 1\right) \tag{C.2k}$$

$$B_1{}' = \frac{I_{bl}\gamma_{bl}\Omega^2}{8}\left[\left(\widehat{\mu}_{tc} + \overline{r}_{eff}^2 + 1\right)\theta_0 + \frac{4\widehat{\lambda}_{pc}}{3} - 2\Omega_{sgn}\left(\theta_0\overline{r}_{eff} - \frac{\overline{p}_{eff}\widehat{\mu}_{tc}}{3} + \frac{2\overline{r}_{eff}\widehat{\lambda}_{pc}}{3}\right)\right] + K_\beta\overline{a}_0 \tag{C.3a}$$

$$\begin{aligned} B_2{}' = \frac{I_{bl}\Omega^2}{3}\Bigg[\Bigg(\left(\theta_0 + \frac{3\widehat{\lambda}_{pc}}{4}\right)\widehat{\mu}_{tc} - \Omega_{sgn}\left(\theta_0\widehat{\mu}_{tc}\overline{r}_{eff} - \frac{3\overline{p}_{eff}}{8}\right) - \frac{3\overline{r}_{eff}\overline{p}_{eff}}{8}\Bigg)\gamma_{bl} \\ - 6\overline{q}_{i,tot} + 3\Omega_{sgn}\left(2\overline{q}_{i,tot}\overline{r}_{i,eff} + \frac{\dot{p}_{i,eff}}{\Omega^2}\right)\Bigg] \end{aligned} \tag{C.3b}$$

$$B_3 = \frac{I_{bl}\Omega^2}{8}\left(16\overline{r}_{i,eff}\overline{p}_{i,eff} - \frac{8\dot{q}_i}{\Omega^2} - 16\Omega_{sgn}\overline{p}_{i,eff} - (\overline{q}_{tot} - \Omega_{sgn}\overline{q}\overline{r}_{eff})\gamma_{bl}\right) \tag{C.3c}$$

$$B_4 = -\frac{I_{bl}\gamma_{bl}\Omega^2 N}{R}\left[\frac{\theta_0}{6}\left(\overline{r}^2_{eff} - \overline{r}^2 C^2_\eta + \frac{3\widehat{\mu}^2_{tc}}{2} + 1\right) + \frac{\widehat{\lambda}_{pc}}{4} - \Omega_{sgn}\left(\frac{\theta_0\overline{r}_{eff}}{3} + \overline{r}_{eff}\widehat{\lambda}_{pc} - \frac{\overline{p}_{eff}\widehat{\mu}_{tc}}{2}\right)\right] \tag{C.3d}$$

$$B_1 = B'_1 - A_{14}\lambda_i \tag{5.81c}$$

$$B_2 = B'_2 - A_{24}\lambda_i \tag{5.81d}$$

$$\overline{p}_X = \frac{p_X}{\Omega} \tag{C.4a}$$

$$\overline{q}_X = \frac{q_X}{\Omega} \tag{C.4b}$$

$$\overline{r}_X = \frac{r_X}{\Omega} \tag{C.4c}$$

$$\overline{\dot{\eta}} = \frac{\dot{\eta}}{\Omega} \tag{C.4d}$$

$$\overline{p}_{eff} = \overline{p}C_\eta - \overline{r}S_\eta \tag{C.4e}$$

$$\overline{r}_{eff} = \overline{p}S_\eta + \overline{r}C_\eta \tag{C.4f}$$

$$\overline{p}_{i,eff} = \overline{p}_i C_\eta - \overline{r}_i S_\eta \tag{C.4g}$$

$$\overline{r}_{i,eff} = \overline{p}_i S_\eta + \overline{r}_i C_\eta \tag{C.4h}$$

$$\overline{r}_{w,eff} = \overline{p}_w S_\eta + \overline{r}_w C_\eta \tag{C.4i}$$

$$\dot{p}_{i,eff} = \dot{p}_i C_\eta - \dot{r}_i S_\eta \tag{C.4j}$$

$$\overline{q}_{tot} = \overline{q} + \overline{\dot{\eta}} \tag{C.4k}$$

$$\overline{q}_{i,tot} = \overline{q}_i + \overline{\dot{\eta}} \tag{C.4l}$$

Table C.1: Description of subscripts of combined rotational rates.

Subscript	Description
[none]	Aerodynamic rate - motion of the air wrt. the tilt-rotor, consisting of an inertial rate and a wash rate. Example - aerodynamic yaw rate $r = r_i - r_w$. Detailed description can be found on page 118.
i	Inertial rate - motion of the tilt-rotor wrt. an inertial frame of reference. Detailed description can be found on page 118.
w	Wash rate - motion of the air wrt. an inertial frame of reference. Detailed description can be found on page 118.
eff	'Effective' rate - combination of two orthogonal rates forming a single rate as a sinusoidal function of the nacelle tilt angle. Detailed description can be found on page 127.
tot	'Total' rate - combination of two rates acting around the same axis. Detailed description can be found on page 127.
X	Any valid combination of the subscripts i, w, eff, and tot.

C.2. Linearized Thrust and Inflow Ratio Solver

As described in section 5.2, an iterative approach is nominally employed in order to solve for the disk tilt angles, rotor inflow, and rotor thrust due to the non-linearity of several of the involved expressions. However, considering the computational cost of this iterative approach, an attempt has been made to linearize the appropriate expressions in order to form a linear system which yields the solution for the disk tilt angles, rotor inflow, and rotor thrust in one computation step instead. This approach does employ several additional simplifications which do introduce noticeable changes to the solution, as shall be discussed later.

The formation of the linear system starts with the linearization of the momentum thrust expression (i.e. eq. (5.92), repeated below for clarity) around a linearization state (LS) with the use of a multivariable first order Taylor expansion as shown in eq. (C.5). This translates to the momentum thrust evaluated at a desired state $\widehat{\boldsymbol{a}}$ being approximately equal to the same expression evaluated at the linearization state $\widehat{a}_{\text{LS}}$ plus the gradient (∇) of the momentum thrust evaluated at that same linearization state dot-multiplied by the vector difference from the linearization state to the desired state. Note that the gradient of $\widehat{T}_M$ involves taking the partial derivatives of the expression with respect to the elements of vector $\widehat{\boldsymbol{a}}$, and the result must be arranged into row-vector form. Since the momentum thrust does not depend on the coning angle $\widehat{a}_0$, its corresponding partial derivative is directly set to zero.

$$\widehat{T}_M = 2\lambda_i \rho \pi R^4 \Omega^2 \sqrt{(\widehat{\mu}_{tc} - \widehat{a}_1 \widehat{\lambda}_{pc})^2 + (\widehat{b}_1 \widehat{\lambda}_{pc})^2 + (\widehat{a}_1 \widehat{\mu}_{tc} + \widehat{\lambda}_{pc} - \lambda_i)^2} \tag{5.92}$$

$$\begin{aligned} \widehat{T}_M\big|_{\widehat{\boldsymbol{a}}} &\approx \widehat{T}_M\big|_{\widehat{\boldsymbol{a}}_{\text{LS}}} + \nabla \widehat{T}_M\big|_{\widehat{\boldsymbol{a}}_{\text{LS}}} (\widehat{\boldsymbol{a}} - \widehat{\boldsymbol{a}}_{\text{LS}}) \\ &= \widehat{T}_M\big|_{\widehat{\boldsymbol{a}}_{\text{LS}}} + \begin{pmatrix} 0 & \frac{\partial \widehat{T}_M}{\partial \widehat{a}_1}\Big|_{\widehat{\boldsymbol{a}}_{\text{LS}}} & \frac{\partial \widehat{T}_M}{\partial \widehat{b}_1}\Big|_{\widehat{\boldsymbol{a}}_{\text{LS}}} & \frac{\partial \widehat{T}_M}{\partial \lambda_i}\Big|_{\widehat{\boldsymbol{a}}_{\text{LS}}} \end{pmatrix} \begin{pmatrix} \widehat{a}_0 - \widehat{a}_{0_{\text{LS}}} \\ \widehat{a}_1 - \widehat{a}_{1_{\text{LS}}} \\ \widehat{b}_1 - \widehat{b}_{1_{\text{LS}}} \\ \lambda_i - \lambda_{i_{\text{LS}}} \end{pmatrix} \end{aligned} \tag{C.5}$$

Evaluating the dot-product, rearranging the result, and expanding the $\widehat{\boldsymbol{a}}$ vector by an additional unknown makes it possible to place the momentum thrust expression within the linear system of equations as shown in eq. (C.6), with the definition of the newly added matrix elements of the fifth row shown in eq. (C.7).

$$\boldsymbol{A_{5\times5}} \widehat{\boldsymbol{a}}' = \boldsymbol{B'_{1\times5}} \tag{C.6a}$$

$$\begin{bmatrix} A_{11} & A_{12} & 0 & A_{14} & 0 & 0 \\ A_{21} & A_{22} & 0 & A_{24} & 0 & 0 \\ A_{31} & A_{32} & A_{33} & 0 & 0 & 0 \\ 0 & A_{42} & 0 & A_{44} & -1 & 0 \\ 0 & A_{52} & A_{53} & A_{54} & 0 & -1 \end{bmatrix} \begin{pmatrix} \widehat{a}_0 \\ \widehat{a}_1 \\ \widehat{b}_1 \\ \lambda_i \\ \widehat{T}_{\text{BEM}} \\ \widehat{T}_{\text{M}} \end{pmatrix} = \begin{pmatrix} B'_1 \\ B'_2 \\ B_3 \\ B_4 \\ B_5 \end{pmatrix} \tag{C.6b}$$

$$K_{\text{sqrt}}\big|_{\widehat{\boldsymbol{a}}_{\text{LS}}} = \frac{\widehat{T}_M\big|_{\widehat{\boldsymbol{a}}_{\text{LS}}}}{2\lambda_{i_{\text{LS}}} \rho \pi R^4 \Omega^2} = \sqrt{(\widehat{\mu}_{tc} - \widehat{a}_{1_{\text{LS}}} \widehat{\lambda}_{pc})^2 + (\widehat{b}_{1_{\text{LS}}} \widehat{\lambda}_{pc})^2 + (\widehat{a}_{1_{\text{LS}}} \widehat{\mu}_{tc} + \widehat{\lambda}_{pc} - \lambda_{i_{\text{LS}}})^2} \tag{C.7a}$$

$$A_{52} = \left.\frac{\partial \widehat{T}_M}{\partial \widehat{a}_1}\right|_{\widehat{\boldsymbol{a}}_{\text{LS}}} = 2\lambda_{i_{\text{LS}}} \rho \pi R^4 \Omega^2 \frac{(\widehat{\mu}_{tc}^2 + \widehat{\lambda}_{pc}^2)\widehat{a}_{1_{\text{LS}}} - \widehat{\mu}_{tc} \lambda_{i_{\text{LS}}}}{K_{\text{sqrt}}\big|_{\widehat{\boldsymbol{a}}_{\text{LS}}}} \tag{C.7b}$$

$$A_{53} = \left.\frac{\partial \widehat{T}_M}{\partial \widehat{b}_1}\right|_{\widehat{\boldsymbol{a}}_{\text{LS}}} = 2\lambda_{i_{\text{LS}}} \rho \pi R^4 \Omega^2 \frac{\widehat{b}_{1_{\text{LS}}} \widehat{\lambda}_{pc}^2}{K_{\text{sqrt}}\big|_{\widehat{\boldsymbol{a}}_{\text{LS}}}} \tag{C.7c}$$

$$A_{54} = \left.\frac{\partial \widehat{T}_M}{\partial \lambda_i}\right|_{\widehat{\boldsymbol{a}}_{\mathbf{LS}}} = 2\lambda_{i_{\mathrm{LS}}}\rho\pi R^4\Omega^2\frac{\lambda_{i_{\mathrm{LS}}} - \widehat{\lambda}_{pc} - \widehat{\mu}_{tc}\widehat{a}_{1_{\mathrm{LS}}}}{K_{\mathrm{sqrt}}|_{\widehat{\boldsymbol{a}}_{\mathbf{LS}}}} + 2\rho\pi R^4\Omega^2\, K_{\mathrm{sqrt}}|_{\widehat{\boldsymbol{a}}_{\mathbf{LS}}} \tag{C.7d}$$

$$\begin{aligned} B_5 &= \left.\frac{\partial \widehat{T}_M}{\partial \widehat{a}_1}\right|_{\widehat{\boldsymbol{a}}_{\mathbf{LS}}} \widehat{a}_{1_{\mathrm{LS}}} + \left.\frac{\partial \widehat{T}_M}{\partial \widehat{b}_1}\right|_{\widehat{\boldsymbol{a}}_{\mathbf{LS}}} \widehat{b}_{1_{\mathrm{LS}}} + \left.\frac{\partial \widehat{T}_M}{\partial \lambda_i}\right|_{\widehat{\boldsymbol{a}}_{\mathbf{LS}}} \lambda_{i_{\mathrm{LS}}} - \widehat{T}_M|_{\widehat{\boldsymbol{a}}_{\mathbf{LS}}} \\ &= A_{52}\widehat{a}_{1_{\mathrm{LS}}} + A_{53}\widehat{b}_{1_{\mathrm{LS}}} + A_{54}\lambda_{i_{\mathrm{LS}}} - \widehat{T}_M|_{\widehat{\boldsymbol{a}}_{\mathbf{LS}}} \end{aligned} \tag{C.7e}$$

The above system is still underdetermined, however, as there are fewer equations than unknowns since the BEM thrust and momentum thrust are not considered equivalent (hence two separate thrust unknowns, i.e. $\widehat{T}_{\mathrm{BEM}}$ and $\widehat{T}_{\mathrm{M}}$, in the $\widehat{\boldsymbol{a}}'$ vector). This is due to the fact that the two thrusts are determined in different reference frames and therefore some transformation must first take place before the equivalence constraint may be imposed. It must be remembered, however, that the BEM thrust is not the resultant force generated by the rotor. Instead, the H- and S-forces must also be determined which, together with the BEM thrust, finally form a resultant rotor force that may undergo the necessary transformation from the (wind axis) control plane into the (wind axis) disk plane in order to perform the comparison between the thrust obtained with the blade element method and momentum theory. If, however, $\widehat{a}_1$ and $\widehat{b}_1$ are considered small, then the transformation of the BEM forces may be omitted and instead the BEM thrust may be assumed to be equal to the momentum theory thrust directly and thus both expressions may be linked with the same unknown variable $\widehat{T}$ as shown in eq. (C.8) forming a 5 by 5 linear system.

$$\boldsymbol{A}_{\mathbf{5\times5}}\widehat{\boldsymbol{a}}' = \boldsymbol{B}'_{\mathbf{1\times5}} \tag{C.8a}$$

$$\begin{bmatrix} A_{11} & A_{12} & 0 & A_{14} & 0 \\ A_{21} & A_{22} & 0 & A_{24} & 0 \\ A_{31} & A_{32} & A_{33} & 0 & 0 \\ 0 & A_{42} & 0 & A_{44} & -1 \\ 0 & A_{52} & A_{53} & A_{54} & -1 \end{bmatrix} \begin{pmatrix} \widehat{a}_0 \\ \widehat{a}_1 \\ \widehat{b}_1 \\ \lambda_i \\ \widehat{T} \end{pmatrix} = \begin{pmatrix} B'_1 \\ B'_2 \\ B_3 \\ B_4 \\ B_5 \end{pmatrix} \tag{C.8b}$$

Unfortunately the above system does not incorporate the lateral disk tilt angle correction (given by eq. (5.83)) which is non-linear as well. Its inclusion into the system would only be possible if it were to be linearized, however this may prove to be a more difficult task than expected due to the presence of an absolute value function. Fortunately there exists a different solution to the problem which yields an invertible $\boldsymbol{A}$ matrix while still allowing for the inclusion of the lateral disk tilt angle correction, as is described next.

If the order of each function of $\widehat{b}_1$ ($O^{f(\widehat{b}_1)}$) within the momentum theory thrust expression is higher than the tailored significance threshold ($T_{\mathrm{tail}}|_{\widehat{T}_M}$), then all of these functions are considered insignificant and thus may be removed from the expression resulting in element A_{53} being equal to zero, as formally described by eq. (C.9). The application of the ordering scheme to the momentum theory thrust does indeed indicate that all functions of $\widehat{b}_1$ are considered insignificant within the expression supporting the acceptability of this simplification.

$$O^{f(\widehat{b}_1)} > T_{\mathrm{tail}}|_{\widehat{T}_M} \implies A_{53} = 0 \tag{C.9}$$

As a consequence only the third row now depends on $\widehat{b}_1$ therefore both the row and $\widehat{b}_1$ may be removed from the system reducing it to four equations and four unknowns as shown by eq. (C.10).

$$\boldsymbol{A}_{\mathbf{4\times4}}\widehat{\boldsymbol{a}}' = \boldsymbol{B}'_{\mathbf{1\times4}} \tag{C.10a}$$

$$\begin{bmatrix} A_{11} & A_{12} & A_{14} & 0 \\ A_{21} & A_{22} & A_{24} & 0 \\ 0 & A_{42} & A_{44} & -1 \\ 0 & A_{52} & A_{54} & -1 \end{bmatrix} \begin{pmatrix} \widehat{a}_0 \\ \widehat{a}_1 \\ \lambda_i \\ \widehat{T} \end{pmatrix} = \begin{pmatrix} B'_1 \\ B'_2 \\ B_4 \\ B_5 \end{pmatrix} \tag{C.10b}$$

Inverting the system, as shown in eq. (C.11), yields the solution which may then be used to evaluate the lateral disk tilt angle and its correction with eq. (5.80c) and eq. (5.83) respectively, repeated below for clarity.

$$\begin{pmatrix} \widehat{a}_0 \\ \widehat{a}_1 \\ \lambda_i \\ \widehat{T} \end{pmatrix} = \begin{bmatrix} A_{11} & A_{12} & A_{14} & 0 \\ A_{21} & A_{22} & A_{24} & 0 \\ 0 & A_{42} & A_{44} & -1 \\ 0 & A_{52} & A_{54} & -1 \end{bmatrix}^{-1} \begin{pmatrix} B'_1 \\ B'_2 \\ B_4 \\ B_5 \end{pmatrix} \tag{C.11}$$

$$\widehat{b}_1 = \frac{1}{A_{33}} \left(B_3 - A_{31}\widehat{a}_0 - A_{32}\widehat{a}_1 \right) \tag{5.80c}$$

$$\widehat{b}_{1,corr} = \widehat{b}_1 + \Omega_{sgn} \frac{K_{b1}\lambda_i}{1 + \widehat{\mu}_{tc}^2/2} \tag{5.83a}$$

$$K_{b1} = \frac{1.33\widehat{\mu}_{tc} / \left|\widehat{\lambda}_{tot}\right|}{1.2 + \widehat{\mu}_{tc} / \left|\widehat{\lambda}_{tot}\right|} \tag{5.83b}$$

As such this approach yields the solution for the disk tilt angles, rotor inflow, and rotor thrust in one computation step as compared to the iterative approach which must repeat its calculations (typically) tens of times in order to converge onto a solution. When considering real-time simulation, the linearized disk tilt solver may be an attractive option, however it does entail two drawbacks that have to be taken into account.

First of all, the rotor model developed for this thesis work does not take into account disk tilt dynamics, nor inflow dynamics, hence the disk tilt angles and rotor inflow may radically change from one simulation step to the next. Since the thrust expression must be linearized around some linearization state (typically the rotor state solution from the previous simulation step), a too large of a change in one or more of the rotor states could possibly introduce very large errors. For this reason this approach is not advised for the rotor model at hand. Secondly, two significant simplifications are employed, namely the removal of $\widehat{b}_1$ from the momentum theory thrust, and the omittance of the H and S forces in the calculation of the BEM thrust defined in the disk plane. Both may contribute to a significant deviation of the solution from the one obtained with the iterative approach (assumed to be the correct solution), hindering the validity of the model which may be considered a significant drawback. Coupling this effect with the notion of using a previous solution as the linearization state, there exists a possibility that the deviation of the solutions grows with the run time of the simulation due to an accumulation of the error as a result of a growing incorrect linearization point.

In order determine whether the simplifications mentioned above have a significant impact on the determination of the solution, trim curves showing the variation of the rotor states as a function of nacelle tilt angle and velocity have been generated using both the iterative and linear disk tilt solvers. After a brief visual inspection, a small yet still observable difference has been observed in the results of the two approaches, the largest being part of the lateral disk tilt and rotor inflow ratio trim curves. For this reason only the latter is included in this report and is shown in fig. C.1 where the trim curves formed by the line patters correspond to the linear solver, while the ones formed by the shapes correspond to the iterative solver. Note that only the portion of the trim curves where the difference is most observable is presented. The difference between the two methods is almost non-existent in airplane configuration (i.e. $\eta = -90°$) and at velocities lower than 65 knots for all nacelle tilt angles. Apart from the airplane configuration, the difference between the linear and iterative solvers grows larger both with velocity and nacelle tilt, where the linear solver tends to underestimate the inflow ratio.

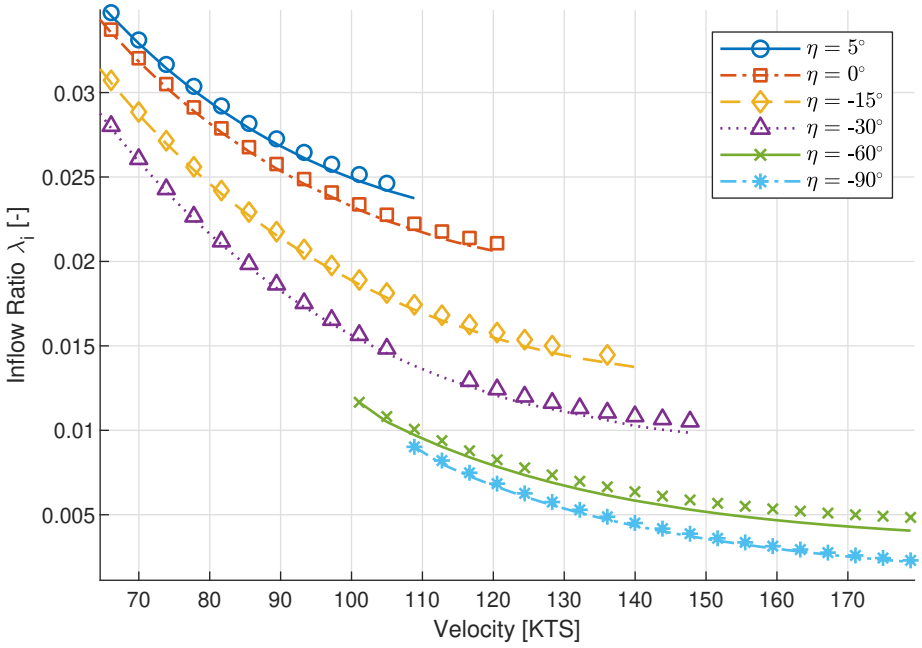

Figure C.1: Comparison of the inflow ratio trim curves between the linear and iterative disk tilt solvers. Line patterns correspond to the linear solver while shapes to the iterative solver. Only fragment of complete trim curve plot shown.

At this point it is known that the linear disk tilt solver does produce results that are noticeably different from the ones of the iterative approach. It is not clear, however, whether this source of error stems from the applied simplifications or from an accumulation of error due to the fact that each new trim solution is found using the previous trim solution as the linearization state. Although the latter seems to be the obvious culprit due to the observed growth of error with velocity, generating a new set of trim curves where the current trim solution (note: not even the previous solution!) obtained with the iterative approach is used as the linearization state, the linear disk tilt solver surprisingly yields (almost) the same results as before. Two conclusions may be taken out of this. First of all, the main source of the error must be caused by the simplifications, i.e. the removal of the lateral disk tilt from the momentum theory thrust expression, and the omittance of the H and S force of the BEM thrust defined in the disk plane. Second of all, it seems that the Taylor expansion of the momentum theory thrust is not very sensitive to the choice of the linearization point, or at least it is not sensitive enough for its effect to be observable when compared to the effect of the mentioned simplifications.

Although the error that the linear disk tilt solver introduces may be considered significant enough for it to be discarded from the model, it is still worthwhile to mention the computational performance improvements that it brings when compared to the iterative solver. As such, the trim algorithm using the linear disk tilt solver generated a complete set of trim curves 30% to 60% faster than the iterative solver. Although during simulation the rotor is not the only component that consumes computational resources, the linear disk tilt solver does have the potential to significantly improve simulation performance if such a need arises in the future.

D

Maple Files Overview

This appendix presents a graphical overview of all the Maple files used in the derivation of the rotor expressions starting with a top-level relationship diagram of the different derivation groups, followed by the legend corresponding to the file relationship diagrams of all of the groups presented next. Finally a list of all Maple files used in the rotor derivation are shown at the end, sorted according to the suggested order of their execution, which is accompanied by a table showing the file name abbreviation convention.

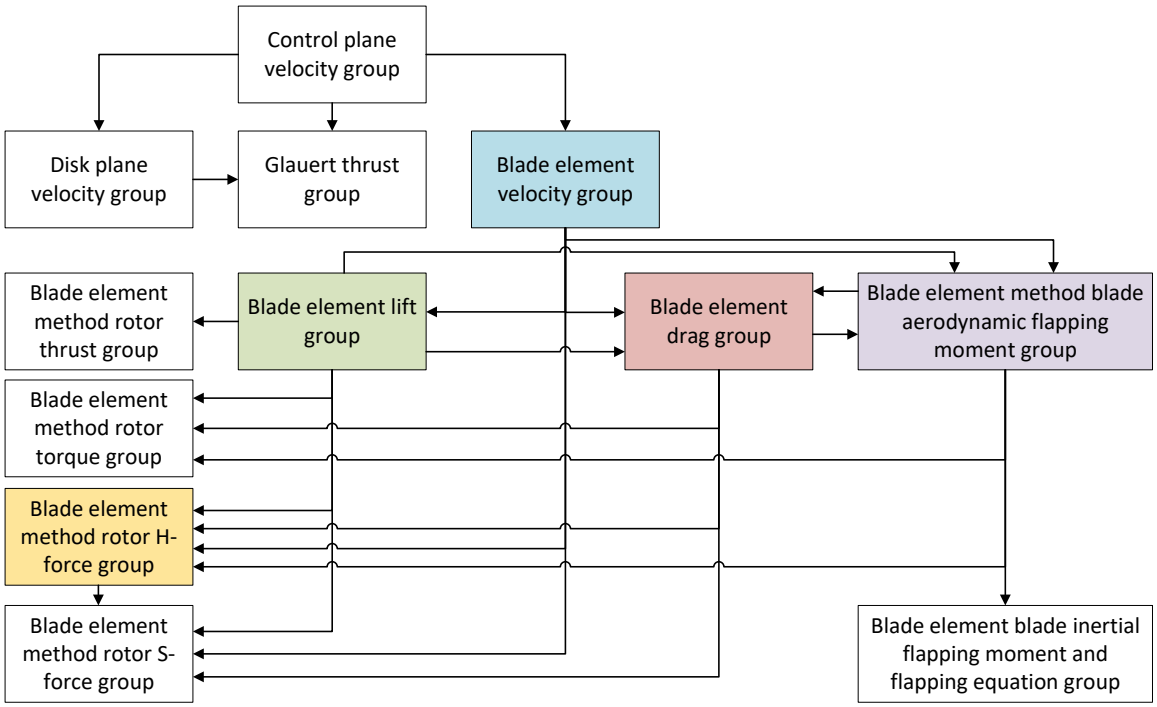

Figure D.1: General overview of the relationships between the Maple file groups.

Table D.1: List of elements, their description, and graphical representation used in the Maple derivation map.

Element Name	Description	Graphical Representation
Worksheet block	Indicates maple worksheet file (.mw) where specific outputs (.mpl files) are not relevant in the current diagram.	.mw file name
Worksheet with save output block	Indicates maple worksheet file and its outputs.	.mw file name ❑ Output .mpl file name 1 ❑ Output .mpl file name 2 ❑ ...
Underlined output	Indicates output file that should be reduced by the automatic ordering scheme.	.mw file name ❑ Output to be reduced ❑ Output that is not reduced
Read .mpl arrow	Solid arrow line with text. Indicates which output file is read by the next worksheet.	
Reference without read arrow	Dash-dot arrow line. Indicates where an expression is mentioned but not expanded in the current worksheet.	
Copy-paste expression arrow	Dashed arrow line with no text. Indicates where one or more expressions have been manually copied from a different worksheet and pasted into the current worksheet. No .mpl files are read in this case.	
Directly read .mpl arrow	Solid arrow line with no text. Links off-page element to parent worksheet. Off-page element specifies output name therefore it is not repeated on the arrow.	
Off-page reference element	Indicates link with the output from a worksheet shown on another page. Worksheet groups (partially) color coded: ▪ blue - BE velocity ▪ green - BE lift ▪ red - BE drag ▪ purple - BE AFM ▪ yellow - rotor H-force	
Worksheet block with red outline	Indicates worksheet where disk tilt approximation is implemented.	.mw file name
Red font worksheet name	Indicates worksheet where the derivative of $\widehat{\psi}$ is taken.	.mw file name
Worksheet block with green background	Indicates worksheet where Ω_{sgn} is introduced.	.mw file name

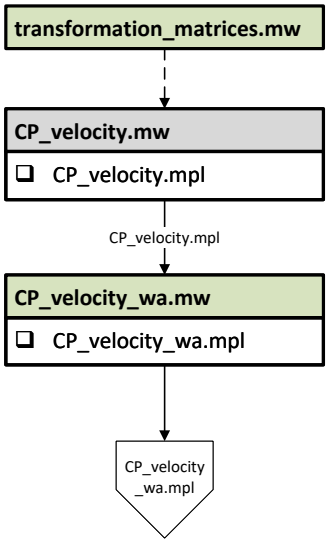

Figure D.2: Maple file relationship diagram for the derivation of the wind axis control plane velocity components.

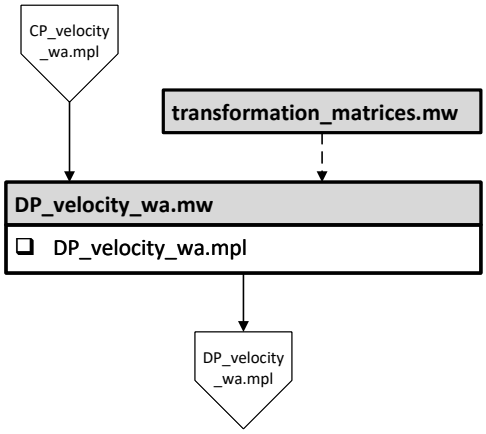

Figure D.3: Maple file relationship diagram for the derivation of the wind axis disk plane velocity components.

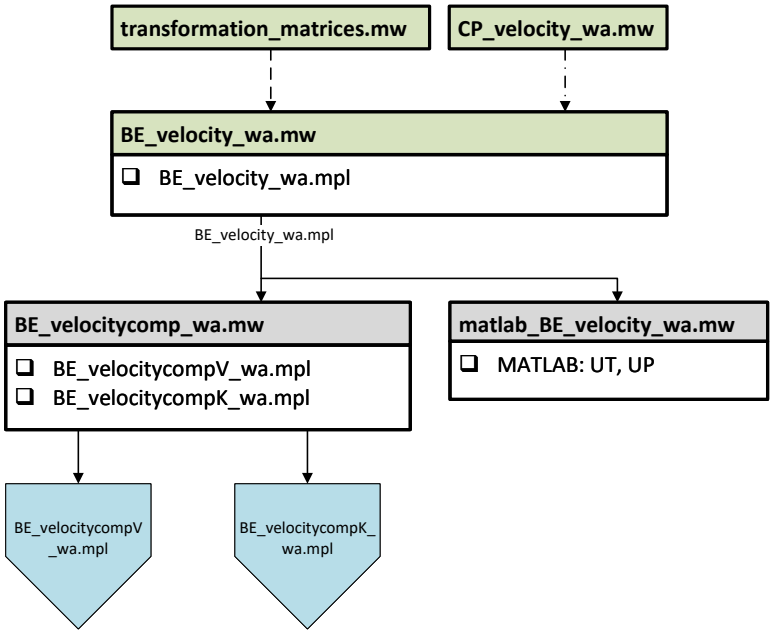

Figure D.4: Maple file relationship diagram for the derivation of the blade element velocity components, with the flapping angle measured from the wind axis control plane.

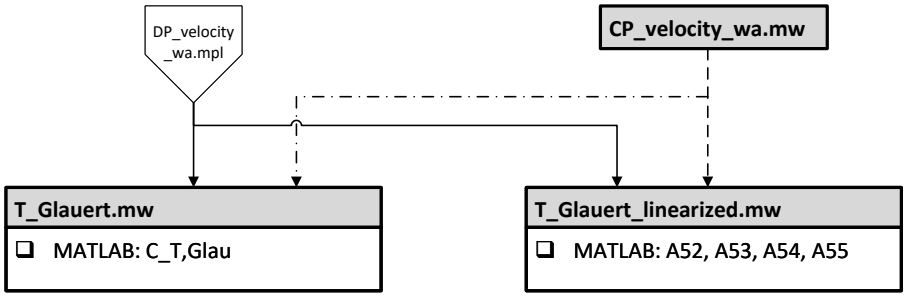

Figure D.5: Maple file relationship diagram for the derivation of the Glauert rotor thrust defined in the wind axis disk plane.

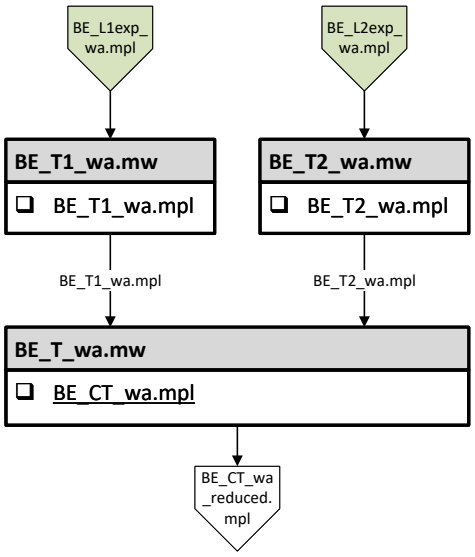

Figure D.6: Maple file relationship diagram for the derivation of the rotor thrust defined in the wind axis control plane.

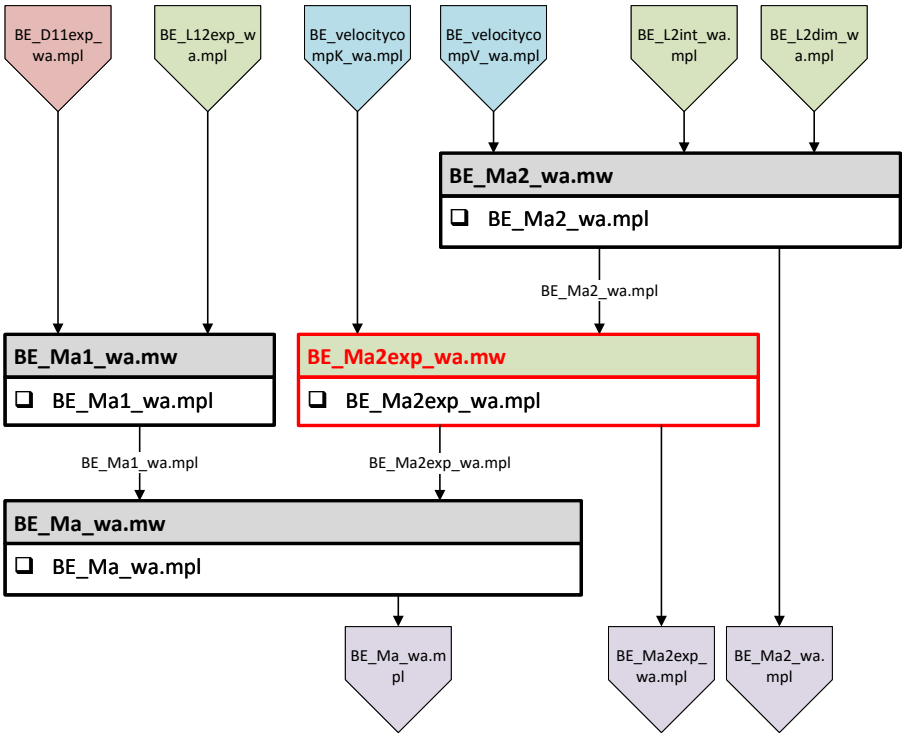

Figure D.7: Maple file relationship diagram for the derivation of the blade element aerodynamic flapping moment.

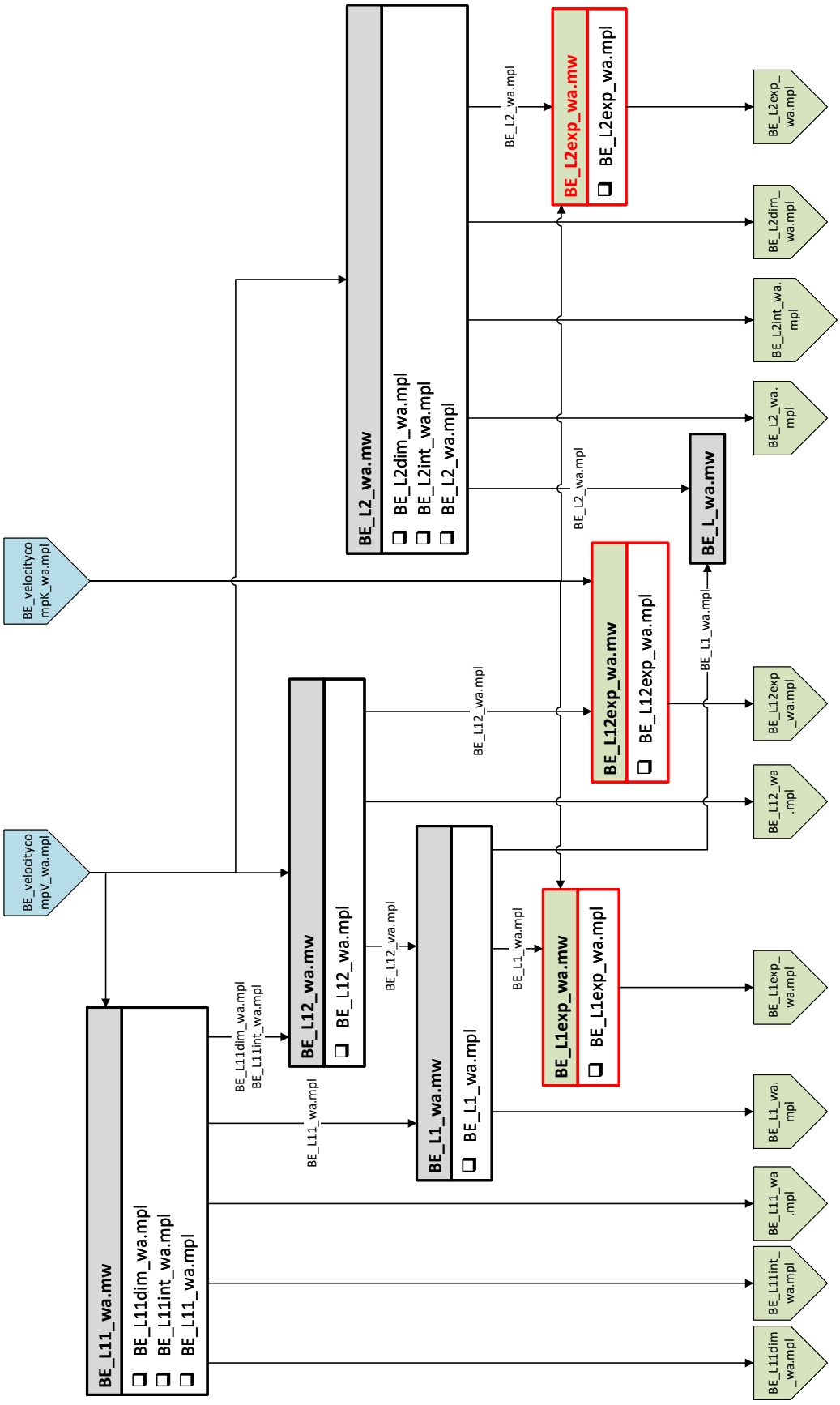

Figure D.8: Maple file relationship diagram for the derivation of the blade element lift.

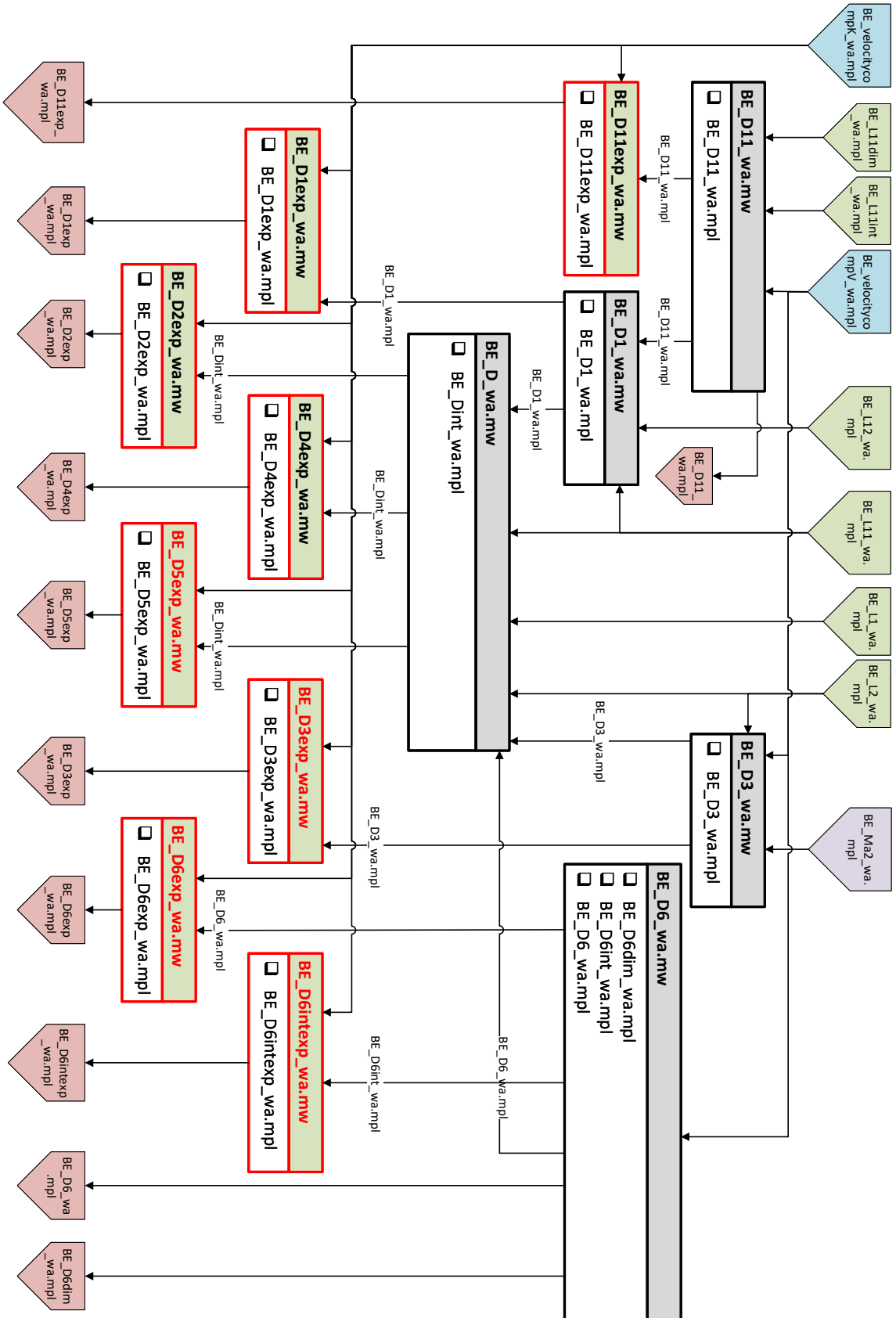

Figure D.9: Maple file relationship diagram for the derivation of the blade element drag.

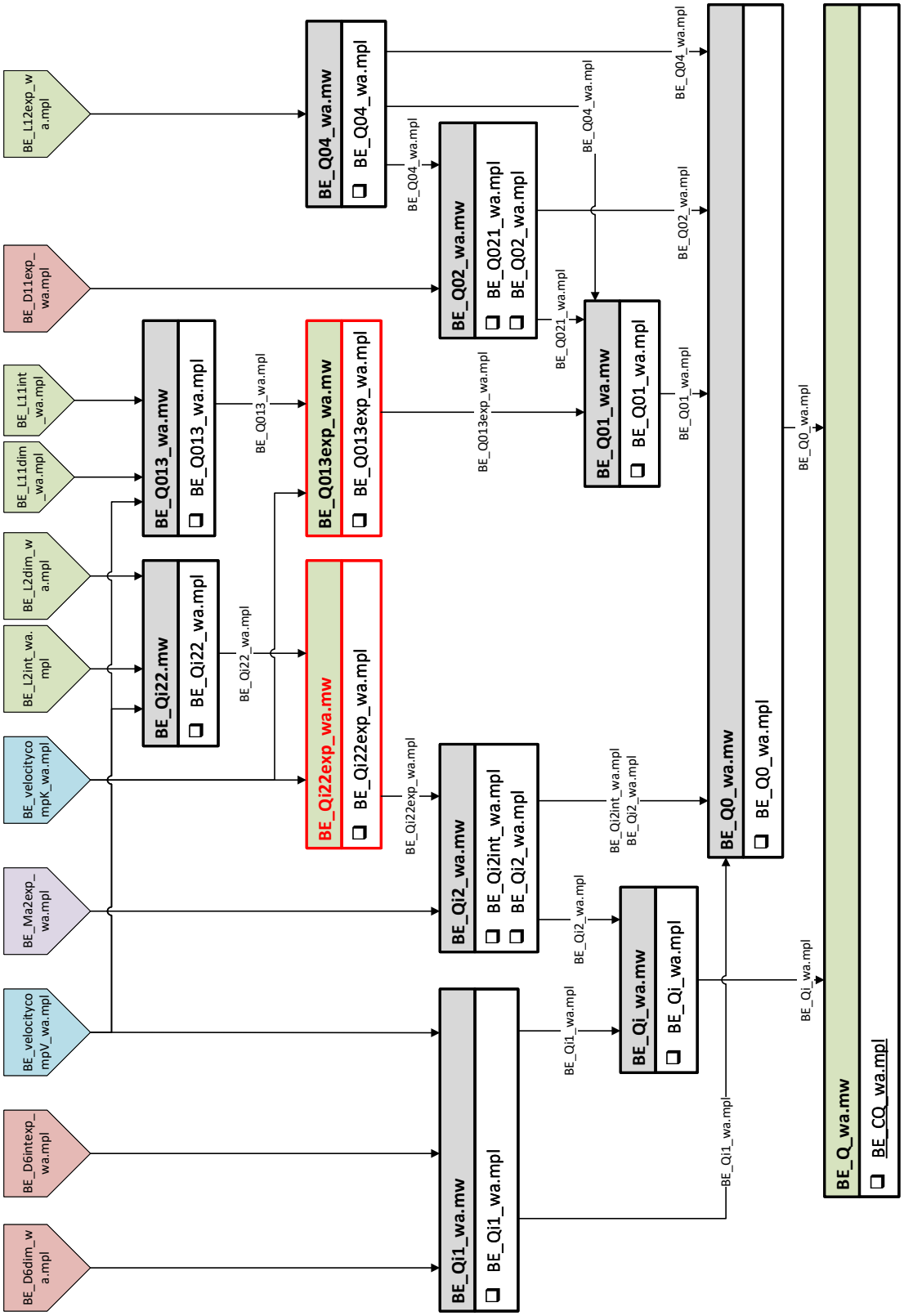

Figure D.10: Maple file relationship diagram for the derivation of the rotor torque defined in the wind axis control plane.

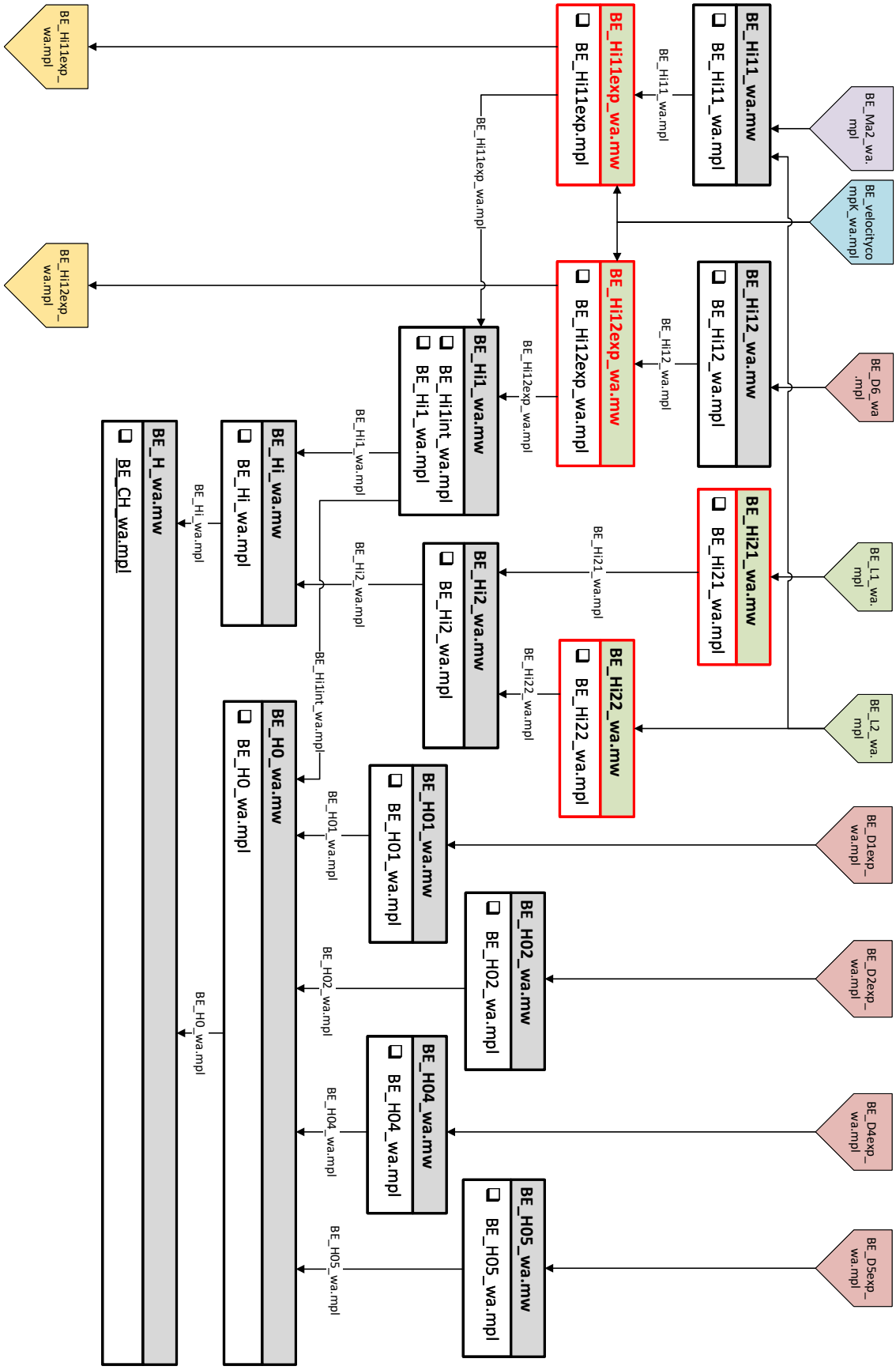

Figure D.11: Maple file relationship diagram for the derivation of the rotor H-force defined in the wind axis control plane.

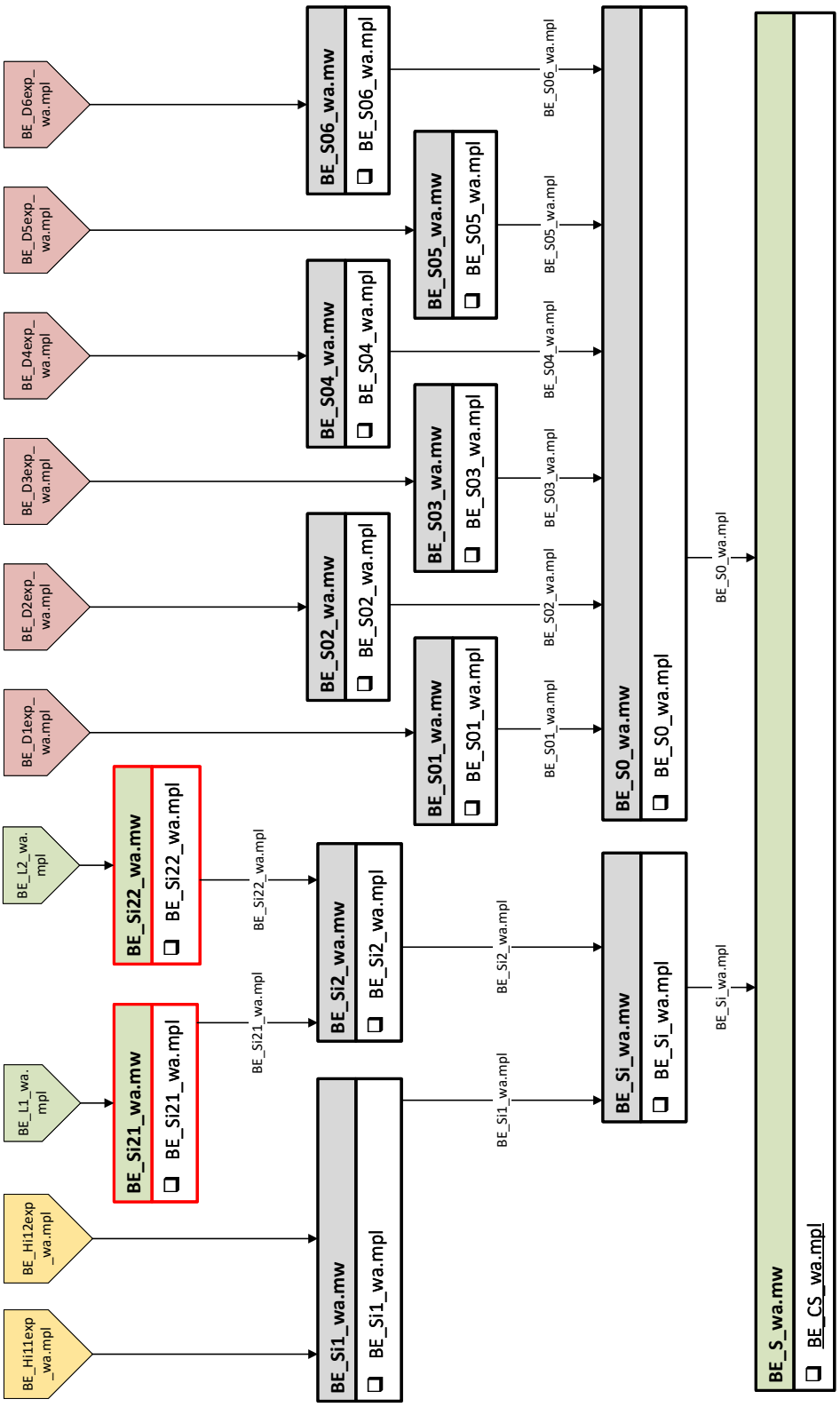

Figure D.12: Maple file relationship diagram for the derivation of the rotor S-force defined in the wind axis control plane.

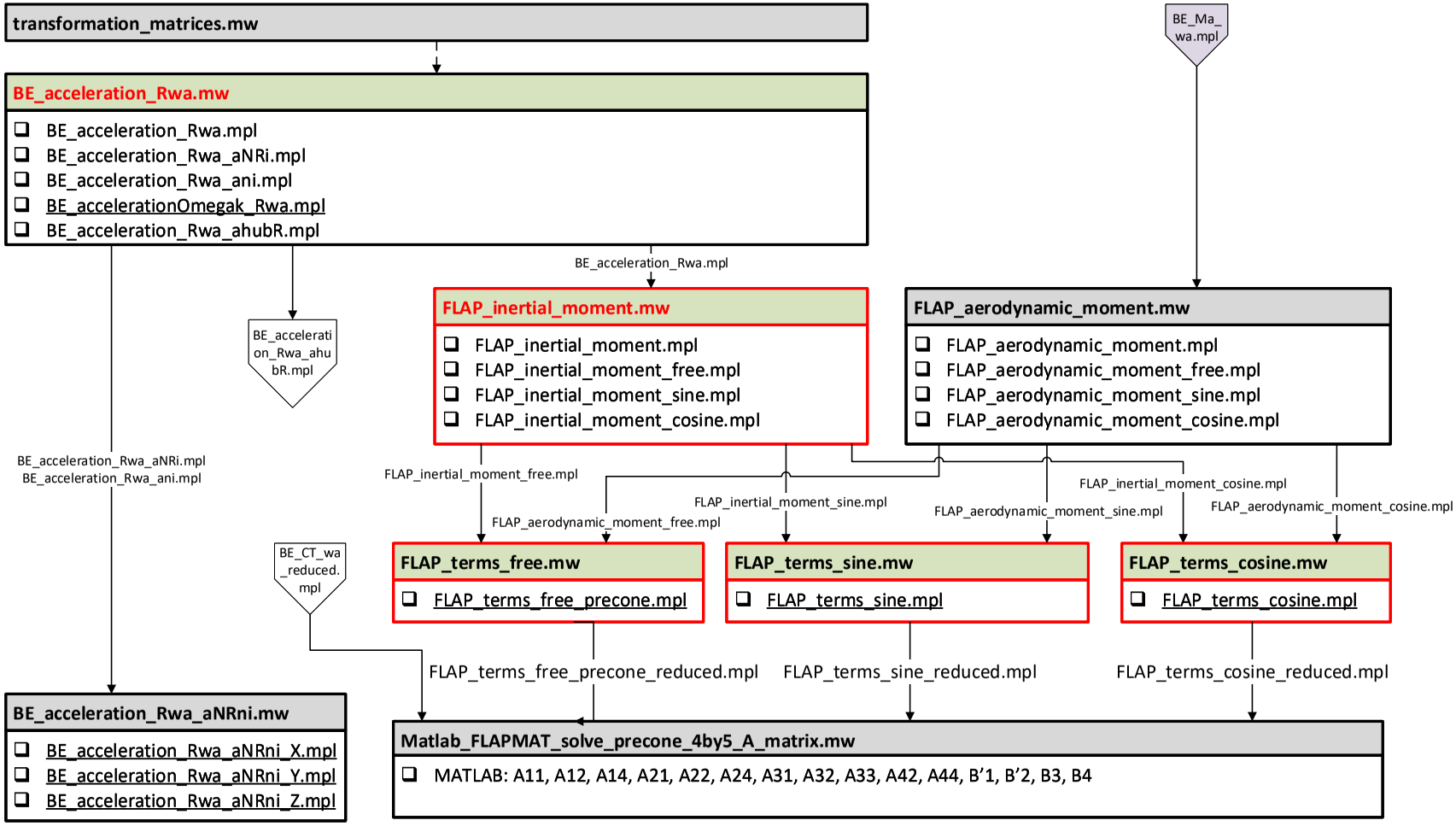

Figure D.13: Maple file relationship diagram for the derivation of the flapping equation terms.

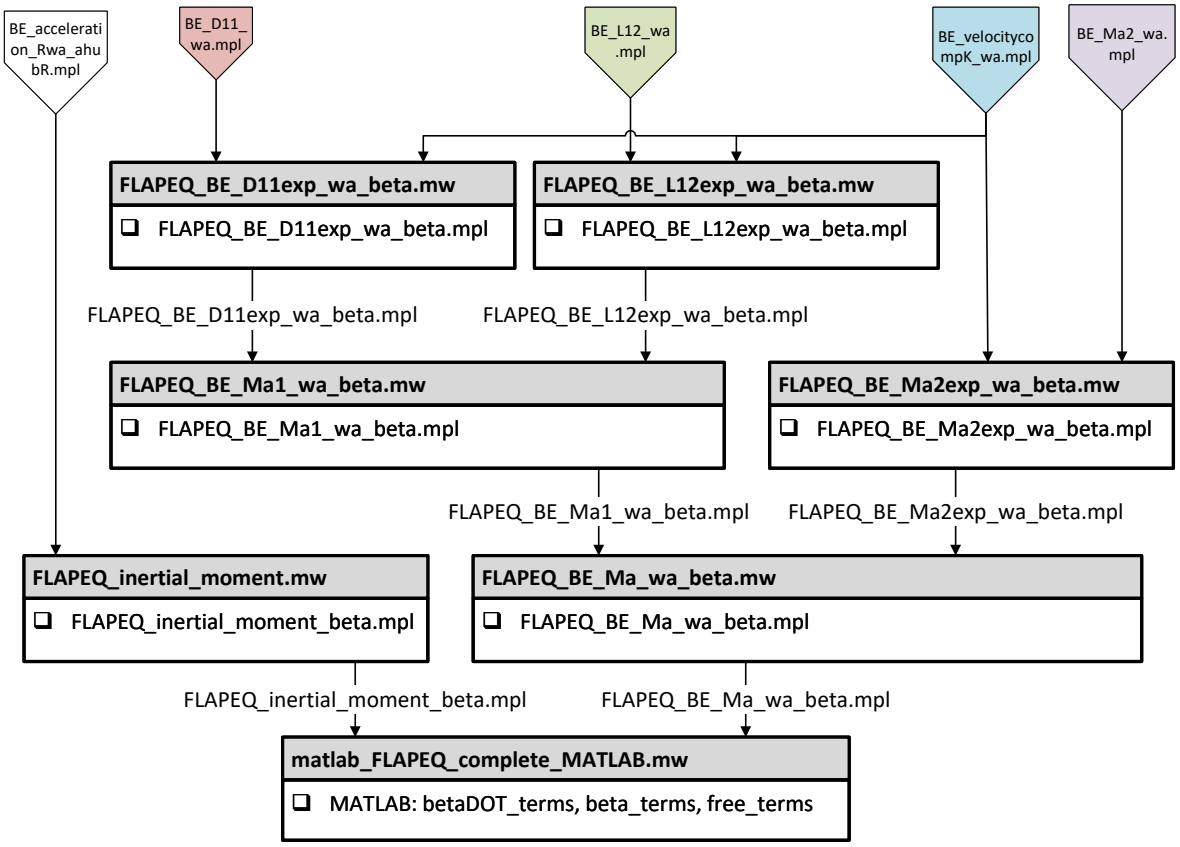

Figure D.14: Maple file relationship diagram for the derivation of the flapping equation.

Table D.2: Maple file naming abbreviation legend.

Abbreviation	Description
CP	control plane
DP	disk plane
wa	wind axis
BE	blade element or indication of derivation with the use of the blade element method
L	lift
D	drag
Ma	aerodynamic flapping moment
H	H-force
S	S-force
T	thrust
Q	torque
Xi	lift dependent force or moment, where X may be replaced by H, S, or Q
X0	drag dependent force or moment, where X may be replaced by H, S, or Q
CX	force or moment coefficient, where X maybe be replaced by H, S, T, or Q
comp	compression of expressions in order to simplify notation
exp	expansion of expressions to expose $\widehat{\psi}$ and other terms necessary in the execution of the automatic ordering scheme
int	intermediate derivation step

Table D.3: List of all Maple files - shown in the suggested order of execution.

1. coefficient_definitions.mw
2. Transformation_matrices.mw.mw
3. CP_velocity[a].mw
4. CP_velocity_wa[a].mw
5. DP_velocity_wa[a].mw
6. T_Glauert.mw
7. T_Glauert_linearized.mw
8. BE_velocity_wa[a].mw
9. BE_velocitycomp_wa[b].mw
10. matlab_BE_velocity_wa.mw
11. latex_BE_velocity_wa.mw
12. BE_L11_wa[b].mw
13. BE_L12_wa[b].mw
14. BE_L12exp_wa.mw
15. BE_L1_wa.mw
16. BE_L1exp_wa.mw
17. BE_L2_wa[b].mw
18. BE_L2exp_wa.mw
19. BE_L_wa.mw
20. BE_T1_wa.mw
21. BE_T2_wa.mw
22. BE_T.mw
23. AOS: BE_CT_wa.mw
24. latex_BE_T_wa[a].mw
25. BE_Ma2_wa[b].mw
26. BE_D11_wa[b].mw
27. BE_D11exp_wa.mw
28. BE_D1_wa.mw
29. BE_D1exp_wa.mw
30. BE_D3_wa.mw
31. BE_D3exp_wa.mw
32. BE_D6_wa[b].mw
33. BE_D6exp_wa.mw
34. BE_D6intexp_wa.mw
35. BE_D_wa.mw
36. BE_D2exp_wa.mw
37. BE_D4exp_wa.mw
38. BE_D5exp_wa.mw
39. BE_Ma1_wa.mw
40. BE_Ma2exp_wa.mw
41. BE_Ma_wa.mw
42. BE_Qi1_wa[b].mw
43. BE_Qi22_wa[b].mw
44. BE_Qi22exp_wa.mw
45. BE_Qi2_wa.mw
46. BE_Qi_wa.mw
47. BE_Q013_wa[b].mw
48. BE_Q013exp_wa.mw
49. BE_Q04_wa.mw
50. BE_Q02_wa.mw
51. BE_Q01_wa.mw
52. BE_Q0_wa.mw
53. BE_Q_wa.mw
54. AOS: BE_CQ_wa.mw
55. latex_BE_Q_wa.mw
56. BE_Hi11_wa.mw
57. BE_Hi11exp_wa.mw
58. BE_Hi12_wa.mw
59. BE_Hi12exp_wa.mw
60. BE_Hi1_wa.mw
61. BE_Hi21_wa.mw
62. BE_Hi22_wa.mw
63. BE_Hi2_wa.mw
64. BE_Hi_wa.mw
65. BE_H01_wa.mw
66. BE_H02_wa.mw
67. BE_H04_wa.mw
68. BE_H05_wa.mw
69. BE_H0_wa.mw
70. BE_H_wa.mw
71. AOS: BE_CH_wa.mw
72. latex_BE_H_wa.mw
73. BE_Si1_wa.mw
74. BE_Si21_wa.mw
75. BE_Si22_wa.mw
76. BE_Si2_wa.mw
77. BE_Si_wa.mw
78. BE_S01_wa.mw
79. BE_S02_wa.mw
80. BE_S03_wa.mw
81. BE_S04_wa.mw
82. BE_S05_wa.mw
83. BE_S06_wa.mw
84. BE_S0_wa.mw
85. BE_S_wa.mw
86. AOS: BE_CS_wa.mw
87. latex_BE_S_wa.mw
88. BE_acceleration_Rwa.mw
89. AOS: BE_accelerationOmegak_Rwa.mw
90. BE_acceleration_Rwa_aNRni.mw
91. AOS: BE_acceleration_R(...)_X/Y/Z.mw
92. FLAP_inertial_moment.mw
93. FLAP_aerodynamic_moment.mw
94. FLAP_terms_free.mw
95. FLAP_terms_sine.mw
96. FLAP_terms_cosine.mw
97. AOS: FLAP(...)_free_precone/sine/cosine.mw
98. matlab_FLAPMAT(...)_4by5_A_matrix.mw
99. latex_FLAPMAT(...)_3by3_A_matrix.mw
100. FLAPEQ_inertial_moment.mw
101. latex_FLAPEQ_inertial_moment.mw
102. FLAPEQ_BE_L12exp_wa_beta.mw
103. FLAPEQ_BE_D11exp_wa_beta.mw
104. FLAPEQ_BE_Ma1_wa_beta.mw
105. FLAPEQ_BE_Ma2exp_wa_beta.mw
106. FLAPEQ_BE_Ma_wa_beta.mw
107. matlab_FLAPEQ_complete_MATLAB.mw
108. latex_FLAPEQ_BE_Ma_wa_beta.mw
109. BE_OP_wa.mw

[a] Some expressions in this file are manually pasted instead of read from a different file.
[b] Some results within this file are manually altered instead of being solved automatically.

E

AOS Example

This appendix provides a worked-out example of an expression being reduced by the automatic ordering scheme.

Consider the total yaw rate of the rotating frame from eq. (5.50d) in non-dimensional form as shown here in eq. (E.1) which shall be fed into the automatic ordering scheme (AOS) to be reduced.

$$\overline{\omega}_{\widehat{R}|Z\widehat{R},i} = C_\eta\, S_{\theta 1s}\, \overline{p}_i - S_\eta\, C_{\theta 1s}\, \overline{p}_i - C_\eta\, C_{\theta 1s}\, \overline{r}_i - S_\eta\, S_{\theta 1s}\, \overline{r}_i + \Omega_{sgn} \tag{E.1}$$

The AOS parameters are chosen as follows: $\epsilon = 0.5$; $\Delta_0 = 4$; $RF = 1.01$. With the values of the terms taken from table A.17, the resulting orders of the products of terms are shown in eq. (E.2).

$$\overline{\omega}_{\widehat{R}|Z\widehat{R},i} = \left[C_\eta\, S_{\theta 1s}\, \overline{p}_i\right] O(\epsilon^7) - \left[S_\eta\, C_{\theta 1s}\, \overline{p}_i\right] O(\epsilon^4) - \left[C_\eta\, C_{\theta 1s}\, \overline{r}_i\right] O(\epsilon^5) - \left[S_\eta\, S_{\theta 1s}\, \overline{r}_i\right] O(\epsilon^8) + \left[\Omega_{sgn}\right] O(\epsilon^1) \tag{E.2}$$

The minimum and maximum means' order powers determined by the automated ordering scheme are the same and equal to 2.177. In accordance with eq. (6.27), the threshold extension is equal to 3.538. The resulting tailored significance threshold works out to be 5.715 as shown in eq. (E.3).

$$T_{tail} = O^{M,\overline{\omega}_{\widehat{R}|Z\widehat{R},i}} + T_{ext} = 2.177 + 3.538 = 5.715 \tag{E.3}$$

As a result all terms with an order power higher than 5.715 are removed as demonstrated in eq. (E.4), with the orders of the remaining terms still shown.

$$\overline{\omega}_{\widehat{R}|Z\widehat{R},i} = -\left[S_\eta\, C_{\theta 1s}\, \overline{p}_i\right] O(\epsilon^4) - \left[C_\eta\, C_{\theta 1s}\, \overline{r}_i\right] O(\epsilon^5) + \left[\Omega_{sgn}\right] O(\epsilon^1) \tag{E.4}$$

The resulting reduced expression is given by eq. (E.5) with the maximum error that the reduction scheme introduced being no greater than 6.25%. It can be seen that out of the 5 product of terms that constitute $\overline{\omega}_{\widehat{R}|Z\widehat{R},i}$, only 3 of them are considered significant resulting in a 40% expression reduction rate.

$$\overline{\omega}_{\widehat{R}|Z\widehat{R},i} = -S_\eta\, C_{\theta 1s}\, \overline{p}_i - C_\eta\, C_{\theta 1s}\, \overline{r}_i + \Omega_{sgn} \tag{E.5}$$

Finally, the AOS provides the minimum and maximum values of $\overline{\omega}_{\widehat{R}|Z\widehat{R},i}$ which are equal to -1.062 and 1.062 respectively, both falling under the category of terms with an order of $O(0.5^{-1})$.

F

Matlab and Simulink Implementation Diagrams

This appendix presents the 6DoF model implementation diagrams starting with the Matlab model class relationships, followed by several Simulink implementation block diagrams, and concludes with the throttle-power curve approximations of the XV-15 tilt-rotor.

F.1. Matlab Class Relationships

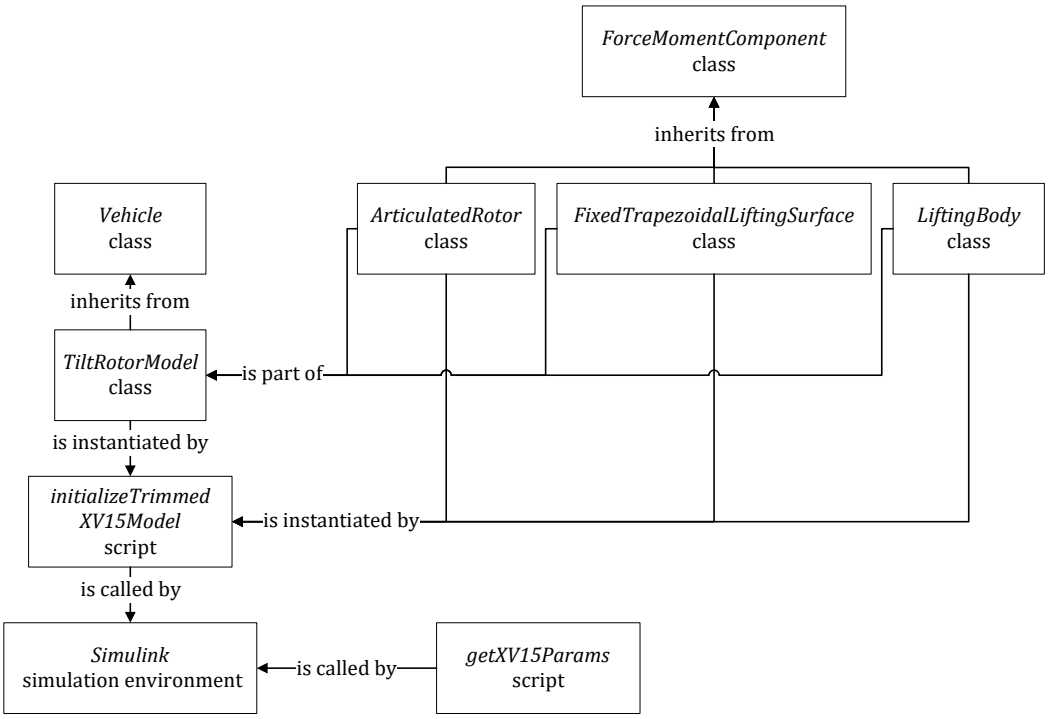

Figure F.1: Diagram of the relationships between the classes of the Matlab implementation of the 6-DoF tilt-rotor model, the Simulink simulation environment, and auxiliary Matlab scripts.

F.2. Simulink Block Diagrams

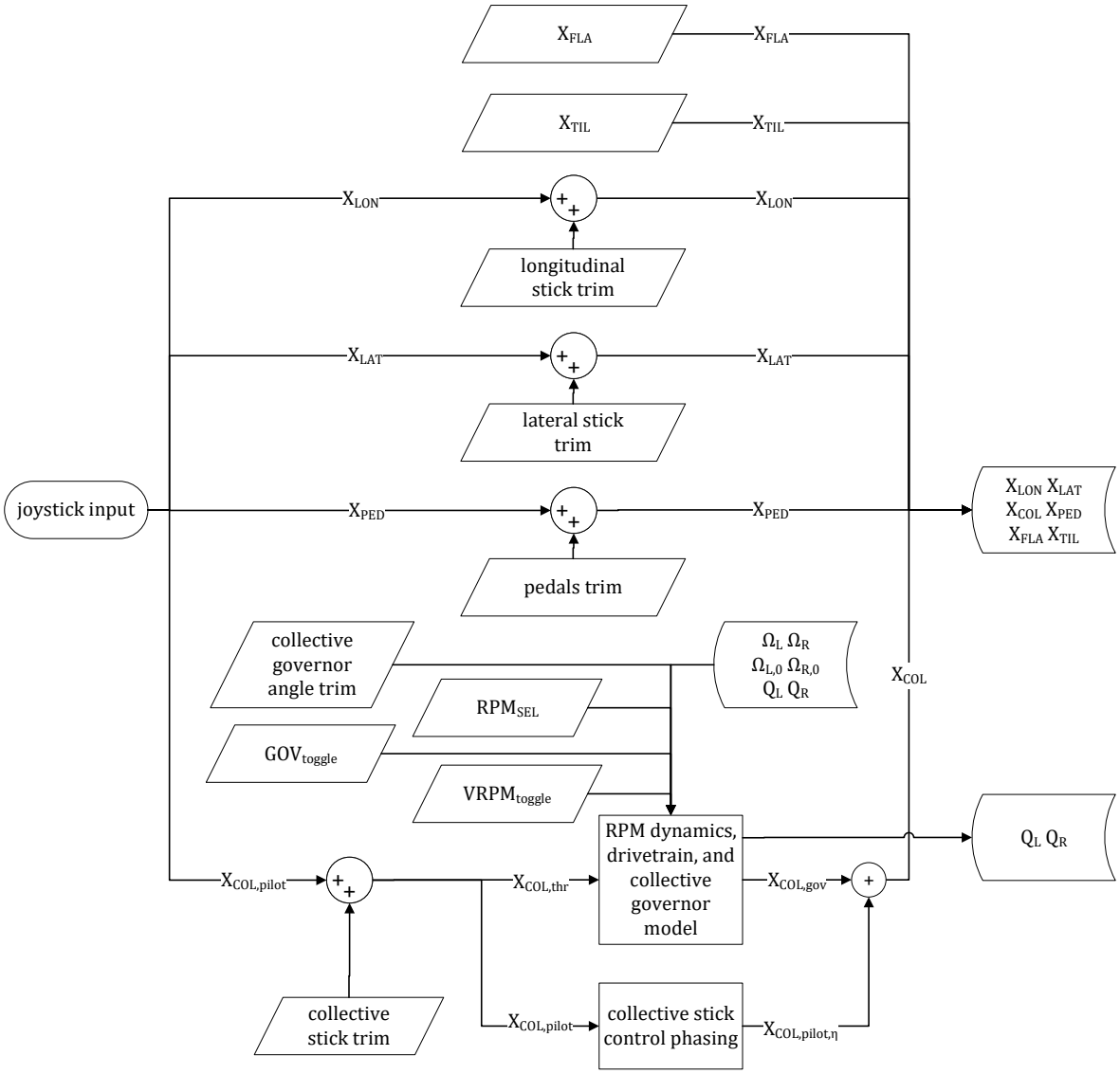

Figure F.2: Block diagram of the pilot inputs, RPM dynamics, drivetrain, and collective governor model block shown in fig. 7.3.

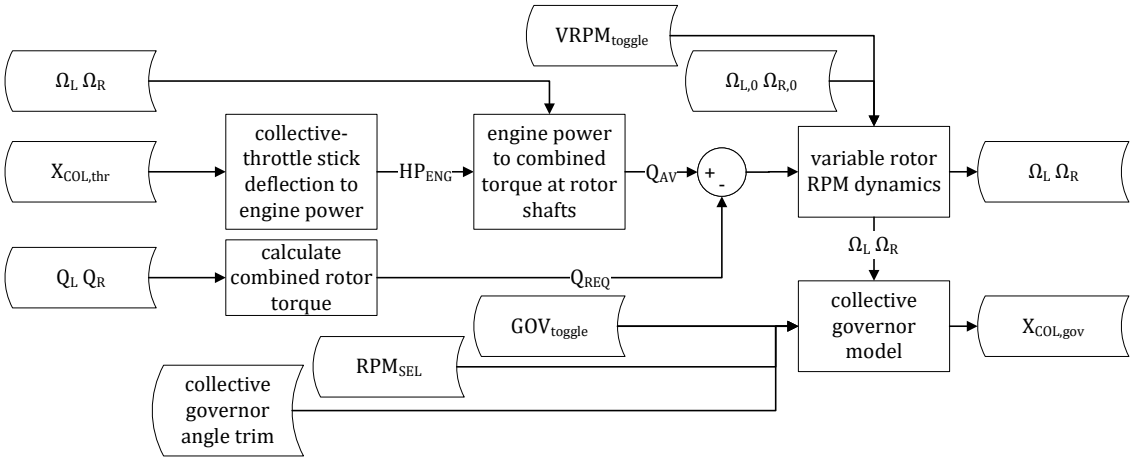

Figure F.3: Block diagram of the RPM dynamics, drivetrain, and collective governor model block shown in fig. F.2.

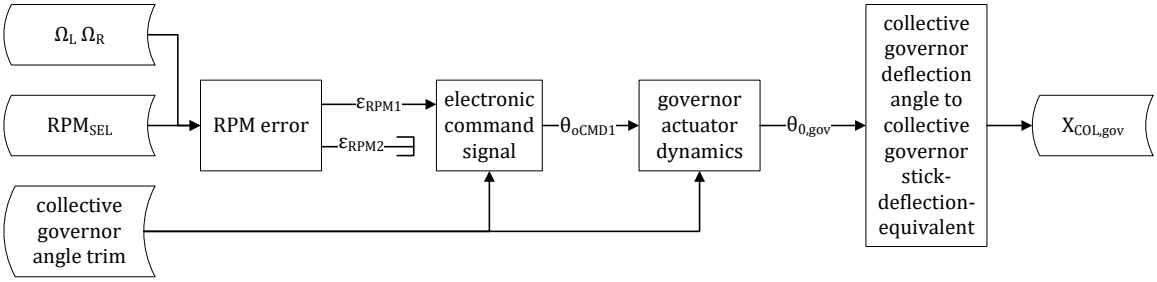

Figure F.4: Block diagram of the simplified collective governor model shown in fig. F.3.

F.3. Simulink Implementation Throttle-Power Curves

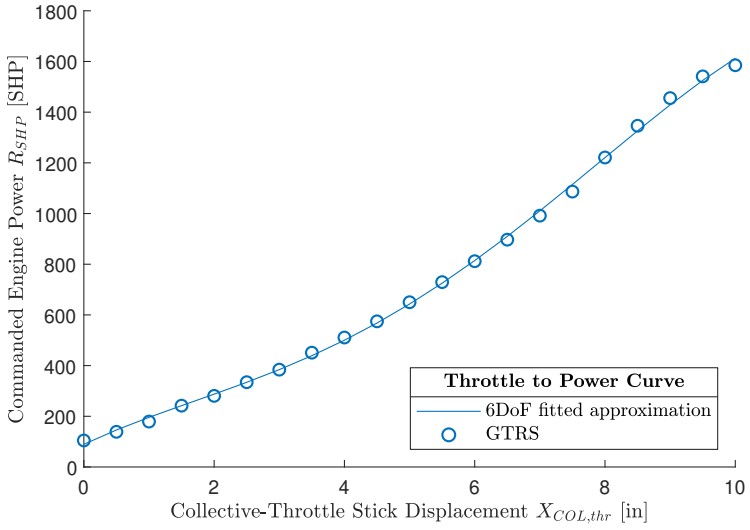

Figure F.5: Actual and approximated relationship between the collective-throttle stick deflection $X_{\mathrm{COL,thr}}$ and the commanded engine horsepower R_{SHP}. Reference data based on [6, tab. 8a-VI, tab. 18-I].

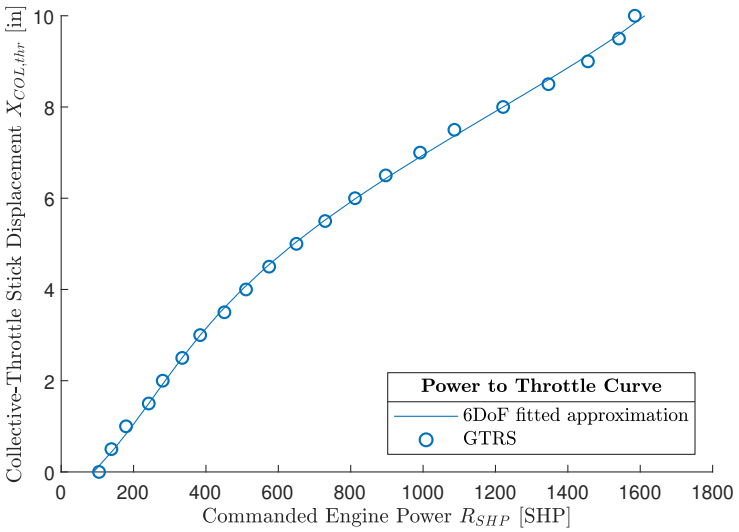

Figure F.6: Actual and approximated relationship between the commanded engine horsepower R_{SHP} and the collective-throttle stick deflection $X_{\mathrm{COL,thr}}$. Reference data based on [6, tab. 8a-VI, tab. 18-I].

G

Supplementary Simulation Results

This appendix presents additional simulation results of the 6DoF model XV-15 implementation starting with the rotor disk distribution contour plots, followed by the longitudinal and level flight trim and pseudo trim curves, and concludes with the climbing flight Haffner diagrams.

G.1. Variation of Blade Element Aerodynamic States Across the Rotor Disk

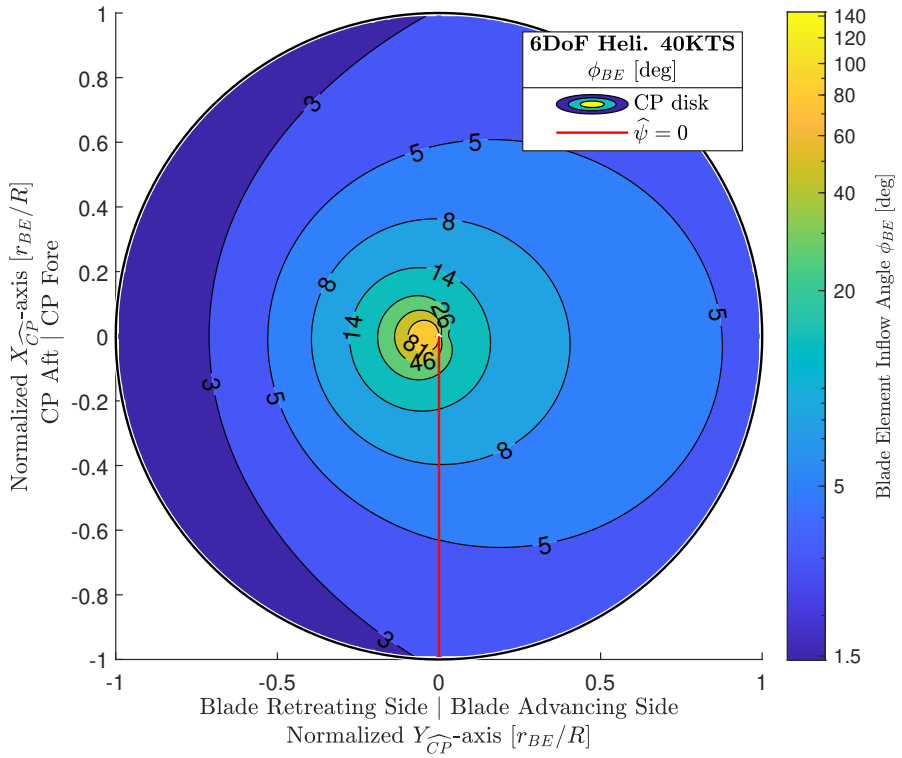

Figure G.1: Variation of the blade element inflow angle across the rotor disk of the 6DoF tilt-rotor model in helicopter level forward flight (40 knots).

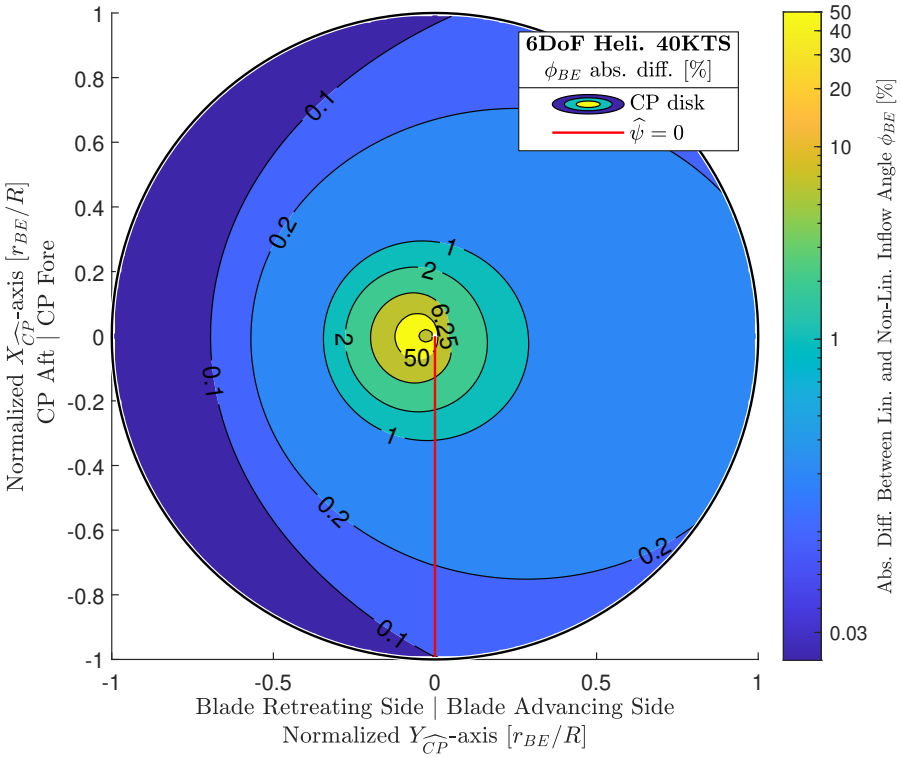

Figure G.2: Variation of the percentage difference between the non-linear and linearized blade element inflow angle across the rotor disk of the 6DoF tilt-rotor model in helicopter level forward flight (40 knots).

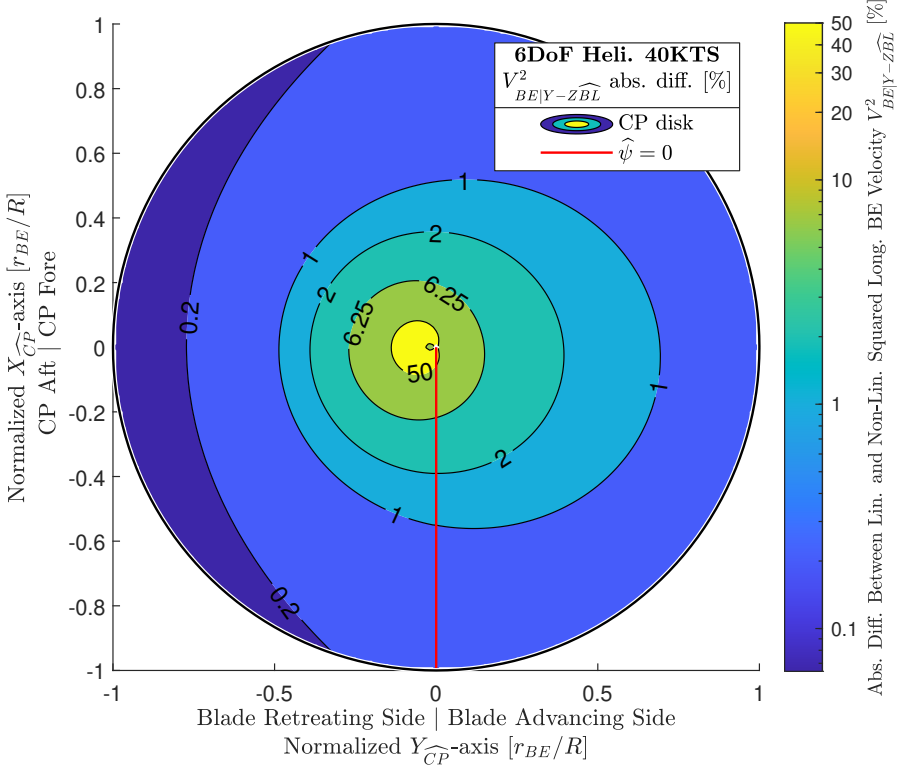

Figure G.3: Variation of the percentage difference between the complete and simplified blade element total longitudinal velocity across the rotor disk of the 6DoF tilt-rotor model in helicopter level forward flight (40 knots).

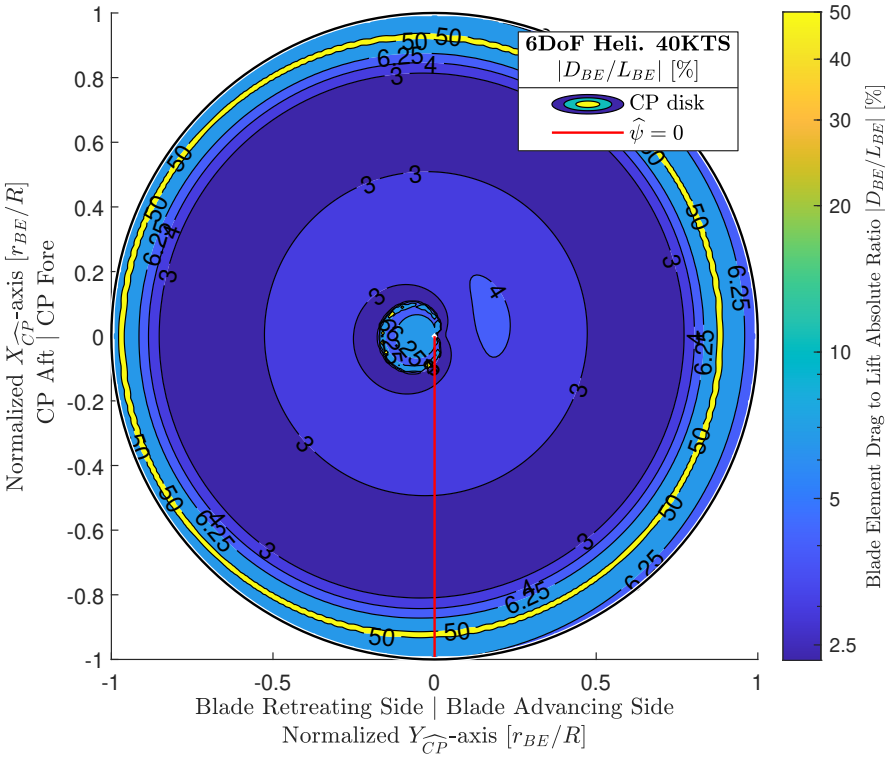

Figure G.4: Variation of the percentage ratio between the drag and lift of the blade element across the rotor disk of the 6DoF tilt-rotor model in helicopter level forward flight (40 knots).

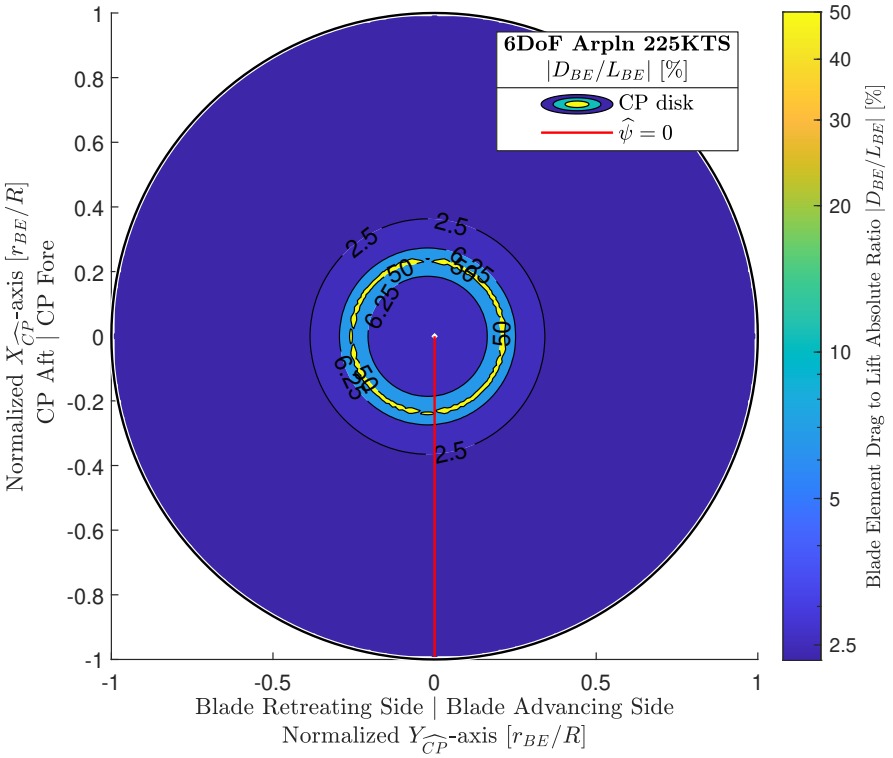

Figure G.5: Variation of the percentage ratio between the drag and lift of the blade element across the rotor disk of the 6DoF tilt-rotor model in airplane level flight (225 knots).

G.2. Trimmed Longitudinal and Level Flight Analysis and Validation

G.2.1. Whole-Model Validation

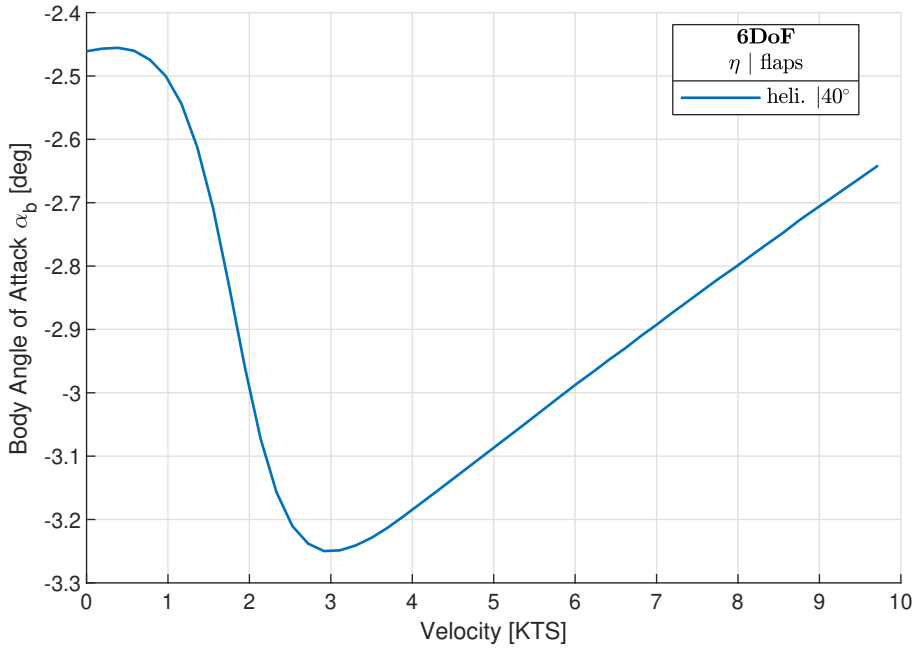

Figure G.6: Detailed view of the body angle of attack trim curve of the 6DoF tilt-rotor model in helicopter configuration near hover. Nacelle tilt η and flap deflection angles indicated in legend.

G.2.2. Subsystem Trim Curve Trend Validation

Rotor

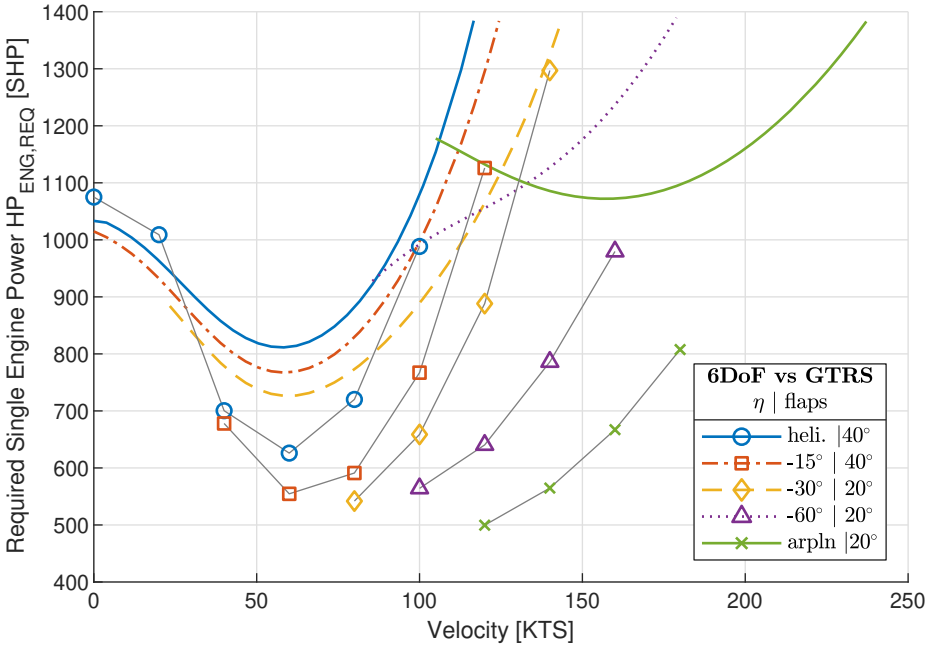

Figure G.7: Comparison between the required single engine power trim curves of the 6DoF tilt-rotor model and the GTRS. Color line patterns correspond to the 6DoF model while shapes connected with gray lines correspond to the GTRS data[5, app. A]. Nacelle tilt η and flap deflection angles indicated in legend.

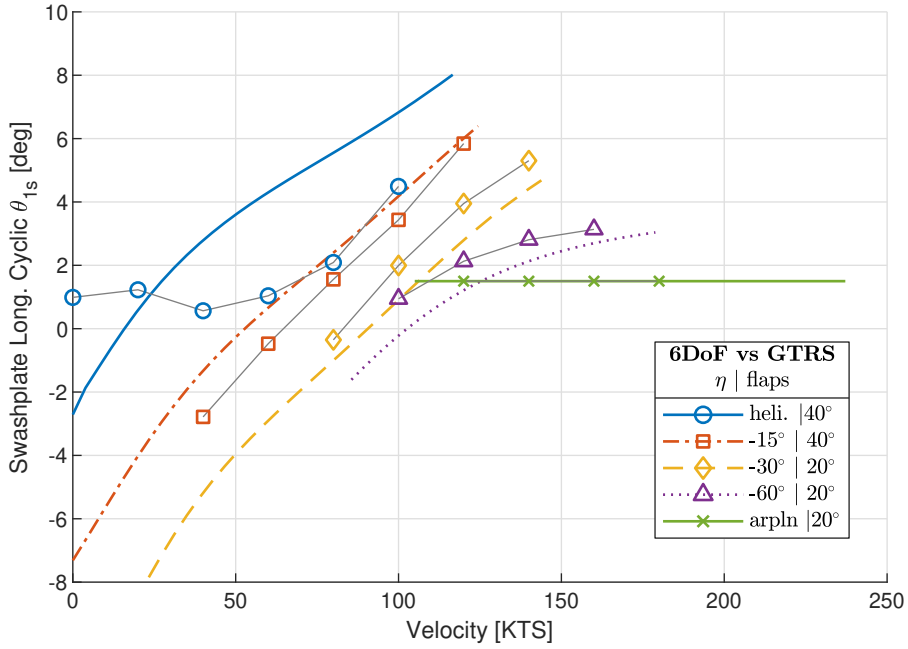

Figure G.8: Comparison between the longitudinal swashplate cyclic trim curves of the 6DoF tilt-rotor model and the GTRS. Color line patterns correspond to the 6DoF model while shapes connected with gray lines correspond to the GTRS data[5, app. A]. Nacelle tilt η and flap deflection angles indicated in legend.

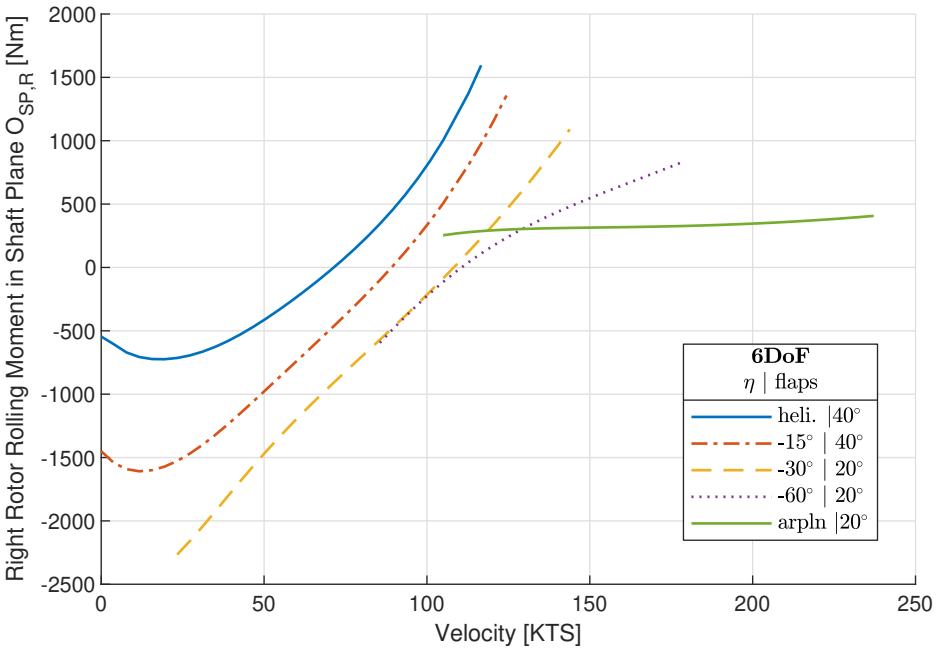

Figure G.9: Comparison between the right counter-clockwise rotating rotor shaft plane spring reaction rolling moment trim curves of the 6DoF tilt-rotor model and the GTRS. Color line patterns correspond to the 6DoF model while shapes connected with gray lines correspond to the GTRS data[5, app. A]. Nacelle tilt η and flap deflection angles indicated in legend.

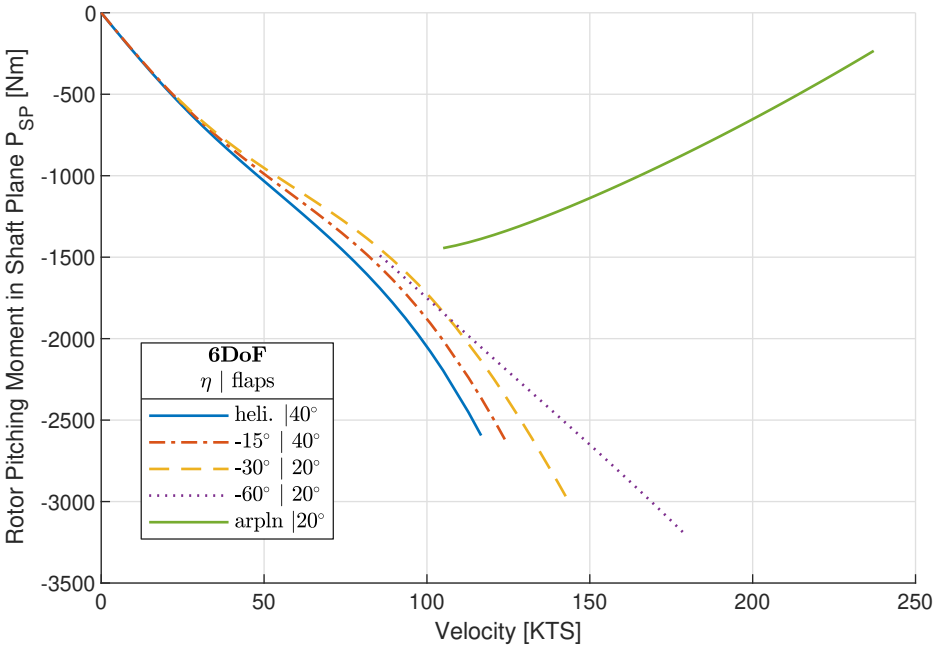

Figure G.10: Comparison between the shaft plane rotor spring reaction pitching moment trim curves of the 6DoF tilt-rotor model and the GTRS. Color line patterns correspond to the 6DoF model while shapes connected with gray lines correspond to the GTRS data[5, app. A]. Nacelle tilt η and flap deflection angles indicated in legend.

Main Wing

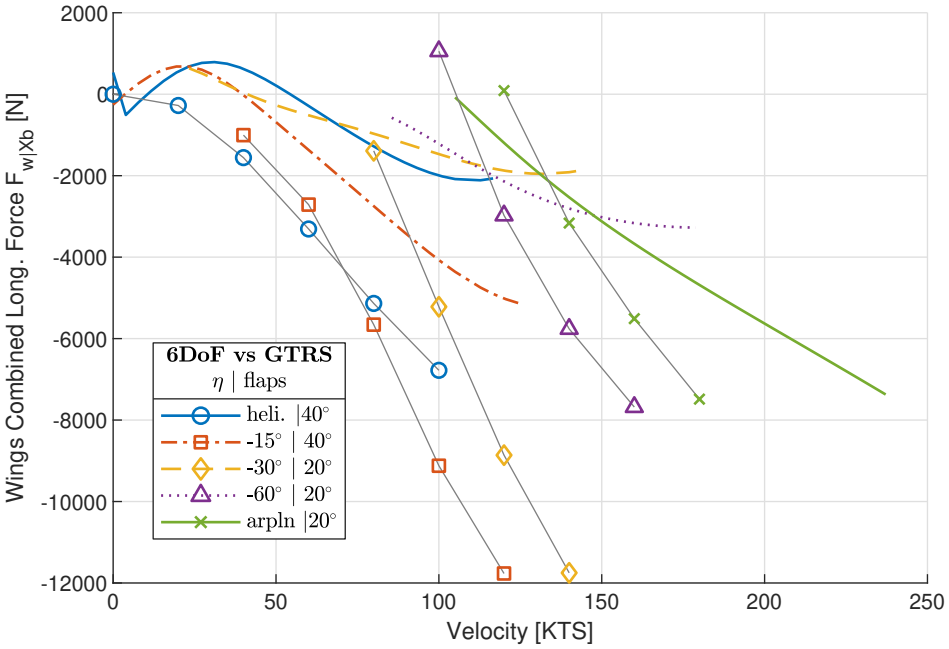

Figure G.11: Comparison between the combined wing longitudinal body force trim curves of the 6DoF tilt-rotor model and the GTRS. Color line patterns correspond to the 6DoF model while shapes connected with gray lines correspond to the GTRS data[5, app. A]. Nacelle tilt η and flap deflection angles indicated in legend.

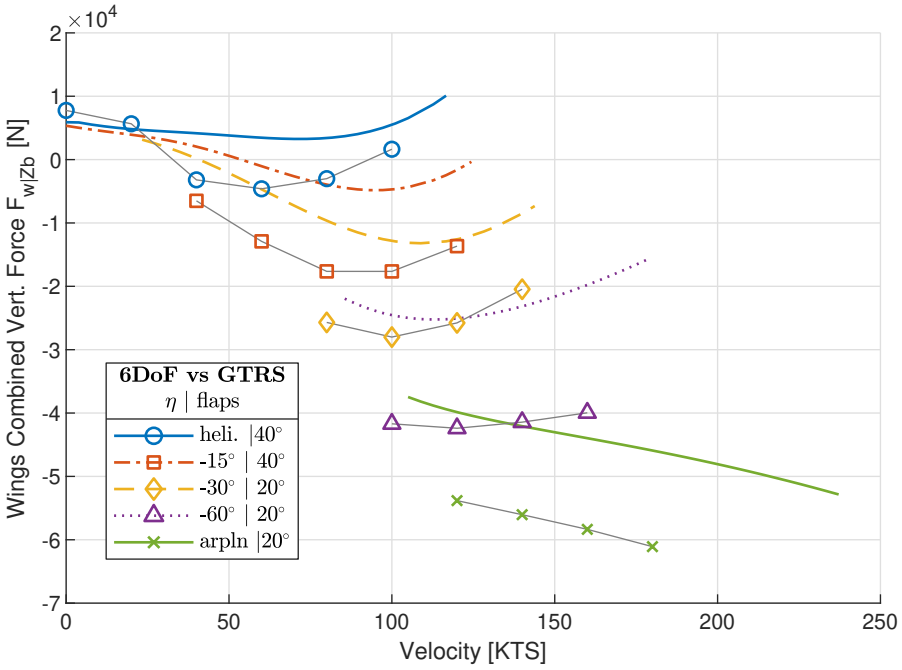

Figure G.12: Comparison between the combined wing vertical body force trim curves of the 6DoF tilt-rotor model and the GTRS. Color line patterns correspond to the 6DoF model while shapes connected with gray lines correspond to the GTRS data[5, app. A]. Nacelle tilt η and flap deflection angles indicated in legend.

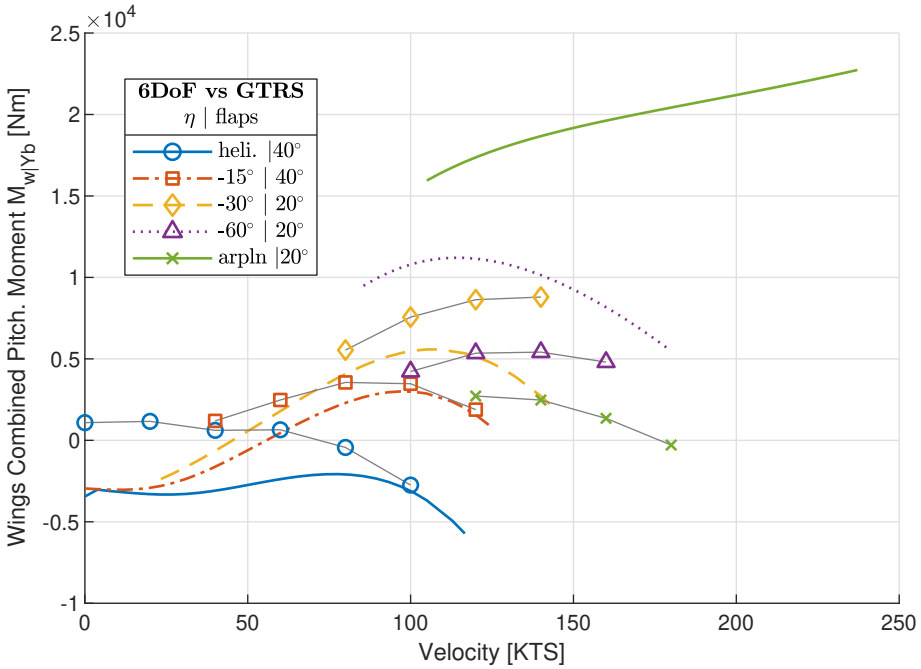

Figure G.13: Comparison between the combined wing body pitching moment trim curves of the 6DoF tilt-rotor model and the GTRS. Color line patterns correspond to the 6DoF model while shapes connected with gray lines correspond to the GTRS data[5, app. A]. Nacelle tilt η and flap deflection angles indicated in legend.

Horizontal Stabilizers

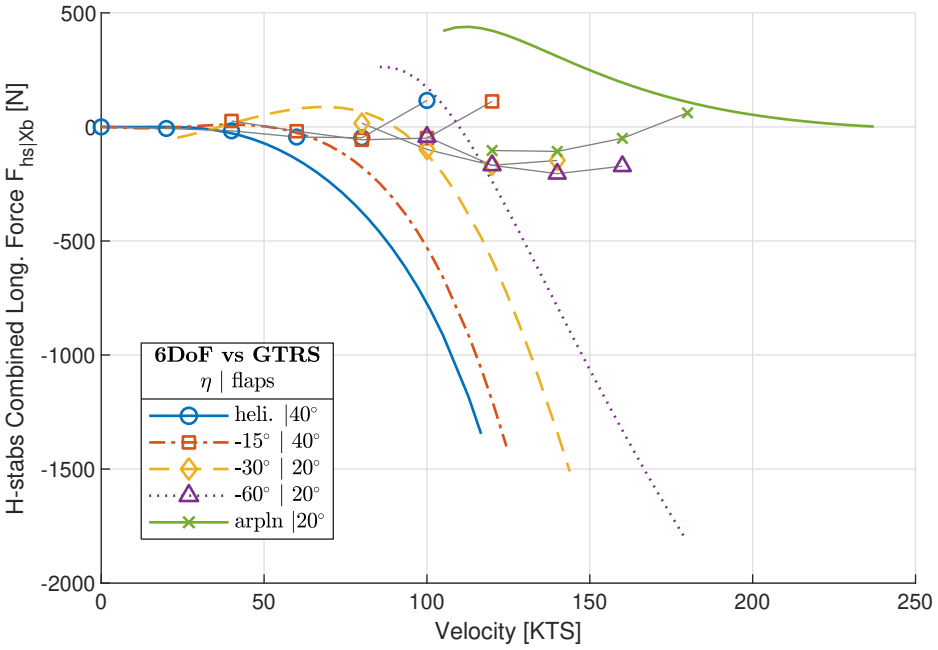

Figure G.14: Comparison between the combined horizontal stabilizer longitudinal body force trim curves of the 6DoF tilt-rotor model and the GTRS. Color line patterns correspond to the 6DoF model while shapes connected with gray lines correspond to the GTRS data[5, app. A]. Nacelle tilt η and flap deflection angles indicated in legend.

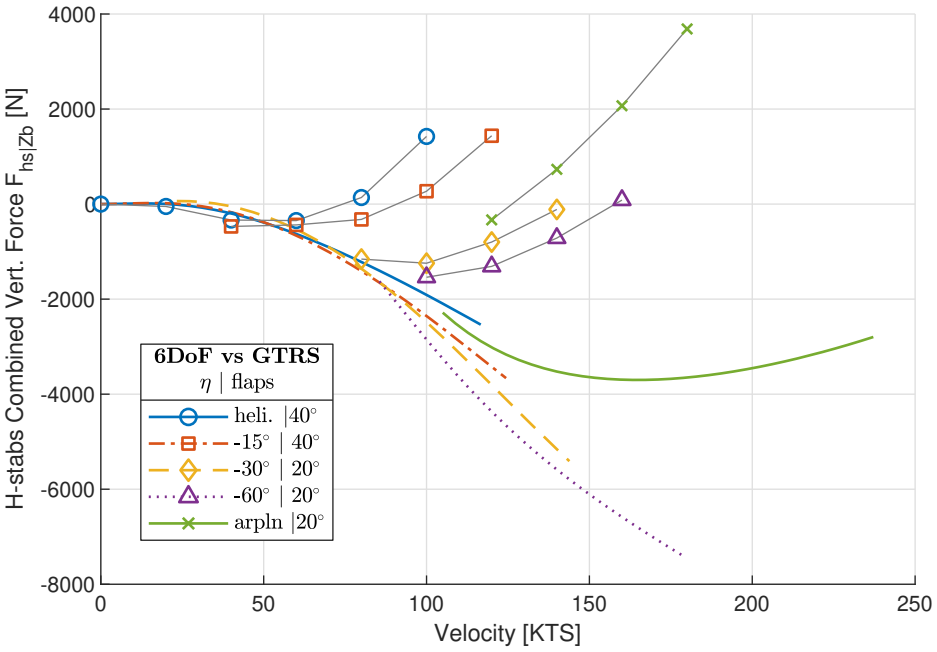

Figure G.15: Comparison between the combined horizontal stabilizer vertical body force trim curves of the 6DoF tilt-rotor model and the GTRS. Color line patterns correspond to the 6DoF model while shapes connected with gray lines correspond to the GTRS data[5, app. A]. Nacelle tilt η and flap deflection angles indicated in legend.

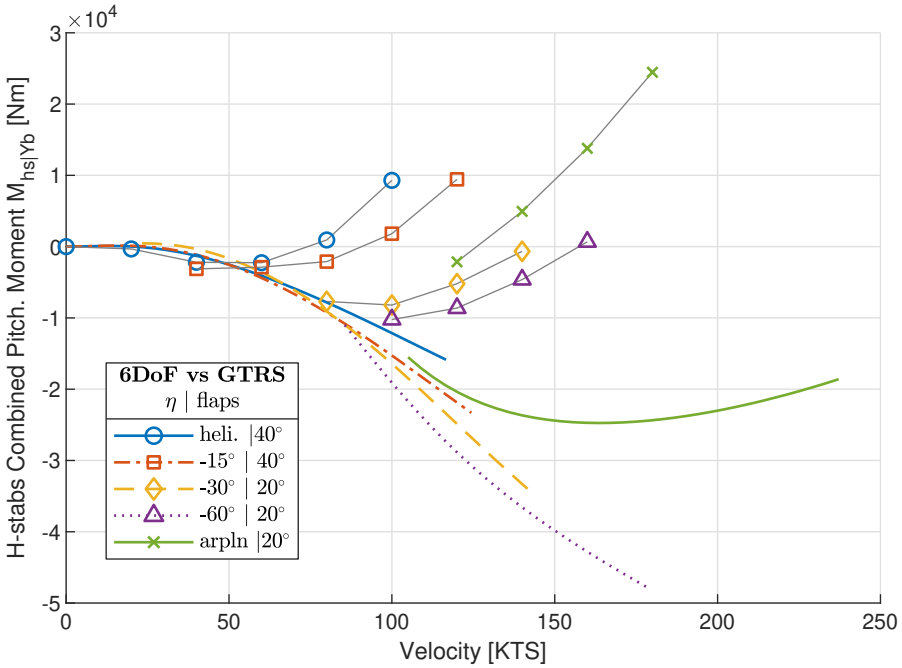

Figure G.16: Comparison between the combined horizontal stabilizer body pitching moment trim curves of the 6DoF tilt-rotor model and the GTRS. Color line patterns correspond to the 6DoF model while shapes connected with gray lines correspond to the GTRS data[5, app. A]. Nacelle tilt η and flap deflection angles indicated in legend.

Fuselage

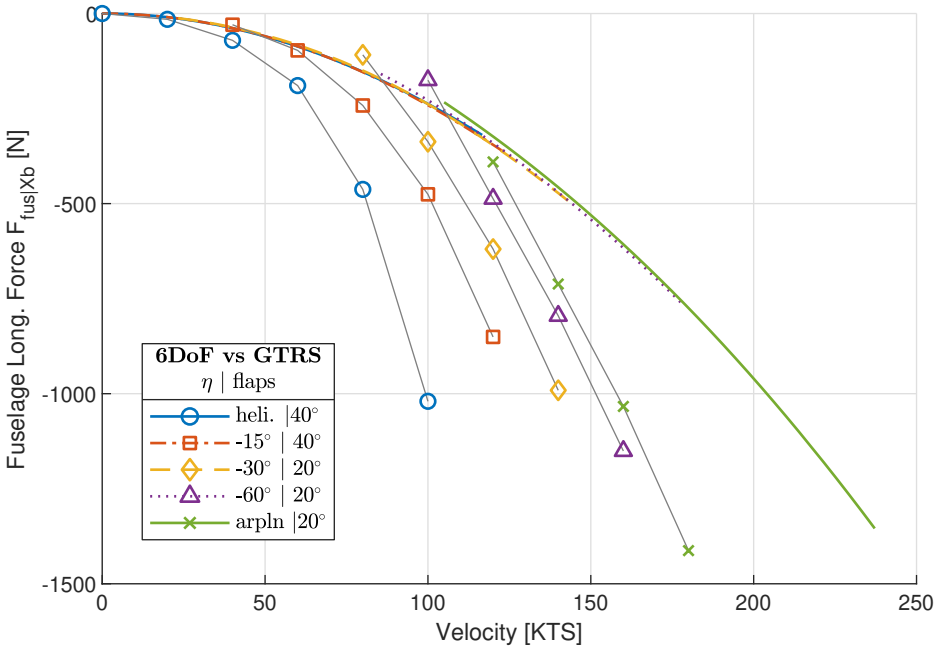

Figure G.17: Comparison between the fuselage longitudinal body force trim curves of the 6DoF tilt-rotor model and the GTRS. Color line patterns correspond to the 6DoF model while shapes connected with gray lines correspond to the GTRS data[5, app. A]. Nacelle tilt η and flap deflection angles indicated in legend.

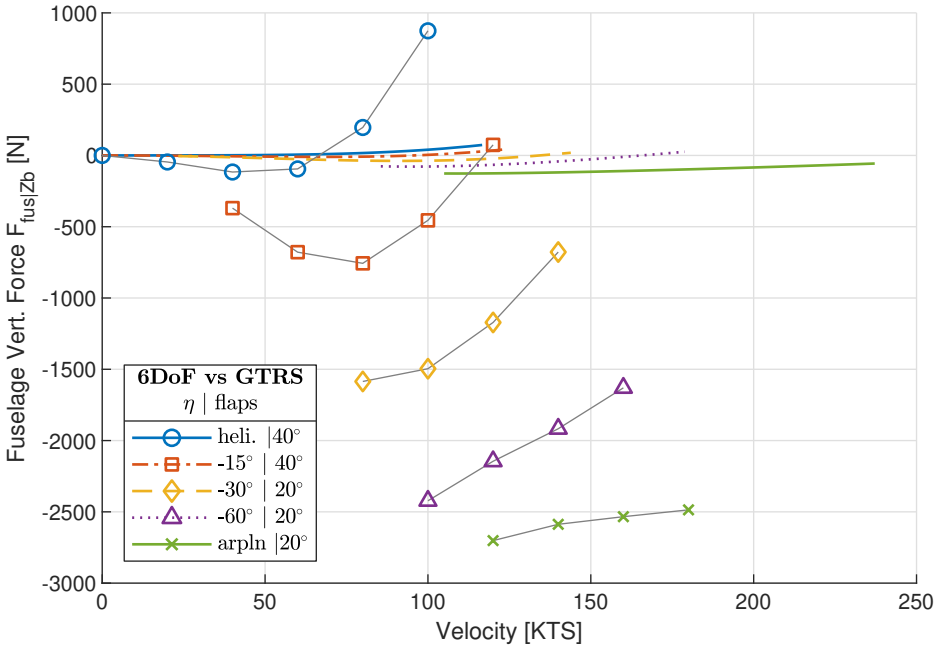

Figure G.18: Comparison between the fuselage vertical body force trim curves of the 6DoF tilt-rotor model and the GTRS. Color line patterns correspond to the 6DoF model while shapes connected with gray lines correspond to the GTRS data[5, app. A]. Nacelle tilt η and flap deflection angles indicated in legend.

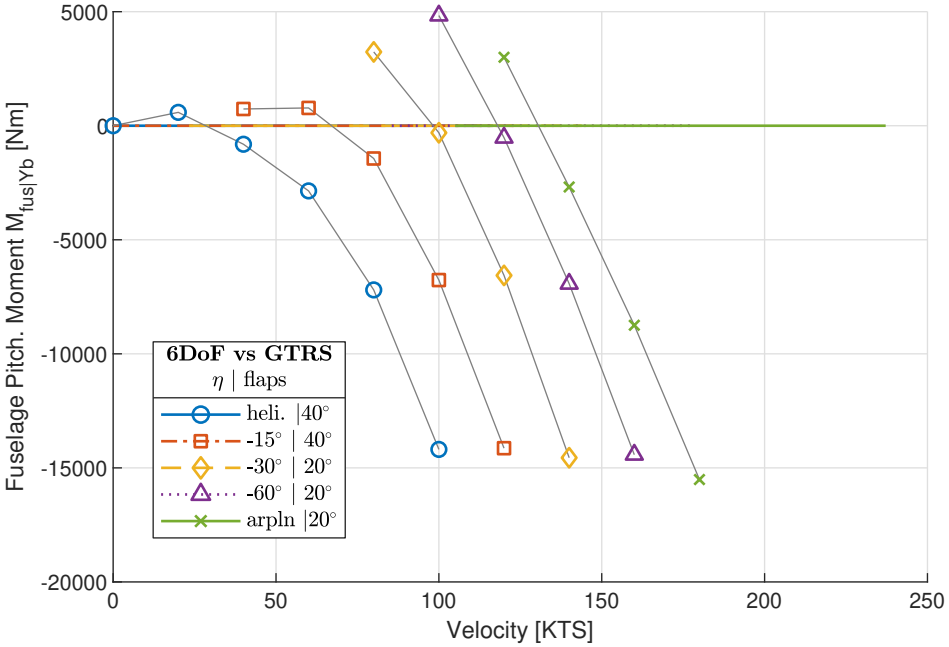

Figure G.19: Comparison between the fuselage body pitching moment trim curves of the 6DoF tilt-rotor model and the GTRS. Color line patterns correspond to the 6DoF model while shapes connected with gray lines correspond to the GTRS data[5, app. A]. Nacelle tilt η and flap deflection angles indicated in legend.

G.2.3. Effect of Nacelle Tilt Rate on Handling and Performance

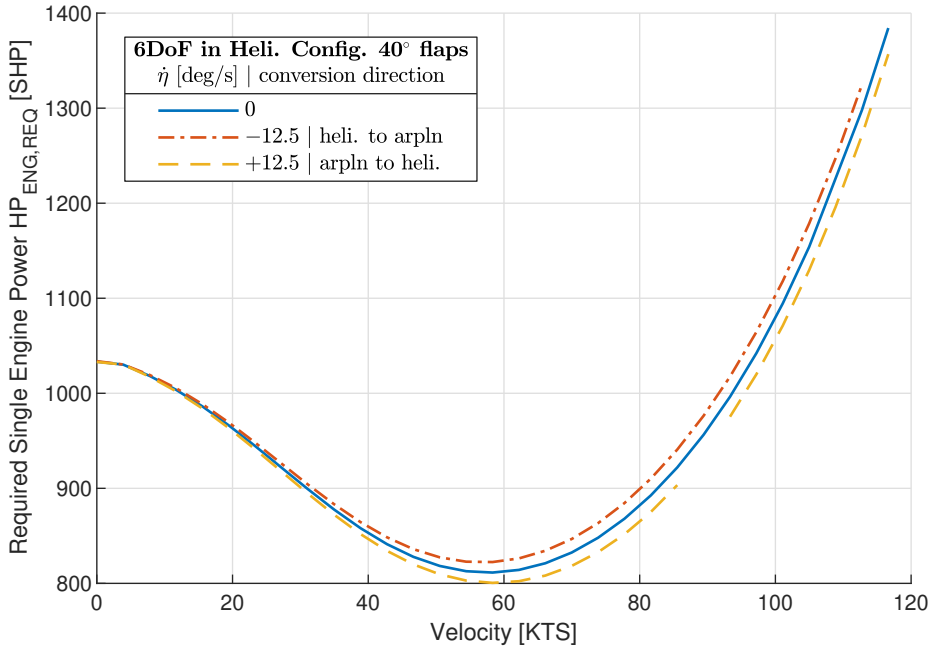

Figure G.20: Effect of nacelle tilt rate on the required single engine power $HP_{ENG,REQ}$ trim curves of the 6DoF tilt-rotor model in helicopter configuration. Nacelle tilt rate $\dot{\eta}$ indicated in legend.

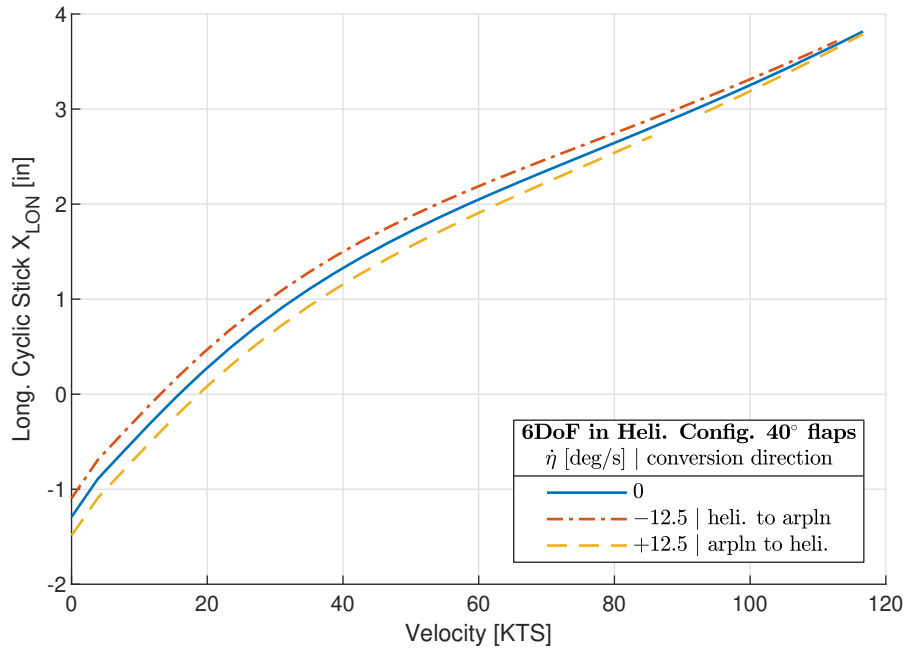

Figure G.21: Effect of nacelle tilt rate on the longitudinal stick deflection trim curves of the 6DoF tilt-rotor model in helicopter configuration. Nacelle tilt rate $\dot{\eta}$ indicated in legend.

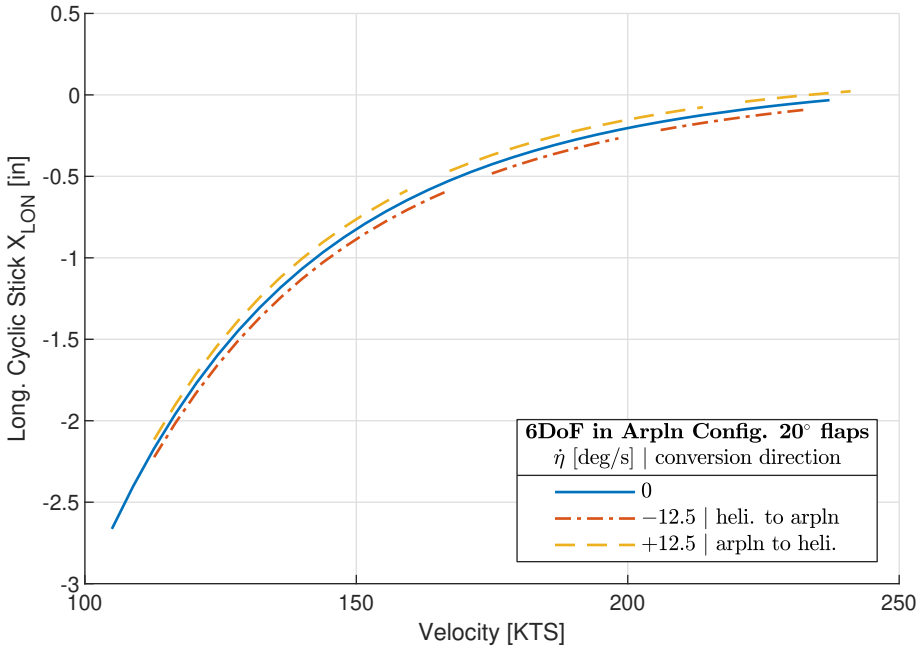

Figure G.22: Effect of nacelle tilt rate on the longitudinal stick deflection trim curves of the 6DoF tilt-rotor model in airplane configuration. Nacelle tilt rate $\dot{\eta}$ indicated in legend.

G.2.4. Subsystem Validation

Rotor

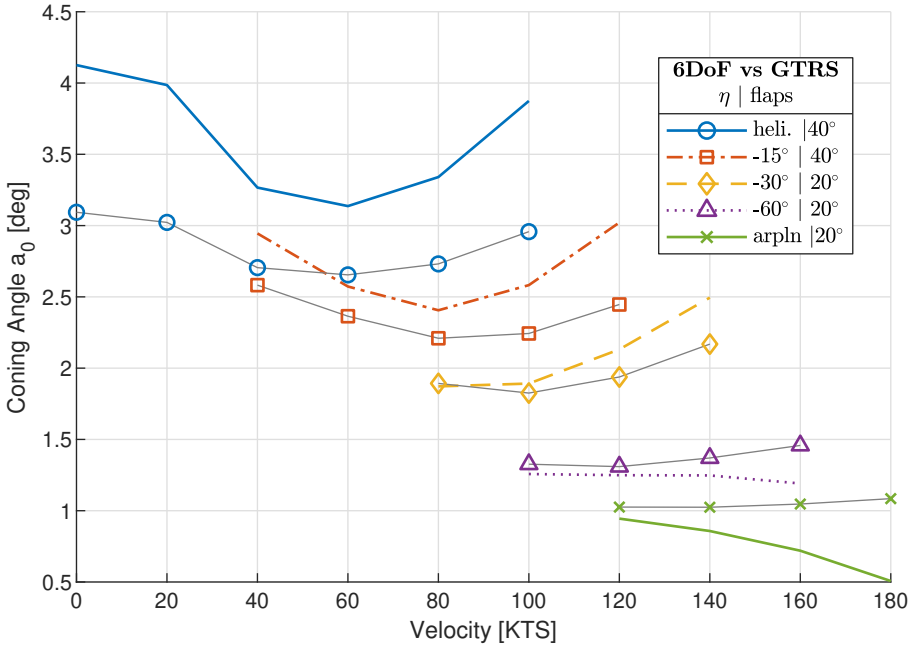

Figure G.23: Comparison between the coning angle pseudo trim curves of the 6DoF tilt-rotor model and the GTRS. Color line patterns correspond to the 6DoF model while shapes connected with gray lines correspond to the GTRS data[5, app. A]. Nacelle tilt η and flap deflection angles indicated in legend.

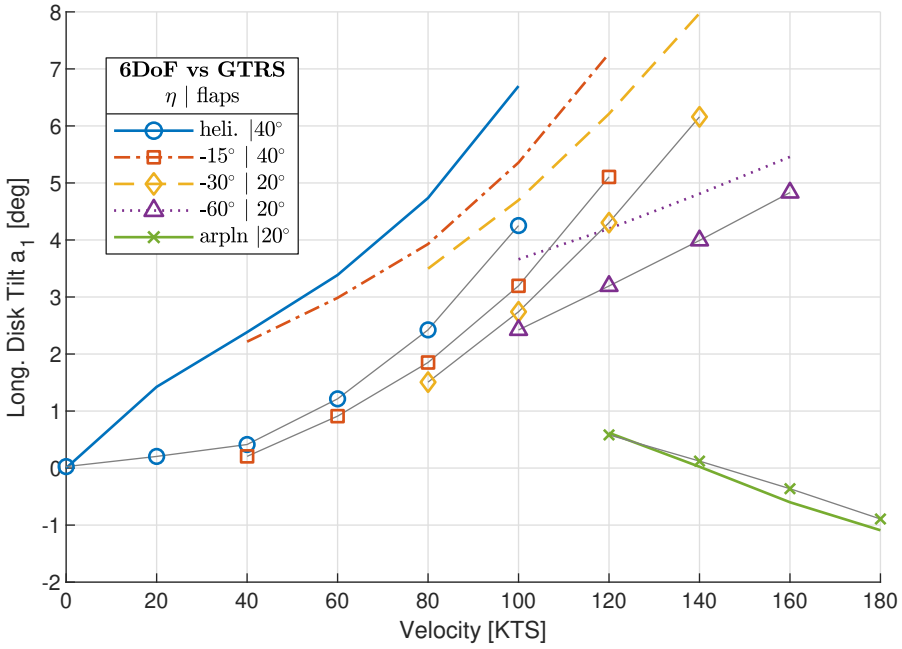

Figure G.24: Comparison between the longitudinal disk tilt angle pseudo trim curves of the 6DoF tilt-rotor model and the GTRS. Color line patterns correspond to the 6DoF model while shapes connected with gray lines correspond to the GTRS data[5, app. A]. Nacelle tilt η and flap deflection angles indicated in legend.

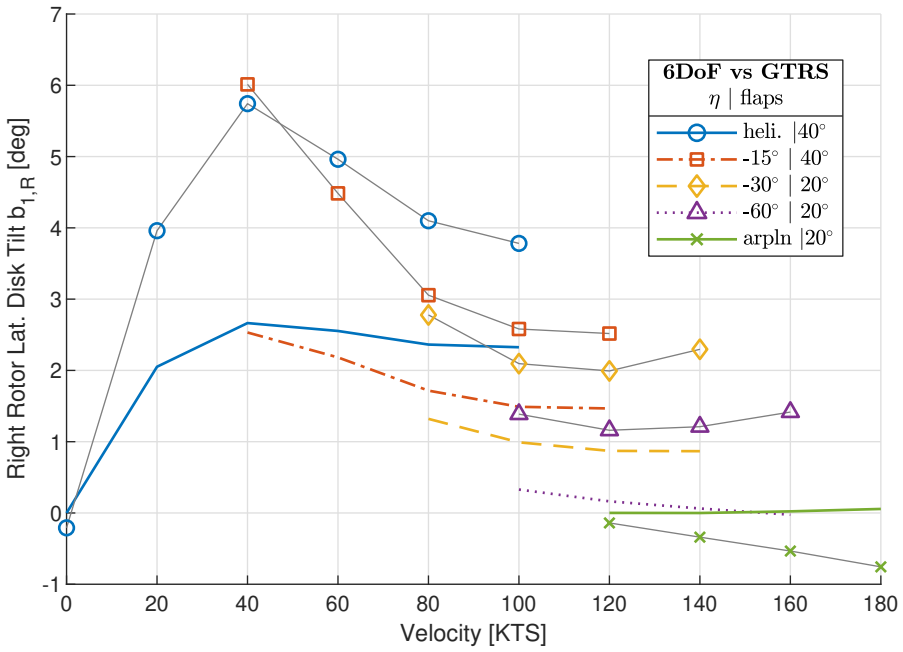

Figure G.25: Comparison between the lateral disk tilt angle pseudo trim curves of the 6DoF tilt-rotor model and the GTRS. Color line patterns correspond to the 6DoF model while shapes connected with gray lines correspond to the GTRS data[5, app. A]. Nacelle tilt η and flap deflection angles indicated in legend.

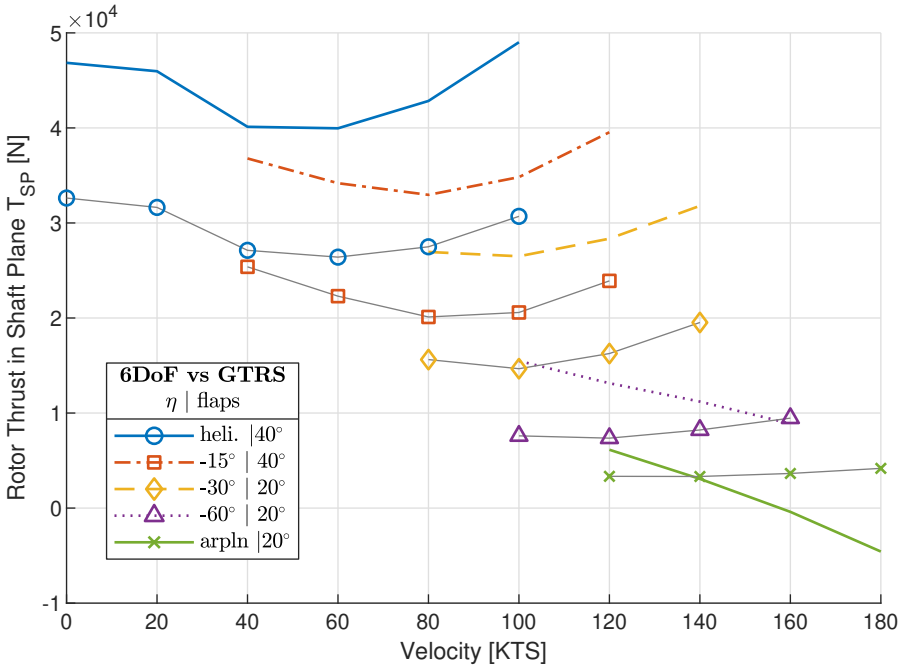

Figure G.26: Comparison between the shaft plane rotor thrust pseudo trim curves of the 6DoF tilt-rotor model and the GTRS. Color line patterns correspond to the 6DoF model while shapes connected with gray lines correspond to the GTRS data[5, app. A]. Nacelle tilt η and flap deflection angles indicated in legend.

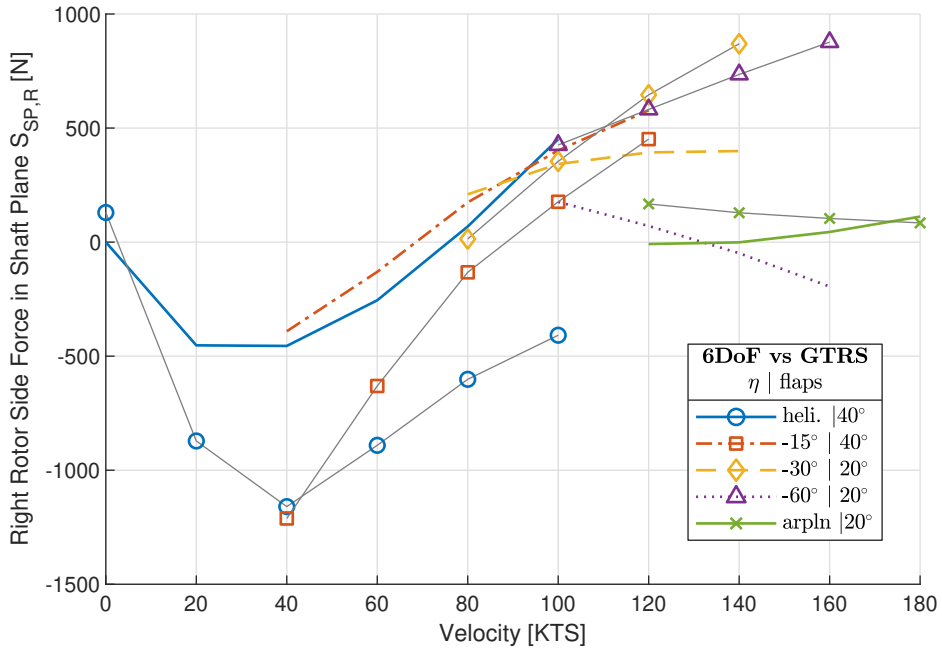

Figure G.27: Comparison between the right counter-clockwise rotating rotor shaft plane side force pseudo trim curves of the 6DoF tilt-rotor model and the GTRS. Color line patterns correspond to the 6DoF model while shapes connected with gray lines correspond to the GTRS data[5, app. A]. Nacelle tilt η and flap deflection angles indicated in legend.

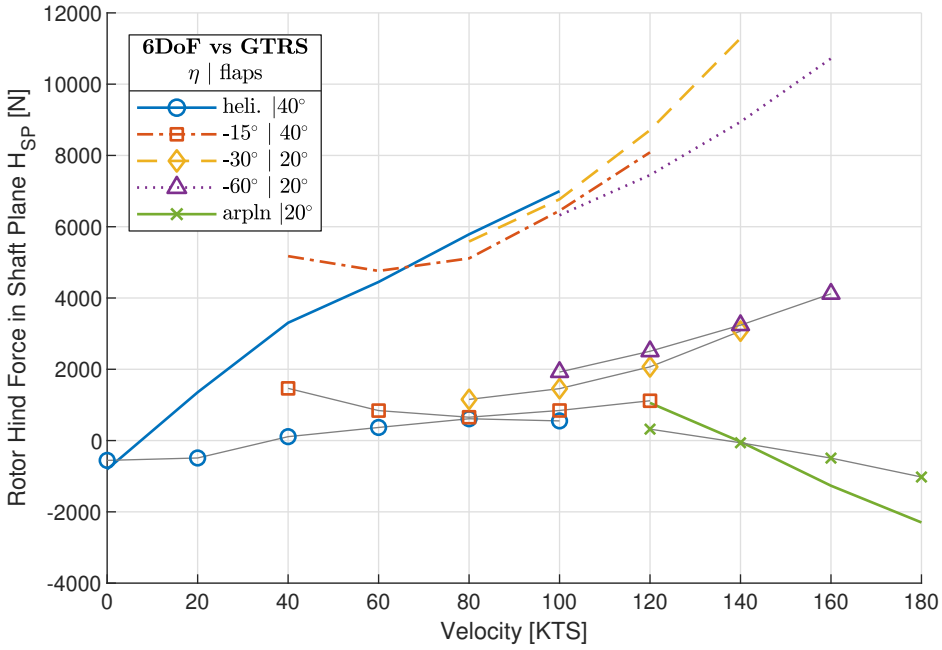

Figure G.28: Comparison between the shaft plane rotor hind force pseudo trim curves of the 6DoF tilt-rotor model and the GTRS. Color line patterns correspond to the 6DoF model while shapes connected with gray lines correspond to the GTRS data[5, app. A]. Nacelle tilt η and flap deflection angles indicated in legend.

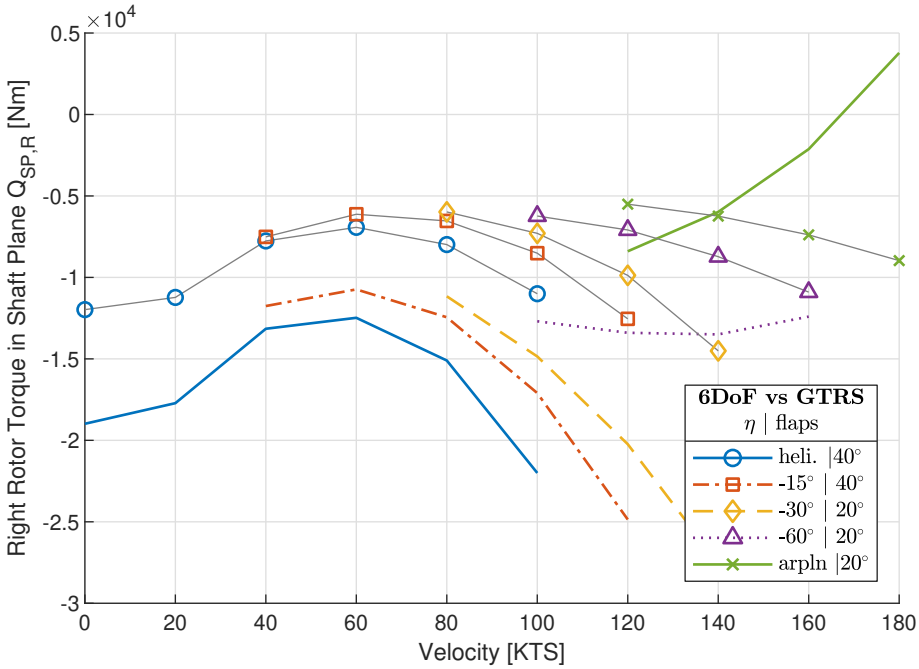

Figure G.29: Comparison between the right counter-clockwise rotating rotor shaft plane torque pseudo trim curves of the 6DoF tilt-rotor model and the GTRS. Color line patterns correspond to the 6DoF model while shapes connected with gray lines correspond to the GTRS data[5, app. A]. Nacelle tilt η and flap deflection angles indicated in legend.

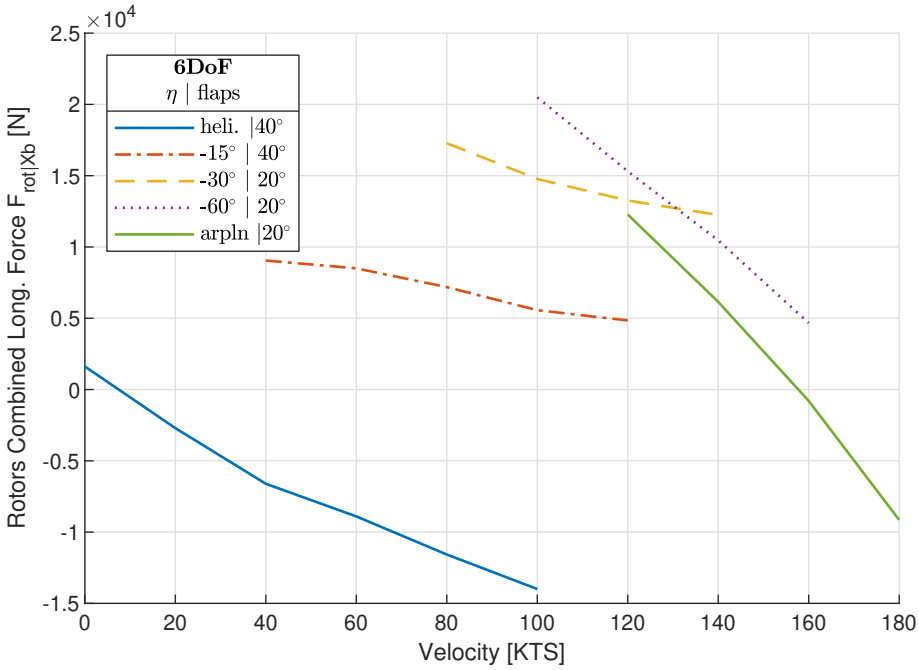

Figure G.30: Combined left and right rotor longitudinal body force pseudo trim curves of the 6DoF tilt-rotor model. Nacelle tilt η and flap deflection angles indicated in legend.

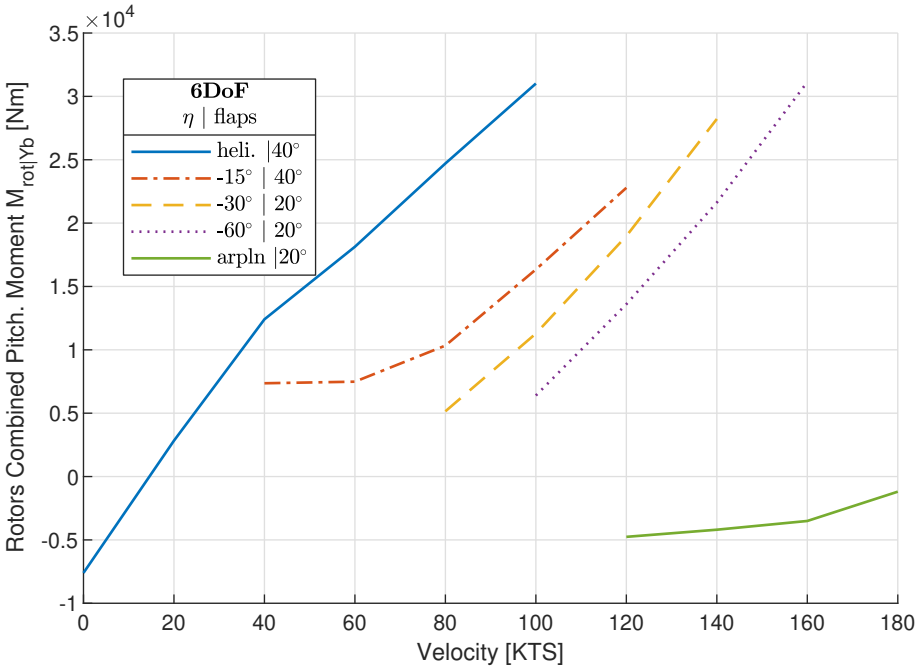

Figure G.31: Combined left and right rotor body pitching moment pseudo trim curves of the 6DoF tilt-rotor model. Nacelle tilt η and flap deflection angles indicated in legend.

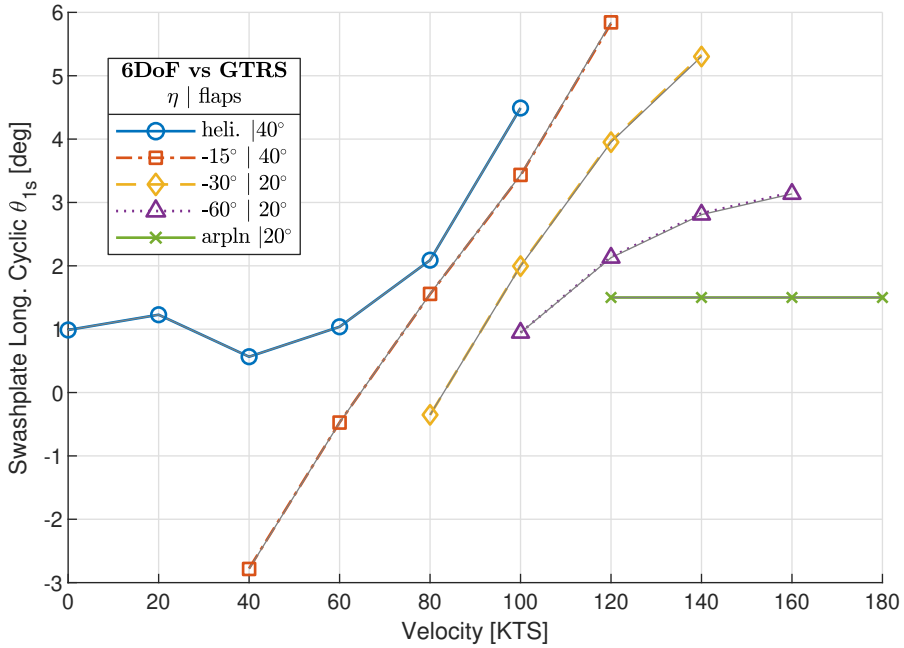

Figure G.32: Comparison between the swashplate longitudinal cyclic pseudo trim curves of the 6DoF tilt-rotor model and the GTRS. Color line patterns correspond to the 6DoF model while shapes connected with gray lines correspond to the GTRS data[5, app. A]. Nacelle tilt η and flap deflection angles indicated in legend.

Main Wing

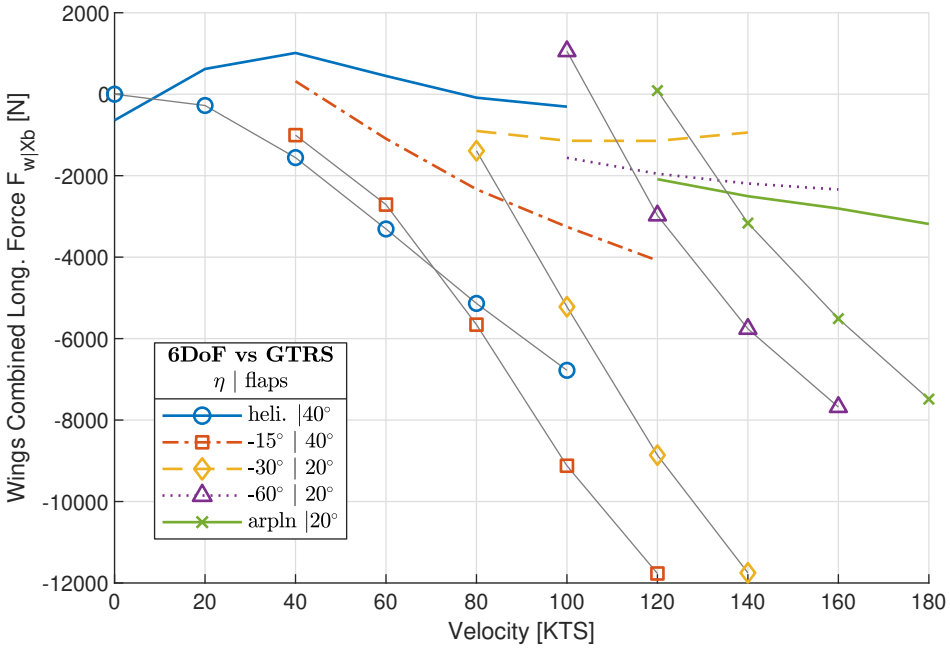

Figure G.33: Comparison between the combined wing longitudinal body force pseudo trim curves of the 6DoF tilt-rotor model and the GTRS. Color line patterns correspond to the 6DoF model while shapes connected with gray lines correspond to the GTRS data[5, app. A]. Nacelle tilt η and flap deflection angles indicated in legend.

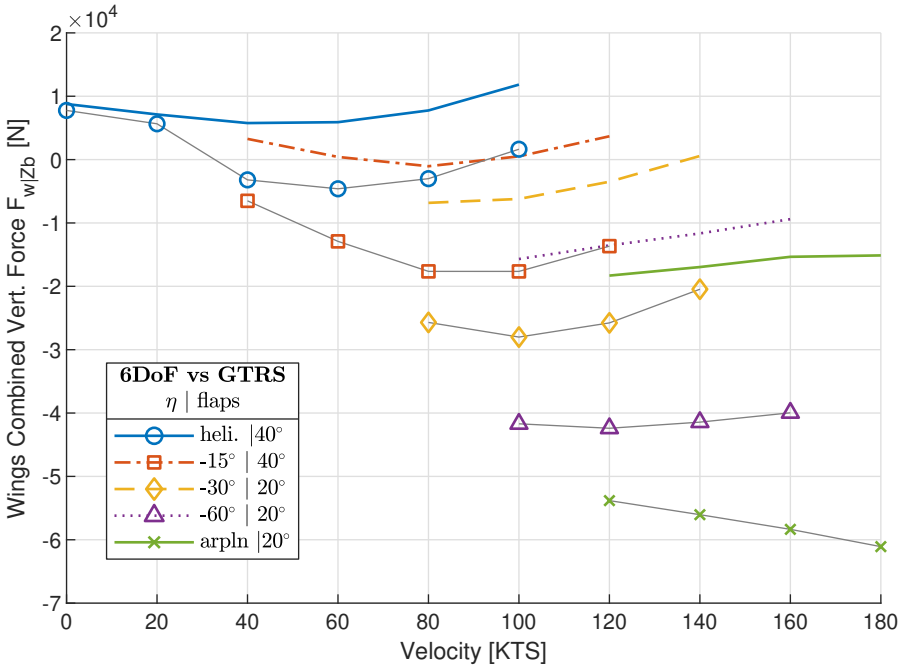

Figure G.34: Comparison between the combined wing vertical body force pseudo trim curves of the 6DoF tilt-rotor model and the GTRS. Color line patterns correspond to the 6DoF model while shapes connected with gray lines correspond to the GTRS data[5, app. A]. Nacelle tilt η and flap deflection angles indicated in legend.

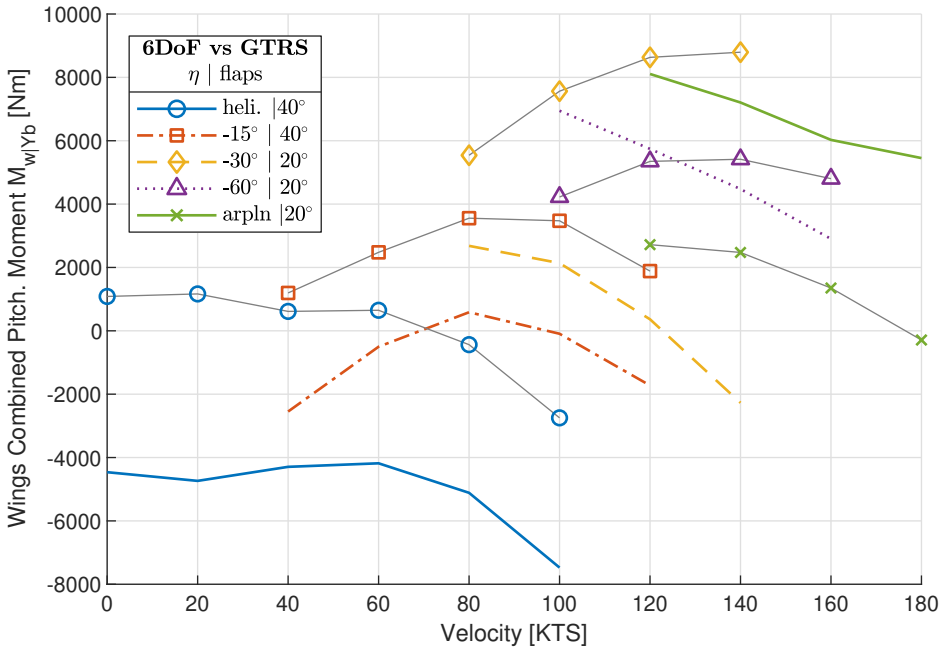

Figure G.35: Comparison between the combined wing body pitching moment pseudo trim curves of the 6DoF tilt-rotor model and the GTRS. Color line patterns correspond to the 6DoF model while shapes connected with gray lines correspond to the GTRS data[5, app. A]. Nacelle tilt η and flap deflection angles indicated in legend.

Horizontal Stabilizers

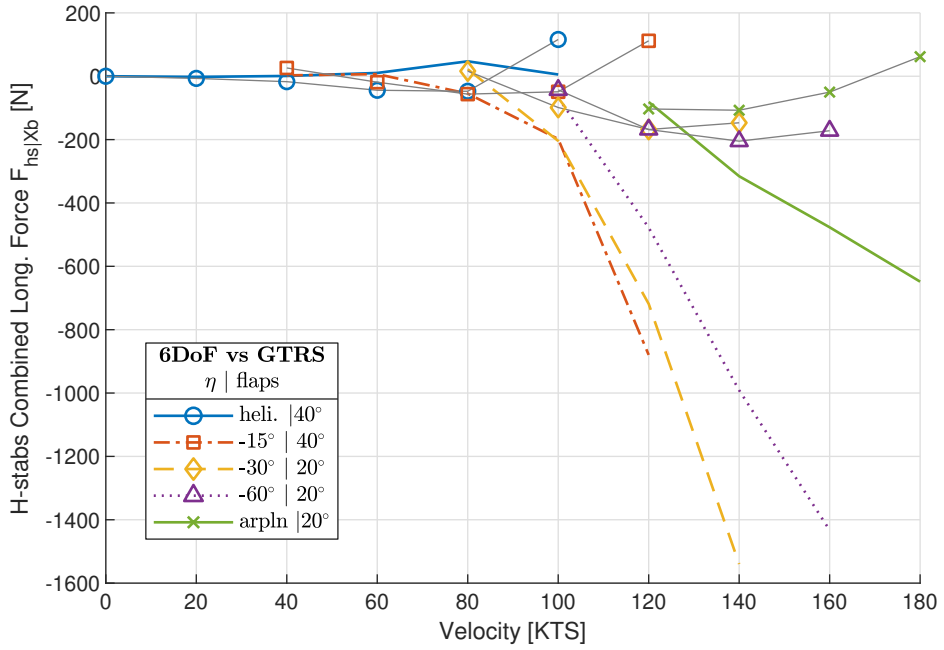

Figure G.36: Comparison between the combined horizontal stabilizer longitudinal body force pseudo trim curves of the 6DoF tilt-rotor model and the GTRS. Color line patterns correspond to the 6DoF model while shapes connected with gray lines correspond to the GTRS data[5, app. A]. Nacelle tilt η and flap deflection angles indicated in legend.

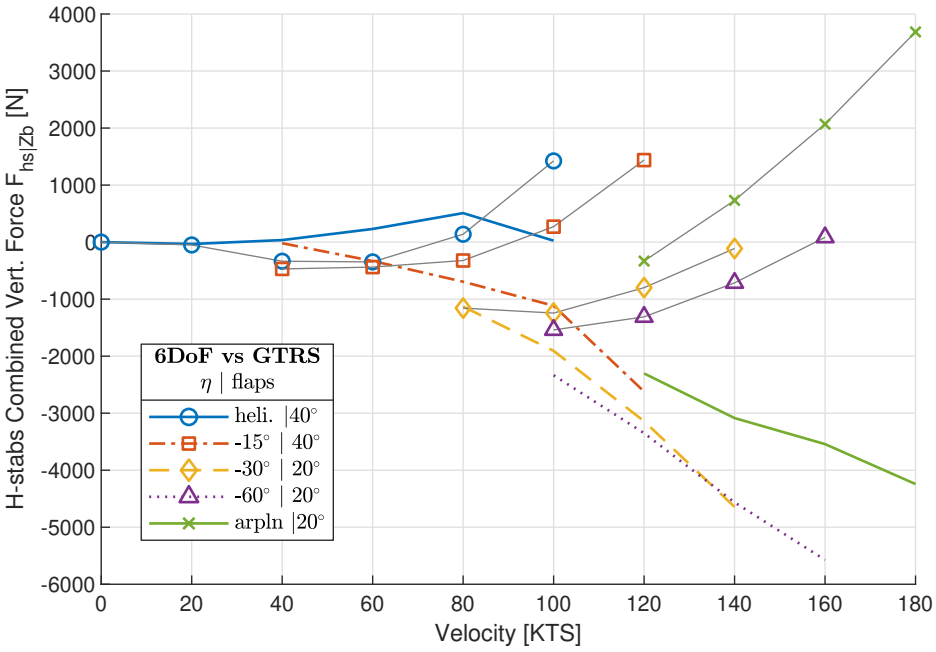

Figure G.37: Comparison between the combined horizontal stabilizer vertical body force pseudo trim curves of the 6DoF tilt-rotor model and the GTRS. Color line patterns correspond to the 6DoF model while shapes connected with gray lines correspond to the GTRS data[5, app. A]. Nacelle tilt η and flap deflection angles indicated in legend.

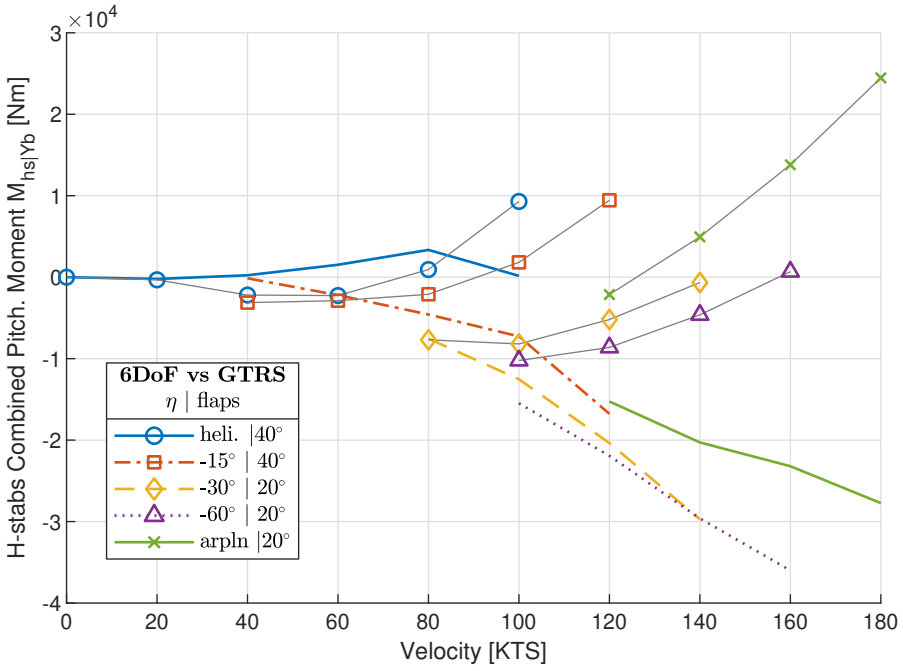

Figure G.38: Comparison between the combined horizontal stabilizer body pitching moment pseudo trim curves of the 6DoF tilt-rotor model and the GTRS. Color line patterns correspond to the 6DoF model while shapes connected with gray lines correspond to the GTRS data[5, app. A]. Nacelle tilt η and flap deflection angles indicated in legend.

Vertical Stabilizers

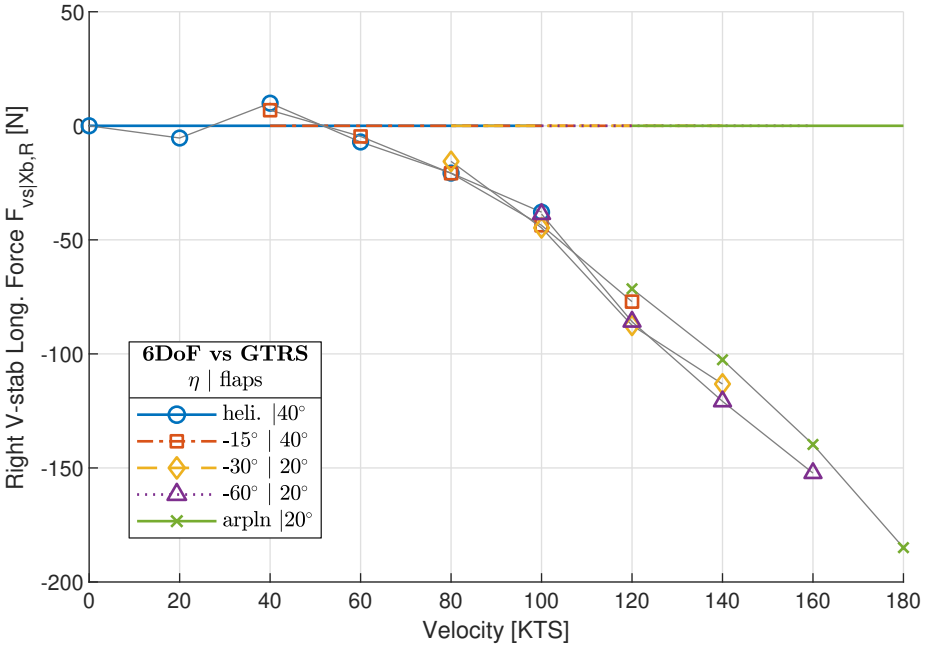

Figure G.39: Comparison between the right vertical stabilizer longitudinal body force pseudo trim curves of the 6DoF tilt-rotor model and the GTRS. Color line patterns correspond to the 6DoF model while shapes connected with gray lines correspond to the GTRS data[5, app. A]. Nacelle tilt η and flap deflection angles indicated in legend.

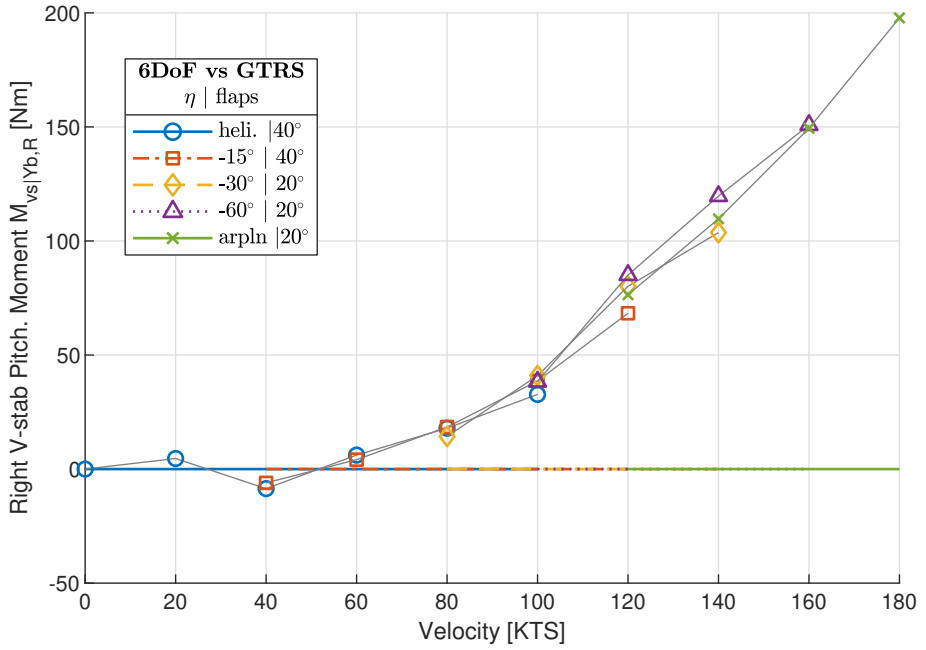

Figure G.40: Comparison between the right vertical stabilizer body pitching moment pseudo trim curves of the 6DoF tilt-rotor model and the GTRS. Color line patterns correspond to the 6DoF model while shapes connected with gray lines correspond to the GTRS data[5, app. A]. Nacelle tilt η and flap deflection angles indicated in legend.

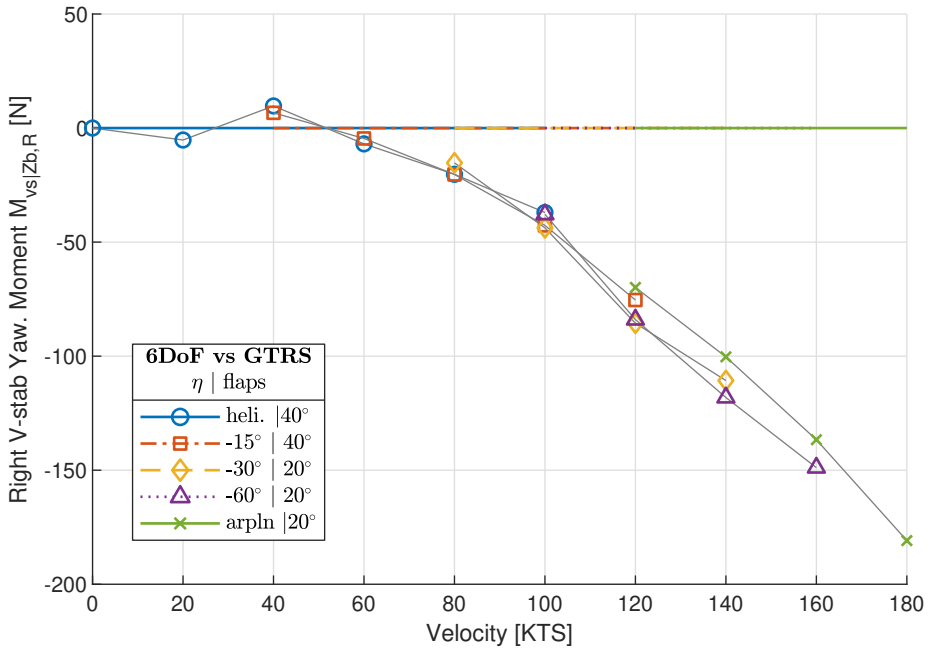

Figure G.41: Comparison between the right vertical stabilizer body yawing moment pseudo trim curves of the 6DoF tilt-rotor model and the GTRS. Color line patterns correspond to the 6DoF model while shapes connected with gray lines correspond to the GTRS data[5, app. A]. Nacelle tilt η and flap deflection angles indicated in legend.

Fuselage

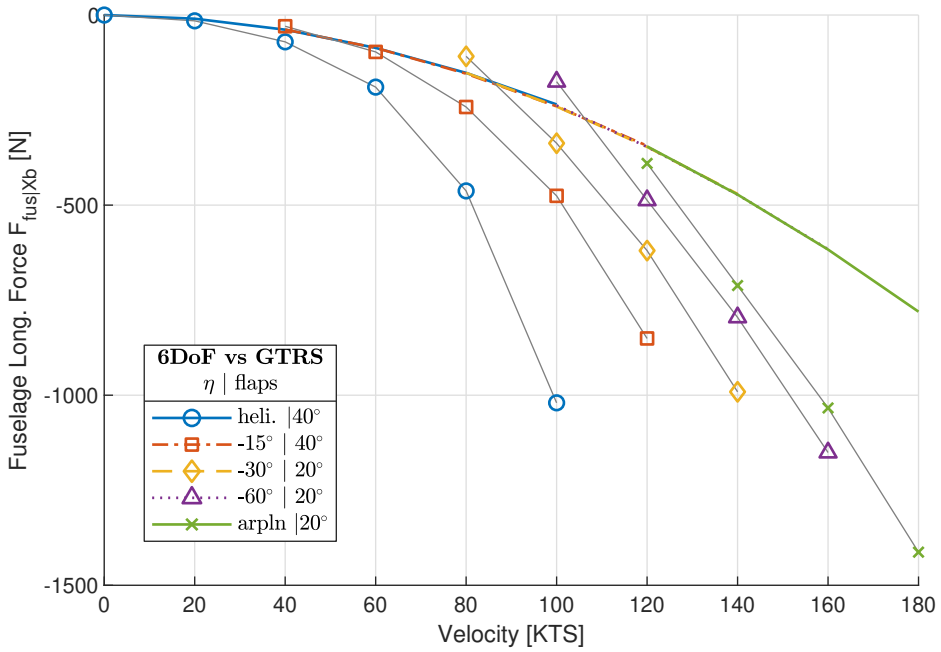

Figure G.42: Comparison between the fuselage longitudinal body force pseudo trim curves of the 6DoF tilt-rotor model and the GTRS. Color line patterns correspond to the 6DoF model while shapes connected with gray lines correspond to the GTRS data[5, app. A]. Nacelle tilt η and flap deflection angles indicated in legend.

Verification of Rotor Torque Dependent Subsystems

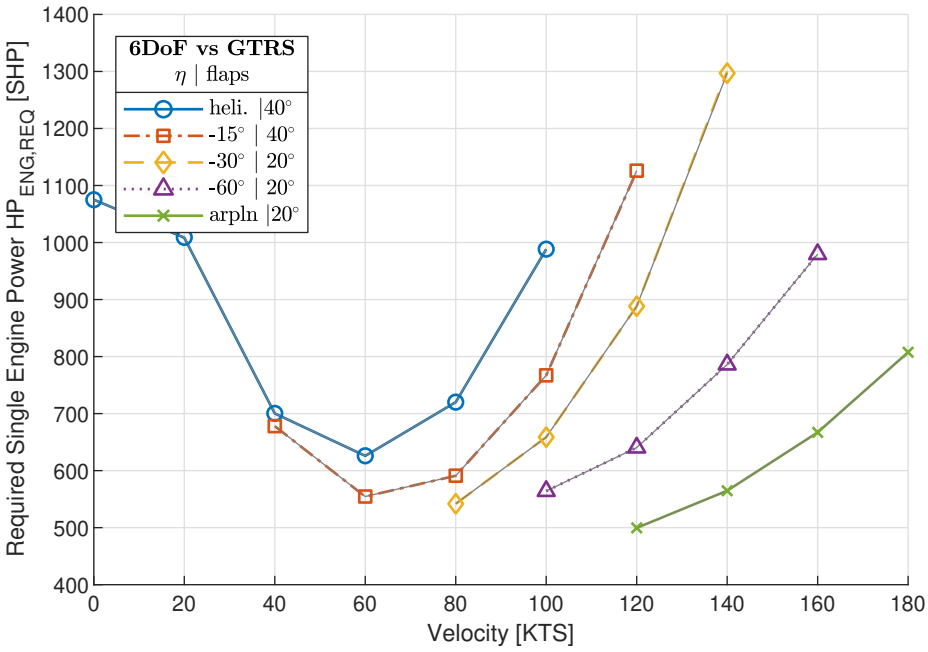

Figure G.43: Comparison between the required single engine power pseudo trim curves of the 6DoF tilt-rotor model and the GTRS. Color line patterns correspond to the 6DoF model while shapes connected with gray lines correspond to the GTRS data[5, app. A]. Nacelle tilt η and flap deflection angles indicated in legend.

G.3. Haffner Diagrams

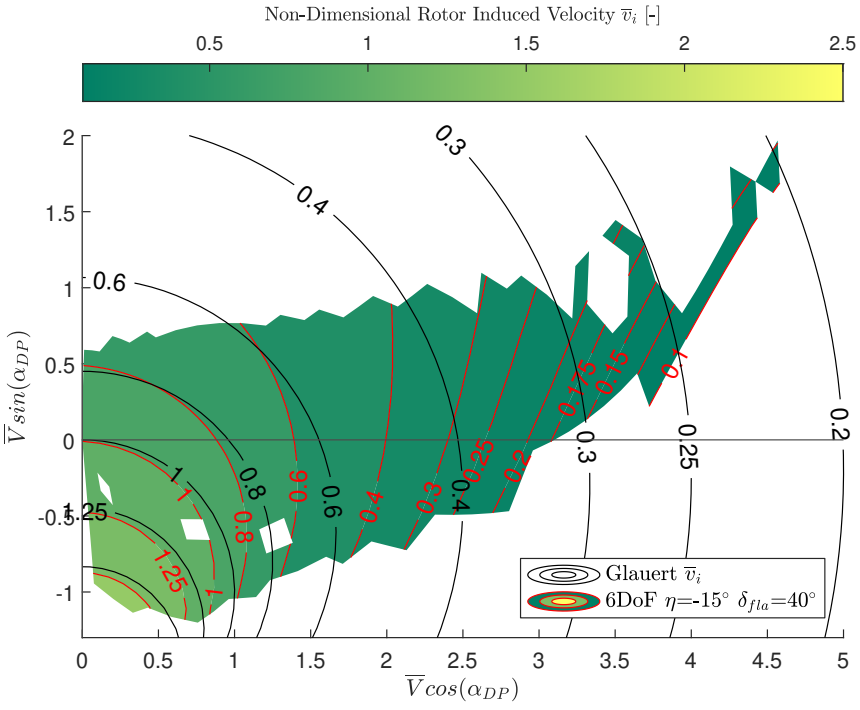

Figure G.44: Haffner diagram corresponding to the 6DoF tilt-rotor in $\eta = -15°$ conversion flight plotted against the Glauert Haffner contours. Flap deflection angle indicated in legend.

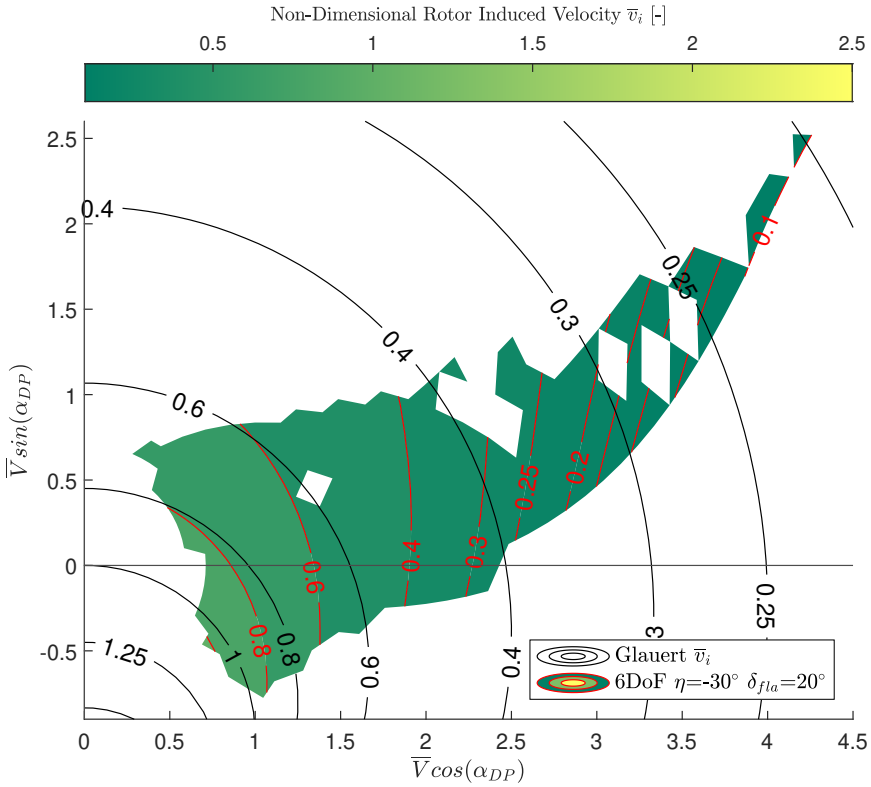

Figure G.45: Haffner diagram corresponding to the 6DoF tilt-rotor in $\eta = -30°$ conversion flight plotted against the Glauert Haffner contours. Flap deflection angle indicated in legend.

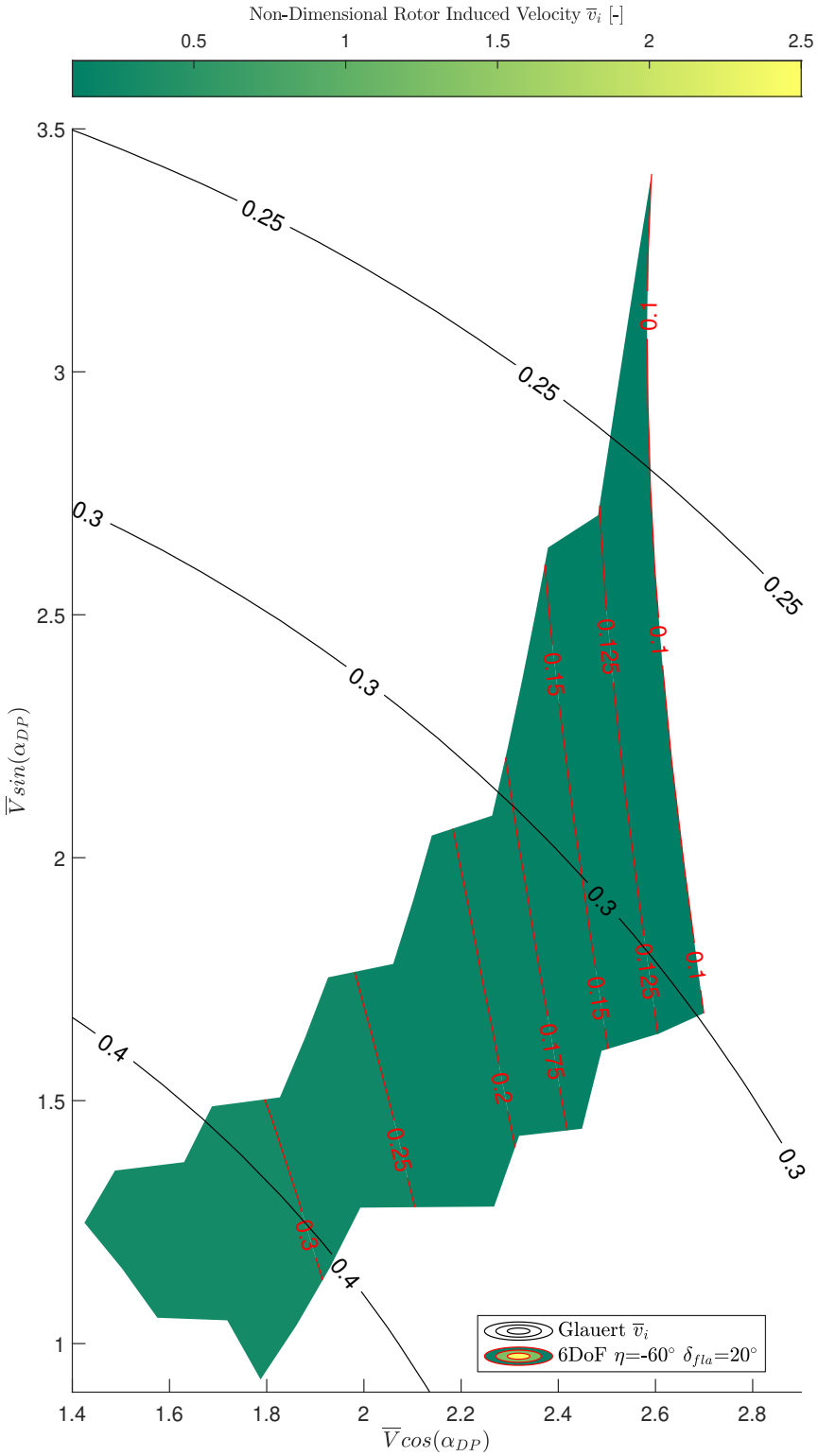

Figure G.46: Haffner diagram corresponding to the 6DoF tilt-rotor in $\eta = -60°$ conversion flight plotted against the Glauert Haffner contours. Flap deflection angle indicated in legend.